The University of Adelaide

Department of Mechanical Engineering

Control and Optimisation of Mixing and Combustion from a Precessing Jet Nozzle

Ph.D. Thesis

Jordan James Parham

December 2000

Abstract

The present study seeks to examine the effects of co-flow, confinement and a shaping jet on the mixing and combustion characteristics of a precessing jet flow. In particular, scientific analysis is used to investigate the physical mechanisms by which the control and optimisation of heat transfer and pollutant emissions from natural gas burners for rotary kilns can be achieved. To achieve these aims, a range of experimental techniques in reacting, non-reacting, confined and unconfined conditions have been employed. The precessing jet, in conjunction with a shaping jet, is shown to provide continuous control of mixing characteristics and corresponding combustion characteristics. Hence the optimum mixing characteristics for the maximum heat transfer and minimum emissions and the conditions under which the precessing jet nozzle produces such mixing characteristics are determined. A scaling procedure is also proposed for the precessing jet nozzle that, for the first time, provides a method to relate the results of small-scale isothermal mixing experiments to operating rotary kilns.

Flow visualisation using a two colour planar laser-induced fluorescence technique in an unconfined, isothermal environment is used to demonstrate that a central axial jet is the most effective form of shaping jet for controlling the mixing from a precessing jet nozzle. The characteristics of the combined jet flow are shown, by a semi-quantitative image processing technique, to be controlled by the ratio of the central axial jet momentum to the combined jet momentum, denoted by $\Gamma_{CAJ}=G_{CAJ}/(G_{PJ}+G_{CAJ})$. The flow visualisation results also demonstrate that, when the momentum ratio is in the range $0\leq \Gamma_{CAJ} \leq 0.2$, corresponding to low proportions of flow through the central axial jet, the combined flow field visually appears to be "precessing jet dominated". For momentum ratios in the range $0.23\leq \Gamma_{CAJ} \leq 1$, the flow appears visually to be dominated by the features of the central axial jet.

The effect of a central axial jet on the characteristics of a precessing jet flame is assessed in an unconfined environment by recording the visible flame luminescence photographically. The results demonstrate that a significant change in the flame volume, length and width is achieved by varying the proportion of central axial jet to total flow rate and hence the momentum ratio, Γ_{CAJ}. These parameters were correlated with changes in the global residence time, radiant fraction and NO_x emissions based on scaling criteria from the literature. These correlations suggest that, consistent with the flow visualisation results, the momentum ratio, Γ_{CAJ}, controls the combustion characteristics, which in turn change significantly in the precessing jet and central axial jet dominated flow regimes.

Confined combustion experiments are undertaken in a pilot-scale cement kiln simulator to quantify the heat flux and NO_x emission characteristics as a function of the combined precessing jet and central axial jet flows and to compare them with that of a conventional burner in a well controlled, confined facility. These experiments demonstrate that the central axial jet provides good control over the heat flux profile, consistent with the experience in industrial installations. Furthermore, the heat transfer from a precessing jet burner is shown to be enhanced relative to a conventional burner and the NO_x emissions reduced if the relationship between heat transfer, emissions and process interaction is taken into account.

To quantify the mixing characteristics of each of the above flows and so to provide insight into the characteristics of relatively "good" and "bad" mixing for the optimisation of combustion in rotary kilns, concentration measurements are performed in a confined, isothermal environment. The effect of co-flow, confinement and the central axial jet on the mixing from a precessing jet nozzle are also assessed. The experiments are performed in a water-tunnel using a quantitative planar laser-induced fluorescence technique to provide measurement of a conserved scalar. The effect of the central axial jet is quantified with respect to its influence upon concentration decay, concentration fluctuations, jet width and probability distribution functions. The effect of co-flow and confinement are also quantified by measurement of the concentration decay, concentration fluctuations, jet width and probability distribution functions. The data is used to develop equations relating the flow conditions and geometry to the mean concentration on the jet axis and jet spread. These equations can be used to describe the entire mean concentration distribution in the far field of the precessing jet flow. Based on the modelling equations, a scaling procedure is proposed that provides a method to scale the precessing jet flow, i.e. to relate isothermal laboratory scale investigations to full scale plant. The scaling procedure is based on a first order assessment of the separate effects of confinement, velocity ratio and mass flow ratio on the scalar mixing. The final scaling parameter represents an additional correction to a modified form of the well known Thring-Newby scaling criterion which distorts the mixture fraction ratio, i.e. the air-fuel ratio, in the model from that in the industrial scale. This correction enables similarity of the jet mixing characteristics to be preserved while correcting for the geometric distortion of the confinement ratio. The new scaling procedure is used to show that the isothermal concentration measurements are representative of the mixing conditions within the pilot-scale combustion facility and hence that the scaling procedure is appropriate for the precessing jet nozzle.

The optimum combustion characteristics of the precessing jet nozzle, defined as the maximum heat transfer and minimum NO_x emissions, are shown to occur at the maximum momentum ratio that still generates a flow characterised as precessing jet dominated. The mixing characteristics associated with high radiation and low NO_x emissions are shown, by the quantitative mixing experiments, to be associated with the maximum mean concentration and the widest range of instantanteous concentrations measured on the jet axis of any flows produced by the combined precessing jet and central axial jet flows. This suggest that such mixing characteristics are desired from any natural gas burner for the maximum heat transfer and minimum emissions in a rotary kiln. The optimal mixing characteristics for the maximum efficieny and lowest emissions from a gas-fired rotary kiln are hence shown to be generated by the precessing jet-central axial jet nozzle at a momentum ratio of $0.17 \leq \Gamma_{CAJ} \leq 0.23$.

Table of Contents

List of Tables

Figure **Page number**

Chapter 2

Chapter 3

Chapter 4

Chapter 5

Chapter 6

Appendix B

List of Figures

Figure **Page number**

Chapter 1

Chapter 2

Chapter 3

Chapter 4

Chapter 5

Chapter 6

Appendix A

Appendix C

Notation

Abbreviations and Constants

AAJ	Adjacent Annular Jet
ASJ	Annular Shaping Jet
CAJ	Central Axial Jet
CCD	Charge-Coupled Device
$EINO_x$	Emission Index of Nitrogen Oxides
FPJ/PJ	Fluidic Precessing Jet
MCB	Multi-Channel Burner
MPJ	Mechanical Precessing Jet
Nd:YAG	Neodium Yttrium Aluminium Garnet laser
PDF/pdf	Probability Distribution Function
PLIF	Planar Laser-Induced Fluorescence
RMS	Root Mean Square
SNR	Signal to Noise Ratio
σ	Stefan-Boltzmann constant = $5.67\times10^{-8}W/m^2.K^4$

Roman Symbols

A_{ij}	Correction for the spatial distribution of absorption of laser intensity
b	Absolute path length (m)
$b_{ij}(r)$	Position of pixel (i,j) along the r-axis of a CCD camera image
$b_{ij}(x)$	Position of pixel (i,j) along the x-axis of a CCD camera image
$b_{ij}'(r)$	Corrected position of pixel (i,j) along the r-axis of a CCD camera image
$b_{ij}'(x)$	Corrected position of pixel (i,j) along the x-axis of a CCD camera image
B_{ij}	Spatial distribution of the background noise of a CCD camera
c, C	Fluid concentration
C_{ij}	Fluid concentration measured at pixel location (i,j)
C_{ref}	Reference concentration representing 100% jet fluid
d	Jet exit diameter (m)
d_c	Centre-body diameter (m)
d_{CAJ}	Central axial jet exit diameter (m)
d_ε	Momentum or effective diameter of a jet (m)
d_{or}	PJ nozzle inlet orifice diameter (m)
d_{PJ}	PJ nozzle chamber diameter (m)
d_2	PJ nozzle exit orifice diameter (m)
D	Molecular diffusion coefficient (m^2/s)

D_{duct}	Diameter of a confining duct (m)
D_{kiln}	Diameter of a kiln (m)
f	Frequency (Hz)
f_p	Frequency of precessional motion (Hz)
F	Fluorescence intensity
G	Jet source momentum (N or kg.m/s^2)
G_{CAJ}	Momentum of the central axial jet at the jet exit (N or kg.m/s^2)
G_{ij}	Spatial distribution of the gain response of a CCD camera and optics
G_{PJ}	Momentum of the precessing jet calculated at the upstream orifice inlet to the nozzle chamber (N or kg.m/s^2)
$G_{shaping}$	Momentum of the shaping jet at the jet exit (N or kg.m/s^2)
G_0	The excess momentum flux of a jet relative to the surrounding co-flow (N or kg.m/s^2)
I_{ij}	Spatial distribution of laser intensity
I_0	Incident laser intensity
K_1	Concentration decay constant
K_2	Spreading rate (slope) of the jet concentration half-width
l_{CAJ}	Protrusion distance of the central axial jet exit from the face of the centre-body (m)
l_x	Local length scale in a flow (m)
l_c	Distance between the upstream face of the centre-body and the inlet orifice of the PJ nozzle chamber (m)
l_c	Momentum radius of a jet in a co-flow (m)
L	Chamber length of the PJ nozzle (m)
L	Spatial resolution of a measurement probe or volume (m)
L_{flame}	Flame length (m)
m	Craya-Curtet scaling parameter
$\dot{m}$	Mass flow rate (kg/s)
m_a	Mass flow rate of co-flow/secondary fluid (kg/s)
m_0	Mass flow rate of jet fluid (kg/s)
P_n	Instantaneous laser power in image n
P_{min}	Minimum instantaneous laser power in a set of images
P_{max}	Maximum instantaneous laser power in a set of images
P_{ref}	Calculated reference laser power for the correction of laser power fluctuations
Q	Rate of energy transfer (W)
Q_{rad}	Total measured rate of radiant energy transfer (W)
Q_{loss}	Rate of total heat transfer through the kiln simulator walls (W)
$Q_{wall,abs}$	Rate of radiant energy absorbed by the kiln simulator walls (W)
$Q_{wall,emit}$	Rate of radiant energy transfer emitted by the kiln simulator walls (W)
Q_{flame}	Rate of radiant energy transfer directly emitted by the flame (W)
Q_f	Energy input in the fuel (W)
r	Span-wise (radial) location in cylindrical co-ordinates (m)

r_{CCD}	Size of the CCD array in pixels along the r-axis
r_{break}	Radial distance from the PJ nozzle axis at which the jet edge "breaks" due to the effects of confinement (m)
$r_{1/2}$	Jet centreline concentration half-width (m)
s_c	Ocular distance of the optical system of a CCD camera
S_p	Average signal strength from the laser power reference cell
S_{cref}	Average signal strength from the jet reference concentration cell
$\overline{S}_{ij}$	Spatial distribution of fluorescence intensity
R	Background dye concentration
t	Time (s)
T_f	Non-adiabatic flame temperature (°K)
T_w	Wall surface temperature (°K)
Th	Becker scaling parameter
u	Fluid velocity (m/s)
U	Bulk mean fluid velocity (m/s)
U_a	Bulk mean velocity of co-flow/secondary air or water (m/s)
$U_{e\text{-}PJ}$	Estimated velocity of the precessing jet at the exit of the nozzle chamber (m/s)
U_{or}	Velocity of the precessing jet at the inlet orifice to the PJ nozzle chamber (m/s)
V_{flame}	Flame volume (m^3)
w_c	Axial width of the centre-body (m)
W_{flame}	Maximum flame width (m)
x	Stream-wise (axial) location in cylindrical co-ordinates (m)
x_{break}	Axial distance from the PJ nozzle exit at which the jet edge "breaks" due to the effects of confinement (m)
x_{CCD}	Size of the CCD array in pixels along the x-axis
$x_{0,1}$	Virtual origin based on the inverse concentration (m)
$x_{0,2}$	Virtual origin based on the jet concentration half-width (m)

Greek Symbols

α	Constant of proportionality in the equation relating the Kolmogorov and Batchelor length scales
β	Ratio of the laser power signal strength to the jet reference concentration signal strength
χ	Non-dimensional axial distance on the jet axis, $= (z - z_{0,1})/d_\varepsilon$
χ_r	Flame radiant fraction
Δ	Difference
ε	Extinction coefficient of a fluorescent dye
ε	Emissivity
η	Non-dimensional radial distance from the jet axis, $= r/(z - z_{0,2})$
ϕ	Quantum efficiency of a fluorescent dye
Γ^*	Momentum ratio based similarity parameter for swirl and bluff-body nozzles

$\Gamma_{shaping}$	Ratio of shaping jet momentum to the sum of the momentum of the precessing jet, calculated at the upstream orifice inlet to the nozzle chamber, and shaping jet = $G_{shaping}/(G_{PJ} + G_{shaping})$
Γ_{CAJ}	Ratio of central axial jet momentum to the sum of the momentum of the precessing jet, calculated at the upstream orifice inlet to the nozzle chamber, and central axial jet = $G_{CAJ}/(G_{PJ} + G_{CAJ})$
κ	Reference concentration ratio scaling parameter
λ	Resolution length scale (m)
λ_b	Batchelor length scale (m)
λ_k	Kolmogorov length scale (m)
μ	Experimental uncertainty
θ	Thring-Newby parameter
ρ	Fluid density (kg/m^3)
σ	Standard deviation
τ_G	Global flame time scale (s)
τ_b	Batchelor time scale (s)
τ_{pulse}	Laser pulse-fluorescence time scale (s)
τ_{frame}	Laser pulse repetition rate and camera frame rate (s)
ξ	Conserved scalar jet concentration
ξ_{ij}	Conserved scalar jet concentration measured at pixel location (i,j)
$\overline{\xi}$	Mean jet concentration
ξ_{rms}	Root mean square of jet concentration fluctuations
$\Psi_{shaping}$	Mass proportion of the total jet flow rate through the shaping jet = $\dot{m}_{shaping}/(\dot{m}_{PJ} + \dot{m}_{shaping})$
Ψ_{CAJ}	Mass proportion of the total jet flow rate through the central axial jet = $\dot{m}_{CAJ}/(\dot{m}_{PJ} + \dot{m}_{CAJ})$

Non-Dimensional Parameters

Re	Reynolds number = $\frac{ud}{\nu}$
Sc	Schmidt number = $\frac{\nu}{D}$
Fr	Froude number = $\frac{U}{\sqrt{gl}}$
St_{ex}	Strouhal number of jet excitation = $\frac{fd}{u}$
St_M	Strouhal number of precession from the fluidic precessing jet nozzle, based on jet source momentum = $\frac{f_p\sqrt{\rho}d_{PJ}^{\,2}}{\sqrt{G}}$
St_p	Strouhal number of precession from the mechanical precessing jet = $\frac{fd}{U}$

Subscripts

a	Denotes quantity in the co-flow/secondary flow
$e\text{-}PJ$	Estimated quantity for the precessing jet
f	Flame
ij	Denotes quantity at a given pixel (i,j) of a CCD array

min	Minimum value
max	Maximum value
n	n^{th} measurement, e.g. image number
r	radiation
ref	Reference value
rms	Root Mean Square of fluctuating component
w	Wall
0	Denotes quantity at the jet source
∞	Denotes quantity in the ambient environment/far-field
$\bar{}$	Time mean value

Statement of Originality

The material in this thesis is original and has not been submitted or accepted for the award of a degree or diploma at any other university and to the best of my knowledge and belief, the thesis contains no material previously published or written by another person except where due reference is made in the text of the thesis.

Jordan Parham

Permission to Copy

The author consents to the thesis being made available for loan and photocopying provided that the thesis is accepted for the award of the degree.

Jordan Parham

Acknowledgment

The completion of this research project has only been possible thanks to the generosity of a wide range of people. In particular, the academic leadership of Emeritus Professor Sam Luxton and Dr. Gus Nathan has successfully guided the research to fruition and contributed significantly to a rewarding research and life experience. The patience, dedication, friendship and inspiration of Gus will always be remembered.

The experiments conducted in this research have benefited significantly from the contributions made by members of the Turbulence, Energy and Combustion (TEC) group. Thanks must go to the many postgraduate students in the TEC group, especially those who have spent time in room S217, for their ideas, assistance and conversation. Dr. David Nobes, Dr. Greg Newbold, Dr. Neil Smith, Mr. Philip Cutler and Mr. Bad Ghazali have especially helped to focus, strengthen and execute the aims of this research. The generosity of Dr. Richard Kelso in providing access to the water-tunnel, image recording and frame-grabbing equipment is most appreciated. The major quantitative mixing experiments would not have been possible without the assistance of Associate Professor Keith King of the Department of Chemical Engineering in securing the Infinity Nd:YAG laser. The contribution of equipment, advice and comments by Dr. David Nobes towards these experiments (which continued from the other side of the world!) was extremely generous. The laser wizardry of Dr. Zeyad Alwahabi ensured the laser based experiments were conducted safely and to the highest standards.

The efforts of the many and varied staff members of the Department of Mechanical Engineering contributed to the development (and repair) of much of the experimental equipment used throughout this research. In particular the contributions of Mr. Graham Kelly, Mr. Anthony Sherry, Mr. Ron Jager, Mr. Craig Price and Mr. Billy Constantine are greatly appreciated. The co-operation and technical input of the staff of the International Flame Research Foundation, especially Mr. Jochen Haas, in conducting the pilot-scale combustion experiments is much appreciated.

This project was made possible by the financial assistance of Fuel and Combustion Technology Ltd. and the Australian Research Council through the Collaborative Grants Scheme. However, the contribution of Fuel and Combustion Technology Ltd. to this research has extended well beyond their financial support. The provision of industrial data, advice, ideas and years of industrial experience from Mr. Steven Hill, Dr. Barrie Jenkins and Dr. Peter Mullinger has ensured a successful commercial and academic outcome from this research.

I am very grateful for the love and support of my partner, Cassie White, and my family who have both helped to share in the highs and lows of the last few years.

Many thanks to you all,

Jordan Parham, December 2000

Chapter 1

Introduction

1.1 Background and Motivation

1.1.1 Combustion of Fossil Fuels and the Environment

Recent research has demonstrated a strong correlation between changes in the composition of the Earth's atmosphere since the advent of the industrial revolution and global climate change (IPCC, 1995). An overwhelming proportion of the change in the composition of the atmosphere is due to pollution generated by the combustion of fossil fuels such as coal, oil and natural gas (Prather and Logan, 1994). Combustion of fossil fuels generates carbon dioxide, CO_2, water, H_2O, and trace amounts of other compounds including nitrogen oxides, NO_x, sulfur oxides, SO_x, carbon monoxide, CO, and hydrocarbons in different quantities depending upon the conditions of combustion. Concern over the production of these pollutants focusses on global problems such as the greenhouse effect and depletion of the ozone layer, and on local problems such as acid rain and photochemical smog. Awareness of the impact of combustion generated pollution on the environment and health has led to the regulation of atmospheric emissions from industrial plants by many national governments. For example Europe has introduced the Large Combustion Plant (LCP) directive and the USA has introduced the 'Reasonably Available Control Technology' (RACT) legislation (Mullinger, 1994). In order to meet the requirement of decreased emission levels while also satisfying the commercial pressure to increase energy efficiency and rate of production, the optimisation of combustion to match the requirements of a particular process has become paramount.

1.1.2 NO_x Emissions

Nitrogen oxides are particularly targeted in the regulation of atmospheric pollution as fossil fuel combustion is the largest single global source of NO_x and has led to a fourfold increase in the source of tropospheric NO_x (Prather and Logan, 1994). NO_x is the single most important oxidant in the atmosphere and can affect human health through ozone production, is the major component of smog and can cause the acidification of rain. NO_x is also classed as a greenhouse gas and was estimated to account for 6% of the enhanced greenhouse effect in the 1980s (Sloss, 1991 in Bowman, 1992).

NO_x is generated in a flame via the "thermal", "prompt" and "fuel" routes. Fuel NO_x is produced by the oxidation of organic nitrogen containing compounds in the fuel and is therefore produced principally in coal and oil flames and is generally absent from natural gas flames. Prompt NO_x production is defined as NO that is formed at a rate

faster than that calculated from the simple equilibrium thermal NO mechanism due to the rapid fixation of atmospheric nitrogen by hydrocarbon fragments. Thermal NO_x is formed by the combination of nitrogen and oxygen from the atmosphere and becomes significant at temperatures above 1400°C. The basic mechanism for thermal NO_x is the Zel'dovitch reaction of molecular oxygen and nitrogen radicals. The high activation energy of the Zel'dovitch reaction and its strong dependence on oxygen availability and residence time means that the production rate of thermal NO_x is strongly dependent on the local flame temperature and oxygen concentration. Bowman (1992) has shown that the maximum production rate of NO can be expressed as:

$$\frac{d[NO]}{dt} = 1.45 \times 10^{17} T^{-1/2} \exp\left(\frac{-69460}{T(K)}\right) \cdot \frac{[O_2]_{eq}^{1/2}}{[N_2]_{eq}} \qquad \textbf{Equation 1-1.}$$

Due to the exponential dependence of Equation 1-1 on temperature, the most concentrated source of combustion generated NO_x emissions are industries that require high flame temperatures. The highest industrial flame temperatures are obtained in glass-melting furnaces, in which peak temperatures are over 2000°C and gas temperatures remain above 1800°C for a significant proportion of the furnace residence time resulting in emissions typically in the range 900 to 2800ppm at 3% O_2 (Nakamura *et al.*, 1993). Transportation is also a significant source of NO_x emissions due to the combustion conditions in internal combustion engines. It is estimated that in the USA, transportation engine emissions accounted for 42% by weight of all anthropogenic air pollution in 1980 and 44% by weight of all NO_x emissions (EPA, 1982 in Marks, 1996). Rotary kilns also contribute significantly to global atmospheric pollution due to relatively high NO_x emissions and the emission of dust and carbon dioxide from the raw feed in cement kilns. A recent OECD report estimates that the cement industry alone contributes 5% of global energy and process related CO_2 emissions (Ellis, 2000). Global cement production in 1995 was estimated to be 1.45 billion tons, generating 1.1 billion tons of CO_2 emissions (Ellis, 2000). Rotary kilns for lime production are estimated to account for a further 2% of global CO_2 emissions. The contribution of rotary kilns to global NO_x emissions is likely to be somewhat greater than these proportions due to the high flame temperatures required for high heat transfer (Mullinger, 1994).

1.1.3 Rotary Kilns

High temperatures are required for the processing of a wide range of materials including lime, alumina, nickel, zinc, cement, chrome ore and chrome oxide, clays, petroleum coke, titanium dioxide and mineral and tar sands. High flame temperatures are required to achieve the high radiant heat transfer rates necessary to drive the chemical reactions which transform these raw materials, such as the clinkering reaction in cement production, which only occurs at temperatures above 1400°C. Rotary kilns are relatively efficient at high temperature radiant heat transfer and can achieve the required reaction temperatures in a continuous process. Hence they are currently the most effective means for processing such minerals.

A schematic diagram of a typical rotary kiln plant for cement production is shown in Figure 1-1. The kiln itself may be from 30 to 230m in length, and 2 to 8 metres in internal diameter, consisting of a brick-lined steel shell which is inclined at about 2° to the horizontal. To induce the feed to move through the kiln, the whole kiln is rotated

at about one revolution per minute. Fuel, through a burner nozzle, and combustion air around it enter co-axially from the lower end of the kiln, so that they move in a direction opposite to that of the bed material. The clinkering reaction in a cement kiln is exothermic (releases energy) and occurs at temperatures of around 1450°C in the "burning zone" (the hottest region of the kiln where the product glows). The calcining reaction takes place in the back half of the kiln at about 800°C and is endothermic (absorbs energy). The combustion air is usually pre-heated to between 400°C and 1000°C by passing the hot product through a cooler. Peak flame temperatures of around 2000°C are typically achieved. Optimum clinker quality is achieved using a relatively short, hot burning zone close to the exit of the kiln (Ono, 1980). The cost of energy can represent up to 40% of the cost of cement production, so there is considerable commercial pressure to increase productivity and energy efficiency.

1.1.4 Low Emission Burners for Rotary Kilns

The production rate of NO_x emissions within a flame is determined by the temperature, oxygen availability and residence time experienced by the gases within a flame volume. These variables are interdependent and vary with time and space in a flame depending on the mixing characteristics of the burner-furnace system and the feedback from the process. Hence most techniques to minimise NO_x emissions seek to either reduce the flame temperature, especially the peak flame temperature, or to modify the flame stoichiometry.

A wide range of low NO_x burners have been developed for the power industry (Bowman, 1992; Garg, 1994). However, techniques such as flue gas recirculation and combustion staging are not generally applicable to rotary kilns because of the increased mechanical complexity required to implement them and the requirement for high radiant heat transfer which necessitates relatively high flame temperatures (McQueen *et al.*, 1995). Hence NO_x control in rotary kilns is usually attempted by controlling the mixing characteristics between the fuel and the air. However, many attempts to produce low NO_x kiln burners have met with limited success because the reduction in emissions is achieved by poorer mixing of the fuel and air, resulting in inadequate heat transfer to the product feed and the flame impinging on the walls of the kiln, reducing both product quality and production (Mullinger, 1994). To design an effective low NO_x rotary kiln burner it is therefore necessary to limit the local oxygen concentration and peak temperatures in the flame, yet at the same time ensure that mixing rates are sufficiently high to obtain adequate heat transfer from the flame to the charge. Since the burner design significantly influences the mixing within a flame, it is one of the most critical components of a kiln system.

In a rotary kiln environment, a complex feedback mechanism exists between the process and the flame, so that the NO_x emissions are dependent upon these heat transfer processes in addition to the mixing characteristics of the burner and the aerodynamics in the kiln. The significance of the thermal feedback between the flame, the process and the walls is well illustrated by the fact that NO_x emissions have been used as an important control parameter in cement kilns, since the temperature of the hottest part of the clinker bed affects both the quality of the cement clinker and the thermal NO_x emissions (Lowes and Evans, 1989). The interdependence between the heat flux requirements of the clinker and the temperature of the flame implies that for an optimal rotary kiln burner design, minimisation of NO_x emissions cannot be achieved without consideration for the optimisation of the thermal profile (Nathan and Manias, 1995; Nathan and Rapson, 1995). Viskanta (1991) identifies that heat transfer and pol-

lutant emissions are also intimately coupled in other high temperature industries such as glass manufacture, chemical processing and materials processing industries, and hence must be tackled simultaneously.

Nearly all rotary kiln systems are dissimilar from each other due to differences in geometry such as kiln shell shape, firing hoods, clinker coolers and other factors such as fuel type and composition of the feed. Hence the optimum firing configuration varies from plant to plant as well, yet the overall objective is the same: maximise product quality, rate of production, energy efficiency and achieve complete combustion with minimal polluting emissions. Hence to achieve these aims, for the reasons outlined above, the correct amount of heat must be transferred to the bed at each stage of the process by controlling and optimising the flame shape and radiant fraction for each plant and process. A burner that provides adequate adjustment and control of flame shape to optimally match the requirements of a particular application and installation will therefore be of major benefit in achieving the maximum efficiency and minimum emissions.

A recently developed type of burner which uses a Precessing Jet (PJ) nozzle (Nathan *et al.*, 1998, Luxton *et al.*, 1991) produces a short, intense heat flux profile which makes it ideal for rotary kiln applications. Industrial installations of the PJ burner also incorporate a secondary jet for flame shaping which can achieve substantial changes in the heat flux profile of rotary cement kilns and hence match the optimal requirements of a particular kiln (Hill *et al.*, 1995). However, while the characteristics of the PJ burner with shaping jet have been demonstrated in practice, neither the mechanism for the benefits nor the details of how the two flows interact are fully understood. Advancing this understanding for optimisation and predictive capability, is the major motivation for the present investigation.

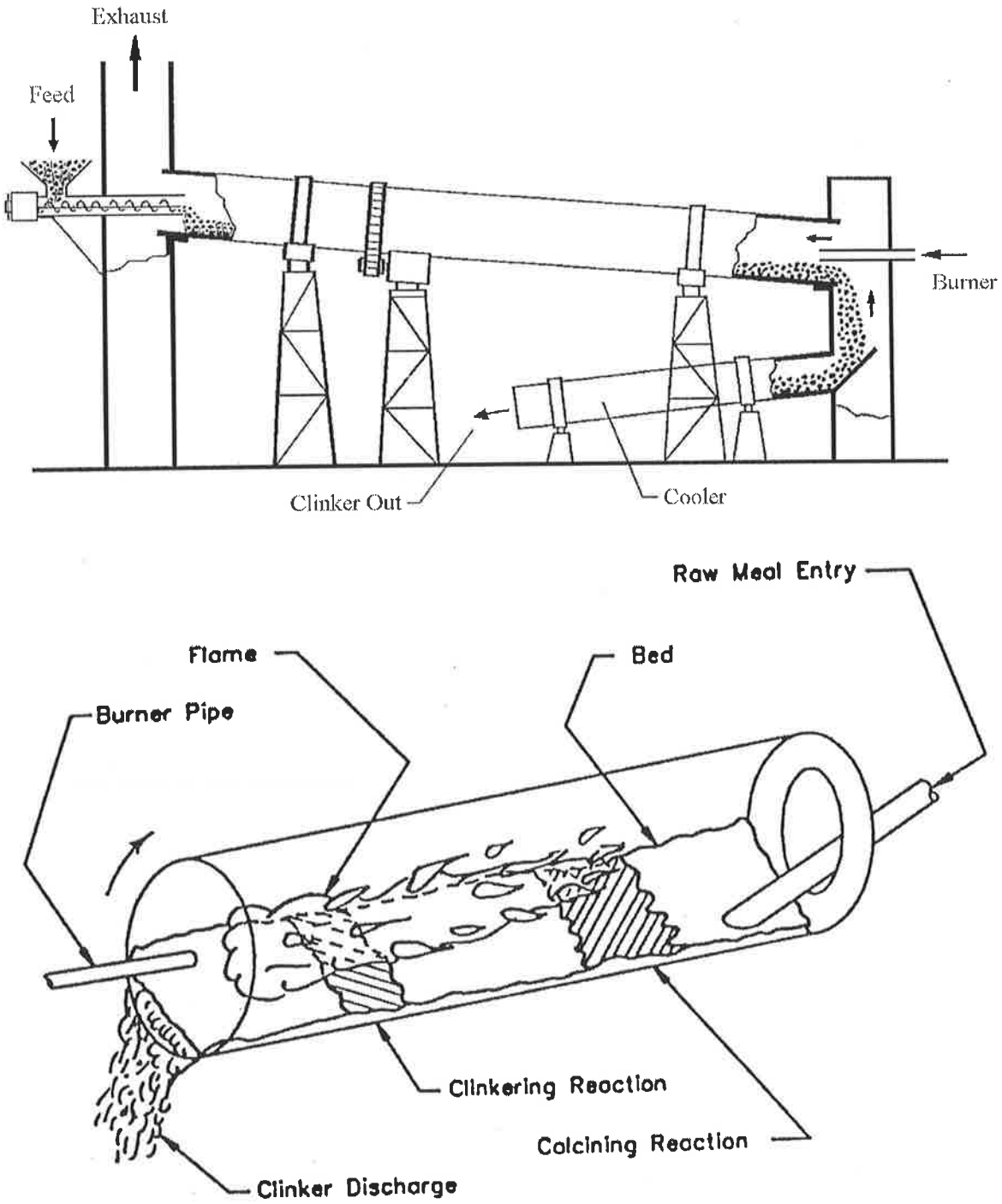

Figure 1-1. Schematic diagrams of the main elements of a rotary kiln. Top: major plant components in the production of cement clinker (Nobes, 1996). Bottom: the reaction zones inside a wet process cement kiln (Nathan and Rapson, 1995).

1.2 The Optimisation of Combustion in a Rotary Kiln

1.2.1 Mixing and Combustion

All combustion processes have the following stages which, in order, are: mixing, ignition, chemical reaction and dispersal of products. The rate of combustion of natural gas in industrial flames is limited by the slowest of the above stages, which is the rate at which the reactants are mixed within specified concentration ratios corresponding to the flammability limits. Hence the combustion is said to be "mixing limited" and control of combustion is achieved by control of the underlying mixing phenomena. The emissions and luminosity characteristics of a flame are strongly influenced by the mixing field through their dependence upon residence times at a given local temperature and mixture fraction.

The dominant mechanism for the mixing of fuel and air in most burners is by jet entrainment. Entrainment results from the combined action of the gulping or enfolding of ambient fluid by large coherent eddies and the small-scale turbulent diffusion processes which mix the reactants at the molecular scale (Brown and Roshko, 1974). McManus *et al.* (1990) concluded that "*control over the formation of these (large-scale) structures presents a possible means to enhance the turbulent transport processes affecting mixing and entrainment rates in these flows and in similar reacting flows*". Gutmark *et al.* (1989, 1990) also emphasised that the ability to control the dynamics of a turbulent flow and redistribute the energy between different turbulent length scales could enhance the bulk mixing of air and fuel selectively at locations where they should be mixed while maintaining the high degree of small-scale mixing required for a high rate of energy release. Small-scale mixing is important because although large-scale structures are critical for mixing in non-premixed flames, bulk mixing is not sufficient and small-scale turbulence leading to the molecular mixing of reactants is crucial for complete combustion. The importance of controlling the spectrum of turbulence scales as well as just the turbulence intensity or the nozzle momentum in providing optimum mixing for minimising emissions and maximising radiant heat transfer has also been highlighted by Nathan *et al.* (1997).

1.2.2 Control of Combustion

The basic building block of most gas burners and mixing investigations is a high velocity turbulent jet of fuel issuing from a "simple" axisymmetric nozzle. The mixing from a simple jet is characterised by small-scale turbulent mixing generated by intense shear in the jet mixing layers, which results in high local temperatures in flames and accompanying high levels of thermally generated NO_x. Simple jet flames are also relatively long and it is very difficult to adjust the flame shape from such a burner nozzle as the flame length typically scales with the nozzle diameter (Hawthorne *et al.*, 1951).

The rate of mixing from a simple jet can be altered by exciting the large-scale structures present in a turbulent flow. This can be achieved by using acoustic, mechanical or fluidic forcing. Acoustic and mechanical modes of excitation of structures in jet flows for the "enhancement" of mixing have been known for some time. For example, Parekh *et al.* (1987) used dual-mode acoustic excitation to produce a bifurcating jet, Badri Narayanan and Platzer

(1987) used oscillating vanes on either side of a jet to increase the spreading rate of a non-reacting jet. Lovett and Turns (1990) used strong axisymmetric pulsing to significantly change the structure of a free, vertical turbulent jet diffusion flame. However, acoustic and mechanical excitation methods do not allow continuous control of mixing as they are restricted to either a limited operating range or planar geometry. They also have practical limitations for industrial application.

A range of fluidic means for altering the mixing from a simple jet have also been developed. A method for altering the mixing characteristics of a jet that has found wide application in industrial systems is the use of swirl. Swirl improves flame stability due to the formation of a central recirculation zone and achieves fast mixing at the boundaries of this zone. The high flame stability of swirl burner flames makes them amenable to NO_x reduction strategies such as staged combustion in boilers. Control of the mixing and flame characteristics is achieved by varying the swirl number, which results in four broad types of flames dependent on the influence of the recirculation zone on flame stabilisation (Claypole and Syred, 1982). Chen *et al.* (1990) has demonstrated that flame properties from a swirl burner in which air is swirled around a central jet is achieved by controlling the vortex strength of the swirling flow and the fuel jet momentum. This results in a degree of control that is not possible in simple jet flames.

Another widely investigated method for controlling combustion with good flame stability is by using a bluff-body nozzle. This nozzle consists of a central fuel jet issuing into a surrounding annular air flow. Large-scale, time-varying structures have been observed in bluff-body stabilised flames and in isothermal conditions (Namazian *et al.*, 1992). Bluff-body flames can be characterised as either air-flow or fuel-jet dominated, depending on whether the annular air velocity is high or low and hence whether the fuel jet penetrates the recirculation region (fuel-jet dominated) or is turned back (air-jet dominated). Four different flame types have been demonstrated by Namazian *et al.* (1992), depending on the velocity ratio. Chen *et al.* (1990) has demonstrated that a momentum ratio based similarity parameter can be used to characterise the flow and flame properties of bluff-body and swirl nozzles with a central fuel jet and hence this a universal controlling parameter for all jet flows with recirculation.

Swirl burners can be designed to incorporate low-NO_x emission features and to produce a heat release profile appropriate for boilers. However these low emission burner designs are not generally applicable in rotary kilns due to the different heat release profile requirements, the need for high radiant heat transfer which necessitates relatively high flame temperatures, and their complex design and control. The precessing jet nozzle is both mechanically simple and has significant advantages in rotary kiln applications. Industrial installations have also demonstrated that a secondary fuel jet can be used to alter the mixing and hence flame shape to match the optimal process requirements.

1.2.3 Optimisation of Mixing for Combustion

The optimal combustion properties and hence the optimal mixing characteristics of a burner nozzle depend on the relative importance of heat transfer (radiation or convection), flame size (large or small) and emissions (nitrogen oxides or carbon monoxide). Hence the variation in the literature as to what constitutes "good" or "bad" mixing depends to an extent on the different models that have been developed to correlate heat transfer, flame size and

emissions and the application of the model. For example, in some interpretations, rapid mixing of fuel and air is considered to be best: "*Recirculation is accompanied by high turbulence intensities and enhanced turbulent mixing rates*" (Schefer *et al.*, 1987) or "*The bluff-body and the swirl vanes ... can improve the fuel-air mixing rates and thereby significantly shorten the flame*" (Chen *et al.*, 1990). Hence a thermal scaling criterion for turbulent jet flames, which correlates a reduction in NO_x emissions with a reduction in the flame length and global residence time, has been derived by Chen and Driscoll (1990). In this model a short flame with high mixing rates is considered optimal. In contrast, Mi *et al.* (1997) have shown that the gross precession of a jet increases the large-scale mixing between the jet and the surrounding flow and simultaneously reduces the mean flow strain rate, thereby suppressing the generation of small-scale turbulence. This mixing, which could be labelled "poor" based on the previous interpretations, has been shown to increase radiant fraction and decrease NO_x emissions by 15% to 25% in unconfined flames (Nathan *et al.*, 1996).

Newbold *et al.* (2000) has reviewed the many scaling models developed for correlating NO_x emissions, radiant fraction and flame volume of unconfined flames and compared these models with measurements from a wide range of burner types. The results demonstrate that, for all burner types, an increase in radiant fraction correlates with an increase in global residence time and a decrease in global strain (Newbold *et al.*, 1997). The production rate of NO is shown to correlate with the global flame temperature. Hence the reduction in NO_x emissions by strongly recirculating flows from swirl and bluff-body burners, relative to those from turbulent jet flames, is inferred to be a consequence of the recycling of NO. However, these flames also have high CO emissions and a high ratio of NO_2/NO_x due to the increased mixing rates in the recirculation dominated flow regime. Precessing jet flames are found to reduce NO_x emissions compared with turbulent jet flames, a result that is attributed to an increase in the global residence time and radiant fraction, consistent with the scaling model of Turns and Myhr (1991). Hence Newbold (1997) concludes that this "*trend implies that the effect of radiation on the temperature of jet flames can become significant when the structure of jet turbulence, and hence the mixing characteristics, have been modified to reduce the characteristic strain rate of the reacting flow. It also provides a mechanism whereby NO_x emissions can be reduced and radiant heat transfer increased simultaneously by proper control of turbulent mixing parameters.*"

A range of burner types have been developed and applied in rotary kilns, each with widely different mixing characteristics and, in turn, differing heat flux and NO_x emission characteristics. However no single comparison of performance exists under well defined conditions. The respective mixing characteristics of burner types has also yet to be quantified. Therefore, the second major aim of the present research is to develop an understanding of what the optimal turbulent mixing parameters are for the optimal radiant heat transfer, flame shape and emissions in a rotary kiln and how these parameters can be controlled via the interaction between a shaping jet and a precessing jet.

1.3 The Precessing Jet Nozzle

Precession describes the motion of a jet (or another body) about an axis other than its own. Precession occurs in a Fluidic Precessing Jet (FPJ) nozzle due to a natural fluid dynamic instability within an axisymmetric nozzle following a large sudden expansion (Nathan *et al.*, 1998; Luxton *et al.*, 1991), see Figure 1-2. The exit angle, frequency and direction of rotation of the emerging jet can change greatly with time (Nathan, 1988). Hence in order to control the frequency, direction and exit velocity of the precessing jet and thereby advance the fundamental understanding of the effect of precession on mixing, a Mechanical Precessing Jet (MPJ) has been developed which produces many similar flow characteristics (Nathan *et al.*, 1997). The nozzle investigated in the present research is the fluidic nozzle, which is denoted by the abbreviation "PJ" throughout the remainder of this thesis.

1.3.1 The Effect of Jet Precession on Mixing

Jet precession is characterised by a dimensionless Strouhal number relating the precessional frequency to the jet velocity and geometric nozzle size. Control of the mixing and combustion characteristics is realised in an MPJ nozzle by varying the Strouhal number, $St_p=f_p d/U$, where d is the jet exit diameter, U is the jet exit velocity and f_p the frequency of rotation of the jet. At low Strouhal number ($St_p<0.01$) the cold-flow mixing characteristics are somewhat analogous to a fully pulsed jet (Schneider *et al.*, 1997). At high Strouhal number ($St_p>0.03$), the jet assumes a helical path and mixing occurs on the scale of the jet helix. The original jet completely loses its identity within 10 diameters of the nozzle exit (Schneider *et al.*, 1997). The velocity decays rapidly and is an order of magnitude greater than that of a non-precessing jet flow. Nobes (1997) has demonstrated that, relative to a non-precessing jet, the flow from a high Strouhal number regime MPJ nozzle reduces the concentration decay rate, increases the jet spreading rate, increases the intensity of concentration fluctuations and broadens the range of concentrations measured on the jet axis. This is consistent with the results of Nathan *et al.* (1997), who showed that jet precession in the high St_p regime acts to increase the size of the largest scale of mixing and to shift the energy in the spectrum of turbulence toward these larger scales and away from the fine scales.

The flow produced by naturally occurring precession cannot be controlled in the same manner as that from an MPJ nozzle. The characteristic Strouhal number of precession from the commercial design of a PJ nozzle, whose geometric ratios are fixed, is a constant, $St_M=0.08$, based on the momentum of the jet entering the chamber, see Equation 1-2, where ρ is the density of the jet fluid, d_{PJ} is the diameter of the PJ nozzle chamber and G_{or} is the momentum of the jet from the inlet orifice to the nozzle chamber. The frequency of precession depends to a minor extent on the geometry of the nozzle and the Reynolds number. The emerging jet does not fill the exit plane of the PJ nozzle and leaves at angles between 45° and 60°. An extensive description of the PJ flow and the conditions under which it arises is given by Nathan *et al.* (1998).

$$St_M = \frac{f_p \sqrt{\rho} d_{PJ}^{\,2}}{\sqrt{G_{or}}} \approx 0.08 \qquad \textbf{Equation 1-2.}$$

The mixing characteristics of the fluidic precessing jet have been shown to differ significantly from those of simple jet flows and are consistent with the mixing characteristics of the high St_p regime of the MPJ nozzle. Within a short distance from the PJ nozzle exit, the velocity of the jet fluid is reduced by two orders of magnitude relative to the velocity at which it enters the chamber. This is associated with the formation of large-scale roller structures in the near field, close to the nozzle, resulting in turbulence of a scale many times that of the nozzle. The large-scale structures result in enhanced large-scale engulfment of ambient fluid and suppressed fine-scale mixing between the jet and the ambient fluid streams (Newbold, 1997). Hence significantly more ambient fluid is found on the jet centreline of a precessing jet flow compared with a simple turbulent jet (Newbold and Nathan, 1998).

The differences between the mixing of the simple jet from the inlet orifice of the PJ nozzle and the mixing with the addition of the PJ chamber have been quantified by Newbold (1997) from unconfined concentration measurements. These results indicate that the addition of the PJ chamber results in the concentration decay along the jet axis being halved, the jet spreading rate being almost doubled and the intensity of concentration fluctuations along the jet axis being increased by about 50%. The increase in the size of the large-scale structures was quantified by calculation of the macroscopic length-scales and in particular the integral length scale of the concentration fluctuations, which increased by a factor of 2. The distribution of mixed fluid concentrations on the jet centreline was also found to increase. The local strain rate (based on the aspect ratio of the integral length scale calculations) was found to decrease.

1.3.2 The Effect of Jet Precession on Combustion

The change in mixing characteristics with Strouhal number in an MPJ nozzle have been shown to correspond to significant changes in the combustion characteristics, as expected. In the low-St_p regime, the flames are non-luminous, short and broad compared with conventional flames. In the high-St_p regime, the flames are highly luminous and of a shape which is between that of a conventional jet flame and the low-St_p flame (Nathan *et al.*, 1996). The radiant fraction is found to increase with St_p in proportion with the visible flame luminosity. The emissions of NO_x were also found to be functions of St_p, with a maximum reduction of 25% compared to conventional flames. The lift-off height is reduced by a factor of 5 to 10 relative to a conventional jet flame and there is a corresponding increase in flame stability.

Extensive investigations into the properties of unconfined flames from PJ nozzles have been performed by Newbold *et al.* (1997) and Newbold and Nathan (1998). High speed image sequences from vertically fired PJ flames show significant differences compared with momentum dominated flames. Large-scale buoyant structures are observed to dominate the mixing and entrainment of surrounding fluid in the region downstream from the stabilization region of the open flames. Oscillations in the flame length due to the burning out of the large-scale buoyant structures closely resemble the "puffing" oscillations observed in pool fires. The oscillations in the flame length are also deduced to indicate that the strain rate at the flame tip is reduced by an order of magnitude compared with momentum dominated flames. At the same time, the global residence time is also increased. The reduced strain rate and increased residence time correlate with an increase in the radiant fraction, reduced flame temperature and

reduced NO_x emissions from precessing jet flames (Newbold *et al.*, 1997). This is consistent with the findings of Turns and Myhr (1991) and the result of Nathan *et al.* (1996) for flames from an MPJ nozzle.

1.3.3 Precessing Jet Burners for Rotary Kilns

The highly luminous flame from a PJ nozzle produces a short, intense heat flux profile which makes it ideal for rotary kiln applications. Industrial installations of the PJ nozzle have produced remarkable benefits, consistent with the reduction in emissions and increase in radiant fraction measured at the laboratory scale. The PJ nozzle has been found to improve the stability of natural gas flames significantly and reduce NO_x emissions by 30-60% (Manias and Nathan, 1993, 1994) while simultaneously increasing the radiation from the flame relative to conventional burner flames (Nathan and Luxton, 1992; Nathan *et al.* 1993). The higher radiant heat transfer from the flame results in a shorter heat flux profile leading to reduced exit gas temperatures, reduced dust losses, increased production of 3-11% and savings in specific fuel consumption of 3-8% (Nathan and Manias, 1995; Videgar 1997).

As the characteristic Strouhal number of precession from a fluidic precessing jet nozzle is constant, the mixing and hence combustion from an PJ nozzle cannot be varied easily by altering this flow. Initial installations of the PJ in rotary kilns making product produced such a short heat flux profile that the stability of the kiln operation was reduced (Manias and Nathan, 1993). The flame also spread so rapidly that it impinged on the raw material resulting in poor product quality. Hence in order to alter the flame shape and so to avoid these problems and match the optimal thermal profile in a rotary kiln, several modifications were made to the basic PJ nozzle shown in Figure 1-2. Control of the mixing and combustion was achieved by combining the PJ flow with a shaping jet, such as an annular or axial fuel jet, to modify the flame shape. Rapson *et al.* (1995) and Hill *et al.* (1995) have demonstrated that the interaction of a precessing jet and a secondary jet for flame shaping can achieve substantial changes in the heat flux profile of rotary cement kilns. However, while the performance of the PJ burner with annular or axial shaping jet has been demonstrated in commercial operation, the most effective type of shaping jet and the physical mechanism for control of the flame properties is not understood. Hence, in order to control and optimise the flame characteristics of a PJ nozzle, the present study seeks the form of a single controlling parameter that can be used to characterise the interaction between precessing and shaping jet flows and its effect on the combustion and mixing properties of the combined flow.

1.3.4 Modelling of the Precessing Jet Burner

In addition to understanding the effect of shaping the flow from a PJ nozzle on the mixing and combustion characteristics, it is also desirable to be able to predict the performance of a PJ burner in a given kiln installation so that the flame shape can be matched to the optimal process requirements. Despite the growth in computer modelling, physical modelling in small-scale test facilities is still technically the most effective method for determining flame shape and characteristics in rotary kilns (Mullinger, 1999).

An ideal model of a combustion system should maintain complete similarity of the fluid mechanics, heat transfer and chemical processes from the plant to the small-scale test facility. However, as the requirements of similarity

theory are so numerous and indeed many of the requirements are often conflicting, exact scaling of a combustion process is practically impossible. Hence the partial modelling approach, in which similarity of the most important parameters is maintained while others are relaxed, is often the only option available to study combustion systems (Spalding, 1962).

Useful modelling of many combustion systems can be undertaken in isothermal conditions, to investigate the mixing, and in combustion facilities, to investigate the flame properties. Most scaling criteria for small-scale combustion modelling of burner designs aim to ensure similarity of the turbulent mixing conditions is achieved, usually by employing either constant velocity or constant residence time scaling criteria (Smart and Morgan, 1994). These methods seek to ensure similarity of the large macro-scale turbulent mixing processes and the global chemical reaction times in a flame respectively, but necessarily compromise on the Reynolds number.

A range of scaling criteria have been developed for the small-scale combustion and isothermal modelling of conventional burner flames in an enclosure which restricts the amount of air available for combustion. A feature of all jets is that, due to their excess momentum over the surroundings, they entrain sufficient fluid to satisfy the entrainment capacity of the particular jet. While free jets encounter no limit in the quantity of entrainable fluid, enclosed jets do. A situation can arise with a jet in a confined co-flow in which the entrainment capacity of the jet exceeds the supply of co-flowing fluid and the phenomenon of recirculation takes place. In the case of a simple turbulent jet flame in a rotary kiln, recirculation is the most important factor for determining the flame shape and length.

The most widely used criteria for characterising the degree of recirculation in ducted jet systems were developed by Thring and Newby (Thring and Newby, 1953), Craya and Curtet (Curtet, 1958) and Becker (Becker *et al.*, 1963). These criteria have been validated for the modelling of large-scale industrial flows in small-scale models in which air or water is the working fluid (Mullinger, 1999). The Thring-Newby parameter, θ, was originally developed for modelling momentum dominated flames in furnaces by distorting the burner nozzle size in the model to take into account density differences in the full-scale kiln. It consists of two components: a correction for the relative confinement based on the change in densities from the combusting environment to the isothermal model (Equation 1-3) and the calculation of the Thring-Newby criterion (Equation 1-4):

$$d_0' = d_0 \sqrt{\frac{\rho_0}{\rho_f}} \qquad \textbf{Equation 1-3.}$$

$$\theta = \frac{\dot{m}_0 + \dot{m}_a}{\dot{m}_a} \cdot \frac{d_0'}{D_{kiln}} \qquad \textbf{Equation 1-4.}$$

where d_0 is the characteristic nozzle diameter, D_{kiln} is the kiln diameter, ρ_0 is the density of the jet fluid at the nozzle exit (i.e. the fuel in a burner), ρ_f is the average density of the combustion products at the end of the flame and m_0 and m_a are the mass flow rates of the jet fluid and co-flowing fluid respectively. The distorted nozzle diameter, d_0', simulates a nozzle through which fluid of the density of the entrained fluid flows but with the same mass flow rate and momentum as that of the actual jet. If the mass flux ratio is maintained constant between the full-scale and the model, the Thring-Newby criterion reduces to keeping the ratio between the distorted nozzle diameter and kiln diameter constant, as long as the nozzle diameter is small relative to the characteristic dimension of the

confined volume, i.e. $d_0'/D_{kiln}<0.05$. However, the Thring-Newby density correction shown in Equation 1-3 usually results in a nozzle diameter in the model typically 2-3 times greater than the actual nozzle diameter (e.g. at a flame temperature of 2300°K). Hence the Thring-Newby parameter is not generally used for kiln modelling since the value of d_0'/D_{kiln} is commonly greater than 0.05.

The Craya-Curtet parameter, m, and Becker parameter, Th, are considered the most suitable scaling criteria for modelling of enclosed flames by Moles *et al.* (1972). Both theories were specifically developed for the modelling of an enclosed flame by solving the Navier-Stokes and continuity equations in the far field of a simple jet by assuming the jet can be treated as a point source of momentum. Recirculation is shown to occur for $m>1.5$ and $Th<0.4$. Moles *et al.* (1972) therefore concluded from a review of the typical operating conditions of a wide range of rotary kilns that "*the rotary kiln system to be of medium to low recirculatory intensity*". Hence typical values of the similarity parameters in cement kilns are:

- Thring-Newby parameter: $0.35 < \theta < 0.80$.
- Craya-Curter parameter: $2.0 < m < 10.0$.
- Becker parameter: $0.20 < Th < 0.45$.

The main assumption in the derivation of the Craya-Curtet and Becker similarity parameters is that the burner nozzle can be treated as a point source of momentum. This enables the diameter of the nozzle to be distorted relative to the kiln without significantly affecting the flow. This is an appropriate assumption for a simple, axisymmetric jet nozzle but cannot be assumed *a priori* to be appropriate for the precessing jet nozzle, as previous experiments have shown that the flow field from an PJ nozzle differs significantly from the flow field of a simple jet and the mixing and entrainment characteristics are not momentum dominated, see Section 1.3.1. Hence the Craya-Curtet and Becker scaling criteria cannot be assumed to be valid in the modelling of precessing jet flows in rotary kilns.

The Thring-Newby scaling criterion does not assume the mixing characteristics of a particular jet type as it is based on a simple assumption of the physical behaviour of a jet. Hence Nathan *et al.* (1995) have proposed that a modified Thring-Newby parameter can be applied to the modelling of precessing jet flows in rotary kilns. The modified form of the Thring-Newby parameter corrects for the relative difference in density between the jet fluid and co-flowing or secondary fluid, ρ_a, instead of the density of the combustion products, ρ_f. The density of the co-flowing fluid is used by Nathan *et al.* (1995) in order to preserve the mixing characteristics of the precessing jet in the near-burner region, by maintaining the momentum and mass flow ratios constant in the small-scale non-reacting model and the large-scale reacting facility. This correction also avoids the uncertainty associated with calculating an average density of combustion products in a flame. However, the modified Thring-Newby scaling criterion for the precessing jet has not been tested. Therefore, at present, no validated criterion exists to relate small-scale model results using a PJ nozzle to industrial applications and consequently the ability to predict how a PJ burner will perform in a given kiln installation is limited. Hence the third major aim of the present research is to understand the behaviour of the mixing from a PJ nozzle in a confined, co-flowing environment so that a model to accurately predict the characteristics of a flame from PJ nozzle in an operating rotary kiln can be developed.

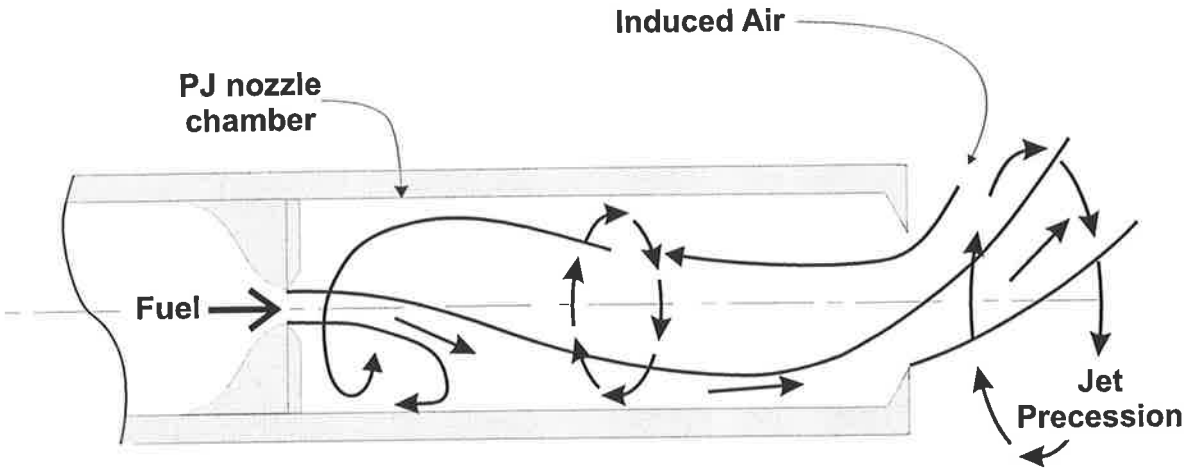

Figure 1-2. A schematic diagram of the fluid motions within an axisymmetric fluidic precessing jet nozzle.

1.4 Thesis Outline

1.4.1 Research Objectives

Optimisation of combustion in rotary kilns is necessary to simultaneously reduce atmospheric pollution caused by the emission of nitrogen oxides and carbon dioxide and increase fuel efficiency. Due to the interaction of the process and flame, differences in kiln geometries and changes in the process requirements, the optimal flame shape to match these needs also changes. The precessing jet burner has been shown to have a significantly different flow field to other types of burners, resulting in a stable, luminous, low temperature flame which can be easily shaped to suit the process requirements of a rotary kiln.

The majority of previous research on the precessing jet burner has focussed on trying to describe and understand the characteristics of the flow field produced by an unconfined precessing jet acting alone. There has also been significant fundamental research into the properties of the flow generated by a mechanically rotated precessing jet which is analogous to the fluidic precessing jet. However most industrial designs of the precessing jet burner utilise a fluidic precessing jet nozzle with a secondary jet for flame shaping. The interaction between a shaping jet and a precessing jet has not hitherto been investigated. The effect of confinement and co-flow velocity on the mixing and combustion from a PJ nozzle has also not been investigated previously. Without such knowledge it is not possible to provide reliable prediction of flame shape or to optimise the burner configuration for a given process requirement. Hence the specific objectives of this research are:

- To investigate the turbulent mixing processes that arise from the interaction of a precessing jet and shaping jet and their effect upon the combustion properties of the combined flow.
- To investigate the effects of confinement and co-flow on the reacting flow and non-reacting flow from a precessing jet nozzle.
- To develop a model for the prediction and control of a gas-fired burner with a combined precessing jet and shaping jet flow in a rotary kiln.
- To characterise the interaction between a shaping jet and a precessing jet to assess how turbulent mixing parameters can be controlled for the optimisation of radiant heat transfer, flame shape and emissions.

1.4.2 Thesis Structure

The aims of the thesis have been addressed by conducting both non-reacting mixing studies and combustion experiments. The mixing studies were performed in water facilities to allow more detailed quantitative measurement than is possible in flames. Combustion experiments were performed to quantify the flame shape, emissions and heat transfer characteristics of the PJ nozzle with shaping jet. Details of the apparatus and jet nozzles used for each experiment are described in Chapter 2.

Flow visualisation of the interaction between the jet from a PJ nozzle and different shaping jets is described in Chapter 3. A two colour Planar Laser-Induced Fluorescence (PLIF) technique in an unconfined, isothermal environment provided a simple and effective means for determining the separate effect of an annular jet, an adjacent axial jet and a central axial jet on the mixing from a PJ nozzle. The central axial jet is found to be the most effective means for controlling the combined jet flow field. A semi-quantitative image processing technique is also used to demonstrate that the ratio of shaping jet momentum to the combined jet momentum controls the spreading rate and size of the large-scale structures in the combined flow.

The effect of a central axial jet on the characteristics of a PJ flame were assessed in an unconfined environment using the visible flame luminescence. The results, outlined in Chapter 4, demonstrate that a significant change in the flame volume, length and width can be achieved by varying the proportion of central axial jet to total flow rate and hence the momentum ratio. These parameters are correlated with changes in the global residence time, radiant fraction and NO_x emissions based on scaling criteria from the literature and suggest that the heat transfer and emissions can be optimised by control of the momentum ratio.

Confined combustion experiments undertaken in a pilot-scale cement kiln simulator are described in Chapter 5. These experiments quantify the heat flux and NO_x emission characteristics of a combined precessing jet/central axial jet burner relative to a conventional burner in a well controlled, confined facility. The results confirm the experience in industrial facilities that the central axial jet provides good control over the heat flux profile. The heat transfer from a PJ burner is also shown to be enhanced relative to a conventional burner and the NO_x emissions reduced if the relationship between heat transfer, emissions and process interaction is taken into account.

To quantify the mixing characteristics of each of the above flows, and so to provide insight into the characteristics of "good" and "bad" mixing for combustion in a rotary kiln, concentration measurements were performed in a confined, isothermal environment. The effect of co-flow, confinement and the central axial jet on the mixing from the combined precessing jet and central axial jet flows were assessed separately. The experiments were performed in a water-tunnel using a quantitative PLIF technique to provide measurement of a conserved scalar marking the jet fluid. The results presented in Chapter 6 are used to develop a scaling criterion and hence to provide a predictive model for the average mixture field from a PJ nozzle. The mixing characteristics associated with high radiation and low NO_x emissions are also quantified and are consistent with the results of the other experimental investigations.

Chapter 7 draws together the results presented in Chapter 3 to Chapter 6, presents the overall conclusions of the research conducted in this thesis and recommendations for further work.

Chapter 2

Experimental Apparatus

2.1 Experimental Jet Nozzles

2.1.1 Precessing Jet Nozzles

The Precessing Jet (PJ) nozzle studied in the present investigation is based on a fluid dynamic instability within an axisymmetric chamber following a large sudden expansion. In its simplest form, the PJ nozzle consists of an inlet orifice-cylindrical chamber-exit orifice geometry, see Figure 1-2. Hill *et al.* (1992) and Nathan *et al.* (1998) have shown that this geometry results in two bi-stable flow modes: an asymmetric precessing jet mode and a symmetric "axial jet" mode. In the asymmetric precessing jet mode, the local jet emerging through the sudden expansion is deflected asymmetrically to the inside of the chamber wall. The jet is deflected across the nozzle axis at an angle between 45° and 60° when it encounters the lip at the exit orifice and azimuthal pressure gradients within the nozzle chamber cause the point of attachment of the initial jet and therefore the whole flow field to rotate about the jet axis and hence precess. The initial flow field outside the nozzle is dominated by turbulence of a scale many times that of the nozzle, resulting in very large-scale mixing between the jet and surrounding medium. The angle, frequency and direction of rotation of the exiting jet can fluctuate significantly with time (Nathan, 1988; Nathan *et al.*, 1998).

To maximise the occurrence of the PJ mode over the axial jet mode, Hill *et al.* (1992) identified an optimum geometry for the PJ nozzle. The optimal geometry includes a centre-body within the nozzle chamber, see Figure 2-1. The addition of the centre-body results in a significant reduction in the amount of ambient fluid that is entrained into the chamber but does not alter the essential character of the precessing motion of the exiting jet or the external flow field. The probability of the PJ mode is effectively 1 if the Reynolds number of the jet through the inlet orifice to the nozzle chamber is greater than 20,000. The design of the fluidic PJ can be scaled for any size, based on the ratio of each dimension to the chamber diameter, d_{PJ}. The optimum geometric ratios, as determined by Hill (2000a), are included in the confidential Appendix B.

In order to shape the flame produced by a PJ nozzle so that it better matches the requirements of a particular process, several control techniques have been developed. Nathan *et al.* (1991) used a co-annular gas stream around the outside of the PJ burner which caused some increase in the flame length and decrease in the spread of the flame with increasing flow through the annular jet, see Figure 2-2. The most recent concept, which is also the most prevalent form of shaping jet in industrial installations of the PJ burner, is the Central Axial Jet (CAJ) design, in which a secondary fuel flow stream is introduced through the centre-body along the nozzle axis, see Figure 2-3.

Hill *et al.* (1995) and Rapson *et al.* (1995) have shown that relatively small proportions of gas, $\Psi_{CAJ} = \dot{m}_{CAJ}/(\dot{m}_{PJ} + \dot{m}_{CAJ}) < 30\%$, are required through the CAJ to achieve very substantial changes to the spreading angle and flame length. Consequently the PJ-CAJ configuration is chosen for detailed investigation in the present study.

All PJ nozzle configurations used in the present experiments conform to the optimum geometric proportions found by Hill *et al.* (1992) to yield a maximum stability of the PJ flow mode. The complete dimensional ratios of all experimental PJ nozzles are presented in investigated in Appendix B. A summary of the inlet conditions and sizes of the critical diameters are included in Table 2-1. The nozzles are characterised in the text by reference to the chamber diameter, d_{PJ}. Details of the experimental nozzle designs are presented in the following sections.

2.1.1.1 PJ Nozzle for Unconfined Flow Visualisation

Two PJ nozzles, both with d_{PJ}=44mm, were used for the unconfined isothermal flow visualisation experiments. The first nozzle, which did not incorporate a CAJ, is the same design as that used by Newbold (1997). This nozzle was used for visualisation of the effect of annular and adjacent axial shaping jets. The second nozzle is also identical in dimensions to Newbold's nozzle, but incorporates feed pipes to supply fluid to the CAJ. Three feed pipes connect the CAJ to a common manifold located outside and at the rear of the PJ nozzle and then to a supply hose. The diameter and length of the CAJ nozzle tip can be altered by using interchangeable inserts that can be screwed into the centre-body. Both PJ nozzles were mounted on a common inlet orifice section. A 950mm long one inch nominal bore pipe was mounted in-line and connected the PJ nozzle to a supply hose.

2.1.1.2 PJ Nozzles for Confined Quantitative Concentration Experiments

Two PJ nozzles were used for the quantitative isothermal concentration experiments. The main nozzle, d_{PJ}=38mm, incorporates an annular arrangement to supply jet fluid to the CAJ via three symmetrical pipes which also locate and support the centre-body. The second nozzle, d_{PJ}=28mm, does not incorporate a CAJ. A smooth contraction inlet of the required dimensions for each nozzle was connected to a common supply pipe, which was a 1000mm long one inch nominal bore pipe. The geometric ratios for both nozzles are identical, including the "bluff-body" ratio of the diameter of the face of the nozzle to the chamber diameter.

2.1.1.3 PJ Nozzle For Unconfined Flame Visualisation

The PJ nozzle used for the open flame visualisation experiments is the same as that used by Anderson and Johnston (1997). The fuel to the CAJ is supplied through an annular chamber to the centre-body via three feed pipes. The inlet to the PJ nozzle chamber is a conical contraction.

2.1.1.4 PJ Nozzle for Pilot-Scale Combustion Experiments

A d_{PJ}=56mm PJ nozzle was used for the pilot-scale combustion studies. The inlet orifice diameter of d_{or}=10.5mm was sized to provide 100% of the thermal input (160kg/hr) using natural gas at 200kPa. The CAJ diameter was selected to match the diameter ratios typical of those used in industry so that the momentum ratio of CAJ to PJ is comparable with the isothermal experiments. Fuel to the CAJ was supplied via an annular chamber and two feed pipes, which also locate the centre-body. Unlike many industrial installations, the experimental burner does not include a co-annular primary air channel.

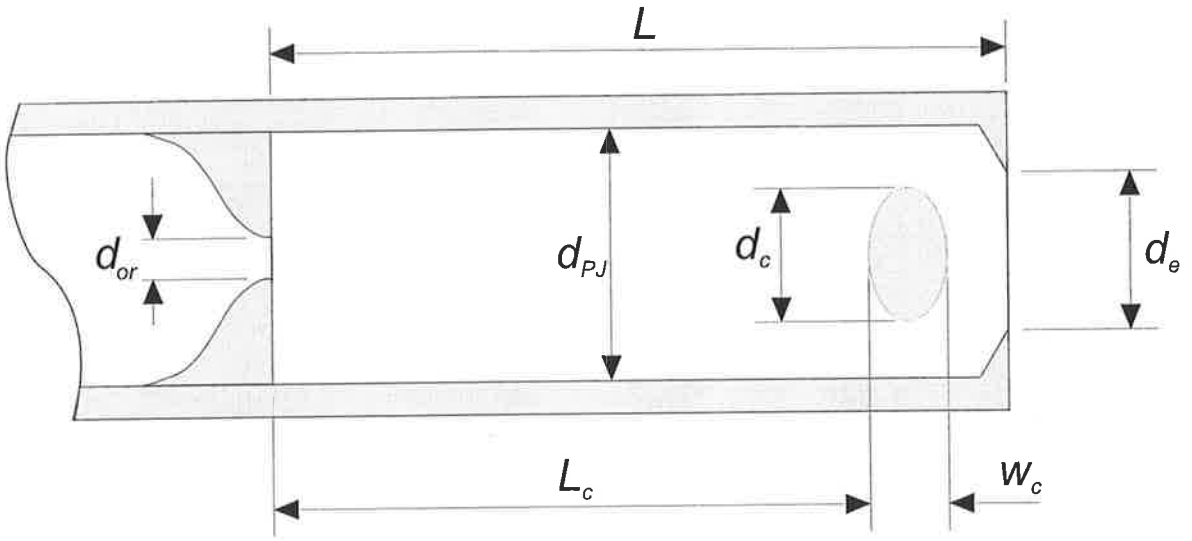

Figure 2-1. Schematic diagram of the precessing jet nozzle with centre-body showing the dimensional notation used here. Note that a range of different configurations of the inlet orifice are used in the present investigation.

Dimension		Isothermal Experiments			Combustion	
Description	**Notation**	**Visualis-ation**	**Confined PLIF**		**Visualis-ation**	**Pilot-Scale**
Chamber diameter (mm)	d_{PJ}	44	38	28	10	56
Upstream orifice diameter	d_{or}/d_{PJ}	0.17	0.20	0.20	0.2	0.19
Central axial jet diameter (see Figure 2-3)	d_{CAJ}/d_{PJ}	0.09-0.14	0.12	-	0.15	0.13
Inlet conditions	-	Sudden orifice	Smooth contr.	Smooth contr.	Conical contr.	Rounded contr.

Table 2-1. Summary of the inlet conditions and ratios of the critical diameters for the experimental precessing jet nozzles used in the present investigations. The complete geometric ratios are compared with the optimal geometric ratios derived by Hill *et al.* (1992) in Appendix B. The notation for the dimensions are shown in Figure 2-1, except for d_{CAJ}, the internal diameter of the central axial jet nozzle.

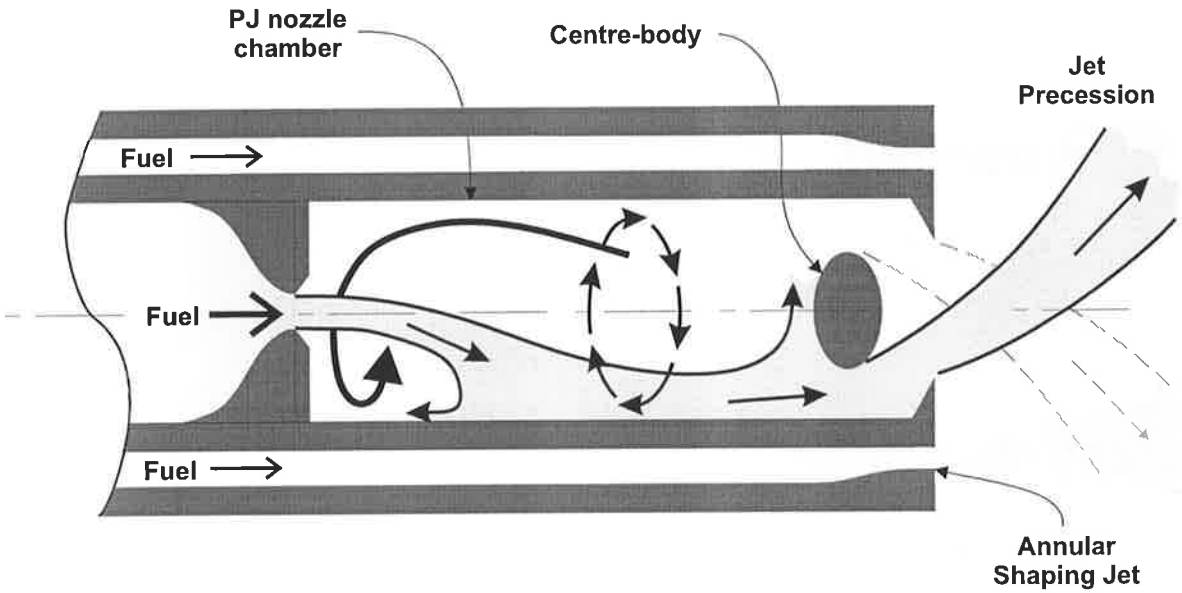

Figure 2-2. Schematic diagram of the precessing jet nozzle with an annular shaping jet for flame shaping.

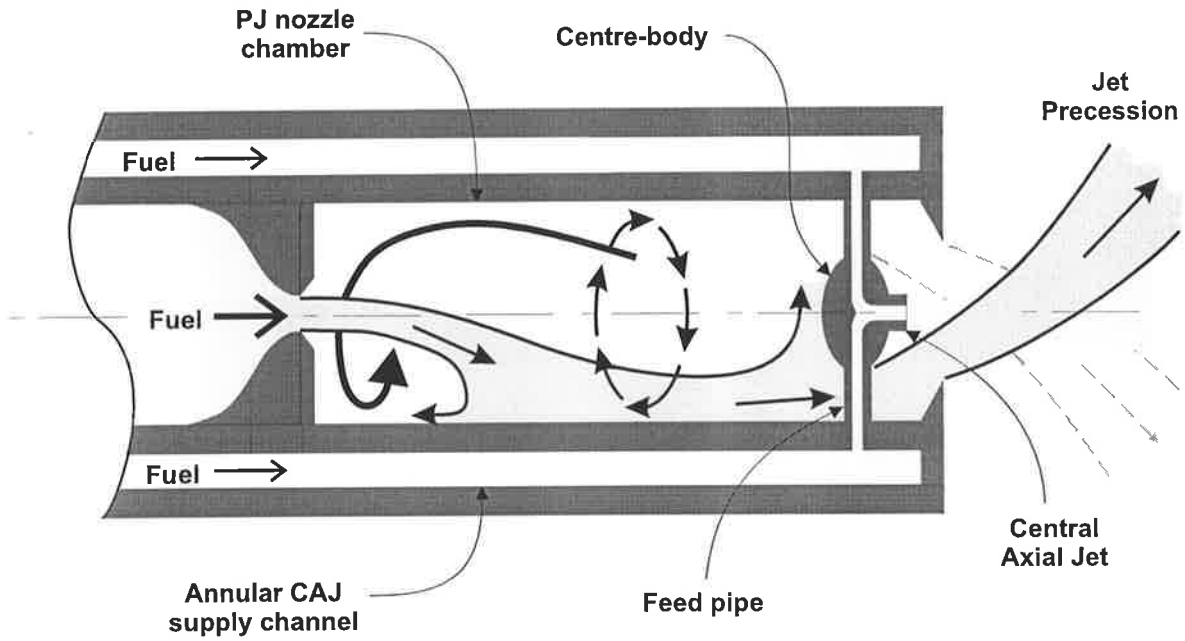

Figure 2-3. Schematic diagram of the precessing jet nozzle with a central axial jet for flame shaping. In the configuration shown, fluid to the central axial jet is supplied via an annular channel and two symmetrical feed pipes.

2.1.2 Conventional Jet Nozzles

In order to benchmark the properties of the PJ nozzle, various reference nozzles were required for each experimental technique. For the unconfined cold flow visualisation and unconfined flame visualisation experiments, the jet issuing from the central axial jet nozzle alone was used as the reference condition. To validate the technique for the quantitative PLIF experiments, a pipe jet was used, while a conventional type burner nozzle was used as the reference condition for the pilot-scale experimental investigation.

2.1.2.1 Pipe Jet for Confined Quantitative Concentration Experiments

A pipe jet was used to validate the quantitative concentration measurement technique described in Section 2.2.3. A pipe jet was selected as it is a class of jet flow that has been widely investigated by previous researchers and provides well defined exit conditions. A pipe jet also minimises the complexity associated with the external boundary layer and bluff-body effects arising from a smooth contraction nozzle in a co-flow.

The pipe jet used for the validation experiments is a 9.45mm internal diameter, 14.0mm external diameter brass pipe, 1000mm (106 diameters) in length. The pipe was connected to supply hoses by a barbed tail fitting which was fitted with a honeycomb screen to reduce any swirl in the inlet flow. The exit of the pipe was sharpened to a knife edge with an external chamfer of approximately 10° to render insignificant any possible external boundary layer and bluff-body effects on the downstream mixing from the jet.

2.1.2.2 Conventional Burner Nozzle for Pilot-Scale Combustion Experiments

The conventional burner, used to provide a basis for comparison with the PJ burner, is a generic (International Flame Research Foundation generic Multi-Channel Burner (MCB), shown in Figure 2-4. For further details on the MCB nozzle design see van de Kamp and Smart (1992). There is provision for a wide combination of swirl and axial flows on both the gas and the air-streams in this design. In the pilot-scale trials 65% of the 2MW thermal input of natural gas was fed through channel 2 (103kg/hr) and 35% through channel 0 (57kg/hr). The primary air supply, channel 1, has a swirled component imparted by 45° swirl vanes, to provide a stable flame anchored close to the burner tip. Two different flames were generated from the MCB nozzle by varying the amount of primary air through channels 2, 4 and 5.

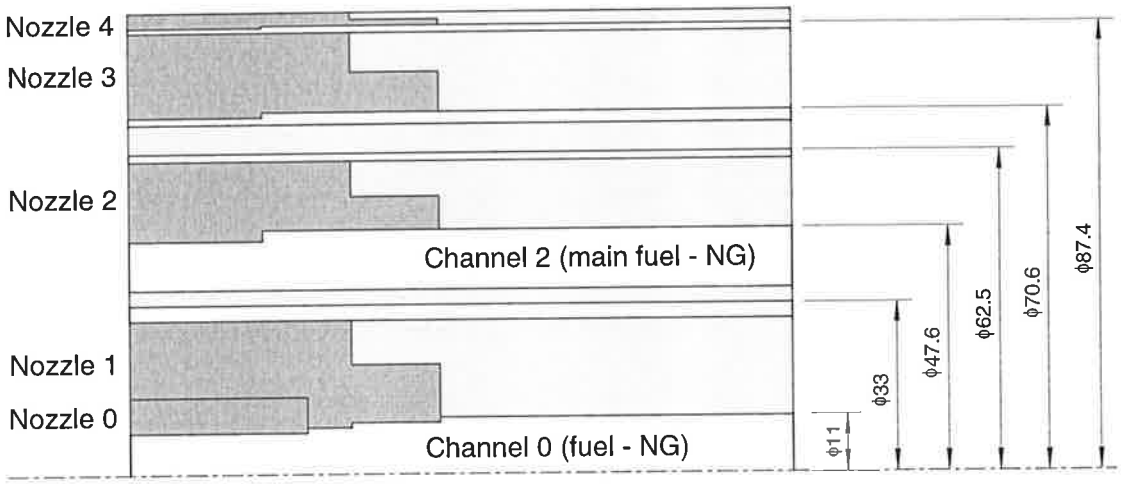

Figure 2-4. Schematic diagram of the multi-channel burner used for the pilot-scale cement kiln simulator experiments. The fuel and air channels are numbered outwards from the nozzle axis. Air is supplied through channels 1 (swirled by 45° vanes), 4 and 5 (unlabelled).

2.2 Isothermal Experiments

2.2.1 Planar Laser-Induced Fluorescence Fundamentals

The study of the diffusion of a passive scalar quantity, such as temperature or concentration, in a turbulent flow has been investigated widely because of its relevance to the fundamental understanding of fluid mechanics. It is also used in the design of industrial heat exchangers, mixing devices and combustion equipment. Planar Laser-Induced Fluorescence (PLIF) is a powerful and non-intrusive technique which is used in the present isothermal experiments to investigate the mixing of a passive scalar from different jets with their surroundings. One experiment uses PLIF as a flow visualisation technique and the other uses PLIF for quantitative measurement of concentration. Both isothermal experiments were performed in water using different laser sources and different fluorescent dyes to mark the jet flows.

PLIF involves recording the light emitted by a fluorescent substance within a measurement volume. The intensity of the fluorescence is proportional to the intensity of the light source and the concentration of the fluorescent substance within the measuring volume. The basic principles of PLIF as applied in the present experiments are well documented by authors such as Guilbault (1973) and Walker (1987). When excited by the absorption of a photon from a laser source, an electron of a fluorescent molecule is excited from the ground state to a higher singlet state. Within an extremely short time, of the order of 10ns, fluorescence occurs if the electron falls back to the ground state from the lowest vibrational level in the singlet state. The photon emitted as part of this de-excitation has a longer wavelength than the original absorbed photon. This process is known as Stokes fluorescence. During the delay between photon absorption and emission, the molecule spins randomly. Hence, for a typical fluorescent molecule, this ensures that the fluorescence is randomly polarised and the intensity is independent of direction.

The relationship between fluorescence intensity, F, and molar concentration, c, is given by:

$$F = \phi I_0(1 - e^{-\varepsilon bc}) \qquad \textbf{Equation 2-1.}$$

where ϕ is the quantum efficiency (the ratio of emitted to absorbed energy), I_0 is the incident laser intensity, ε is the molar absorbtivity and b is the absolute path length. Theoretically, the fluorescence intensity should increase with increasing incident light intensity. In practice, photo-decomposition of a fluorescent sample can occur, limiting the emitted intensity. For very dilute concentrations, Arcoumanis (1990) has shown that Equation 2-1 can be reduced to:

$$F = 2.3\phi I_0 \varepsilon bc \qquad \textbf{Equation 2-2.}$$

Hence, at low concentrations, the fluorescence intensity varies linearly with the molar concentration of fluorescent dye and laser light intensity, reaching a maximum at higher concentrations. According to Walker (1987), linearity exists over five orders of magnitude of dye concentration, beyond which attenuation is no longer small and the fluorescence intensity can actually decrease (the inner-cell effect). In order to correct for the effects of attenuation, a fluorescent dye and laser system for PLIF experiments must also obey the Beer-Lambert Law. The Beer-Lambert

law governs the absorption of light as a laser beam passes through a fluorescent medium, causing the fluorescence signal to diminish exponentially. Hence the choice of fluorescent dye and its concentration to match the laser source for linear characteristics with respect to intensity, concentration and absorption is crucial for obtaining accurate PLIF results.

Quantitative PLIF provides two-dimensional measurement of the distribution of concentration in a flow. To accomplish quantitative measurement, a laser beam is formed into a laser-sheet and aligned with the jet centreline or another selected geometric plane. The fluorescence generated by the interaction of the laser sheet and fluorescent dye hence marking the jet fluid is captured by a camera. Karasso (1994) notes that the PLIF signal or recorded image depends on the spectroscopic processes, the optical arrangement (laser sheet and collection optics) and the characteristics of the imaging sensor. For the purposes of quantitative concentration measurements, each of these factors affecting the PLIF signal must be quantified and corrected for by suitable image processing to yield the correct molar concentration of the fluorescent marker. For flow visualisation purposes, exact determination of the dye concentration is not required and hence corrections for the optics and imaging system are not necessary. In all cases it is highly desirable that the laser-dye system be linear with respect to concentration and absorption.

The major limitation of performing PLIF experiments in water is that the spatial resolution of the measurements is often much poorer than the smallest length scales in the flow being investigated. For measurements of the concentration of a passive scalar, the Batchelor scale represents the smallest physical scale at which scalar gradients exist in a turbulent flow. The Batchelor scale, λ_b, can be estimated using the expression:

$$\lambda_b = \alpha l_x Re^{-0.75} Sc^{-0.5} \qquad \textbf{Equation 2-3.}$$

where l_x is the local length scale of the flow, *Re* is the Reynolds number, *Sc* is the Schmidt number and α is a constant of proportionality. Adequate spatial resolution of PLIF experiments in water is extremely difficult to achieve because the Schmidt number of fluorescent dye in water is about $Sc \approx 1000$, approximately three orders of magnitude greater than in air. For example, typical PLIF measurement resolutions are of the order of 500μm, while typical Batchelor scales in liquid turbulent flows are of the order of 1μm. Breidenthal (1981) has shown that any measurement technique that does not resolve down to the Batchelor scale results in an over-estimate of the actual amount of mixing. Therefore, this presents a limitation and source of error in the present aqueous PLIF experiments.

2.2.2 Unconfined Flow Visualisation Using Two-Colour PLIF

Flow visualisation of the interaction between a precessing jet and a shaping jet was conducted using PLIF in a large water tank. The PLIF technique enabled the use of two different dyes, which fluoresce at different wavelengths, to mark the shaping and precessing jets and hence highlight the interaction of the jets and their respective influence on the combined flow mixing characteristics. The experimental arrangement is shown in Figure 2-5. PLIF image sequences and image processing results are presented in Section 3.3.

The PJ nozzle was directed vertically downwards into a water tank of dimensions 750×750×1500mm. The PJ nozzle chamber diameter is d_{PJ}=44mm so the confinement is very low. The nozzle was mounted on a frame separate from that of the tank. The nozzle exit was 800mm below the surface of the water, which was maintained at a constant level by a knife edge lip on the top of the tank that drains excess, overflowing fluid. The recirculating flow induced in the water tank is estimated to have a velocity of less than 1% of the local mean centreline velocity, based on the conservation of mass flux through a horizontal plane.

Three types of shaping jet were investigated. Of most interest is the Central Axial Jet (CAJ), located in the centrebody of the PJ nozzle. Various CAJ inserts allowed the length of the exit and the diameter of the jet to be changed so that the jet location and momentum could be varied independent of the flow rate. An Adjacent Axial Jet (AAJ) 5mm in diameter, located parallel to the PJ nozzle axis and 29mm from it, was also investigated. The d_{PJ}=44mm PJ nozzle (without CAJ) was used for the AAJ experiments and to investigate an Annular Shaping Jet (ASJ). For the ASJ experiments, the annular jet consisted of an annular gap created by a larger perspex pipe section located by three grub screws around the outside of the PJ nozzle (50mm inner diameter, 56mm outer diameter). The annular jet was supplied via a supply hose with meshes and screens to ensure the annular distribution of flow was uniform at the jet exit.

The dyes marking the jet flows were mixed in two separate 200 litre capacity storage tanks adjacent to the main working tank. A Fischer and Porter rotameter was used to measure the flow to the precessing jet nozzle, with a 1-GNSVT-64A float in a 1-27-G-10 tube. The flow to the shaping jet (CAJ, AAJ, or ASJ) was monitored by a Fischer and Porter rotameter with a 1/2-GSVT-44A float in a 1/2-27-G-10 tube. The nominal accuracy on the rotameters is ±2% of the maximum capacity. The flow rate through the CAJ was maintained as nearly constant as possible within the range of flow ratios investigated. By varying the mass flow rate through the PJ, the proportion of CAJ to total flow rate, and thus the momentum ratio, was altered.

A 1mm thick light sheet was produced from an Argon-Ion (Spectra Physics) laser. The laser was operated in multiline mode and the output power was estimated to be 2.3W. The laser sheet was aligned to pass through the centreline of the nozzle. The mixing characteristics in a plane perpendicular to the nozzle centreline were also investigated by rotating the laser optics through 90° to produce a horizontal laser sheet and hence a transverse cross-section through the flow field. Rhodamine B, (concentration: 0.045mg/L), which fluoresces red, marked the PJ fluid and fluorescein (concentration: 0.04mg/L), which fluoresces yellow, marked the CAJ fluid. Rhodamine 6G (concentration: 0.04mg/L) was also used to mark the precessing jet on its own. The concentrations used are within the limits recommended by Arcoumanis (1990) for a linear response to the incident light and also take into consid-

eration the higher quantum efficiency of fluorescein compared to rhodamine B. Hence, as the laser attenuation is not significant, for the purposes of flow visualisation the recorded signal intensity of the fluorescence can be used as a direct measure of the jet concentration.

Temporal sequences of the flow visualisation images were recorded on Hi-8 digital videotape by a "lipstick" video camera (Panasonic WV-KS152) with zoom lens (Sony 12.5-75mm *f*/1.8). A Pentax SLR camera with zoom lens (Tamron 80-200mm) using Fuji ISO-800 film was used to capture high quality still images of the flow field. Both cameras were positioned normal to the laser sheet, as close as possible together and focussed on the laser sheet so that their imaging windows were almost identical. The precessional frequency was sufficiently slow for the framing rate of the video camera (25 frames per second) to capture multiple images during each precessional cycle.

To minimise spurious illumination, data acquisition was performed with the room darkened. Two water filters were used in tandem to filter the supply water. Since the tank has no co-flow, the run time was limited to about two minutes. Background fluorescence became significant with longer run times. The tank water was emptied after each run and replaced with clean water for every jet condition investigated. An exposure time of t=1/1000s was sufficient for both video and photographic images to adequately freeze the motion of the exiting jets. A high-pass optical filter to remove scattered laser light from the acquired PLIF images was found to cause a significant reduction in signal intensity, making it extremely difficult to obtain acceptable images at an exposure time of 1/1000s. In addition, the high-pass filter reduced the visual contrast between the fluorescent colours of the two dyes in video and photographic images. Many other published PLIF investigations use some form of filter to reduce the effect of scattered laser light. However, Stapountzis *et al.* (1992) did not use a filter as they concluded that elastic scattering was small due to the similarity in shape of fluorescence versus distance curves. Prasad and Sreenivasan (1990) demonstrated that filtered and unfiltered PLIF results only differ in the peak wavelength detected and the measured intensity. Hence it was concluded that, for the purposes of flow visualisation, it was acceptable not to use a filter provided care was taken to minimise the presence of bubbles and particles so that the amount of scattered light was minimised.

Images were digitised using a colour frame grabber on a PC-compatible computer. The images were captured at a resolution of 640×480 pixels in RGB 8-bit colour format and stored as bitmaps.

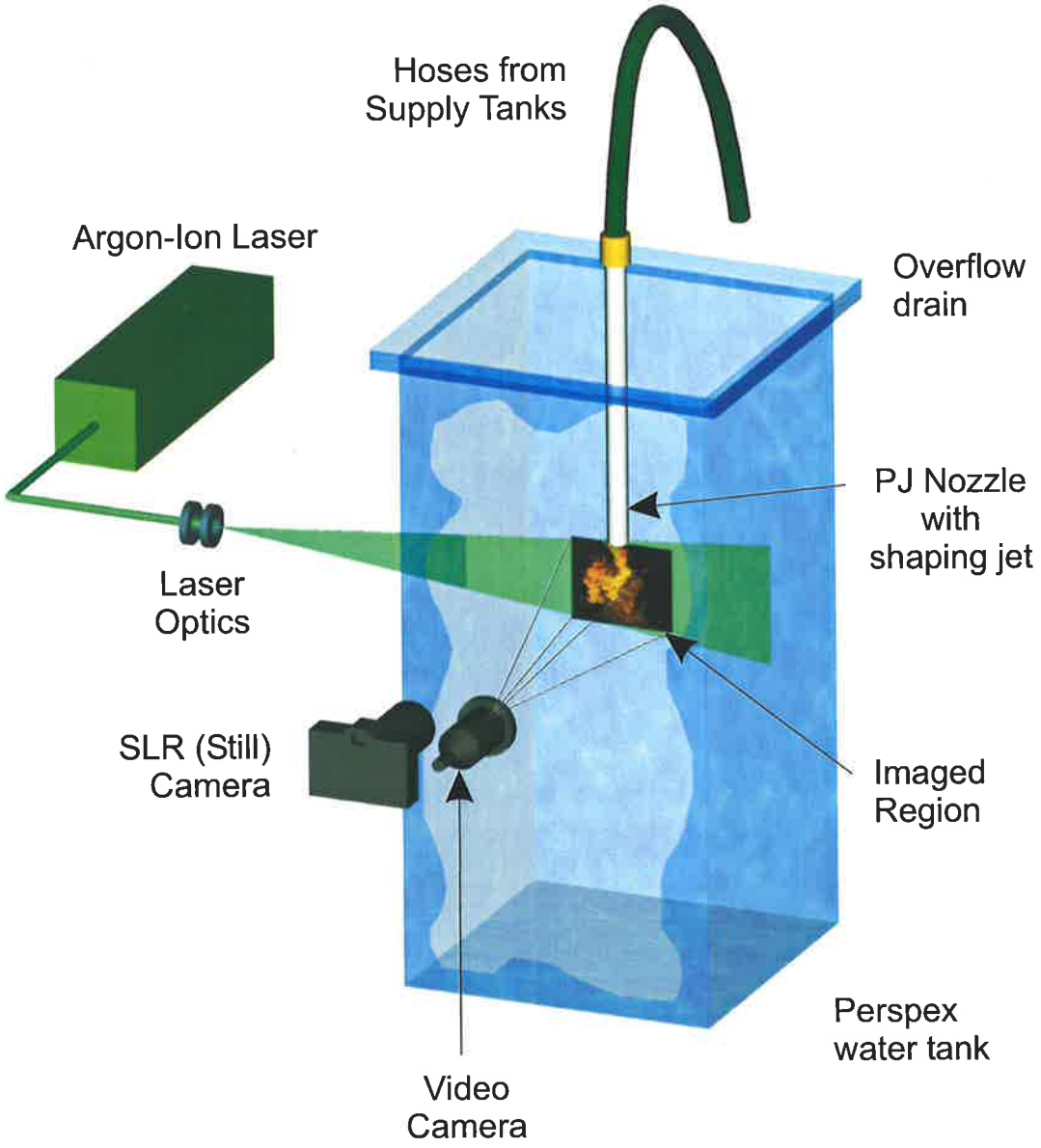

Figure 2-5. Schematic diagram of the experimental arrangement for flow visualisation of the interaction between a shaping jet and precessing jet by one and two colour planar laser-induced fluorescence on the nozzle centreline.

2.2.3 Confined Quantitative Concentration Measurement

2.2.3.1 Experimental Apparatus

Experiments to determine the effect of co-flow and confinement on the passive scalar mixing field from a precessing jet nozzle were undertaken in the water-tunnel facility shown in Figure 2-6. The effects of co-flow, confinement and central axial jet flow proportion on a precessing jet flow were determined by quantitative measurement of the jet concentration. A large region was imaged and statistical information has been calculated based on these measurements. Quantitative measurement of the jet concentration was achieved using a PLIF technique based on the laser-dye system used by Karasso and Mungal (1996, 1997a) for the investigation of shear layers. The results of the quantitative PLIF investigation are presented in Section 6.4 and Section 6.5.

The closed-circuit water-tunnel shown schematically in Figure 2-6 provided a uniform co-flow around the jet nozzles. The working section of the water-tunnel is made of perspex and has dimensions of 0.5×0.5×2.0m. Calibration of the water speed in the working section to the frequency of the pump recirculating the water in the tunnel ensures the co-flow velocity can be precisely controlled. A series of perforated plates, a honeycomb section and mesh screens are used to condition the flow which emerges from the pump outlet and provide a uniform velocity profile at the exit of the contraction section. A weir at the return end of the tunnel ensures a constant water level is maintained in the working section.

The d_{PJ}=38mm and d_{PJ}=28mm PJ nozzles described in Section 2.1.1.2 were used in the water-tunnel experiments. A simple jet flow produced from a 9.45mm diameter pipe, see Section 2.1.2.1, was used to validate the PLIF experimental technique. The precessing jet and simple jet nozzles were supplied with dye from a 200L external supply tank and controlled via a rotameter (Fischer and Porter 1-35-G-10 tube with a 1-GSVT-69 float) with a nominal accuracy of ±2% of the full scale. The flow to the central axial jet of the 38mm PJ nozzle was supplied from a second 200L external supply tank and also controlled via a rotameter (Fischer and Porter 3/4-27-G-10 tube with a 3/4-GNSVGT-54-T60 float). The same pumps used in the flow visualisation experiments supplied the jet fluid from the storage tanks through the rotameters and the jet nozzles.

The jet nozzles were mounted in the contraction section of the water-tunnel so that they were coincident with the axis of symmetry of the working section. The nozzles were mounted by two vertical airfoil sections to an overhead frame that was connected in turn to the water-tunnel frame. Two extra horizontal airfoil supports were required for the PJ nozzles to prevent horizontal vibration of the nozzle tip. A cylindrical shroud was used to enclose the supply pipe and hoses of the d_{PJ}=38mm PJ nozzle to avoid flow separation in the co-flow.

The effects of confinement were investigated by using three different acrylic perspex tube sections. The 2m long, 290mm internal diameter tube and the 390mm ID tube, consisting of two 0.5m long sections taped together, were mounted on vertical supports to ensure that they were concentric with the working section and jet centrelines. The 490mm ID tube did not require any external support as it filled the working section of the water-tunnel exactly. All perspex tubes had a wall thickness of 5mm. The leading edge of all tubes was shaped to form a parabolic profile

to minimise flow disturbance. The leading edge of each tube was located approximately 50mm downstream from the start of the working section. The exit plane of the jet nozzles was located approximately 150mm downstream from the same reference point. Just under one half of each tube was covered in black "contact" to provide a uniformly dark and non-reflective background for the captured images. As the index of refraction of water and perspex is nearly identical, any optical distortion due to the tubes is confined to the very edge of the cylinders. A perspex sheet was mounted on top of the free surface to provide a transition interface between the water and air and so avoid perturbations in the water surface that would otherwise distort the image detected by the camera.

The laser used for the quantitative PLIF experiments was a Nd:YAG laser (Coherent, Infinity 40-100). The fundamental wavelength of the laser was frequency doubled to 532nm and the pulse duration was approximately 3ns. The laser was operated at its maximum energy output (250mJ/pulse at 532nm) and a repetition rate of 10Hz for the simple jet experiments and 6Hz for the precessing jet experiments. The telescope in the laser head of the Infinity was removed to prevent possible back reflections which would damage other optical components in the laser system. The laser beam was focussed by a 1m focal length spherical lens located 1.25m from the jet centreline and then spread by a 12.5mm negative cylindrical lens. The horizontal laser sheet was approximately 0.5mm thick at the jet centreline and aligned to pass through the axis of the jet nozzle. A second Nd:YAG laser (Continuum Surelite II, 230mJ/pulse at 532nm) was used for some of the final experiments due to problems with the operation of the Infinity laser.

A biochemical molecular tracer, 5(&6) carboxy-2',7'-dichlorofluorescein, was used as the fluorescent marker for the quantitative PLIF experiments. This follows the finding of Karasso and Mungal (1997b) that this dye is the only one to display linear fluorescence behaviour with respect to concentration and absorption when excited by a Nd:YAG laser. However, in order to obtain a sufficiently high signal, a much higher concentration of 3.5mg/L (7.9×10^{-6} M) was used for the present experiments compared to the concentration used by Karasso of 0.6mg/L (1.4×10^{-6} M). Preliminary tests demonstrated that at the significantly higher dye concentration the carboxy-dichlorofluorescein dye still obeyed linear fluorescence characteristics. The only limitation of the dye is its high cost (~$100 per 100mg), which meant that the conservation of dye was a very important consideration in planning and implementing the experiments. Recent experiments by Law and Wang (2000), which investigated the mixing of a pipe jet in water, indicate that rhodamine B may also suitable (and much cheaper) for quantitative PLIF experiments using a Nd:YAG laser. However, this information was not available before the present experiments were planned and conducted.

The carboxy-dichlorofluorescein dye was dissolved in methanol in a glass beaker before being added to the main supply tank and thoroughly stirred to obtain a uniform concentration. If both supply tanks were required for the precessing jet and central axial jet, mixed dye was transferred from the main tank to the second tank to ensure a consistent concentration. The tunnel and supply tanks were filled with filtered tap water with a pH of 7.2. Due to the large volume of water in the water-tunnel it was not possible to buffer the system at a pH above 8. As carboxy-dichlorofluorescein is highly dependent on pH at this value, it is possible that there are some effects of pH on the present results.

The emitted fluorescence caused by the interaction of the laser light and fluorescent dye was collected at right angles to the laser sheet by a camera positioned above the water-tunnel. The image capture system consisted of a Kodak MegaPlus ES1.0, class 1 camera connected to a PC-compatible computer via an EPIX image capture board. The MegaPlus CCD array consists of 1008×1018 pixels of size 9.0×9.0μm with 10-bit greyscale resolution. Although the exact size of the imaged area is unique for each case, it is approximately 505×510mm so the nominal pixel resolution based on the imaged area is about 500×500μm. Space limitations above the tunnel and the large imaged area necessitated the use of a one inch, 12.5mm fixed focal length, *f*/1.4 Fujinon wide-angle lens (model CF12.5A). The lens was operated at an f-stop of *f*/2.0 to ensure images had a good signal to noise ratio. A long-pass filter (OG-550, Melles Griot) was placed in front of the camera lens to block scattered light from the laser, but allow the longer wavelength fluorescence to be detected by the camera.

The camera was triggered by the laser so that the fluorescence from each laser pulse was captured. Each image was then transferred into the computer's RAM. A maximum of 152 images could be held in the RAM before being transferred to the computer hard-drive for temporary storage. Due to the need to conserve dye, the jet was stopped while images were transferred from the RAM to the hard-drive. The camera was operated with the factory background setting deactivated and in single-channel mode to reduce any additional noise generated by the camera.

2.2.3.2 Experimental Procedure

Over forty individual jet conditions were investigated in the quantitative PLIF study. A number of different conditions were grouped together within an experimental "run", depending on the number of images required and the flow rate of the jet. The water-tunnel was refilled between each run and the camera and laser reset. Hence, to minimise experimental error between experimental runs, a systematic procedure was used to collect the raw experimental images and to obtain the data required for the image correction procedures. Once the major components of equipment were in position, the experimental procedure was as follows:

1. The jet was positioned in the water-tunnel and aligned with the centreline of the tunnel working section and confining duct, if used. The fluorescent dye was mixed in the supply tanks to the required concentration.
2. The laser sheet was aligned with the geometric axis of the jet.
3. A target test pattern was mounted on the jet nozzle in the imaged region. The test pattern was used to ensure the laser sheet was correctly aligned with the geometric axis, to check that the camera was focussed on the laser sheet and the camera was aligned correctly with the jet axis. It was also used as a reference to calculate the spatial resolution of the experiment.
4. A small perspex reference cell containing dye from the supply tanks was positioned in the laser sheet and image area, but outside the flow region. This reference cell was used to monitor the pulse-to-pulse fluctuations in the laser power and to calculate the reference concentration of 100% jet fluid.
5. Air bubbles were cleaned from all surfaces, the room was darkened and a batch of images was taken with the laser off to measure the background noise.

6. The laser was turned on and allowed to reach a stable operating condition. The room was darkened and a batch of images was taken with the laser on to measure the background noise.

7. If the experiment was with a precessing jet, a second reference cell was located near the nozzle exit. A batch of images was taken with the laser on to determine the reference concentration for these experiments. The second reference cell was removed.

8. The water-tunnel was set to the required co-flow velocity. The jet was set to the required flow rate and checked to ensure that the dye concentration was stable at the nozzle exit.

9. A batch of images was recorded.

10. The jet was turned off while the batch of images was transferred to the computer's hard-drive. Any air bubbles that appeared on the perspex surfaces were also removed in-between batches.

11. Steps 8 to 10 were repeated until the background concentration became significant (typically about 4 or 5 batches). Some water was emptied from the water-tunnel and refilled with fresh water.

12. Batches of experimental data were recorded until there was no dye left in the supply tanks.

13. The water-tunnel was turned off, the working section containing the confining cylinder was sealed using plastic lining and extra dye added to the enclosed volume. A small fish tank pump circulated the fluid in the sealed volume for approximately one hour to ensure a uniform dye concentration. A set of images was then recorded with the laser on to measure the spatial distribution of the laser sheet intensity.

14. The water-tunnel was emptied and cleaned and the recorded images were transferred to compact disc for permanent storage.

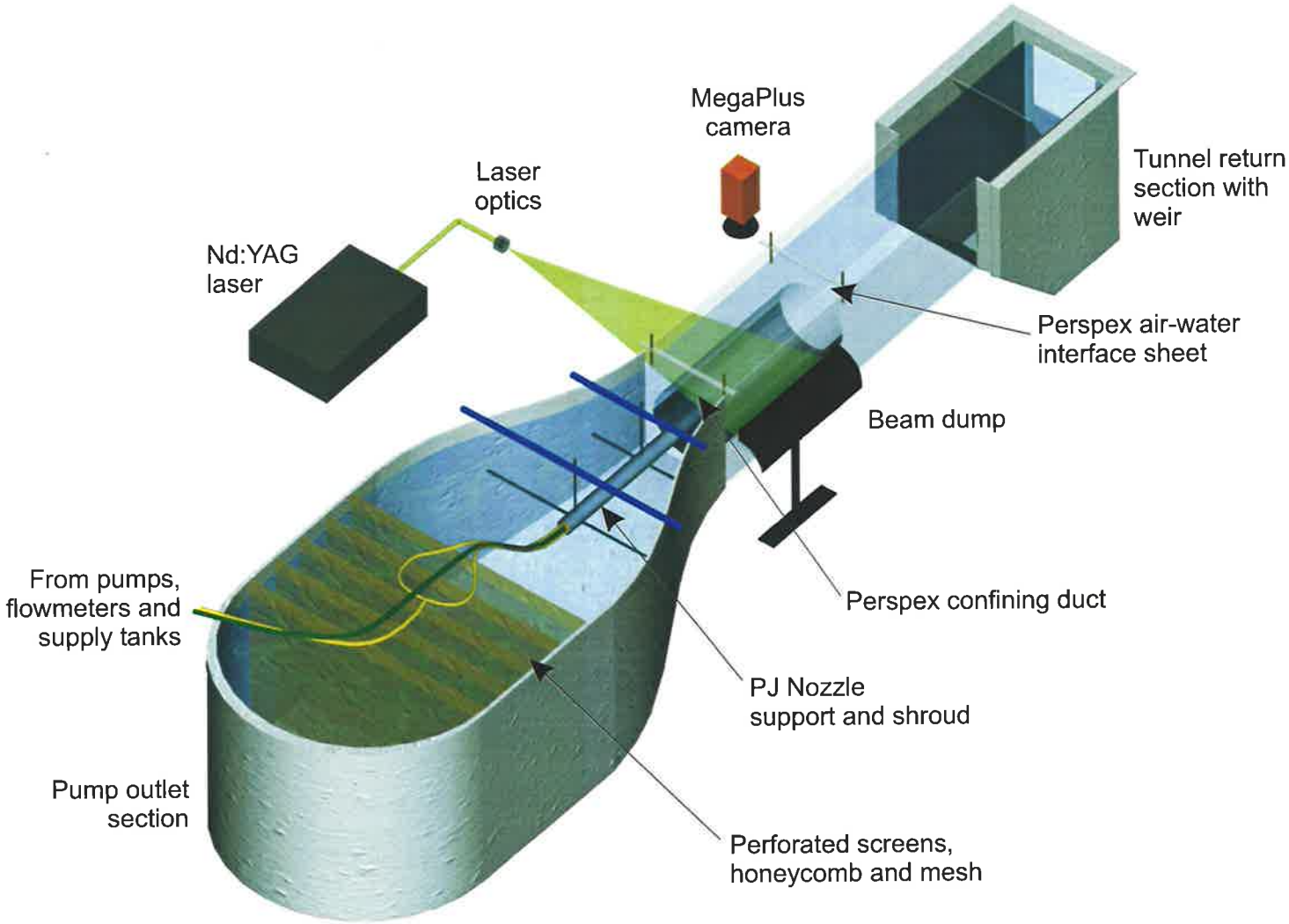

Figure 2-6. Schematic diagram of the water-tunnel facility and mounting arrangement of the precessing jet nozzle for the confined quantitative PLIF experiments.

2.3 Combustion Experiments

2.3.1 Unconfined Flame Visualisation

Visualisation of the visible flame envelope was performed to characterise the effect of the central axial jet on the macroscopic properties of the flame from a PJ nozzle. Visualisation was accomplished by taking "instantaneous" images of the flame using short exposure times and time-averaged images using long exposure times. The instantaneous and time-averaged photographs are presented in Section 4.3.

The geometry of the d_{PJ}=10mm PJ nozzle used for the unconfined flame visualisation experiments is detailed in Table 2-1. The nozzle tip was orientated vertically upwards underneath an exhaust extraction hood. The nozzle tip was positioned approximately 900mm above the floor and the exhaust hood is about 3m above the floor. The effect of cross-drafts was minimised by placing the PJ burner within a 3m×3m×2.5m enclosure of heavy duty welding curtains, with ventilation provided by a gap of 150mm at the bottom of the curtains. Black cloth was placed over the rear curtain to ensure a uniform dark background for the photographs.

Liquid Petroleum Gas (LPG) was used as the fuel for the flame visualisation following the results of Newbold *et al.* (1997), who found it produces a highly luminous flame of nearly uniform light intensity. LPG consists predominantly of propane (C_3H_8), with a nominal heating value of 80MJ/m^3. The bottled supply of fuel was controlled using two rotameters. The gas supply to the PJ nozzle was metered using a Fischer and Porter 1/2-27-G-10 tube with a 1/2-GUSVT-414 float and the gas supply to the CAJ was metered using a Fischer and Porter 1/2-27-G-10 tube with a 1/2-GUSVT-414 float. The nominal accuracy of both flow-meters is ±2% of the full scale. The total flow rate to the burner was maintained at a constant input equivalent to 20kW while the proportion of fuel to each jet was varied, to alter the flame shape.

The camera was positioned within the enclosure on a tripod and operated from outside the enclosure by means of a remote cable. Photographs were captured using a Canon EOS 50 SLR camera with a 35-105mm *f*/1.2 Ultrasonic lens. Instantaneous images of the flame structure were acquired with an exposure time of t=1/250s and an aperture of *f*/6.7 or *f*/8 using ISO-400 colour film. Time-averaged images of the flame were acquired with an exposure time of t=8s and an aperture of *f*/22 using ISO-100 colour film. Images were also taken zoomed in on the base of the flame with an exposure time of t=8s and an aperture setting of *f*/27 using ISO-100 colour film. Each set of images was developed using identical processing settings. The images were digitised using a Hewlett-Packard ScanJet 6300C colour scanner and identical scanner settings for each image set.

2.3.2 Pilot-Scale Cement Kiln Experiments

The confined combustion experiments were conducted in the 2MW cement kiln simulator facility at the International Flame Research Foundation (IFRF), IJmuiden, The Netherlands, shown in Figure 2-7. The experiments enabled the flame characteristics from a confined precessing jet burner to be quantitatively determined in an environment as close as possible to that which exists in a real cement kiln. The temperature, heat-flux and emission measurements from the pilot-scale combustion investigations are discussed in Section 5.3.

A comprehensive description of the IFRF pilot-scale kiln simulator facility is given by van de Kamp and Daimon (1996) and van de Kamp (1996). The facility is a refractory lined cylindrical combustor with air pre-heat and probe access. It is non-rotating and does not make product. The load is simulated by a water-cooled shell designed so that the typical heat flux is comparable with that in a full-scale cement kiln. However, the heat flux through the shell cannot be controlled independently from the flame since the possible variation of the cooling water temperature is negligible compared to the temperature differential across the refractory lining, which is about 1000°K. The test section of the combustor has an internal diameter of 756mm and a length to internal diameter ratio of 15. Thus the facility simulates a region corresponding to the "burning zone" (a term referring to the exothermic reaction in the clinker and not to the flame) of a cement kiln or the calcination region of a lime kiln. The kiln shell is constructed of fifteen water-cooled segments, each 707mm in length. Six access ports were used for in-flame measurements.

In the present investigation the thermal input based on fuel was 2.0MW and the co-flowing combustion (or "secondary") air temperature was set to 640°C for the comparison of a precessing jet burner and a multi-channel burner. The combustion air was heated by a gas-fired pre-combustor utilising a low NO_x burner to minimise NO_x emissions entering the kiln. Pure oxygen is added to the flue gases from the pre-combustor to correct the oxygen concentration back to 21% by volume. The combustion air passes through a "U" bend between the pre-combustor and kiln. Two high pressure-drop "baffle plates", made from castable refractory with 40mm diameter holes to give a blockage ratio of 80%, are located at the inlet to the kiln. The baffle plates are intended to correct the non-uniformities and secondary patterns introduced into the combustion air flow by the bends.

The experimental burners were scaled relative to typical full scale conditions using the constant velocity similarity criteria (Smart and Morgan, 1994). The nozzles were mounted within a refractory-lined and water cooled housing and the burner tip was inserted a distance of 475mm (0.6 kiln diameters or 12 baffle hole diameters) downstream from the "baffle plates" in order to minimise the effect of the turbulence generated by the baffle plate on the flame. Sufficient time was allowed between each burner configuration to ensure the cement kiln simulator reached a steady state condition.

All measurements were conducted using IFRF designed equipment (Chedaille and Braud, 1972). Radiative heat flux was measured using a calibrated stainless steel water-cooled hollow ellipsoidal total radiation pyrometer inserted into the kiln through access ports. The instrument measures total hemi-spherical radiation and thus includes the combined incident radiation from the flame and the furnace walls. The furnace refractory wall temperature was measured using surface mounted thermocouples. From these temperatures and measurement of the cooling water temperature, in combination with the physical properties of the refractory brick, a simple heat bal-

ance can be used to determine the local heat flux. An alternative measure of the total heat flux is obtained by summing the contributions of each ellipsoidal radiation measurement, although this includes the total radiation from the flame and that re-radiated from the walls.

In-flame gas species were sampled and water-quenched with a stainless steel water-cooled probe. On-line instrumentation was used to measure NO_x, O_2, CO and CO_2. Measurements of the in-flame gas species concentration were conducted at six axial positions downstream of the burner tip. At each axial position ten radial measurements were made for most of the flames investigated in detail. The flue gas emissions were measured just upstream from the flue gas exit duct on the combustion chamber axis and thus are only an accurate measure of the total emissions if the profile is uniform. A spatially averaged measure of emissions has therefore been calculated for comparison with the single point data where possible.

All flame input settings with the exception of the exact supply settings for the CAJ were logged on the IFRF's facility data acquisition system. Wall temperatures, cooling water measurements for each segment and emissions were also logged.

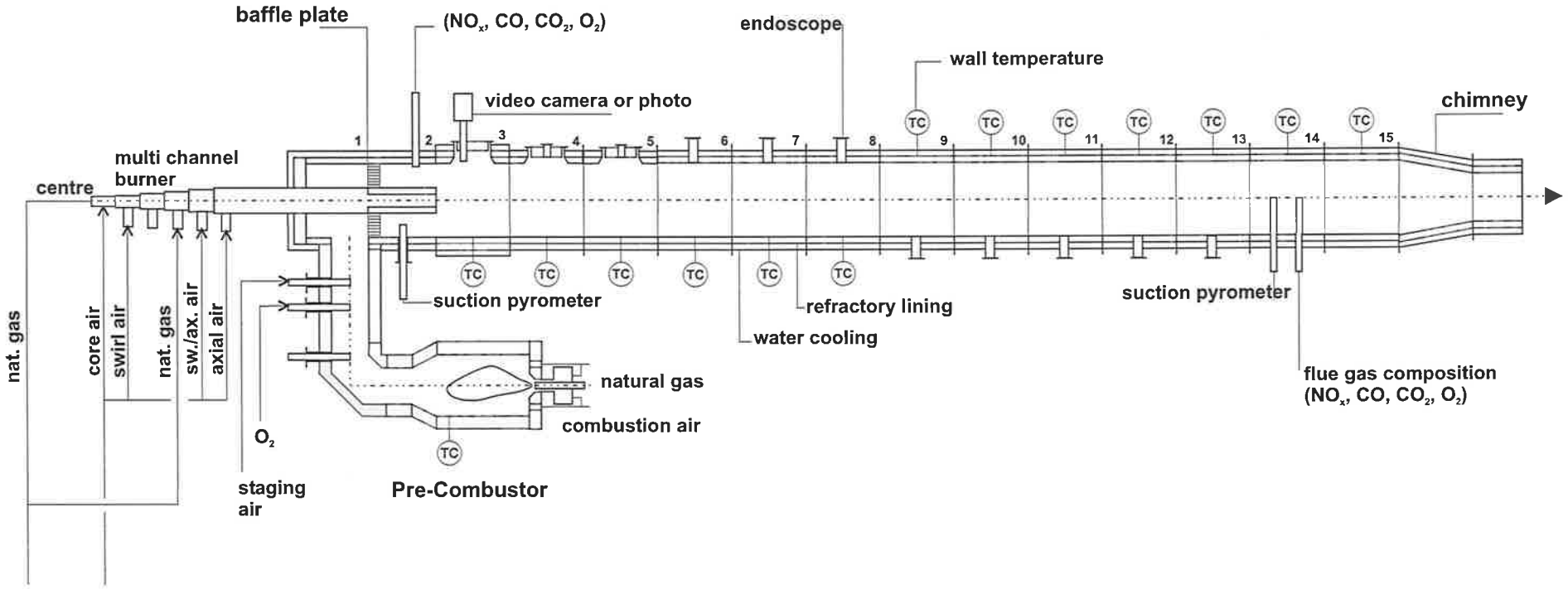

Figure 2-7. Schematic diagram of the pilot-scale cement kiln simulator facility at the International Flame Research Foundation showing the main kiln section, pre-combustor and supply lines for the IFRF multi-channel burner.

Chapter 3

Flow Visualisation of the Interaction Between a Precessing Jet and a Shaping Jet

3.1 Introduction

The use of a jet in combination with another flow to control the shape of a flame is not new. Investigations of bluff-body flames, in which fuel is supplied through a central jet and air through a concentric annular jet separated from the central jet by a bluff-body, have shown that a wide range of flame shapes can be produced, from "fuel-jet flow dominated" to "air-flow dominated" (Namazian *et al.*, 1992). Li and Tankin (1987) found that the penetration of the fuel jet into the bluff-body recirculation zone and hence the location of the fuel jet stagnation point correlates with the momentum ratio of the fuel jet to air flow and the diameter ratio of the fuel jet to bluff-body. An annular swirling flow concentric with a fuel jet resembles, perhaps more closely, the present nozzle configuration. Chen *et al.* (1990) derived a momentum ratio based similarity parameter which enables flows from a swirl nozzle with central jet to be compared with equivalent flows from bluff-body nozzles. Chen *et al.* (1990) suggest that the ratio of vortex-induced momentum ratio to the fuel jet momentum, Γ^*, is a universal parameter for recirculating flows.

Industrial installations of the PJ nozzle have demonstrated that a PJ flow combined with a secondary jet can provide flame shaping and alter the heat flux distribution in a rotary kiln (Hill *et al.*, 1995). Commercial installations have trialled annular jets, adjacent axial jets and central axial jets. A constant heat output from a PJ burner is achieved by distributing the total flow rate between the PJ nozzle and the shaping jet at different mass proportions to achieve different flame shapes. However no systematic investigation of the interaction between a shaping jet and a precessing jet has been performed previously. Hence one aim of the present experiments is to conduct such a systematic investigation and to assess the effectiveness of alternative means of shaping the flow from a PJ nozzle. The change in mixing characteristics of the combined flow at different proportions of flow through each jet are also assessed and a parameter that characterises the change in mixing characteristics determined.

As the technical requirements to quantify scalar mixing in flames are far more extreme than for isothermal conditions, investigations of the mixing characteristics of burner designs are often first performed in isothermal (non-reacting) conditions. Furthermore, before proceeding to a detailed quantitative study, it is often wise to undertake a preliminary qualitative study. The present experiments were hence designed to investigate a wide range of jet conditions and nozzle configurations using a flow visualisation technique. A significant advantage of flow visualisation is the ability to rapidly and relatively simply acquire instantaneous and spatially dense information about large flow regions (Pashereit *et al.*, 1992). Flow visualisation is also more adept at revealing information about

large-scale coherent motions, such as those first detected by Brown and Roshko (1974), than are single point techniques.

Planar Laser-Induced Fluorescence (PLIF) has been widely used for flow visualisation by other researchers to investigate turbulent flows, most commonly using the passive scalar property of fluorescent dyes for concentration measurements. For example, Yoda and Fiedler (1996) used PLIF for flow visualisation of a round jet in a uniform counter flow and Dahm and Dimotakis (1987) used a PLIF technique in water to demonstrate the controlling role played by large-scale structures in mixing and entrainment processes. Dahm *et al.* (1992) used two dyes which fluoresce at different wavelengths to visualize the structure of vortex patterns from coaxial jets and the dynamics of their interactions. PLIF was used for the present experiments principally for this purpose, so that the precessing jet and the shaping jet could be marked separately and hence their interaction examined. Conducting the experiments in water also results in a 14-fold reduction in flow velocities for the same Reynolds number as in air, allowing the use of less expensive imaging equipment. Furthermore, the same PLIF technique has also been used previously within the Department of Mechanical Engineering by Newbold (1997) and Schneider (1997) to investigate the flow characteristics of fluidic and mechanically rotated precessing jet flows.

3.2 Experimental Conditions

Details of the apparatus and jet nozzles used for the flow visualisation PLIF experiments are presented in Section 2.2.2. Briefly, an Argon-Ion laser was used to create a thin laser sheet aligned with the centreline of the jet nozzle. The nozzle was directed vertically downwards into a large, quiescent water tank. Rhodamine B was used to mark the precessing jet fluid and fluorescein was used to mark the shaping jet fluid. The fluorescence due to the excitation of the fluorescent dye by the laser source was captured by a video camera and a still camera positioned at right angles to the laser sheet. No optical filter was used since this reduced the detected signal intensity and the contrast between the fluorescence from the two dyes. The imaged area is approximately the same for all conditions, about 240×180mm. Experiments were also performed with the laser sheet forming a transverse cross-section through the jet by orientating the laser sheet perpendicular to the nozzle centreline and placing the video camera underneath the water tank.

The experimental program was devised to focus on the shaping characteristics of a Central Axial Jet (CAJ) issuing from the centre-body of the PJ nozzle, because industrial trials have found this method to be effective at controlling the flame shape. The effects of an Annular Shaping Jet (ASJ) and Adjacent Axial Jet (AAJ) on shaping the flow from the PJ nozzle were also studied as these methods have been applied in operating rotary kilns. The PJ nozzle used for all the present experiments has a chamber diameter of d_{PJ}=44mm and a sudden contraction orifice at the inlet to the PJ nozzle chamber. Details of the nozzle and shaping jet designs are presented in Section 2.1.1.

The mass ratio of shaping jet flow rate to the total jet flow rate is defined by $\psi_{shaping} = \dot{m}_{shaping}/(\quad\quad_{shaping})$. Most experiments were performed at three ratios of shaping jet to PJ flow, $\psi_{shaping}$=15%, 30% and 40%. These proportions matched typical ratios used in industrial installations of the PJ nozzle and also spanned the range of flow types which could be generated by the experimental facilities. Other intermediate values of $\psi_{shaping}$ were investigated for some configurations. In the case of the CAJ and AAJ experiments, the mass flow through the shaping jet was maintained as close to a constant value as possible and hence only the precessing jet component of the total flow rate was altered. For the ASJ, higher flow proportions were investigated and the jet flow rates were slightly different. The conditions for each shaping jet and corresponding value of $\psi_{shaping}$ are shown in Table 3-1. For the CAJ, the effect of jet momentum was also examined by varying the CAJ diameter for the same mass flow rate. The CAJ diameters investigated were 4mm, 5mm and 6.2mm. The effect of the axial position of the CAJ exit was examined by using interchangeable jet inserts for the 5mm CAJ that protrude 1mm, 5mm and 10mm from the surface of the PJ nozzle centre-body.

Table 3-1 shows that the Reynolds numbers of the precessing jet, based on conditions at the inlet to the nozzle chamber, was varied between 18,200 and 49,600 depending on the shaping jet proportion. Precession was ensured for $\psi_{shaping}$=40%, when the Reynolds number was below the critical value of 20,000 for guaranteed precession, by first increasing the flow rate to exceed the critical value and then lowering it to the required setting. The ratio of shaping jet momentum to the sum of precessing jet and shaping jet momentum, denoted by the symbol $\Gamma_{shaping}=G_{shaping}/(G_{PJ}+G_{shaping})$, is also included in Table 3-1 as a momentum ratio is expected to be the dominant parameter controlling the combined jet mixing, rather than the mass ratio, $\psi_{shaping}$. The present form of the

momentum ratio was selected as it spans a bounded range between 0 (precessing jet only) to 1 (shaping jet only) rather than an unbounded range produced by a ratio of the form $G_{shaping}/G_{PJ}$, which approaches infinity as $\psi_{shaping}$ approaches 100%. The momentum of the shaping jet is calculated based on the bulk flow properties at the jet exit. The momentum of the precessing jet is calculated at the inlet to the PJ chamber, as the flow conditions are well defined at this plane. The momentum at the PJ nozzle exit, although physically the most appropriate scaling condition, cannot be calculated due to the poorly defined character of the jet at the exit plane (Nathan and Luxton, 1991).

The frequency of precessing of jet precession varies with flow rate, according to the definition of the Strouhal number for the PJ nozzle given by Hill *et al.* (1992) in Equation 1-2. Hence for the present experiments f_p is estimated to vary between 0.7Hz and 2.3Hz. Newbold (1997) has shown that, despite the precession frequency and flow rate changing with Reynolds number, the spreading angle of the precessing jet flow is only weakly affected within the range presently investigated.

It is widely known that a range of natural frequencies exist in a simple jet flow. It is necessary to assess whether these frequencies in the shaping jet can couple with those in the PJ flow. Past research has shown that the mixing of jets can be altered by applying axisymmetric forcing, characterised by the Strouhal number, $St_{ex}=fd/U$, where d is the jet exit diameter, U is initial jet velocity and f is the frequency of excitation. Taking the forcing frequency of the CAJ to be the frequency of precession, the Strouhal number of the "excitation" of the central axial jet, St_{ex}, can be reduced to:

$$St_{ex} = 0.08 \times \sqrt{\frac{\pi}{4}} \times \sqrt{\frac{G_{...}}{G_{CAJ}}} \times \left(\quad \right)^2 \qquad \textbf{Equation 3-1.}$$

The excitation Strouhal number for the central axial jet is shown for the different jet diameters and shaping jet proportions in Table 3-1. The results demonstrate that the Strouhal number of precession is several orders of magnitude lower at all conditions than the excitation Strouhal numbers associated with the vortex structures in a jet and the Strouhal number range for axisymmetric excitation of jet structures, St_{ex}=0.1-0.9 (Crow and Champagne, 1971; Lovett and Turns, 1992). However Badri Narayanan (1987) has shown that the Strouhal number for strong excitation is quite different from the one associated with the natural disturbances in a jet. This was demonstrated by producing significantly different mixing from a plane jet using twin vane excitation at a Strouhal number of St_{ex}=0.037, based on the jet width. This Strouhal number is still an order of magnitude greater than the excitation Strouhal number due to the precession of the emerging jet from the PJ nozzle, $0.0005< St_{ex} <0.007$. Hence excitation of large-scale structures in the CAJ by the precessing jet, if present, occurs at a much lower Strouhal number than for any of the excitation mechanisms outlined above. As the exiting jet is a three-dimensional fluidic forcing mechanism and the precession frequency of the exiting jet is not constant, so the characteristic excitation Strouhal number changes, such excitation of the CAJ may still have an effect on the combined jet mixing characteristics.

Description	$\Psi_{shaping}$ (%)	Precessing Jet	Shaping Jet Conditions		
		Reynolds number	Reynolds number	$\Gamma_{CAJ} = \frac{G_{shaping}}{G_{PJ}+G_{shaping}}$	St_{ex}
PJ Only	0	49,600	0	0	0
4mm CAJ	15	49,600	16,400	0.10	0.0018
	30	20,400	16,400	0.39	0.0007
	40	18,200	22,700	0.61	0.0005
5mm CAJ/5mm AAJ	15	49,600	13,000	0.07	0.0035
	30	20,400	13,000	0.29	0.0014
	40	18,200	18,000	0.49	0.0009
6mm CAJ	15	49,600	10,300	0.04	0.0070
	30	20,400	10,300	0.21	0.0028
	40	18,200	14,300	0.38	0.0018
ASJ	15	34,500	1,100	0.02	-
	40	24,400	1,100	0.04	-
	50	20,300	1,400	0.08	-

Table 3-1. Experimental configurations and conditions for the PLIF flow visualisation experiments for different shaping jets and different shaping jet proportions, $\Psi_{shaping} = \dot{m}_{shaping}/(\dot{m}_{PJ} + \dot{m}_{shaping})$. The momentum of the PJ nozzle, G_{PJ}, is calculated at the chamber inlet; the momentum of the shaping jets, G_{CAJ}, is calculated at the jet exit. St_{ex} is the Strouhal number of the "excitation" of the central axial jet based on the characteristic frequency of the precessing jet motion.

3.3 Flow Visualisation Results

Sequences from the video footage of the flow visualisation experiments are shown in Figure 3-1 to Figure 3-9. The images were obtained by frame grabbing each image from the video onto a computer and digitally enhancing the colour characteristics of each image sequence to improve the contrast between the dyes marking the precessing jet and shaping jet fluid. The PJ nozzle can be seen protruding into the top of the imaged region in each sequence.

3.3.1 Characteristics of the Combined Central Axial Jet and Precessing Jet

The video sequences and high quality still photographs shown in Figure 3-1 to Figure 3-7 highlight the dramatic differences in the structure of the combined flow-field as the proportion of central axial jet flow to total flow, ψ_{CAJ}, is varied. The images shown are for the 5mm CAJ diameter nozzle with the intermediate length (5mm protrusion) insert. In the case of the precessing jet flow alone, Figure 3-1, the visually coherent structures generated immediately downstream from the nozzle are of a very large scale, spanning the width of the flow. The precession of the exiting jet is visible as a flapping motion of the jet to the left and right due to the laser sheet slicing through the three-dimensional movement of the jet. The initial spreading of the jet in the plane of the laser sheet is very wide and large-scale structures emerge at a high angle to the nozzle centreline. The large-scale structures cause ambient fluid, shown as large dark pockets, to be entrained into the jet very close to the nozzle exit. These features are similar to those observed by Newbold (1997).

The effect of the CAJ at ψ_{CAJ}=15% for the 5mm central axial jet (Γ_{CAJ}=0.07) is illustrated in the still image, Figure 3-2a, and the sequence of video images in Figure 3-3. A noticeable change in flow characteristics can be observed relative to the ψ_{CAJ}=0% case. The flow field retains the dominant features of the precessing jet flow acting alone, as can be seen from the presence of the large-scale flow structures and the out-of-plane motions, indicating large entrainment of ambient fluid. The two jets interact strongly, causing the jet fluid from the CAJ to also precess strongly, although it does not spread as widely as the precessing jet fluid. The relatively high velocity of the CAJ causes the convection velocity of the large-scale structures to increase and the average size of these structures to decrease, although they still span the full extent of the flow. The spreading of the combined jet flow has been reduced and although some very large structures are expected because the precessing jet fluid emerges at a wide angle, many of the smaller structures are drawn toward the CAJ and nozzle centreline.

At ψ_{CAJ}=30% for the 5mm diameter CAJ (Γ_{CAJ}=0.29), the character of the flow is very different, see Figure 3-2b and Figure 3-4. In this case, the flow field is now dominated by the CAJ. While the two jets still interact strongly, the jet fluid from the CAJ appears to penetrate through the PJ flow. Hence the CAJ precesses only weakly and does not deviate from the nozzle axis significantly. The spreading of the combined jet flow has been decreased significantly, as has the size of the largest-scale structures. The precessing jet still has a wide spreading angle within the immediate region of the nozzle exit. The spreading of the PJ further downstream is curtailed by the central axial jet, which entrains some of the precessing jet fluid, although much of the precessing jet fluid remains distinct.

At ψ_{CAJ}=40% for the 5mm diameter CAJ (Γ_{CAJ}=0.49), the flow field is completely dominated by the CAJ flow, see Figure 3-5. The CAJ fluid does not exhibit any significant precession and any deflection from the centreline is small. The precessing jet generates very few large-scale structures, and those that do leave the nozzle at an angle to the centreline are entrained back into the central axial jet fluid by the time they leave the viewing area.

The video footage of a cross-section through the combined flow reveals additional information about the interaction of the jets from the PJ nozzle and the CAJ. The images shown in Figure 3-6 and Figure 3-7 were obtained one chamber diameter (d_{PJ}=44mm) downstream from the PJ nozzle exit. At ψ_{CAJ}=15% (Γ_{CAJ}=0.07), Figure 3-6 shows clearly the red fluid from the precessing jet moving about the nozzle centreline in a generally anti-clockwise direction. However, the movement of the jet is not smooth or regular. Instead, the jet appears to intermittently "burst" through the plane of the laser sheet and "bounce" around the viewing area with a chaotic component so that the jet is even observed to cross the centreline of the nozzle on some occasions. This is consistent with the observations for 100% of the total flow through the PJ nozzle. Close examination of the pattern of movement of the jet fluid also suggests a triangular pattern to the jet bursts and path. The triangular pattern coincides with the gaps between the three feed pipes to the centre-body. Hence it appears that drag exerted by the CAJ feed pipes on the PJ flow is significant, causing the jet to favour the locations between the feed pipes. The strong interaction between the PJ and the shaping jet noted previously is also illustrated distinctly in Figure 3-6. The two jets clearly move together and the CAJ fluid also appears to be "pushed" by the fluid from the PJ nozzle, so that it leads the movement of the "bursts" of fluid across the end-view.

The cross-sectional PLIF experiments also reveal the distinct change in the flow field when ψ_{CAJ} is changed from 15% to 30% of the total flow for the 5mm CAJ (momentum ratio changes from Γ_{CAJ}=0.07 to Γ_{CAJ}=0.29). For ψ_{CAJ}=30%, the CAJ wobbles slightly as a large PJ structure passes and although some CAJ fluid is drawn into the PJ fluid, the majority remains concentrated around the nozzle centreline, see Figure 3-7. The triangular pattern of precessing jet movement is again observed.

The results of the flow visualisation experiments using the long 5mm diameter CAJ insert (10mm protrusion) and short 5mm diameter CAJ insert (1mm protrusion) are not included in the current presentation. The flow visualisation images indicate that the axial location of the CAJ has a small but noticeable effect on the mixing from a PJ nozzle. At low values of ψ_{CAJ}, the overall flow field appears similar but jet fluid from the short insert is broken up rapidly and quickly mixes with the PJ structures while with the long CAJ insert, the jet fluid from the CAJ and PJ remain more distinct. At higher values of ψ_{CAJ}, the difference in the combined structures is less clear and the only discrepancy seems to be a reduction in the spreading of the jet with the long CAJ insert. Hence moving the axial position of the CAJ exit downstream appears to decreases the interaction and merging of the CAJ and PJ fluid, which visually makes the combined flow appear to be more CAJ dominated at the same mass flow proportion and momentum ratio.

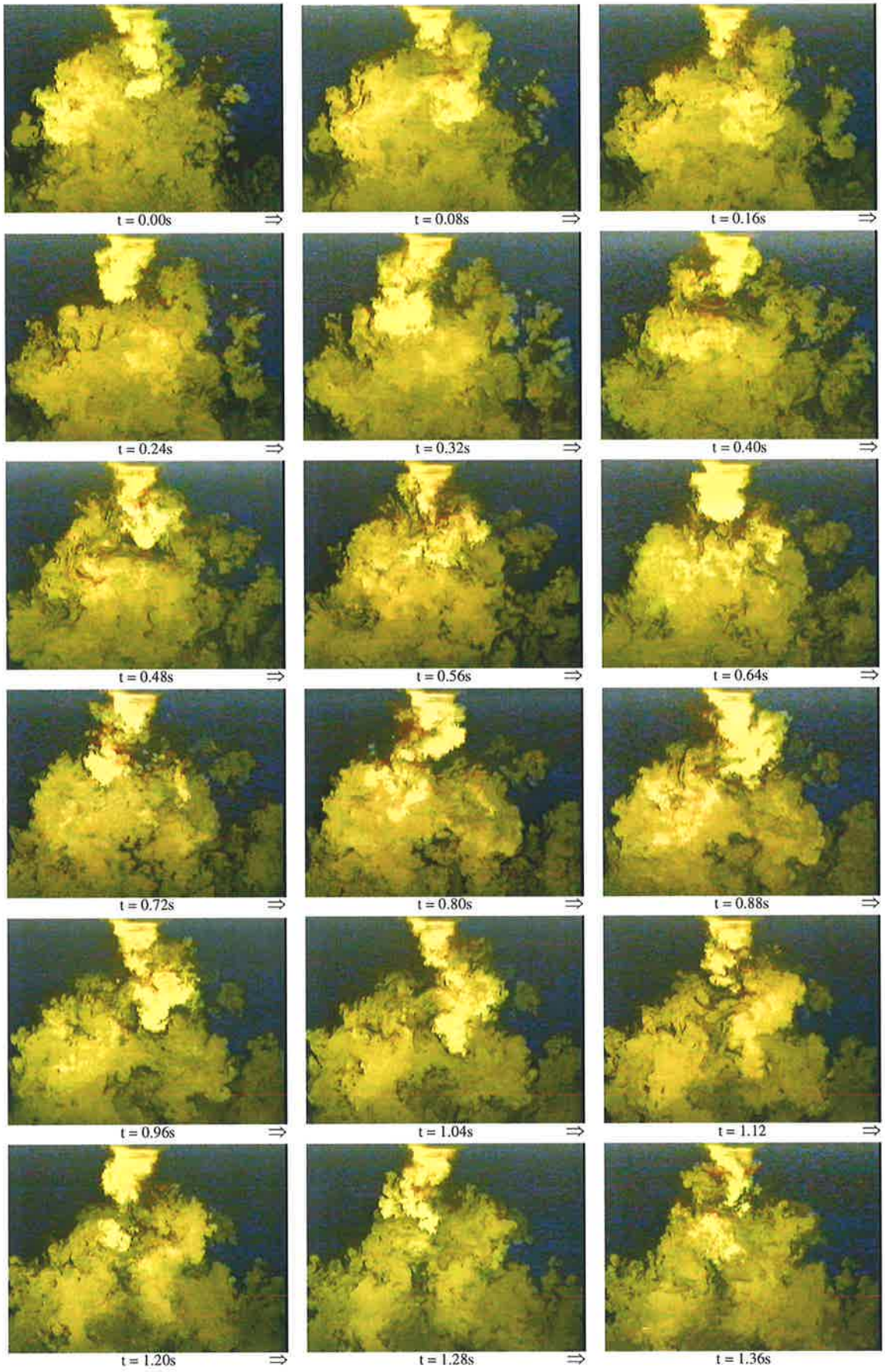

Figure 3-1. Video images of precessing jet flow only, ψ_{CAJ}=0%, Γ_{CAJ}=0, from the d_{PJ}=44mm PJ nozzle (dye: rhodamine 6G, optical filter used). Refer to Table 3-1 for jet conditions. Every second frame shown, t=1/1000s exposure time.

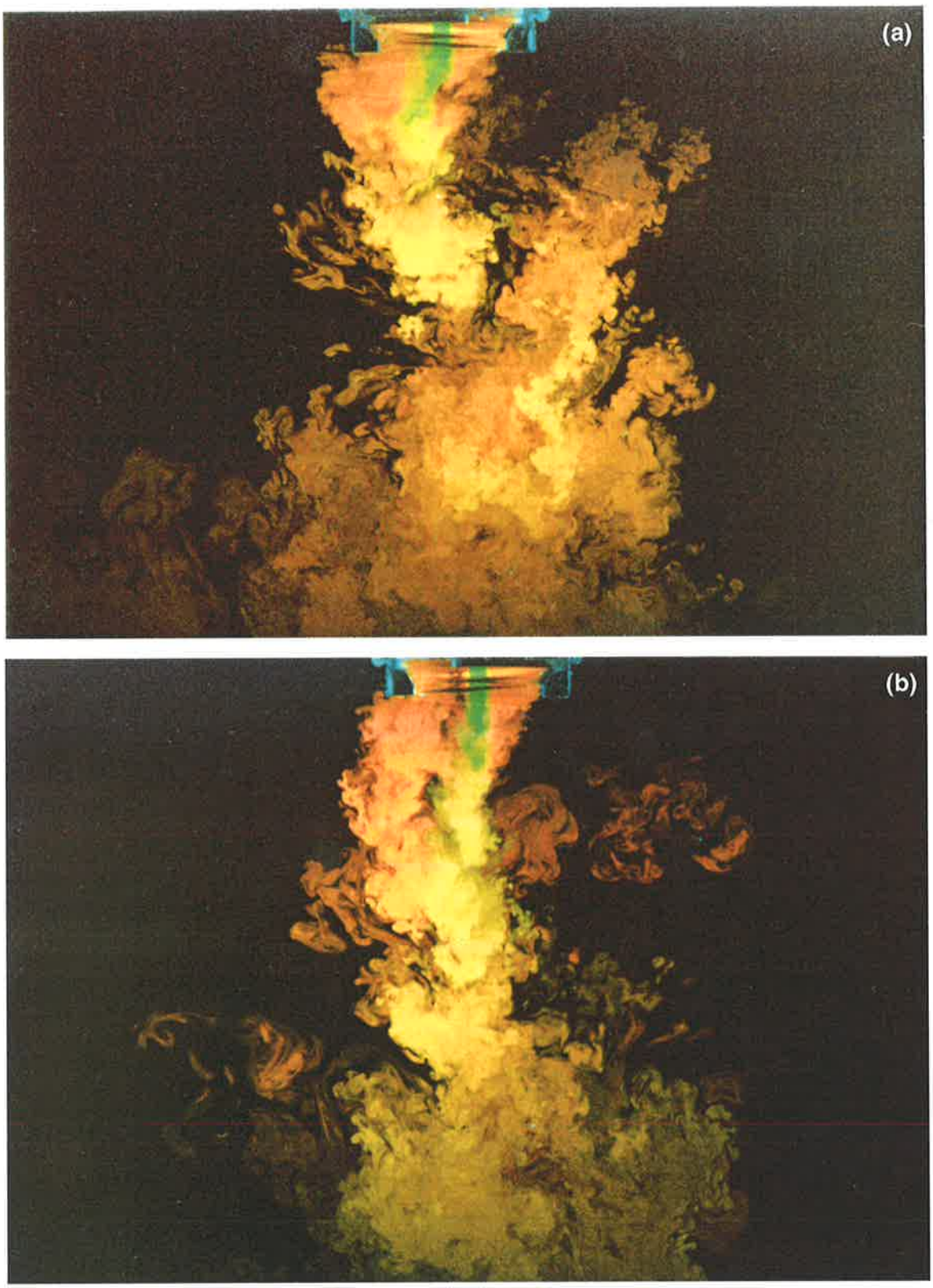

Figure 3-2. High quality flow visualisation photographs of the interaction of the 5mm diameter, intermediate length insert, central axial jet and precessing jet fluid. Pure PJ fluid is red, pure CAJ fluid is yellow, t=1/1000s exposure time. Refer to Table 3-1 for detailed conditions: (a) ψ_{CAJ}=15%, Γ_{CAJ}=0.07; (b) ψ_{CAJ}=30%, Γ_{CAJ}=0.4.

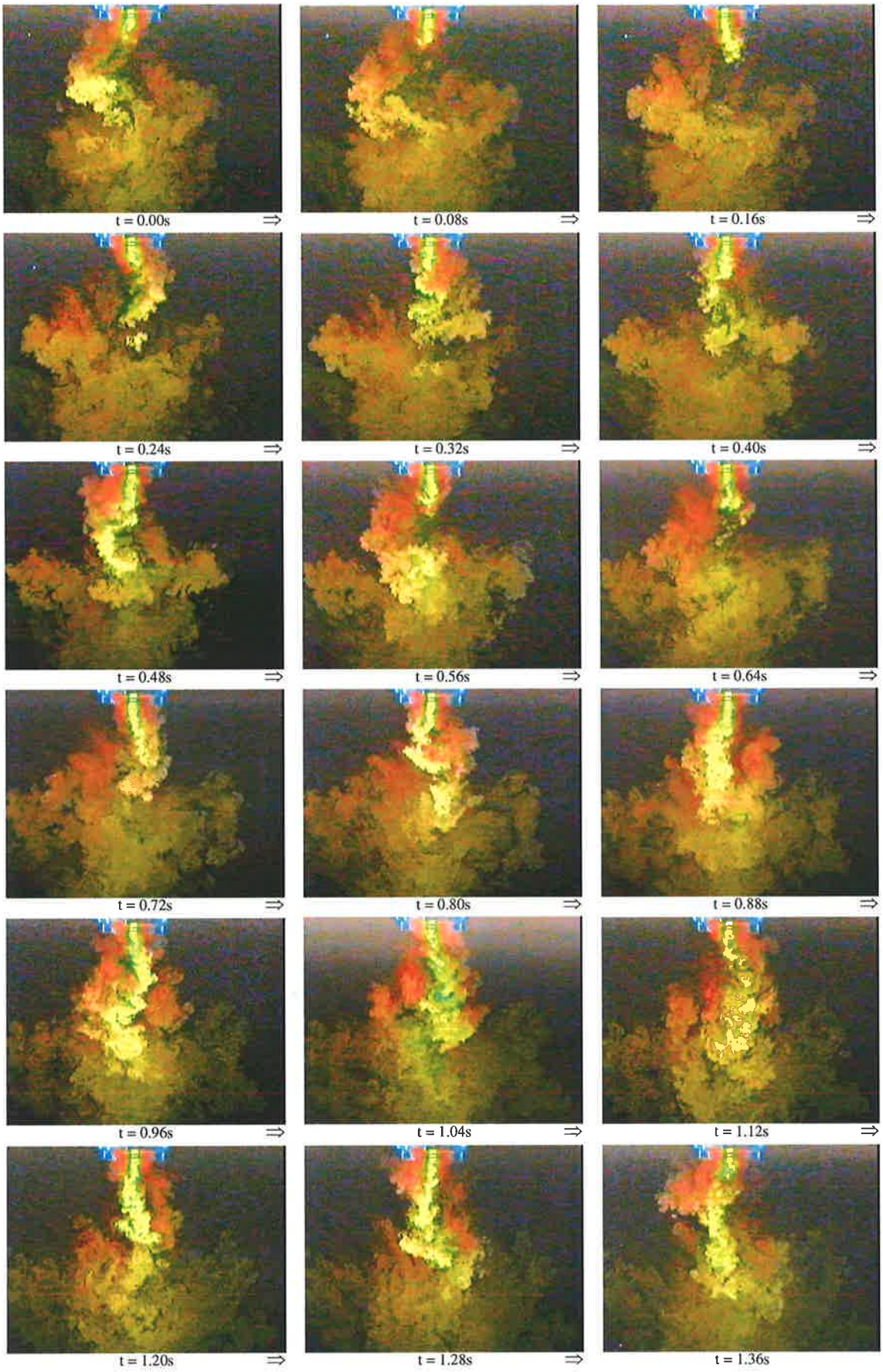

Figure 3-3. Video images of the 5mm diameter central axial jet, intermediate length insert, with the precessing jet. Pure PJ fluid is red, pure CAJ fluid is yellow. Mass flow proportion is ψ_{CAJ}=15%, momentum ratio is Γ_{CAJ}=0.07, conditions as per Table 3-1. Every second frame shown, t=1/1000s exposure time.

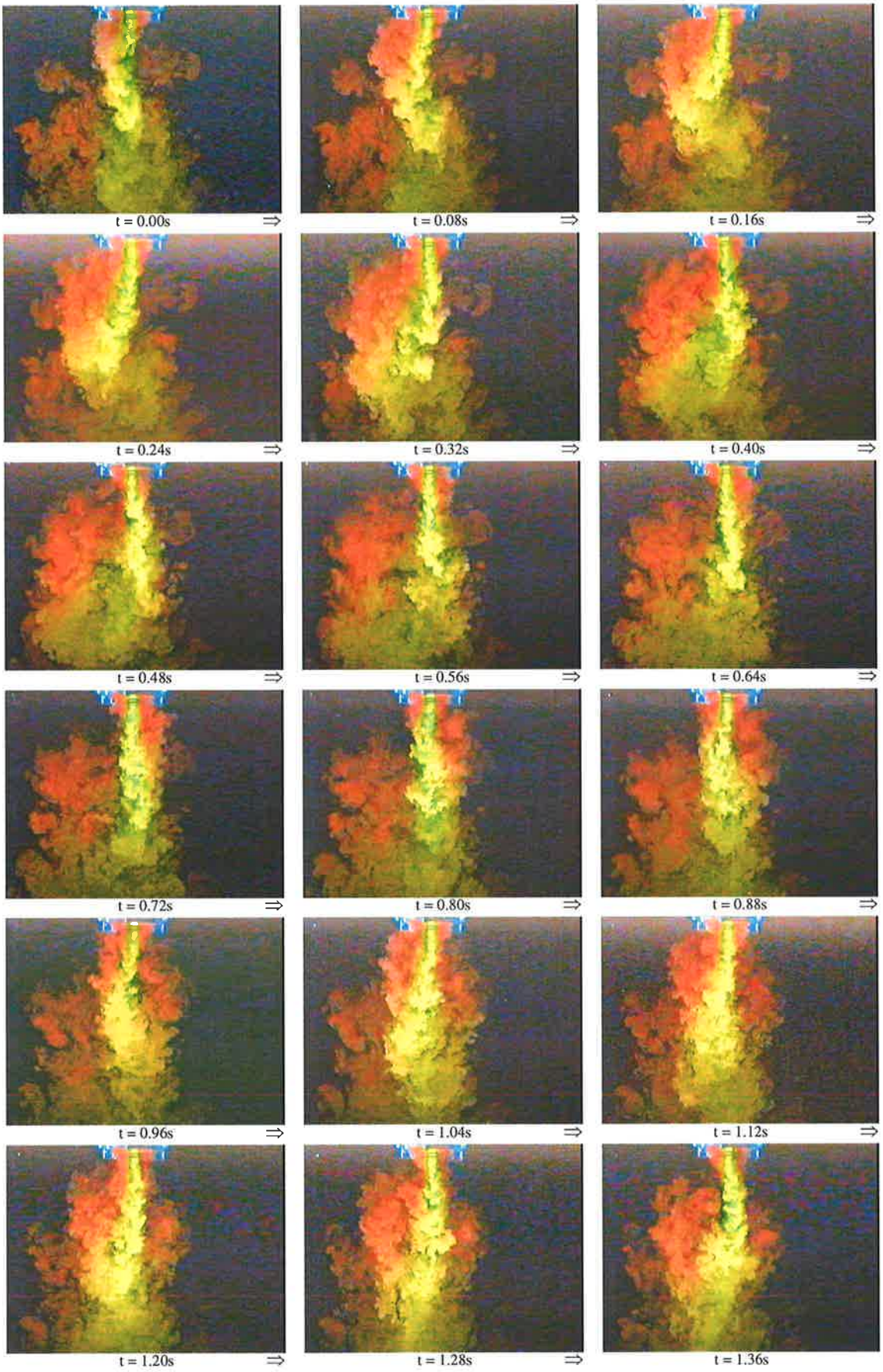

Figure 3-4. Video images of the 5mm diameter central axial jet, intermediate length insert, with the precessing jet. Pure PJ fluid is red, pure CAJ fluid is yellow. Mass flow proportion is ψ_{CAJ}=30%, momentum ratio is Γ_{CAJ}=0.29, conditions as per Table 3-1. Every second frame shown, t=1/1000s exposure time.

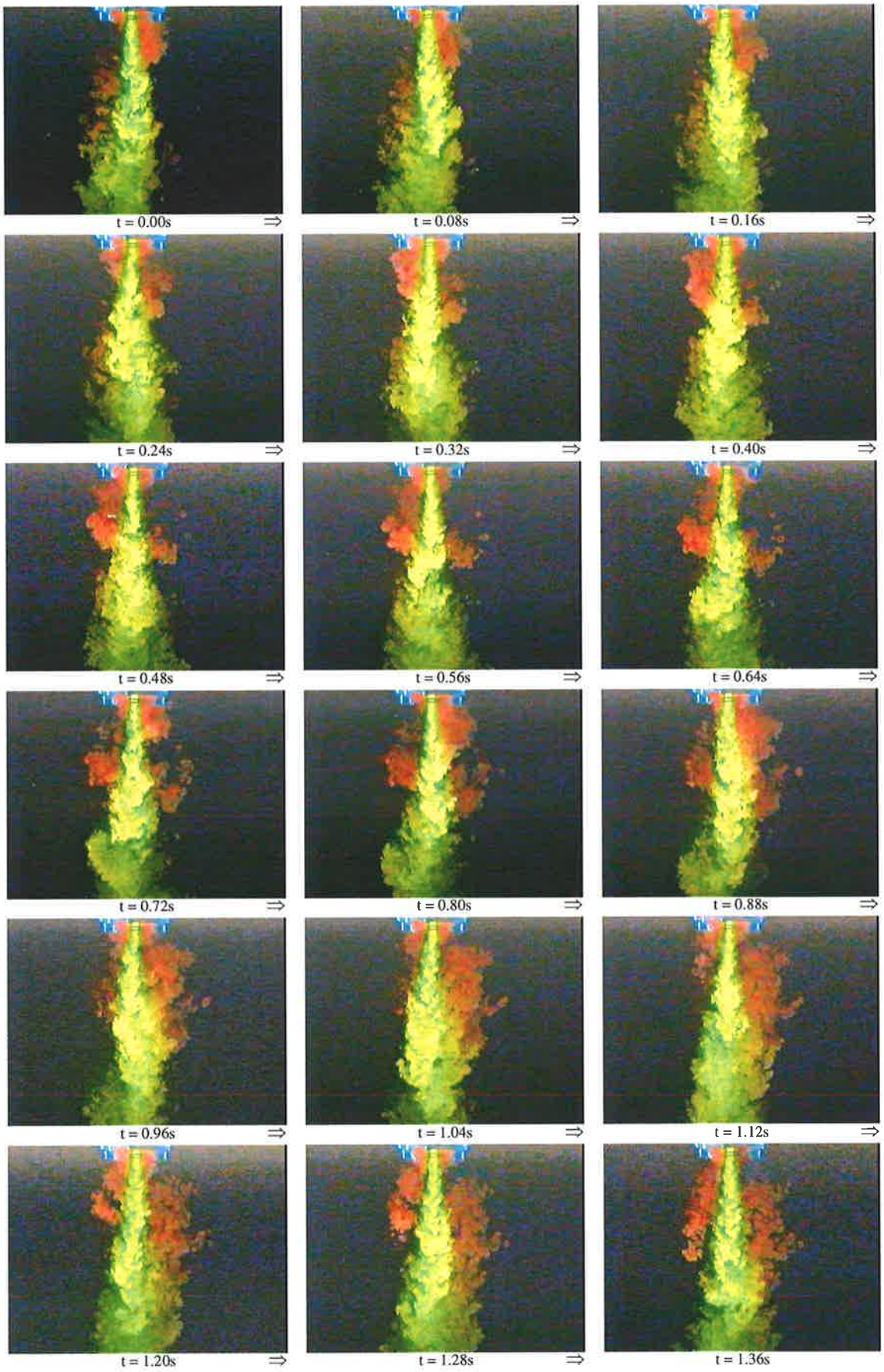

Figure 3-5. Video images of the 5mm diameter central axial jet, intermediate length insert, with the precessing jet. Pure PJ fluid is red, pure CAJ fluid is yellow. Mass flow proportion is ψ_{CAJ}=40%, momentum ratio is Γ_{CAJ}=0.49, conditions as per Table 3-1. Every second frame shown, t=1/1000s exposure time.

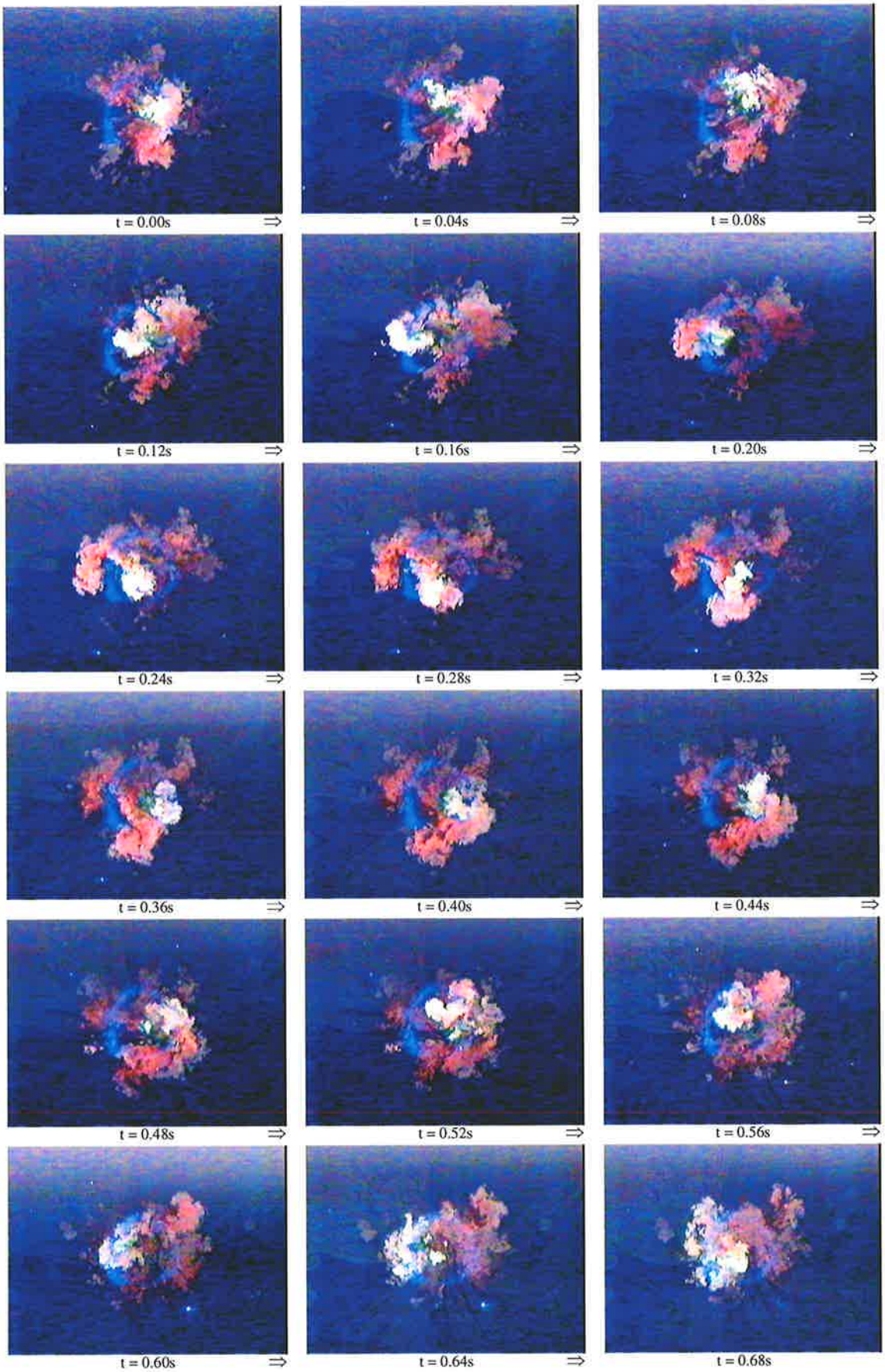

Figure 3-6. Cross-section PLIF experiments: video images of the 5mm diameter central axial jet, intermediate length insert, with the precessing jet, one chamber diameter (d_{PJ}=44mm) downstream of the nozzle tip. Pure PJ fluid is red, pure CAJ fluid is yellow. Mass flow proportion is Ψ_{CAJ}=15%, momentum ratio is Γ_{CAJ}=0.07, conditions as per Table 3-1. Every frame shown, t=1/1000s exposure time.

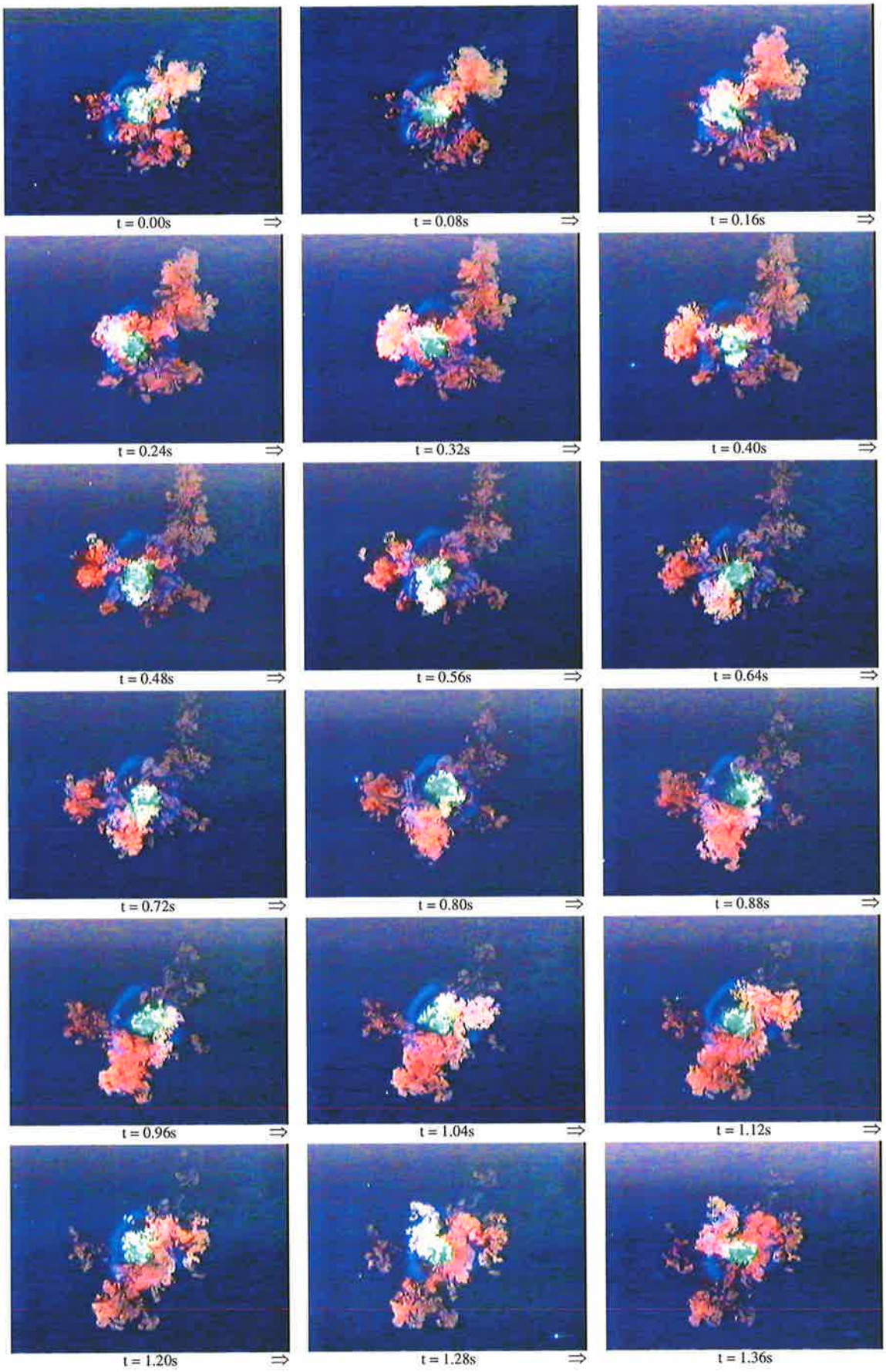

Figure 3-7. Cross-section PLIF experiments: video images of the 5mm diameter central axial jet, intermediate length insert, with the Precessing Jet, one chamber diameter (d_{PJ}=44mm) downstream of the nozzle tip. Pure PJ fluid is red, pure CAJ fluid is yellow. Mass flow proportion is ψ_{CAJ}=30%, momentum ratio is Γ_{CAJ}=0.29, conditions as per Table 3-1. Every second frame shown, t=1/1000s exposure time.

3.3.2 Characteristics of the Combined Adjacent Axial Jet and Precessing Jet

Figure 3-8 shows a sequence of images illustrating the typical instantaneous flow structures created by the interaction of a precessing jet flow and an adjacent axial jet. The proportion of the total flow rate through the AAJ is Ψ_{AAJ}=15% (momentum ratio, Γ_{AAJ}=0.07) and hence the shaping jet characteristics are exactly the same as that of the CAJ shown in Figure 3-3. Therefore, although the exit conditions of the shaping jets are slightly different, the major difference between the CAJ and AAJ is the location of the jet exit. Despite the fact that the intensity of the dye marking the precessing jet flow is not as great in Figure 3-8 (AAJ) as in Figure 3-3 (CAJ), it can be clearly seen that the relative radial location of the origin of the two shaping jets on the mixing characteristics of the combined jet flow is very significant. The AAJ has a much weaker influence on the overall PJ flow structure than the CAJ. The two jets do not interact strongly together for most of the time and instead the flow field appears to be a superposition of precessing jet and simple jet flows, except for the occasional interaction as a large structure from the precessing jet passes through the AAJ.

The cross-sectional view through the flow-field of the PJ with AAJ, not shown here, also highlights the weakness of the interaction between the two jets as described above. The AAJ fluid tends to remain on its geometric axis while the PJ fluid precesses around its nozzle axis, so that the two jets interact only when a burst of PJ fluid passes directly into the path of the AAJ. Hence the adjacent jet does not appear to be effective for controlling the mixing and combustion characteristics of a precessing jet flow.

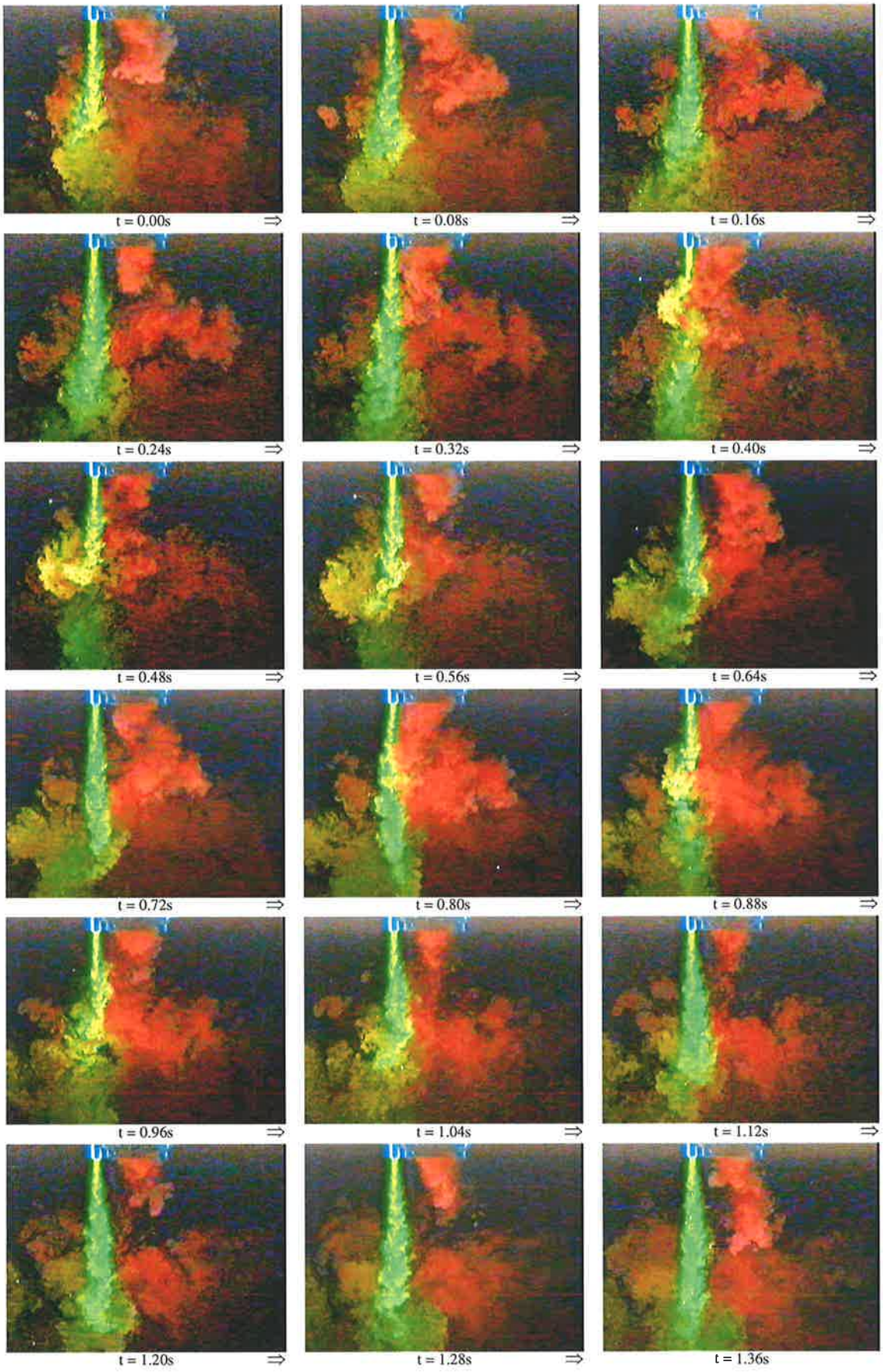

Figure 3-8. Video images of the 5mm diameter adjacent axial jet with the precessing jet. Pure PJ fluid is red, pure AAJ fluid is yellow. Mass flow proportion is ψ_{AAJ}=15%, momentum ratio is Γ_{AAJ}=0.07, conditions as per Table 3-1. Every second frame shown, t=1/1000s exposure time.

3.3.3 Characteristics of the Annular Shaping Jet and Precessing Jet

The mixing characteristics of the combined annular shaping jet (ASJ) and PJ flows were examined at slightly different conditions to those of the previous experiments. This was due to the need for a higher flow rate through the ASJ to ensure a uniform distribution of velocity and concentration at the jet exit. The effect of ψ_{ASJ}=40% (momentum ratio Γ_{ASJ}=0.04) on the instantaneous flow field is shown in Figure 3-9. The results demonstrate that, even with such a high proportion of flow through the shaping jet, the flow field is qualitatively similar to that with the PJ nozzle on its own. At values of ψ_{ASJ} less than 30%, the jet exiting from the PJ nozzle entrains the annular jet fluid from all directions so the annular fluid appears to "leak" into the flow field around the edges of the precessing jet fluid. At moderate values of ψ_{ASJ}, such as that shown in Figure 3-9, the fluid from the annular jet quickly merges with the large-scale structures from the PJ nozzle so that the large-scale features dominate the mixing and there is significant entrainment of ambient fluid onto the jet centreline. At values of ψ_{ASJ} greater than 50% (not shown), the annular jet appears similar to a bluff-body flow, with the precessing jet emerging from where the recirculation zone would otherwise be located. Close to the nozzle exit the jets interact strongly so that, in general, the two flows merge and the spreading angle is significantly reduced, with high velocity puffs of precessing jet fluid still occasionally penetrating the annular jet flow.

The effect of the ASJ on the PJ flow is weak at ψ_{ASJ}=40%, as shown in Figure 3-9. The present experiments indicate that, using the ASJ, a significant change in the flow field only occurs for ψ_{ASJ}>50%. The results presented in Section 3.3.1 demonstrate that a much lower proportion of the total flow rate is required to produce a substantial change in the jet structure using a central axial jet. However, in addition to the comparing the location of the shaping jet it is also necessary to consider the momentum ratio of shaping jet to precessing jet for the ASJ and CAJ. Values for the present form of the momentum ratio, $\Gamma_{shaping}=G_{shaping}/(G_{PJ}+G_{shaping})$, are shown in Table 3-1. The momentum ratio for the ASJ at ψ_{ASJ}=40%, Γ_{ASJ}=0.04, is of the same order as that from the CAJ at ψ_{CAJ}=15% for all jet exit diameters, Γ_{CAJ}=0.04-0.1. The jet features at all these conditions are dominated by the precessing jet. To achieve the same shaping jet momentum ratio at the same value of $\psi_{shaping}$ with an annular and axial shaping jet requires that the jet exit area is identical. For the present PJ nozzle with a 5mm CAJ, this implies an annular gap of 0.25mm, which is not practical as any small eccentricity, misalignment or machining error results in a large bias of the exit flow, with a detrimental effect on the combined jet mixing characteristics.

The findings described above are consistent with the finding of Smith (2000) who also investigated the effect of an annular jet on a PJ nozzle. The flow visualisation technique used by Smith was identical to the present experiments but was for the purposes of developing a coal-fired precessing jet burner. Using a range of PJ nozzle and annular geometries, Smith was able to deduce that *"similarity in the interaction between precessing and annular jets relies on the momentum ratio between streams, which controls entrainment rates, rather than on the instantaneous position of the emerging PJ flow. Likewise, similarity does not rely on maintenance of a constant ratio of precession cycle time-scale ($1/f_p$) to annular fluid residence time in the near burner zone"*. Hence the momentum ratio of shaping jet to a combination of the precessing and shaping jet appears to be the principal controlling parameter for determining the features of the combined jet mixing field, consistent with the results for bluff-body and swirling jet flows (Chen *et al.*, 1990). A semi-quantitative image processing technique is used in the following section to determine the relationship between the combined jet spreading rate and the momentum ratio.

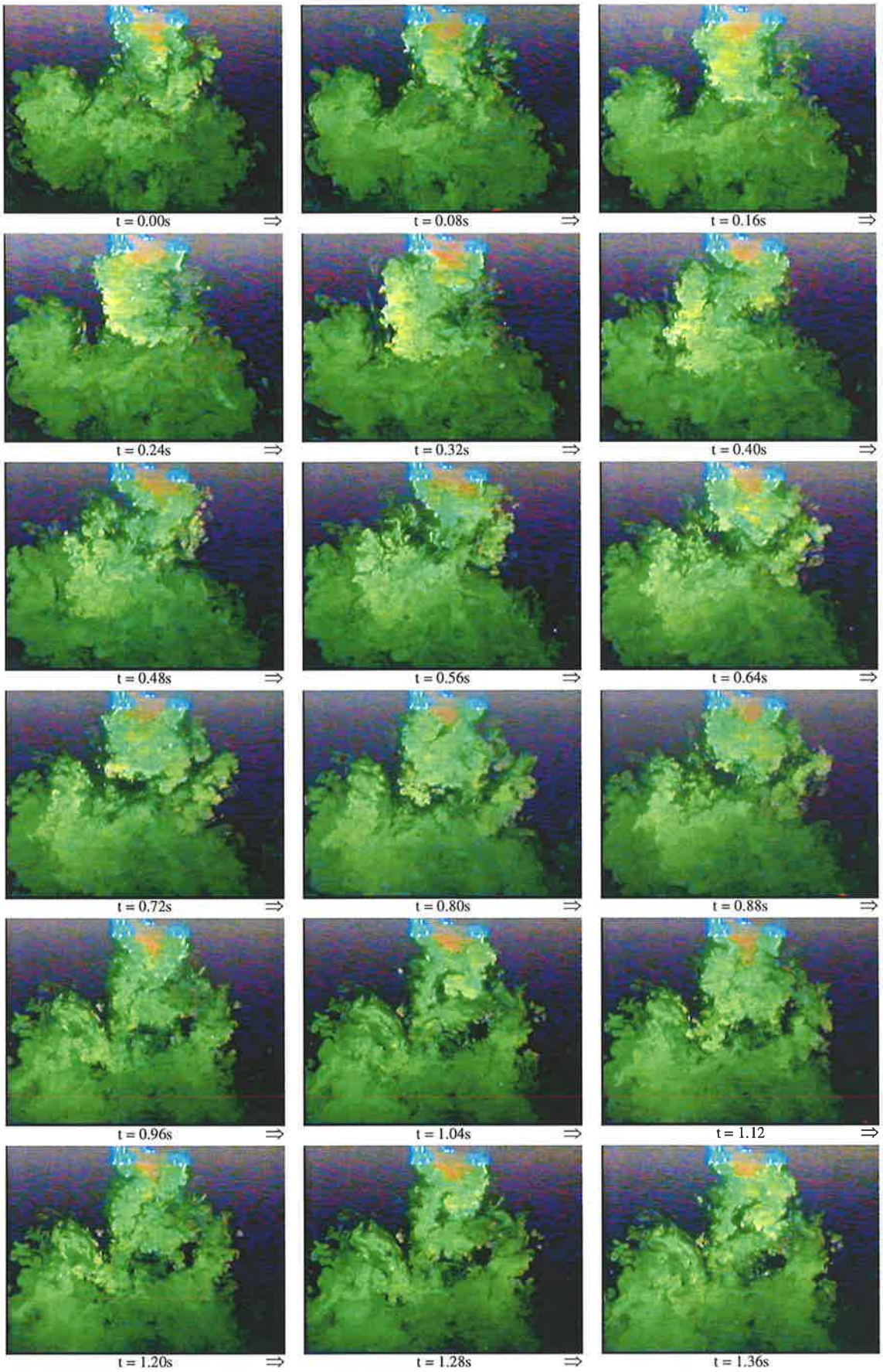

Figure 3-9. Video images of the annular shaping jet with precessing jet. Pure PJ fluid is red, pure ASJ fluid appears yellow-green in this sequence. Mass flow proportion is ψ_{ASJ}=40%, momentum ratio is Γ_{ASJ}=0.04, conditions as per Table 3-1. Every second frame shown, t=1/1000s exposure time.

3.4 Image Processing

3.4.1 Introduction

The qualitative information obtained from the flow visualisation experiments about the structure of the jet turbulence in the combined shaping jet and precessing jet flows can be extended to provide some semi-quantitative information by suitable image processing. The present flow visualisation results are not suitable for obtaining quantitative measurements of absolute mixture fraction due to the use of two different dyes and the limited laser power which prevents good temporal resolution and limits the signal to noise ratio. However a semi-quantitative procedure developed by Newbold (1997) can be used to calculate the jet half-width with reasonable accuracy. This technique is sufficiently accurate to quantify large differences in flow features and so is adequate for the present requirements, which are primarily comparative.

3.4.2 Image Processing Technique

The video footage of the flow visualisation experiments was converted to digitised still images using a colour frame-grabber. The colours in each raw digitised image were enhanced to balance the signal intensity from the different dyes and then converted into an 8-bit greyscale format. The resolution of the digital images is 640×480 pixels, so the nominal spatial resolution is about 375μm per pixel in each dimension. The image processing was conducted using a commercially available package, "Transform", from Fortner Research Ltd. Using Transform, an average of approximately 50 to 100 images was calculated for each flow condition. The images were taken from a large portion of video footage and hence provided independent measurements.

The spreading rate of a jet has been quantified by other researchers by calculating the radial contour where the mean concentration is exactly half the centreline value. The half-width is also a measure of the scale of the largest flow structures, assuming that large-scale coherent structures span the width of the jet (Tennekes and Lumley, 1972). Due to the nature of the flow and the limitations of the present data, the local fluorescence signal intensity was scaled relative to the maximum radial value instead of the centreline value. This normalisation allows for the fact that the maximum concentration is not always located on the nozzle axis and for the fact that signal attenuation due to the laser passing through the dyed field causes the maximum signal to be located away from the jet axis. Since each row of the mean digital image represents equal distances from the nozzle origin, the normalisation was calculated along each image pixel row. The maximum angle of a light ray in the laser sheet to a pixel row is less than 10°, so the radial variation in laser intensity along each pixel row is small and hence the axial variations in laser sheet intensity do not greatly effect the results. A reference for "pure" jet fluid is also not required.

The spreading rate of the jet was determined by fitting a line of best fit through the 0.5-maximum contour in the imaged region beginning one nozzle diameter away from the nozzle tip and extending to approximately x/d_{PJ}=3-3.5 from the nozzle tip. The spreading angle was defined as the maximum calculated angle from either side of an average image of the jet (i.e. near to the laser or left hand side of the image and far from the laser or right

hand side of the image). The spreading angle was generally based on the measurement closest to the incident laser sheet due to the higher fluorescence signal strengths and hence better contours in this region. However, in some cases for which the 0.5-maximum contours differed significantly on either side of the nozzle centreline, an average value was used.

3.4.3 Image Processing Results

The results of the image processing and averaging were generally satisfactory and the 0.5-maximum contour provides a reasonable measure of the spreading of the jet. The reduction in spreading angle with increased mass flow proportion through the CAJ, ψ_{CAJ}, seen visually, is also evident in the processed results, e.g. Figure 3-10. For each step change in ψ_{CAJ}, the spreading angle changes by approximately 10°. The spread-angle of the combined flows are plotted against ψ_{CAJ} in Figure 3-11 for the different CAJ exit diameters investigated, the ASJ experiments and for a series of experiments in which the total flow rate was maintained constant and ψ_{CAJ} was changed simultaneously. Figure 3-11 demonstrates that, although the spread-angle generally decreases with increasing shaping jet proportion for a given shaping jet configuration, there is no clear relationship between the spread-angle of the combined flow and the mass ratios ψ_{CAJ} or ψ_{ASJ}.

The effect of the shaping jet on the spreading rate of the combined flow from a PJ nozzle is demonstrated more clearly when plotted against the momentum ratio $\Gamma_{CAJ}=G_{CAJ}/(G_{PJ}+G_{CAJ})$, see Figure 3-12. Figure 3-12 demonstrates that for $0\leq \Gamma_{CAJ}<0.6$ the spread-angle varies linearly with the momentum ratio for all the experimental conditions. The regression coefficient for the line of best fit with momentum ratio was 0.70, compared to 0.44 for the correlation with mass flow rate proportion. At high momentum ratios, $0.6< \Gamma_{CAJ}\leq 1.0$, the influence of the PJ flow weakens and the spread-angle is approximately the same as the shaping jet alone. The spread-angle of the 5.0mm CAJ on its own was measured to be 8°. This is larger than the spread-angle of 6° determined by Becker *et al.* (1967a) for an axisymmetric jet issuing from a smooth contraction and the spread-angle of 5.5° determined by Newbold (1997) for a jet from an orifice using an identical technique to the present experiments. However, due to the physical design of the CAJ nozzle, see Figure 2-3, the initial conditions of the central axial jet are likely to result in greater turbulence intensity and increased jet spreading rate, consistent with the effect of jet exit conditions on the far field mixing characteristics determined by Mi *et al.* (2000a). Hence the agreement of the present measurements with previous investigations, although not perfect, is reasonable.

Within the limits of the image processing technique and the limited range of conditions examined, the data used to calculate the line of best fit provides satisfactory evidence that the momentum ratio between the shaping jet and combined precessing and shaping jet, Γ_{CAJ}, to a first order, controls the jet spreading rate. As the flow visualisation results demonstrate that visually coherent large-scale motions occur across the entire width of the jet, Figure 3-12 also implies that the scale of the largest turbulent flow motions varies with the momentum ratio. A decrease in spreading angle can also be expected to correlate with increased jet velocity. For a burner nozzle, this would result in the bulk of the flame volume being pushed further away from the nozzle tip.

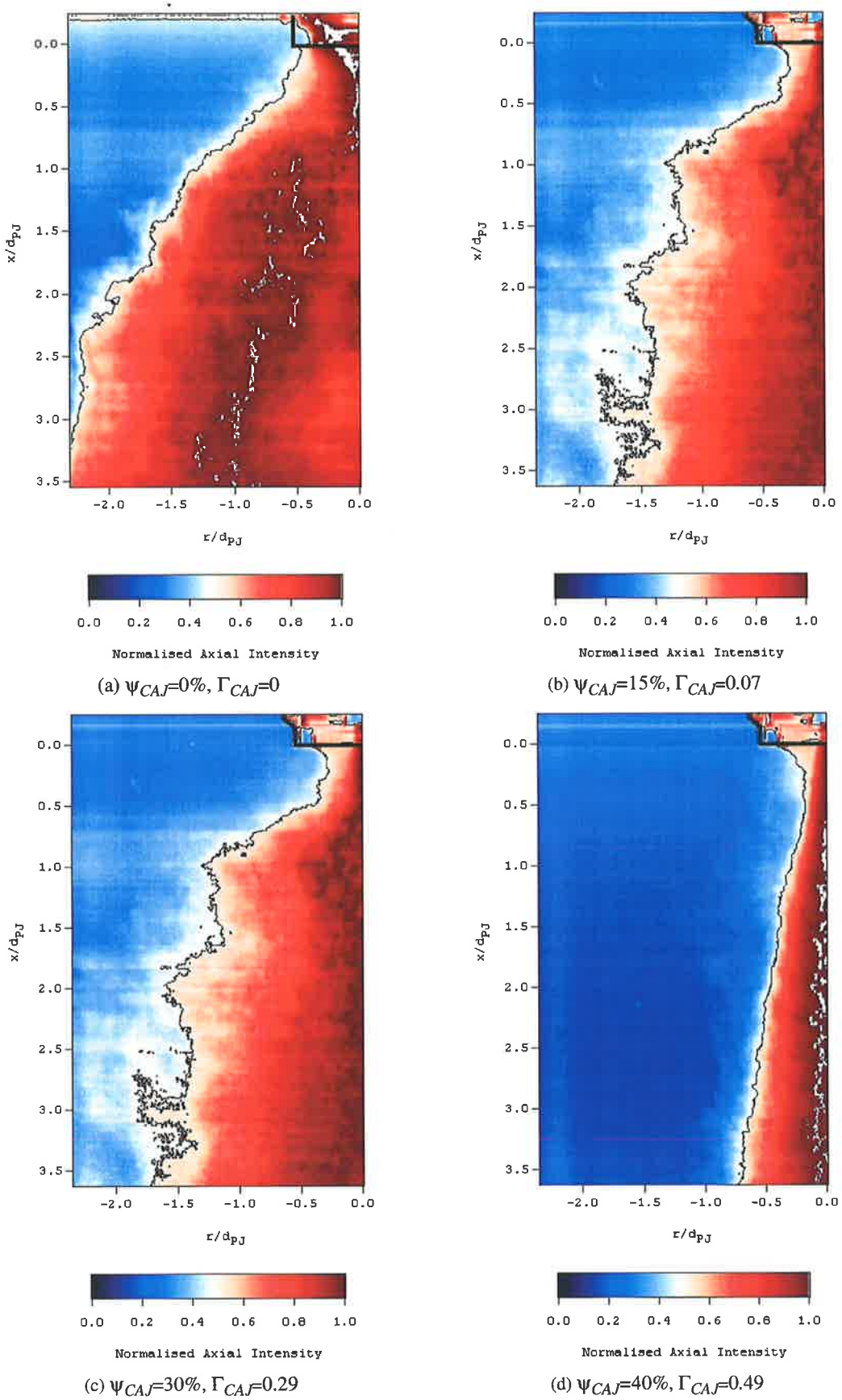

Figure 3-10. The concentration half-widths of combined precessing jet and central axial jet flows, determined from local normalisation of every pixel to the maximum value in each row. Images shown are for the 5mm, intermediate length CAJ insert. Refer to Table 3-1 for the jet conditions.

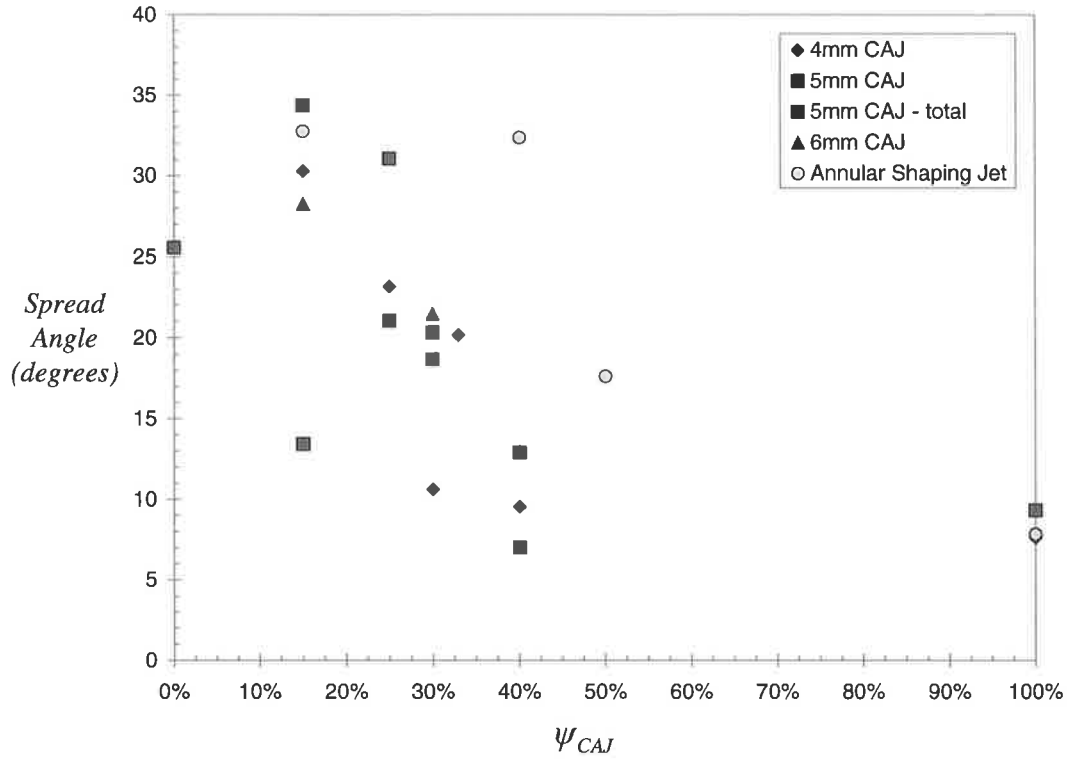

Figure 3-11. Variation in jet spread-angle for the combined precessing jet and central axial jet flows with CAJ proportion, $\psi_{CAJ} = \dot{m}_{CAJ}/(\dot{m}_{PJ} + \dot{m}_{CAJ})$, for different CAJ exit diameters and Reynolds number conditions. Also shown is the variation in spread-angle for the annular shaping jet.

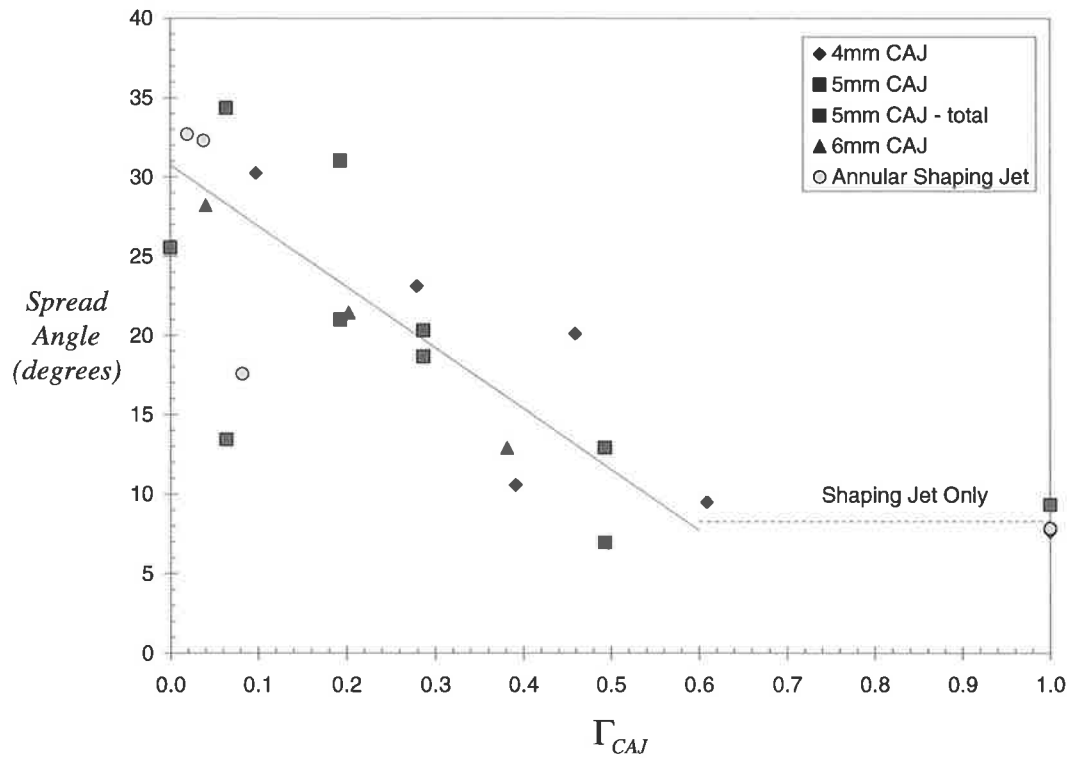

Figure 3-12. Variation in jet spread-angle for the combined precessing jet and central axial jet flows with momentum ratio, $\Gamma_{CAJ}=G_{CAJ}/(G_{PJ}+G_{CAJ})$, for different CAJ exit diameters and Reynolds number conditions. Also shown is the variation in spread-angle for the annular shaping jet. The trend line is based on a line of best fit through all data, excluding the data for ψ_{CAJ}=100% and data points greater than 10 degrees from the mean trend.

3.5 Conclusions

A flow visualisation technique has been used to demonstrate that the initial scale of the largest turbulent motions in a combined jet flow, incorporating a precessing jet and a shaping jet, can be controlled by altering the proportion of flow rate through each jet. The proportion of flow through the shaping jet, relative to the total flow through both jets, is denoted by $\psi_{shaping}$. Visual images show that the two flows combine and that the largest motions span the entire flow, so the jet half-width can be used a measure of the largest motions in the flow. Hence the results of a semi-quantitative technique, based on the image processing of video images, demonstrates that the jet spread, and therefore the size of the largest scale motions, is controlled by the ratio of shaping jet momentum to combined precessing jet and shaping jet momentum, $\Gamma_{shaping}=G_{shaping}/(G_{PJ}+G_{shaping})$. This is consistent with the results of Smith (2000) who investigated different annular shaping jet and PJ nozzle configurations and Chen *et al.* (1990) and Li and Tankin (1987) for swirling and bluff-body flows with central fuel jets, although the form of the momentum ratio and relationship with the combined jet characteristics is different.

The flow visualisation sequences and image processing calculations have demonstrated that the interaction between a precessing jet and a shaping jet depends upon the relative momentum of the two jets. As a source of high momentum, an axisymmetric "simple" jet requires the smallest proportion of the total combined flow rate, $\psi_{shaping}$, to produce a significant change in flow characteristics and hence is the most effective form of shaping jet. However the flow visualisation results have also shown that the effectiveness of a simple jet in altering the mixing characteristics depends upon the relative location of the jet exit. Experiments using a Central Axial Jet (CAJ) located in the centre-body of the PJ nozzle, demonstrated a broad spectrum of flow characteristics, from those typical of a precessing jet flow to those typical of a simple jet flow, can be generated. Experiments using an adjacent axial jet, in which the jet exit was located next to the PJ nozzle, demonstrated a limited ability to influence the overall mixing characteristics. Increasing the length of the CAJ insert was also found to decrease the interaction with the precessing jet flow, similar to increasing the momentum ratio of shaping jet to combined jet flow. Hence the CAJ with a protrusion length of about one CAJ diameter or one-tenth of the PJ chamber diameter, or less, is considered to be the most effective means for controlling the combustion characteristics of a PJ burner. The effectiveness of the CAJ is shown to be, in part, due to the excitation of flow structures in the CAJ by the precessing jet. The excitation of the CAJ occurs at a Strouhal number associated with the precessing motion, which is at least an order of magnitude lower than the values determined by previous investigators to excite the natural disturbances in a jet.

Observation of the flow visualisation results indicates that the jet fluid from the CAJ and PJ nozzles interact strongly and merge. Increasing the CAJ proportion, ψ_{CAJ}, increases the momentum ratio, Γ_{CAJ} and causes a decrease in the amount of ambient fluid being entrained into the centre of the jet, a reduction in the angle at which the large-scale structures initially move away from the centreline and hence a reduction in the initial spreading angle of the jet. The decrease in spreading angle is inferred to increase the speed at which the structures in the combined flow are convected downstream, which would result in the flame being pushed further downstream from the nozzle tip. For momentum ratios in the range $\Gamma_{CAJ}<0.2$ (corresponding to low ψ_{CAJ}), the flow-field can be characterised as precessing jet dominated, while at momentum ratios of approximately $\Gamma_{CAJ}>0.23$ the flow appears visually dominated by the features of the central axial jet. This compares with the results of the semi-quantitative

technique for determining the spread-angle of the combined flows, which indicates that above momentum ratios of 0.6 the spread-angle is approximately the same as that of a simple axisymmetric jet. Within the range $0 \leq \Gamma_{CAJ} < 0.6$, the spread-angle is, to a first order, linearly dependent on the momentum ratio.

Chapter 4

Measurement of Unconfined Precessing Jet Flame Dimensions

4.1 Introduction

Global parameters which can be determined from photographs of unconfined flames have been used by previous researchers as a relatively quick and easy method to evaluate the effect of different jet mixing conditions on combustion. Long exposure times that produce time-averaged images have been used by Lovett and Turns (1990) to show that pulsing a turbulent jet at different frequencies produces variations in the average length and maximum width of propane jet flames; Newbold *et al.* (2000) demonstrated that altering the mixing from a jet with constant fuel nozzle conditions but a range of different fluid mixing devices produces substantial changes in the visible flame shape; Nathan *et al.* (1996) has demonstrated that the Strouhal number of a mechanically rotated precessing jet burner can cause significant differences in the colour and shape of methane flames. Instantaneous images of a flame, representing the instantaneous location of the stoichiometric surface, were used by Li and Tankin (1987) to reveal the effect of different mixing conditions on the combustion from a bluff-body burner. High speed sequences of instantaneous flame images have been used by Mungal *et al.* (1991) and Newbold *et al.* (1997) to reveal the role of large-scale structures in determining the global and temporal properties of flames from smooth contraction and precessing jet nozzles respectively.

The simplicity of photographing an unconfined flame using either short or long exposure times belies some of the important information that can be obtained from this technique. A number of authors have proposed correlations between flame dimensions - typically the mean flame length, L_{flame}, maximum mean width, W_{flame}, and mean volume, V_{flame}, which can be easily determined from time-averaged images - and the fraction of the input energy converted to radiation, χ_r, the non-adiabatic flame temperature, T_f, and the NO_x emission index, $EINO_x$. Although there has been considerable development towards the correlation of flame properties with geometrical and fluid mechanical parameters, a single, consistent and satisfactory model has not yet been devised.

Some of the earliest measurements from an unconfined simple jet by Bilger and Beck (1975), found that characteristic NO_x production rates decrease with Reynolds number at constant jet Froude number. Explaining this seemingly anomalous result has been a theme in many subsequent experimental and analytical studies (Turns and Myhr, 1991). For example, Bilger (1976) and Kent and Bilger (1977) developed the idea that superequilibrium oxygen concentration broadened the reaction zone of NO_x formation and was responsible for the Reynolds number depen-

dency. Buriko and Kuzntsov (1978) conducted an experimental and analytical study of propane jet flames and concluded that the Reynolds number dependence was due to the effects of flame radiation.

The observed experimental *Re* and *Fr* scaling detected previously was not, however, demonstrated in the seminal experimental and theoretical correlation of flame geometry and properties by Peters and Donnerhack (1981). The scaling model proposed by Peters and Donnerhack is based upon a flamelet model with a purely thermal analysis that accounts for scalar fluctuations and neglects the effects of radiation, superequilibrium oxygen chemistry and prompt NO. For these conditions, the NO_x emission index for a turbulent jet flame is predicted to be equal to:

$$EINO_x = 0.057\left(\frac{L_f^3}{d_\varepsilon^2}\right)S_{NO,b}\varepsilon\frac{\rho_{ST}}{\rho_A} \qquad \textbf{Equation 4-1.}$$

where $S_{NO,b}$ and ε are constants that depend on the known thermal NO kinetics, the equilibrium gas concentrations and the gas temperature, d_ε is the momentum (or effective) jet diameter, ρ_A is the air density and ρ_{ST} is the density of the stoichiometric mixture. Peters and Donnerhack also assumed that the time-average conserved scalar profiles of the jet fluid are self-similar, implying that the volume of the thin, wrinkled (and strained) reaction zone should scale with the cube of the flame length. Hence, via Equation 4-1, $EINO_x$ is predicted to scale linearly with the reaction zone volume, which is expected to be proportional to a global residence time, τ_G if the jet achieves self-similarity. Hence, as flame length is proportional to d_ε for simple jets, thermal $EINO_x$ is predicted by the Peters and Donnerhack model to scale with a global residence time given by the expression:

$$\tau_G \propto \frac{L_{flame}^3}{Ud^2} \qquad \textbf{Equation 4-2.}$$

where U is the velocity of the fuel at the burner exit and d is the diameter of the burner nozzle exit. Peters and Donnerhack also show that Reynolds and Froude numbers are significant factors in NO_x production.

Turns and Lovett (1989) and Turns and Myhr (1991) similarly characterised unconfined simple jet flames in terms of a global residence time, thereby demonstrating that flame radiation plays an important role in NO_x scaling, consistent with the concept advanced by Buriko and Kuznetsov (1978). In their model, the entire flame is considered to be a uniform source of heat release and radiation and, as per Peters and Donnerhack (1981), propose that the formation of nitrogen oxide in jet flames scales with a characteristic time scale in the flow that is in turn proportional to the reaction zone volume. Physically the global residence time represents the time required for a stoichiometric mixture of hot products to pass through a volume equal to that occupied by the visible flame. It is expected to be proportional to the residence time in a final homogeneous eddy. Hence the general form of the relationship between the global residence time and flame volume is given by the relationship:

$$\tau_G \propto \frac{V_{flame}}{Q_f} \qquad \textbf{Equation 4-3.}$$

where Q_f is the fuel input flow rate.

Turns and Myhr (1991) simplified Equation 4-3 by assuming the flame volume from a simple jet nozzle can be modelled as a cone, such that.

$$\tau_G \propto \frac{L_{flame} W^2_{flame}}{Ud^2} \qquad \textbf{Equation 4-4.}$$

For momentum dominated flames, Turns and Myhr (1991) have demonstrated experimentally that τ_G is directly proportional to the convective time scale at the jet exit, *d/u*. For buoyancy dominated flames, the two time scales are no longer directly proportional, with large changes in the jet exit convective time scale producing relatively small changes in τ_G.

For some flame conditions, the predicted emissions based on the model proposed by Turns and Myhr (1991) differ significantly from the actual emissions measured in laboratory experiments. This occurs for C_3H_8 and C_2H_4 flames with characteristic temperatures below approximately 2050K, which suggests that the relative significance of the prompt NO_x formation mechanism is greater in these luminous low temperature flames. The good agreement over the rest of the range leads to the conclusion that radiation can indeed play a significant role in NO_x formation and should be an essential ingredient in models that seek to predict NO_x emissions from jet flames.

In contrast to the above conclusion of Turns and Myhr (1991), Rokke *et al.* (1992, 1994) developed an alternative NO_x scaling model that is derived solely from the underlying chemical kinetics, flamelet structure and buoyancy-controlled turbulent-jet behaviour and did not explicitly include the effect of radiant energy loss. Their model uses a laminar diffusion method incorporating both thermal and prompt NO_x mechanisms. Simplified expressions for the flame volume, chemical kinetics and a flamelet model are used to correlate NO_x emissions from previous data in the literature and new experimental results covering momentum and buoyancy dominated simple jet flames of different sizes with strain rate and Froude number via the expression:

$$E_{NO_x}\left(\rho_0 \frac{u_0}{d_0}\right) = 44 Fr^{3/5} \qquad \textbf{Equation 4-5.}$$

Rokke *et al.* hence conclude that the leading order parameter for NO_x is the flame volume, which is proportional to $Fr^{3/5}$.

Another, more recently developed scaling model is that proposed by Broadwell and Lutz (1998). Their model is based upon the hypothesis that NO formation in flames takes place primarily in regions near the flame tip, where the combination of high temperature and high concentrations of O and CH radicals influence the thermal and prompt mechanisms respectively. They develop a model that is independent of the flame sheet structure and show that NO production is significantly influenced by radiation, controlling the temperature, and by buoyancy, which controls entrainment. Broadwell and Lutz conclude that radiant losses and buoyancy both act to reduce the residence time, which explains how the flamelet model of Rokke *et al.* is successful without explicitly considering flame radiation. Their model predicts that the thermal NO mechanism is responsible for 75% of the total NO_x emission from methane jet flames.

The most recent review and experimental investigation of scaling models for flame properties has been conducted by Newbold *et al.* (2000) using propane. In this study, the scaling methods outlined previously were tested against experimental measurements of flame geometry and emissions and radiation from flames produced by simple jet, bluff-body, swirl and precessing jet burners. Newbold found that the correlation of radiant fraction with global residence time detected by Turns and Myhr (1991) is valid for both momentum and buoyancy dominated turbulent jet flames and the wide range of dissimilar burners investigated so that, for this fuel:

$$\chi_r \propto \tau_G \qquad \textbf{Equation 4-6.}$$

This finding is consistent with treatment of the flame as a uniform source of radiation and the assumption of an optically thin flame, more typical of flames dominated by gas-chromatic radiation.

The correlation of flame radiation with residence time across a wide range of different flames demonstrates a correlation between the non-adiabatic flame temperature, T_f, related to radiant losses from the flame and the flame length, L_{flame}, related to the flame volume and mass flux (Newbold *et al.*, 2000). Consistent with the model of Turns and Myhr (1991), Newbold *et al.* (1997) has shown that the increase in the flame radiant fraction and decrease in NO_x emissions from a PJ burner, compared to a simple jet flame is related to a decrease in the strain rate at the flame tip. Newbold and Nathan (1999) demonstrates that the characteristic strain rate (the reciprocal of the global residence time), is related to the size of the structures at the flame tip, which can be estimated from the ratio of the flame width to the flame length. Hence the thermal NO_x emissions, as characterised by the emission index, $EINO_x$, can be estimated using the expression:

$$EINO_x \propto \frac{W_{flame}}{L_{flame}} \qquad \textbf{Equation 4-7.}$$

Newbold *et al.* (2000) has also demonstrated that, for the PJ nozzle, a reduction in flame length normalised to the nozzle exit diameter corresponds to a reduction in the NO_x emission index, attributed to a reduction in the global strain rate and increase in the global residence time, such that:

$$EINO_x \propto \frac{L_{flame}}{d} \qquad \textbf{Equation 4-8.}$$

where, for the PJ nozzle, d is the diameter of the inlet to the nozzle chamber.

Hence, while much of the development of models for scaling flame properties from measurements of flame dimensions has been based on research that used simple jet burners, Newbold *et al.* (2000) has demonstrated that appropriate scaling methods, in particular that of Turns and Myhr (1991), can be extended to other flames including those from precessing jet burners. For example, Newbold *et al.* (2000) concludes that all of the global emission models discussed here provide reasonable agreement with the scaling of NO_x emission indices for unconfined propane turbulent-jet diffusion flames. However, the model is not complete. Departure of measured NO_x emissions from strongly recirculating flames (swirl, bluff-body nozzles) from the purely thermal prediction is attributed to inappropriate scaling of the reaction zone volume with the flame volume. In the case of the precessing jet nozzle, the difference between measured and predicted emissions is attributed to the increased importance of the prompt mech-

anism caused by a reduction in the flame temperature. Therefore the correlation of NO_x emission index with flame geometry and residence time embodied in Equation 4-7 and Equation 4-8 can be expected to predict the trends in the thermal NO_x production. However they cannot provide an absolute prediction of NO_x emissions and cannot account for prompt NO_x. Yet the model is still relevant to the present investigation because the flame temperatures in the both pilot-scale and full scale rotary kiln burner installations are such that NO_x is expected to be produced overwhelmingly via the thermal mechanism.

The analysis shown above demonstrates that simple measurements of the average flame dimensions can be used to assess important flame properties that are relevant to the optimisation of a burner for industrial application. The results of Section 3.4 demonstrated that the central axial jet is the most effective means of altering the mixing from a PJ nozzle. The aim of the present experiments therefore, is to visualise flames from an unconfined PJ nozzle at different proportions of central axial jet, ψ_{CAJ}, and hence momentum ratio, $\Gamma_{CAJ}=G_{CAJ}/(G_{PJ}+G_{CAJ})$, and so deduce implications regarding the expected effect of ψ_{CAJ} and Γ_{CAJ} on the radiant fraction, global residence time, global strain rate and thermally generated NO_x emissions.

4.2 Experimental Conditions

The layout of equipment and apparatus for the present experiments is detailed in Section 2.3.1. Briefly, a d_{PJ}=10mm PJ nozzle with an annular supply of fuel to the central axial jet was positioned vertically underneath a ventilation hood and isolated from the effects of cross-drafts by an enclosure of welding curtains. A camera was positioned on a tripod within the ventilation enclosure and operated remotely to acquire instantaneous and long exposure images of the flame. Instantaneous images of the entire flame were acquired with an exposure time of t=1/250s and an aperture setting of f/8. Long exposure images were acquired with the shutter open for 8s and an aperture of f/22 for the whole flame and with a t=8s exposure and an aperture of f/27 for the base of the flame. Each set of photographs as developed and digitised using identical settings.

Liquid petroleum gas (LPG), i.e. commercial propane, was used as the fuel. The total flow rate through the PJ nozzle and CAJ was maintained at a constant rate so the flame output was always 20kW and hence only the mixing of the fuel and air is altered. The full range of possible mass proportions, ψ_{CAJ}, from 0% to 100% were investigated, as shown in Table 4-1, corresponding to the full range of momentum ratios, Γ_{CAJ}=0-1. The output of 20kW was the maximum flow rate for which the flame at ψ_{CAJ}=100% was guaranteed to be stable. Note that the Reynolds number of the jet through the PJ nozzle drops below 20,000 at ψ_{CAJ}=50%, which implies that the probability of jet precession is slightly less than 1 for 50%< ψ_{CAJ} <100%. However the flame did not exhibit any visually detectable intermittent behaviour, so this influence is deduced to be small.

The t=8s exposure images represent the time-averaged appearance of the flame. Hence the images of the entire flame are used to calculate the mean flame length, width and volume. The images of the flame base are used to measure the initial spreading of the flame and the lift-off height. These parameters were quantified by digitising the flame photographs using a Hewlett-Packard colour scanner with identical exposure settings for each image region. Image processing was then performed to convert the pictures to greyscale images and extract the contour corresponding to the edge of the flame, which is a constant value corresponding to approximately 20% of the maximum signal intensity. The flame length is defined as the distance from the nozzle tip to the maximum axial location of the constant value contour, the flame width is the maximum width of the contour. The flame volume was estimated by calculating the cross-sectional area from the number of pixels within the flame edge contour.

ψ_{CAJ} (%)	Precessing Jet		Central Axial Jet		Γ_{CAJ}
	Jet Output (kW)	Reynolds number	Jet Output (kW)	Reynolds number	
0	20	36,900	0	0	0
15	17	31,300	3	7,400	0.19
30	14	25,800	6	14,700	0.36
40	12	22,100	8	19,700	0.47
50	10	18,400	10	24,600	0.57
75	5	9,200	15	36,900	0.80
100	0	0	20	49,200	1

Table 4-1. Experimental conditions for the unconfined flame experiments at different proportions of flow through the central axial jet, ψ_{CAJ}. The fuel is LPG (propane).

4.3 Results

4.3.1 Instantaneous Images

The effect of the central axial jet on the instantaneous flame structure from the PJ nozzle is illustrated in Figure 4-1 at selected values of ψ_{CAJ}. The dimensions of the photographs are approximately 650mm×980mm. For ψ_{CAJ}=0% the flame structure is very similar to that shown by Newbold *et al.* (1997) for a 44kW flame from a d_{PJ}=13mm PJ nozzle. Large "puff" structures at the base and further downstream from the nozzle exit are visible, with a narrow neck in the flame between the puffs. The dimensions of the puff structures are significantly larger than the scale of the large-scale structures visualised in Section 3.3. Newbold *et al.* (1997) has demonstrated that the frequency of the "puffing" oscillations is much lower than, and not correlated with, the frequency of the precessing jet. Instead the puff structures are more similar to those observed from buoyant flames in pool fires.

As ψ_{CAJ}, and hence Γ_{CAJ} is increased, the size of the puff structures decreases and the number of structures observed within the flame increases. This is consistent with the results of Newbold (1997), who noted that two to three structures are generally observed at any one time for a precessing jet flame, while in momentum dominated turbulent jet flames Mungal *et al.* (1991) typically observed eight visible structures. The collection of photographs, from which the images shown in Figure 4-1 were selected, indicate that as ψ_{CAJ} is increased, the structures at the flame tip also become more blurred, suggesting an increase in the flame convection velocity. Hence it appears that increasing ψ_{CAJ} reduces the effect of buoyancy on the flame characteristics and the momentum of the combined jet flow becomes more significant.

Figure 4-1. Instantaneous images of the visible flame structure from an unconfined PJ nozzle at different proportions of central axial jet to total flow rate. The fuel is propane at a constant input of 20kW, t=1/250s camera exposure time, f/8 aperture setting. Flow conditions: (a) Ψ_{CAJ}=0%, Γ_{CAJ}=0; (b) Ψ_{CAJ}=30%, Γ_{CAJ}=0.36; (c) Ψ_{CAJ}=50%, Γ_{CAJ}=0.57 and (d) Ψ_{CAJ}=100%, Γ_{CAJ}=1.

4.3.2 Time-Averaged Images

The effect of varying ψ_{CAJ} and hence Γ_{CAJ} on the time-averaged flame shape from a PJ nozzle is presented in Figure 4-2. The images are eight second exposures of an experimental region with dimensions of approximately 650mm×980mm. The flames at low values of ψ_{CAJ} possess the broad, bulbous flame shape also observed by Newbold *et al.* (2000) for a fluidic precessing jet nozzle and Nathan *et al.* (1996) for a high Strouhal number mechanically rotated precessing jet nozzle. The appearance of the flames for ψ_{CAJ}=75% and ψ_{CAJ}=100% (Γ_{CAJ}=0.8 and Γ_{CAJ}=1) are significantly different, with a much narrower width and slightly shorter length more characteristic of flames from simple turbulent jet nozzles.

A time-averaged image of the base of the flame is presented for ψ_{CAJ}=0% in Figure 4-3. The effect of ψ_{CAJ} on the structure of the base of the flame is demonstrated in Figure 4-4 by overlaying the constant value contours defining the edge of the flames. The lift-off height of the flames is approximately constant at x/d_{PJ}=2.5 for all ψ_{CAJ}. Newbold *et al.* (1997) notes that photographic film is generally more sensitive to wavelengths in the orange part of the visible spectrum than wavelengths in the blue part of the spectrum, which are likely to occur in the flame stabilisation region. However since the imaged region is a close-up of the base of the flame it is expected that the present measurements are not very sensitive to colour. Using images of the entire flame, Newbold *et al.* (1997) estimated the lift-off height to be x/d_{PJ}=3.8-7.7 for a 44kW flame at ψ_{CAJ}=0% from a PJ nozzle with d_{PJ}=13mm. Note that the extent of the imaged region of the isothermal experiments described in Chapter 3 was approximately x/d_{PJ}=3.5 and hence the present experiments demonstrate that combustion only occurs in a limited region within this axial distance. For $\psi_{CAJ}\leq$50%, the base of the flame appears as a "W" shape with the region of the flame on the centreline stabilising further downstream than the surrounding flame. This resembles the lobed structure at the base of the mechanically rotated precessing jet concentration field described by Nobes (1997).

Figure 4-4 demonstrates that the central axial jet has a significant effect upon the initial spreading rate of the flame from the PJ nozzle. The maximum flame spread occurs for ψ_{CAJ}=15% (Γ_{CAJ}=0.19) and is greater than that of the PJ only flame. For $\psi_{CAJ}\geq$30% ($\Gamma_{CAJ}\geq$0.36), increasing ψ_{CAJ} causes a progressive decrease in the flame spreading rate, especially for $\psi_{CAJ}\geq$75%, at which point the flame resembles a momentum dominated flame rather than that typical of a flame from a precessing jet nozzle. The observed change in the flame contour is in contrast to the results of the isothermal experiments presented in Section 3.4.3, which found that the 0.5-maximum jet spread reduces monotonically with ψ_{CAJ} and Γ_{CAJ}. However, this can be attributed to the fact that the flame boundary represents the edge of the stoichiometric contour, while the 0.5-maximum contour is normalised to the maximum concentration at each axial position. The combination of the observed change in stoichiometric contour and 0.5-maximum contour implies that the concentration decay, approximately on the jet centreline, is least rapid for ψ_{CAJ}=15% (Γ_{CAJ}=0.19).

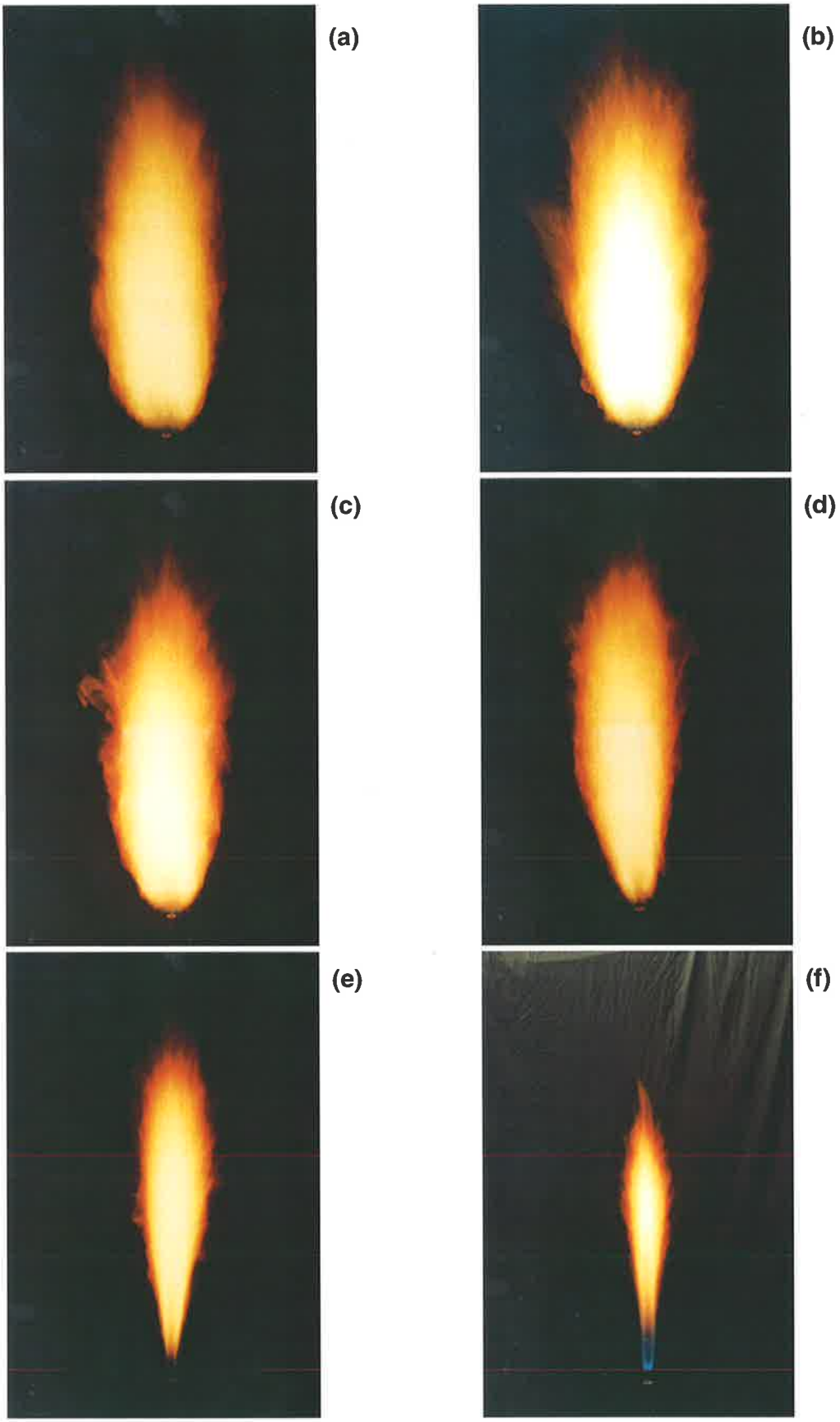

Figure 4-2. Time-averaged images of the visible flame from an unconfined PJ nozzle at different proportions of central axial jet to total flow rate. The fuel is propane at a constant input of 20kW, t=8s exposure time, f/22 aperture setting. Flow conditions: (a) ψ_{CAJ}=0%, Γ_{CAJ}=0; (b) ψ_{CAJ}=15%, Γ_{CAJ}=0.19; (c) ψ_{CAJ}=30%, Γ_{CAJ}=0.36; (d) ψ_{CAJ}=50%, Γ_{CAJ}=0.57; (e) ψ_{CAJ}=75%, Γ_{CAJ}=0.80 and (f) ψ_{CAJ}=100%, Γ_{CAJ}=1 (aperture of f/19).

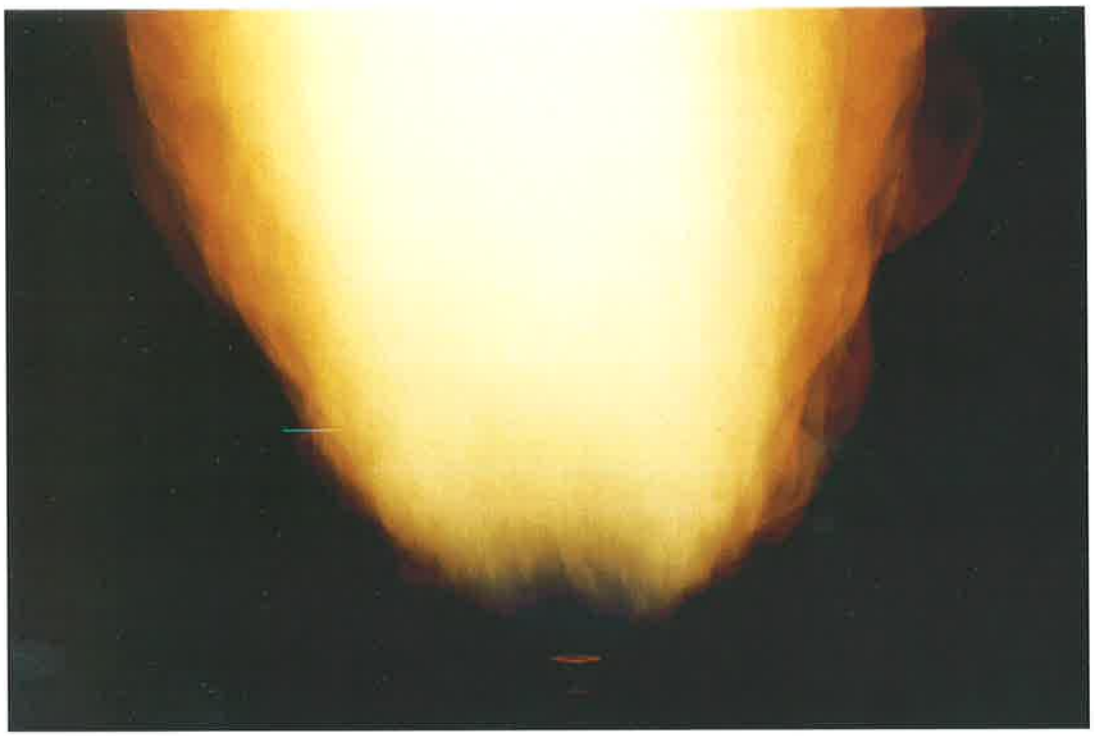

Figure 4-3. Time-averaged image of the base of the flame from an unconfined PJ nozzle at ψ_{CAJ}=0%. The fuel is propane at a constant input of 20kW, *t*=8s camera exposure time, *f*/27 aperture setting.

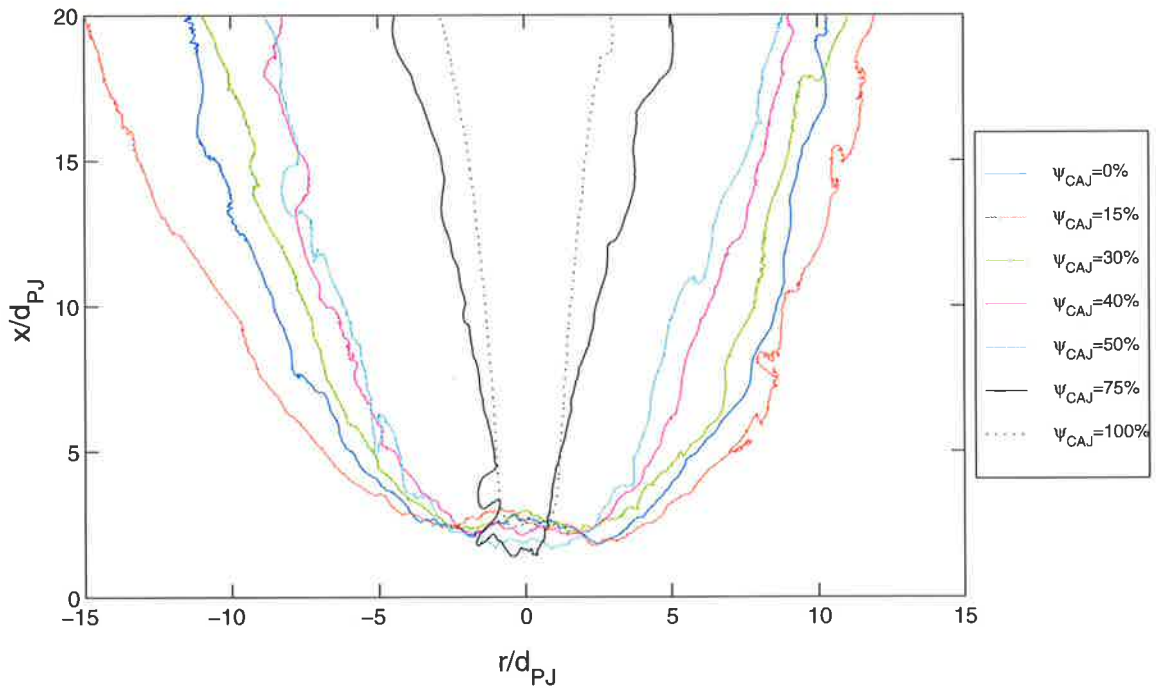

Figure 4-4. Comparison of the constant value signal intensity contours defining the edge of the flame from the time-averaged images of the base of the PJ nozzle flame at different ψ_{CAJ}. Momentum ratios are shown in Table 4-1.

4.3.3 The Effect of the Central Axial Jet on Flame Dimensions

The variation in flame volume, length, width and visible radiation signal intensity are plotted in Figure 4-5 to Figure 4-8 against the momentum ratio, Γ_{CAJ}, following the results of the isothermal flow visualisation experiments, which indicate that this is the controlling parameter of the combined precessing and central axial jet flows.

The variation in average flame volume, normalised to the value at $\Gamma_{CAJ}=0$, with the momentum ratio is presented in Figure 4-5. The flame volume was determined using both the "exact" method based on the cross-sectional area within the flame contour and the conical approximation of Turns and Myhr (1991), where $V_{flame} \propto L_{flame} \times W^2_{flame}$. The time-averaged images of the flames presented in Figure 4-2 demonstrate that the flame shape from the PJ nozzle changes with CAJ proportion and hence the canonical approximation is not appropriate for the purposes of comparison. Figure 4-5 indicates that the maximum flame volume occurs at $\Gamma_{CAJ}=0.19$ ($\psi_{CAJ}=15\%$) and increasing the momentum ratio further gradually decreases the flame volume. The flame volume is less than that of the PJ only case for $\Gamma_{CAJ} \geq 0.36$ based on the exact method and $\Gamma_{CAJ} \geq 0.49$ based on the conical approximation method. This is consistent with the change in flow regime from precessing jet dominated to central axial jet dominated at a momentum ratio of $\Gamma_{CAJ} \approx 0.2$-0.23 noted in the isothermal experiments.

For the present experiments, the fuel input energy was 20kW for all flame configurations. The analysis presented in Section 4.1 demonstrates that, for constant fuel flow rate, the global residence time, τ_G, and radiant fraction, χ_r, scale with the flame volume. Therefore Figure 4-5 also provides information about the variation in τ_G and χ_r with momentum ratio. In particular, the maximum residence time and radiant fraction can be deduced to also occur at $\Gamma_{CAJ}=0.19$ and to decrease with momentum ratio for $\Gamma_{CAJ}>0.2$. The flame volume and hence residence time and radiant fraction are approximately 20% greater at $\Gamma_{CAJ}=0.19$ compared to the precessing jet on its own.

As each photograph was taken with the same camera settings and then processed and digitised with the same scanner settings, the integrated signal from the entire flame volume represents a crude measurement of the visible radiation from each flame. No saturation was present in the long exposure images. Hence, assuming the spectrum of radiation from the flame does not change with ψ_{CAJ}, the integrated signal is a relative measure of the radiant fraction. The variation in integrated signal intensity with momentum ratio, normalised to the PJ only case ($\Gamma_{CAJ}=0$) is presented in Figure 4-6. The maximum signal intensity of each image, normalised to the value at $\Gamma_{CAJ}=0$ is also included as a further check on the trend in flame radiation. As different camera settings were used for the CAJ only flame, the relative radiation could not be calculated for this case. The trend in integrated intensity follows a very similar trend to the variation in radiant proportion deduced from Figure 4-5. The peak integrated intensity value occurs for $\Gamma_{CAJ}=0.19$ ($\psi_{CAJ}=15\%$) and increasing the momentum ratio in the CAJ dominated flow regime causes the intensity to decrease approximately linearly. The maximum value of the normalised peak intensity also occurs at $\Gamma_{CAJ}=0.19$, but the decrease in peak intensity in the CAJ dominated flow regime is not as marked as that based on the integrated intensity.

The variation in mean flame length, normalised to the value at $\Gamma_{CAJ}=0$, with the momentum ratio is shown in Figure 4-7. The variation in the mean flame length is broadly similar to the variation in normalised flame width and volume with momentum ratio, Figure 4-5 and Figure 4-8. This normalisation indicates that the flame length is greatest for $\Gamma_{CAJ}=0.19$ ($\psi_{CAJ}=15\%$) and further increasing the momentum ratio results in a general decrease in the

flame length, with the minimum value occurring when all the flow is introduced through the CAJ. The flame length for Γ_{CAJ}>0.47 is less than for flow through the PJ nozzle only. The decrease in flame length with momentum ratio in the CAJ dominated flow regime is much less than the decrease in flame volume or maximum flame width, Figure 4-8.

The variation of flame width to length with momentum ratio, Figure 4-8, is very similar to the trend of flame volume with momentum ratio, Figure 4-5, and intensity, Figure 4-6. The trend of W_{flame}/L_{flame} to decrease with Γ_{CAJ} in the CAJ dominated flow regime implies that size of the puff structures in the flame decreases, the number of large-scale structures increases and hence the characteristic strain rate in the flame increases. The maximum flame width to length ratio at Γ_{CAJ}=0.19 indicates that the flame strain rate is a minimum at this flow condition. The present measurements of W_{flame}/L_{flame}=0.37 at ψ_{CAJ}=0% and W_{flame}/L_{flame}=0.17 at ψ_{CAJ}=100% compare with the measurements of W_{flame}/L_{flame}=0.3 for the PJ only flame and W_{flame}/L_{flame}=0.18 for the flame from a simple jet by Newbold *et al.* (2000). The close agreement in overall flame shape of the two measurements contrasts with the significantly different normalised flame lengths. The flame length was measured by Newbold *et al.* (2000) to be L_{flame}/d_{or}=200 for the PJ only flame and L_{flame}/d=217 for a simple turbulent jet flame, much shorter than the present measurements of L_{flame}/d_{or}=351 and L_{flame}/d_{CAJ}=415 respectively. The cause of this discrepancy is unclear, but may be due to an error in scaling the measurements from the photographs to their actual physical dimensions or the effect an induced co-flow due to the overhead ventilation hood. A scaling error does not affect any of the trends deduced from the present results as all the measurements are normalised to the value at Γ_{CAJ}=0. It may also be because of the different jet conditions at the upstream orifice in each experiment.

Newbold *et al.* (2000) has shown that a reduction in $EINO_x$ for the PJ nozzle, compared to a flame from a simple jet burner, correlates with a decrease in flame length normalised by the burner diameter. The increase in normalised flame length detected in the present measurements, from L_{flame}/d_{or}=351 for PJ only flow to L_{flame}/d_{CAJ}=415 for CAJ only flow suggests that the thermal NO_x emissions are higher for the CAJ only flame than the PJ only flame. However, it is not possible from Figure 4-7 to infer the effect of momentum ratio on NO_x emissions because, for a CAJ proportion in between the limits of ψ_{CAJ}=0% and ψ_{CAJ}=100%, it is not clear what diameter should be used to normalise the flame length. The effect of momentum ratio and CAJ proportion on NO_x emissions is instead deduced from the variation in global residence time, based on Figure 4-5, and the ratio of flame width to length, Figure 4-8.

From the analysis outlined above it can be deduced that the variation of thermal NO_x emissions with momentum ratio and CAJ proportion is likely to scale inversely with the trend in the flame volume and the width to length ratio. Hence the minimum thermal NO_x emissions are expected to occur for Γ_{CAJ}=0.19 (ψ_{CAJ}=15%), and the emissions to increase with momentum ratio in the CAJ dominated flow regime, Γ_{CAJ}>0.2. The correlation between flame radiation and temperature on the production rate of NO_x via the thermal mechanism implies that the non-adiabatic flame temperature should also vary with Γ_{CAJ} in a similar fashion to $EINO_x$. As described above, Newbold *et al.* (2000) has demonstrated that the prompt mechanism of NO_x production can be significant in unconfined precessing jet flames due to the lower temperature of these flames. However the influence of prompt NO_x is not significant in the pilot-scale results and it is readily apparent that the trends in the open flame shape are consistent with the measured trends in NO_x emissions and radiation in the pilot-scale facility.

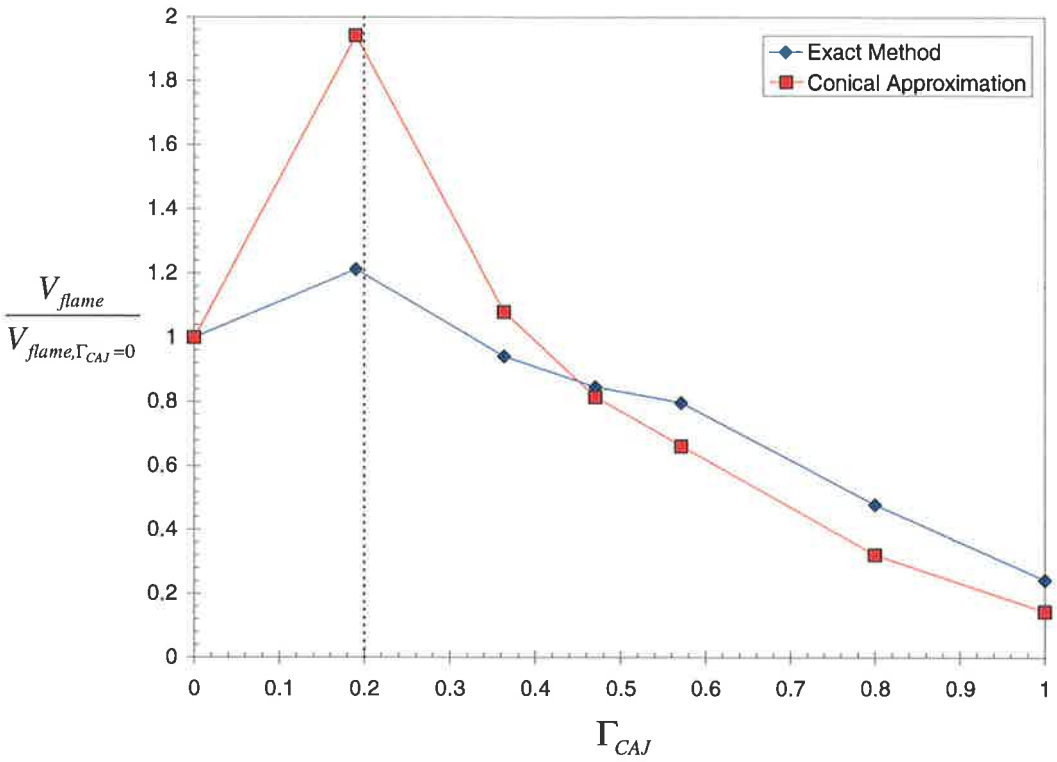

Figure 4-5. The variation in flame volume, normalised to the value at Γ_{CAJ}=0, with momentum ratio at constant total fuel flow rate. The "exact" method is based upon the area within the contour defining the time-average flame edge and the "conical approximation" is based upon the simplified equation derived by Turns and Myhr (1991). See Table 4-1 for jet conditions. The dashed line indicates the transition from PJ to CAJ dominated flow regime.

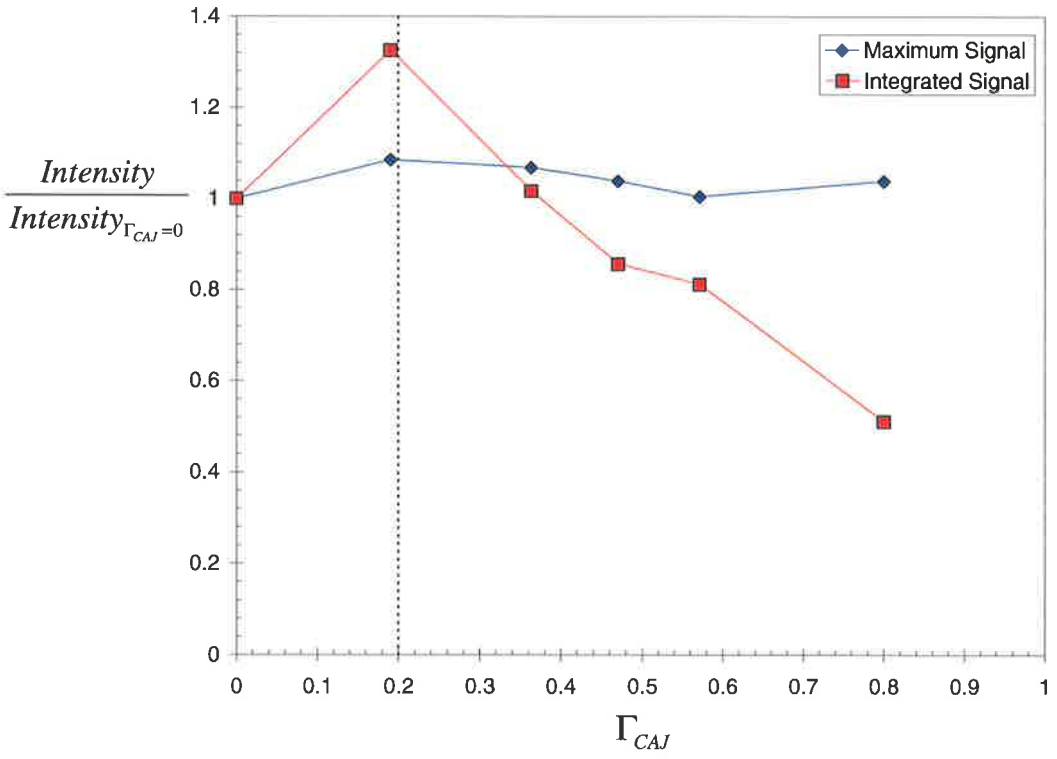

Figure 4-6. The variation in signal intensity of the visible flame radiation, normalised to the value at Γ_{CAJ}=0, with momentum ratio at constant total fuel flow rate. The integrated signal is based on the sum of the measured pixel intensities within the flame volume. See Table 4-1 for jet conditions. The dashed line indicates the transition from PJ to CAJ dominated flow regime.

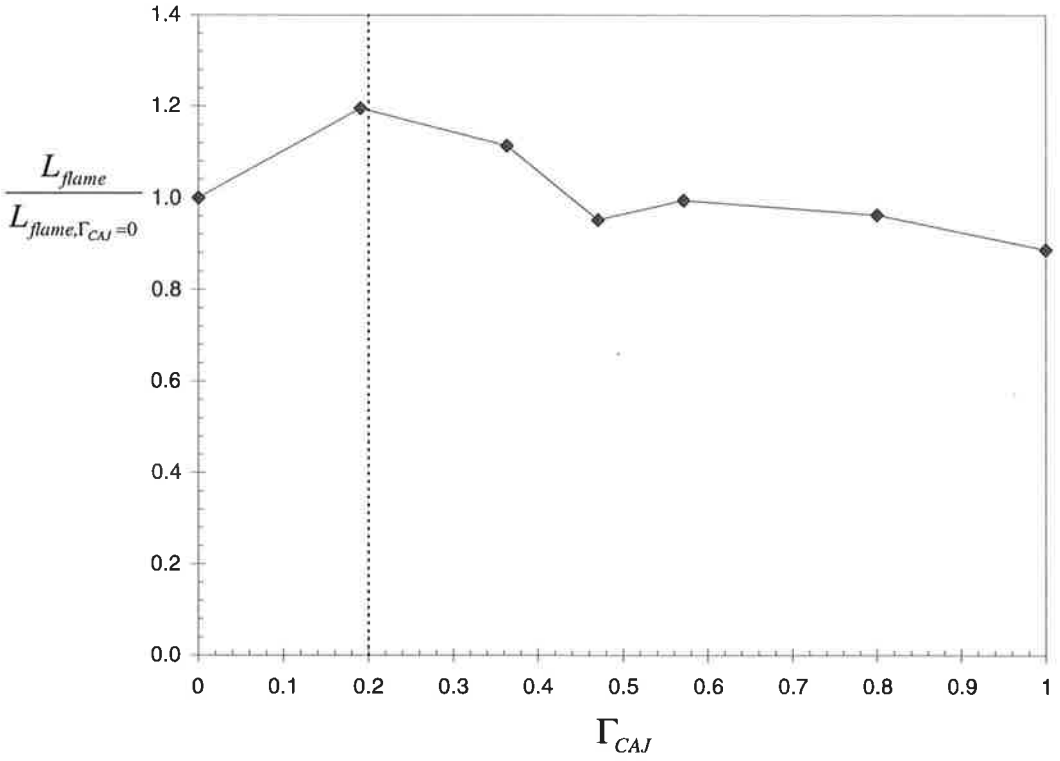

Figure 4-7. The variation in flame length, normalised to the value at Γ_{CAJ}=0, with momentum ratio at constant total fuel flow rate. See Table 4-1 for jet conditions. The dashed line indicates the transition from PJ to CAJ dominated flow regime.

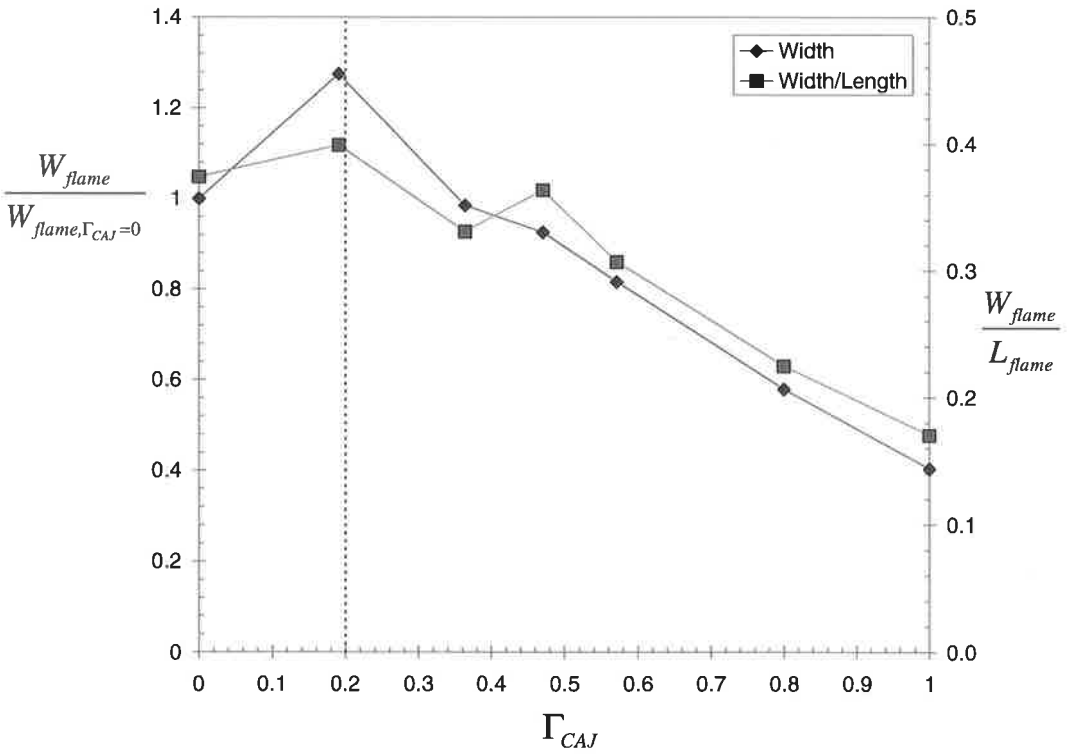

Figure 4-8. The variation in maximum flame width, normalised to the value at Γ_{CAJ}=0, and the ratio of flame width to length with momentum ratio at constant total fuel flow rate. See Table 4-1 for jet conditions.The dashed line indicates the transition from PJ to CAJ dominated flow regime.

4.4 Conclusions

Instantaneous and time-averaged photographs have been used to visualise the effect of the central axial jet on the length, width and volume of the flame from an unconfined precessing jet nozzle at constant total fuel flow rate. The results demonstrate that the proportion of central axial jet mass flow rate, ψ_{CAJ}, causes significant changes in both the instantaneous flame structure and the average flame shape. Consistent with the isothermal results reported in Section 3.4.3, the present results indicate the momentum ratio, $\Gamma_{CAJ}=G_{CAJ}/(G_{PJ}+G_{CAJ})$, also controls the variation in combustion characteristics of the combined precessing and central axial jets. In particular, the relationship of flame volume, length, width and intensity with momentum ratio is different for $\Gamma_{CAJ}<0.2$, the precessing jet dominated flow regime, and $\Gamma_{CAJ}>0.23$, the CAJ dominated flow regime. Photographs of the base of the entire flame demonstrate that the lift-off height and hence flame stability is not affected by the change in dominant flow regime and is constant for $0\leq \Gamma_{CAJ} \leq 0.57$ ($0\%\leq \psi_{CAJ} \leq 50\%$). The present results also suggest a separate transition occurs from buoyancy dominated flames to momentum dominated flames at a shaping jet momentum ratio of about $\Gamma_{CAJ}>0.57$ ($\psi_{CAJ}>50\%$). This was deduced from the change in the number and the perceived velocity of structures observed in the flame.

Within the PJ dominated flow regime, increasing the momentum ratio, Γ_{CAJ}, increases the spread and size of the structures within the flame, while in the CAJ dominated flow regime the spread and size of the structures decrease with increasing momentum ratio. Hence the spread and size of the flame are a maximum at a momentum ratio within the range $0.19\leq \Gamma_{CAJ} <0.36$. This trend is observed to be the case for the mean flame volume, flame length, width and signal intensity. The measured variation in flame volume, length and width with momentum ratio have been correlated with other properties of unconfined flames based on scaling relationships described in the literature. The radiant fraction and global residence time are expected to follow the same trend with momentum ratio as the flame volume and signal intensity. Hence the radiant fraction and global residence time are expected to be a maximum in the range $0.19\leq \Gamma_{CAJ} <0.36$ and decrease with a further increase in momentum ratio. At the condition producing the maximum radiant fraction and global residence time in the present experiments, $\Gamma_{CAJ}=0.19$, the magnitude of these parameters is deduced to be approximately 20% greater than for the PJ only case and five times greater than for the CAJ only case. The emission index of nitrogen oxides is predicted to follow an inverse trend such that the minimum thermal NO_x emissions are expected to occur in the range $0.19\leq \Gamma_{CAJ} <0.36$ and further increasing the momentum ratio increases the NO_x emission index. This is consistent with the measurement of the flame length normalised to the jet orifice diameter, which implies the thermal NO_x emissions for the CAJ flow only case are 20% greater than those of the PJ flow only case. The above results and deductions are consistent with the measurements reported in Chapter 5 of heat flux and emissions of confined PJ burner flames in a pilot-scale cement kiln simulator.

At the momentum ratio $\Gamma_{CAJ}=0.19$, the flame volume reaches the maximum measured value of a factor of 1.21 greater than the PJ only case and the measured flame width to length ratio is also at its maximum value of 0.40, compared to a value of 0.37 for the PJ only case and 0.17 for the CAJ only case. These results imply that at this flow condition the global strain rate at the tip of the flame from the combined PJ and CAJ nozzle is a minimum. The momentum ratio of $\Gamma_{CAJ}=0.19$ is also close to the momentum ratio that defines the transition from precessing

jet to central axial jet dominated flow regime detected in Chapter 3 of Γ_{CAJ}≈0.2-0.23. The isothermal experiments presented in Section 3.4.3 indicate that the 0.5-maximum jet spread reduces linearly with momentum ratio for Γ_{CAJ}<0.6. The present experiments demonstrate that the spread of the flame boundary and hence the stoichiometric contour is a maximum at Γ_{CAJ}=0.19 and decreases with further increases in the momentum ratio in the CAJ dominated flow regime. These results imply that the centreline concentration decay rate is a minimum at a momentum ratio in the range 0.19≤ Γ_{CAJ} <0.36. Hence the optimal condition for the maximum heat transfer and minimum emissions from the PJ nozzle predicted from the measurement of unconfined flame dimensions is the same as that measured in the pilot-scale facility.

Chapter 5

Combustion Properties of Confined Pilot-Scale Precessing Jet Flames

5.1 Introduction

The ability to produce a wide range of flame types by combining a central axial jet with a precessing jet burner has been demonstrated in Chapter 4 and in commercial rotary kiln installations. Rapson *et al.* (1995) and Hill *et al.* (1995) for example, deduced that substantial changes in the heat flux profile of flames within a rotary cement kiln can be obtained by varying the proportion of the total flow through the central axial jet. These deductions were based on measured differences in kiln performance. However, the heat flux and NO_x emissions of these combined flows have yet to be quantified or compared with those of a conventional burner in a well controlled confined facility. Hence the aims of the present experiments were to document the range of flame shapes, heat fluxes and NO_x emissions from the combined PJ-CAJ burner and to compare them with those of conventional gas-fired burners in rotary kilns.

Pilot-scale trials in a well controlled environment are often chosen as a cost effective and reliable method to evaluate the effectiveness of new burner designs for use in an industrial environment. However the results of reduced scale experiments can only be related to full scale plant if similarity is maintained between the experiments and the industrial application. Maintenance of complete similarity of all relevant dimensionless parameters is not possible in combustion modelling as many physical and chemical processes do not scale in the same manner. Hence the goal is to ensure that similarity of the most important parameters is maintained (Spalding, 1962). Most scaling studies aim to ensure similarity of the turbulent mixing conditions is achieved, usually by employing either constant velocity or constant residence time scaling criteria (Smart and Morgan, 1994). These methods seek to ensure similarity of the large macro-scale turbulent mixing processes and the global chemical reaction times in the flame respectively, but necessarily compromise on the Reynolds Number. Additionally, pilot facilities cannot adequately simulate the relationship between the flame and the furnace system, which differs between the model and industrial scales. Since complete similarity between facilities of different scale can never be maintained, there is no unique or universal "scaling criterion" to relate the results from a pilot-scale trial to operating plant, so that engineering and scientific principals must be applied to scale flame properties such as heat flux and pollutant emissions.

Many of the studies specifically related to the scaling of NO_x emissions from turbulent flames are based on circular jets and other simple burner designs in open flame conditions. For example, Chen and Driscoll (1990) and Driscoll *et al.* (1992) have shown that NO_x emissions from open turbulent diffusion flames vary with global residence time,

based on measured flame volume and radiant fraction, as has Nathan *et al.* (1996) for open precessing jet flames. Turns and Myhr (1991) varied the emissivity of open gas flames by changing fuel type and developed a relationship which scales a reduction in flame temperature, and hence NO_x emissions, with increased radiant fraction. However, the scaling of NO_x emissions for practical purposes is more difficult due to the complex geometry of industrial burners, the presence of high temperature furnace walls and pre-heated combustion air, which result in increased emissions of NO_x (Tomeczek *et al.*, 1995).

The scaling of emissions from swirl stabilised confined natural gas flames in boiler type conditions has been investigated extensively as part of the "Scaling 400" study. An analysis of the principal energy flows in the Scaling 400 flames by Weber (1996), suggests that the flame temperature and hence the NO_x emissions, can be related to the radiant fraction, the ratio of entrained combustion products to the inlet flow rate and the fraction of the total thermal input extracted in the post-flame zone. For a furnace environment with system dependent heat sinks, the energy analysis described above can also be used to show that NO_x emissions from swirl stabilised natural gas flames in cylindrical furnaces are directly related to the heat extraction rate. Hence Weber (1996) proposes that the primary thermal similarity criterion in scaling from experimental to industrial scales, is to achieve identical furnace exit temperatures. As part of the Scaling 400 program, Sayre *et al.* (1994) also investigated a non-sooting flame in two furnaces with similar aerodynamics but very different heat extraction rates. The flame in the water-cooled furnace was shown to have lower flame temperatures and NO_x emissions than that in the refractory lined furnace. They attribute the different flame temperatures to different entrained furnace gas temperatures, which are in turn controlled by radiant heat transfer, hence confirming the existence of a strong relationship between radiant heat transfer and NO_x emissions in both open and confined flames. Hsieh *et al.* (1998) demonstrated that excellent agreement between the Scaling 400 model and measured NO_x emissions can be achieved across a wide range of different burner scales when the furnace heat flux characteristics and burner type, and hence mixing characteristics, are truly similar.

Each of the above components of the Scaling 400 study were conducted under conditions in which every effort was made to ensure mixing similarity at different scales. However pilot-scale facilities can also be used to compare the flames from burners with intentionally different mixing conditions, as in the present study. In the past such studies have tacitly assumed that changes in the mixing conditions do not influence other similarity criteria such as thermal similarity. For example, Beltagui *et al.* (1993) conducted detailed measurements of the aerodynamics, heat transfer and pollutant emissions of swirling natural gas flames over a wide range of swirl numbers in a vertical cylindrical furnace. However, the effect of swirl on NO_x emissions was considered independently of the effect of swirl on the heat flux profiles and heat extraction. Tomeczek *et al.* (1995) also did not consider any changes in heat transfer in comparing the NO_x emissions of two very different natural gas burners. The present investigation addresses the effect of different mixing conditions on thermal similarity by a comparison of flames with different mixing conditions, both in a pilot-scale facility and in full scale plant. It should also be noted that the present investigation is conducted in a rotary kiln environment, as distinct from all the above studies, which were conducted in boiler simulators.

The present study also compares measurements from the pilot-scale facilities with those from full scale plant to examine the effect of process-flame interaction on the relationship between heat flux and NO_x emissions. In a rotary kiln environment, a complex feedback mechanism exists between the feed material and the flame, so that the NO_x emissions are dependent upon these heat transfer processes in addition to the mixing characteristics of the burner and the aerodynamics in the kiln. The interdependence between the heat flux requirements of the feed material and the temperature of the flame implies that for an optimal rotary kiln burner design, minimisation of NO_x emissions cannot be achieved without consideration for the optimisation of the thermal profile (Nathan and Rapson, 1995; Nathan and Manias, 1995).

In an operating rotary kiln, the principal requirement is to achieve a specified time-temperature profile for the product, which equates reasonably well to a specified wall temperature profile. If an increase in heat flux from the flame can be achieved, for example by a modification to the fuel or burner, this allows an increase in the rate of product throughput and hence heat extraction, while the wall temperature profile remains more or less unchanged to maintain the product temperature within the specifications. By contrast, in most experimental kiln facilities, the heat load of the product is usually simulated by careful choice of insulating bricks and a surrounding water cooled jacket. The control over the wall surface temperatures that can be achieved by such a facility in response to variations in test conditions and hence heat extraction is negligible, so that wall temperatures increase with an increase in flame radiant heat flux produced, for example, by a change in burner. Hence thermal similarity between the experimental and the industrial scale, which is influenced by the thermodynamic feedback between the walls and the combustion process will be compromised in a comparison between flames with different heat flux profiles. This issue is also addressed in the present study by a comparison of similar burners in a pilot-scale kiln simulator and in operating rotary kilns.

5.2 Experimental Conditions

The confined combustion experiments were conducted in a 2-MW cement kiln simulator facility at the International Flame Research Foundation (IFRF), IJmuiden, The Netherlands. A comprehensive description of the facility, measurement equipment and burner designs is given in Section 2.3.2. Experiments were conducted at a combustion (or "secondary") air pre-heat temperature of 640°C for the comparison of a PJ burner and a conventional burner. This pre-heat temperature is typical of many cement and lime kilns, although some modern cement plants use temperatures as high as 1000°C. The result is to provide wall temperatures that are closer to those of lime kilns than cement kilns. Additional experiments using the precessing jet burner alone were conducted at a pre-heat temperature of 840°C.

The experimental burners are a PJ nozzle with CAJ for flame shaping with d_{PJ}=56mm and an IFRF generic multi-channel burner (MCB) design used as a conventional burner for comparison. Both burners were scaled using the constant velocity similarity criterion. The different CAJ proportions, ψ_{CAJ}, momentum ratios, Γ_{CAJ}, and settings of the PJ burner investigated are shown in Table 5-1. The MCB nozzle was configured to provide two different flames based on the extent of external recirculation between the flame and the kiln walls, as determined by calculating the Craya-Curtet parameter, m, see Section 1.3.4. The Craya-Curtet parameter was altered by varying the flow rate of primary air to the MCB nozzle, which changes the momentum of the flame relative to the secondary air and hence controls the degree of external recirculation, see Table 5-1. Moles *et al.* (1972) state that for recirculation to occur, m must be greater than 1.5 and that good recirculation in practical kiln systems is observed when $2.0< m <2.5$. One of the present burner arrangements had m=0.6 (MCB-CC0.6), typical of an "under-recirculatory" flame. The other flow condition had m=2.7 (MCB-CC2.7), to provide a typically good recirculatory flame.

Flame	Flow rates (kg/hr)						Γ_{CAJ}
	Fuel Channels		Primary Air Channels				
	0-A†/PJ	2-A/CAJ	1-S‡	3-A	4-A	5-A	
MCB-CC2.7	57	103	107	0	107	107	-
MCB-CC0.6	57	103	20	0	20	20	-
PJ-ψ0-T640/840/840*	160	0	-	-	-	-	0
PJ-ψ8-T840*	147	13	-	-	-	-	0.05
PJ-ψ13-T840*	139	21	-	-	-	-	0.10
PJ-ψ15-T640/840	136	24	-	-	-	-	0.11
PJ-ψ19-T840*	130	30	-	-	-	-	0.17
PJ-ψ25-T640/840	120	40	-	-	-	-	0.25
PJ-ψ31-T840	111	49	-	-	-	-	0.32

Table 5-1. Fuel and primary air flow rates for the two multi-channel burner configurations and the precessing jet burner with different central axial jet proportions (ψ_{CAJ}). The notation for the precessing jet flames also includes the secondary air pre-heat temperature. Symbols indicate: * - the burner tip was retracted flush with the inlet baffle plates, while in all other cases the nozzle tip protrudes 475mm beyond the baffle; † - axial channel; ‡ - swirled channel.

5.3 Results

5.3.1 Heat Flux Measurements

Figure 5-1 and Figure 5-2 demonstrate clearly that the mixing characteristics of a burner nozzle can influence the heat flux characteristics of a flame in a rotary kiln. The variation in radiative heat flux with axial distance along the kiln simulator for different ψ_{CAJ} at a secondary air pre-heat temperature of 840°C is shown in Figure 5-1. This quantifies that an increase in ψ_{CAJ} translates the heat flux profile downstream, consistent with trends found in industrial kilns by Rapson *et al.* (1995) and Hill *et al.* (1995). The axial distance from the tip of the burner to the peak of the heat-flux profile increases by approximately one kiln diameter as ψ_{CAJ} is increased from 0% to 31% (momentum ratio increased from Γ_{CAJ}=0 to Γ_{CAJ}=0.32). The data also suggests that the peak heat flux is greatest when ψ_{CAJ}=15% (Γ_{CAJ}=0.11). The difference between the minimum and maximum peak heat flux is about 3%, see Table 5-2. The effect of pushing the peak heat flux down the kiln by increasing ψ_{CAJ} can also be seen in Figure 5-2 which presents the data for 640°C air pre-heat.

The heat flux characteristics of the MCB and PJ burners at 640°C pre-heat are compared in Figure 5-2. It is evident that two of the three PJ burner flames produce higher radiant heat flux than either of the MCB flames. The radiant heat flux from the PJ-ψ0-T640 flame, as measured by the ellipsoidal radiometer, is lower than that produced by the PJ-ψ15-T640 and PJ-ψ25-T640 cases, in contrast to the radiant output measured for the comparable flames with 840°C pre-heat (Figure 5-1). The trend in Figure 5-2 however, is consistent with the measured wall temperature profiles in which the PJ-ψ0-T640 flame also produces comparable heat flux with that of the MCB-CC2.7 flame and lower heat flux than those of the PJ-ψ15-T640 and PJ-ψ25-T640 flames, see Figure 5-4.

The shape of the heat flux profile of the typically good Craya-Curtet parameter MCB flame is broadly comparable with that produced by the PJ burner flames. However it produces a peak heat flux, as measured by an IFRF ellipsoidal radiometer, about 7% lower than that of the PJ-ψ15-T640 and PJ-ψ25-T640 flames, see Table 5-2. The total heat release as measured by the integrated radiation measurements is 12% lower than the PJ burner flames, although it is only 3% lower as measured by the total heat transfer through the walls. The shape of the m=0.6 MCB flame is much longer than any of the other flames with a peak some two kiln diameters further down the kiln. The peak heat flux is also much lower than the PJ burner flames (approximately 12%). The total radiative and wall heat transfer measured from the MCB-CC0.6 flame is 20% and 8% lower than that from the other flames, respectively. This highlights the importance of external recirculation in achieving good burner design for a jet entrainment type burner, as emphasised by Mullinger (1999).

Table 5-2 shows that the internal consistency in the trends of heat transfer as measured by total radiative heat flux, the total heat transfer through the walls and total calculated direct flame radiant energy, is good for the case with 640°C pre-heat and poorer with 840°C pre-heat. The variation in total heat output with ψ_{CAJ} is within 3% for each technique, except for that determined by total radiation from the PJ-ψ100-T640 flame. Thus the dominant operational effect of changing ψ_{CAJ} is to "stretch" the shape of the heat flux profile so that the peak heat flux location and magnitude can be controlled, with a simultaneous influence on the total heat release.

5.3.1.1 Error Analysis

The ellipsoidal radiometer measures total hemispherical radiation incident on the instrument. Therefore the radiation measurements presented in Table 5-2 include both the direct radiation from the flame and the indirect radiation from the walls. To check the accuracy of the data, an energy balance of the dominant heat transfer paths in each segment of the kiln, ignoring the effects of convection and absorption from the flame, was calculated. For each segment, the difference between the total radiant energy measured by the ellipsoidal radiometer, Q_{rad}, and the total energy removed through the kiln simulator wall segments, Q_{loss}, should equal the sum of the radiant heat absorbed by the walls, $Q_{wall,abs}$, and the radiant heat emitted by the walls, $Q_{wall,emit}$, such that:

$$\dot{Q}_{rad} - \dot{Q}_{loss} = \dot{Q}_{wall,\,abs} + \dot{Q}_{wall,\,emit} \qquad \textbf{Equation 5-1.}$$

Q_{loss} is calculated from the rate of heat transfer to the cooling water flowing around the exterior of each kiln segment. Based on a constant wall emissivity of ε=0.68 and an equal value for the wall absorptivity, Equation 5-1 can be reduced to the relationship shown in Equation 5-2, where σ is the Stefan-Boltzmann constant and T_w is the surface wall temperature measured in each kiln segment of the simulator facility:

$$\dot{Q}_{rad} - \dot{Q}_{loss} \approx (1+\varepsilon)\varepsilon\sigma T_w^{\,4} \qquad \textbf{Equation 5-2.}$$

The results of the heat flux and wall temperature measurements were used to calculate the values of the left and right hand sides of Equation 5-2. The discrepancy between the heat transfer difference, Q_{rad} - Q_{loss}, and the sum of the radiant heat absorbed and emitted by the walls, $Q_{wall,abs}$ + $Q_{wall,emit}$, is 5.7% for all flames with a standard deviation of ±3.3%. Considering the assumptions made in the calculations and analysis, the small discrepancy in the energy balance represents excellent agreement of the measured results.

The above energy analysis also indicates that the direct flame radiation, Q_{flame}, is equal to the difference between the total radiant heat measured by the radiometer and the radiant heat emitted by the walls:

$$\dot{Q}_{flame} = \dot{Q}_{rad} - \dot{Q}_{wall,\,emit} \qquad \textbf{Equation 5-3.}$$

The calculated values for the total radiant heat from each flame are shown in Table 5-2 and show that the highest radiant heat transfer for each air pre-heat temperature occurs for PJ flames with ψ_{CAJ}=15-25% (Γ_{CAJ}=0.11-0.25). The flames from the MCB nozzle are also shown to produce significantly less radiant heat (approximately 15%), consistent with the total radiation and total wall heat transfer measurements.

Flame	Peak radiant heat flux, Q_{rad}		Integrated wall heat release		
	Value	Location	Net measured radiation, Q_{rad}	Wall temperature differential, Q_{loss}	Calculated direct flame radiation, Q_{flame}
	(kW/m^2)	(x/D_{kiln})	(kW)	(kW)	(kW)
PJ-ψ0-T640	344	2.5	4,983	1,295	2,907
PJ-ψ15-T640	388	2.7	5,383	1,311	3,203
PJ-ψ25-T640	379	3.1	5,289	1,315	3,083
MCB-CC2.7	356	2.6	4,707	1,278	2,669
MCB-CC0.6	335	5.0	4,288	1,204	2,587
PJ-ψ0-T840	454	2.2	6,394	1,442	3,503
PJ-ψ15-T840	458	2.6	6,351	1,437	3,532
PJ-ψ25-T840	444	3.2	6,446	1,429	3,681
PJ-ψ31-T840	450	3.0	6,411	1,435	3,617
PJ-ψ0-T840*	-	-	-	1,459	-
PJ-ψ8-T840*	-	-	-	1,466	-
PJ-ψ13-T840*	-	-	-	1,433	-
PJ-ψ19-T840*	-	-	-	1,425	-

Table 5-2. Summary of the peak heat flux and total heat release produced by all PJ burner and MCB flames at 640°C and 840°C pre-heat. The total radiant heat from the flame is calculated from a heat balance of the main heat transfer paths in each kiln segment. A correction has been made for the effective increase in kiln length and hence total heat flux when the burner is mounted flush with the inlet baffle plate, as indicated by the symbol *.

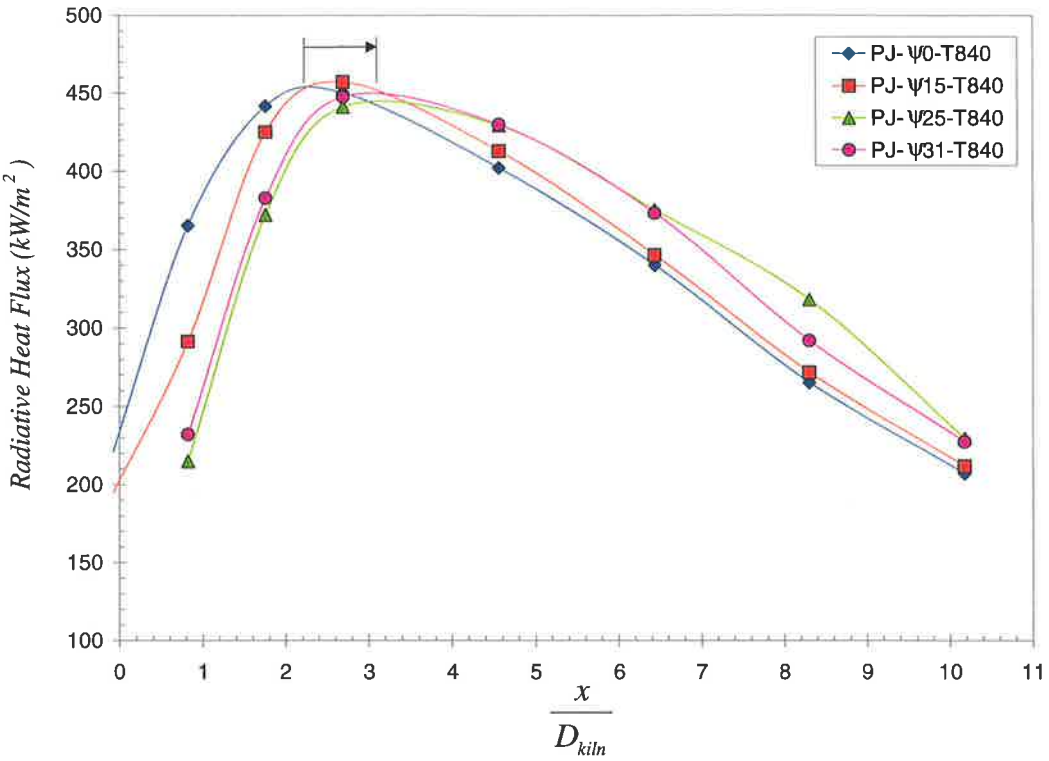

Figure 5-1. Profiles of the radiative heat flux, Q_{rad}, from precessing jet flames with various proportions of central axial jet to total flow rate, ψ_{CAJ}. The arrow indicates the axial distance which the peak in the heat flux profile is shifted by variation of axial jet proportion. Conditions: 2MW fuel input, 840°C pre-heat, see Table 5-1 for momentum ratios, Γ_{CAJ}.

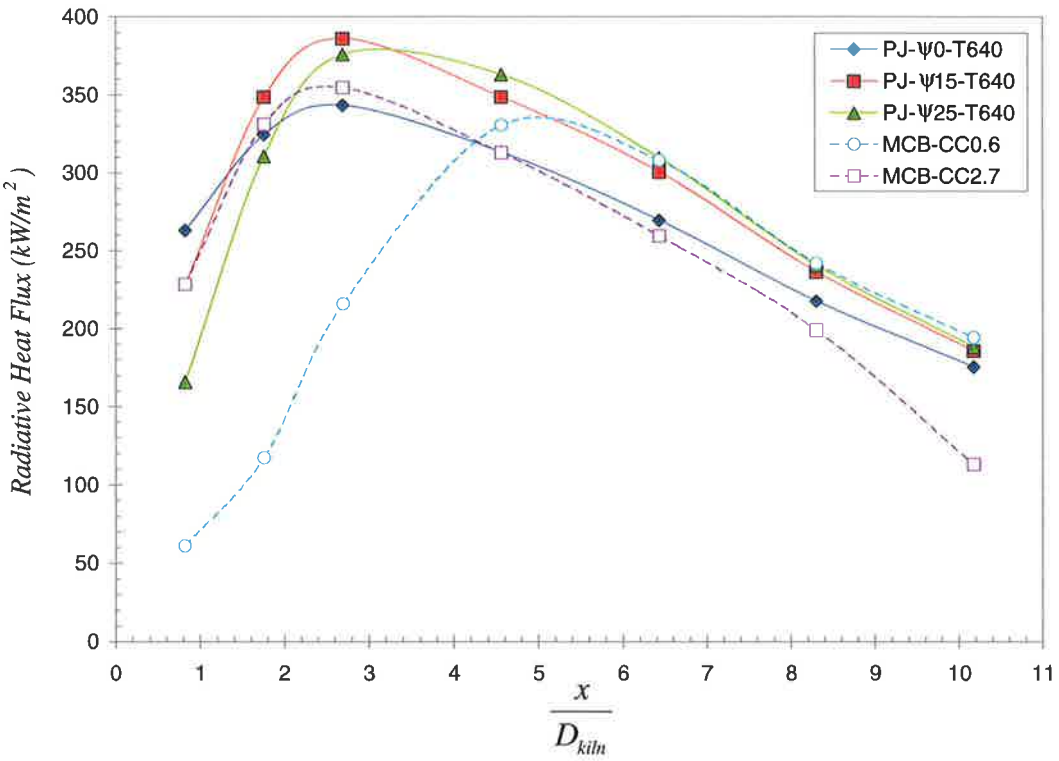

Figure 5-2. Profiles of the radiative heat flux, Q_{rad}, from precessing jet flames with various proportions of central axial jet to total flow rate, ψ_{CAJ}, compared to a low recirculation flame (MCB-CC0.6) and a typically good recirculation flame (MCB-CC2.7) from a multi-channel burner. Conditions: 2MW fuel input, 640°C pre-heat, see Table 5-1 for momentum ratios, Γ_{CAJ}.

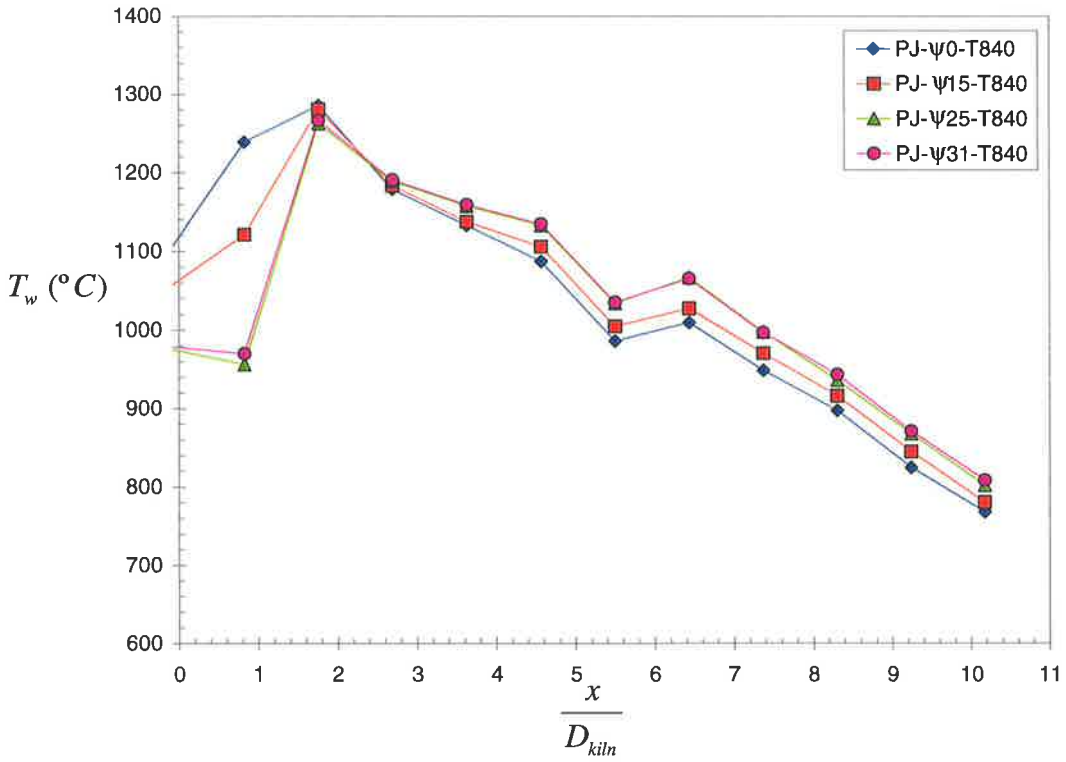

Figure 5-3. Profiles of the temperature at the inner surface of the kiln wall, T_w, for precessing jet flames with various proportions of central axial jet to total flow rate, ψ_{CAJ}. Conditions: 2MW fuel input, 840°C pre-heat, see Table 5-1 for momentum ratios, Γ_{CAJ}.

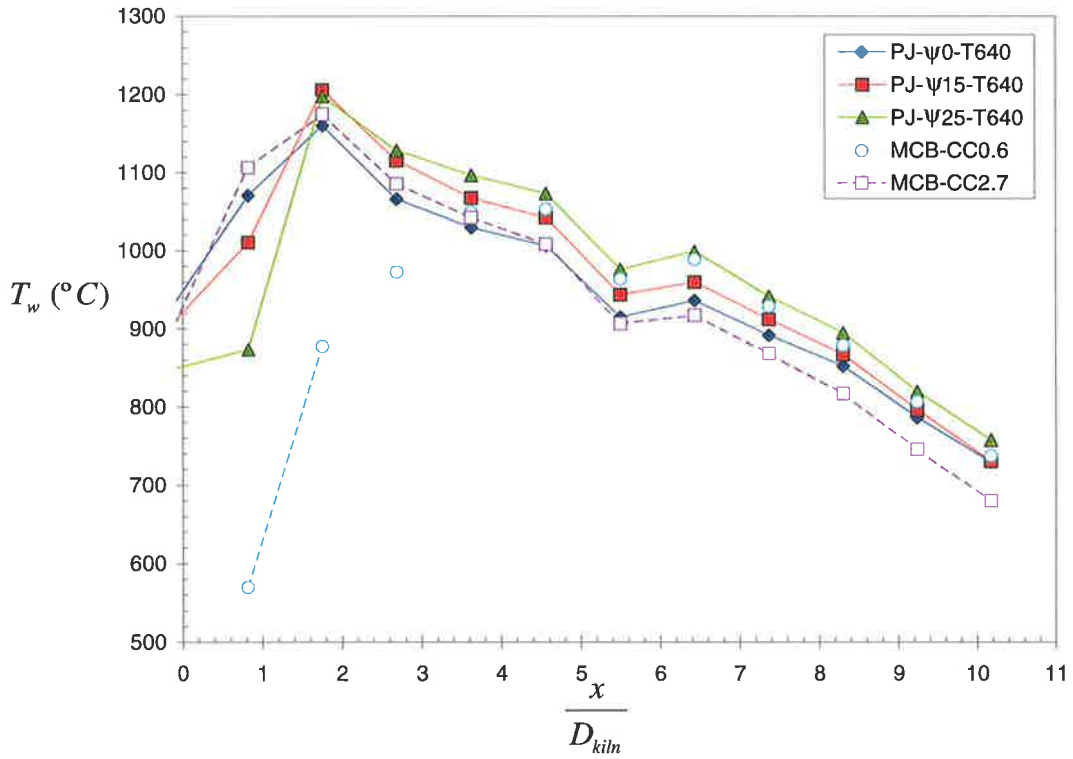

Figure 5-4. Profiles of the temperature at the inner surface of the kiln wall, T_w, for precessing jet flames at various proportions, ψ_{CAJ}, compared to a low recirculation flame (MCB-CC0.6) and a typically good recirculation flame (MCB-CC2.7) from a multi-channel burner. Conditions: 2MW fuel input, 640°C pre-heat, see Table 5-1 for momentum ratios, Γ_{CAJ}.

5.3.2 In-Flame Measurements

In-flame measurements of gas species concentration were made by traversing the gas sampling probe across the full diameter of the pilot kiln through access ports. Ten radial measurements were made at each of the six access ports. Due to the large number of measurement points and the time required to achieve a stable measurement at each location, complete maps of the gas species concentration are only available for three flames: the two multi-channel burner flames MCB-CC0.6 and MCB-CC2.7 and one precessing jet flame, PJ-ψ25-640. Partial concentration maps were recorded for some other precessing jet cases and are presented in Appendix A.

Concentration maps of in-flame NO_x and carbon monoxide for the three complete measurements are presented in Figure 5-5 to Figure 5-10. A consistent colour-map is used for each gas species. In the case of carbon monoxide, no data is presented below a concentration 0.5% as this contour level is defined by Beltagui *et al.* (1993) to represent the edge of a flame and hence represents the boundary of the flame volume in the present results.

5.3.2.1 CO Emissions

The in-flame concentration of carbon monoxide, CO, is shown for the three complete data sets in Figure 5-5, Figure 5-7 and Figure 5-9. The flame volume, as defined by the 0.5% concentration contour, shows that the flame from each burner configuration occupies a significant proportion of the pilot-scale kiln simulator. In an operating rotary kiln manufacturing product, the kiln length is typically 15-30 diameters, giving more opportunity for complete burnout than occurs in the present kiln simulator.

Flame asymmetry is clearly visible in each burner configuration, though it is most evident in the MCB-CC2.7 flame, which has a high degree of swirl. The volume of the flame from the PJ nozzle is approximately twice that of the MCB-CC2.7 flame, although the latter has a significant and long tail which runs along one side of the kiln and is not fully burned out by the last measurement station. By contrast the volume of the MCB-CC0.6 flame is much larger than the other three flames so that burnout is not complete within the kiln. The asymmetry in the CO measurements can be attributed principally to residual bias in the co-flowing air stream. Laser Doppler Annememtry (LDA) measurements conducted after the present experiments indicated that the velocity profile of the co-flowing air 1m from the baffle plate was biased to the positive or right hand side of the kiln, see Figure 5-11, and a slight tangential or swirling component was present, see Figure 5-12, despite the mitigating influence of the baffle plates.

Measurements of the in-flame CO concentration were carried out over a limited region within the kiln simulator for precessing jet burner flames at 840°C pre-heat (PJ-ψ0-T840 and PJ-ψ25-T840). Comparison of the CO profiles from this data, shown in Appendix A, and Figure 5-5 indicates that the air pre-heat temperature and hence co-flow air velocity does not have a significant effect upon the precessing jet flame volume at ψ_{CAJ}=25%. The limited data available to compare the effect of the central axial jet demonstrated that the concentration of CO is significantly lowered along the kiln wall at approximately two kiln diameters from the burner tip. This indicates that increasing the proportion of central axial jet reduces the proximity of the flame volume to the kiln walls and the concentration

of carbon monoxide present on the walls. This is particularly relevant to the manufacture of cement (and to a lesser extent lime) as it is known that reducing conditions are detrimental to clinker properties.

5.3.2.2 NO_x Emissions

The in-flame NO_x profiles are shown in Figure 5-6, Figure 5-8 and Figure 5-10. The profiles are characterised by a peak at about 4 to 6 kiln diameters from the burner tip and a general trend of increasing concentration of NO_x with axial distance, consistent with the significance of residence time in the dominant thermal mechanism of NO_x formation in kilns (Hsieh *et al.*, 1998). The in-flame profiles show significant asymmetry, consistent with the carbon monoxide measurements, reinforcing the conclusion that the single point "flue" measurements may not be a representative value of the true NO_x emissions for each flame in which flow asymmetry is evident.

The location of the peak NO_x concentration region in the PJ-ψ25-640 and MCB-CC2.7 flames correlates with the location of the flame boundary, as defined by the 0.5% CO concentration contour. The peak NO_x region is just within the flame tip of the PJ nozzle flame with ψ_{CAJ}=25% and in between the edge of the main flame volume and the extended tail down the right hand side of the kiln of the MCB-CC2.7 flame. The location of the peak NO_x concentration in the MCB-CC0.6 flame however, is close to the location of the peak CO concentration and not near the end of the flame, consistent with a significantly different combustion environment in this flame. The peak NO_x concentration measured in the PJ nozzle flame is 890ppm. The peak NO_x concentration measured in the conventional burner flames are lower, 767ppm in the MCB-CC2.7 flame and 390ppm in the MCB-CC0.6 flame.

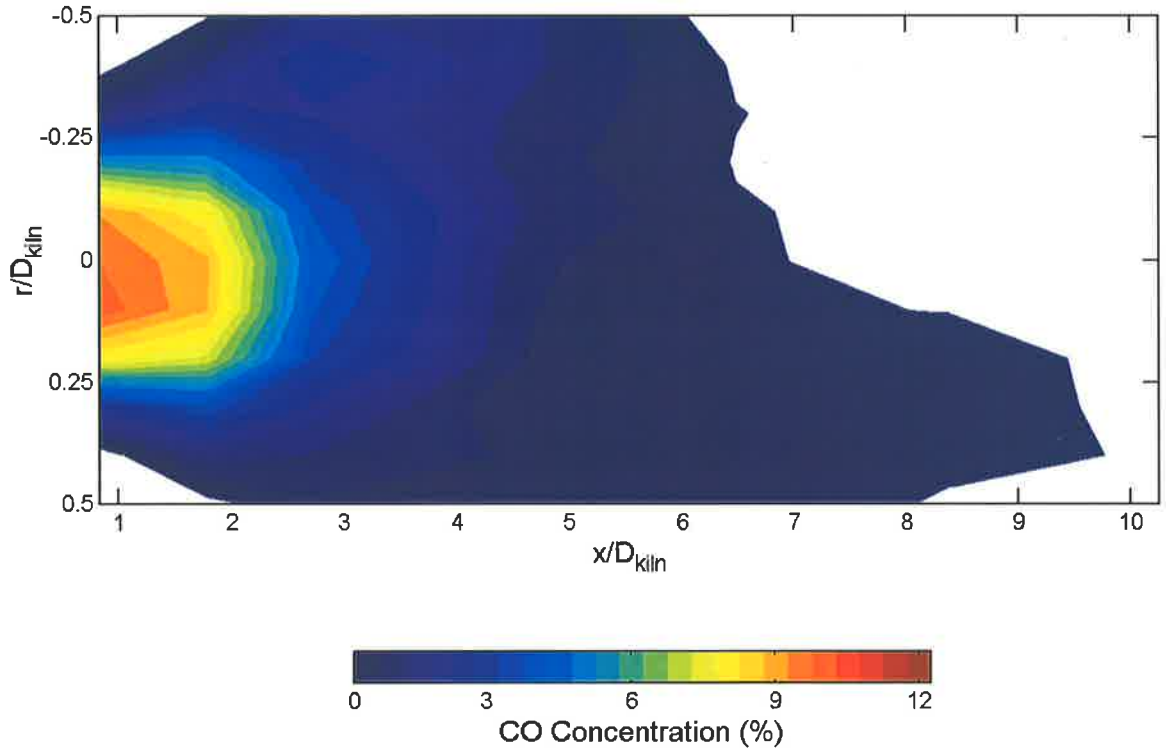

Figure 5-5. Concentration contours of carbon monoxide measured in the kiln simulator for the precessing jet burner with ψ_{CAJ}=25% (PJ-ψ25-640 flame). Contours are in steps of 0.5%. See Table 5-1 for the jet conditions.

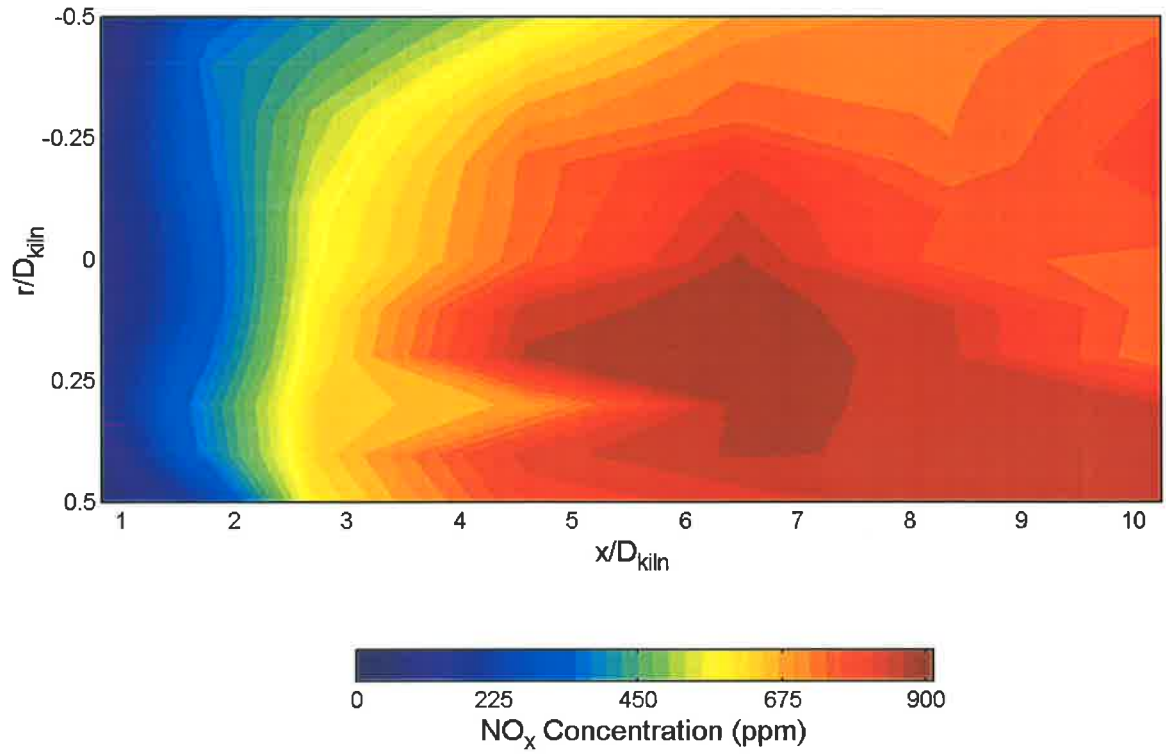

Figure 5-6. Concentration contours of NO_x measured in the kiln simulator for the precessing jet burner with ψ_{CAJ}=25% (PJ-ψ25-640 flame). Contours are in steps of 25ppm. See Table 5-1 for the jet conditions.

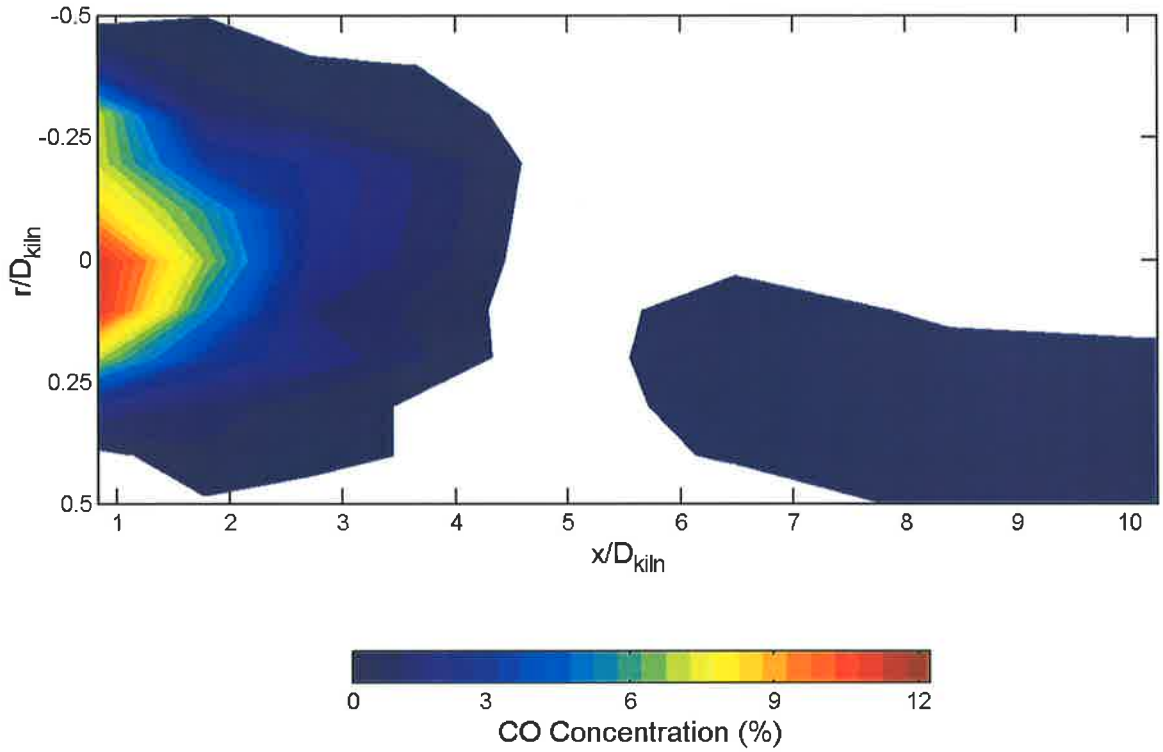

Figure 5-7. Concentration contours of carbon monoxide measured in the kiln simulator for the multi-channel burner with typically good recirculation (MCB-CC2.7 flame). Contours are in steps of 0.5%. See Table 5-1 for the jet conditions.

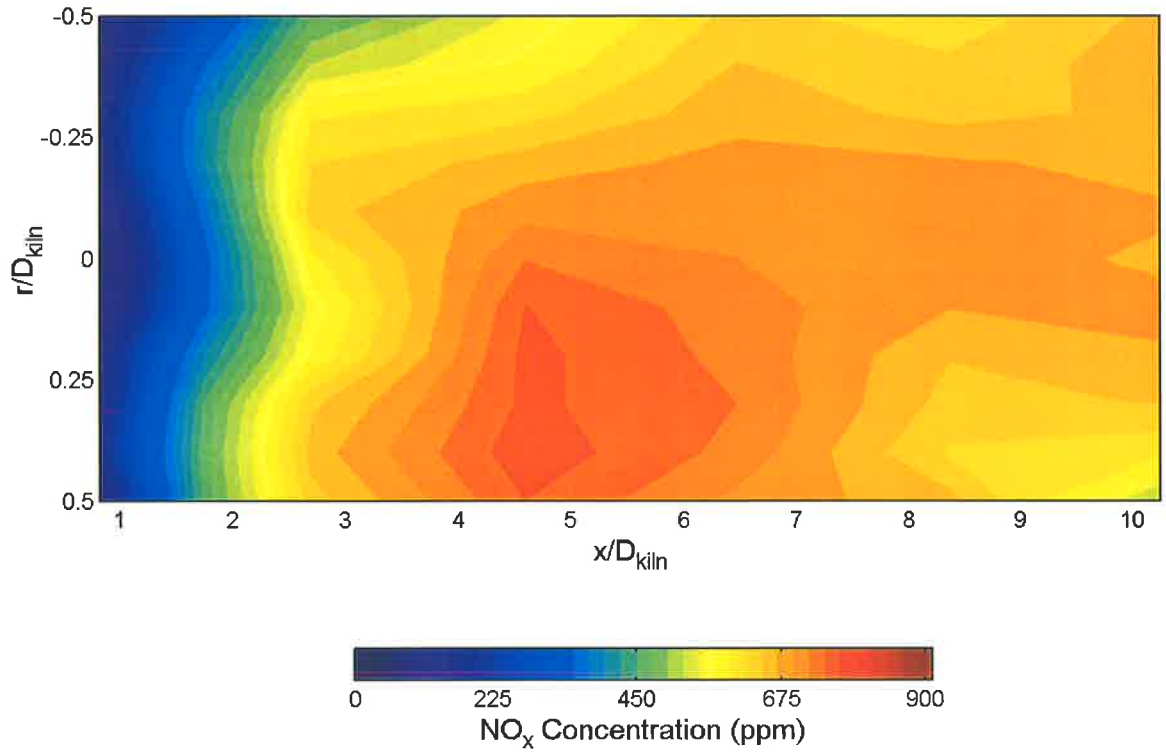

Figure 5-8. Concentration contours of NO_x measured in the kiln simulator for the multi-channel burner with typically good recirculation (MCB-CC2.7 flame). Contours are in steps of 25ppm. See Table 5-1 for the jet conditions.

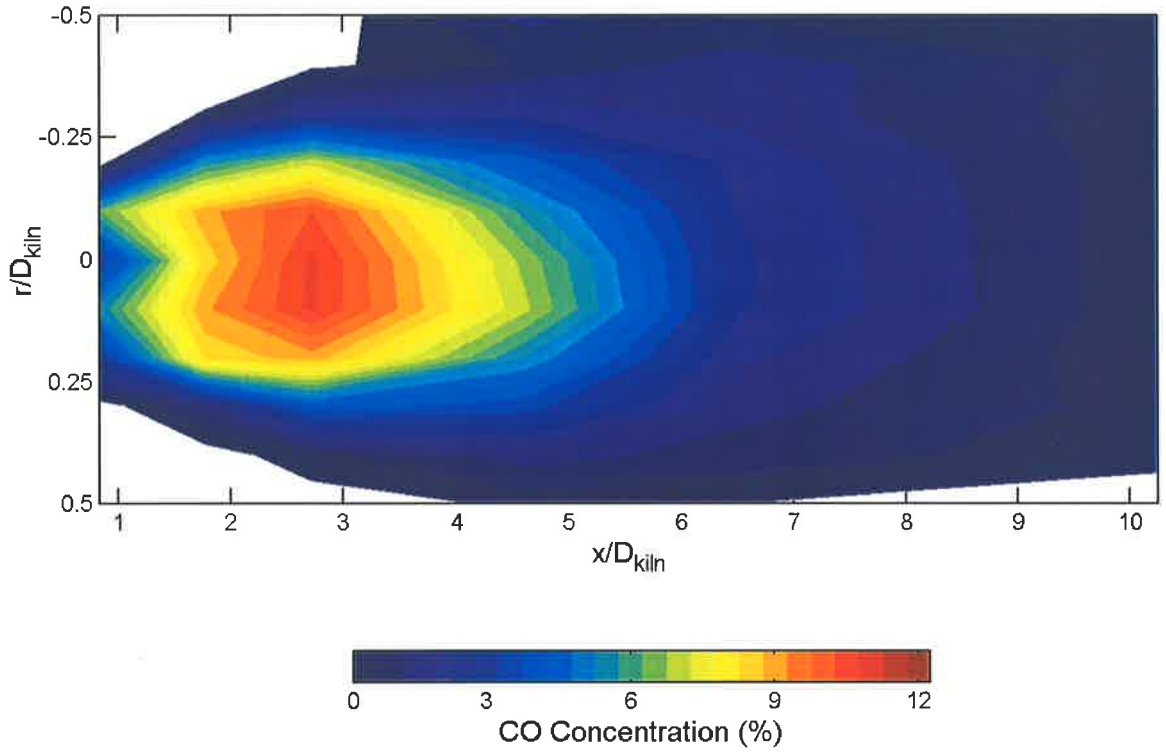

Figure 5-9. Concentration contours of carbon monoxide measured in the kiln simulator for the multi-channel burner with low recirculation (MCB-CC0.6 flame). Contours are in steps of 0.5%. See Table 5-1 for the jet conditions.

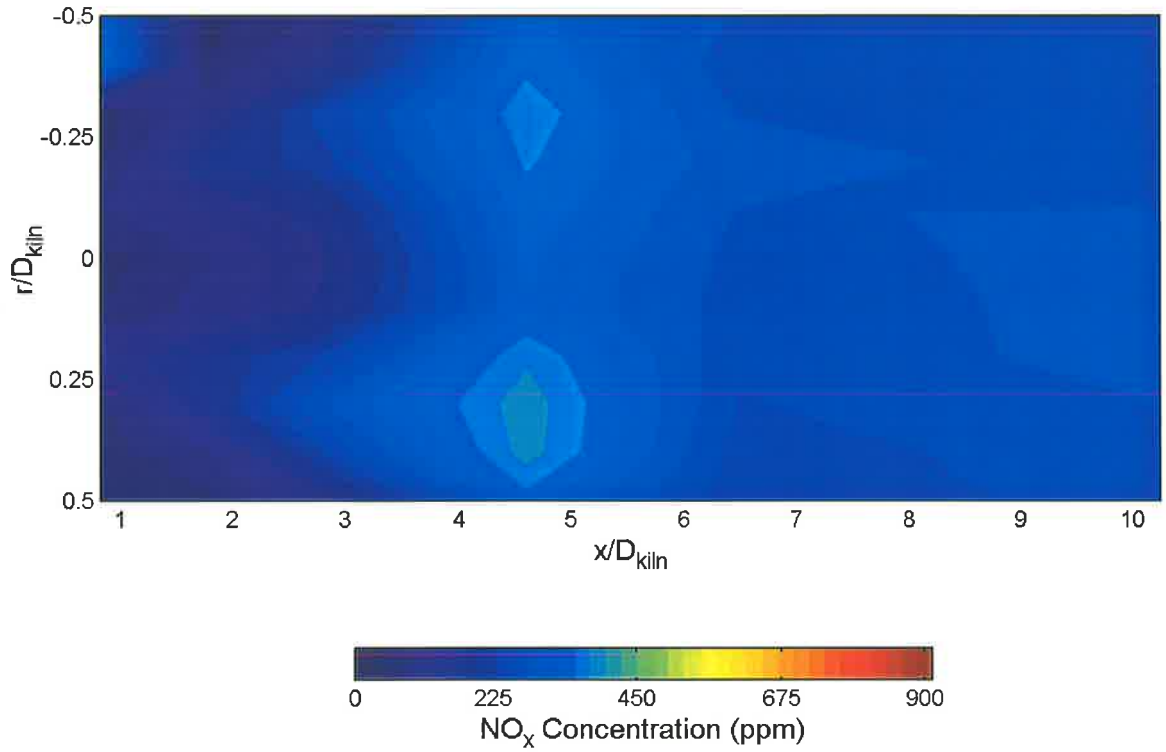

Figure 5-10. Concentration contours of NO_x measured in the kiln simulator for the multi-channel burner with low recirculation (MCB-CC0.6 flame). Contours are in steps of 25ppm. See Table 5-1 for the jet conditions.

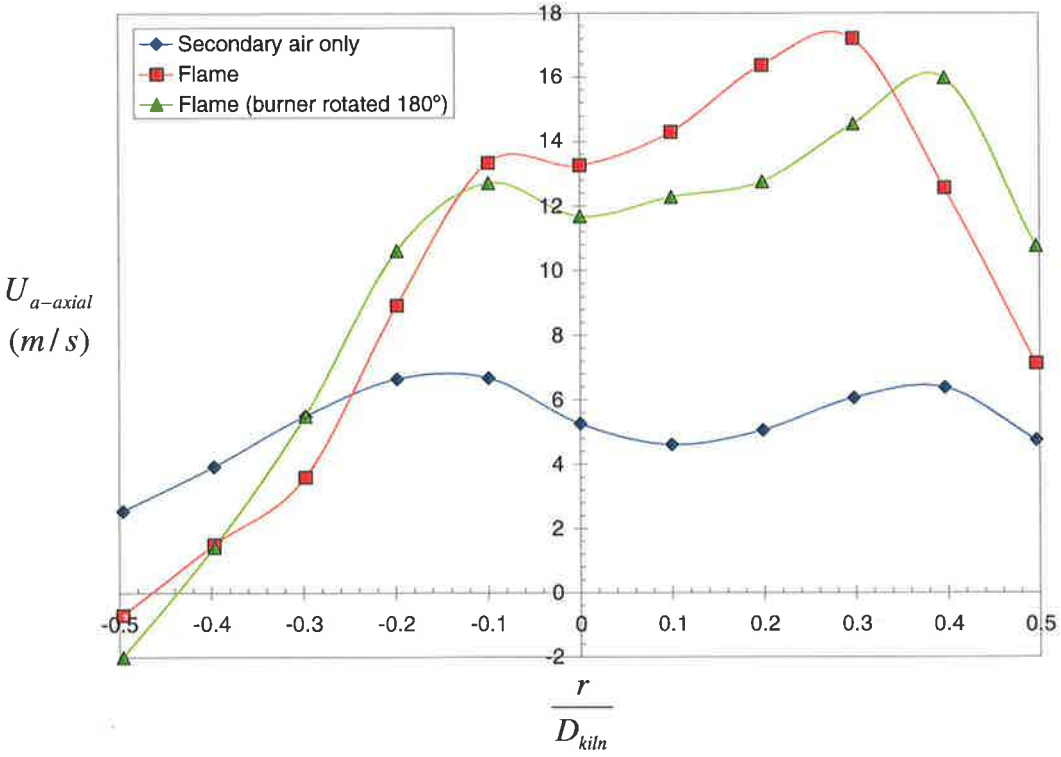

Figure 5-11. LDA measurements of the axial component of velocity 1m from the inlet baffle plates with only secondary air flowing and a coal flame from the Multi-Channel Burner (CEMFLAME3 condition B50-NG). In the no-flame condition a small amount of primary air was passed through the MCB. The MCB was tested with the burner in two angular positions, to check the contribution of the burner to any asymmetry. The burner housing was flush with the inlet baffle plate.

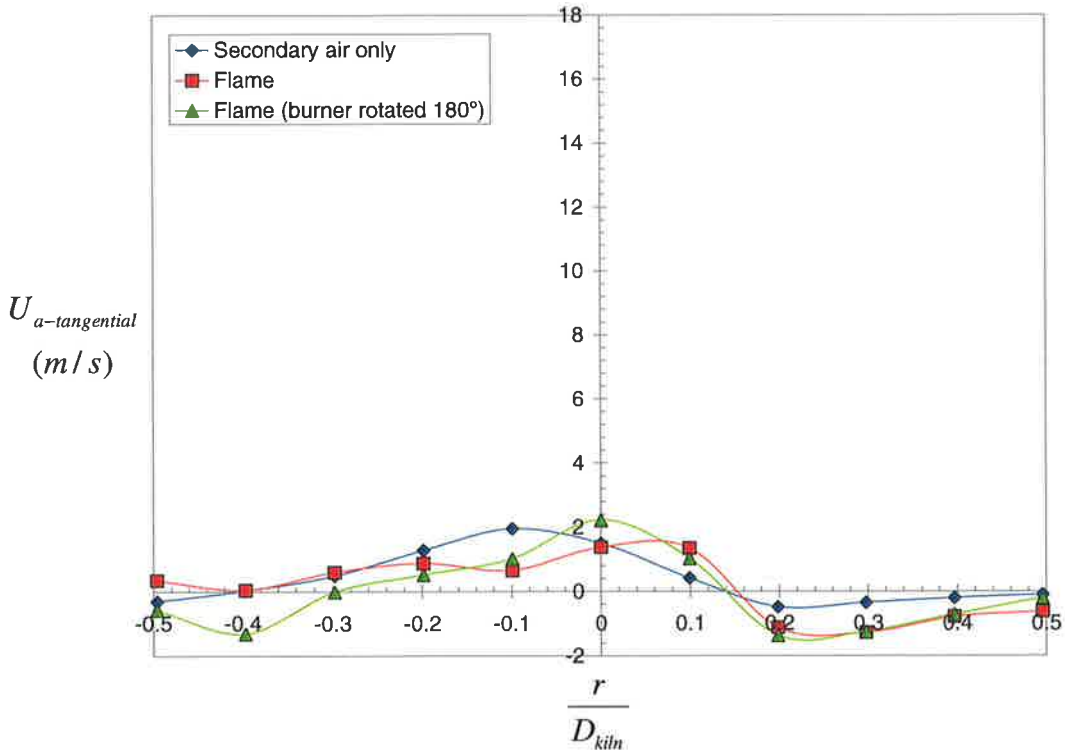

Figure 5-12. LDA measurements of the tangential component of velocity 1m from the inlet baffle plates with only secondary air flowing and a coal flame from the multi-channel burner. Conditions as for Figure 5-11.

5.3.3 Flue Gas Emission Measurements

The total flue NO_x and carbon monoxide measurements in the pilot-scale facility are presented in Table 5-3. In this table, one set of data is taken from the single point measurement in the last segment of the kiln and one from an integrated average, based on the cross-sectional area, of the traverse through the access port furthermost down-stream from the burner tip. Integrated average values are only presented for those conditions in which full traverses were undertaken. The single point data is higher than the integrated data by 12.5±2%, showing good agreement and providing an expected trend of increased NO_x with increased residence time since the single point data was measured further down the kiln than the measurements at the last axial location shown in Figure 5-5 to Figure 5-10.

Table 5-3 shows that the total NO_x emissions from the PJ burner flames are broadly comparable with those from the MCB-CC2.7 flame. A trend of increased NO_x emission with ψ_{CAJ} is evident such that the PJ-ψ0-T640 flame shows a 20% reduction in NO_x emissions relative to the MCB-CC2.7 flame based on the single point data, while the PJ-ψ25-T640 flame shows a 15% increase. The trend of increased NO_x emission with ψ_{CAJ} is consistent with a trend of increasing flue temperature with increasing ψ_{CAJ}, corresponding to a longer heat flux profile. The level of CO emissions at the end of the pilot-scale facility is an indication of both the air to fuel ratio used in the experiments and how near the combustion process is to completion. In an ideal facility operated at the stoichiometric ratio of air to fuel and with perfect mixing of the fluids, the CO emissions far downstream of the burner tip would be zero. For the present facility, in which case the excess air levels were constant and the measurement point the same, the trend of CO emissions to decrease with increased ψ_{CAJ} suggests the degree of intimate mixing of air and jet fluid is increased and combustion is closer to completion.

The lowest NO_x emissions are produced by the low Craya-Curtet parameter MCB flame, consistent with generally reduced wall temperatures and poor heat flux, suggesting lower flame temperatures. The poor heat flux profile and output of the MCB-CC0.6 flame would preclude it from application in a rotary kiln for efficient production. The relatively high CO emissions measured from the MCB-CC0.6 flame compared to the other flames further illustrates the poor combustion characteristics of an "under" recirculating flame.

In contrast to the trend at 640°C air pre-heat, in which NO_x emissions increase with increasing ψ_{CAJ}, when the pre-heat temperature is 840°C no consistent trend is found in the effect of ψ_{CAJ} on NO_x emissions for the case with the burner pushed 475mm past the baffle plate (Table 5-3). The measured levels are all within ±10% of each other. In contrast, by retracting the tip of the burner so that it is flush with the baffle plate, which results in increased fine scale turbulence in the combustion air in the near burner zone, a clear trend of decreasing NO_x emissions with increasing ψ_{CAJ} is seen. The trend in this case is opposite to that found at 640°C with the burner protruding 475mm into the kiln. Although the case of the burner mounted flush with the baffle plate is unlikely to occur in real rotary kilns, it does illustrate that both the scale and intensity of turbulence in the secondary air has a significant influence on NO_x generation in a flame.

Flame	Flue NO_x emissions		Flue CO emissions		Flue gas temperature
	Single point measurement	Integrated average	Single point measurement	Integrated average	
	(ppm)	(ppm)	(%)	(%)	(°C)
PJ-ψ0-T640	621	-	0.45	-	1,425
PJ-ψ15-T640	807	-	0.24	-	1,454
PJ-ψ25-T640	886	803	0.18	0.29	1,467
MCB-CC2.7	773	678	0.14	0.44	1,418
MCB-CC0.6	320	283	0.34	0.68	1,433
PJ-ψ0-T840	1,997	-	0.45	-	1,470
PJ-ψ15-T840	1,774	-	0.37	-	1,481
PJ-ψ25-T840	2,028	1,666	0.21	0.28	1,488
PJ-ψ31-T840	1,921	-	0.22	-	1,489
PJ-ψ0-T840*	2,104	1,756	0.31	0.47	-
PJ-ψ8-T840*	1,964	-	0.38	-	1,535
PJ-ψ13-T840*	1,697	-	0.50	-	1,508
PJ-ψ19-T840*	1,510	-	0.55	-	1,512

Table 5-3. Flue gas temperatures and emission levels (corrected to 3% O_2) for all MCB and PJ burner flames at different ψ_{CAJ} and secondary air pre-heat temperatures. The symbol, *, indicates the burner was mounted flush with the inlet baffle plate.

5.4 Flame and Process Interaction

The present finding that NO_x emissions from PJ burner configurations in the pilot-scale facility are broadly comparable with those of the conventional MCB nozzle appears, at first sight, to contradict previous findings in industrial installations in which NO_x emissions have been found to be lowered. For example, Manias and Nathan (1993, 1994) and Videgar (1997) found that the replacing an original "conventional" type burner with a PJ burner resulted in NO_x emissions being reduced by 30-60%. This apparent discrepancy between results from the pilot-scale facility and those in industrial plant are attributed to the different thermal environment in the experimental facility and industrial installations, as is demonstrated below.

The significance of considering the control of heat flux in experimental kilns that do not make product, and in accounting for different heat flux characteristics produced by different burners, is clearly evident in Figure 5-13. Figure 5-13 plots the relationship between total axial heat flux and NO_x emissions for a given type of burner nozzle in the pilot-scale facility. A clear trend of increasing NO_x emissions with increasing heat flux is evident for a given type of burner nozzle. This is because, for the pilot kiln with a fixed wall heat transfer coefficient, an increase in heat flux inevitably results in increased wall temperature for a constant air pre-heat temperature. However, it is also evident that there is a significant difference in the relationship between the NO_x emissions and the heat flux for the MCB compared with that of the PJ burners. This difference can only be attributed to the different mixing characteristics of the two nozzles since all other parameters (e.g. air pre-heat temperature and fuel flow rate) are identical. It is this different relationship which is deduced to be consistent with trends found in industrial installations. The same trend is evident in the measurements of flames at 840°C pre-heat, where a different relationship between NO_x emissions and heat flux is found for the case with the burner mounted flush with the baffle and that when the burner tip is retracted – a result also attributable to differences in mixing.

The importance of control of heat flux in maintaining thermal similarity is well illustrated by comparing the above trends with the relationship between heat flux and NO_x emission in operating plants. Figure 5-14 shows the variation in NO_x emissions with heat input from a 300 ton/day gas-fired rotary kiln (Manias and Nathan, 1993). Although not precisely the same as heat flux, heat input is used in the comparison of industrial data as it equates to the heat extracted by the product and kiln and is more easily measured than the heat flux profile. The original burner in this kiln was a high velocity single channel axial burner. The PJ burner nozzle was mounted with the high velocity axial burner adjacent to it so that any ratio of the two flows could be obtained. Hence while the configuration is broadly comparable with that in the present pilot-scale investigation, there is a significant difference in that the axial jet was mounted adjacent to the PJ nozzle, rather than co-axially. Figure 5-14 demonstrates that, in an operating rotary kiln, NO_x emissions from a PJ flame are very weakly dependent on heat input, in contrast to the trend in the simulator, in which increased heat flux results in increased wall temperatures. The difference in trend arises from the fact that in the operating plant, increased heat flux is compensated by increased throughput to maintain similar product and wall temperatures. Thus a change in total heat input of 8% results in only a 15% change in NO_x emissions, while in the simulator, a change in heat flux of 2% results in a 20% change in NO_x emissions.

An alternative data set for comparing the differences in combustion performance of a conventional and precessing jet burner can be obtained from recent installations in two very similar gas-fired rotary kilns, both nominally rated to produce 750 tons of cement clinker per day. Nathan and Manias (1995) have shown that NO_x emission reductions of 25-30% were achieved in Kiln 2 after a burner using multiple jets to generate a weak swirl was replaced by a PJ burner without a CAJ. The most recent installation of a PJ burner incorporating a CAJ for flame shaping, replacing an identical original burner in Kiln 1 also demonstrates a reduction in NO_x emissions in the order of about 20% for a typical production rate, see Figure 5-15.

During the commissioning of Kiln 1, the effect of varying ψ_{CAJ} was not assessed so that a direct comparison of NO_x emissions to energy input for each burner setting, as in Figure 5-14, is not possible. However, a comparison of NO_x emissions against fuel input can be made at constant specific fuel consumption, see Figure 5-16. The "constant" specific fuel consumption for each burner was selected on the basis of the most common operating specific heat consumption range. Figure 5-16 demonstrates that increased energy input into the kiln results in a slight decrease in NO_x emissions, in contrast to the trends in the pilot-scale facility, Figure 5-13. For the precessing jet burner an increase in total heat input of 7% results in a 7% reduction in NO_x emissions. Hence as the input energy into the kiln increases, the production level also increases such that the wall temperatures remain approximately constant and the NO_x emissions decrease slightly. The relationship between heat flux and NO_x emissions for the original burner and the PJ burner are also similar, although the PJ burner has a slightly lower NO_x level. In practice, Figure 5-15 and Figure 5-16 imply that for a given tonnage of cement, the PJ burner results in about 20% lower NO_x emissions.

A comparison of Figure 5-13, Figure 5-14 and Figure 5-16 demonstrates that a different relationship between NO_x emissions and heat flux exists in an operating rotary kiln, in which the control of the kiln results in the wall temperature profile being maintained more or less constant, and the present pilot-scale kiln, in which the wall temperature cannot be independently controlled. While the total heat flux is, at best, a crude way of accounting for the complex heat flux profile and its interaction with the flame, it is nevertheless useful. For example, it is interesting that extrapolation of the data from the PJ flames to provide the same heat flux output of the MCB-CC2.7 flame (see Figure 5-13), equates to a 48% reduction in NO_x emissions. Alternatively, if the comparison is based on the total radiative heat flux, the equivalent reduction in NO_x emissions is about 37%. While any extrapolation must be treated with caution, these reductions are in the same range as found in many industrial installations of the PJ burner, for example at the Ash Grove Durkee cement plant (Videgar, 1997), although slightly higher than those in Figure 5-15. This result underscores the importance of considering heat flux and NO_x emissions together in any comparison of the performance of different burners in experimental facilities. It also highlights the importance of considering the control of heat flux in maintaining thermal similarity in pilot-scale facilities.

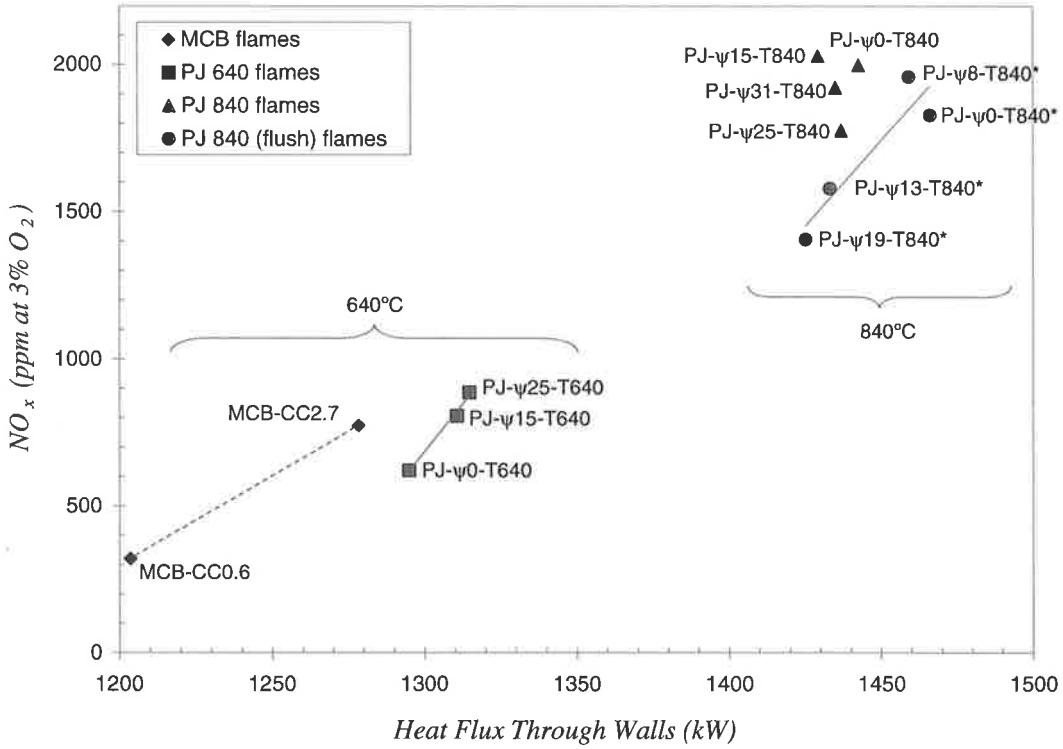

Figure 5-13. Variation in NO_x emissions with total heat flux through the kiln walls for the precessing jet (PJ) and multi-channel burner (MCB) configurations. To account for the effective increase in kiln length and hence increased residence time of the combustion products in the kiln, a correction has been made to the measured NO_x emissions from the flames where the PJ burner is mounted flush with the inlet baffle plate, indicated by the symbol *.

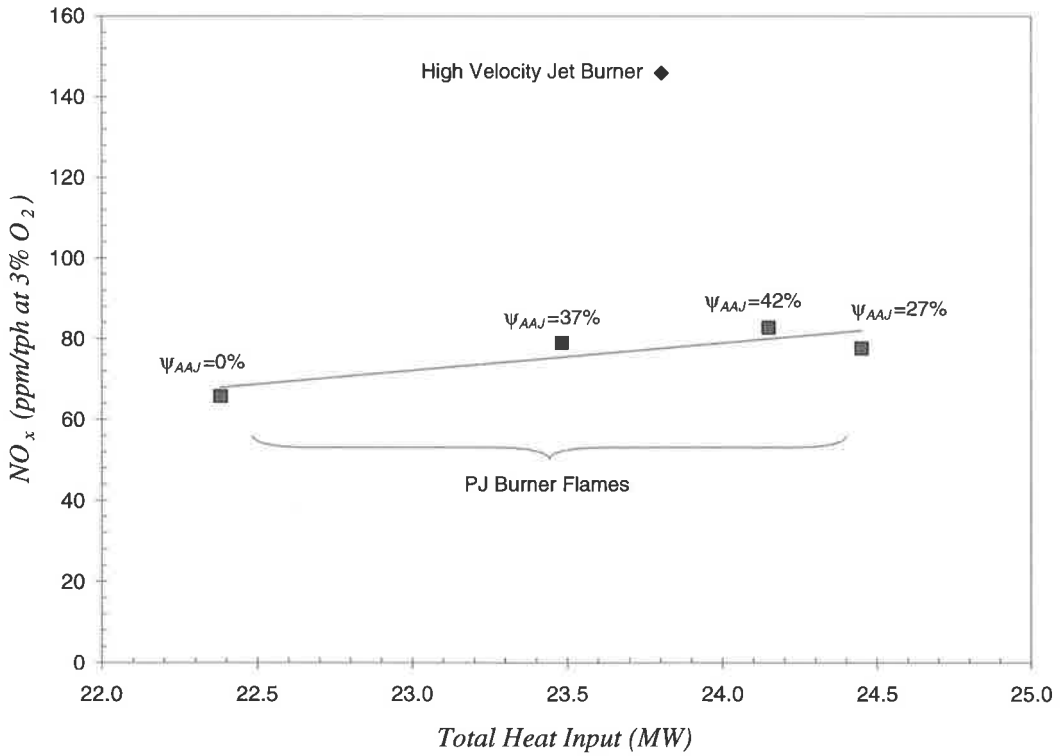

Figure 5-14. Variation in NO_x emissions (normalised to the production rate) with heat input from a 300 ton/day gas-fired rotary cement kiln. The original burner produces a high velocity jet of fuel and is compared to a precessing jet using the adjacent axial jet burner at various flow rate proportions, ψ_{AAJ}, to provide flame shaping.

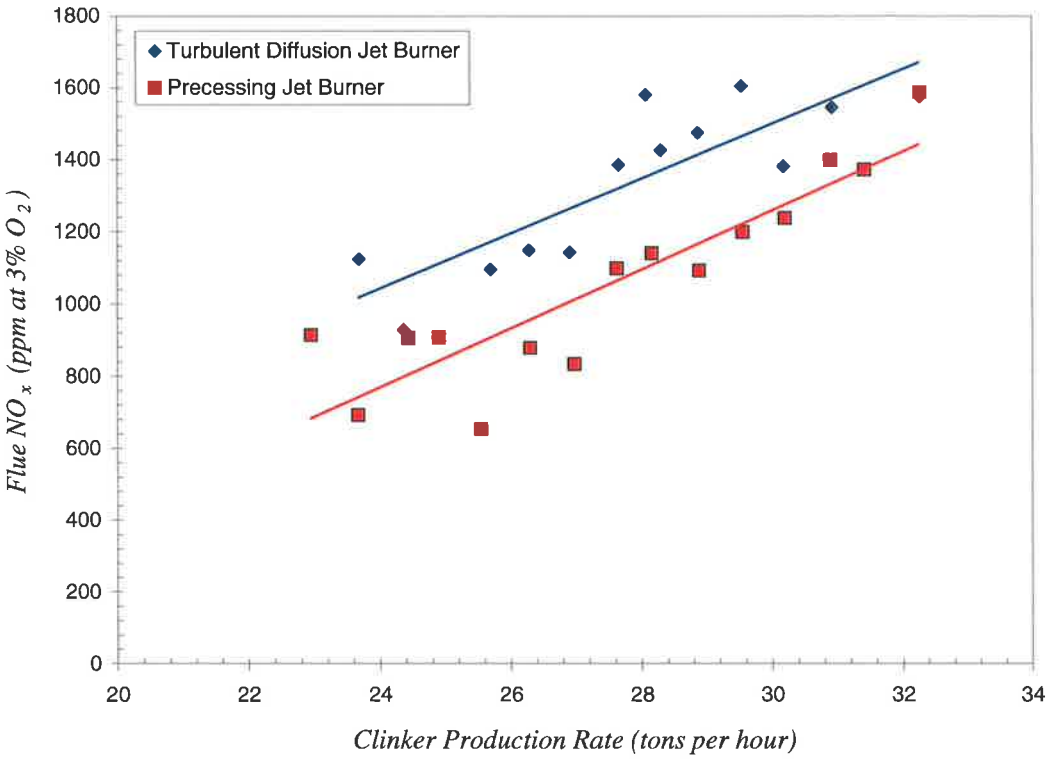

Figure 5-15. Variation in NO_x emissions with production rate in a 750 ton/day gas-fired rotary cement kiln. The turbulent jet diffusion type burner incorporates multiple gas jets and is compared to a precessing jet burner with central axial jet for flame shaping. Averaged data points are taken from approximately three months continuous operation of each burner. Secondary air temperature is approximately 1000°C. Data courtesy of Lafarge (Canada).

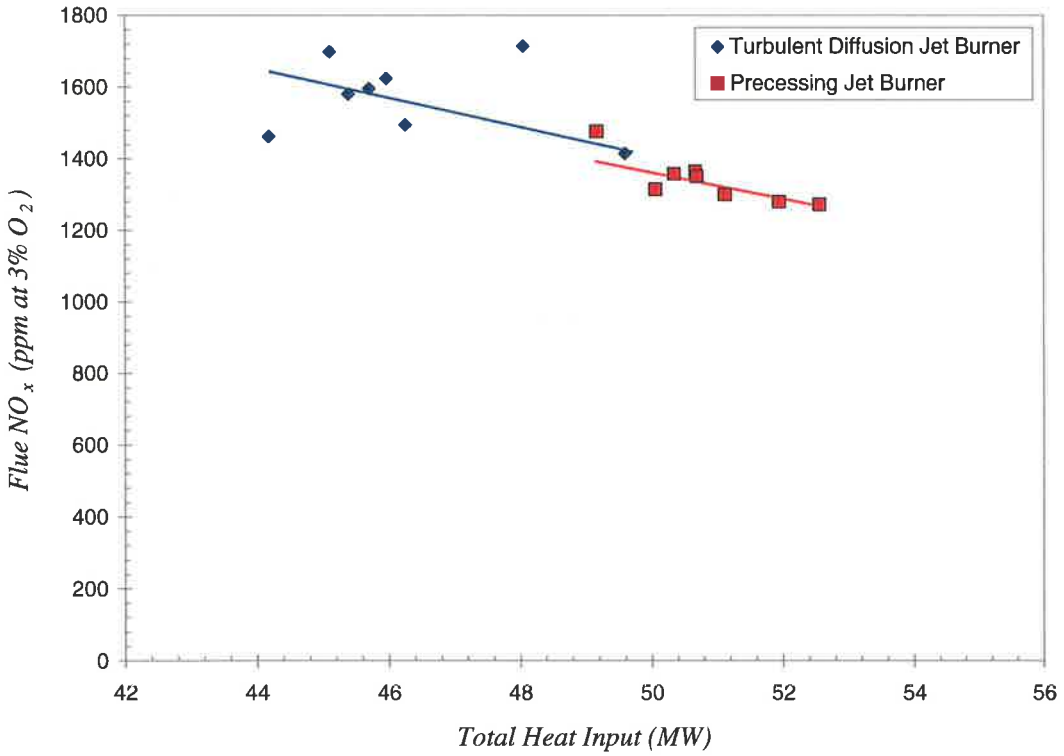

Figure 5-16. Variation in NO_x emissions with input fuel energy at constant specific fuel consumption in a 750 ton/day gas-fired rotary cement kiln. The constant specific fuel consumption selected for each burner corresponds to the most common operating condition of each burner. Operating range for the turbulent diffusion jet burner = 5,350-5,500 MJ/ton, PJ burner = 5,400-5,550 MJ/ton.

5.5 Conclusions

A comparison of the relationship between heat flux and NO_x emissions for two different burner designs has been conducted in a pilot-scale kiln simulator and in operating rotary kilns. Measurements in the pilot-scale facility indicate that for a secondary air pre-heat temperature of 640°C, flames from a precessing jet burner produced more total heat for the same NO_x emissions compared to a multi-channel burner configured to provide strong external recirculation. The general shape of the heat release profile of the flame from the multi-channel burner with typically good external recirculation (MCB-CC2.7) is comparable with those of the PJ burner flames. However the shape of the heat release profile from a low recirculation flame (MCB-CC0.6) is significantly different, peaking some two kiln diameters further downstream. The peak heat flux from the MCB-CC2.7 flame was 7% lower than that of the PJ burner flames. Based on the measured wall surface temperatures, the heat transfer through the kiln walls shows that the PJ burner flames also typically produce 3% more total heat release than the MCB-CC2.7 flame over the first ten kiln diameters, and 8% more total heat release than the MCB-CC0.6 flame. Using the radiation measurements, the PJ burner flames produced 12% more total radiation heat release than MCB-CC2.7 flame and 20% more than the MCB-CC0.6 flame.

The heat flux measurements clearly demonstrate that good control of the heat flux profile of a precessing jet flame can be accomplished by varying the ratio of central axial jet fuel flow rate to PJ fuel flow rate and hence the momentum ratio. Increasing the proportion of CAJ to total gas flow, ψ_{CAJ}, over the range 0-31% (Γ_{CAJ}=0-0.32) pushes the heat flux further down the kiln by approximately one kiln diameter and also broadens the profile so that the peak heat flux is slightly reduced. The total heat release varies by approximately 3%, depending on ψ_{CAJ}, with the highest total heat flux appearing to be produced from flames with ψ_{CAJ}=15-25% (Γ_{CAJ}=0.11-0.25). This result is consistent with the observations in Section 4.3 which indicate that the flame volume and hence radiant fraction is maximised with the same range of flow proportions and momentum ratios. The trends in the high momentum burners are consistent with previous predictions based on the Craya-Curtet parameter: the high momentum, low recirculation flame (MCB-CC0.6) has poor heat transfer, low NO_x and high CO emissions and the high Craya-Curtet flame has good heat transfer characteristics and good burnout. The in-flame measurements of gas-species concentration, although limited, also highlighted the differences between the flames from the PJ burner and the two multi-channel burner flames.

When considered in isolation, the trends in NO_x emissions from the MCB and PJ burners in the pilot-scale facility appear to be irreconcilable with those obtained in full scale operating rotary kilns. However, it has been found that a comparison of the relationship between the heat flux and NO_x emissions enables reasonable agreement to be found in the trends of the performance of the different burner systems when compared in the different facilities. The results also highlight the difficulties in maintaining thermal similarity between experimental facilities and operating plant. This is particularly true when comparing either different combustion systems, for example those with different mixing characteristics, or when the control of heat flux in the pilot facility is different from that in the operating plant.

A crude method of describing the relationship between heat flux and NO_x emissions is proposed by plotting total heat flux through the walls against total NO_x emissions. Extrapolation of the heat flux from the PJ burner to equal that from the comparable typically good multi-channel burner flame (MCB-CC2.7), results in an apparent reduction in NO_x emissions of 35-50%, the same order as those measured in full-scale plant. This result demonstrates that different types of mixing within a flame can result in a different relationship between NO_x emissions and heat flux with all other parameters held constant, for both the pilot-scale facility and the operating plant.

Chapter 6

Mixing Characteristics of a Confined Precessing Jet Flow

6.1 Quantitative Measurement of Concentration

6.1.1 Introduction

A rotary kiln and burner system can be idealised as a jet of fuel issuing into a concentric confining cylinder with a surrounding uniform co-flow of air. Extensive investigations by previous researchers have demonstrated that the proximity of the confining walls and the velocity of the co-flowing stream can have a significant impact upon the behaviour of an enclosed flame and hence the operation of a rotary kiln.

In the case of a confined simple turbulent jet, the dominant factor governing flame characteristics is the degree of recirculation induced in a rotary kiln due to the interaction of the duct walls with the natural entrainment of the jet. The most widely used criteria for characterising the degree of recirculation in ducted jet systems are the Thring-Newby, Craya-Curtet and Becker parameters, see Section 1.3.4. The Craya-Curtet and Becker scaling criteria, which assume the jet can be treated as a point source of momentum in the far field, are considered by Moles *et al.* (1972) to be the best methods for modelling enclosed flames. However, due to the fundamentally different nature of the mixing of a precessing jet from that of a simple jet, the Craya-Curtet and Becker scaling criteria cannot necessarily be applied to precessing jet flows. Nathan *et al.* (1995) has suggested that a modified form of the Thring-Newby criterion is suitable for modelling the PJ nozzle, but this has yet to be tested. Hence, there is at present no validated scaling criterion for the PJ nozzle to relate small-scale model results and industrial applications. The principle aim of the present investigation is therefore to develop and validate such a model for the behaviour of a ducted PJ nozzle with shaping jet. A further aim of the experiments is to quantitatively determine the effect of the central axial jet on the mixing from a PJ nozzle and incorporate this into the modelling criterion. The effect of the central axial jet is also quantified to investigate the optimum combustion properties and mixing characteristics of a precessing jet flow in a confined, co-flowing environment.

To develop a model of the characteristics of a confined PJ flow, it is necessary to assess quantitatively the separate effects of co-flow velocity, confinement and shaping jet ratio. The effect of a co-flow and confinement and hence recirculation on the mixing characteristics of simple jet nozzles has been widely investigated by previous researchers. For example, velocity measurements were made by Yule and Damou (1991) and Khodadadi and Vlachos (1989) and extensive measurements of the mean and fluctuating components of the concentration of a passive

scalar tracer have been made by Becker *et al.* (1963, 1965 and 1967b). All these experiments used single point techniques. However, two-dimensional imaging has the advantage of capturing the instantaneous spatial distribution of the mixing field, which is advantageous for the highly transient and three-dimensional nature of the flow from a PJ nozzle. The instantaneous measurement of the two-dimensional distribution of the velocity field from a precessing jet using a technique such as Particle Image Velocimetry (PIV) has severe limitations and difficulties due to the wide distribution of magnitude and direction of velocity in the flow from a PJ nozzle (Newbold, 1997). Scalar measurements are not subject to these problems because there is no directional sensitivity.

6.1.2 Quantitative PLIF

Planar Laser-Induced Fluorescence (PLIF) is a powerful, non-intrusive technique for the measurement of passive scalar concentration and hence is chosen for the present investigation. PLIF is a well developed diagnostic tool in fluid mechanics. Examples of quantitative measurements of the concentration of a jet in water include Dahm and Dimotakis (1990), Dimotakis *et al.* (1983), Law and Wang (2000) and Papanicolau and List (1988). The technique used by Karasso and Mungal (1996, 1997a) for the investigation of plane and curved shear layers is the basis of the PLIF technique chosen for the present study.

The pulsed Neodium Yttrium Aluminium Garnet (Nd:YAG) laser and carboxy-dichlorofluorescein dye system used by Karasso and Mungal (1996, 1997a) was selected for the present PLIF experiments due to the need to acquire instantaneous, time-resolved images of the jet concentration field. For a continuous laser, the temporal resolution of a PLIF image is determined by the shutter speed of the camera, which is usually limited by the laser power and hence fluorescence signal strength. A typical value for the temporal resolution of a continuous laser PLIF system, such as that used for the two-colour experiments described in Chapter 3, is 1ms, which is not adequate to temporally resolve the fluid motions near to the jet exit. For a pulsed laser, such as the Nd:YAG laser, the temporal resolution is determined by the pulse duration and fluorescence time scale, which are both typically less than 10ns. As the smallest time scales in a turbulent flow are greater than these time scales, the PLIF images so acquired are fully temporally resolved. The Nd:YAG laser also offers the advantage of considerably more energy than the Argon-Ion source used for the flow visualisation experiments in Chapter 3. Karasso and Mungal (1997b) have demonstrated that a Nd:YAG laser (at approximately 40mJ/pulse) produces at least two orders of magnitude more energy per exposure than a 20W Argon-Ion system in which the laser beam is swept through the imaged region. Hence, in order to acquire two-dimensional images of the scalar mixing field of a PJ nozzle in a co-flowing, confined environment, the Nd:YAG laser is clearly the superior choice as the excitation source.

The selection of an appropriate fluorescent dye for a particular laser source is vital for ensuring the acquired PLIF images can be used to determine quantitatively the jet concentration throughout the experimental region. Karasso and Mungal (1997b) examined the selection of an appropriate dye for PLIF measurements with the Nd:YAG laser and found that a commonly used dye, fluorescein, was unsuitable for quantitative measurements as it did not obey the Beer-Lambert Law governing absorption decay. They found only one dye suitable for use with the Nd:YAG laser: 5(&6)carboxy-2′7′-dichlorofluorescein. Hence, this dye was chosen for the present experiments.

6.1.3 Quantitative PLIF Image Processing Fundamentals

The raw fluorescence signal detected in a PLIF experiment is a function of the jet concentration, camera optics and laser intensity distribution. Following the notation used by Karasso (1994), the signal intensity detected by a camera aligned at right angles to and focussed on the plane of a laser sheet can be expressed by Equation 6-1. The overbar symbol in Equation 6-1 refers to an acquired two-dimensional image, i and j are the column and row index respectively for the pixel under consideration, B_{ij} refers to the camera's background noise, G_{ij} is the camera's fixed pattern gain and includes the collection optics and camera non-uniformities, I_{ij} is the spatial distribution of laser intensity, $[\phi C]_{ij}$ is the spatial distribution of fluorescence intensity and R is the background concentration of the image flow field:

$$\bar{S}_{ij} = B_{ij} + G_{ij}(I_{ij}[\phi C_{ij}] + R) \qquad \textbf{Equation 6-1.}$$

Assuming a linear relationship between dye concentration and fluorescence intensity, then ϕ, the effective quantum efficiency, is constant and Equation 6-1 can be reduced to Equation 6-2. The concentration of jet fluid can then be calculated by applying Equation 6-3:

$$C_{ij} = \frac{1}{I_{ij}} \times \frac{\bar{S}_{ij} - B_{ij}}{G_{ij}} \qquad \textbf{Equation 6-2.}$$

$$\zeta_{ij} = \frac{C_{ij} - R}{C_{ref} - R} \qquad \textbf{Equation 6-3.}$$

where C_{ref} is the reference concentration, usually determined in a region of the image where 100% dye fluid is known to be present.

Equation 6-1 demonstrates that, in order to determine quantitatively the concentration of dye in the flow being investigated, each of the correction factors, B_{ij}, G_{ij}, I_{ij}, C_{ref} and R must be known. Hence the camera background noise, the camera gain and the spatial distribution of laser intensity distribution must be measured across the imaged area of each experiment. The procedures taken to account for all of these systematic corrections in an image are described in Section 6.2.2.

6.2 Quantitative PLIF Technique

6.2.1 Experimental Apparatus

A detailed description of the experimental apparatus used for the quantitative PLIF experiments, including the jet nozzles, is given in Section 2.2.3. Briefly, the jet nozzle was aligned on the axis of symmetry of a 0.5×0.5m cross-section, closed-circuit water-tunnel. Fluorescent dye stored in supply tanks of limited volume, was pumped through the jet at flow rates controlled by Fischer and Porter rotameters. The horizontal laser sheet from a Coherent Infinity 40-100 Nd:YAG laser was aligned through the jet axis with the intensity distribution configured to minimise the reduction in fluorescence signal along the jet axis by matching the intensity profile to the decay in jet concentration as much as possible. The laser was operated at its maximum power output of 250mJ/pulse at 532nm and a repetition rate of 10Hz for the validation experiments and 6Hz for the precessing jet experiments. A Kodak MegaPlus camera was positioned at right angles to the laser sheet and a Fujinon CF12.5A wide-angle lens was used to focus the fluorescence image onto the large CCD array of the camera. Images were captured in batches of 152 images, which were temporarily stored in the RAM of the camera's controlling computer and then transferred for permanent storage on the computer's hard-drive. The jet flow was stopped in between capturing each batch of images. Perspex tubes of different diameters were used to provide different levels of confinement relative to the jet and the frequency of the water-tunnel pump was adjusted to provide control over the co-flow velocity.

6.2.2 Image Processing Corrections

6.2.2.1 Correction for Background Noise, B_{ij}

For the present experiments, two measurements of the camera background noise, B_{ij}, were acquired. The first measurement was taken with the laser off and the room darkened while the second measurement was performed with the room darkened and the laser operating exactly as for the data collection procedure. The camera settings were identical to those used in acquiring the data images. A total of 152 images were acquired and averaged to determine the camera background noise.

6.2.2.2 Correction for Camera Gain Effects, G_{ij}

The camera gain effect, G_{ij}, is a product of the performance of the camera CCD array and the transfer function of the optical system described in detail in Section 2.2.3. Accurate determination of the present camera gain effects was difficult due to the requirement of generating a perfectly uniform illuminated target. However, as Equation 6-2 shows, it is not necessary to determine the camera gain response and laser intensity distribution separately, although this was done by Karasso (1994), as long as a measurement incorporating both elements can be used to determine the product $I_{ij}\times G_{ij}$. The procedure to measure this product accurately is described in Section 6.2.2.4. An estimate of G_{ij} is still necessary to correct the measurement of $I_{ij}\times G_{ij}$ for the effects of dye absorption as described in Section 6.2.2.5.

Non-uniformities in the Fujinon lens and MegaPlus CCD array were tested by measuring the response of the camera when viewing an approximately uniformly illuminated target. The camera settings were as used in experiments, but with the lens unfocused. A total of 152 images were acquired and averaged and the camera's background noise subtracted to determine the spatial distribution of the camera's gain response, G_{ij}. At an f-stop of *f*/2 the spatial gain response is not uniform as progressively less light is detected by pixels in the CCD array the greater their distance from the centre of the image. Although the response becomes more uniform at larger f-stops, a higher f-stop also reduces the signal intensity detected by the CCD and significantly lowers the signal-to-noise ratio of the experiments. Hence an f-stop of *f*/2 was chosen for all the present experiments.

6.2.2.3 Correction for Geometric Distortion

Due to the wide-angle lens used in the PLIF experiments, geometric distortion is present at the edges of the images. This is evidenced by a slight "barrelling" of the true image. To determine the true measurement location of each pixel, the geometric distortion due to the optical lens must be corrected. The method presented by Lu *et al.* (1994), as shown in Equation 6-4 and Equation 6-5, was used to account for the optical distortion and reconstruct each image. An image of a target test-pattern was used to quantify the level of distortion and the accuracy of Lu's method.

$$b_{ij}'(r) = b_{ij}(r)\sqrt{\frac{s_c^2 + b_{ij}^2(x)}{s_c^2 + x_{CCD}^2}} \qquad \textbf{Equation 6-4.}$$

$$b_{ij}'(x) = b_{ij}(x)\sqrt{\frac{s_c^2 + b_{ij}^2(r)}{s_c^2 + r_{CCD}^2}} \qquad \textbf{Equation 6-5.}$$

where $b_{ij}(r)$ and $b_{ij}(x)$ are the positions of pixel (i,j) along the r-axis and x-axis respectively, $b_{ij}'(r)$ and $b_n'(x)$ are the corrected pixel positions, s_c is the ocular distance and r_{CCD} and x_{CCD} are the height and width of the CCD array in pixels. Note that the cylindrical co-ordinate system is used here such that x represents distance parallel to the main flow direction and r represents radial distance.

6.2.2.4 Correction for Laser Spatial Intensity Distribution, I_{ij}

The spatial distribution of the laser intensity varies significantly throughout the image area of each experimental configuration. This is principally due to the Gaussian distribution of intensity caused by spreading a laser beam into a two-dimensional sheet using a cylindrical lens. The laser operation, streaks caused by scratches† in the perspex surfaces of the water-tunnel and cylindrical ducts and absorption through the experimental region also affected the spatial intensity distribution. For the reasons discussed in Section 6.2.2.2 the laser intensity distribution and camera gain effects were measured simultaneously in the present experiments.

†. Note that the walls of the tunnel were polished to reduce many scratches, but some optical distortion still remained.

The combined product $I_{ij} \times G_{ij}$ was measured with the combined optical arrangement, including ducts, for each configuration by recording the fluorescence signal intensity generated when either the entire water-tunnel or a section of the water-tunnel was at a uniform dye concentration. Measurements in which the entire water-tunnel was at a uniform concentration were conducted at selected intervals during and at the conclusion of each experimental run. For these measurements the tunnel was left running for several minutes to circulate the fluid and ensure uniform dye concentration. For measurements when only a closed off section of the tunnel was used, extra dye was added to increase the signal strength of the measurements. A separate small fish-tank pump was then left running to mix the fluid within the sealed section for approximately an hour to ensure uniform dye concentration. The laser and camera were operated as during the data collection stage. The raw images were checked for fluctuations in the laser's operation and any spurious images eliminated. A small perspex cell containing a fixed concentration of fluorescent dye was used to monitor the pulse-to-pulse fluctuations in laser power. Approximately 152 images were acquired for every different experimental arrangement and averaged, correcting for variations in laser power, P, and background noise as shown in Equation 6-6. As the dye concentration is uniform, the recorded signal, $\overline{S}_{ij}$, depends only on the laser intensity distribution and the camera gain effects. However, as the laser signal passes through the image area some of the light is absorbed due to the interaction of the dye and the laser. Correction for this absorption is required to determine the true product of I_{ij} and G_{ij}.

$$I_{ij} \times G_{ij} = \frac{1}{n} \sum_{t=1}^{n} \frac{P_{ref}}{P_n} (\overline{S}_{ij,n} - B_{ij}) \qquad \textbf{Equation 6-6.}$$

6.2.2.5 Correction for Absorption

The absorption of a linear laser-dye system for PLIF experiments is characterised by the Beer-Lambert law. As outlined in Section 6.1.2, Karasso and Mungal (1997b) found that the only dye that is suitable for quantitative PLIF experiments with a Nd:YAG laser source is carboxy-dichlorofluorescein, whose absorption characteristics follow the Beer-Lambert Law.

In order to calculate the absorption for each experimental configuration, it is necessary to separate the intensity distribution and camera gain effects. The camera gain distribution, G_{ij}, was estimated as described in Section 6.2.2.2. The corrected laser intensity distribution image was then calculated from $I_{ij} = (G_{ij} \times I_{ij})/G_{ij}$. The change in signal intensity due to absorption was then calculated between two points by applying the approximate form of the Beer-Lambert Law for a laser beam passing between two points (i=0 to i=k, in intervals of Δr), through a uniformly dyed medium, as shown in Equation 6-7, where ε is the molar absorbtivity of the dye and C is the concentration of dye in the imaged region.

$$\frac{I_{kj}}{I_{0j}} = \exp\left[-\sum_{i=0}^{k} \varepsilon C \Delta r\right] = \exp[-k(\varepsilon C \Delta r)] \qquad \textbf{Equation 6-7.}$$

One measurement point was chosen just to the near-laser side of the duct (right hand side of the images) and the other just to the far-laser side of the duct (left hand side of the images) so that any optical attenuation of the fluorescence signal due to the perspex cylinders is eliminated. Each point lies on the same pixel row which is coincident with the direction of propagation of the laser sheet. The signal intensity was averaged over five pixel values in the same row, centred around the measurement point.

The theoretical change in signal due to absorption was calculated from the absorption characteristics for carboxydichlorofluorescein dye with a Nd:YAG laser determined by Karasso and Mungal (1997b) and Equation 6-7. The distance between the measurement points ($k\Delta r$) was calculated from the resolution of each experiment (~500μm). The concentration of each condition was calculated based on the estimated quantity of dye present in the water-tunnel or sealed off segment. The dye concentration used in the intensity distribution measurements varied between 0.06×10^{-6}M and 1.8×10^{-6}M, or a factor of 0.04 to 1.2 relative to that of Karasso. Hence it is expected that even though the experimental arrangements are vastly different, the absorption behaviour of the dye should be identical. The lowest concentrations correspond to measurements of the background concentration in the middle of experimental runs and the highest concentrations correspond to cases in which extra dye has been added to a sealed off segment. The theoretical change in signal due to absorption is compared to the measured change in Table 6-1.

Experimental Run Name	Dye Concentration (relative to Karasso)	Measured Intensity Change (I_{far}/I_{near})	Theoretical Intensity Change (I_{far}/I_{near})
SimpleCon	1.12	0.53	0.73
PJ3901 - background	0.11	0.93	0.96
PJ3901 - doped	1.25	0.73	0.64
PJ3902 - background	0.17	0.89	0.94
PJ3903 - background	0.14	1.02	0.95
PJ390cofl - background	0.10	1.05	0.96
PJ2902 - background	0.10	0.91	0.97
PJ2903 - background	0.11	0.88	0.97
PJ2903 - doped	1.13	0.75	0.73
28PJ290 - background	0.07	0.91	0.98
28PJ290 - doped	0.58	0.80	0.85
28PJ390 - background	0.09	0.84	0.97
28PJ390 - doped	0.32	0.78	0.89
Swirl - background	0.14	0.98	0.96
Swirl - intensity	0.29	0.97	0.92

Table 6-1. Comparison of the theoretical and measured change in fluorescence intensity in the spatial intensity distribution measurements due to the effects of absorption.

A number of experimental conditions are not listed in Table 6-1. The PJ4901 intensity distribution measurements are not listed as the perspex duct filled the entire water-tunnel cross-section and hence it was not possible to measure the effect of absorption independent of the effect of signal attenuation due to the duct interface. The simple jet experiments used to validate the PLIF technique are not included due to the effect of reflections from the rear water-perspex-air interface. In the absence of any duct to disrupt the optical path of the laser sheet, the reflections from the rear interface were sufficiently strong to cause the laser intensity distribution to appear to increase with distance in the experimental region. Reflections from the rear interface were detected at various intensities in a number of other experimental configurations. However they were most significant in the validation case. A reflection between the rear interface and the far-laser side of the duct, where it is terminated, locally increases the laser intensity in the PJ3903 and PJ390cofl cases so that the fluorescence signal between the near and far sides appears to increase.

Table 6-1 indicates a number of important results. The first and most critical point is that, with consideration given to the effect of reflections and refractions from each perspex surface, the nature of the camera gain measurement and the estimation of the actual background concentration, there is very good agreement between the theoretical and measured absorption. Hence it is possible to incorporate a correction for absorption in the calculation of the product of the laser intensity distribution and camera effects, $I_{ij} \times G_{ij}$. The second point is that the highest amount of absorption present in an experiment has been quantified and is of the order of 4% across the width of the duct at the end of an experimental run, when the background concentration is highest.

The theoretical absorption for each condition was calculated across the image array, A_{ij}. This was then incorporated into the calculation of the true product of the laser intensity distribution and camera gain effects:

$$(I_{ij} \times G_{ij})' = \frac{(I_{ij} \times G_{ij})}{A_{ij}} \qquad \textbf{Equation 6-8.}$$

The effect of absorption on the measurement of $I_{ij} \times G_{ij}$ is illustrated in Figure 6-1. Figure 6-1a shows the calculated theoretical absorption for the PJ3902 case and Figure 6-1b shows the combined intensity distribution and camera gain distribution for the PJ3902 configuration, which has been corrected for absorption.

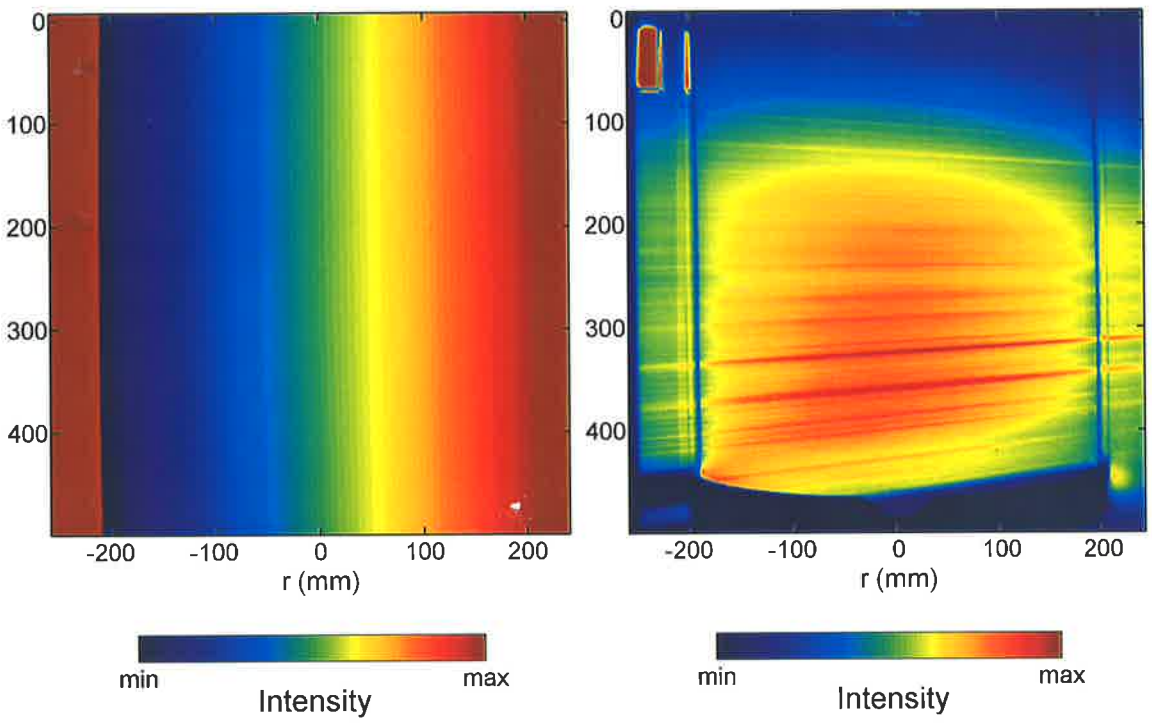

(a) Absorption correction

(b) Intensity distribution

Figure 6-1. Correction Images used in the image processing of raw PLIF images from the PJ3902 experiments: (a) Absorption correction image, A_{ij}; (b) Intensity distribution, corrected for absorption, $I_{ij} \times G_{ij} / A_{ij}$. The colourmap used to represent each image is normalised to the minimum and maximum values to show the relative distribution of actual values.

6.2.3 Image Processing Procedure

The image processing procedure was consistent for every condition, although there is a significant difference in the calculation of the reference concentration for the simple jet case and precessing jet cases. The first step in the image processing was to determine the systematic corrections outlined in Section 6.2.2 for each experimental run:

Step	Image Processing Procedure	Mathematical Implementation
1	Review all raw images and discard any spurious images with significant changes in the laser sheet distribution or incorrect image capture.	-
2	Calculate the average camera background noise with the laser off.	$B_{off} = \frac{1}{n}\sum_{k=1}^{n} S_{ij,n}$
3	Calculate the average camera background noise with the laser on.	$B_{on} = \frac{1}{n}\sum_{k=1}^{n} S_{ij,n}$
4	Calculate the combined product of the laser intensity and camera gain distributions:	-
4a	Determine the instantaneous laser pulse power for every image, P_n, by averaging the signal strength over a number of pixels ($w \times h$) in a reference cell at a fixed dye concentration.	$P_n = \frac{1}{w \times h}\sum_{i=r}^{r+wx+h}\sum_{j=x} (S_{ij,n} - B_{off,ij})$
4b	Calculate laser reference power - the mean laser pulse power.	$P_{ref} = \frac{1}{n}\sum_{k=1}^{n} P_n$
4c	Determine the bounds of the 95% confidence range of the Gaussian distribution of laser pulse powers. Images with laser powers outside the limits defined by P_{min} and P_{max} are excluded from subsequent image processing.	$P_{min} = P_{ref} - 1.96 \times P_{rms}$ $P_{max} = P_{ref} + 1.96 \times P_{rms}$
5	Correct and average the intensity images:	-
5a	Determine the instantaneous laser pulse power for every image, P_n, by averaging the signal strength over a number of pixels ($w \times h$) in a reference cell at a fixed dye concentration.	$P_n = \frac{1}{w \times h}\sum_{i=r}^{r+wx+h}\sum_{j=x} (S_{ij,n} - B_{off,ij})$
5b	If $P_{min} < P_n < P_{max}$, correct for pulse to pulse power fluctuations.	$(I \times G)_{ij,n} = \frac{P_{ref}}{P_n}(S_{ij,n} - B_{on,ij})$
5c	Calculate average intensity and camera gain distribution.	$\overline{(I \times G)_{ij}} = \frac{1}{n}\sum_{k=1}^{n} (I \times G)_{ij,n}$
5d	Calculate theoretical absorption distribution.	$= A_{ij}$
5e	Calculate true intensity and camera gain distribution, corrected for absorption in the experimental measurement.	$\overline{(I \times G)'}_{ij} = \frac{\overline{(I \times G)_{ij}}}{A_{ij}}$

Table 6-2. The image processing procedure to determine the systematic correction images for background noise, absorption, camera gain response and laser sheet intensity distribution.

The image processing to determine the corrections for camera noise and laser intensity and camera gain distribution were only calculated for each experimental run as the corrections for each experimental condition are the same for each run in which the configuration of the laser, camera and jet is the same. The next step was to conduct the image processing on the actual data to determine the average jet concentration for a particular experimental condition.

Step	Image Processing Procedure	Mathematical Implementation
1	Determine reference laser powers (see steps (4a-4c) in the processing procedure for corrections).	$= P_{ref}, P_{min}, P_{max}$
2	Correct and average the intensity images:	-
2a	Determine the instantaneous laser pulse power for every image, P_n, by averaging the signal strength over a number of pixels (w×h) in a reference cell at a fixed dye concentration.	$_n = \frac{1}{w \times h} \sum_{i=r}^{r+wx+h} \sum_{j=x} (S_{ij,n} - B_{off,ij})$
2b	If $P_{min} < P_n < P_{max}$, correct for pulse to pulse power fluctuations and laser intensity distribution and camera gain distribution to calculate the concentration distribution.	$C_{ij,n} = \frac{P_{ref}(S_{ij,n} - B_{on,ij})}{P_n \overline{(I \times G)'_{ij}}}$
2c	Determine the instantaneous background concentration, R_n, by averaging the concentration over a number pixels (w×h) in a designated region in the image where no jet is present.	$R_n = \frac{1}{w \times h} \sum_{i=r}^{r+wx+h} \sum_{j=x} C_{ij,n}$
3	Determine the reference concentration:	-
3a	If the experiment is of a simple jet, average the concentration over a number pixels (w×h) in a designated region in the image within the jet potential core (100% jet fluid).	$C_{ref} = \frac{1}{w \times h} \sum_{i=r}^{r+wx+h} \sum_{j=x} C_{ij,n}$
3b	If the experiment is of a precessing jet, repeat steps 1-2b for the images taken at the start of the experiments with the reference cell containing 100% jet fluid.	$= \text{Cjetref}_{ij,n}$
3c	Determine the average signal strength from the laser power reference region (w×h).	$S_P = \frac{1}{w \times h} \sum_{i=r}^{r+wx+h} \sum_{j=x} \text{Cjetref}_{ij,n}$
3d	Determine the average signal strength from the jet reference cell region (w'×h').	$S_{cref} = \frac{1}{w' \times h'} \sum_{i=r'}^{r'+w'x'+h'} \sum_{j=x'} \text{Cjetref}_{ij,n}$
3e	Calculate the ratio between the laser power signal strength and the jet reference signal strength.	$\beta = \frac{S_{cref}}{S_P}$
3f	Calculate the reference concentration for the experiment.	$C_{ref} = \beta \times P_n$
4	Determine the instantaneous jet concentration.	$\zeta_{ij,n} = \frac{C_{ij,n} - R_n}{C_{ref} - R_n}$
5	Average the instantaneous jet concentration measurements.	$\bar{\zeta}_{ij} = \frac{1}{n} \sum_{k=1}^{n} \zeta_{ij,n}$

Table 6-3. Image processing procedure for the calculation of the average jet concentration of an experiment. The procedure is similar for the calculation of the Root Mean Square (RMS) of the concentration fluctuations.

The location of the regions used to monitor the laser power fluctuations, P_n, the background concentration, R_n, and in the case of the simple jet, the reference concentration, C_{ref}, are shown in Figure 6-2 for the validation experiment using a simple jet and a typical precessing jet case.

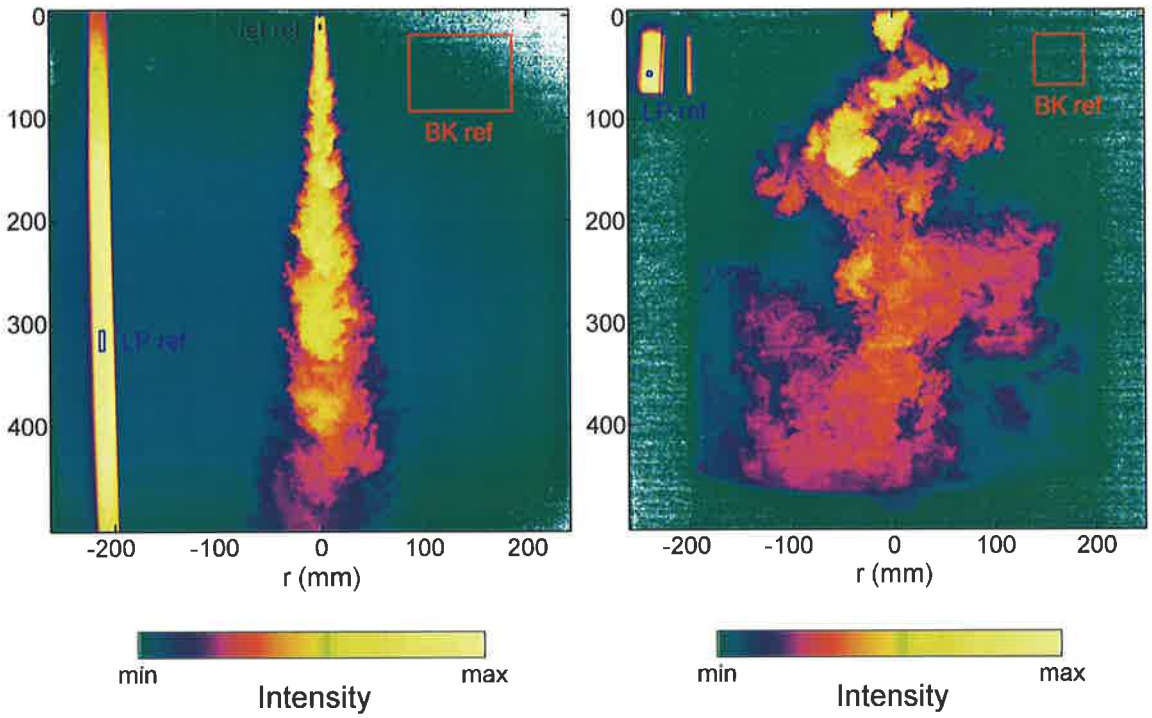

(a) Pipe jet (validation experiment)

(b) Precessing Jet (PJ3902 configuration)

Figure 6-2. The typical location of the regions used in the image processing procedure to calculate the laser power (LP ref, P_n), background concentration (BK ref, R_n) and 100% jet fluid for the pipe jet (Jet Ref, C_{ref}). The images are false-colour representations of raw PLIF images.

6.3 Sources of Experimental Error

6.3.1 Spatial Resolution

The accurate measurement of mean local passive scalar concentration requires that the measurement volume be small compared to the local instantaneous concentration gradient. Accurate measurement of scalar concentration fluctuations requires that the measurement volume must resolve the instantaneous local concentration gradients. The Batchelor scale, λ_b, is the smallest scale at which scalar fluctuations occur. If the resolution of the measurement probe is larger than the Batchelor scale then the Root Mean Square (RMS) of concentration fluctuations will be underestimated as fluctuations smaller than the probe volume cannot be measured. The Kolmogorov scale, λ_k, is the smallest scale at which velocity fluctuations occur in a flow and is given by Equation 6-9, where Re_x is the local Reynolds number and l_x is the local length scale of the flow, which is proportional to the axial distance from the nozzle exit for a jet (i.e. Dahm and Dimotakis (1990) assume l_x=0.44x to calculate the local length scale of their jet flow):

$$\lambda_k = Re_x^{-0.75} l_x \qquad \textbf{Equation 6-9.}$$

The largest Kolmogorov scales in the present experiments are approximately 100μm. Miller and Dimotakis (1991) define a velocity field spatial scale, λ_v, which is some multiple, α, of λ_k, where α has a value of approximately 25 (Dahm and Dimotakis, 1990; Miller and Dimotakis, 1991). The Batchelor scale, λ_b, which is the smallest scale at which scalar fluctuations occur, is related to the velocity field spatial scale by the Schmidt number, Sc, the ratio of the relative importance of turbulent transportation and molecular diffusion in a fluid, see Equation 6-10:

$$\lambda_b = Sc^{-0.5} \lambda_k \qquad \textbf{Equation 6-10.}$$

The Kolmogorov and Batchelor scales in a jet flow vary with axial distance from the jet exit due to the dependence of Equation 6-9 on the local length scale of the flow. The relative resolution of an experiment, defined as L/λ_b for the Batchelor scale and L/λ_k for the Kolmogorov scale, where L is the largest dimension of the probe resolution, therefore also vary throughout the flow field. The Batchelor scale is resolved if $L/\lambda_b<1$ and the Kolmogorov scale is resolved if $L/\lambda_k<1$. Figure 6-3 presents the variation in L/λ_b and L/λ_k along the jet centreline for the principal jet types investigated using the present PLIF technique. The Schmidt number of carboxy-dichlorofluorescein dye in water is assumed to be Sc≈1,900 for the present calculations, based on the measurement of D=5.2×10^{-6} cm^2/s for fluorescein (Ware *et al.*, 1983 in Karasso, 1994). The local length scale in the flow for the PJ nozzle was calculated based on the method of Newbold (1997), in which the jet is assumed to expand at the same rate as a simple jet from the inlet orifice of the nozzle chamber, and an approximate but more realistic measure in which a constant spread half-angle of 40° is assumed.

In the present experiments the resolution was about the same in all three dimensions. The nominal imaged dimensions of each pixel in the CCD array varied from L=496μm to L=510μm depending on the experimental configuration. The spatial resolution out of the plane of the laser sheet is defined by the sheet thickness, which was

approximately 500μm at the nozzle centreline, where most statistics are calculated. Figure 6-3 demonstrates that the measurement resolution is between one and two orders of magnitude greater than the Kolmogorov and Batchelor scales anywhere in the imaged region.At the furthest measurement point from the jet exit the Batchelor scale is approximately 8 times smaller than the measurement resolution and the Kolmogorov scale is approximately 5 times smaller than the measurement resolution. Hence the finest scales of velocity and scalar fluctuations are not resolved. This results in lower values of concentration fluctuation and scalar dissipation rates than the true values. However, the velocity field spatial scale, λ_v, is resolved in most of the imaged area, except for the immediate vicinity of the nozzle exit for all jet types.

6.3.2 Temporal Resolution and Statistical Independence

The temporal resolution required to resolve the Batchelor length scale is defined by the Batchelor time scale, τ_b:

$$\tau_b = \frac{\lambda_b}{u} \qquad \textbf{Equation 6-11.}$$

where u is the local velocity and λ_b is the local Batchelor scale. The temporal resolution of the present experiment is defined by the laser pulse duration of 3ns plus the fluorescence lifetime of approximately 10ns, so that $\tau_{pulse} \approx 13$ns. The Batchelor and Kolmogorov time scales in the current experiments were estimated based on the jet flow rate and spreading angle. The ratio of τ_{pulse} to the smallest time scales, which occur at the jet exit, is shown in Table 6-4, illustrates that the Batchelor and Kolmogorov time scales are well resolved for all jet types.

Jet	τ_b (ns)	τ_k (ns)	τ_b/τ_{pulse}	τ_k/τ_{pulse}
Simple	5.3	5,790	8.4E-06	1.5E-07
Central Axial	5.2	5,625	1.5E-05	7.2E-07
Precessing	24.1	26,293	1.4E-06	6.9E-08

Table 6-4. Estimated ratios of laser pulse-fluorescence duration (τ_{pulse}) to experimental time scales for the principal jet types investigated. Values less than 1 indicate complete independence.

For calculating statistical properties it is necessary to ensure statistical independence of the data. Hence another equally important temporal consideration is the independence of successive images. This is determined by the frame rate of the camera relative to the flow velocities and the imaged area. The most important criterion for image-to-image independence is that based on the convection velocity of the large-scale structures in the flow. This requires that the time between images be greater than the time scale for a typical large-scale structure in the flow to move past a fixed point in space, τ_{convec}. In addition, pixel-to-pixel independence requires that a fluid particle must not be detected in the same pixel from one image to the next. This requires that the time between images exceeds the time for the flow to completely traverse a pixel, τ_{pixel}. In the present experiments, the need for independence had to be balanced with the need to conserve dye, reduce the accumulation of dye in the image background and the limited volume of the supply tanks. Hence the very low camera frame rate required for complete independence based on the convection of a complete structure between successive images, τ_{image}, was not practi-

cal. Nevertheless reasonable independence is assured by maintaining the laser repetition rate and camera frame rate, τ_{frame} greater than $5\times\tau_{pixel}$ in all cases, as shown in Table 6-5. Also shown in Table 6-5 is the comparison of the image capture time scale compared to the time scale for one complete cycle of precession, τ_{prec}. Since typically several hundred images are collated, the statistics are averaged over at least 30 (and more typically at least 100) large structures and cycles of precession.

Jet	Frame Rate (fps)	τ_{frame}/τ_{prec}	$\tau_{frame}/\tau_{pixel}$	$\tau_{frame}/\tau_{convec}$	$\tau_{frame}/\tau_{image}$
Simple	10	-	5.71	0.28	0.12
Central Axial	6	-	9.51	0.035	0.15
Precessing	6	0.48	9.51	0.05	0.01

Table 6-5. Estimated ratios of laser pulse repetition rate and camera frame rate (τ_{frame}) to different jet time scales. Values greater than 1 indicate complete independence. τ_{pixel} and τ_{image} are the time required for a fluid particle, based conservatively on the lowest co-flow velocity, to traverse the length of a pixel or image length respectively. τ_{convec} is the time required for the slowest moving structure at the end of the imaged region to traverse a fixed point.

6.3.3 Limited Number of Measurements

The number of PLIF images that could be used to calculate flow statistics was limited in the present measurements by the amount of memory in the camera's computer, the cost of dye and the number of different jet conditions investigated. The magnitude of the uncertainty associated with a finite number of data point can be estimated using the formula given by Yoda *et al.* (1994):

$$\mu = 2\left(\frac{\sigma}{n^{1/2}}\right) \qquad \textbf{Equation 6-12.}$$

where μ is the uncertainty, n is the number of independent concentration measurements and σ is the standard deviation of the measurements. For the present simple jet measurements, σ is about 0.2, giving an uncertainty of approximately 1.2% for 1100 images. For the precessing jet experiments the number of images used depends on the jet condition. The present measurements indicate σ is about 0.3 in the far field of a precessing jet flow, giving an uncertainty of approximately 1.8% for 1100 images, 3.4% for 304 images and 4.9% for 152 images.

6.3.4 Laser Sheet Intensity Distribution

The correction for the laser sheet intensity distribution, I_{ij}, see Section 6.2.2.4, represents the largest source of error in the image processing of raw PLIF images to obtain quantitative values of jet concentration distribution. Instantaneous deviations from the mean intensity distribution, changes in the mean intensity distribution from the actual jet experiment and the measurement of the intensity profile and the effects of absorption all contribute to the overall error. The effect of instantaneous intensity deviations was reduced by inspecting individual PLIF images and discarding those with gross intensity fluctuations observed in the background. This error was further reduced by eliminating any images with an instantaneous laser power outside the range of one standard deviation greater or less

than the mean laser power signal, based on the measurement from the laser power reference cell. For most experimental conditions the standard deviation of laser power signal was less than 4% of the mean value and the effect of instantaneous intensity distribution fluctuations on the final results is negligible.

The error due to changes in the intensity distribution in the jet experiments and the measurement of the intensity profile at the end of the experiments was primarily caused by slight movements of the experimental apparatus, although changes in the laser operation may have also had an effect. This error was checked by comparing background measurements during and after the experiments. For most configurations, if the final measurement was not suitable, an intermediate background measurement was used. However, this was not possible in the experiments conducted in the 490mm duct and as a result there is a slight peak in the concentration measurements in the middle region of these images. There was also a slight change in the intensity distribution of PJ390cofl experiments, restricted to just the very downstream end of the image region, which could not be accounted for.

The effect of absorption of laser intensity across the laser sheet is addressed in Section 6.2.2.5. This demonstrated that the maximum contribution of absorption across the width of the imaged region is about 4%. The contribution of absorption to the overall error in the spatial intensity distribution correction was reduced by including a correction in the calculation of the laser intensity distribution. However, a separate effect of absorption is to reduce the signal from the reference cell used to correct for laser power fluctuations. Inspection of the reference cell signal indicated that, allowing for the effect of actual laser power fluctuations, the signal intensity from the reference cell decreases by approximately 1-2% over the duration required to acquire eight batches of 152 images and hence the effect of absorption is minimal. This also indicates that any effect of photo-bleaching of the fluorescent dye in the reference cell is also negligible.

6.3.5 Signal to Noise Ratio

The signal-to-noise ratio (SNR) is relevant to the intensity resolution of the fluorescence signal. In the present study, careful orientation of the laser sheet intensity profile with respect to the concentration decay from the different jets resulted in a maximum SNR of the raw PLIF images of approximately 25 for the majority of the precessing jet investigations and the validation experiments. These were obtained using the Infinity Nd:YAG laser. The SNR of the raw images was about 20 for the experiments using the 28mm PJ nozzle due to the use of a different laser. The SureLite Nd:YAG laser, used in these latter experiments, was operated at a non-optimal repetition rate resulting in lower signal than was possible with the Infinity Nd:YAG laser.

6.3.6 Summary

The analysis presented above has quantified the main sources of uncertainty in the present PLIF experiments. The main sources of procedural error occurs in those runs when the number of images captured is only 152. The laser sheet intensity distribution correction provides another source of error. The main source of resolution error is that which is common to all liquid-phase PLIF experiments - the large Schmidt number of fluorescent dye in water, which results in a separation of the concentration and velocity scales. The present experiments are shown to have

a spatial resolution which is significantly poorer than the scale of the smallest concentration fluctuations, the Batchelor scale and the scale of the smallest velocity fluctuations, the Kolmogorov scale. Nevertheless the present spatial resolution is comparable with that of other PLIF investigations such as Dahm and Dimotakis (1990). The Nd:YAG/ dichloro-fluorescein system has been shown to completely resolve the time scales associated with velocity and scalar fluctuations in the jet flows investigated. Hence the instantaneous images of the passive scalar concentration are effectively "frozen". On the scale of the measurement resolution, an image pixel, the images of concentration distribution are independent while at larger scales independence of the measurements is necessarily compromised due to other experimental factors. Therefore the accuracy of mean jet concentration calculations is expected to be good, while the accuracy of concentration fluctuation calculations should be satisfactory but slightly lower than the actual values, sufficient to quantify the gross characteristics of the flow field from a PJ nozzle for the present purposes. However, an estimate of the overall uncertainty is difficult due to the unique combination of possible errors and jet conditions in each experimental configuration. Hence the simple jet experiments, in addition to validating the PLIF technique, provide a means of assessing the uncertainty experimentally by comparing the present measurements with previous results for a simple jet condition.

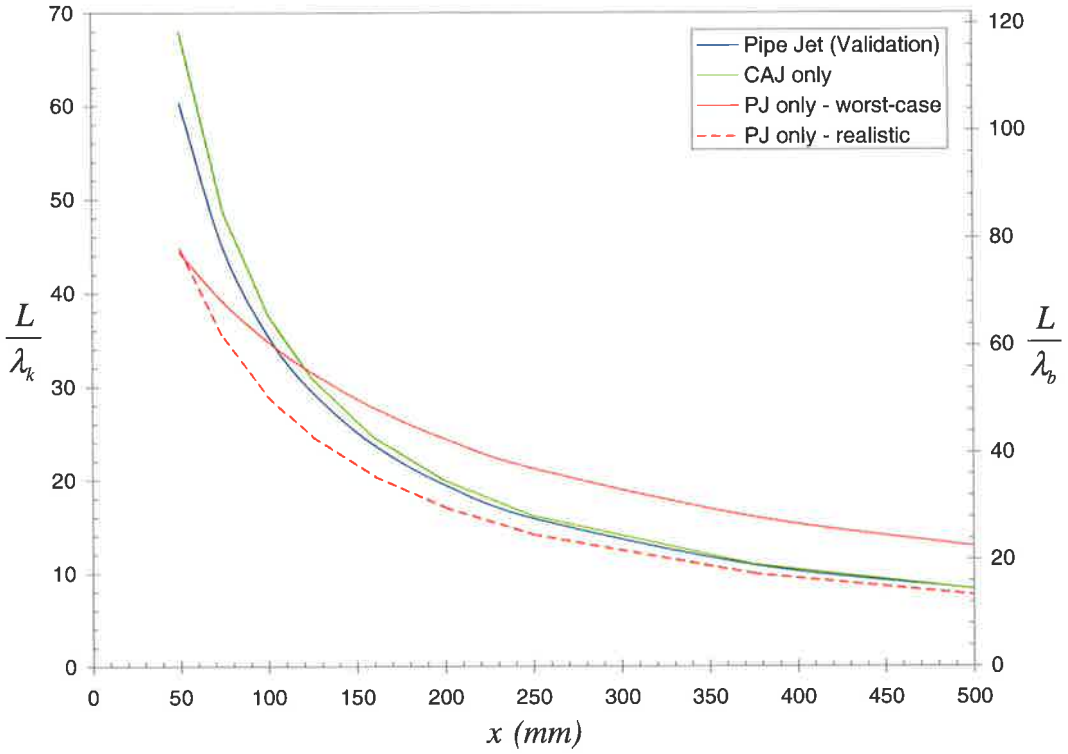

Figure 6-3. Variation in the Batchelor scale, λ_b, and Kolmogorov scale, λ_k, relative to the spatial resolution of the camera, L, with axial distance for the principal jet types used in the present PLIF experiments. For the "worst case" calculation of the PJ nozzle, the jet is assumed to expand at the same rate as a simple jet issuing from the inlet orifice of the nozzle chamber. For the "realistic" calculation a constant spread half-angle of 40° is assumed from the PJ nozzle exit.

6.4 Experimental Validation

6.4.1 Introduction

6.4.1.1 Properties of Axisymmetric Simple Jets

The present experimental technique is validated by comparing the results from the investigation of a simple, axis-symmetric jet with those from previous studies. The turbulent transport of a conserved scalar from a circular free jet has been investigated widely for many years both because of its wide industrial application and its significance as a class of turbulent flow.

According to the classical theory of the distribution of a passive scalar from a round, momentum-driven, free-turbulent jet, the mean and fluctuating concentration fields should display self-similarity with increasing normalised downstream distance, $\chi = (x - x_{0,1})/d_\varepsilon$, where x is the distance from the jet exit in cylindrical co-ordinates, $x_{0,1}$ is the virtual origin of the jet flow in the far field and d_ε is the jet momentum diameter. The mean concentration, $\overline{\xi}$, of jet fluid on the nozzle centreline should decay as χ^{-1}, such that in the far field, the inverse concentration on the centreline can be expressed as:

$$\frac{1}{\overline{\xi}_c} = \frac{1}{K_1}\left(\frac{x - x_{0,1}}{d_\varepsilon}\right) \qquad \textbf{Equation 6-13.}$$

where K_1 is a decay constant determined by experiment. The spreading of a free-turbulent jet, can be quantified by calculating the concentration half-width of the jet, $r_{1/2}$, which is defined as the radial location at which the concentration is exactly half the centreline concentration. In the far field, the jet spread should become self-similar and hence can be expressed as:

$$\frac{r_{1/2}}{d_\varepsilon} = K_2\left(\frac{x - x_{0,2}}{d_\varepsilon}\right) \qquad \textbf{Equation 6-14.}$$

where K_2 is the spreading rate determined by experiment and $x_{0,2}$ is the jet-spread virtual origin determined from the far field data. The radial profiles of the mean and RMS concentration fluctuations, ξ_{rms}, are self-similar when plotted against the appropriate normalised dimension, $\eta = r/(x - x_{0,2})$, where r is the distance from the jet centreline. This implies that the fluctuation intensity of jet concentration on the nozzle centreline, $\xi_{rms}/\overline{\xi}$, also termed the unmixedness, should approach a constant value in the jet far field. Values for the virtual origins, $x_{0,1}/d$ and $x_{0,2}/d$, decay constant, K_1, and spreading rate, K_2, determined in previous jet experiments are summarised in Table 6-6 for a variety of single point, linear and planar techniques in both gas and aqueous mediums. Values for the asymptote of concentration fluctuation intensity and the ratio of the maximum RMS to centreline RMS, $\xi_{rms}/\xi_{rms\text{-}c}$ are also included in Table 6-6.

While the Reynolds number is the major similarity parameter in non-reacting jet flows, other factors have recently been found to have a secondary influence on the far field mixing characteristics. However such a wide variety of different initial conditions, different boundary conditions, different experimental techniques and different spatial

resolutions have been used in previous jet experiments (see Table 6-6) that it is difficult to separate out their respective influences and so explain the wide spread in the data. Indeed, it is only recently that Mi *et al.* (2000b) demonstrated conclusively that significant differences exist throughout the scalar field of a jet issuing from a smooth contraction relative to that from a long pipe. They also showed that these differences explain many of the apparent discrepancies between previous data sets. However, the role of molecular diffusion, as characterised by the Schmidt number, $Sc=\nu/D$, the ratio of turbulent to molecular diffusivity, is less clear in jets, despite the large difference between aqueous ($Sc\sim1000$) and gaseous ($Sc\sim1$) mediums. As the present experiments are found to suggest an influence of Schmidt number on the mixing from a simple jet, the role of Schmidt number in mixing is reviewed in detail.

6.4.1.2 The Effect of Schmidt Number on Mixing

Evidence for the effect of Schmidt number on mixing can be readily found in the results of shear layer experiments. Koochesfahani and Dimotakis (1985) found that the probability of observing unmixed ambient fluid on the centre of liquid mixing layers is 10%, compared to 6% in gaseous layers at comparable Reynolds numbers. Broadwell and Mungal (1991), in reviewing previous experiments, found the mixed fluid composition to be more uniform across a liquid shear layer than in a gaseous layer, indicative of a Schmidt number effect even at high Reynolds number. Mungal and Dimotakis (1984) showed that ramp-like features exist in the instantaneous time traces of product concentration in gaseous shear layers, while no such features are detected in the liquid shear layer experiments of Koochesfahani and Dimotakis (1985). Broadwell and Mungal (1991) propose a two-stage Lagrangian model to explain the mixing of shear-layers and jets based on discrete, large-scale engulfment of ambient fluid and large-scale unsteadiness in the flow. The effect of Schmidt number is accounted for by the contribution to the mixing by the diffusion layer, or Taylor scale, which is negligible in high Schmidt shear layer experiments and significant for low Schmidt number shear layers. Finally, Karasso and Mungal (1996) in comparing the mixed fluid distribution from a shear layer in water and gas experiments, concluded that molecular diffusion has a significant effect and hence it "*becomes imperative to incorporate this Schmidt-number dependency in models and calculations of scalar mixing in any turbulent flow*".

The effect of Schmidt number on the mixing from free jets is, however, less clear. Some results demonstrate an obvious effect of Schmidt number on mixing in turbulent jets. For example, Dahm and Dimotakis (1990) estimate that in the limit of perfect spatial resolution of aqueous jet experiments using PLIF, the fraction of the jet centreline in the far field occupied by ambient fluid decreases from nearly 30% to less than 4% as the Reynolds number is increased from 1,500 to 5,000. No pure ambient fluid is measured on the jet centreline in experiments using gas jets at comparable Reynolds numbers. Dahm and Dimotakis (1990) also note that, in time traces of the jet fluid concentration on the jet centreline, the characteristic large-scale ramp-like features reported in gaseous turbulent jets are not observed in liquid-phase jets, consistent with the observations in shear layers. Dowling and Dimotakis (1990) demonstrate a Schmidt number effect (at constant Reynolds number) off the jet centreline by an increase in the normalised value of the RMS of the concentration fluctuations. This is deduced to be due to a reduction in diffusivity (associated with the increase in Sc) causing an increase in the local concentration fluctuation at the jet edge. On the centreline, Miller and Dimotakis (1991) show that in high Schmidt number jets the RMS of concentration

fluctuations decrease with increasing Reynolds number and do not reach an asymptotic value by Re=24,000. In low Schmidt number jets however, the concentrations fluctuations do not change significantly with Reynolds number. Dimotakis (2000) concludes that as "*lower fluctuation levels correspond to more homogeneous mixing ... we see that, at least for the case of a liquid-phase jet, the flow transitions to a more well-mixed state as the Reynolds number is increased, as in the shear layer, even though in a more gradual manner.*" This Schmidt number effect is deduced to be due to molecular diffusion in low-*Sc* jets bridging recently entrained reservoir-fluid filaments at low Reynolds numbers, improving homogenisation, while for high-*Sc* jets, higher Reynolds numbers are required to increase the molecular mixing by increasing the surface-to-volume ratio of fluid filaments.

The variation in concentration fluctuations with Reynolds number reported by Miller and Dimotakis (1991) is consistent with a narrowing in the normalised far field probability distribution. This implies that in liquid phase jets, the "flame length", defined by a specified jet-ambient fluid mixture fraction, should decrease with increasing Reynolds number. The finding that simulated flame length varies with Reynolds number in liquid jets contradicts previous research, which suggests that this quantity is independent of Schmidt number and Reynolds number, at least above a critical Reynolds number. Kristmanson and Danckwerts (1961) and Wilson and Danckwerts (1964) found the simulated flame length of jets in water and air is different. Wilson and Danckwerts (1964) conclude that the simulated flame length is 9 percent greater for water jets compared to air jets, consistent with the notion that if all other flow and fluid quantities are fixed, increasing the Schmidt number can only decrease the rate of molecular mixing and the amount of mixed fluid, thereby resulting in longer simulated flame lengths.

The observations noted above for jet and shear layers are perhaps best summarised by Miller and Dimotakis (1991), who state that "*experimental and theoretical arguments in the last few years suggest that the turbulent mixing process is sensitive to the value of the molecular diffusion coefficients, even at Reynolds numbers typically regarded as high. We recognise that this remains a controversial proposal, at this writing, especially in the case of turbulent jet mixing.*" One of the main difficulties with the concept of the Schmidt number altering jet entrainment is that there is no clear physical mechanism whereby a change in Schmidt number can result in a change to the bulk entrainment rate of ambient fluid by a jet and hence overall flow statistics such as the rate of decay of mean concentration on the centreline, K_1 (Dahm and Dimotakis, 1990). In addition, the two-stage Lagrangian model proposed by Broadwell and Mungal (1991), which demonstrates that the Schmidt number alters the bulk entrainment in shear layer experiments, also shows that the Schmidt number should not alter the centreline entrainment characteristics of a jet. This is consistent with the observations of Dowling and Dimotakis (1990) which show no difference in the far field probability distribution function of liquid or gaseous jets.

6.4.1.3 Previous Studies of the Scalar Mixing from a Turbulent Simple Jet

Despite the fact that there is evidence that the Schmidt number may have a significant, albeit secondary influence on the mixing characteristics of a jet, the wide variety of different jet exit conditions, boundary conditions, experimental techniques and spatial resolutions of previous simple jet investigations has made it difficult to separate out a possible Schmidt number effect. To address the difference in scalar mixing of jets, the results of previous simple jet experiments summarised in Table 6-6 are organised according the jet type and phase (i.e. liquid or gas) of the

jet and ambient fluid. The results are separated based on the type of exit conditions following the analysis of Mi *et al.* (2000b), which demonstrated that the far field characteristics of a simple jet from a smooth contraction nozzle differ from those from a pipe flow. The experiments conducted using gas-phase jets are separated from those using liquid-phase jets to illustrate any differences due to the change in Schmidt number.

The most extensive range of data available to compare the effects of Schmidt number on the mixing from a simple jet is for smooth contraction nozzles. For measurements in air, the average inverse concentration decay constant, K_1, is 4.845 (standard deviation, σ=0.587) and the average jet spreading rate, K_2, which is less sensitive to experimental errors, is 0.1125 (σ=0.0144). For measurements in water, the average inverse concentration decay constant, K_1, is 5.537 (σ=0.638) and the average jet spreading rate, K_2, is 0.1120 (σ=0.0033). Hence it appears that the change in Schmidt number from liquid to gas phase, may have an effect of increasing K_1 and slightly decreasing K_2, consistent with a reduced mixing rate. The measurement of K_1=6.34 by Papanicolau and List (1988) for a smooth contraction nozzle may therefore be partly attributed to the effect of Schmidt number and not just experimental error as proposed by the authors.

The data available to compare the effect of Schmidt number is less extensive for pipe jets. From measurements in air, the average concentration decay constant is K_1=4.61 (σ=0.382) and the average jet spreading rate is K_2=0.1019 (σ=0.0151). Only two measurements of the concentration decay constant are available for pipe jets in water, Law and Wang (2000) and Dahm and Dimotakis (1990), with an average value of K_1=5.36. (Note the value reported by Law and Wang (2000) of K_1=5.26 has been corrected here for the momentum diameter, assuming a fully developed pipe jet). There are also only two measurements of the jet spreading rate of pipe jets in water, Law and Wang (2000) and Chu *et al.* (1999) with an average value of K_2=0.109. Hence the effect of the change in Schmidt number from air to water for pipe jets appears also to increase the value of K_1 by 16%, consistent with the increase of 14% determined for jets from smooth contractions. It should be noted that the jet used by Dahm and Dimotakis (1990) was a smooth contraction followed by a pipe section 8 diameters in length and hence the exit conditions are likely to be between those of a pipe jet and a smooth contraction jet, but closer to those of a pipe jet since it usually takes about 10 diameters to attain similarity in the mean data. The jet used by Law and Wang (2000) was from a long pipe and their PLIF technique is very similar to the present experiment, as it also used a MegaPlus CCD camera and Nd:YAG laser, but with rhodamine B as the fluorescent dye tracer. Law and Wang (2000) demonstrated that the properties of the Nd:YAG/rhodamine B PLIF system are linear with respect to concentration and absorption.

It is important to note that following the results of Mi *et al.* (2000b), the concentration decay constant should be higher and the jet spreading rate lower for pipe jets than for smooth contraction jets. This is satisfied for the average values of K_2 but not for the average value of K_1, probably due to the high value determined by Papanicolau and List (1988) of K_1=6.34 for a smooth contraction jet in water, who acknowledged that experimental errors may have contributed to this value. The jet spreading rate for pipe jets also appears to be greater in water than in air, contradicting the findings for smooth contraction jets. The present experiments, intended as a validation case for the quantitative PLIF technique, provide further statistics to assess the effect of Schmidt number on the mixing from a jet.

6.4.2 Validation Experiments

The equipment and procedures used in implementing the quantitative PLIF technique for the simple jet validation experiment are described in detail in Section 2.2.3. A well defined initial condition for the simple jet was achieved by using fully developed pipe flow. A pipe with a length of more than 100 diameters (1000mm long, 9.45mm internal diameter pipe) was selected for this purpose. The Reynolds number at the jet exit based on the bulk jet flow velocity was 28,200. The jet was aligned with the axis of symmetry of the water-tunnel working section and the laser sheet was aligned to the geometric axis of the nozzle. A rod containing a fixed concentration of fluorescent dye to monitor the laser power fluctuations was located in the image area and incident with the laser sheet, but sufficiently far away from the jet so that it did not disturb the flow. Eight batches of 152 images were collected, corresponding to a total of 1216 images of data. Image processing to calculate the instantaneous, average and fluctuating jet concentration fields was performed according to the procedures outlined in Section 6.2.3.

The water-tunnel was operated at a slight co-flow, approximately 2% of the bulk jet exit velocity. The effect of this slight co-flow on the jet mixing can be estimated using the "momentum radius", l_c, defined by Maczynski (1962):

$$l_c^2 = \frac{G_0}{\pi \rho_a U_a^2}$$ **Equation 6-15.**

where ρ_a is the density of the co-flowing stream, U_a is the velocity of the co-flow and G_0 is the excess momentum flux of the jet relative to the co-flow. The co-flow has little effect on the jet if, at a distance x from the nozzle exit, x/l_c is less than one. Assuming a uniform flow at the jet exit, $G_0 = \pi \rho_0 r_0^2 (U_0/U_a - 1) U_0/U_a$, where 0 indicates a property at the jet exit, and the maximum value of x/l_c is 0.13 for the present simple jet experiment. Hence the co-flow has negligible influence on the jet asymptotic state.

The momentum diameter, d_ε, or effective diameter of a simple jet nozzle has been shown to collapse the results of a wide variety of experiments using different nozzle designs and jet-reservoir densities (Dowling and Dimotakis, 1990). Although the velocity profile at the exit to the pipe used in the present experiments has not been measured, the momentum diameter was corrected following the findings of Mi *et al.* (2000b) that $d_\varepsilon \approx 0.99 \times d$ for fully developed pipe flow, where d is the physical jet exit diameter.

6.4.3 Results of the Validation Experiments

6.4.3.1 Planar Data

The spatial distribution of the scalar mixing field from a jet can be characterised by instantaneous, mean and fluctuating jet concentration measurements. A typical instantaneous image and images of the mean and RMS of the jet concentration from the pipe flow are shown in Figure 6-4. A consistent colour map spanning the range $0<\xi<0.5$ is used for the instantaneous and average images, where white represents pure, unmixed ambient fluid and black represents concentration values greater than $\xi=0.5$.

The instantaneous image shown in Figure 6-4 reveals the large-scale structures and local, instantaneous deviation from symmetry in the developing and far field regions that has been noted by Dahm and Dimotakis (1990) and van Cruyningen *et al.* (1990). The average and RMS images are symmetrical about the jet axis and also exhibit the same features noted by previous planar simple jet investigations. No unmixed fluid is visible on the jet centreline, consistent with the photographs and trends of Dahm and Dimotakis (1990) for a Reynolds number above 20,000. A more detailed comparison of the present results with previous simple jet investigations is made in the following section by plotting statistics of the concentration measurements along radial and axial profiles through the jet flow field.

6.4.3.2 Statistical Analysis

Figure 6-5 plots the inverse concentration on the jet centreline, $1/\overline{\xi}_c$, compared to other reported measurements of pipe jets in water (Sc~1000) and air (Sc~1). The present results demonstrate the expected inversely proportional relationship between distance from the nozzle and the mean concentration. A line of best fit through the data for $x/d_\varepsilon>20$ defines the relationship between the mean concentration and non-dimensional axial distance to be:

$$\frac{1}{\overline{\xi}_c} = \frac{1}{6.36}\left(\frac{x-0.84}{d_\varepsilon}\right) \qquad \textbf{Equation 6-16.}$$

The value of the centreline concentration decay constant determined here, $K_1=6.36$, is higher than the values reported in the literature, see Table 6-6, which are between 4.16 and 5.44 for gaseous pipe jets and the measurements in water by Dahm and Dimotakis (1990) in which $K_1=5.41$ and Law and Wang (2000) in which $K_1=5.31$. The location of the virtual origin, $x_{0,1}/d=0.84$ lies within the values reported in the literature of -1 to 5.8 for gaseous pipe jets.

The jet spread is quantified by determining the concentration half-width, $r_{1/2}$. The half-width was calculated using an average of the values for each side of the nozzle centreline (i.e. the near-laser and far-laser sides of the jet centreline) at a given axial location. The normalised half-width, $r_{1/2}/d$, is plotted as a function of axial distance in Figure 6-7 and compared to other data for pipe jets. The graph shows a constant rate of jet spread, with a linear relationship found to be:

$$\frac{r_{1/2}}{d_\varepsilon} = 0.094\left(\frac{x-0.05}{d_\varepsilon}\right) \qquad \textbf{Equation 6-17.}$$

The rate of jet growth, K_2=0.094, is at the lower end of the rates determined previously in gaseous pipe jet experiments, which vary from 0.089 to 0.132, see Table 6-6. This is consistent with the low rate of concentration decay along the jet centreline. The present measurement of jet spreading rate is also lower than the value of K_2=0.104 determined by Chu *et al.* (1999) and K_2=0.108 determined by Law and Wang (2000), which are the only other data for comparable pipe jet experiments in water. The location of the concentration half-width virtual origin, $x_{0,2}/d$=0.05, is within the values reported in the literature of -0.35 to 4.3 for gas-phase pipe jet experiments.

The radial profiles of mean and fluctuating jet concentration, $\overline{\xi}$ and ξ_{rms}, normalised to the centreline value, are shown in Figure 6-9 to Figure 6-12. Within the axial extent of the present experimental region, the radial profiles have become identical, indicating the jet has reached self-similarity. As for the centreline inverse concentration and jet half-width, the present results compare well with previous investigations for pipe jets, the only difference being a slightly narrower spread of the present data.

One of the best tests of the accuracy of an experimental technique for the investigation of the scalar concentration from a jet is the intensity of jet concentration fluctuations, $\xi_{rms\text{-}c}/\overline{\xi}_c$, or unmixedness. The concentration fluctuation intensity along the jet centreline is compared to other pipe jet measurements in Figure 6-8. The results indicate that the profile of the concentration fluctuation intensity is very similar to the gas-phase measurements of Pitts and Kashiwagi (1984) and Birch *et al.* (1978), although the value of the far field asymptote is lower for the present case. This is consistent with the spatial resolution not resolving the concentration fluctuations at the Batchelor scale. The present profile of $\xi_{rms\text{-}c}/\overline{\xi}_c$, is greater than the liquid-phase jet measurements of Nakamura *et al.* (1982) and Dahm and Dimotakis (1990) but less than the measurements of Law and Wang (2000), who also used a PLIF technique in water. The asymptotic concentration fluctuation intensity value in the jet far field of the present experiments is $\xi_{rms\text{-}c}/\overline{\xi}_c$=0.194, compared to values shown in Table 6-6, which vary from 0.15 to 0.225 for liquid-phase pipe jets and 0.21 to 0.23 for gas-phase pipe jet experiments.

6.4.4 Discussion

The statistical analysis of the mean and fluctuating components of jet concentration shown in the previous section demonstrate that the results of the present pipe jet experiments compare well with the results obtained by other researchers. The consistent difference in all the results is that the present measurements indicate that the jet is narrower, with lower rates of the mean concentration decay and spreading, resulting in a higher value of the decay constant, K_1, and lower jet spreading rate, K_2, than for previous pipe jet measurements. The contribution of experimental error to these differences will outlined first, followed by a discussion of the effect of differences in experimental conditions.

There are a number of potential experimental factors that may contribute to the different results of the present and previous investigations. Great care was taken to align the camera focal plane and the laser sheet, so any overall error due to this source is expected to be small. The large spatial resolution compared to the Batchelor scale is also expected to have a minimal effect on the calculation of K_1 and K_2 due to the reasons outlined in Section 6.3, which show a resolution effect should only affect the measurement of fluctuation calculations and other higher order sta-

tistics. An error in the calculation of 100% jet fluid would have a significant effect upon the centreline jet mixing statistics, but will not effect the normalised calculations such as the jet spreading rate and radial profiles. As the difference in centreline and normalised statistics of the present measurements and previous experiments are consistent, the effect of an error due to the reference concentration is expected to be small. Another possible source of error is the limited experimental region, which only extends to just over 50 jet nozzle diameters, compared to much larger regions investigated in the literature. However, Mi *et al.* (2000b) have shown that a pipe jet is fully developed by x/d=50, although smooth contraction jets required more distance, x/d=70. The present measurements indicate the radial profiles of mean and fluctuating concentration have become self-similar by x/d=20, so that measurements downstream of this location are in the far field.

We return now to the issue of the influence of Schmidt number discussed in Section 6.4.1.2. The present measurement of K_1=6.36 is greater than the average value in gaseous pipe jet measurements of K_1=4.61, consistent with an increase due to the postulated Schmidt number influence on gas and liquid jets described in Section 6.4.1.2. However the present value of K_1 does not agree with the previous liquid phase measurements of Dahm and Dimotakis (1990), K_1=5.41, and Law and Wang (2000), K_1=5.31. Consistent with the increased concentration decay constant, the present measurements also yield a lower spreading rate, K_2=0.094, relative to both the average measurement for gaseous pipe jets, K_2=0.1019 and the measurements in water by Chu *et al.* (1999), K_2=0.104, Nakamura *et al.* (1982), K_2=0.114, and Law and Wang (2000), K_2=0.108.

The present value for the centreline decay constant in a pipe jet is very similar to the value determined by Papanicolau and List (1988) of K_1=6.34 for a smooth contraction nozzle using a simultaneous velocity and concentration measurement technique. While the authors attributed this relatively high measurement to experimental calibration errors, this deduction was based on the fact that it differed from previous measurements. It is therefore possible that the effect of Schmidt number may be a primary reason for the high measurement. Dahm and Dimotakis (1990) use an integral mass balance and self-similarity analysis in which the theoretical vale of K_1 was determined to be 5.15 with a maximum possible value of 5.70. Hence while there is strong evidence that the Schmidt number plays a role in jet mixing, it is also clear that there are differences between the present data and previous measurements conducted in water. To address this, the differences in physical arrangement of the jet and experimental facilities are examined.

It is well known that the spread angle and decay rate are a function of the ratio of co-flow to jet velocity. They are also effected by the presence or absence of a solid surface through which a jet protrudes. Although the calculation of the momentum radius in Section 6.5.1.1 indicates that the present co-flow is significantly lower than that required to alter the mixing characteristics and hence the calculated statistics within the imaged region, there is a difference in the boundary conditions of the present experiment and those of Dahm and Dimotakis (1990) and Law and Wang (2000). The experiments of Dahm and Dimotakis (1990) and Law and Wang (2000) were both conducted in enclosed water tanks, which results in an induced counter-flow when the jet is in motion. In addition, the jet exit was located close to the free surface of the water in these investigations. Both of these conditions will act to increase the jet mixing and spreading rate compared to the effect of the unrestricted supply and co-flow of ambi-

ent fluid in the present case and hence will, at least in part, account for the higher present value of K_1 and lower value of K_2.

6.4.5 Conclusion

The present implementation of a novel quantitative PLIF technique using a Nd:YAG laser with carboxy-dichlorofluorescein dye has been compared with results reported in the literature of the centreline and radial statistics of a passive scalar issuing from a simple jet. Separating the results of previous simple jet investigations according to the nozzle type (smooth contraction or pipe jet) and phase (liquid or gas) provides strong evidence that the Schmidt number is important in determining the bulk mixing characteristics of simple jets. The results of the present technique, which indicate that the jet is narrower and the concentration decay rate is lower than previous pipe jet measurements, can therefore be attributed, at least in part, to the significant difference in Schmidt number when comparing mixing experiments conducted in water and in gases. The disparity between the present results and those of comparable experiments investigating pipe jets in water using a PLIF technique are attributed to differences in the conditions of the ambient medium. Hence the pipe jet experiments clearly demonstrate that the present implementation of the Nd:YAG/carboxy-dichlorofluorescein PLIF system is an appropriate and accurate technique for the quantitative measurement of passive scalar concentration from a jet.

First Author	Technique	x/d	ρ_0/ρ_∞	U_∞/U_0	Sc	Re_d	K_1	$x_{0,1}/d$	K_2	$x_{0,2}/d$	$\xi_{rms}/\xi_{rms\text{-}c}$ maximum	$\xi_{rms\text{-}c}/\bar{\xi}_c$ (x/d>50)	Experimental Boundary Conditions
Smooth Contraction													
Richards (1993)	Rayleigh scattering	30-50	1.552	0	~1	25,000	4.76	1.6±3.9	0.113±0.009	3.6±0.2	–	0.23	Jet into a quiescent enclosure
Dowling (1990)	Rayleigh scattering	20-80	1.05	0.4%	1.2	16,000	4.73	–	0.114	–	1.17	0.237	Co-flowing jet into a reservoir
Grandmaison (1982)	Mie scattering	2-40	1.0	0	0.7	27,000	5.43	1.67	0.105	1.67	1.15	0.20	No details
Becker (1967)	Mie scattering	0-32	1.0	0	0.7	54,000	5.59	2.4	0.106	2.4	1.17	0.22	Free jet
Ebrahimi (1977)	Mie scattering	0-50	1.1	0	0.63	15,400	4.30	0	–	0	–	0.25	Free jet with exhaust hood
Nobes (1997)	Mie scattering	0-90	1.0	0	0.7	16,400	5.52	-0.68	0.111	1.54	1.28	0.233	Free air jet
Chua (1986)	Cold-wire	0-40	0.91	0	0.7	17,700	4.63	-2.3	0.106	-1.4	–	0.19	Free heated air jet
Mi (2000b)	Cold-wire	0-64	0.85	0	0.7	16,000	4.48	3.5	0.111	-1.0	1.20	0.24	Free heated air jet
Wilson (1964)	Cold-wire	0-100	0.6-0.93	0	0.7	20,000+	5.71	0	0.13	3.8	1.18	0.18	Heated air jet, from flat surface
Corrsin (1950)	Thermometry	0-27	0.65 0.95	0 0	0.7 0.7	55,000 55,000	5.26 3.66	2.16 2.60	0.143 0.086	3 0	- –	– –	Heated free jet, disk around exit
Average value	–	–	–	–	–	–	**4.85**	**1.1**	**0.113**	**1.4**	**1.19**	**0.22**	–
Kristmanson (1961)	Acid-Alkali	8-110	1.0	~0	500	10,000+	4.78	0	0.112	0	–	–	Jet up into water-tank
Papanicolau (1987)	Thermometry	16-40	0.98-1.0	~0	~1000	16,700	5.49	–	0.096	–	~1.4	–	Jet up into water-tank
Papanicolau (1988)	LIF	0-98	0.98-1.0	~0	~1000	11,000	6.34	4.35	0.115	2.51	~1.25	0.22	Jet up into water-tank
Average value	–	–	–	–	–	–	**5.54**	**2.2**	**0.112**	**1.3**	**~1.3**	**0.22**	–
Pipe Jets													
Lockwood (1980)	Thermo-couple	0-50	0.54	0	0.7	50,400	5.44	2.0	0.132	2.0	1.26	0.21	No details
Birch (1978)	Raman scattering	0-70	0.56	0	0.7	16,000	4.44	5.8	0.097	0	1.20	0.27	Free jet
Richards (1993)	Rayleigh scattering	20-60	1.552	0	~1	25,000	4.81	2.1±1.1	0.104	4.2	1.27	0.23	Jet into a quiescent enclosure
Pitts (1991)	Rayleigh scattering	2-31.5	1.02	4.3%	~1	3,960	4.42	-0.35	–	-0.35	–	0.23	Jet into an enclosure
Pitts (1984)	Rayleigh scattering	0-30	0.55	3.3%	~1	4,130	4.50	-1	0.104	0	1.18	–	Jet into an enclosure
Dyer (1979)	Rayleigh scattering	15-30	1.6	3.3%	~1	9,790	4.5	2.4	0.0855	0.5	1.29	–	Free jet with a co-axial air flow
Mi (2000b)	Cold-wire	0-70	0.85	0	0.7	16,000	4.64	4.73	0.102	1.3	1.19	0.218	Free heated air jet
Antonia (1974)	Cold-wire	0-80	0.66	5.9%	0.7	23,500	4.16	0.99	0.089	4.3	~1.26	0.21	Co-flowing jet in wind-tunnel
Average value	–	–	–	–	–	–	**4.61**	**2.0**	**0.102**	**1.5**	**1.23**	**0.23**	–
Nakamura (1982)	Dye-absorption	0-300	1.0	0	~1000	5,000	–	–	0.114	4.37	–	0.208	No details
Chu (1999)	LIF	10-100	1.0	0	~1000	6,000+	–	–	0.104*	–	~1.3	0.15	Co-flowing jet in water-tunnel
Dahm (1990)	LIF	0-300	1.0	~0	~600	5,000	5.41	–	–	–	1.17	0.225	Jet into water tank, near surface
Law (2000)	PLIF	40-80	1.0	~0	~1000	12,700	5.26	0	0.108	0	~1.36	0.224	Jet into water tank, near surface
Average value	–	–	–	–	–	–	**5.36**	**0**	**0.109**	**2.2**	**1.28**	**0.202**	–
Present	**PLIF (water)**	**0-53**	**1.0**	**2.0%**	**~1000**	**28,200**	**6.36**	**0.84**	**0.094**	**0.05**	**1.22**	**0.194**	Co-flowing jet in water-tunnel

Table 6-6. A comparison of the mixing statistics measured in previous investigations into the scalar concentration field from simple axisymmetric nozzles with the present results. The results are separated according to the type of jet nozzle and if the experiments were conducted in water or gas. Experimental boundary conditions and jet conditions are also shown. * - Indicates the concentration half-width spreading rate was estimated from 1/e-concentration contour values.

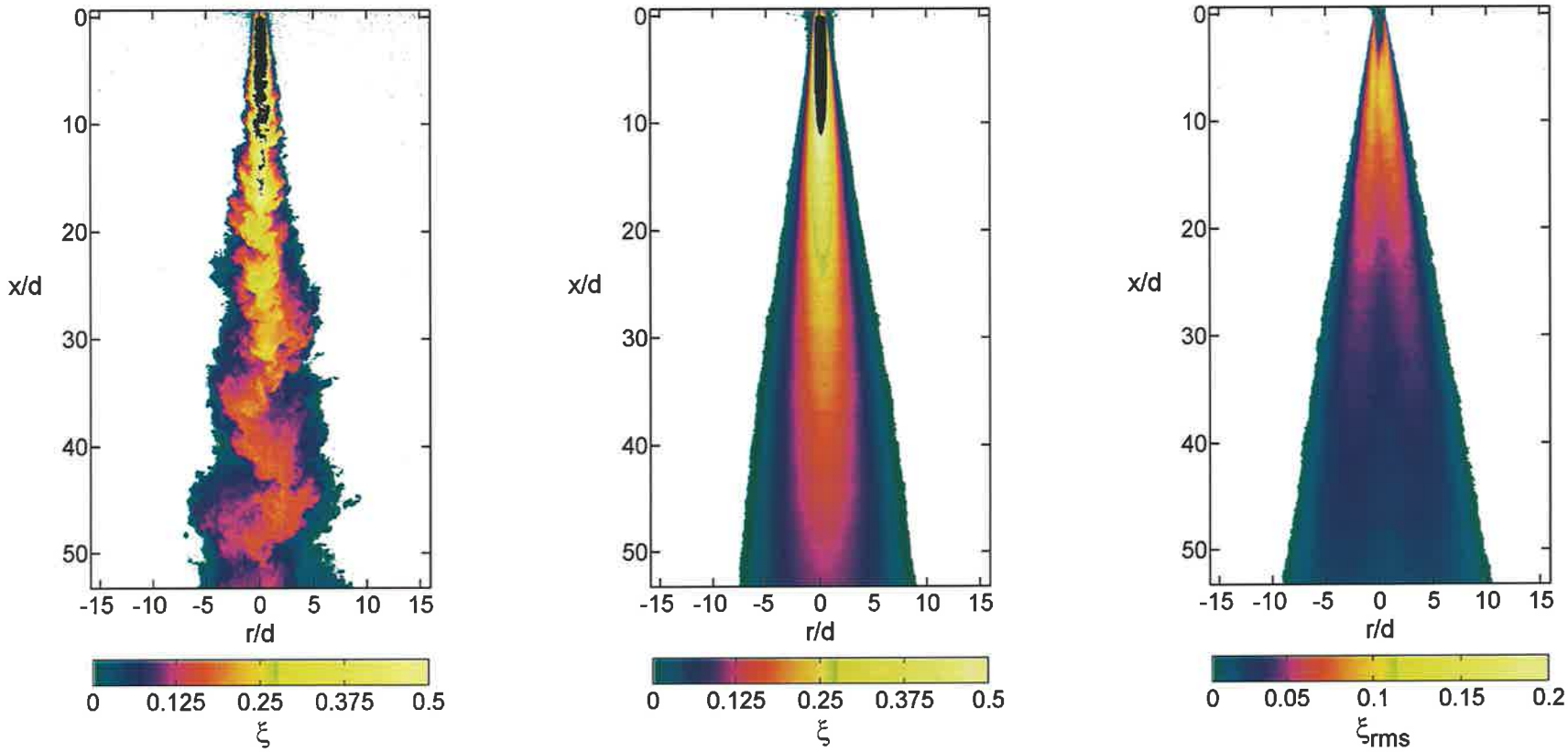

Figure 6-4. False colour images of the spatial distribution of the instantaneous, mean and RMS of the jet concentration, ξ, from the present pipe jet measurements. Conditions: Reynolds number=28,200, co-flow velocity U_a=0.06m/s, jet diameter d=9.45mm, water-tunnel cross-section=500×500mm.

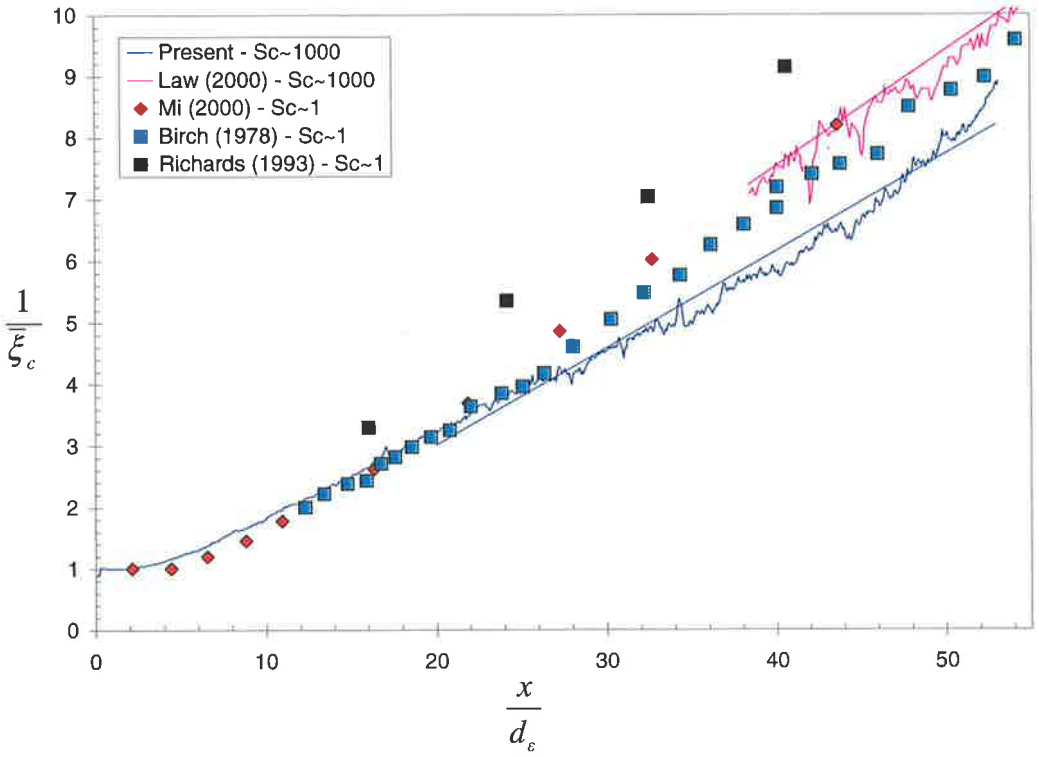

Figure 6-5. Inverse of the mean concentration on the jet centreline, $\overline{\xi}_c$, for the present pipe jet measurements compared with the results of other liquid (Sc~1000) and gaseous (Sc~1) phase pipe jet investigations. Refer to Figure 6-4 and Table 6-6 for the jet conditions.

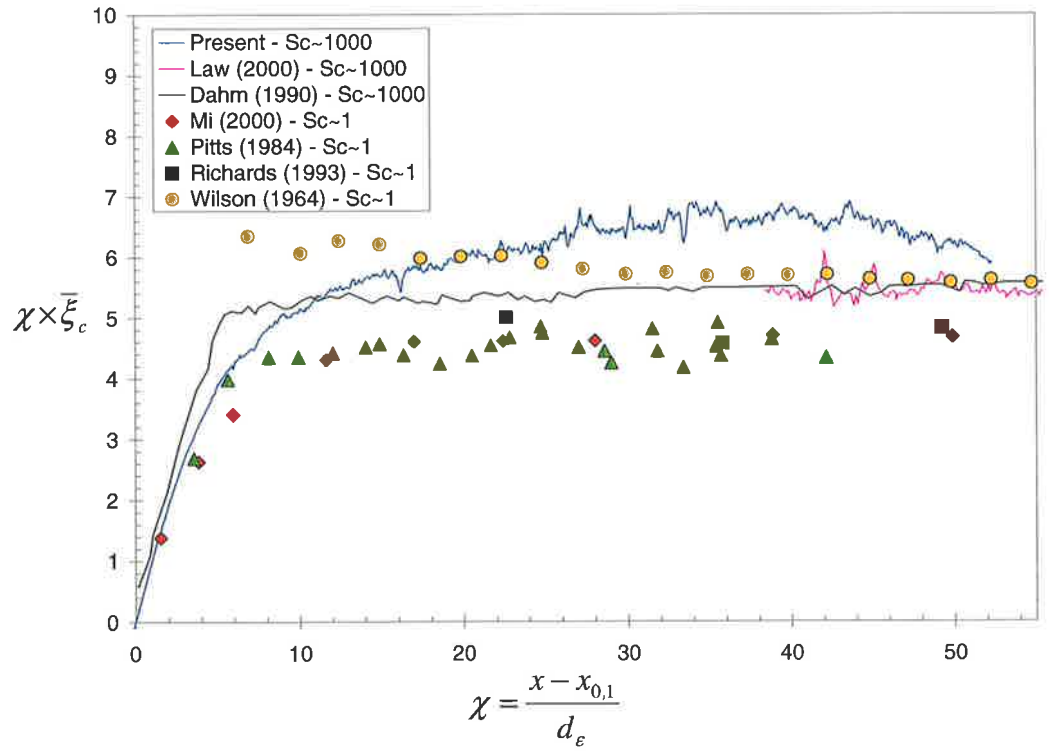

Figure 6-6. The scaled mean centreline concentration, $\chi \times \overline{\xi}_c$, for the present pipe jet measurements compared with the results of other liquid (Sc~1000) and gaseous (Sc~1) phase pipe jet investigations. Refer to Figure 6-4 and Table 6-6 for the jet conditions.

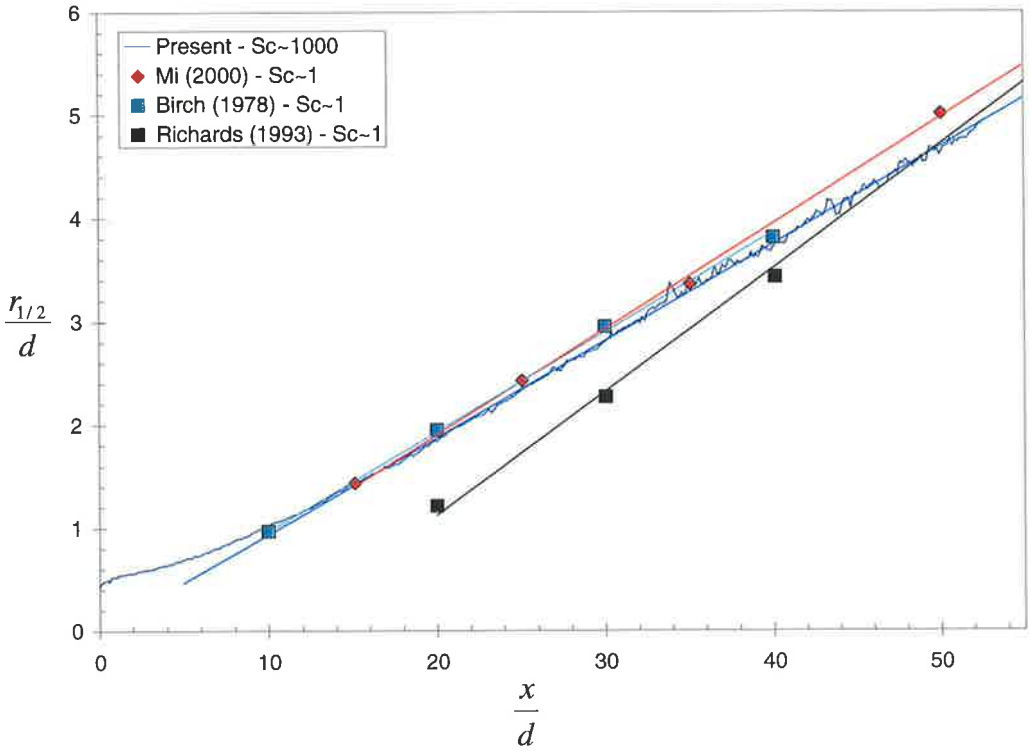

Figure 6-7. The concentration half-width, $r_{1/2}/d$, for the present pipe jet measurements compared with the results of other liquid (Sc~1000) and gaseous (Sc~1) phase pipe jet investigations. Refer to Figure 6-4 and Table 6-6 for the jet conditions.

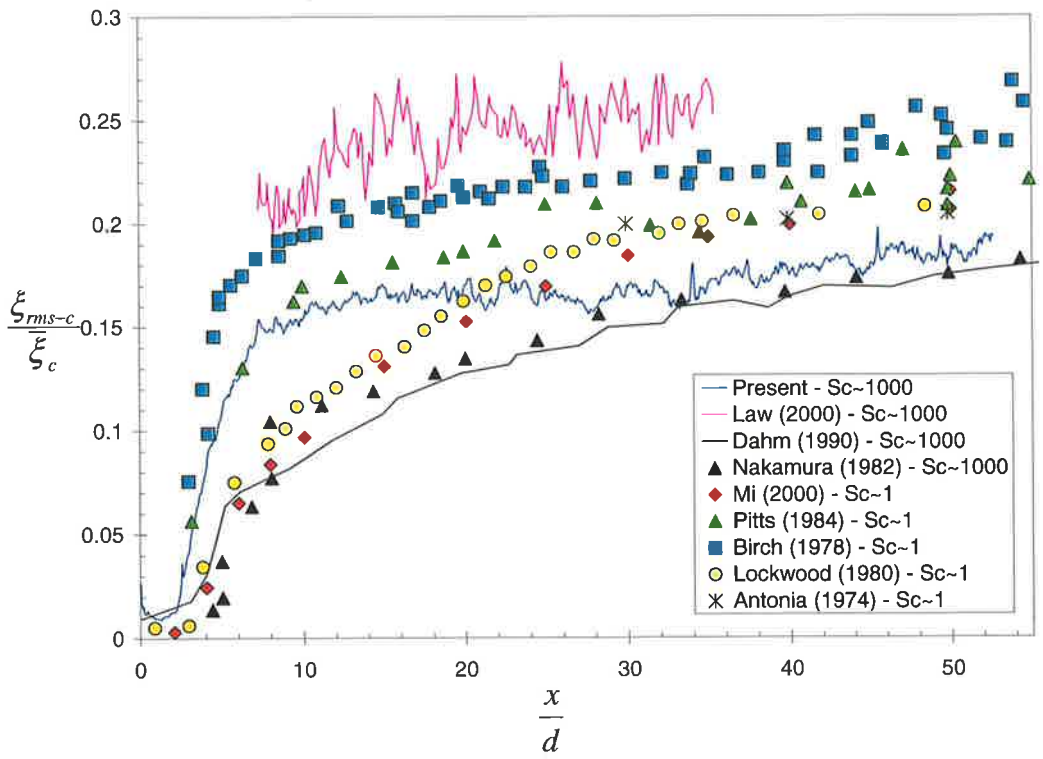

Figure 6-8. The intensity of jet concentration fluctuations along the nozzle centreline, $\xi_{rms-c}/\overline{\xi}_c$, for the present pipe jet measurements compared with the results of other liquid (Sc~1000) and gaseous (Sc~1) phase pipe jet investigations. Refer to Figure 6-4 and Table 6-6 for the jet conditions.

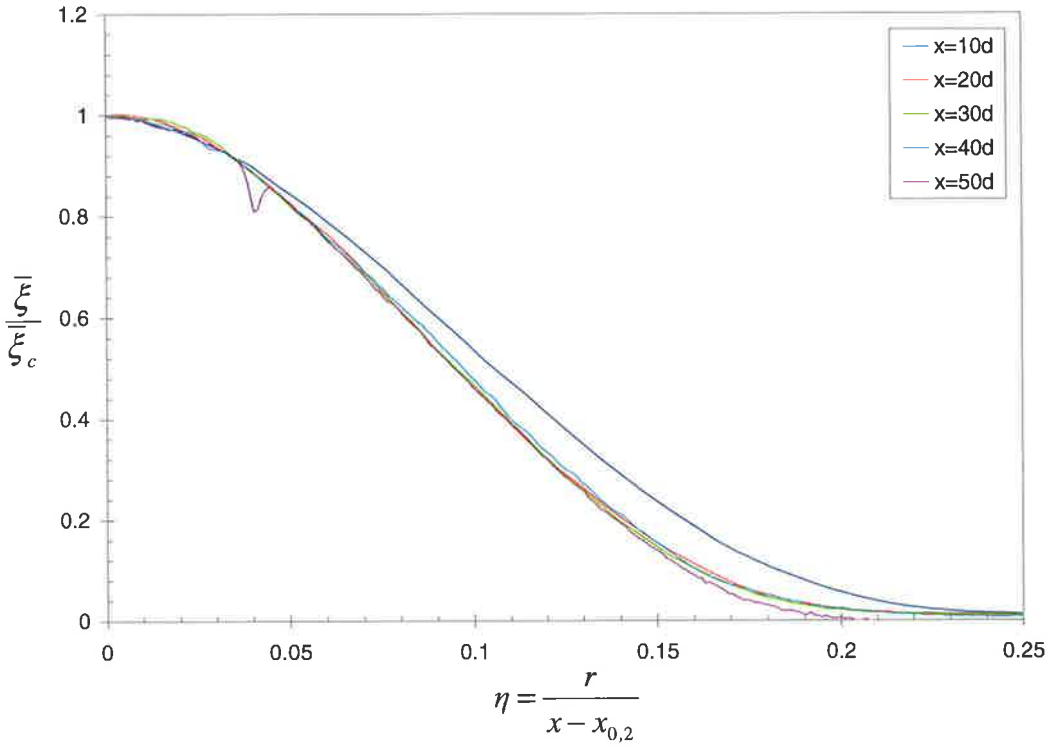

Figure 6-9. Radial profiles of the mean jet concentration normalised to the value on the centreline, $\overline{\xi}/\overline{\xi}_c$, at different axial locations downstream of the jet exit for the present pipe jet measurements. Refer to Figure 6-4 for the jet conditions.

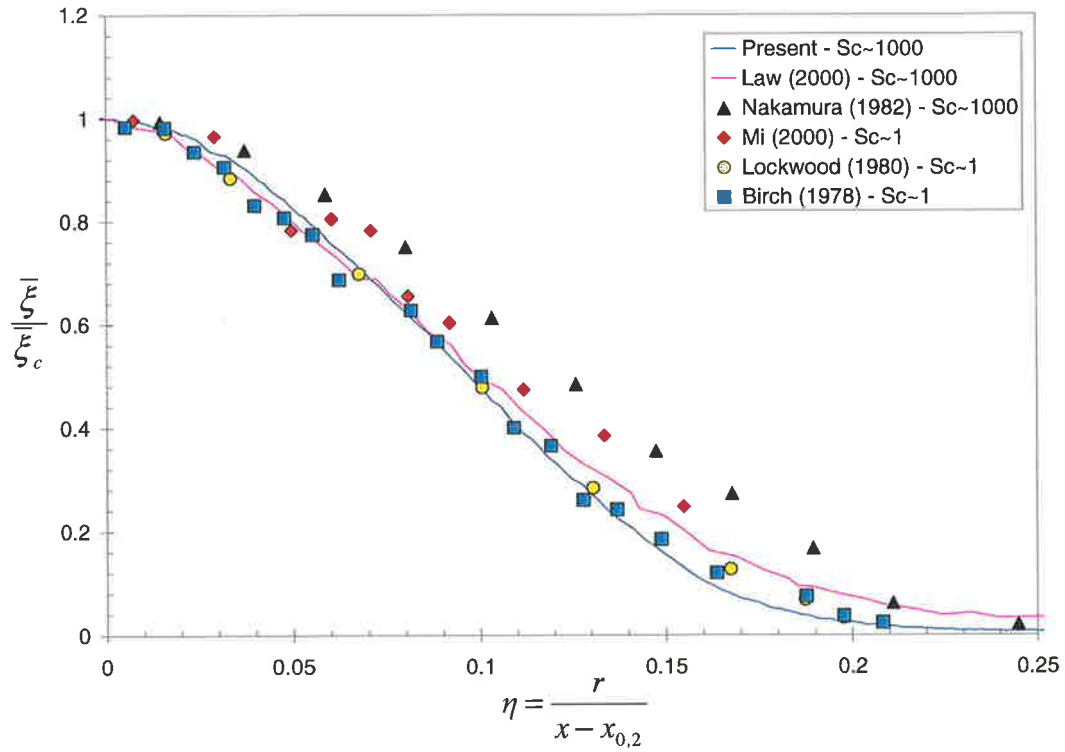

Figure 6-10. Radial profile at x=40d of the mean jet concentration normalised to the centreline value, $\overline{\xi}/\overline{\xi}_c$, for the present pipe jet measurements compared with results in the far field of other liquid (Sc~1000) and gaseous (Sc~1) phase pipe jet investigations. Refer to Figure 6-4 and Table 6-6 for the jet conditions.

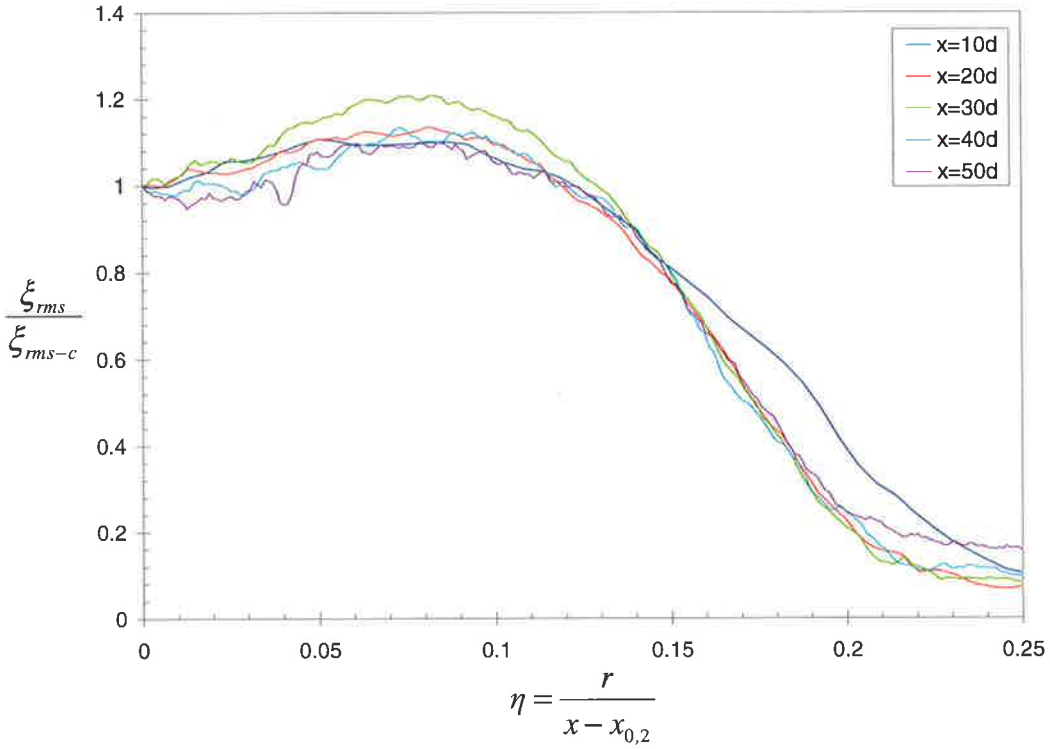

Figure 6-11. Radial profiles of the RMS of jet concentration fluctuations normalised to the value on the centreline, $\xi_{rms}/\xi_{rms\text{-}c}$, at different axial locations downstream of the jet exit for the present pipe jet measurements. Refer to Figure 6-4 for the jet conditions.

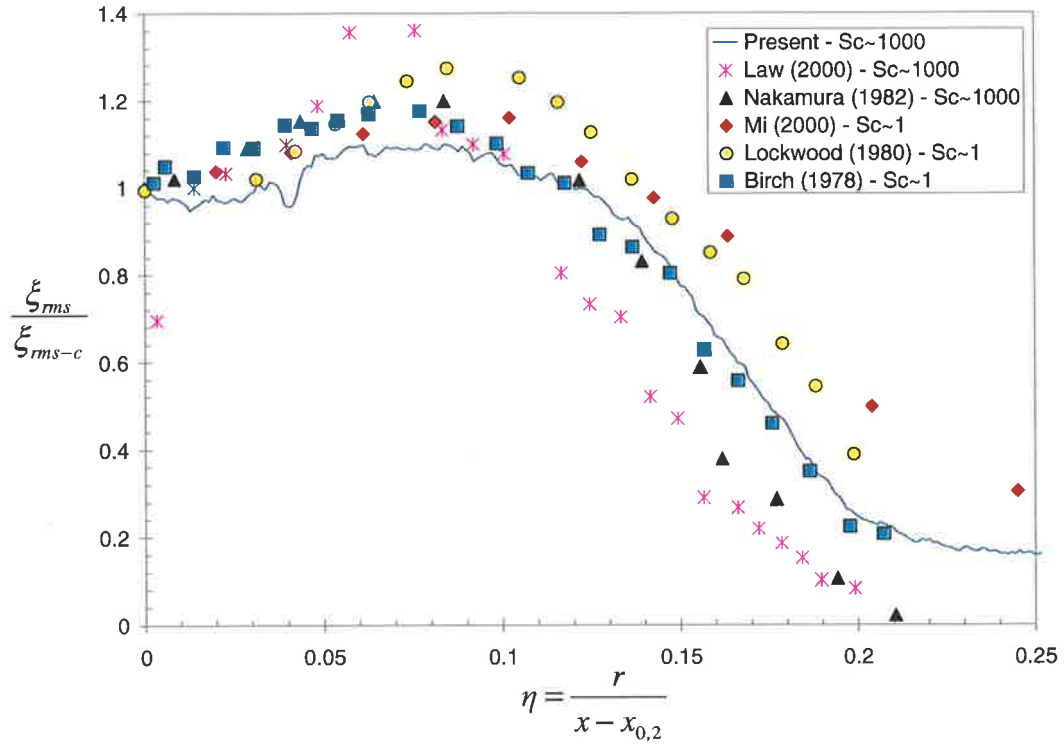

Figure 6-12. Radial profile at x=50d of the RMS of jet concentration fluctuations normalised to the centreline value, $\xi_{rms}/\xi_{rms\text{-}c}$, for the present pipe jet measurements compared with results in the far field of other liquid (Sc~1000) and gaseous (Sc~1) phase pipe jet investigations. Refer to Figure 6-4 and Table 6-6 for jet conditions.

6.5 Precessing Jet Experiments

6.5.1 Experimental Design

6.5.1.1 Precessing Jet Conditions

To assess independently the effects of confinement and co-flow on the combined PJ and CAJ flows, while also minimising the quantity of dye used, careful selection of experimental configurations and conditions was necessary. A matrix of test cases was developed in which the nozzle geometry and jet flow conditions were kept constant while the co-flow velocity and confinement were varied, see Table 6-7. Two nozzle were used, a d_{PJ}=38mm PJ nozzle and a d_{PJ}=28mm PJ nozzle. The non-dimensional geometry of both nozzles was identical. Section 2.1.1 provides full details of the designs. All the conditions shown in Table 6-7 were investigated for constant nozzle conditions with 100% of the flow through the precessing jet nozzle. The Reynolds number at the inlet orifice of the nozzle chamber was 66,100 for the d_{PJ}=38mm PJ nozzle and d_{PJ}=62,400 for the 28mm PJ nozzle. The imaged region corresponds to approximately one duct diameter for the least confinement and 1.7 duct diameters for the highest confinement. This region represents the near-field of the flames investigated in the pilot-scale cement kiln simulator, see Section 2.3.2, where the concentration of carbon monoxide is highest and the heat-flux profile increases rapidly with distance from the burner nozzle exit.

6.5.1.2 Scaling of Precessing Jet Nozzles for the Present Experiments

The PJ nozzle dimensions, flow rates, co-flow velocities and duct diameters of the present experiments were selected to overlap with the scaled conditions from a number of combustion facilities. The primary reference for calculating the geometry and experimental conditions of the present experiments is the pilot-scale combustion facility outlined in Section 2.3.2, although consideration was also given to installations of the PJ burner in operating cement kilns.

Methods (i.e. models) for scaling the dynamics of large-scale industrial combustion facilities to isothermal, laboratory scale conditions have been reviewed in detail by Moles *et al.* (1972) and Rhine and Tucker (1991). The three most important modelling criteria for enclosed jet systems are the Thring-Newby, Craya-Curtet and Becker theories, see Section 1.3.4. The Craya-Curtet and Becker similarity parameters have been validated for the modelling of momentum dominated burner designs in which the burner nozzle can be treated as a point source of momentum. Previous research (e.g. Newbold *et al.*, 1996) and the flow visualisation results of Chapter 3 demonstrate that the mixing of jet and ambient fluids by a precessing jet cannot be characterised solely by the momentum of the jet at its origin. Hence the jet flow in the far field cannot be treated as originating from a point source of momentum. The Craya-Curtet and Becker similarity parameters were estimated for the PJ nozzle in the pilot-scale combustion experiments using some simplifications. However the co-flow velocities or duct dimensions required in the small-scale isothermal experiments to achieve the required similarity parameter values were not sensible as they were significantly greater than the physical dimensions and pump capacity, confirming that these parameters are inappropriate scaling methods for the confined PJ nozzle.

Following the failure of the Becker and Craya-Curtet parameters to provide an appropriate scaling methodology for a confined PJ flow, a modified form of the Thring-Newby parameter, geometric scaling and constant velocity scaling were considered, as they can be applied irrespective of the jet mixing conditions. The modified Thring-Newby parameter, θ_{PJ}, proposed by Nathan *et al.* (1995) and discussed in detail in Chapter 1.3.4, consists of a correction for the nozzle geometry based on the change in densities from the combusting environment to the isothermal model (Equation 6-19) and the calculation of the Thring-Newby criterion (Equation 6-18). The modified Thring-Newby parameter maintains mixing similarity in the near-burner zone by maintaining the momentum ratio and mass flow ratio of jet to co-flowing fluid in the large-scale reacting facility and small-scale non-reacting model.

$$d_0' = d_0\sqrt{\frac{\rho_0}{\rho_a}} \qquad \textbf{Equation 6-18.}$$

$$\theta_{PJ} = \frac{\dot{m}_0 + \dot{m}_a}{\dot{m}_a} \cdot \frac{d_0'}{D_{kiln}} \qquad \textbf{Equation 6-19.}$$

where d_0 is the characteristic nozzle diameter, D_{kiln} is the kiln diameter, ρ_0 is the density of the jet fluid (i.e. the fuel in a burner) at the inlet orifice, ρ_a is the density of the co-flowing fluid (i.e. the secondary air in a rotary kiln) and m_0 and m_a are the mass flow rates of the jet fluid and co-flowing fluid respectively.

The modified Thring-Newby parameter is based on a simple assumption of the physical behaviour of a jet and hence does not assume any particular mixing characteristics of a jet type. Therefore it can be applied to any burner nozzle design, as long as the nozzle diameter is small relative to the characteristic dimension of the confined volume, i.e. $d_0'/D_{kiln}<0.05$, which is generally the case in rotary kilns. While the ratio of internal dimensions of the PJ nozzle are identical in the isothermal model and the pilot-scale kiln simulator, the exit flow from the PJ nozzle is poorly understood and is not well represented by a single nozzle dimension. As a result two Thring-Newby values have been calculated, corresponding to the two extreme nozzle diameters, that of the inlet orifice to the PJ nozzle chamber, d_{or}, and the diameter of the PJ nozzle chamber, d_{PJ}, as shown in Table 6-7 for the small-scale isothermal model and Table 6-8 for the pilot-scale rotary kiln simulator. Commercially sensitive values of the Thring-Newby parameter and other scaling criteria for industrial installations of the PJ nozzle are shown in the confidential attachment Appendix B. The model conditions were designed to ensure an extensive overlap with the values of θ_{PJ} in the combustion cases. In particular the values of θ_{PJ} for the d_{PJ}=38mm PJ nozzle in 390mm duct at 0.06m/s co-flow (38PJ-d390-u060) and d_{PJ}=28mm PJ nozzle in the 290mm duct at 0.044m/s (28PJ-d290-u044) are almost identical to the value of θ_{PJ} in the pilot-scale combustion experiments. It is also important to note that the values of θ_{PJ} in the industrial installations, see Appendix B, are substantially lower than the typical values in cement kilns calculated by Moles *et al.* (1972), indicative of the differences due to the correction relative to the density of the secondary air instead of the average density of combustion products in the flame.

Geometric similarity requires that the ratio of kiln to burner dimensions is maintained from the full-scale to the model. As for the Thring-Newby parameter, two geometric ratios can be calculated: kiln or duct diameter to PJ chamber diameter, d_{PJ}, and kiln or duct diameter to PJ orifice diameter, d_{or}. Table 6-7 shows the values of these ratios for the different model duct diameters, D_{duct}. Comparison of Table 6-7, Table 6-8 and Appendix B indicates that the 38mm PJ nozzle in the 490mm duct (D_{duct}/d_{PJ}=12.9) and the 28mm PJ nozzle in the 390mm duct

(D_{duct}/d_{PJ}=13.9) are geometrically similar to the combustion installations. The experiments with the 38mm PJ nozzle in the 290mm duct (D_{duct}/d_{PJ}=7.6) do not overlap directly any combustion installation, but examine a more highly confined case than is found in present rotary kilns.

Similarity in the mixing processes between the jet and co-flowing fluid close to the nozzle exit at different scales can be achieved by keeping the ratio of co-flow velocity, U_a, to the characteristic nozzle velocity constant in the full-scale and model facilities. This is termed constant velocity scaling. For the PJ nozzle, the characteristic nozzle velocity can again be calculated in two ways: at the inlet orifice of the nozzle chamber where the velocity is known exactly, U_{or}, or using an approximate exit velocity, $U_{e\text{-}PJ}$. For the present calculations the approximate exit velocity from a PJ nozzle is estimated to be one-eighth of the velocity at the inlet orifice of the nozzle chamber based on the PIV measurements of Nobes *et al.* (2000). A comparison of the conditions in the isothermal model and combustion facilities in Table 6-7, Table 6-8 and Appendix B respectively shows that there is a significant overlap in the velocity ratios $U_a/U_{e\text{-}PJ}$ and $U_{or}/U_{e\text{-}PJ}$, implying that the mixing processes within the region investigated in the present small-scale tests span the range of those in the large scale facilities.

For the d_{PJ}=38mm PJ nozzle, a co-flow velocity was calculated for each duct-nozzle geometry such that the mass flux ratio of co-flowing fluid to jet fluid, m_a/m_0, was approximately constant (test configurations 38PJ-d290-u108, 38PJ-d390-u060 and 38PJ-d490-u038 in Table 6-7). The mass flux ratio for these configurations was approximately the same as in the pilot-scale combustion experiments, m_a/m_0=18.1. These test conditions were intended as baseline conditions for comparing scaling effects on the mixing from the PJ nozzle. The effect of the central axial jet on the scalar mixing field was investigated only at these baseline co-flow velocities and confinements. The 28PJ-d290-u080 and 28PJ-d390-u044 cases were also intended as baseline test conditions but at a reduced scale, although the mass flux ratio of m_a/m_0=19.6 for each case is slightly higher than the value of m_a/m_0=18.4 for the 38mm PJ nozzle configurations.

The effect of varying the confinement ratio, D_{duct}/d_{PJ}, at constant co-flow velocity and co-flow velocity ratio, $U_a/U_{e\text{-}PJ}$, at constant confinement, are presented in the following sections. The present data is also compared with the scalar measurements from a fluidic precessing jet nozzle performed by Newbold (1997), in order to further validate the PLIF technique and compare the effect of inlet conditions on the mixing downstream of the PJ nozzle exit.

Test Condition Name	Duct Diameter (mm)	Co-Flow Velocity (m/s)	Mass Flux Ratio (m_a/m_0)	Geometric Ratio		Velocity Ratio		Thring-Newby, θ_{PJ}		Number of Images
				Chamber (D_{kiln}/d_{PJ})	PJ Inlet (D_{kiln}/d_{or})	PJ Exit ($U_a/U_{e\text{-}PJ}$)	PJ Inlet ($U_{or}/U_{e\text{-}PJ}$)	Chamber	PJ Inlet	
38mm PJ Nozzle										
38PJ-d290-u038	290	0.038	6.44	7.6	38.7	0.035	4.31×10^{-3}	0.151	0.0299	304
38PJ-d290-u060	290	0.060	10.17	7.6	38.7	0.055	6.80×10^{-3}	0.144	0.0284	152
38PJ-d290-u108	290	0.108	18.31	7.6	38.7	0.098	12.3×10^{-3}	0.138	0.0273	152
38PJ-d290-u162	290	0.162	27.47	7.6	38.7	0.147	18.4×10^{-3}	0.136	0.0268	152
38PJ-d290-u216	290	0.216	36.63	7.6	38.7	0.196	24.5×10^{-3}	0.135	0.0266	152
38PJ-d390-u038	390	0.038	11.65	10.3	52.0	0.035	4.31×10^{-3}	0.106	0.0209	304
38PJ-d390-u060	390	0.060	18.40	10.3	52.0	0.055	6.80×10^{-3}	0.103	0.0203	1216
38PJ-d390-u108	390	0.108	33.12	10.3	52.0	0.098	12.3×10^{-3}	0.100	0.0198	304
38PJ-d390-u162	390	0.162	49.68	10.3	52.0	0.147	18.4×10^{-3}	0.099	0.0196	152
38PJ-d390-u216	390	0.216	66.24	10.3	52.0	0.196	24.5×10^{-3}	0.099	0.0195	152
38PJ-d490-u038	490	0.038	18.40	12.9	65.3	0.035	4.31×10^{-3}	0.082	0.0161	304
38PJ-d490-u060	490	0.060	29.05	12.9	65.3	0.055	6.80×10^{-3}	0.080	0.0158	304
38PJ-d490-u108	490	0.108	52.28	12.9	65.3	0.098	12.3×10^{-3}	0.079	0.0156	152
38PJ-d490-u162	490	0.162	78.42	12.9	65.3	0.147	18.4×10^{-3}	0.079	0.0155	152
38PJ-d490-u216	490	0.216	104.56	12.9	65.3	0.196	24.5×10^{-3}	0.078	0.0155	152
28mm PJ Nozzle										
28PJ-d290-u044	290	0.044	10.78	10.4	52.7	0.031	3.88×10^{-3}	0.106	0.0207	304
28PJ-d290-u080	290	0.080	19.59	10.4	52.7	0.056	7.05×10^{-3}	0.101	0.0199	304
28PJ-d290-u108	290	0.108	26.45	10.4	52.7	0.076	9.51×10^{-3}	0.100	0.0197	152
28PJ-d290-u162	290	0.162	39.68	10.4	52.7	0.114	14.3×10^{-3}	0.099	0.0194	152
28PJ-d390-u044	390	0.044	19.49	13.9	70.9	0.031	3.88×10^{-3}	0.075	0.0148	304
28PJ-d390-u080	390	0.080	35.44	13.9	70.9	0.056	7.05×10^{-3}	0.074	0.0145	304
28PJ-d390-u108	390	0.108	47.84	13.9	70.9	0.076	9.51×10^{-3}	0.073	0.0144	152
28PJ-d390-u162	390	0.162	71.76	13.9	70.9	0.114	14.3×10^{-3}	0.073	0.0143	152

Table 6-7. The duct size and co-flow velocities of the PJ nozzle experimental conditions. Also shown are the values of the scaling parameters: geometric ratio, velocity ratio and modified Thring-Newby parameter calculated for the inlet jet to the PJ nozzle and the chamber diameter or estimated exit velocity conditions. The highlighted rows indicate the baseline conditions with approximately constant mass flux ratio of co-flowing fluid to jet fluid. The number of images are for precessing jet flow only (Ψ_{CAJ}=0%).

Facility	PJ Chamber Diameter (mm)	Duct Diameter (mm)	Co-Flow Velocity (m/s)	Mass Flux Ratio (m_a/m_0)	Geometric Ratio		Velocity Ratio		Thring-Newby, θ_{PJ}	
					Chamber (D_{kiln}/d_{PJ})	PJ Inlet (D_{kiln}/d_{or})	PJ Exit ($U_a/U_{e\text{-}PJ}$)	PJ Inlet ($U_{or}/U_{e\text{-}PJ}$)	Chamber	PJ Inlet
IFRF	56	756	4.64	18.1	13.8	72.0	0.051	18.3×10^{-3}	0.105	0.0197

Table 6-8. Geometry and conditions of the PJ nozzle experiments conducted in the pilot-scale rotary kiln simulator. Also shown are the values of the scaling parameters: geometric ratio, velocity ratio and modified Thring-Newby parameter calculated for the inlet jet to the PJ nozzle and the chamber diameter or estimated exit velocity conditions. Refer to Appendix B for the geometry and conditions of industrial installations of the PJ nozzle.

6.5.2 Comparison with Previous Data

The only previous quantitative measurement of the concentration of a passive scalar mixing from a fluidic precessing jet nozzle was performed by Newbold (1997). A planar Mie scattering technique in air was applied to the measurement of the jet concentration from a PJ nozzle with a Reynolds number of 20,500 at the inlet orifice of the nozzle chamber issuing into an unconfined, quiescent environment. Results from the present investigation have been compared to the results obtained by Newbold and jet conditions corresponding to the flow from the inlet orifice. The normalisation convention adopted by Newbold for the axial distance from the PJ nozzle exit, $\chi=x/d_{or}$, where x is the distance from the inlet orifice of the nozzle chamber and d_{or} is the diameter of the inlet orifice is used for the present comparison. Note that in subsequent sections the axial distance is normalised to the PJ nozzle chamber diameter and the exit orifice of the PJ nozzle as this is considered to be a more appropriate for the development of a scaling criterion.

6.5.2.1 Planar Data

An image of the instantaneous spatial distribution of scalar concentration measured using the present technique is compared with a similar image from Newbold (1997) in Figure 6-13. The images are displayed at approximately the same dimensionless size, based on normalisation of the axial and radial distances to the diameter of the inlet orifice of the PJ nozzle and the colourmap used to represent the jet concentration is also the same for both images. The results demonstrate the same characteristic flow features of the precessing jet field described in Section 3.3, in particular the presence of large-scale structures that dominate the flow field, entraining ambient fluid deep into the jet towards the jet axis.

6.5.2.2 Jet Axis Statistics

Inspection of the images of the planar distribution of the average and RMS of jet concentration indicate that there is a slight bias to the left of the image (away from the laser source) in the 38mm PJ nozzle and a significant bias to the right of the image (towards the laser source) in the 28mm PJ nozzle. A PJ nozzle is a fluid 'amplifier', so that any small bias in the inlet flow or chamber geometry is amplified in the emerging flow. Bias can arise from a disturbance in the inlet orifice or from eccentricity between the orifice and nozzle chamber. In order to account for the bias in the results, the "jet axis" has been used as the reference co-ordinate for subsequent calculations rather than the nozzle geometric centreline. The jet axis is defined as the line of best fit through the centre of the nozzle exit and the radial position of the maximum local concentration at each axial location corresponding to a pixel row in the camera CCD array.

Statistics along the jet axis for the 38mm PJ nozzle in the least confined case (D_{duct}/d_{PJ}=12.9) with $U_a/U_{e\text{-}PJ}$=0.055 (U_a=0.06m/s) have been compared with the unconfined, free jet results of Newbold (1997) and with other simple jet measurements. The simple jet investigated by Newbold (1997) corresponds to the inlet orifice used in the PJ nozzle of that investigation. Note that the nozzle inlet for the present PJ nozzle is a smooth contraction. Hence the smooth contraction jet investigated by Nobes (1997) is used as a reference case for the effects of precession on the inlet jet of the present experiments. The experiments in air of Nobes (1997) are used as the reference data because

insufficient information was available for liquid-phase jet investigations. The raw data was also readily available from Nobes and the experimental technique was the same as used by Newbold.

The inverse of the mean jet concentration shown in Figure 6-14 demonstrates a number of similarities and differences between the present results and those of Newbold. One common feature is that the majority of the data is linear so that in the far field the mean concentration is inversely proportional to the distance from the inlet orifice of the nozzle chamber. The slight "bump" in the middle section of the present data is caused by a small error in the laser sheet intensity distribution correction, see Section 6.3.4, and is not a result of any jet, co-flow or confinement effect. The rate of decay is much lower for the present measurements than for the results obtained by Newbold. In addition, the present results indicate that the far field decay is preceded by an initial very rapid concentration decay in approximately the first nozzle diameter from the nozzle exit which is not detected by Newbold. One contribution to this difference may be the relative spatial resolution of the experiments. Although the spatial resolution is approximately 500μm per pixel for both techniques, the size of the PJ nozzle used by Newbold was d_{PJ}=13mm compared to d_{PJ}=38mm for the present experiments, so the spatial resolution relative to the PJ nozzle is effectively a factor of 3 better in the present experiments. Hence in the near-field close to the nozzle exit, the steep gradient in mean concentration may be better resolved by the present measurement technique. However another, possibly more significant cause of the discrepancy between the experiments is the different methods used to calculate the reference concentration for determining 100% jet fluid. The use of PLIF in the present experiments allowed the use of a reference cell of dye to determine the signal value corresponding to 100% jet fluid, while Newbold's Mie-scattering technique does not allow such a reference. In the absence of a better alternative, Newbold assumed that the maximum signal in a 3×3 pixel area at the nozzle exit corresponded to 100% jet fluid. The present measurements, although affected by reflections in the region very close to the nozzle exit, indicate an average concentration of approximately $\bar{\xi}$=95% at this point. However, there is significant fluctuation in the maximum concentration. These two difference suggest that the present measurements are more reliable than Newbold's in the near nozzle region.

The mean centreline decay in the far field of the PJ nozzle was derived by Newbold to be given by the relationship:

$$\frac{1}{\bar{\xi}} = \frac{1}{5.88}\left(\frac{x-L}{d_{or}} + 10.4d_{or}\right) \qquad \textbf{Equation 6-20.}$$

while the relationship for the present configuration of the PJ nozzle is derived to be:

$$\frac{1}{\bar{\xi}} = \frac{1}{11.5}\left(\frac{x-L}{d_{or}} + 41.3d_{or}\right) \qquad \textbf{Equation 6-21.}$$

Although the difference between the far field concentration decay rate measured by Newbold, K_J=5.88, and the present experimental technique, K_J=11.5, is significant, it is important to note that there is a similar difference in the decay rate of the two reference jets. Newbold's results indicate that precession acts to roughly halve the concentration decay rate from a sudden contraction orifice, K_J=2.23. The present results indicate the concentration decay rate from the PJ nozzle is roughly half that of a smooth contraction nozzle, K_J=5.52 as measured by Nobes (1997) or K_J=5.537 based on an average of previous liquid-phase jet experimental results, see Table 6-6. Hence

the differences in jet inlet conditions of each PJ nozzle may account for the apparent discrepancy. The calculation of the reference concentration, as outlined previously, may also contribute to the change in decay rate. A third reason for the difference in far field concentration decay rate is the effect of Schmidt number. As outlined in Section 6.4, the increase in Schmidt number between water and air decreases the centreline decay rate of simple jets by an estimated 15%. This is consistent with the trend in the difference between the present inverse concentration decay rate and that measured by Newbold, although the magnitude of the difference is too large to be due to a Schmidt number effect alone.

Calculation of the jet concentration half-width shows good agreement between the present data set and that of Newbold. Figure 6-15 demonstrates that both measurement techniques record a very rapid initial jet spread, followed by a more gradual rate of jet growth, so that the characteristic width of the PJ nozzle jet is much greater than that of a jet issuing from the nozzle inlet (i.e. with the chamber section removed). The jet spread of the present measurement is slightly less than that reported by Newbold. In explaining these differences it is necessary to consider the separate effects of Schmidt number, confinement and co-flow. The radial distribution of the mean jet concentration for the present experiments at the same co-flow, U_a=0.06m/s, and different confinements, D_{duct}/d_{PJ}=10.3 and D_{duct}/d_{PJ}=12.9, are compared with Newbold's measurements in Figure 6-16. The radial profiles are taken at approximately the same non-dimensional axial location and are plotted using the same normalisation scheme for the radial distance as used for the simple jet. The results indicate that the effect of confinement and co-flow in the present measurements are more significant than any Schmidt number effects as the D_{duct}/d_{PJ}=12.9 case approaches the profile of Newbold's free jet closer than that at D_{duct}/d_{PJ}=10.3. All radial profiles follow a Gaussian type distribution of mean concentration. The plot of radial RMS distribution, normalised to the value on the jet axis, Figure 6-17, also demonstrates a slight effect of confinement on the D_{duct}/d_{PJ}=12.9 configuration and a stronger effect on the D_{duct}/d_{PJ}=10.3 configuration. Otherwise, the radial profiles of ξ_{rms} follow the typical double peak distribution observed in other jet flows.

The intensity of jet concentration fluctuations on the jet axis is shown in Figure 6-18. Both the present results and those of Newbold demonstrate a peak close to the nozzle exit. However, the peak is much sharper and closer to the nozzle exit for the present measurements compared to that of Newbold. The combination of improved spatial resolution relative to the PJ nozzle size and improved normalisation method for the reference concentration are sufficient to explain this difference. Note that the magnitude of any Schmidt number effect on the scalar fluctuations from a jet, as described in Section 6.4.1.2 and Section 6.4.3.2, would be too small to account for this difference. Also, the effect of Schmidt number on the spatial resolution would cause the present measurements to underestimate concentration fluctuations, which does not account for the differences between the present measurements and those of Newbold. Figure 6-18 also demonstrates the difference in concentration fluctuation intensity on the jet axis for an orifice jet and smooth contraction jet, which are also characterised by a peak close to the jet exit. Both the present measurement technique and that of Newbold (1997) demonstrate that the fluidic precessing jet nozzle increases the asymptotic value of $\xi_{rms\text{-}ja}/\bar{\xi}_{ja}$ in the far field by approximately 50% compared to a jet issuing from the PJ nozzle inlet orifice with the chamber section removed.

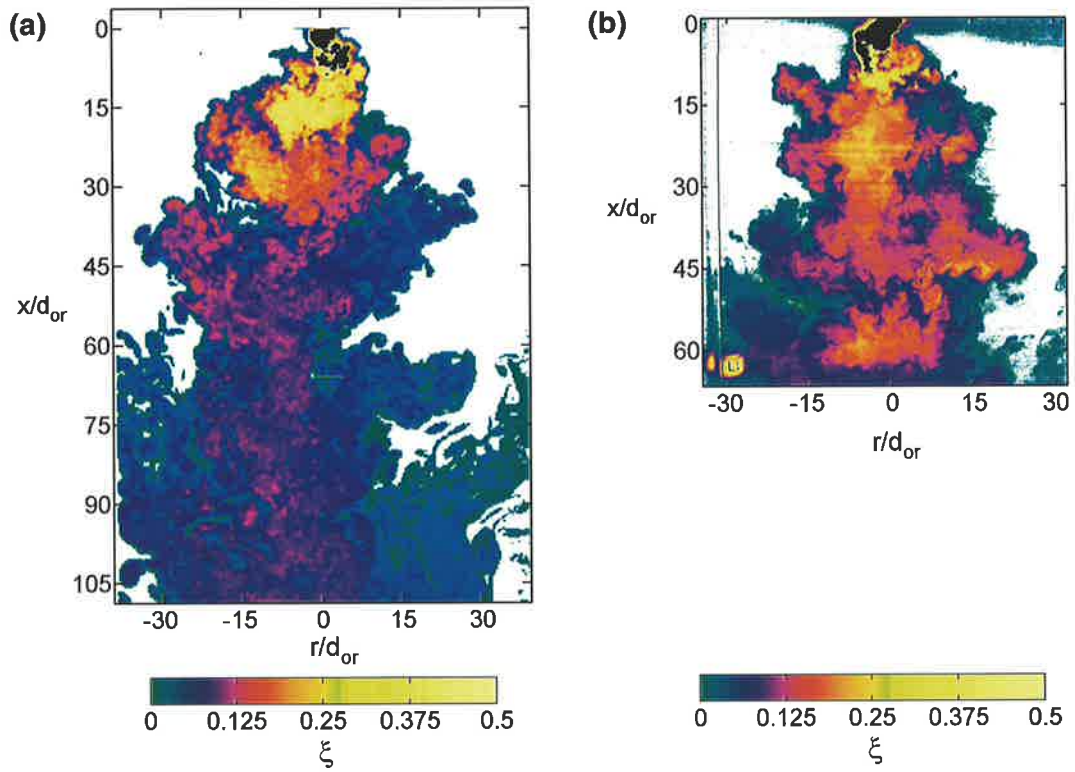

Figure 6-13. Instantaneous images of the scalar concentration field of a precessing jet nozzle: (a) Newbold (1997), Reynolds number=20,500, free jet in air; (b) Present experiments, d_{PJ}=38mm PJ nozzle, Reynolds number=66,100, U_a=0.06m/s co-flow, D_{duct}/d_{PJ}=12.9 confinement in water. Axial and radial distances are normalised to the diameter of the PJ nozzle inlet orifice in both images.

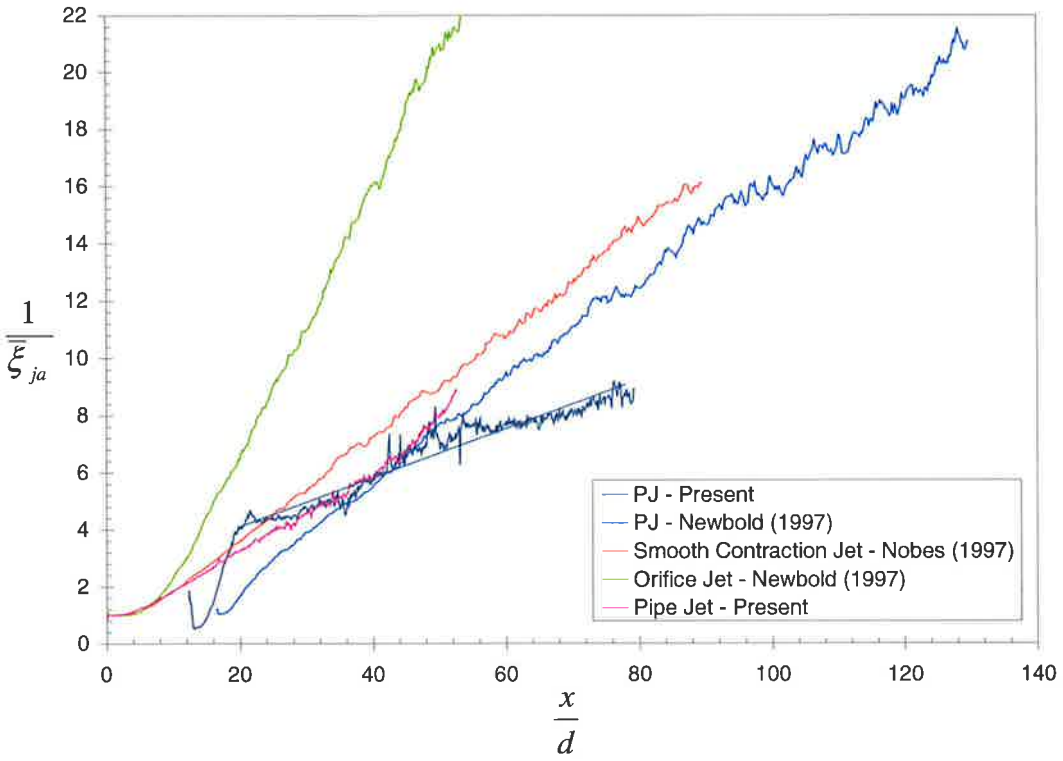

Figure 6-14. Comparison of the inverse mean jet concentration on the jet axis, $\overline{\xi}_{ja}$, of a PJ nozzle for the present technique and the Mie-scattering technique of Newbold (1997) and different simple jet conditions. See Figure 6-13 and Table 6-6 for the jet conditions. Axial distance is normalised to the diameter of the PJ nozzle inlet orifice, d_{or}, for the PJ nozzle jet flows.

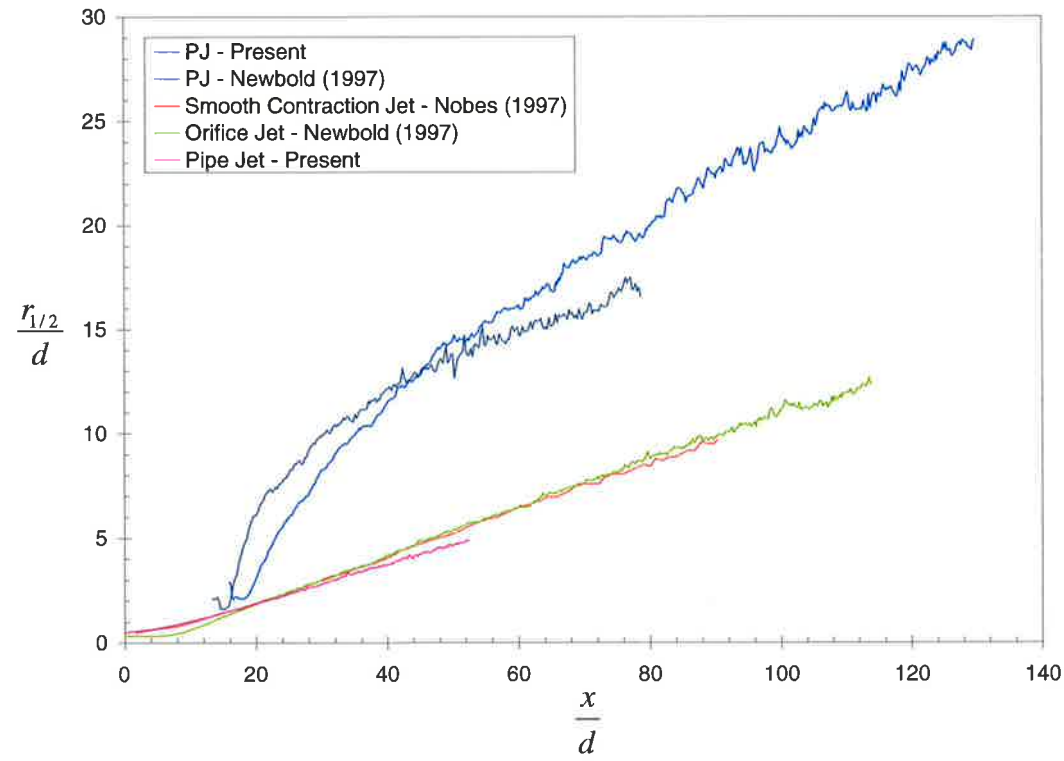

Figure 6-15. Comparison of the jet concentration half-width, $r_{1/2}/d_{or}$, of a PJ nozzle for the present technique and the Mie-scattering technique of Newbold (1997) and different simple jet conditions. See Figure 6-13 and Table 6-6 for the jet conditions. Axial distance is normalised to the diameter of the PJ nozzle inlet orifice, d_{or}, for the PJ nozzle.

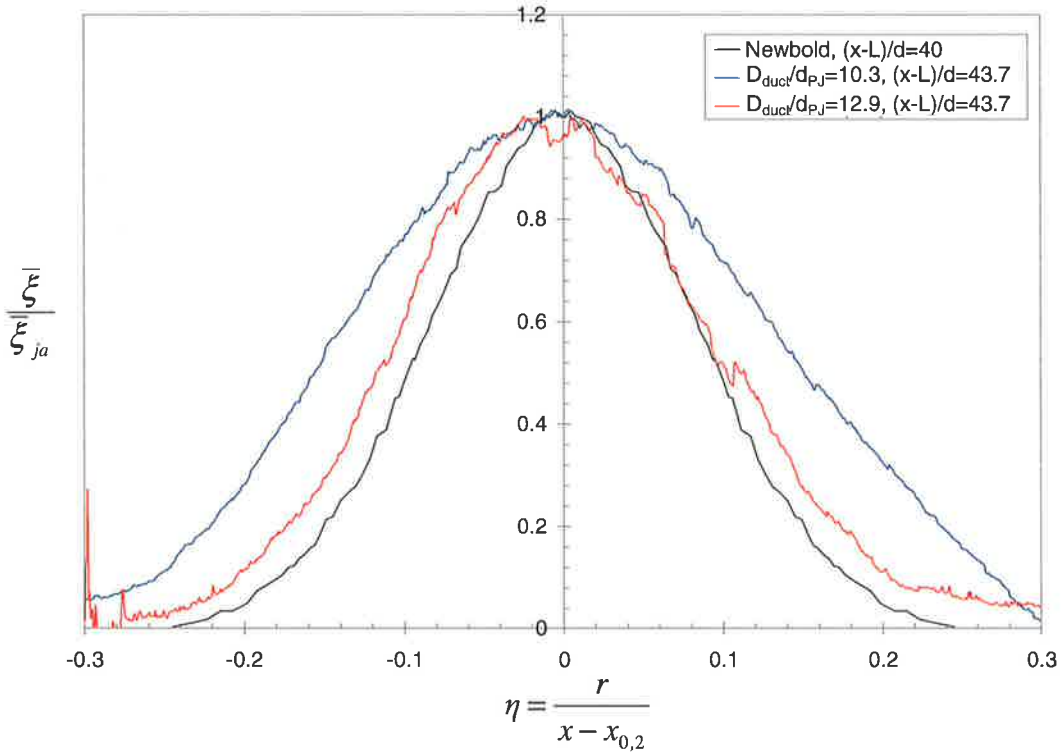

Figure 6-16. Comparison of the far field radial profiles of mean jet concentration normalised to the value on the jet axis, $\overline{\xi}/\overline{\xi}_{ja}$, of a PJ nozzle for the present technique and that of Newbold (1997). See Figure 6-13 for the jet conditions.

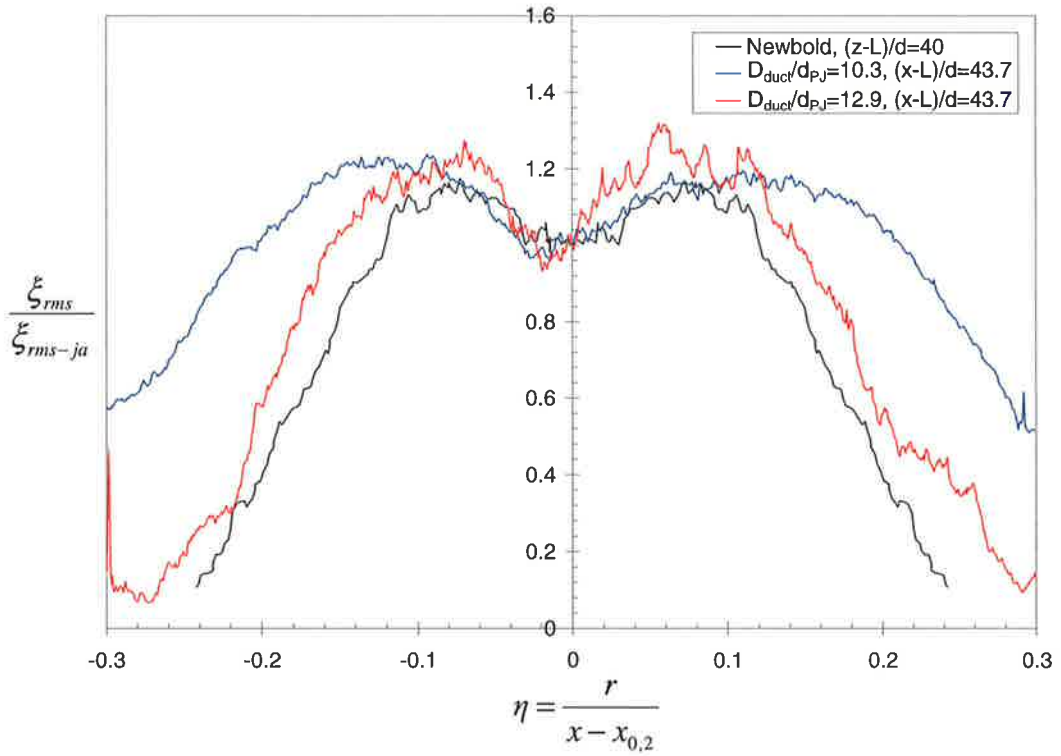

Figure 6-17. Comparison of the far field radial profiles of RMS jet concentration fluctuation normalised to the value on the jet axis, $\xi_{rms}/\xi_{rms\text{-}ja}$, of a PJ nozzle for the present technique and that of Newbold (1997). See Figure 6-13 for the jet conditions.

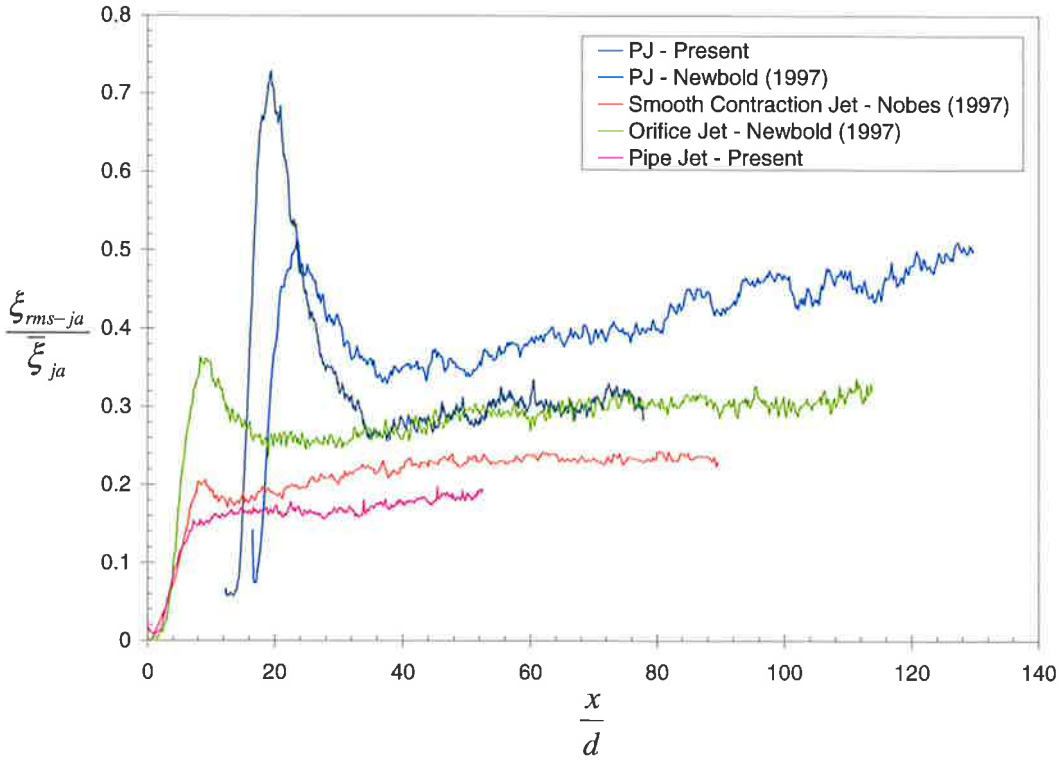

Figure 6-18. Comparison of the concentration fluctuation intensity on the jet axis, $\xi_{rms\text{-}ja}/\overline{\xi}_{ja}$ of a PJ nozzle for the present technique and that of Newbold (1997) and different simple jet conditions. See Figure 6-13 and Table 6-6 for the jet conditions. Axial distance is normalised to the diameter of the PJ nozzle inlet orifice, d_{or} for the PJ nozzle jet flows.

6.5.3 The Effect of Co-Flow Velocity on the Mixing from a PJ Nozzle

6.5.3.1 Qualitative Trends from Planar Data

The effect of co-flow velocity on the spatial distribution of the instantaneous, average and RMS of the jet concentration distribution from the 38mm PJ nozzle is illustrated in Figure 6-19 and Figure 6-20 for the D_{duct}/d_{PJ}=10.3 confinement. The results indicate that increasing the relative co-flow velocity reduces the spread of the jet and impingement upon the confining walls. At the lowest ratio of co-flow to PJ nozzle exit velocity, $U_a/U_{e\text{-}PJ}$=0.035 (U_a=0.038m/s co-flow), visual observation of sequences from the raw PLIF images shows jet fluid moving slightly upstream and recirculating at the point of impingement, i.e. where the jet first comes in contact with the duct walls. For $U_a/U_{e\text{-}PJ}\geq$0.098 (U_a>0.108m/s) jet fluid still comes into contact with the duct walls, but there does not appear to be any recirculation. Increasing the co-flow also causes the pitch of the "helix" generated by the precession of the emerging jet to lengthen in the far field, as illustrated in Figure 6-21. At a low co-flow velocity ratio, the large-scale turbulent "puff" structures and the helix to merge near to the nozzle exit. A higher co-flow velocity ratio causes the helix to stretch downstream from the nozzle exit, so that the puff structures become separated and merging of the helix is reduced or delayed.

6.5.3.2 Jet Axis Statistics

The effect of co-flow velocity on the distribution of jet fluid is quantified by determining the inverse concentration decay and concentration fluctuation intensity on the jet axis as well as the jet concentration half-width for each experimental condition. The results for the D_{duct}/d_{PJ}=10.3 confinement are presented here as an example. The results at confinements of D_{duct}/d_{PJ}=7.6 and D_{duct}/d_{PJ}=12.9 are included in Appendix C.

As outlined in Section 6.5.2, the concentration fluctuation intensity and mean jet concentration decay along the jet axis for the present PJ nozzle results are characterised by two major features. The inverse mean concentration is characterised by an initial, very rapid and constant decay rate which ceases at a point labelled the "elbow" point, approximately x/d_{PJ}=1.3-1.5 from the nozzle exit. At distances further downstream of the elbow point the jet concentration decays at a more gradual and constant rate such that the inverse concentration is inversely proportional to the distance along the jet axis. The fluctuation intensity is characterised by a high peak at approximately the same location as the elbow point and then asymptotes to a single value. Hence the region prior to the elbow point is labelled the jet near-field and the region in which the jet radial profiles collapse to a single profile defines the jet's far field, which begins downstream of the elbow point, at about x/d_{PJ}=4, see Figure 6-23. Figure 6-23 also demonstrates that the radial profile of mean jet concentration from the PJ nozzle is characterised by a Gaussian distribution.

Figure 6-22 indicates that in general, the rate of inverse concentration decay in the near-field and far field does not change with the co-flow velocity ratio. However, the magnitude of the inverse concentration is shifted higher as the velocity ratio increases, so that at a given axial location the value of the inverse concentration increases with increasing co-flow velocity. The exception to this trend for all duct diameters appears to be at $U_a/U_{e\text{-}PJ}$=0.055

(U_a=0.06m/s). There is no clear explanation for this phenomena. In the case of the D_{duct}/d_{PJ}=10.3 confinement the concentration measurements at $U_a/U_{e\text{-}PJ}$=0.055 were conducted in a separate experimental run and 1216 images were collected for image processing, while either 152 or 304 images were used for the other co-flow conditions, so the experimental uncertainty is greater for these case.

The effects of co-flow velocity ratio on the intensity of concentration fluctuations, $\xi_{rms\text{-}ja}/\overline{\xi}_{ja}$ are clearly illustrated in Figure 6-24. As the ratio of co-flow to jet velocity increases, the maximum value of the distinctive peak at the end of the PJ nozzle near-field increases, but the location of the maximum fluctuation intensity does not change significantly. The breadth of the peak is stretched out with increasing co-flow velocity and the asymptotic value of fluctuation intensity in the far field also increases.

The average jet concentration half-widths are compared at different co-flow velocity ratios for D_{duct}/d_{PJ}=10.3 confinement in Figure 6-25. The effects of the velocity ratio on the jet spread are not readily visible in Figure 6-25, but can be more easily compared by calculating the line of best fit in the far field to define the rate of jet spread and the virtual origin of the line of best fit. These calculations demonstrate that increasing the co-flow velocity ratio reduces the far field spreading rate slightly and moves the virtual origin upstream. There does not seem to be any clear effect of co-flow velocity on the jet spreading in the near-field of the jet nozzle.

The trends and behaviour described above are consistent with the results of investigations into the effect of co-flow velocity on the mixing from a simple axisymmetric jet if the range of experimental conditions and the significantly different mixing produced by the PJ nozzle are taken into account. The principal studies of co-flowing jets include the velocity measurements by Maczynski (1962), Antonia and Bilger (1973) and Nickels and Perry (1996) and the measurements of the scalar concentration field by Becker *et al.* (1963) and Chu *et al.* (1999). Note that Becker's investigation was of a confined jet flow, so recirculation effects became significant at certain flow conditions. These investigations have shown that, at a sufficiently high ratio of co-flowing velocity to jet velocity, the mean radial profiles of velocity and concentration achieve similarity in the far-field but do not collapse to a universal self-preserving state. Under these conditions the velocity and concentration half-widths are also shown to vary non-linearly with distance from the source, while at low velocity ratios the mixing conditions can be separated into the components of a jet superimposed on a uniform co-flow.

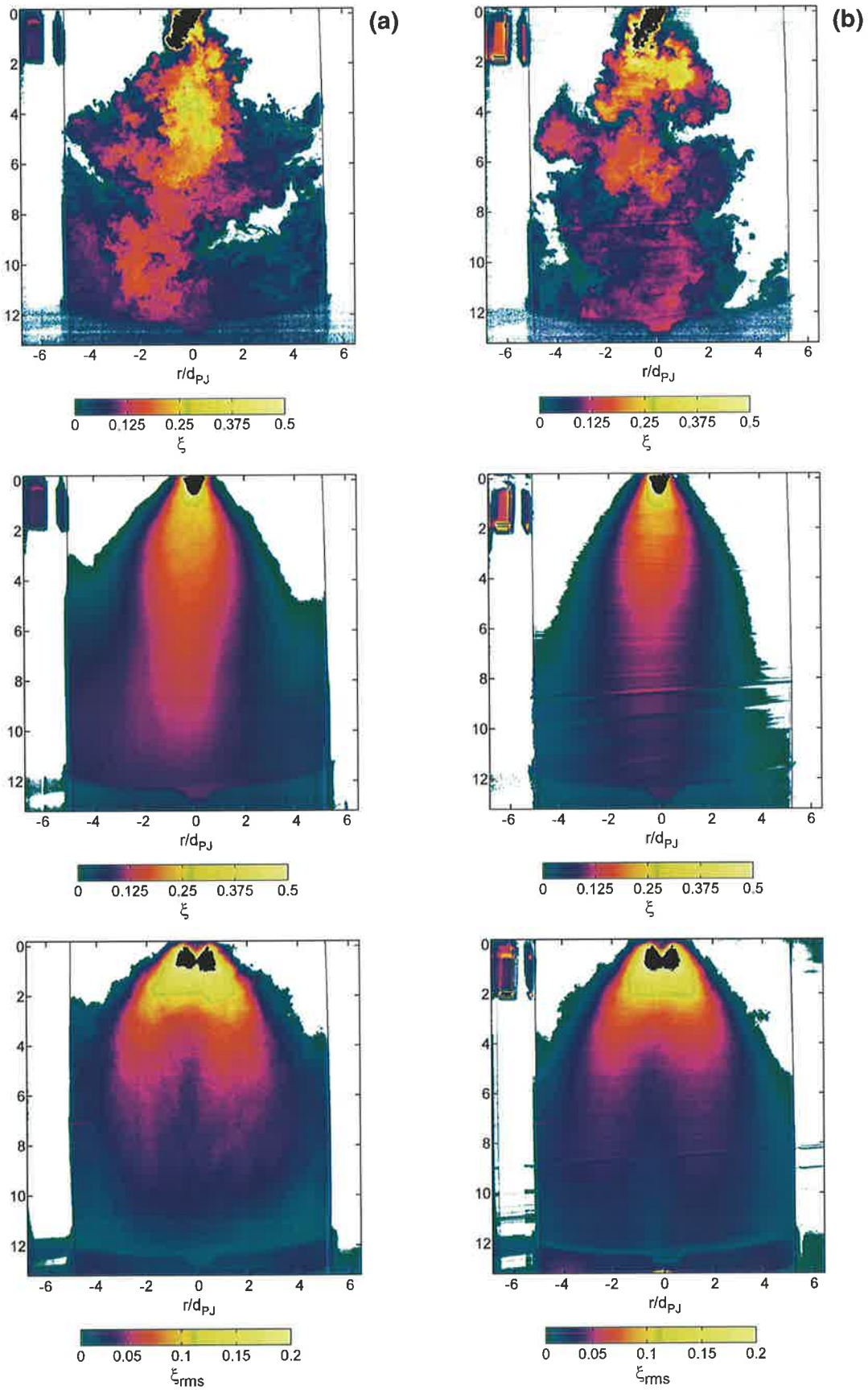

Figure 6-19. False colour images of the spatial distribution of instantaneous, mean and RMS jet concentration, ξ, from the d_{PJ}=38mm PJ nozzle. Conditions: PJ flow only (ψ_{CAJ}=0%), Reynolds number=66,100, D_{duct}/d_{PJ}=10.3, (a) $U_d/U_{e\text{-}PJ}$=0.035, and (b) $U_d/U_{e\text{-}PJ}$=0.055. The band at the bottom of the images is the tape joining the two halves of the duct together.

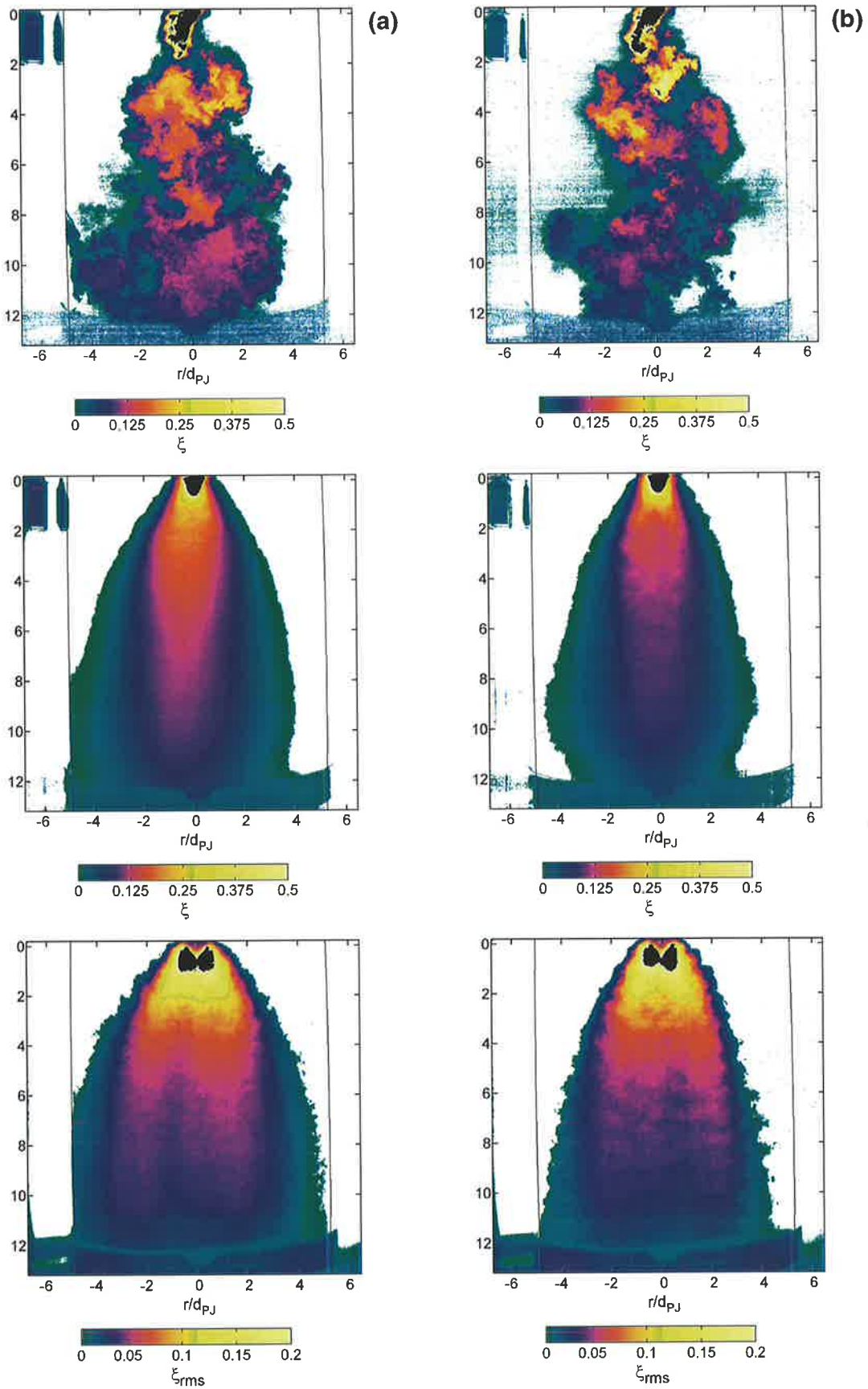

Figure 6-20. False colour images of the spatial distribution of instantaneous, mean and RMS jet concentration. ξ, from the d_{PJ}=38mm PJ nozzle. Conditions: PJ flow only (ψ_{CAJ}=0%), Reynolds number=66,100, D_{duct}/d_{PJ}=10.3, (a) $U_d/U_{e\text{-}PJ}$=0.098, and (b) $U_d/U_{e\text{-}PJ}$=0.196. The band at the bottom of the images is the tape joining the two halves of the duct together.

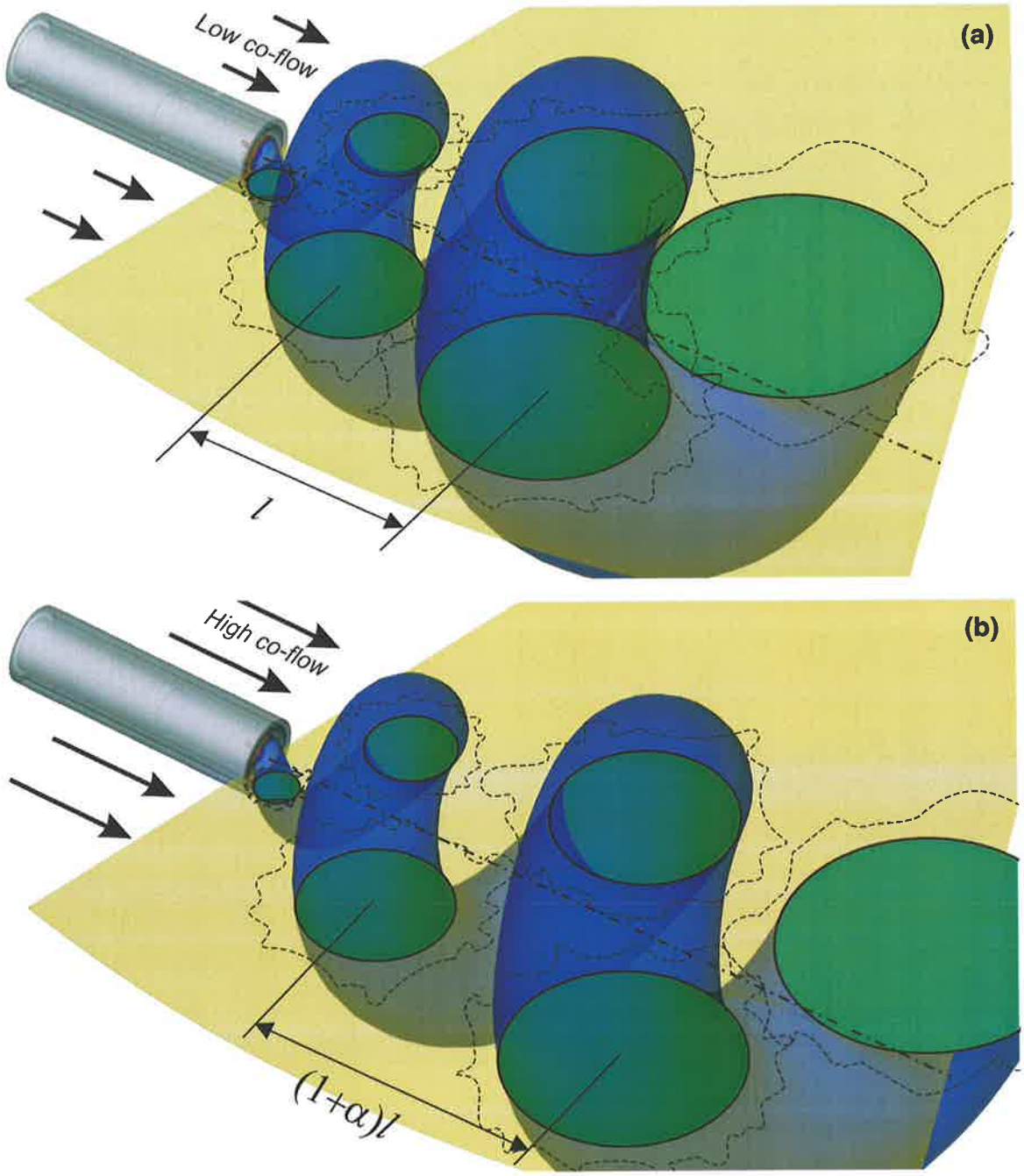

Figure 6-21. Illustration of the effect of the ratio of co-flow velocity to jet velocity on the structure of flow from a precessing jet nozzle: (a) at low velocity ratios, $U_d/U_{e\text{-}PJ} \leq 0.055$, the helix of flow structures formed by the motion of the exiting jet collapse on top of each other close to the nozzle exit and the large-scale structures detected by the PLIF technique are observed to merge; (b) at high velocity ratios, $U_d/U_{e\text{-}PJ} \geq 0.098$, the helix of flow structures is stretched out and hence does not collapse, the relative distance between large-scale structures is increased and merging is reduced.

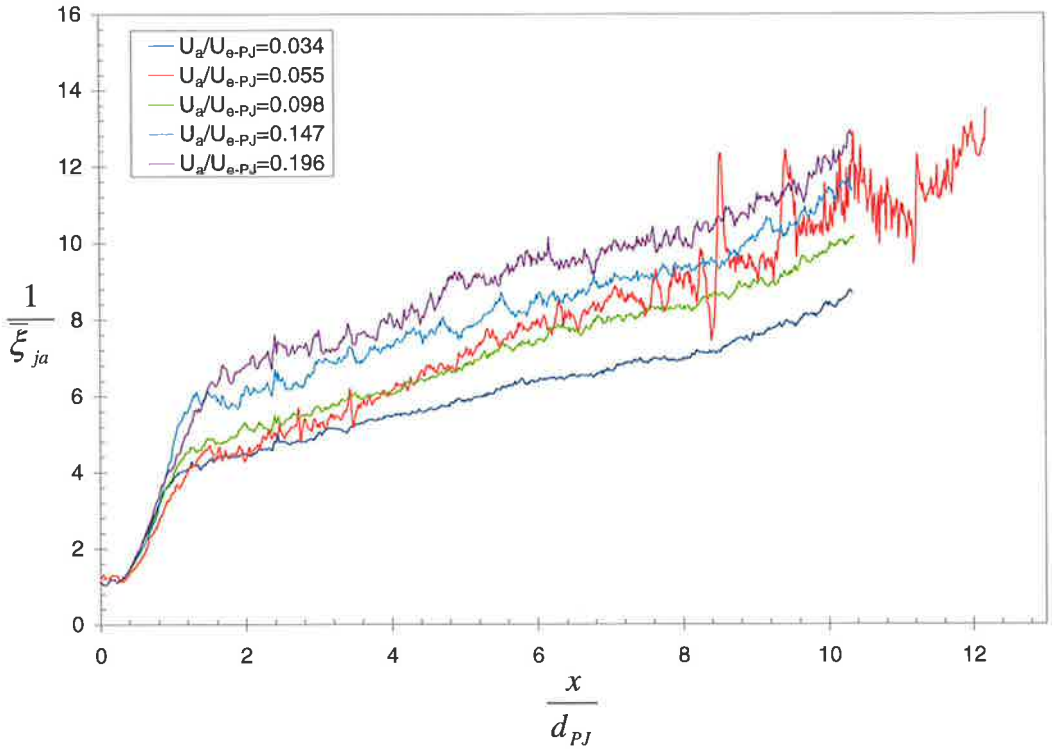

Figure 6-22. The effect of co-flow velocity ratio on the inverse mean jet concentration on the jet axis, $\overline{\xi}_{ja}$, of the d_{PJ}=38mm PJ nozzle. Conditions: PJ flow only (ψ_{CAJ}=0%), Reynolds number=66,100, D_{duct}/d_{PJ}=10.3.

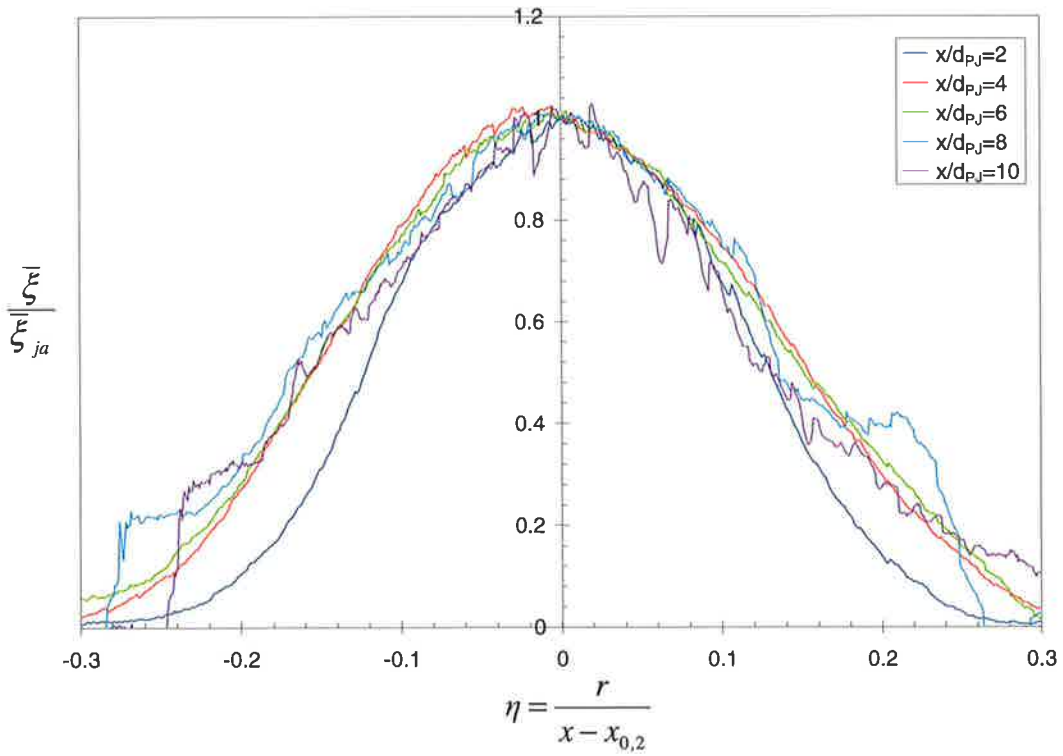

Figure 6-23. The radial distribution of mean jet concentration, normalised to the mean concentration on the jet axis, $\overline{\xi}/\overline{\xi}_{ja}$,at different axial distances downstream of the d_{PJ}=38mm PJ nozzle exit. Conditions: PJ flow only (ψ_{CAJ}=0%), Reynolds number=66,100, D_{duct}/d_{PJ}=10.3, $U_a/U_{e\text{-}PJ}$=0.055.

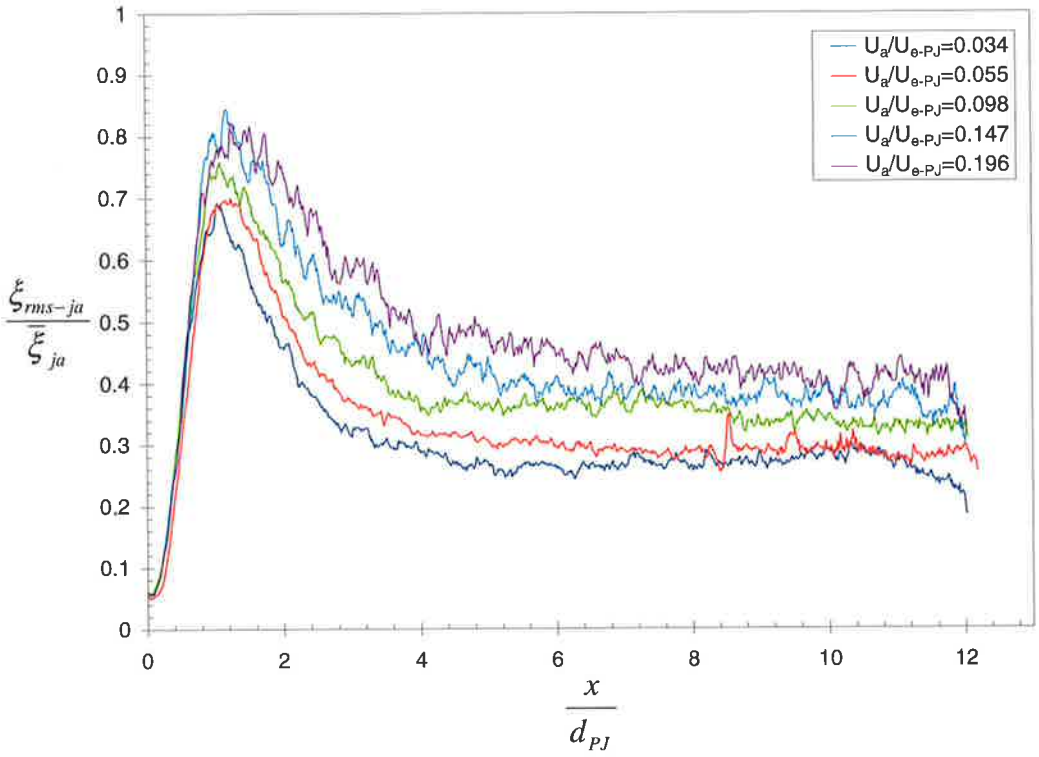

Figure 6-24. The effect of co-flow velocity ratio on the concentration fluctuation intensity, $\xi_{rms\text{-}ja}/\overline{\xi}_{ja}$, on the jet axis of the d_{PJ}=38mm PJ nozzle. Conditions: PJ flow only (ψ_{CAJ}=0%), Reynolds number=66,100, D_{duct}/d_{PJ}=10.3.

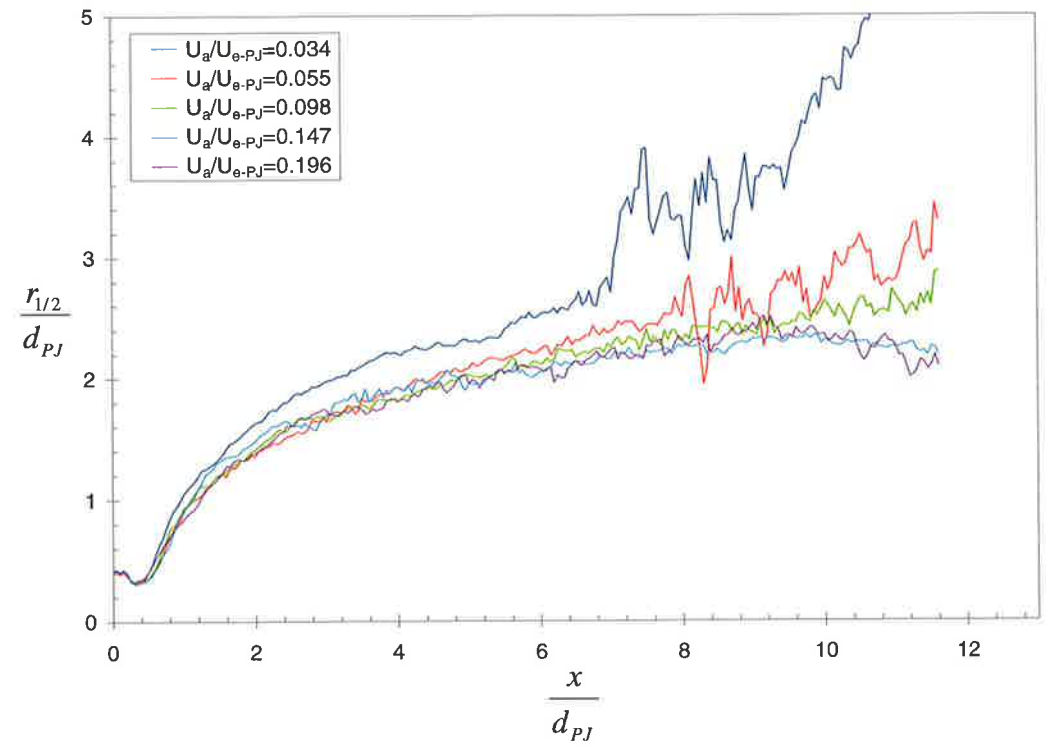

Figure 6-25. The effect of co-flow velocity ratio on the concentration half-width, $r_{1/2}/d_{PJ}$, of the d_{PJ}=38mm PJ nozzle. Conditions: PJ flow only (ψ_{CAJ}=0%), Reynolds number=66,100, D_{duct}/d_{PJ}=10.3.

6.5.4 The Effect of Confinement on the Mixing from a PJ nozzle

6.5.4.1 Qualitative Trends from Planar Data

The effect of confinement on the instantaneous, average and RMS distribution of jet concentration is illustrated in Figure 6-26 at confinement ratios of D_{duct}/d_{PJ}=7.6 and D_{duct}/d_{PJ}=12.9 and a constant a ratio of co-flow to jet velocity of $U_a/U_{e\text{-}PJ}$=0.055. Refer to Figure 6-19b for the results at a confinement of D_{duct}/d_{PJ}=10.3. The instantaneous images suggest that, while confinement exerts little influence on the initial jet trajectory from the nozzle exit (i.e. spreading), the effect is significant in the local region where the jet impinges instantaneously against the wall, increasing the local spreading angle. Impingement in the region x/d_{PJ}<10 is only occasional for the confinement of D_{duct}/d_{PJ}=12.9, but is continuous at a confinement of D_{duct}/d_{PJ}=7.6. Large-scale flow structures are evident in all cases and the presence of ambient fluid is observed downstream from the plane of impingement. The axial position at which puffs of jet fluid impinge against the wall is approximately the same for D_{duct}/d_{PJ}=10.3 and D_{duct}/d_{PJ}=12.9.

6.5.4.2 Jet Axis Statistics

The effect of confinement on the mixing from the PJ nozzle is demonstrated by comparing the inverse concentration decay and concentration fluctuation intensity on the jet axis as well as the concentration half-width at a constant velocity ratio of $U_a/U_{e\text{-}PJ}$=0.055. The trends of the effect of confinement at other velocity ratios are consistent with this result and are included in Appendix C.

Figure 6-27 indicates that, as the ratio of duct to PJ nozzle diameter increases, the profile of the inverse jet concentration along the jet axis is shifted downwards, so that increasing the confinement decreases the mixing rate. Confinement does not appear to alter the near-field concentration decay. However, if the duct diameter is used as the characteristic length scale to normalise the axial distance instead of the nozzle diameter, as in Figure 6-28, the jet axis inverse concentration profiles collapse onto the same line. This demonstrates that, downstream from the elbow point, the mixing rate scales with the duct diameter rather than the nozzle diameter. This result is consistent at all velocity ratios except the lowest, $U_a/U_{e\text{-}PJ}$=0.035 (U_a=0.038m/s).

The effect of confinement upon the concentration fluctuation intensity on the jet axis is illustrated in Figure 6-29. In the case of the fluctuation intensity it appears that the nozzle diameter is the most appropriate normalisation length scale because the main feature, the large peak, is a function of the nozzle characteristics, not the duct. This is also demonstrated by the fact that the maximum value of the peak fluctuation intensity, the location of the maximum and the breadth of the peak are not altered by the confinement ratio. The asymptotic value of the fluctuation intensity in the far field does not seem to be significantly altered by the confinement.

The effect of confinement on the jet concentration half-width, Figure 6-30 is more complex. For x/d_{PJ}<4 the half-width profiles seem to scale best with the nozzle chamber diameter, while further downstream the profiles are most similar when normalised by the duct diameter. Although it cannot be shown from Figure 6-30 alone, the effect of

confinement is reduced as the ratio of co-flow velocity to jet velocity is increased and the concentration half-width contours collapse onto a single curve, see Figure 6-31.

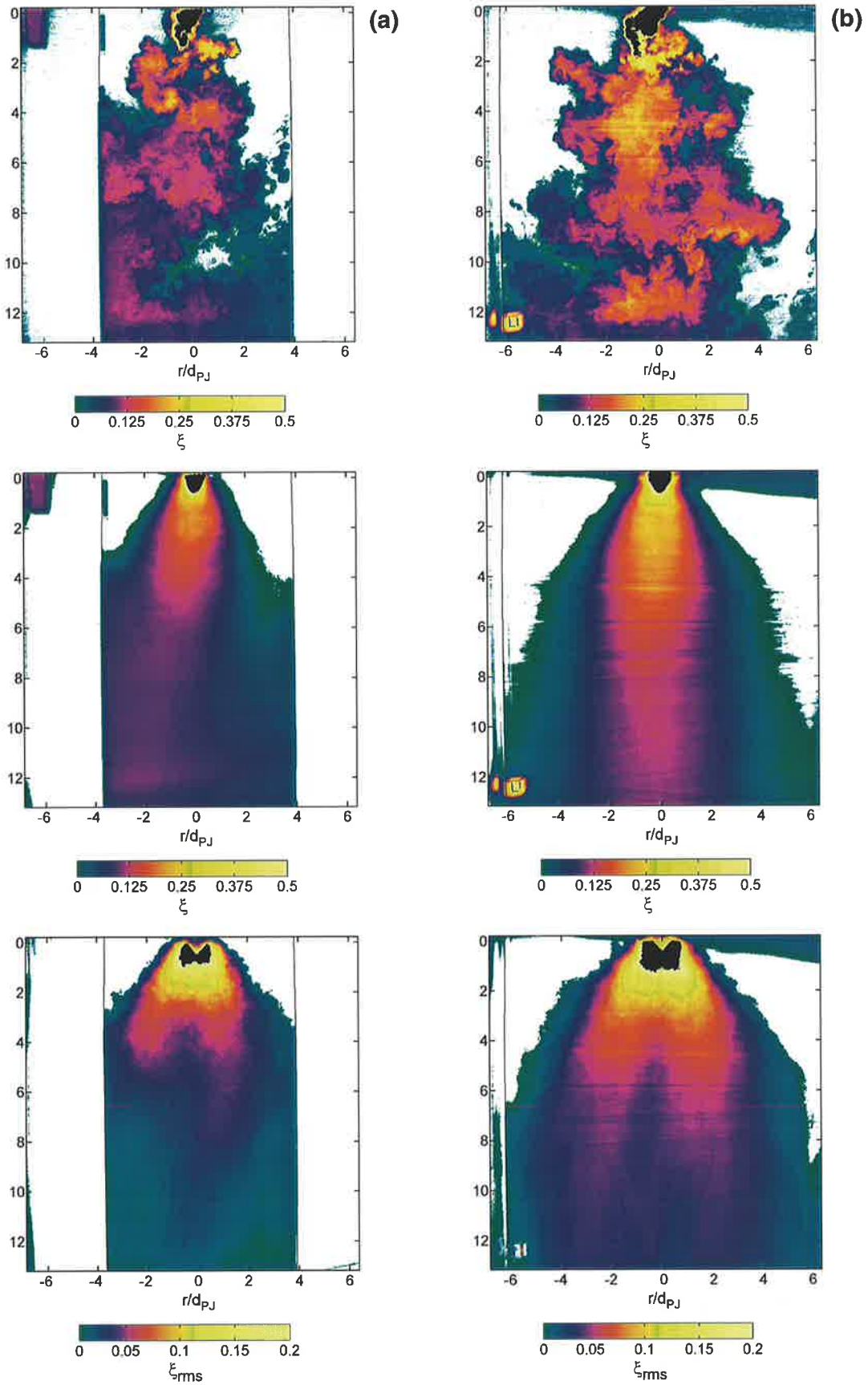

Figure 6-26. False colour images of the spatial distribution of instantaneous, mean and RMS jet concentration, ξ, from the d_{PJ}=38mm PJ nozzle. Conditions: PJ flow only (ψ_{CAJ}=0%), Reynolds number=66,100, $U_a/U_{e\text{-}PJ}$=0.055 (U_a=0.06m/s), (a) D_{duct}/d_{PJ}=7.6 and (b) D_{duct}/d_{PJ}=12.9.

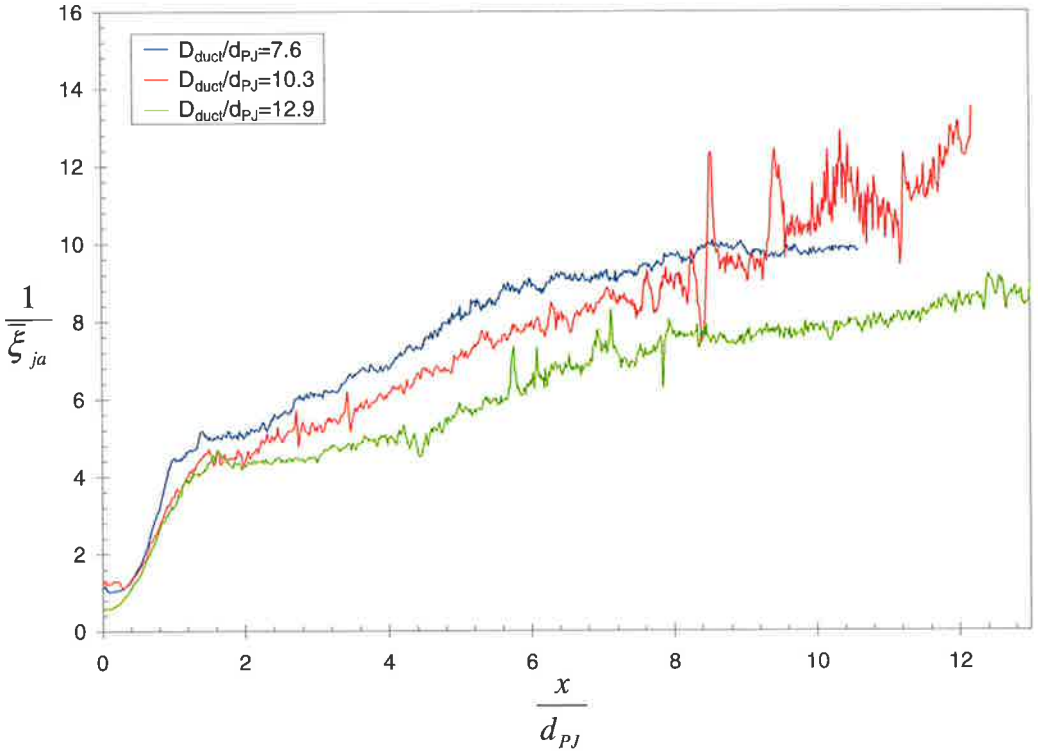

Figure 6-27. The effect of confinement on the inverse mean jet concentration on the jet axis, $\overline{\xi}_{ja}$, of the d_{PJ}=38mm PJ nozzle. Conditions: PJ flow only (ψ_{CAJ}=0%), Reynolds number=66,100, $U_a/U_{e\text{-}PJ}$=0.055 (U_a=0.06m/s). Axial distance from the nozzle exit is normalised to the PJ nozzle chamber diameter, d_{PJ}.

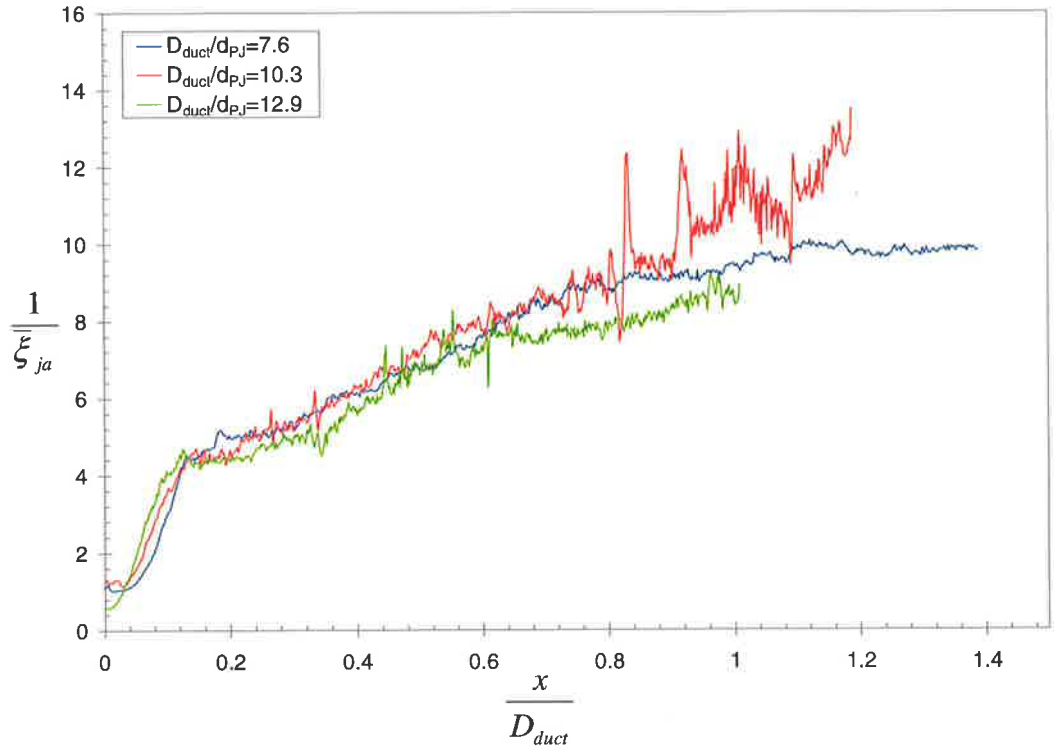

Figure 6-28. The effect of confinement on the inverse mean jet concentration on the jet axis, $\overline{\xi}_{ja}$, of the d_{PJ}=38mm PJ nozzle. Conditions: PJ flow only (ψ_{CAJ}=0%), Reynolds number=66,100, $U_a/U_{e\text{-}PJ}$=0.055 (U_a=0.06m/s). Axial distance from the nozzle exit is normalised to the duct diameter, D_{duct}.

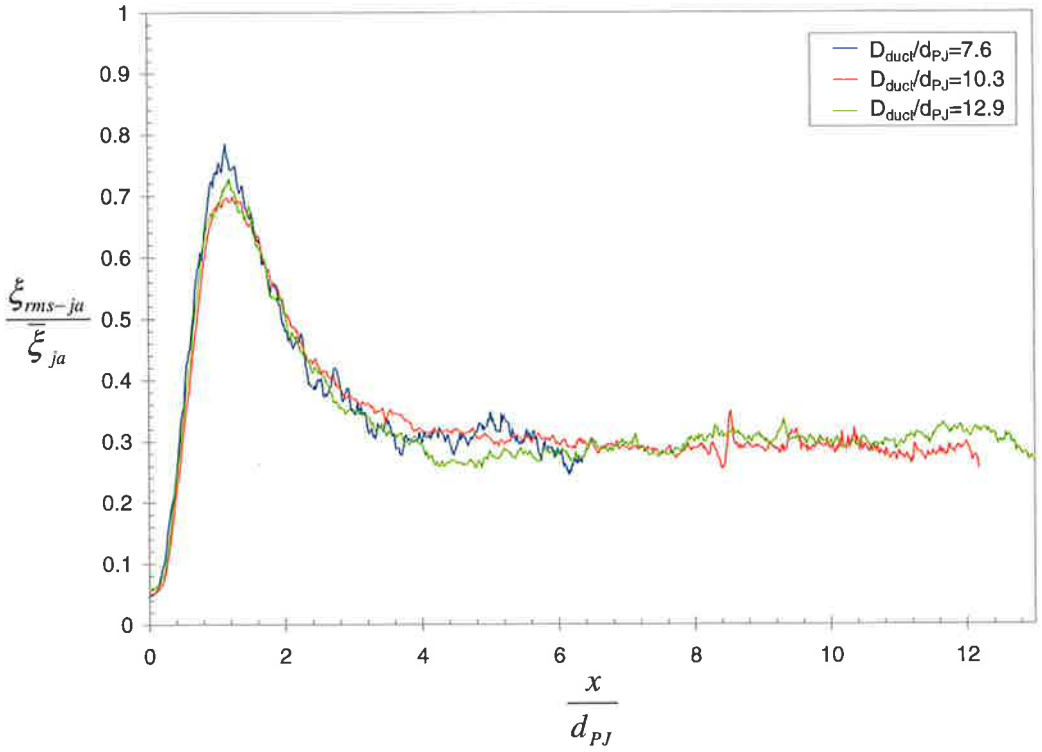

Figure 6-29. The effect of confinement on the concentration fluctuation intensity on the jet axis, $\xi_{rms\text{-}ja}/\bar{\xi}_{ja}$, of the d_{PJ}=38mm PJ nozzle. Conditions: PJ flow only (ψ_{CAJ}=0%), Reynolds number=66,100, $U_a/U_{e\text{-}PJ}$=0.055 (U_a=0.06m/s). Axial distance is normalised to the PJ nozzle chamber diameter, d_{PJ}.

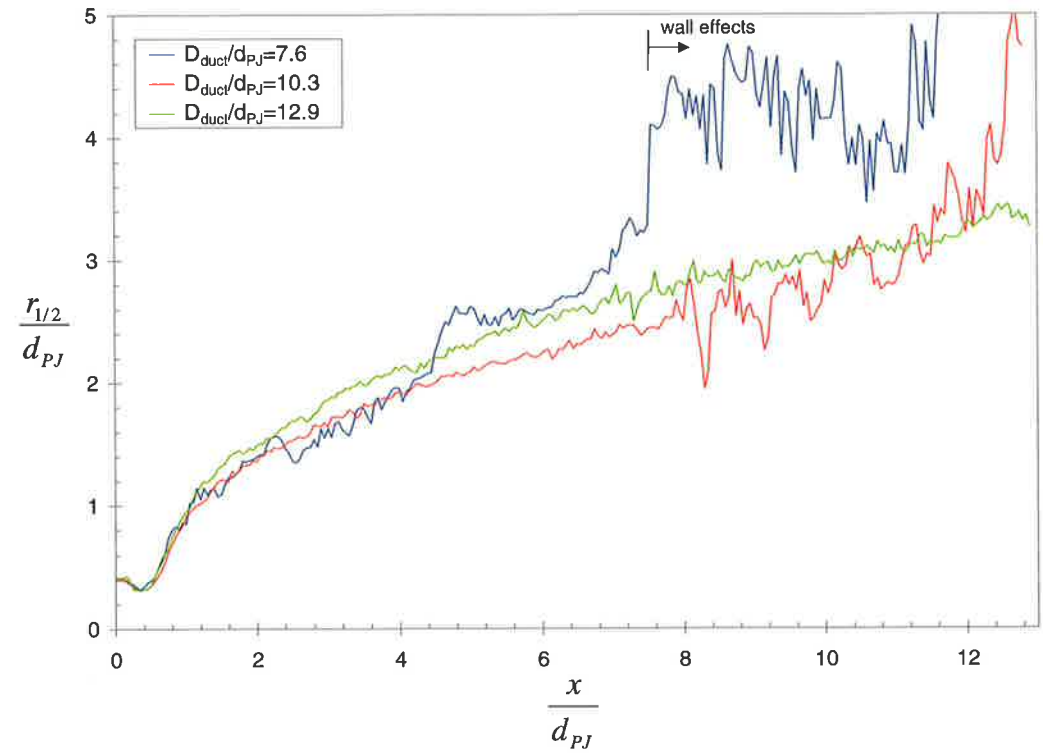

Figure 6-30. The effect of confinement on the concentration half-width, $r_{1/2}/d_{PJ}$, of the d_{PJ}=38mm PJ nozzle. Conditions: PJ flow only (ψ_{CAJ}=0%), Reynolds number=66,100, $U_a/U_{e\text{-}PJ}$=0.055 (U_a=0.06m/s). Axial distance is normalised to the PJ nozzle chamber diameter, d_{PJ}.

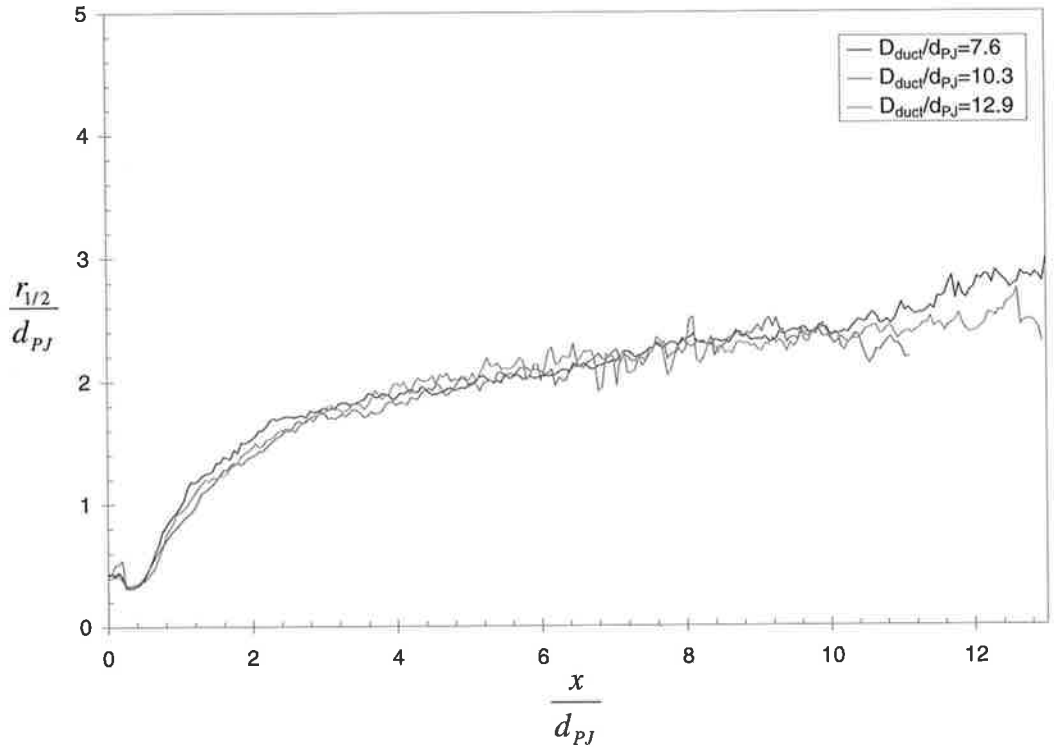

Figure 6-31. The effect of confinement on the concentration half-width, $r_{1/2}/d_{PJ}$, of the d_{PJ}=38mm PJ nozzle. Conditions: PJ flow only (ψ_{CAJ}=0%), Reynolds number=66,100, $U_a/U_{e\text{-}PJ}$=0.196 (U_a=0.216m/s). Axial distance is normalised to the PJ nozzle chamber diameter, d_{PJ}.

6.5.5 The Effect of the Central Axial Jet on the mixing from a PJ nozzle

6.5.5.1 Qualitative Trends from Planar Data

The effect of the central axial jet on the scalar concentration field from the 38mm PJ nozzle is demonstrated by examination of the results obtained at a constant co-flow velocity of U_a=0.06m/s and D_{duct}/d_{PJ}=10.3 confinement, shown in Figure 6-32 and Figure 6-33. Refer to Figure 6-19b for the results with just precessing jet flow only at the same co-flow and confinement. The main feature of these images is the reduced spreading and hence impingement on the duct walls as the CAJ proportion, ψ_{CAJ}, is increased. Note that the ratio of co-flow velocity to PJ nozzle exit velocity is not estimated as the effects of the CAJ on the characteristic jet exit velocity from the PJ nozzle are presently unknown.

6.5.5.2 Jet Axis Statistics

The effect of the central axial jet on the jet axis concentration statistics is illustrated in Figure 6-34 to Figure 6-36 for a co-flow velocity of U_a=0.06m/s and D_{duct}/d_{PJ}=10.3 confinement. The results obtained at approximately the same mass flux ratio, m_a/m_0≈18.4 and confinements of D_{duct}/d_{PJ}=7.6 (U_a=0.108m/s) and D_{duct}/d_{PJ}=12.9 (U_a=0.038m/s) are shown in Appendix C.

The effect of the CAJ proportion, ψ_{CAJ}, on the inverse jet concentration on the jet axis can be clearly seen in Figure 6-34. Note that the axial distance in these figures is normalised by the PJ nozzle diameter, which is consistent, although the appropriateness of this length scale reduces as the proportion of flow through the CAJ nozzle tends to 100%. At low CAJ proportion (0< ψ_{CAJ}<20%) the rate of concentration decay appears similar for all jets. However for ψ_{CAJ}>20% (Γ_{CAJ}>0.11) the CAJ begins to dominate the flow features and the rate of decay tends towards that of the CAJ on its own. The decay constant for ψ_{CAJ}=100% (CAJ only), when normalised to the CAJ exit diameter is K_J=5.95, well within the range reported for simple jets in Table 6-6. Generally the ψ_{CAJ}=25% (Γ_{CAJ}=0.17) case has the lowest inverse concentration value at a given axial position for the experiments conducted in each duct. It is interesting to note that this CAJ proportion corresponds to the configuration in the pilot-scale experiments with the highest measured heat transfer, see Section 5.3.1.

Perhaps the most noticeable feature of Figure 6-34 is that, as ψ_{CAJ} is increased, the rapid decay in concentration on the jet axis in the near-field gradually diminishes until there is no longer a visible "elbow". Hence the presence of the "elbow" may relate to the presence of the dominant near field precessing jet flow regime postulated in Section 3.3. Calculation of the rate of concentration decay and the location of the virtual origin provides further evidence for the existence of two dominant flow regimes. As ψ_{CAJ} is increased to an amount greater than 25%, a step change occurs in the concentration decay rate and the location of the virtual origin. For the present experiments, ψ_{CAJ}=25% corresponds to a momentum ratio of Γ_{CAJ}=0.17. The critical momentum ratio reported in Section 3.5 for the transition from PJ to CAJ dominated flow regime is in the range Γ_{CAJ}≈0.2-0.23.

It is also interesting to note that the relative values of inverse jet concentration on the jet axis for the ψ_{CAJ}=15% (Γ_{CAJ}=0.05) and ψ_{CAJ}=25% (Γ_{CAJ}=0.17) cases are different for each confinement ratio investigated. This is consistent with the raw image sequences, and the observations noted in Section 3.3 which indicate that, in between the extremes of precessing jet only flow and completely CAJ dominated flow (ψ_{CAJ}≈40%, Γ_{CAJ}=0.45), the characteristics of the dominant flow regime are not always present. Hence for ~5%< ψ_{CAJ} <40% the jet behaviour switches modes between the characteristics of a PJ or CAJ dominant regime. For the D_{duct}/d_{PJ}=7.6 and D_{duct}/d_{PJ}=12.9 experiments, in which only 152 images were collected at each CAJ setting, one mode may be favoured in the image sequence and more images are required for a more accurate average. For the D_{duct}/d_{PJ}=10.3 experiments, 608 images were obtained at the same CAJ proportions, reducing the experimental uncertainty and ensuring the full range of flow characteristics is captured.

The presence of a dominant flow regime in the near field is also suggested by the jet axis concentration fluctuation intensity results. Figure 6-35 shows that as the CAJ proportion is increased, the peak fluctuation intensity close to the nozzle gradually diminishes, until at the same flow proportions corresponding to a CAJ dominated flow, it is no longer present. Increasing ψ_{CAJ} also moves the location of the peak fluctuation intensity further downstream of the nozzle exit and results in a slight decrease in the asymptotic value. The asymptotic value of concentration fluctuation intensity for the CAJ on its own is 0.204, which is very similar to the results obtained for other types of simple jet, see Table 6-6, and the present measurement from a pipe jet of 0.194. The asymptotic CAJ fluctuation intensity is less than that of any of the combined CAJ and PJ flows, even for very high ψ_{CAJ}.

The effect of CAJ proportion on the jet concentration half-width is illustrated in Figure 6-36. As for the inverse concentration and the concentration fluctuation intensity plots, the effect of ψ_{CAJ} is very clear and there is evidence of two different flow regimes depending on the CAJ proportion. At low ψ_{CAJ}, there is a very rapid increase in jet spread in the near-field, indicative of a PJ dominated flow, while at higher ψ_{CAJ}, the absence of the rapid rise is indicative of a CAJ dominated flow. In the far field of a jet in the PJ dominated flow regime, increasing the CAJ proportion reduces the jet spreading rate, with the minimum spreading rate occurring at ψ_{CAJ}=20% (Γ_{CAJ}=0.11). Further increasing ψ_{CAJ} increases the jet spreading rate for the range of conditions investigated. The spreading rate of the CAJ only case (ψ_{CAJ}=100%) is quite low when normalised by the PJ nozzle chamber diameter, d_{PJ}, just above the minimum level measured for the PJ nozzle. However, when normalised by the CAJ exit diameter, d_{CAJ}, the spreading rate is K_2=0.090, well within the range reported for simple jets, see Table 6-6. Similar behaviour is also observed for the far field virtual origin, which initially moves downstream as ψ_{CAJ} increases, until reaching a peak at ψ_{CAJ}=20%. Further increasing ψ_{CAJ} leads to a step change in the location of the virtual origin, which then moves upstream.

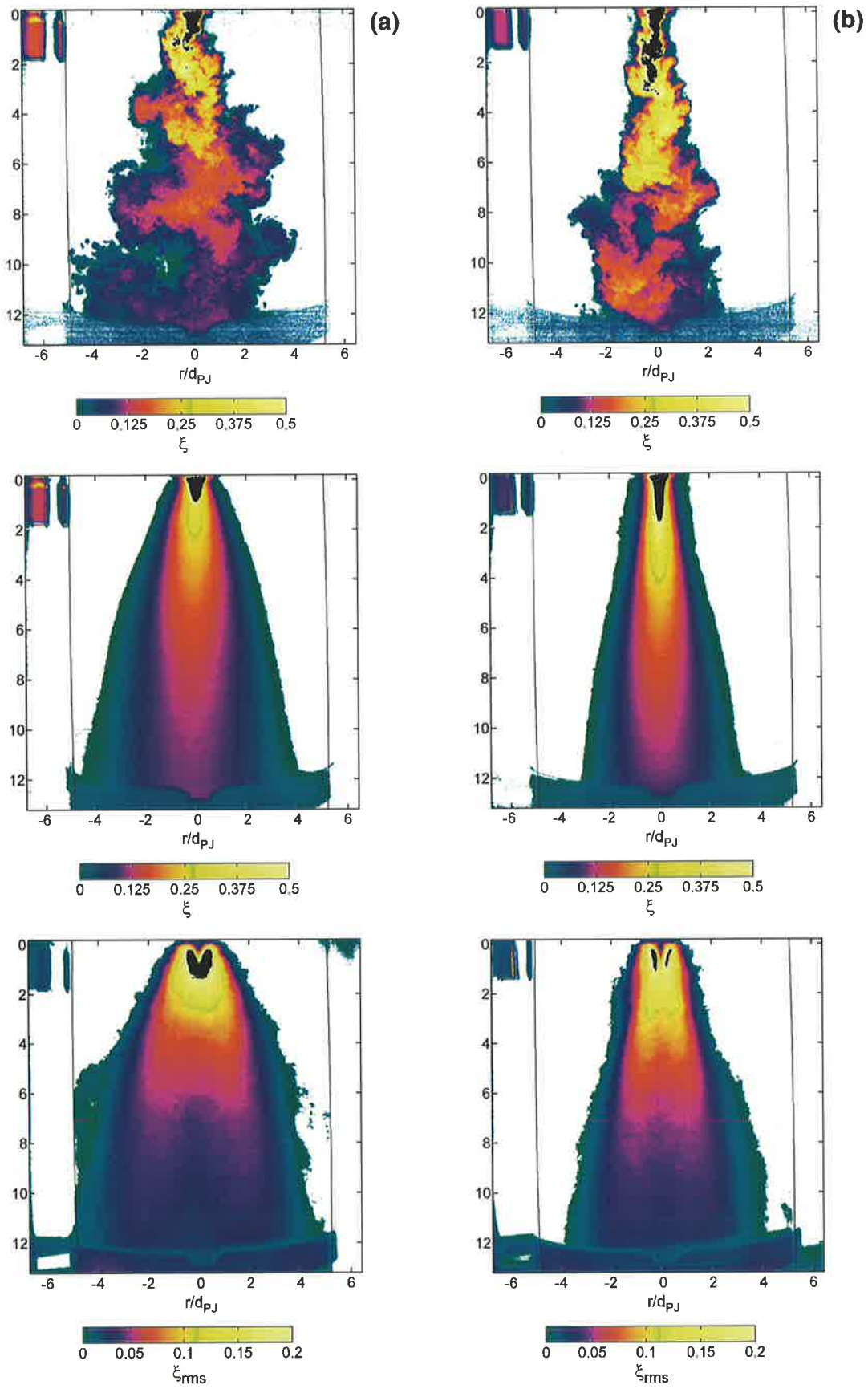

Figure 6-32. False colour images of the spatial distribution of instantaneous, mean and RMS jet concentration, ξ, from the d_{PJ}=38mm PJ nozzle. Conditions: U_a=0.06m/s, D_{duct}/d_{PJ}=10.3, m_a/m_0=18.4; (a) ψ_{CAJ}=15%, Γ_{CAJ}=0.05 and (b) ψ_{CAJ}=25%, Γ_{CAJ}=0.17. The band at the bottom of the images is the tape joining the two halves of the duct together.

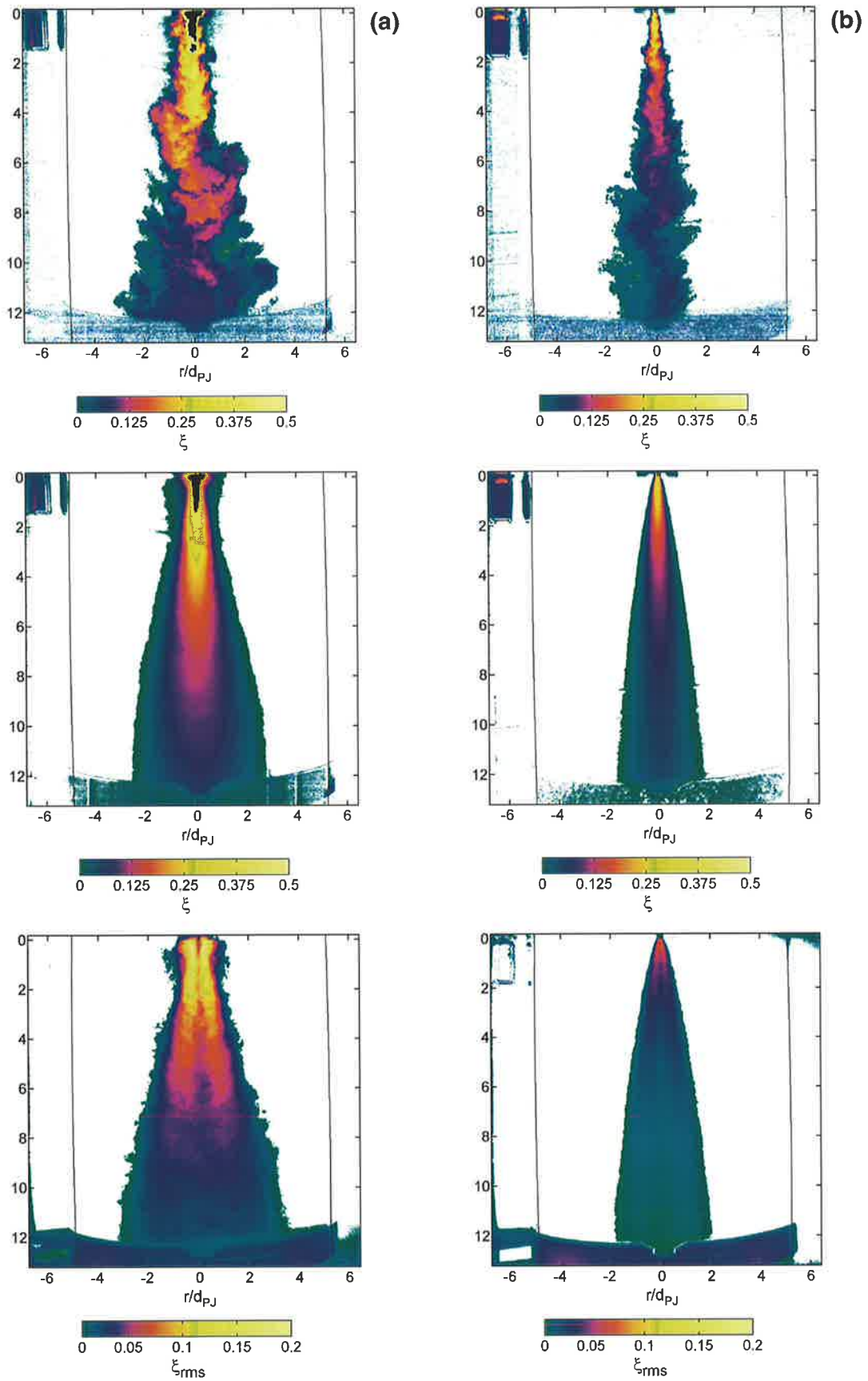

Figure 6-33. False colour images of the spatial distribution of instantaneous, mean and RMS jet concentration, ξ, from the d_{PJ}=38mm PJ nozzle. Conditions: U_a=0.06m/s, D_{duct}/d_{PJ}=10.3; (a) ψ_{CAJ}=40%, Γ_{CAJ}=0.45, m_a/m_0=18.4 and (b) ψ_{CAJ}=100%, Γ_{CAJ}=1.0, m_a/m_0=122. The band at the bottom of the images is the tape joining the two halves of the duct together.

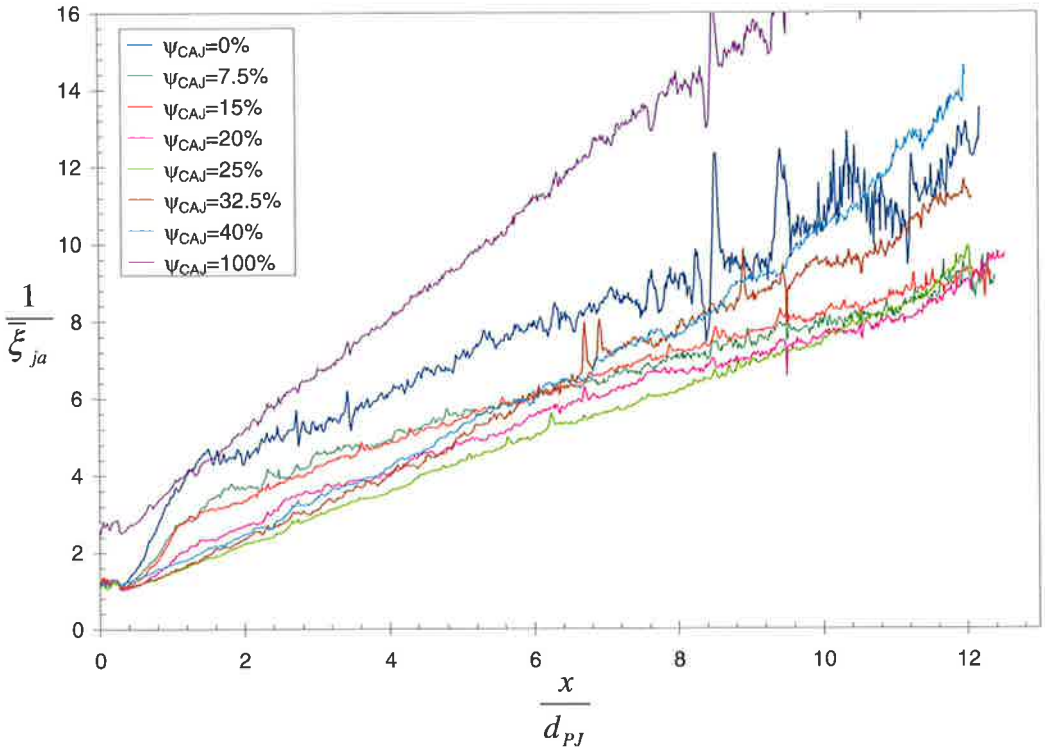

Figure 6-34. The effect of CAJ proportion, ψ_{CAJ}, on the mean jet concentration on the jet axis, $\bar{\xi}_{ja}$, of the d_{PJ}=38mm PJ nozzle. Conditions: U_a=0.06m/s, D_{duct}/d_{PJ}=10.3, m_d/m_0=18.4 except for ψ_{CAJ}=100% (CAJ only, m_d/m_0=122).

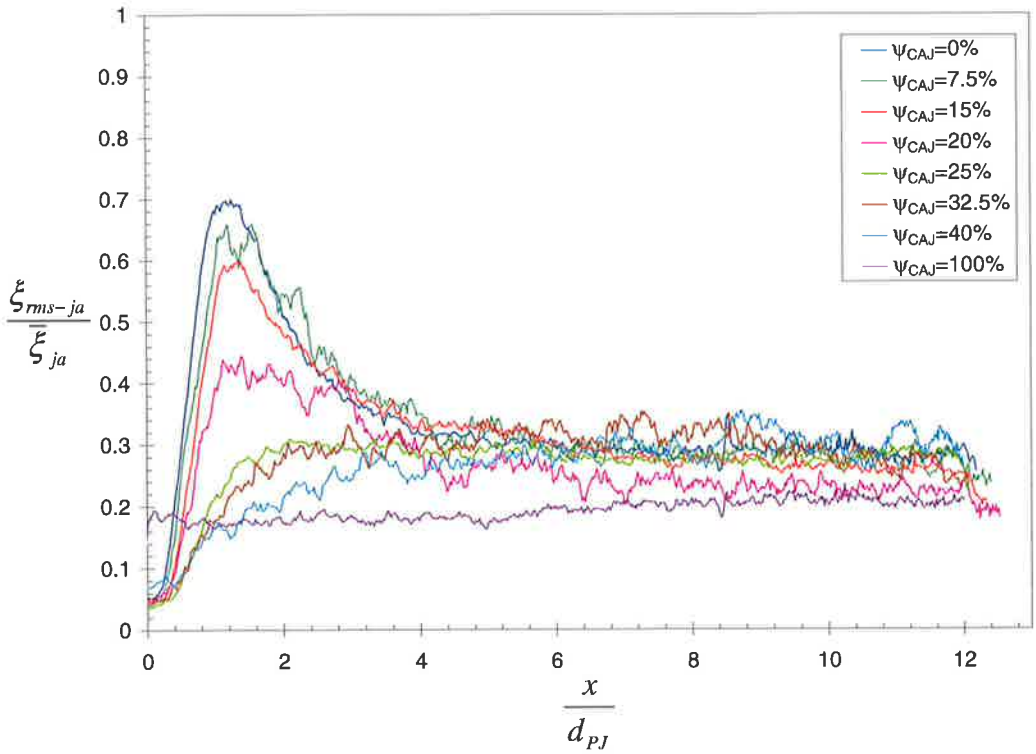

Figure 6-35. The effect of CAJ proportion, ψ_{CAJ}, on the concentration fluctuation intensity, $\xi_{rms\text{-}ja}/\bar{\xi}_{ja}$, on the jet axis of the d_{PJ}=38mm PJ nozzle. Conditions: U_a=0.06m/s, D_{duct}/d_{PJ}=10.3, m_d/m_0=18.4 except for ψ_{CAJ}=100% (CAJ only, m_d/m_0=122).

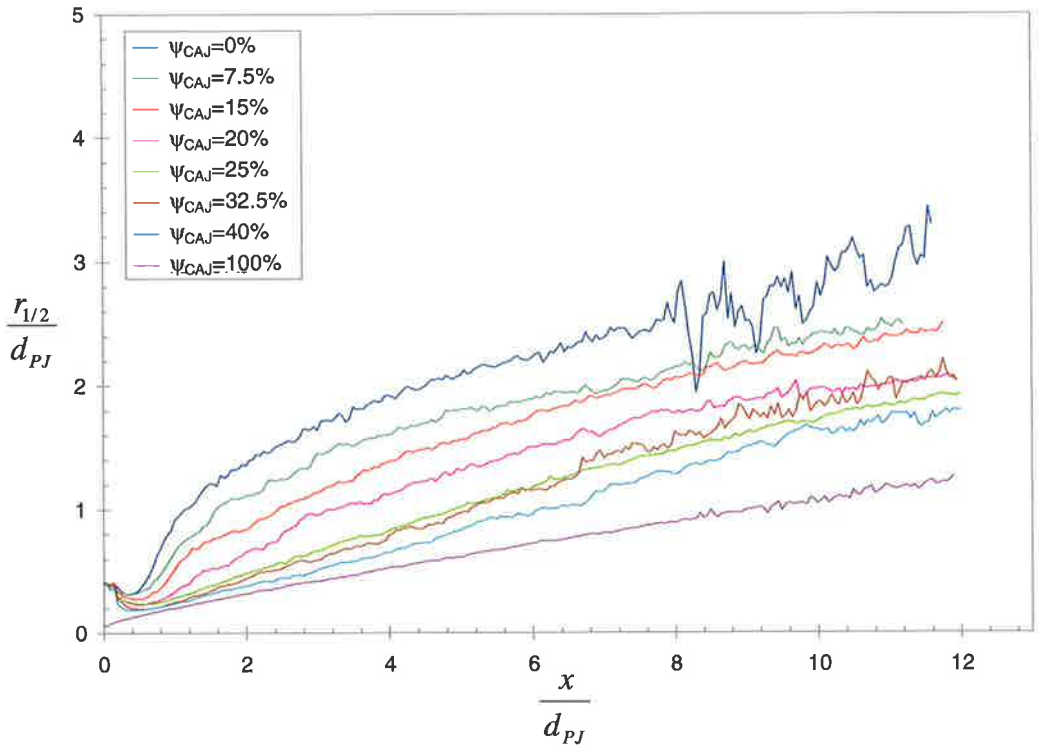

Figure 6-36. The effect of CAJ proportion, ψ_{CAJ}, on the concentration half-width, $r_{1/2}/d_{PJ}$, of the d_{PJ}=38mm PJ nozzle. Conditions: U_a=0.06m/s, D_{duct}/d_{PJ}=10.3, m_a/m_0=18.4 except for ψ_{CAJ}=100% (CAJ only, m_a/m_0=122).

6.5.6 The Probability Distribution of Jet Concentration

The effect of co-flow, confinement and the proportion of central axial jet on the distribution of concentrations in a precessing jet flow can be assessed further by calculating the probability distribution function (p.d.f.) of the jet concentration, *pdf*(ξ), on the jet axis. At a given point, the p.d.f. corresponds to the distribution of probabilities that the instantaneous concentration falls within a given range, $\xi \pm \Delta\xi$. Following the procedure of Newbold (1997), bins of $\Delta\xi$=0.005 were used for the present calculations, so that "pure" ambient fluid corresponds to ξ=0-0.005 and "pure" jet fluid corresponds to ξ=0.995-1. Normalisation of the p.d.f. at each measurement point implies that:

$$\int_0^1 \mathrm{pdf}(\xi)\,d\xi = 1 \qquad \textbf{Equation 6-22.}$$

P.d.f.s have been calculated for a select number of cases. The accuracy of *pdf*(ξ) is dependent on the spatial resolution, the probability "bin" size used for the calculation and the number of data points in the data set. The poor spatial resolution relative to the Batchelor scale of the present technique, see Section 6.3.1, suggests that the p.d.f.s of the measured data will differ from the actual distribution of concentration on the jet axis. However, a qualitative description of the effect of co-flow, confinement and CAJ on *pdf*(ξ) can still be made by comparing the relative distribution of concentration. The selection of data sets for analysis was based primarily on the requirement to have enough data to achieve a smooth distribution and to illustrate the effect of co-flow velocity ratio, confinement and the proportion of CAJ, ψ_{CAJ}. The number of data points used to calculate the p.d.f.s has also been increased by incorporating the data within a span of approximately 5mm (10 pixels) upstream and downstream of each axial position. This has been shown to provide smooth distributions as shown in Figure 6-37 and Figure 6-38.

6.5.6.1 The Effect of Jet Type

Profiles of jet concentration p.d.f.s along the jet axis for the validation pipe jet are shown in Figure 6-37a, while the concentration p.d.f. for the jet from the 38mm PJ nozzle at ψ_{CAJ}=0%, D_{duct}/d_{PJ}=10.3 and $U_a/U_{e\text{-}PJ}$=0.055 (U_a=0.06m/s) case is shown in Figure 6-37b. The same number of images and data points was used to calculate the p.d.f. for each jet case. The *pdf*(ξ) for the pipe jet is compared in the far field with the *pdf*(ξ) for the PJ only case in Figure 6-40. Dowling and Dimotakis (1990) have shown that $\xi/\overline{\xi}$ is the proper similarity variable for jet concentration statistics and hence the p.d.f. of $\xi/\overline{\xi}$ should be self-similar when the jet flow is fully developed. The far field *pdf*($\xi/\overline{\xi}$) is shown in Figure 6-39 using the appropriately normalised co-ordinates. The far field p.d.f.s displayed are taken at the same axial position, corresponding to the maximum downstream location of all conditions not affected by optical distortion or laser sheet intensity correction errors. This position is at 50 diameters from the pipe jet exit and 12 chamber diameters for all the PJ nozzle conditions from the nozzle exit.

The p.d.f. distributions shown in Figure 6-37a and Figure 6-37b reveal significant differences in the mixing characteristics of a simple jet and a precessing jet. Figure 6-40 shows that low concentration fluid is drawn on to the jet axis closer to the nozzle exit by the action of the precessing jet than occurs with the simple jet. Figure 6-39 demonstrates that the shape of the far field normalised *pdf*($\xi/\overline{\xi}$) is generally symmetric about $\xi=\overline{\xi}$ for both jets, but the average p.d.f. of the PJ flow is much broader indicating a wider distribution of jet concentrations. This is also

shown in the non-normalised $pdf(\xi)$, which also indicates that in the far field the probable jet concentrations at the same axial location are much lower for a precessing jet flow. These observations are consistent with the results of Newbold (1997) and demonstrate that a broader, more diluted distribution of jet concentrations exists on the jet axis of the PJ flow than in a simple jet flow. It also agrees with the present finding of increased concentration fluctuation intensity on the jet axis of a PJ nozzle, see Section 6.5.2.

6.5.6.2 The Effect of Co-Flow Velocity

The effect of the ratio of co-flow velocity to jet exit velocity on the distribution of concentration on the jet axis of the 38mm PJ nozzle is well illustrated by the data set obtained using co-flow velocity ratios of $U_a/U_{e\text{-}PJ}$=0.035 and $U_a/U_{e\text{-}PJ}$=0.098 at a confinement of D_{duct}/d_{PJ}=10.3, see Figure 6-38a and Figure 6-38b. The effect of co-flow velocity ratio on the average far field $pdf(\xi)$ and normalised $pdf(\xi/\bar{\xi})$ are illustrated in Figure 6-41 and Figure 6-42. The results show that the change in concentration distribution along the jet axis with co-flow velocity is not large. The normalised profiles, $pdf(\xi/\bar{\xi})$, indicate the range of concentrations on the jet axis in the far field are comparable for all co-flow velocities. However, the non-normalised $pdf(\xi)$ profiles reveal a shift towards lower concentrations as the co-flow velocity increases. This is consistent with the higher mass flow of ambient fluid with increasing velocity. Comparison of Figure 6-38a and Figure 6-38b indicates that this effect is not isolated to just the far field of the PJ nozzle but also occurs near the nozzle tip.

6.5.6.3 The Effect of Confinement

The effect of confinement on jet concentration distribution along the jet axis is illustrated by the p.d.f.s calculated for D_{duct}/d_{PJ}=7.6 and D_{duct}/d_{PJ}=12.9 at constant velocity ratio and nozzle conditions, see Figure 6-38c and Figure 6-38d. Refer to Figure 6-37b for the p.d.f. at D_{duct}/d_{PJ}=10.3. The effect of confinement on the average far field $pdf(\xi)$ and normalised $pdf(\xi/\bar{\xi})$ are shown in Figure 6-43 and Figure 6-44. The results demonstrate that the ratio of duct diameter to PJ nozzle chamber diameter does not significantly affect the probability distribution in the near field. However confinement does act to change the distribution of jet concentrations and the most probable concentration found on the jet axis in the far field. The normalised $pdf(\xi/\bar{\xi})$ reveals that the range of jet concentrations relative to the mean concentration remains approximately the same with increasing confinement ratio, or may decrease slightly. However, Figure 6-43 and Figure 6-44 show that confinement causes a significant change in the non-normalised $pdf(\xi)$. The range of actual concentrations in the far field broadens and the peak of the p.d.f. (maximum probability) increases with increasing confinement ratio. This highlights the important differences between $pdf(\xi)$ and $pdf(\xi/\bar{\xi})$, particularly as the jet concentration distribution within the flammability limits for a given fuel is crucial for accurate modelling of combustion processes.

6.5.6.4 The Effect of Central Axial Jet Proportion

The effect of the flow regime (PJ or CAJ dominated) on the mixing from the PJ nozzle is highlighted by the distribution of jet concentrations on the jet axis. Figure 6-37b to Figure 6-37f show the jet axis concentration distributions for PJ only, ψ_{CAJ}=15%, ψ_{CAJ}=25%, ψ_{CAJ}=40%PJ and CAJ only at the same co-flow velocity ratio and confinement. The effect of CAJ proportion on *pdf*(ξ) and *pdf*($\xi/\overline{\xi}$) is illustrated in Figure 6-45 and Figure 6-46. For the ψ_{CAJ}=0% and ψ_{CAJ}=15% (Γ_{CAJ}=0.06) a wide range of concentrations is observed in the far field as is the rapid concentration decay in the near-field, which is manifested as an increased probability of low concentration fluid very close to the nozzle exit. However, the probability distribution for ψ_{CAJ}=25% (Γ_{CAJ}=0.17) and ψ_{CAJ}=40% (Γ_{CAJ}=0.45) are significantly different, particularly close to the nozzle exit, where the probability of finding low concentration fluid on the jet axis is close to zero.

The average far field profile of *pdf*($\xi/\overline{\xi}$) shows that the range of jet concentrations relative to the mean concentration is not significantly affected by CAJ proportion. The peak value of *pdf*($\xi/\overline{\xi}$) does change with CAJ proportion though, with the minimum value occurring for ψ_{CAJ}=25%. This is more clearly demonstrated by the non-normalised distribution of *pdf*(ξ), in which it can be seen that the ψ_{CAJ}=25% case covers the widest range of actual concentration values. Figure 6-46 indicates that as ψ_{CAJ} is increased from 0% to 25% (momentum ratio increased from Γ_{CAJ}=0 to Γ_{CAJ}=0.17), the distribution of concentrations found in the jet far field increases, however, further increases in the CAJ proportion into the CAJ dominated regime beyond ψ_{CAJ}=25% cause a reduction in the range of jet concentrations. Similarly the most probable concentration also increases with CAJ proportion until it reaches a maximum at ψ_{CAJ}=25% (Γ_{CAJ}=0.17), after which the most probable concentration decreases in value. This result is consistent with the observation in Section 6.5.5 that the inverse centreline concentration is minimised at ψ_{CAJ}=25%. It is also important to note that this condition produced the maximum heat release in the pilot-scale experiments described in Section 5.3.1 and corresponds closely to the momentum ratio found to have the minimum global strain rate and maximum flame volume in Section 4.3.3 (Γ_{CAJ}=0.19).

The distribution of concentration on the jet axis of the central axial jet only flow is very different to that of the PJ cases and is consistent with the p.d.f. of a simple jet. The p.d.f. has a very narrow, sharp peak which covers a smaller range of concentrations than the precessing jet flow and has a much lower value for the most probable jet concentration.

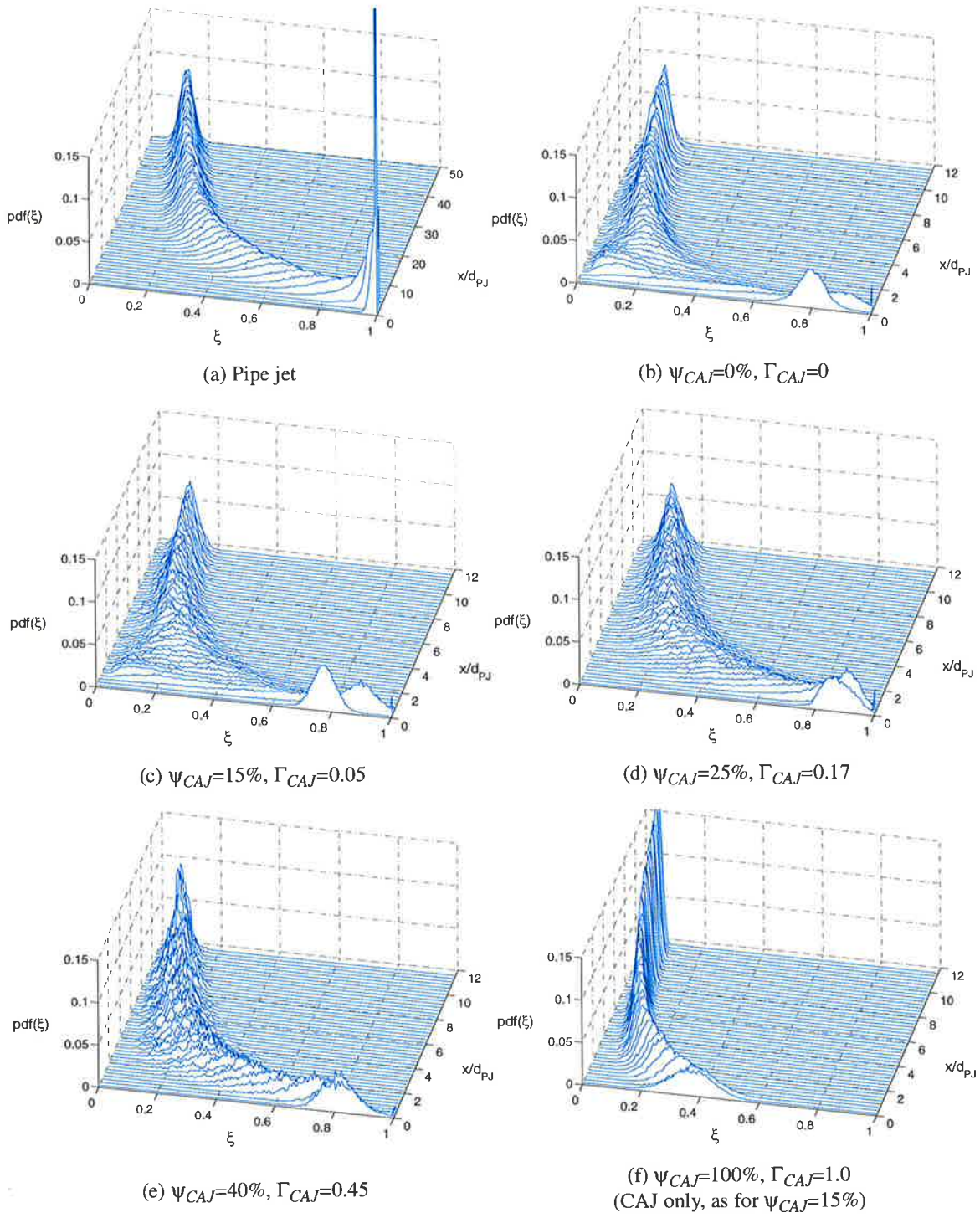

(a) Pipe jet

(b) Ψ_{CAJ}=0%, Γ_{CAJ}=0

(c) Ψ_{CAJ}=15%, Γ_{CAJ}=0.05

(d) Ψ_{CAJ}=25%, Γ_{CAJ}=0.17

(e) Ψ_{CAJ}=40%, Γ_{CAJ}=0.45

(f) Ψ_{CAJ}=100%, Γ_{CAJ}=1.0
(CAJ only, as for Ψ_{CAJ}=15%)

Figure 6-37. The effect of jet type and CAJ proportion, Ψ_{CAJ}, on the probability distribution functions of jet concentration on the jet axis, *pdf*(ξ). Conditions: (a) Pipe jet, Reynolds number=28,200, co-flow velocity U_a=0.06m/s, no confinement; (b) - (e) d_{PJ}=38mm PJ nozzle, co-flow velocity U_a=0.06m/s, D_{duct}/d_{PJ}=10.3, m_a/m_0=18.4 except for Ψ_{CAJ}=100% (m_a/m_0=122).

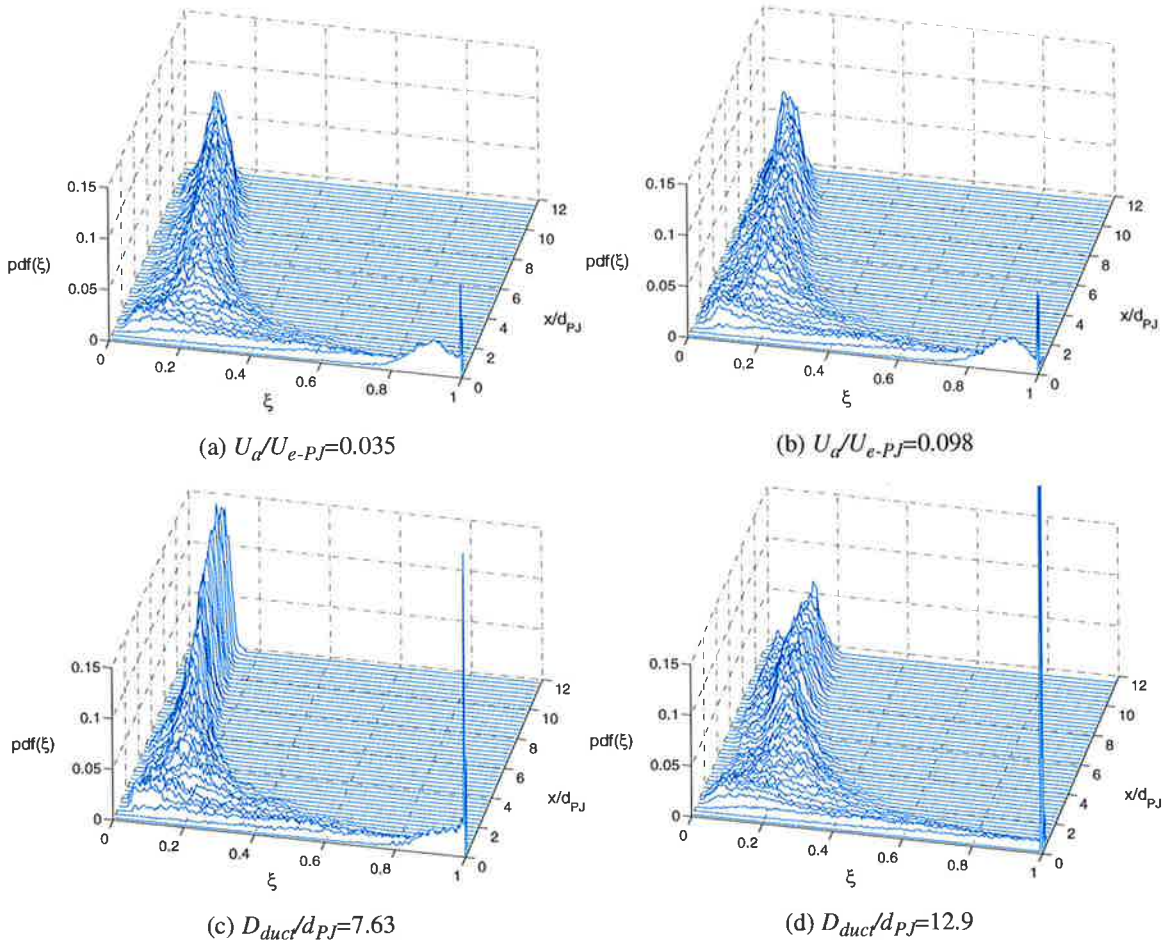

(a) $U_a/U_{e\text{-}PJ}$=0.035

(b) $U_a/U_{e\text{-}PJ}$=0.098

(c) D_{duct}/d_{PJ}=7.63

(d) D_{duct}/d_{PJ}=12.9

Figure 6-38. The effect of co-flow velocity and confinement on the probability distribution functions of the jet concentration on the jet axis, *pdf*(ξ), of the d_{PJ}=38mm PJ nozzle. Conditions: (a) - (b) PJ only flow, Reynolds number=66,100, D_{duct}/d_{PJ}=10.3; (c)-(d) PJ flow only, Reynolds number=66,100, $U_a/U_{e\text{-}PJ}$=0.055 (U_a=0.06m/s).

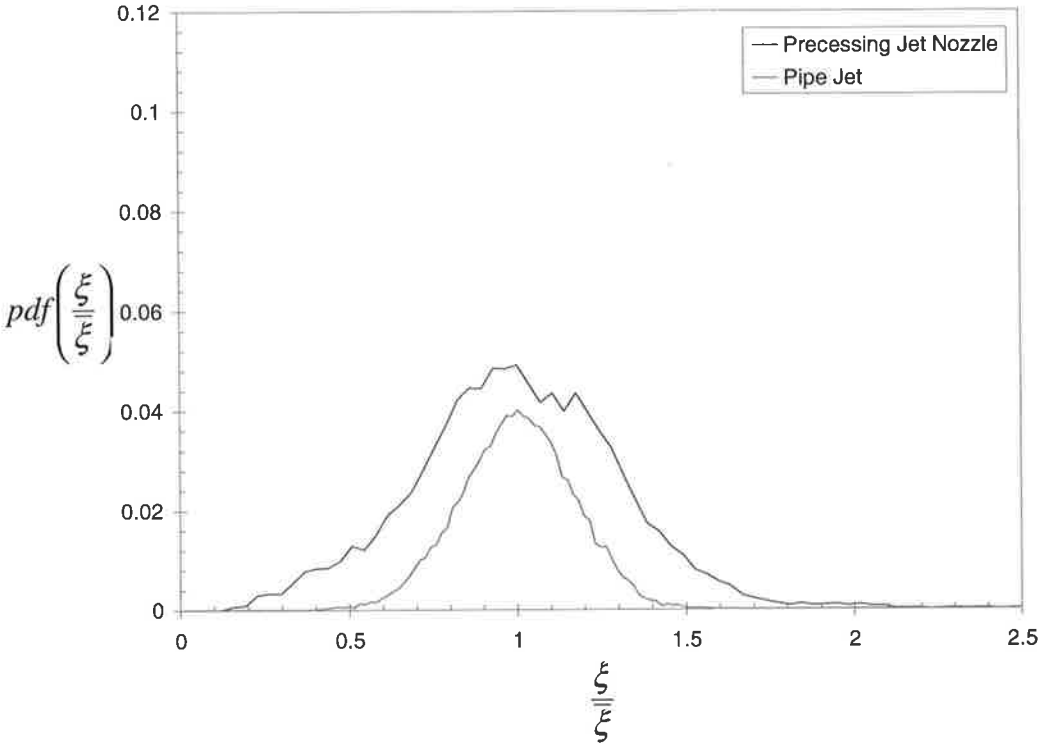

Figure 6-39. Comparison of the probability distribution function of concentration on the jet axis normalised to the local mean jet concentration in the far field of the pipe jet and d_{PJ}=38mm PJ nozzle (x/d_{pipe}≈50, x/d_{PJ}≈12). Conditions: Re_{pipe}=28,200, Re_{PJ}=66,100, U_a=0.06m/s, D_{duct}/d_{PJ}=12.9.

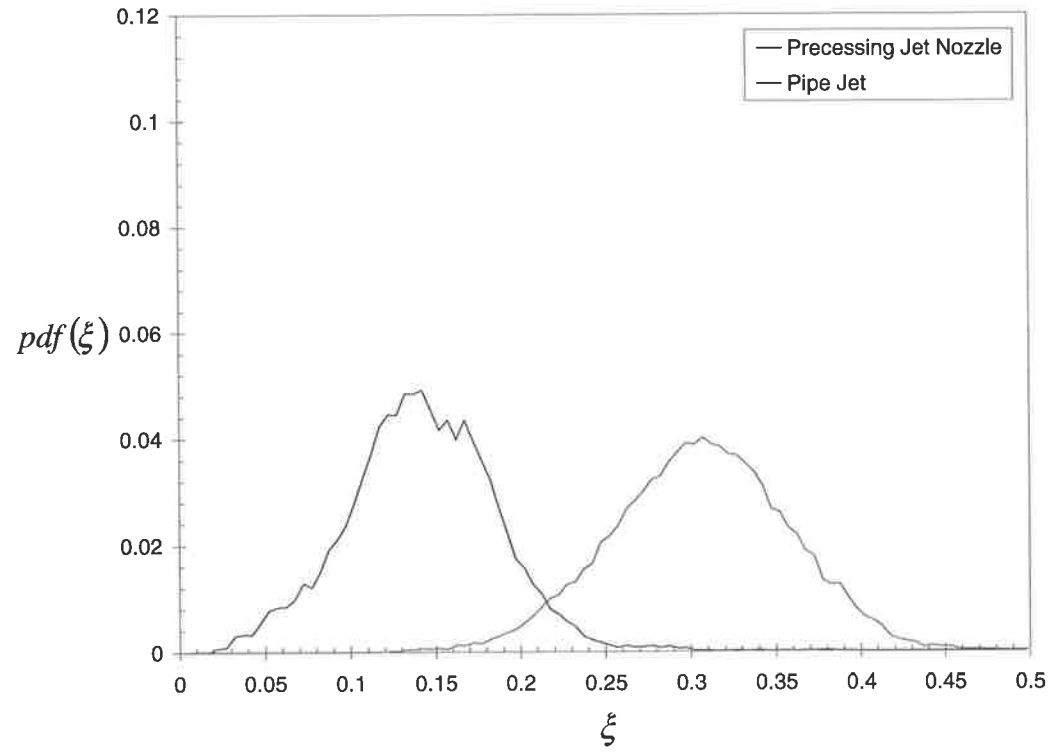

Figure 6-40. Comparison of the probability distribution function of local jet concentration on the jet axis in the far field of the pipe jet and PJ nozzle. Conditions as for Figure 6-39.

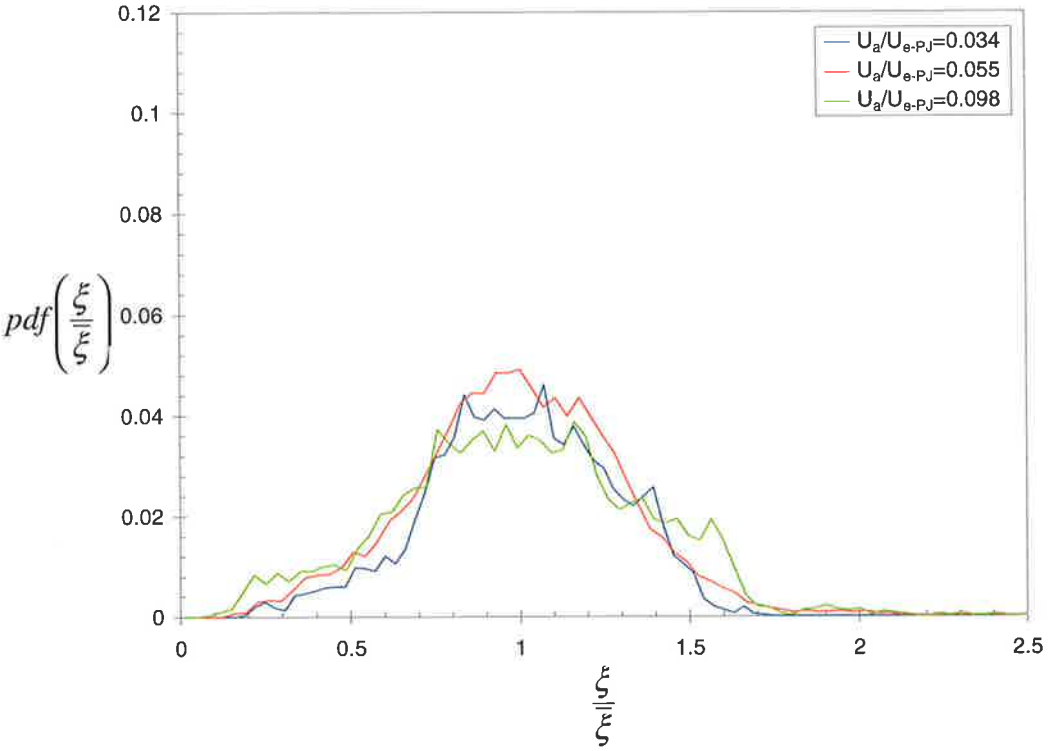

Figure 6-41. The effect of co-flow velocity on the probability distribution function of concentration on the jet axis normalised to the local mean jet concentration in the far field of the d_{PJ}=38mm PJ nozzle ($x/d_{PJ}\approx$12). Conditions: PJ flow only, Reynolds number=66,100, D_{duct}/d_{PJ}=10.3.

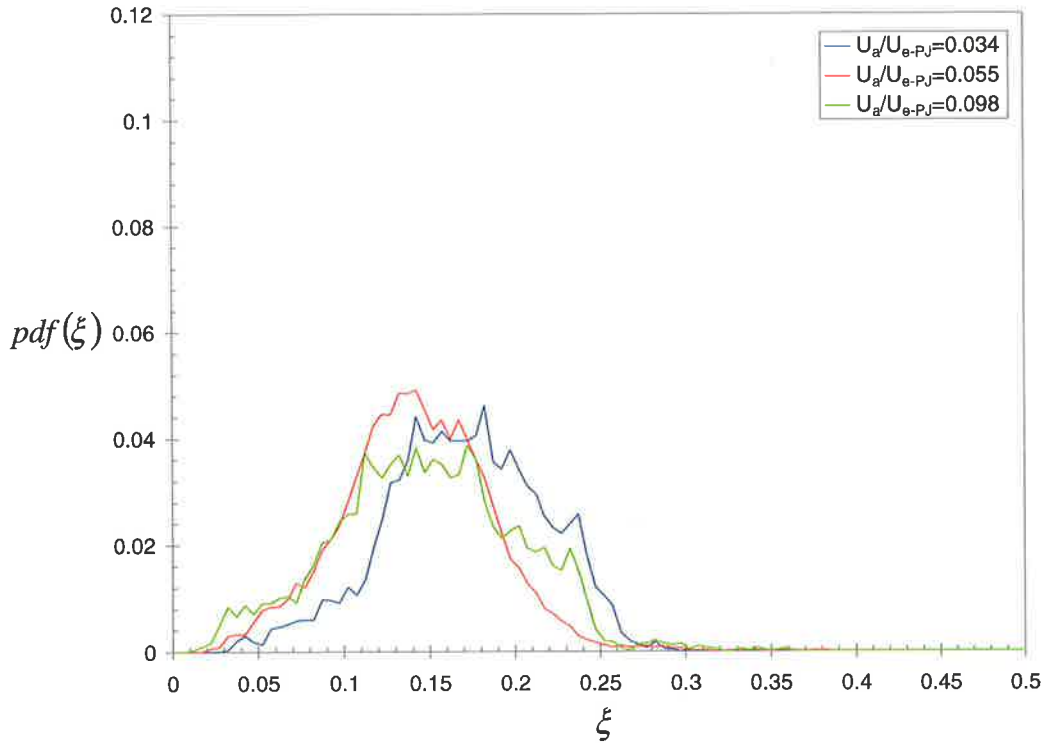

Figure 6-42. The effect of co-flow velocity on the probability distribution function of the local jet concentration on the jet axis in the far field of the PJ nozzle. Conditions as for Figure 6-41.

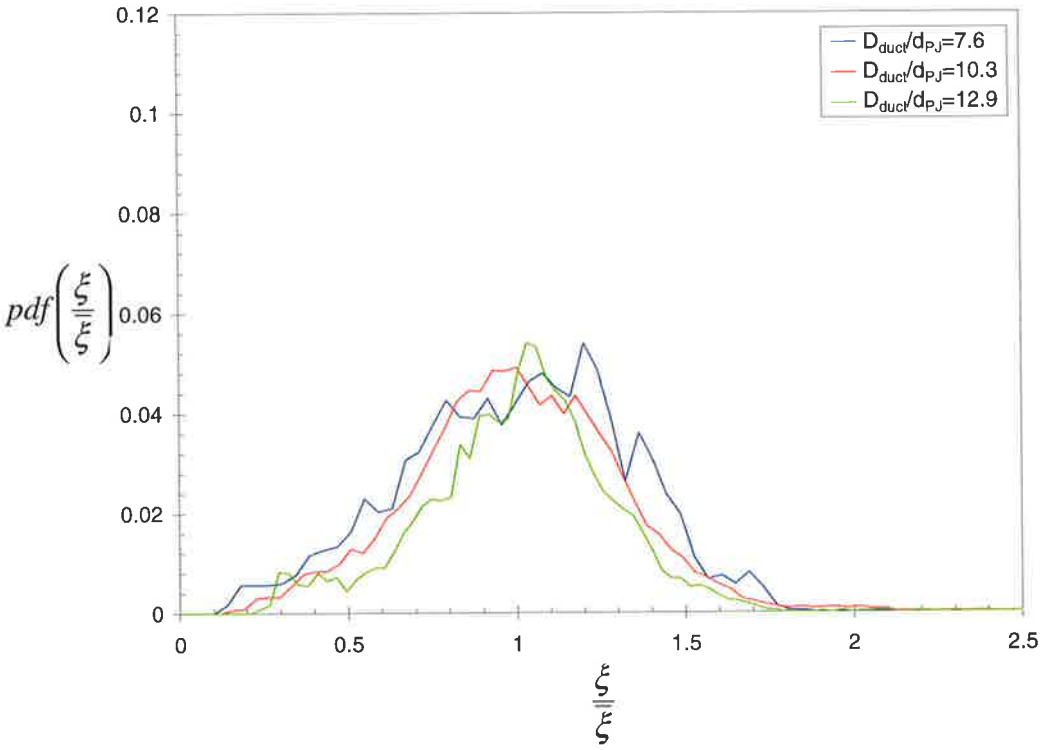

Figure 6-43. The effect of confinement on the probability distribution function of concentration on the jet axis normalised to the local mean jet concentration in the far field of the d_{PJ}=38mm PJ nozzle ($x/d_{PJ}\approx$12). Conditions: PJ flow only, Reynolds number=66,100, $U_a/U_{e\text{-}PJ}$=0.055.

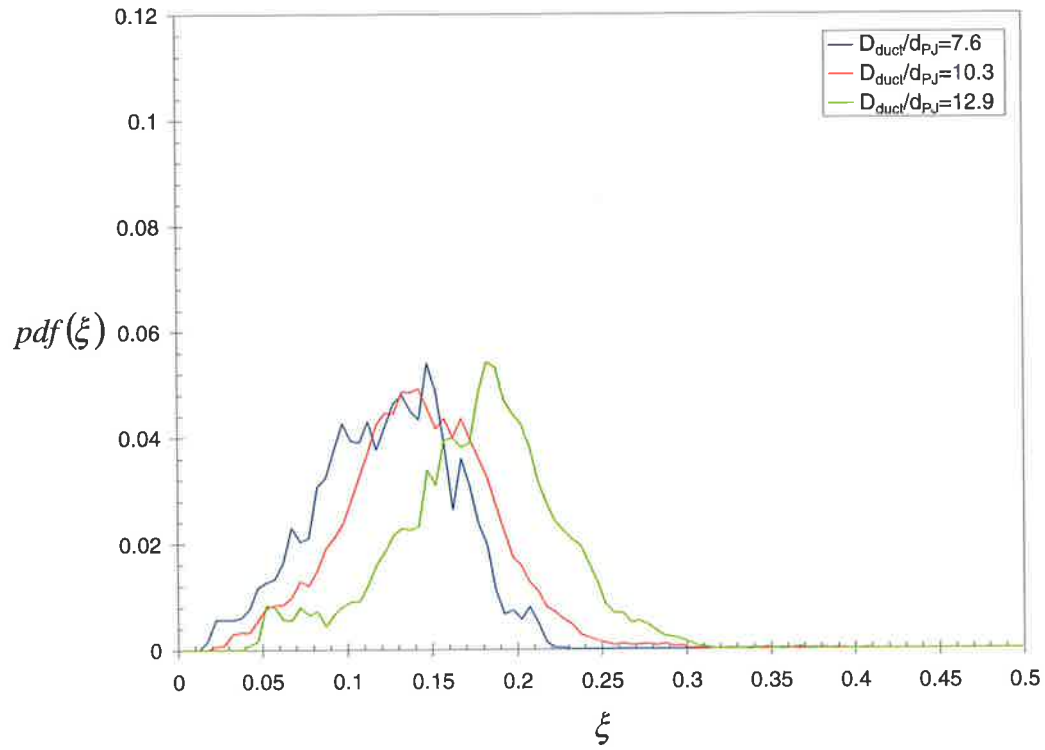

Figure 6-44. The effect of confinement on the probability distribution function of local jet concentration on the jet axis in the far field of the PJ nozzle. Conditions as for Figure 6-43.

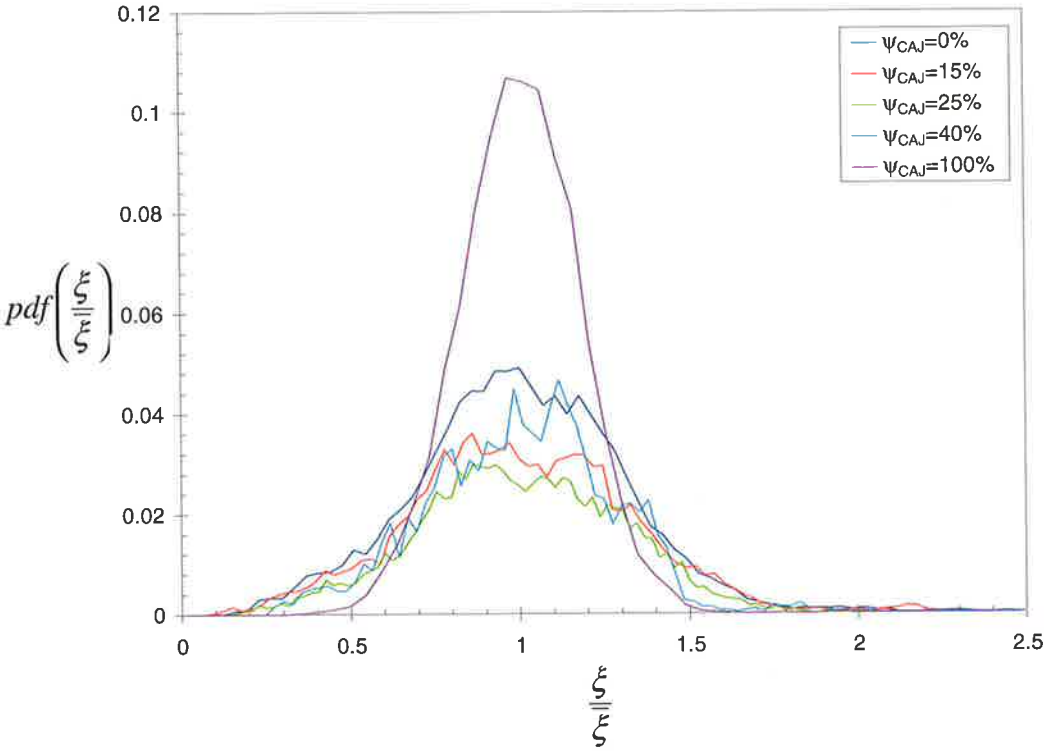

Figure 6-45. The effect of CAJ proportion, ψ_{CAJ}, on the probability distribution function of concentration on the jet axis normalised to the local mean jet concentration in the far field of the d_{PJ}=38mm PJ nozzle (x/d_{PJ}≈12). Conditions: D_{duct}/d_{PJ}=10.3, U_a=0.06m/s, m_a/m_0=18.4 except for ψ_{CAJ}=100% (m_a/m_0=122).

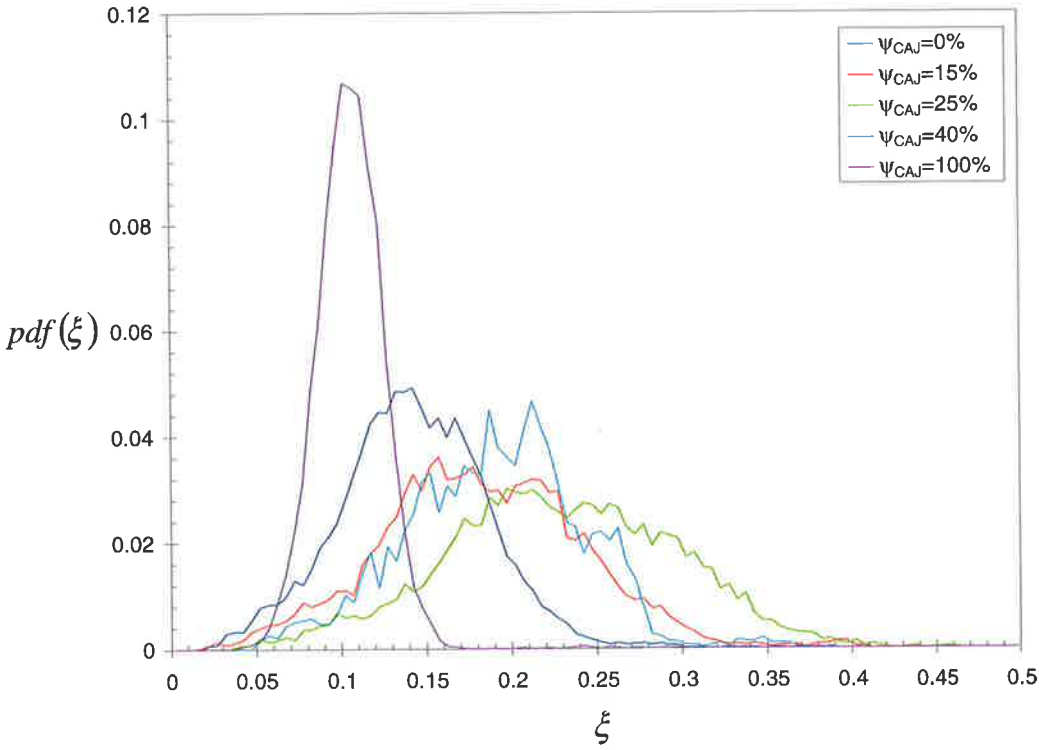

Figure 6-46. The effect of CAJ proportion, ψ_{CAJ}, on the probability distribution function of jet concentration on the jet axis in the far field of the PJ nozzle. Conditions as for Figure 6-45

6.6 Scaling of a Confined Precessing Jet Flow

6.6.1 Description of the Scaling Model

The observations and results described in Section 6.5 demonstrate that the effects of confinement and co-flow on the scalar mixing field from a PJ nozzle are different depending on the axial distance from the nozzle exit. The different regions in the jet and duct are summarised in Figure 6-47.

The identification of dominant flow regions in the jet and duct flows can assist in the development of a semi-empirical model of the confined PJ flow. These regions, illustrated in Figure 6-47, are the jet mixing dominated, interaction and duct mixing dominated regions. The interaction region is of most importance as it is in this zone that the jet conditions, co-flow and confinement interact to determine the nature of the mixing of the jet and co-flowing fluid and if recirculation is important. In most rotary kiln geometries the jet mixing dominated and duct mixing dominated regions are expected to overlap significantly with the interaction region, depending on the precise kiln geometry and conditions.

As outlined in the introduction to this chapter and highlighted by the instantaneous images shown in the previous section, it is not yet possible to mathematically model the scalar mixing from a confined precessing jet nozzle. Hence the scaling model proposed here is based on dimensional arguments and an empirical correlation with the results outlined in Section 6.5 and Appendix C. The fundamental assumption of the proposed model is that, if the inverse concentration decay along the jet axis and the jet half-width can be estimated in the jet far field for any given co-flow velocity ratio and confinement, the mean jet concentration at any location within the duct can be calculated by assuming the radial distribution of concentration is Gaussian. The model is applied only up to the point where the jet reaches the duct walls, which is generally also the limit of the imaged region of the present experiments.

6.6.2 Development of the Scaling Parameters

The characteristics of the jet concentration decay along the jet axis noted in Section 6.5.4 indicate that the duct diameter is the most appropriate dimension for the normalisation of the axial distance and decay rate. The results for the concentration half-width indicate the PJ chamber diameter is the most appropriate length scale for calculating the jet spreading rate. Hence, following Mi *et al.* (2000b) for a simple jet, the far field inverse concentration decay along the jet axis can be described by the linear equation:

$$\frac{1}{\bar{\xi}} = \frac{1}{K_1}\left(x - \frac{x_{0,1}}{D_{duct}}\right) \qquad \textbf{Equation 6-23.}$$

Similarly, the concentration half-width in the precessing jet far field can be expressed as:

$$\frac{r_{1/2}}{d_{PJ}} = K_2\left(x - \frac{x_{0,2}}{d_{PJ}}\right) \qquad \textbf{Equation 6-24.}$$

The radial mean concentration profiles of the PJ nozzle is approximately a Gaussian distribution, as shown in Figure 6-23. Hence if the parameters K_1, $x_{0,1}$, K_2 and $x_{0,2}$ can be calculated for a given geometry and flow condition, the concentration at any point (x,r) in a confined precessing jet flow field can be expressed as:

$$\bar{\xi}(x, r) = \frac{\exp\left(-0.693\left(\frac{r}{K_2(x/d_{PJ} - x_{0,2})}\right)^2\right)}{\frac{1}{K_1}\left(\frac{x}{D_{duct}} - x_{0,1}\right)}$$

Equation 6-25.

The results of Section 6.5.4 indicate that the concentration decay constant, K_1, is significantly influenced by the confinement ratio and that the virtual origin, $x_{0,1}$, is dominated by the effects of the co-flow velocity ratio. The variation in K_1 is plotted against the confinement ratio, D_{duct}/d_{PJ}, in Figure 6-48, for constant co-flow velocity ratio. It can be seen that, for all data sets except $U_a/U_{e\text{-}PJ}$=0.055, the data collapses reasonably well to a linear relationship which is given by:

$$K_1 = 0.00774\left(\frac{D_{duct}}{d_{PJ}}\right) + 0.0948$$

Equation 6-26.

The location of the jet virtual origin, $x_{0,1}/D_{duct}$, is plotted against the co-flow velocity ratio, $U_a/U_{e\text{-}PJ}$, for constant confinement ratio in Figure 6-49. The results demonstrate that there is a good collapse of data onto a single, linear profile, with an exception for the values of $x_{0,1}/D_{duct}$ at $U_a/U_{e\text{-}PJ}$=0.055. The departure of the point at a velocity ratio of $U_a/U_{e\text{-}PJ}$=0.055 from a linear trend is consistent with the variation in K_1 compared to other co-flow velocities. It is considered an aberration since no physical reason for the point of inflection can be found. The aberration may possibly be explained by measurement errors of $x_{0,1}/D_{duct}$ at $U_a/U_{e\text{-}PJ}$=0.035, in which condition confinement effects are more likely to contribute to changes in the jet behaviour, although this is not consistent with the variation in K_1. Based on a line of best fit through all the data points, the linear relationship between the velocity ratio and virtual origin location is specified by:

$$\frac{x_{0,1}}{D_{duct}} = -3.386\left(\frac{U_a}{U_{e-PJ}}\right) - 0.3903$$

Equation 6-27.

The results in Section 6.5.3 and Section 6.5.4 indicated no consistent effect of confinement ratio or co-flow velocity ratio on the jet half-width slope and virtual origin. However, it was found that the variation in K_2 and $x_{0,2}/d_{PJ}$ collapsed reasonably well to a linear profile if plotted against the ratio of the volumetric flow rate of the co-flow and the volumetric flow rate of the PJ nozzle, Q_a/Q_0. In the current isothermal experiments, the volumetric flow rate ratio is the same as the mass flux ratio, m_a/m_o. Figure 6-50 demonstrates that an inverse proportionality exists between the jet spreading rate and the mass flux ratio, so that the relationship is given by:

$$\frac{1}{K_2} = 0.1138\left(\frac{m_a}{m_0}\right) + 4.8311$$

Equation 6-28.

Figure 6-51 demonstrates that the relationship between the jet concentration half-width virtual origin and mass flux ratio is linear and is given by:

$$\frac{x_{0,2}}{d_{PJ}} = -0.2240\left(\frac{m_a}{m_0}\right) - 5.7547 \qquad \textbf{Equation 6-29.}$$

6.6.3 Modelling the Effect of the Central Axial Jet

A full model of the concentration field of a passive scalar issuing from a PJ nozzle must also incorporate the effects of central axial jet proportion, ψ_{CAJ}, on the flow field. It is assumed in the present section that the effects of the CAJ can be modelled independently of the effects of co-flow velocity and confinement.

The results of the two-colour PLIF experiments reported in Section 3.4.3 demonstrate that the mixing characteristics of the combined PJ and CAJ flow field are characterised by the momentum ratio between the CAJ and the sum of the momentum of the PJ at the inlet orifice of the nozzle chamber and the CAJ momentum, Γ_{CAJ}. Hence the mean concentration distribution parameters K_1, $x_{0,1}/D_{duct}$, K_2 and $x_{0,2}/d_{PJ}$ of the present combined CAJ and PJ nozzle measurements are plotted against the CAJ momentum ratio in Figure 6-52 to Figure 6-55 for three different confinements and co-flow velocities but constant mass flux ratio of co-flowing fluid to jet fluid. The results of the D_{duct}/d_{PJ}=10.3 (390mm duct) measurements are considered the most accurate representation of the effect of the CAJ as more images were captured at CAJ proportions of ψ_{CAJ}=15%, ψ_{CAJ}=25% and ψ_{CAJ}=40% and intermediate proportions between these settings were also investigated. The measurements of K_1, $x_{0,1}/D_{duct}$, K_2 and $x_{0,2}/d_{PJ}$ from the D_{duct}/d_{PJ}=7.6 (U_a=0.108m/s) and D_{duct}/d_{PJ}=12.9 (U_a=0.038m/s) experiments are corrected for the effects of confinement and co-flow relative to the D_{duct}/d_{PJ}=10.3 (U_a=0.06m/s) measurements by applying the model equations derived in the previous section. This correction assumes the effects of the CAJ are independent of other factors. The effects of the CAJ proportion are quantified by normalising the measurements of K_1, $x_{0,1}$, K_2 and $x_{0,2}$ at each Γ_{CAJ} to the value at Γ_{CAJ}=0 (ψ_{CAJ}=0%) of each experimental configuration. The duct diameter is used as the characteristic length scale for the jet axis concentration constants and the nozzle diameter is used for the jet concentration half-width normalisation, following the derivation of the scaling parameters in Section 6.6.2.

The results shown in Figure 6-52 to Figure 6-55 generally reflect the analysis presented in Section 6.5.5. The main observation that can be made from these figures is that the major mixing characteristics of the combined PJ and CAJ flow depend significantly on the dominant flow regime and hence the momentum ratio. The present results indicate that the PJ dominated flow regime occurs for Γ_{CAJ}<0.2 and the CAJ dominated flow regime occurs for approximately Γ_{CAJ}>0.25, consistent with the results of Section 3.5.

Figure 6-52 demonstrates that the concentration decay constant, K_1, normalised to the value at Γ_{CAJ}=0, can be modelled reasonably well by a linear relationship with the CAJ momentum ratio. Hence the concentration decay rate is not altered by the dominant flow regime. The linear relationship derived for the present model does not include the measurements from the D_{duct}/d_{PJ}=7.6 experimental configuration as the trend for this configuration is different from the trends for D_{duct}/d_{PJ}=10.3 and D_{duct}/d_{PJ}=12.9. Most rotary kilns also do not operate at this con-

finement ratio. The normalised far field jet spreading rate, K_2, changes significantly depending on the dominant flow regime. It is difficult from Figure 6-53 to determine what relationship best describes the effect of CAJ momentum ratio on the jet spreading rate. Hence the measurements from the d_{PJ}=10.3 (U_a=0.06m/s) experimental configuration are used to derive a model based on a quadratic expression in the PJ dominated flow regime and a linear expression in the CAJ dominated flow regime. The equations to predict the effect of CAJ proportion on the far field concentration decay constant and spreading rate are therefore given by:

For $0<\Gamma_{CAJ}\leq 1$

$$\frac{K_{1,\Gamma}}{K_{1,\Gamma=0}} = -0.7699\,\Gamma_{CAJ} + 1.1136 \qquad \textbf{Equation 6-30.}$$

For $0<\Gamma_{CAJ}<0.2$:

$$\frac{K_{2,\Gamma}}{K_{2,\Gamma=0}} = 11.028\,\Gamma^2_{CAJ} - 1.9294\,\Gamma_{CAJ} + 0.9909$$

For $0.23<\Gamma_{CAJ}\leq 1$:

$$\frac{K_{2,\Gamma}}{K_{2,\Gamma=0}} = -0.8599\,\Gamma_{CAJ} + 1.557 \qquad \textbf{Equation 6-31.}$$

The location of the inverse jet concentration decay and jet spreading rate virtual origins, $x_{0,1}/D_{duct}$ and $x_{0,2}/d_{PJ}$, normalised to the values at Γ_{CAJ}=0, are approximately linearly proportional to the momentum ratio in the PJ dominated flow regime, as shown in Figure 6-54 and Figure 6-55. In the CAJ dominated flow regime however, the locations of the virtual origins are almost independent of the effect of CAJ proportion and there is therefore no need for these values to be normalised to the value at Γ_{CAJ}=0 in Figure 6-54 and Figure 6-55. Hence in the present model, for $\Gamma_{CAJ}>0.23$, $x_{0,1}/D_{duct}$ and $x_{0,2}/d_{PJ}$ are treated as a constant value based on the mean of the measurements in the CAJ dominated flow regime. Therefore the equations to model the effect of the CAJ on the virtual origin locations are:

For $0<\Gamma_{CAJ}<0.2$:

$$\frac{x_{0,1,\Gamma}}{x_{0,1,\Gamma=0}} = -4.7341\,\Gamma_{CAJ} + 1.0753$$

For $0.23<\Gamma_{CAJ}\leq 1$:

$$\frac{x_{0,1,\Gamma}}{D_{duct}} = \frac{x_{0,1,\Gamma=0}}{D_{duct}} = -0.118 \qquad \textbf{Equation 6-32.}$$

For $0<\Gamma_{CAJ}<0.2$:

$$\frac{x_{0,2,\Gamma}}{x_{0,2,\Gamma=0}} = -4.5574\,\Gamma_{CAJ} + 1.1201$$

For $0.23<\Gamma_{CAJ}\leq 1$:

$$\frac{x_{0,2,\Gamma}}{d_{PJ}} = \frac{x_{0,2,\Gamma=0}}{d_{PJ}} = -0.74 \qquad \textbf{Equation 6-33.}$$

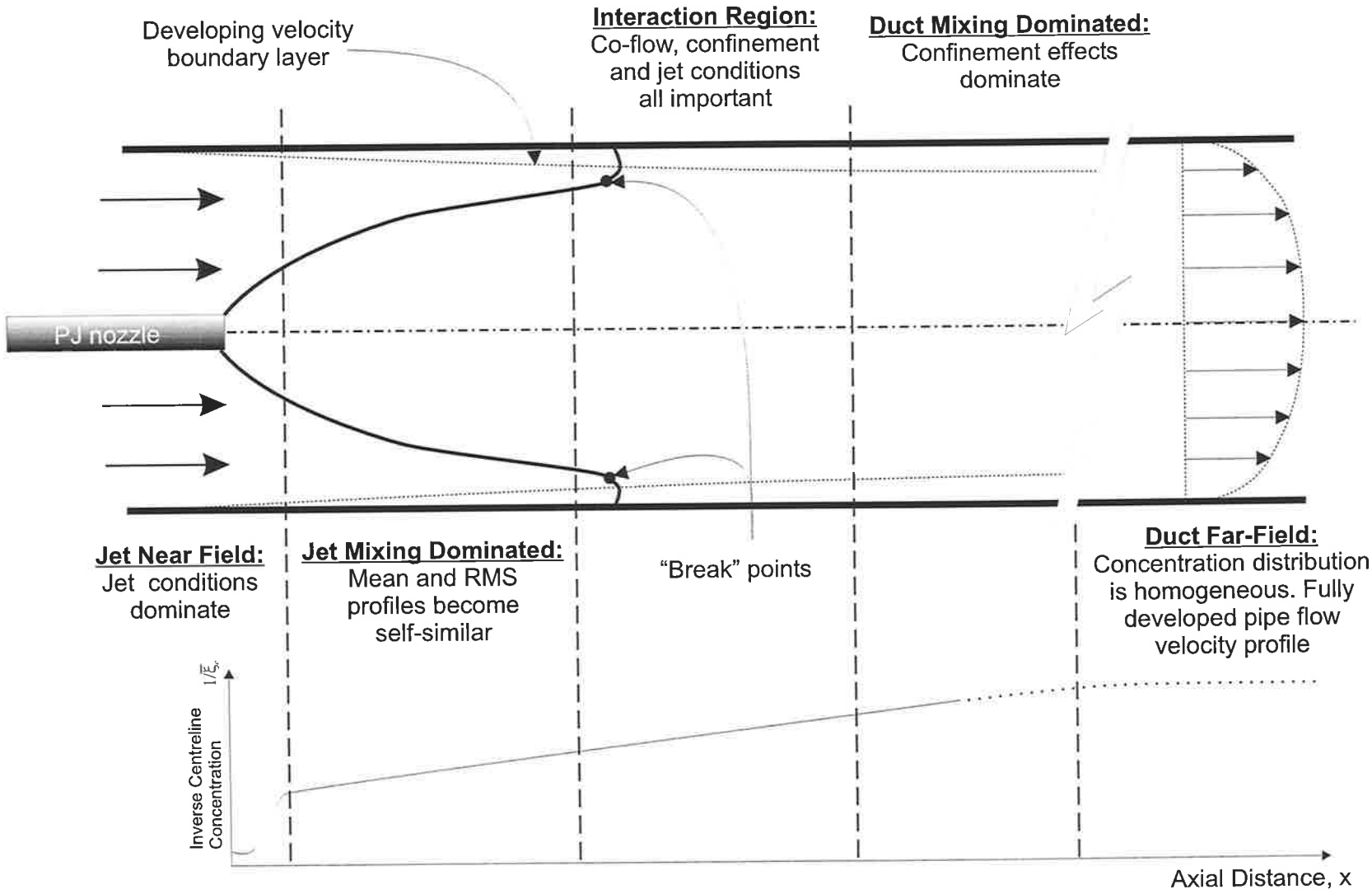

Figure 6-47. Principal regions and mixing conditions for the flow from a precessing jet nozzle in a confined, co-flowing environment.

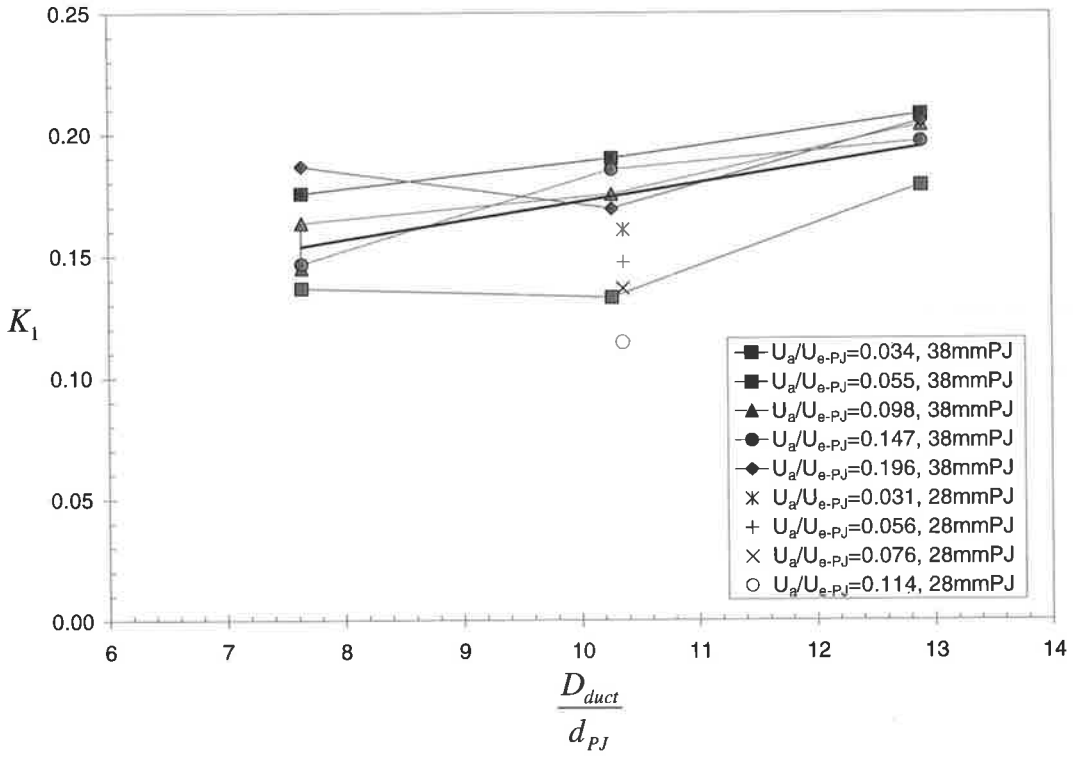

Figure 6-48. Variation in the far field concentration decay constant, K_1, with confinement for different ratios of co-flow velocity to jet exit velocity and constant precessing jet nozzle conditions: PJ flow only (ψ_{CAJ}=0%), Reynolds number=66,100.

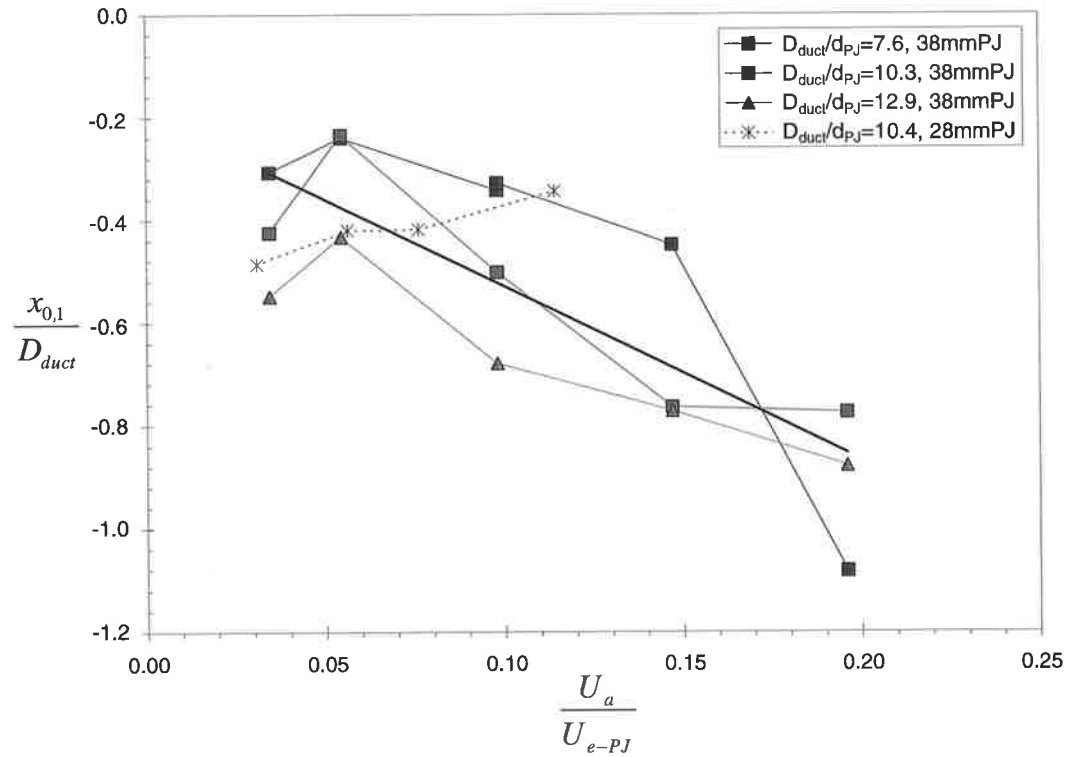

Figure 6-49. Variation in the far field concentration virtual origin, $x_{0,1}/D_{duct}$, with the ratio of co-flow velocity to jet exit velocity for different confinement and constant precessing jet nozzle conditions: PJ flow only (ψ_{CAJ}=0%), Reynolds number=66,100.

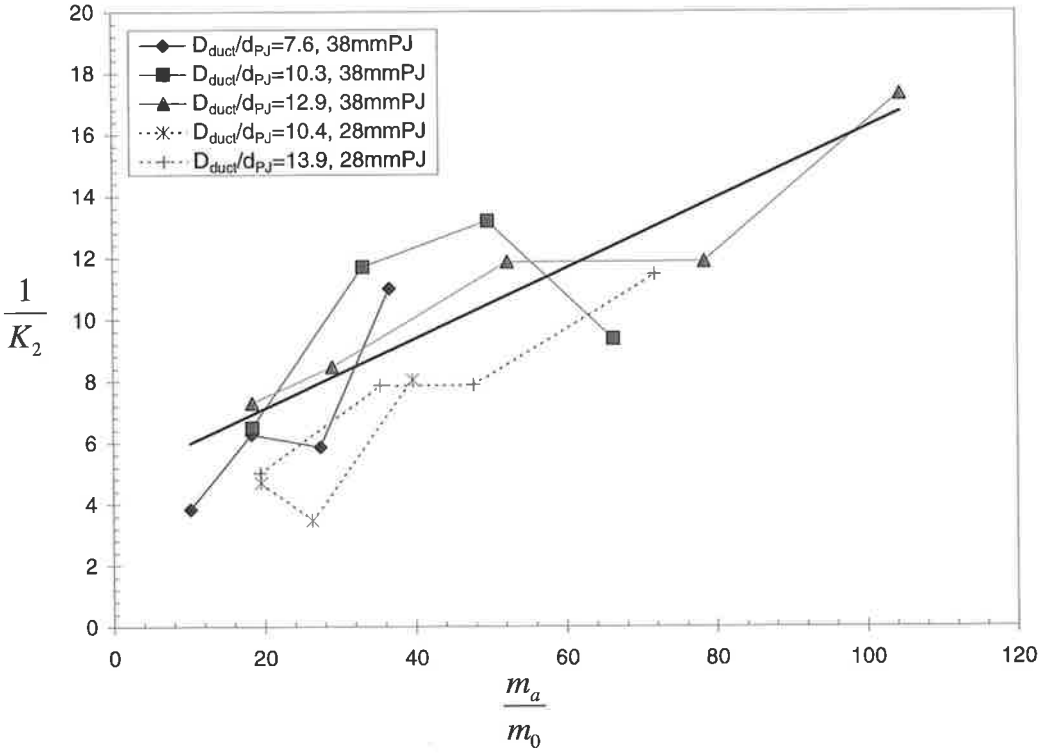

Figure 6-50. Variation in the reciprocal of the far field jet spreading rate, K_2, with the mass flux ratio of co-flowing fluid to jet fluid for different confinements and constant PJ nozzle conditions: precessing jet flow only (ψ_{CAJ}=0%), Reynolds number=66,100.

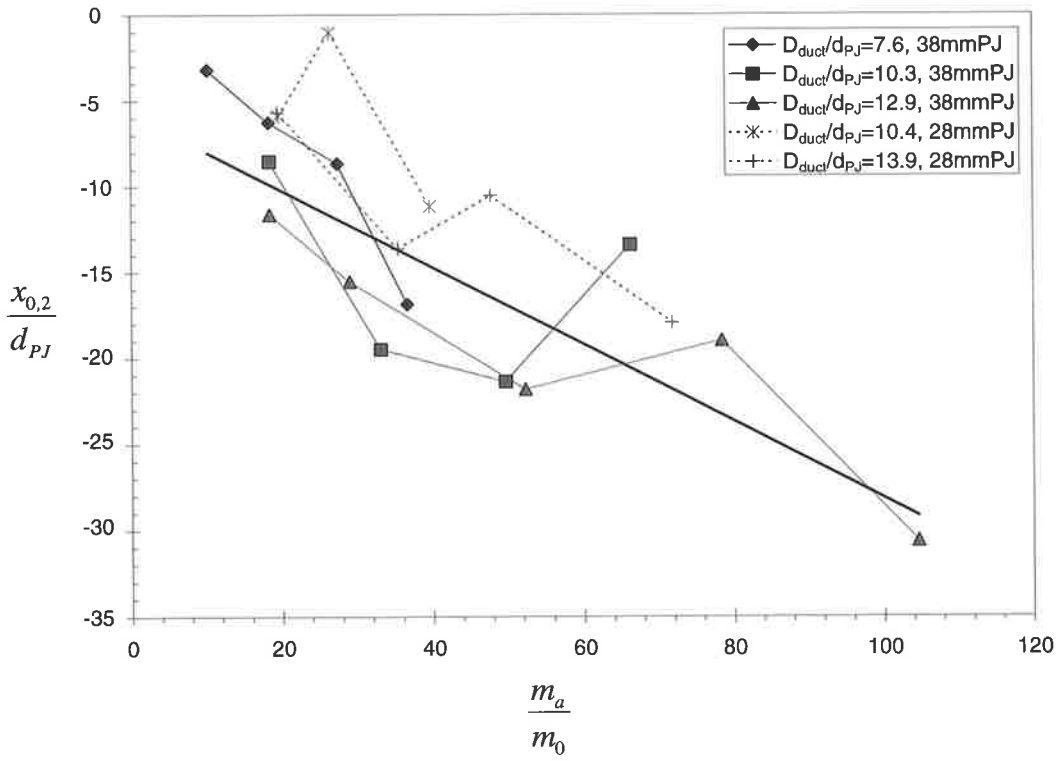

Figure 6-51. Variation in the far field jet spreading rate virtual origin, $x_{0,2}/d_{PJ}$, with the mass flux ratio of co-flowing fluid to jet fluid for different confinements and constant PJ nozzle conditions: precessing jet flow only (ψ_{CAJ}=0%), Reynolds number=66,100.

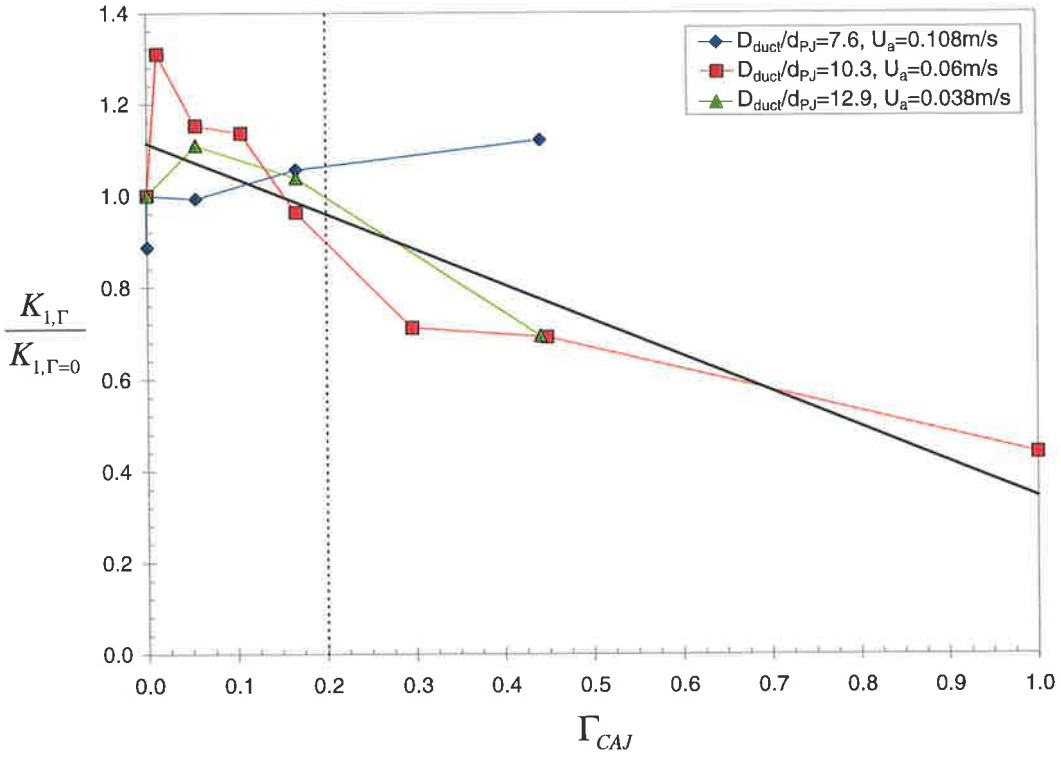

Figure 6-52. Variation in the far field concentration decay constant, K_1, normalised to the value at Γ_{CAJ}=0, with the momentum ratio Γ_{CAJ} for different confinements and constant mass flux ratio. The data for D_{duct}/d_{PJ}=7.6 and D_{duct}/d_{PJ}=12.9 are corrected for the effects of confinement, relative to D_{duct}/d_{PJ}=10.3, using Equation 6-26. The bold line indicates the line of best fit to the data (excluding D_{duct}/d_{PJ}=7.6), the dashed line indicates the transition from PJ to CAJ dominated flow regime.

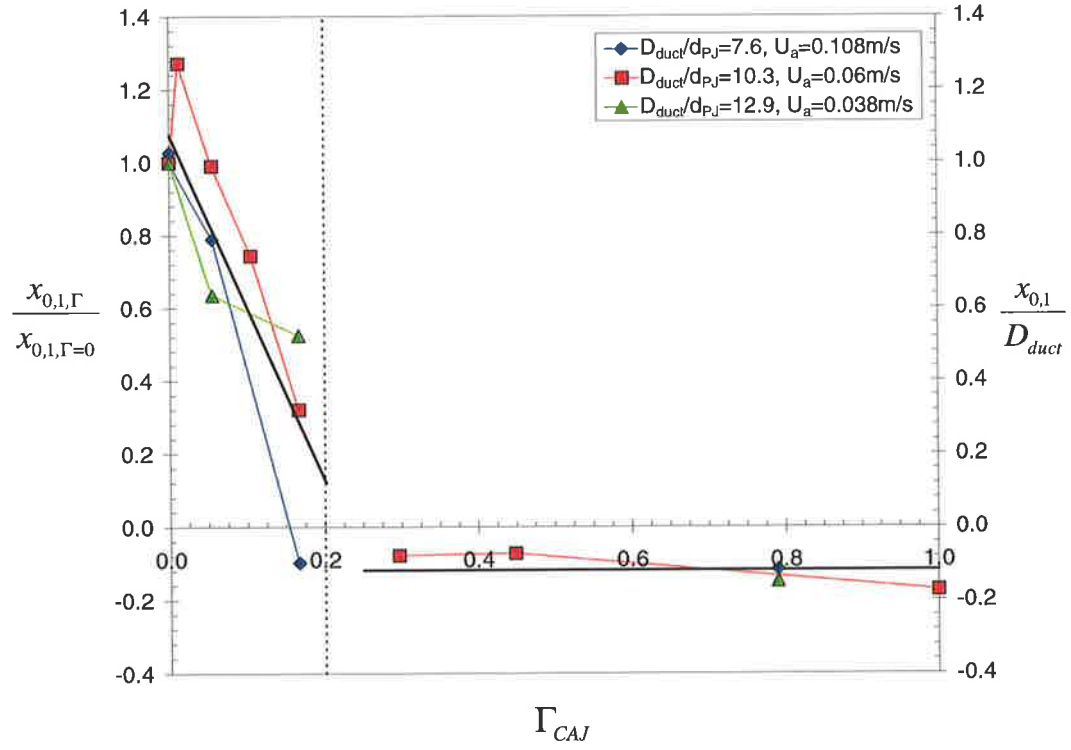

Figure 6-53. Variation in the far field concentration decay virtual origin, $x_{0,1}/D_{duct}$, with the momentum ratio Γ_{CAJ} for different confinements and constant mass flux ratio. The data for D_{duct}/d_{PJ}=7.6 and D_{duct}/d_{PJ}=12.9 are corrected for the effects of confinement, relative to D_{duct}/d_{PJ}=10.3 using Equation 6-27. For Γ_{CAJ}<0.2 the data is normalised to the value at Γ_{CAJ}=0. The bold lines indicate the line of best fit in the respective flow regime, the dashed line indicates the transition from PJ to CAJ dominated flow regime.

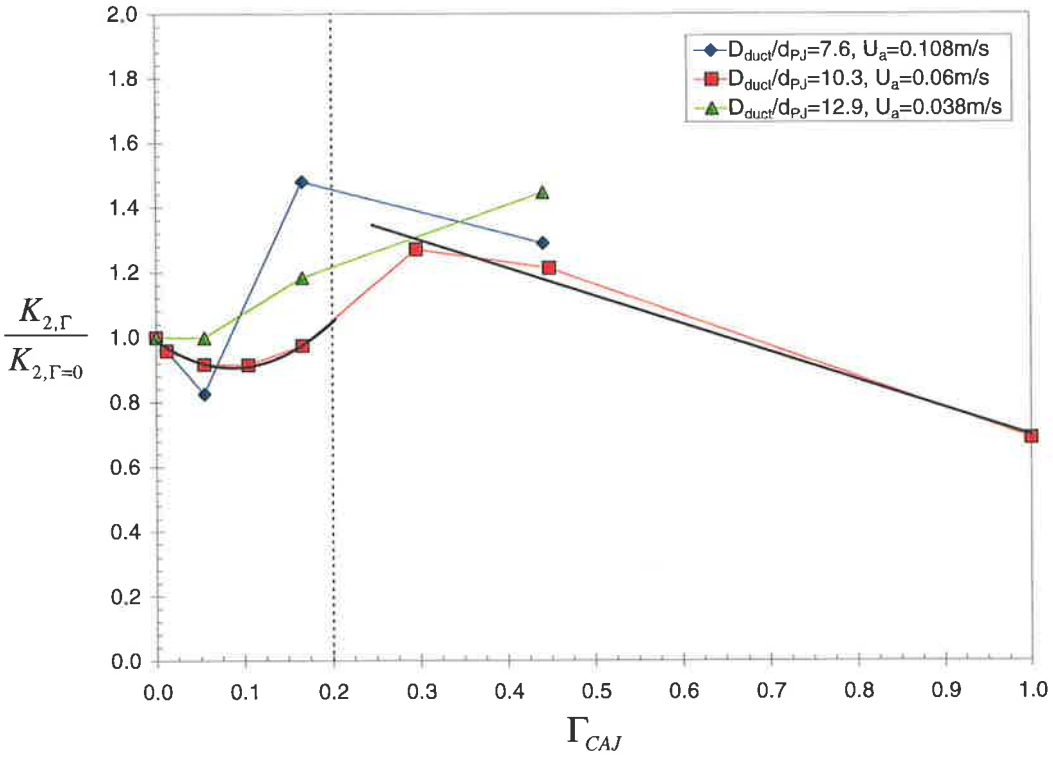

Figure 6-54. Variation in the far field jet spreading rate, K_2, with the momentum ratio Γ_{CAJ} for different confinements at constant mass flux ratio. The data for D_{duct}/d_{PJ}=7.6 and D_{duct}/d_{PJ}=12.9 are corrected for the effects of confinement, relative to D_{duct}/d_{PJ}=10.3 using Equation 6-28. For Γ_{CAJ}<0.2 the data is normalised to the value at Γ_{CAJ}=0. The bold line indicate the line of best fit in the respective flow regime, the dashed line indicates the transition from PJ to CAJ dominated flow regime.

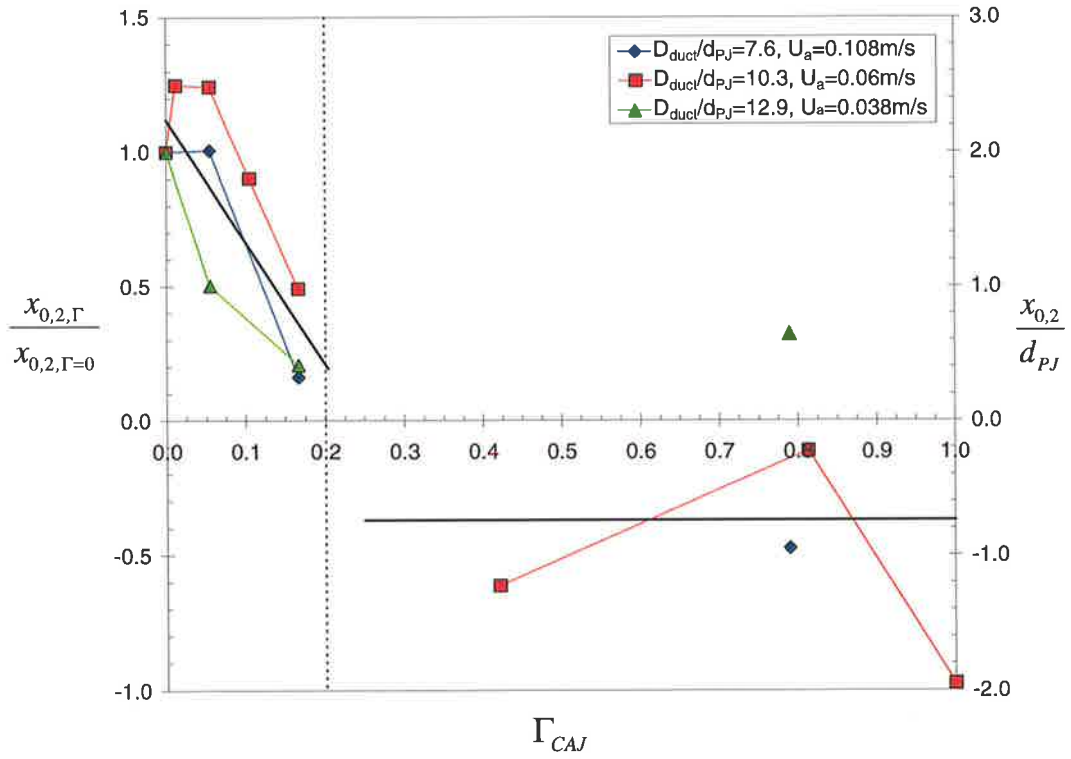

Figure 6-55. Variation in the far field jet spreading rate virtual origin, $x_{0,2}/d_{PJ}$, with the momentum ratio Γ_{CAJ} for different confinement ratios at constant mass flux ratio. The data for D_{duct}/d_{PJ}=7.6 and D_{duct}/d_{PJ}=12.9 are corrected for the effects of confinement, relative to D_{duct}/d_{PJ}=10.3 using Equation 6-29. For Γ_{CAJ}<0.2 the data is normalised to the value at Γ_{CAJ}=0. The bold lines indicate the line of best fit in the respective flow regime, the dashed line indicates the transition from PJ to CAJ dominated flow regime.

6.6.4 Application of the Proposed Model to the Scaling of Operating Rotary Kilns

The proposed model outlined in Section 6.6.2 has been developed based on jet concentration measurements relatively close to the exit of a PJ nozzle in an isothermal facility. The ultimate aim of this model however is to develop a criterion for the prediction of flame characteristics in an operating rotary kiln. This requires an understanding of the dominant physical mechanisms in order to allow the results from a small scale isothermal facility to be usefully related to a large-scale facility in which combustion occurs. The reader is referred to Section 1.3.4, which discusses the power of isothermal modelling as a useful design tool even though an isothermal model can never provide an exact representation of a reacting system.

Equation 6-24 to Equation 6-29, developed from an analysis of the present experimental results, contain the controlling non-dimensional parameters necessary to describe the concentration on the jet axis and the jet half-width and in turn the entire mean concentration field of the PJ nozzle in the far field of the jet. They reveal that the jet half-width contour is controlled, to a first order, by the mass flux ratio. The rate of concentration decay on the jet axis is controlled, to a first order, by the confinement ratio while the location of the virtual origin of the concentration decay is controlled by the velocity ratio. This combination of scaling relationships reveals the most important dimensionless ratios that should be maintained to enable the accurate modelling of the precessing jet burner to maintain reasonable similarity between the mixing characteristics at the laboratory scale and the industrial scale.

Mixing similarity, at least close to the nozzle exit, is achieved by maintaining the momentum ratio of the co-flow (secondary) fluid to jet fluid, G_a/G_0, the same in the model and combustion facility. As a consequence of this, the mass flux ratio, m_a/m_0, and velocity ratio, $U_a/U_{e\text{-}PJ}$, must be constant. However, for the mass flux ratio and velocity ratio to be constant when density ratios are different, the geometric confinement ratio, D_{duct}/d_{PJ}, must be distorted in the model. It can hence be shown that for constant mass-flux and velocity ratios, the geometric distortion is equivalent to the density correction of the modified Thring-Newby criterion proposed by Nathan *et al.* (1995). Hence the distorted nozzle diameter in the isothermal model is the diameter of a nozzle through which fluid of the density of the co-flowing fluid would flow, but with the same mass flow rate and the same momentum as that of the jet. The modified Thring-Newby scaling can be applied with reference to the PJ nozzle inlet diameter or the chamber diameter, but as the conditions are more clearly defined at the jet inlet chamber, in particular the jet density in a burner, and the PJ nozzle is sized on the basis of the required flow rate through the inlet diameter, this is considered the most appropriate location to apply the density correction, see Equation 6-34. The PJ nozzle chamber diameter, d_{PJ}, can then be calculated based on the optimal geometric ratio specified by Hill *et al.* (1992), see Table 2-1.

$$\left(\frac{D_{duct}}{d_{or}}\right)_{model} = \sqrt{\frac{\rho_a}{\rho_0}}\left(\frac{D_{duct}}{d_{or}}\right)_{plant} \qquad \textbf{Equation 6-34.}$$

where d_{or} is the PJ nozzle inlet diameter, ρ_a is the density of the secondary air in the plant and ρ_0 is the density of the fuel at the inlet orifice of the PJ nozzle.

A change in confinement ratio implies, via Equation 6-26, that the concentration decay rate also changes. The dimensionless concentration decay virtual origin, $x_{0,1}/D_{duct}$, will be maintained between the model and combustion facility if the velocity ratio is maintained, as shown by Equation 6-27. For a constant mass flux ratio, the present model demonstrates that the jet half-width contour, as defined by the parameters K_2 and $x_{0,2}/d_{PJ}$, is constant (see Equation 6-28 and Equation 6-29). Hence, similarity in the mean concentration field reduces to ensuring the concentration on the jet axis is identical at the same axial distance, normalised to the duct diameter, in the full-scale plant and model cases. The concentration on the jet axis in the isothermal model is given by Equation 6-35, and the concentration on the jet axis of the reference is combustion case is given by Equation 6-36:

$$\frac{1}{\xi_{model}} = \frac{1}{K_{1,model}}\left(x - \frac{x_{0,1,model}}{D_{duct}}\right) \qquad \textbf{Equation 6-35.}$$

$$\frac{1}{\xi_{plant}} = \frac{1}{K_{1,plant}}\left(x - \frac{x_{0,1,plant}}{D_{kiln}}\right) \qquad \textbf{Equation 6-36.}$$

Note that the present assessment does not consider the effect of combustion itself on the decay rate or mixing rate of a flame. This is beyond the scope of the present study. However, Jenkins (1998) has shown that a linear correction can be made to isothermal calculations of flame length based on a mean flame density, which is sufficiently accurate to solve most industrial problems and provide useful prediction of heat flux. Extending the present work to provide an analogous correction is recommended as useful future work.

As outlined above, based on Equation 6-24 to Equation 6-29 the virtual origin location, $x_{0,1}/D_{duct}$, is identical in the combustion and isothermal facilities as the velocity ratio is scaled to be constant in both cases. Hence equating Equation 6-35 and Equation 6-36, it can be shown that the concentration on the jet axis in the isothermal facility can be related to the concentration on the jet axis in the large-scale combustion facility by the expression:

$$\xi_{model} = \frac{K_{1,model}}{K_{1,plant}}\xi_{plant} \qquad \textbf{Equation 6-37.}$$

Equation 6-37 suggests that while alteration of the confinement ratio will maintain mixing similarity close to the nozzle exit where wall effects are not significant, it will not, on its own, be sufficient to ensure similarity in the mean concentration at a given location. To achieve complete similarity it is necessary to also distort the mixture fraction or the air-fuel ratio in the model. This can be achieved by changing the reference concentration used in the normalisation of the present PLIF experiments (i.e. normalising to a value other than ξ=1), or the stoichiometry in an acid-alkali simulation, as originally suggested by Hill (2000b), by an amount, κ, which is given by:

$$\kappa = \frac{K_{1,model}}{K_{1,plant}} \qquad \textbf{Equation 6-38.}$$

For flow only through the PJ nozzle in the plant and model, the modelling equations derived in Section 6.6.2 show that the concentration decay constants $K_{1,plant}$ and $K_{1,model}$ can be calculated from the confinement ratio, D_{duct}/d_{PJ},

using Equation 6-26. For flow through the precessing jet and central axial jet at a momentum ratio Γ_{CAJ}, the concentration decay constant must be modified using Equation 6-30.

Hence the scaling procedure to allow simulation of the mixing characteristics of a PJ nozzle in a full scale rotary kiln using a small-scale isothermal model is as follows:

1. Calculate the mass flux ratio of secondary fluid to jet fluid, m_a/m_0, in the combustion facility.
2. Calculate the density ratio of secondary air to fuel, ρ_a/ρ_0, in the combustion facility.
3. Calculate the confinement ratio, D_{duct}/d_{PJ}, in the combustion facility.
4. Calculate the predicted jet axis concentration decay constant in the combustion facility, $K_{1,plant}$, using Equation 6-26.
5. If a central axial jet is used, calculate the momentum ratio Γ_{CAJ} and hence the modification to $K_{1,plant}$ using Equation 6-30.
6. Calculate the confinement ratio, D_{duct}/d_{or} in the model using the modified Thring-Newby criterion, Equation 6-34.
7. Either specify the size and flow conditions of the PJ nozzle in the small scale model and hence calculate the duct diameter and co-flow velocity based on maintaining the mass flux ratio constant.
8. Or, alternatively to (7) specify the duct diameter and co-flow velocity in the small scale model and hence calculate the size and flow conditions of the PJ nozzle to satisfy the scaling criterion.
9. Calculate the concentration decay constant in the small scale model, $K_{1,model}$, using Equation 6-26.
10. If a central axial jet is used, calculate the momentum ratio Γ_{CAJ} and hence the modification to $K_{1,model}$ using Equation 6-30.
11. Calculate the reference concentration ratio in the model, κ, using Equation 6-38
12. Correct the measured concentration in the small scale model by κ and hence determine the concentration in the combustion facility.

The scaling procedure above has been used to calculate the geometry of a small-scale isothermal model to simulate the pilot-scale cement kiln presented in Table 6-8 and the industrial installations of the PJ burner presented in Appendix B as a sensibility check. The results, presented in Table 6-9 for the pilot-scale kiln and Appendix B for the industrial installations, show that the present experiments using the 38mm PJ nozzle in the 390mm duct (D_{duct}/d_{PJ}=10.3) and the 28mmPJ nozzle in the 290mm duct (D_{duct}/d_{PJ}=10.4) match the scaled conditions for the pilot-scale facility, which is to be expected as they were designed using the modified Thring-Newby criterion. The confinement ratio is reduced in all of the facilities, except the kiln at QAL. This is attributed to the very low secondary air temperature and velocity in this installation. The concentration reference ratio, κ, is reasonably close to 1 in most cases, indicating that the required correction for stoichiometry is not overly large. The moderate reduction in confinement for most of the facilities also implies that the aerodynamics are not significantly different at the different scales. The fact that κ is less than 1 in most cases suggests that the jet spread is wider in the reacting envi-

ronment, consistent with the effect of density differences between the fuel and air and with the results presented in Section 6.7.

Combustion Facility	Mass Flux Ratio (m_a/m_0)	Geometric Ratio (D_{kiln}/d_{PJ})	Velocity Ratio ($U_a/U_{e\text{-}PJ}$)	Predicted concentration decay constant (K_1)	Model			
					D_{duct}/d_{PJ}	D_{duct} (mm)	K_1	κ
IFRF	18.1	13.8	0.051	0.202	10.7	401.6	0.178	0.88

Table 6-9. The results of applying the present scaling procedure to the pilot-scale cement kiln simulator. The duct diameter for the model is calculated for a d_{PJ}=38mm PJ nozzle as used in the present experiments. Refer to Appendix B for details on the application of the scaling procedure to industrial installations of the PJ nozzle.

6.6.5 Application of the Proposed Model to the Prediction of Impingement

The location at which a flame impinges upon the walls of a rotary kiln is an important operational consideration in mineral processing industries as reducing conditions at the surface of the raw material can lead to severe reductions in product quality. It can also reduce the life of refractory bricks. Due to the rapid spread of the flame from a PJ burner, preventing flame impingement is a major concern in industrial installations and was the original motivation for incorporating the central axial jet into the burner design. To assess the ability of Equation 6-24 to Equation 6-29 to predict the location of impingement, measurements of the location of impingement in the current experimental facility are compared with the calculated locations based on applying the model equations to the flow conditions and geometry.

The proposed model, consisting of Equation 6-24 to Equation 6-29, can be used to predict the mean jet concentration in a given confined PJ flow configuration at any point if the radial distribution of mean concentration is known. An obvious starting point is to assume that it follows a Gaussian profile. Figure 6-23 demonstrates that, in general, this is an appropriate assumption. However, the assumption of a Gaussian distribution of concentration breaks down where wall effects become important. Hence to assess the ability of the present model to predict impingement, the "break point", the location where the jet edge departs from the free path jet due to the influence of the walls on the mixing, is examined. The "break point" was determined from the present experimental results by inspection of the jet edge, which was somewhat arbitrarily defined as the 2% concentration contour. In general, at low co-flow velocity ratios, the 2% contour breaks from the normal path of the jet some distance away from the wall which, from observation of the raw image sequences, appears to be due to recirculation bringing jet fluid upstream along the duct wall. As the co-flow velocity ratio increases, the location of the "break radius" gradually approaches the wall of the duct. The recirculation zone also diminishes in size until it disappears and the jet edge barely impinges on the duct wall in the imaged region, if at all. The effect of co-flow velocity ratio on the 2% concentration contour and the location of the break points is illustrated in Figure 6-56, for flow through the PJ nozzle only (ψ_{CAJ}=0%) at a confinement ratio of D_{duct}/d_{PJ}=10.3.

Within the imaged region of the present experiments, the radial location of the break point, normalised by the half-width of the duct, $r_{break}/0.5\times D_{duct}$, was found to correlate best with the reciprocal of the mass flux ratio, see Figure 6-57. A line of best fit through the data gives the relationship as:

$$\frac{r_{break}}{D/2} = -2.0761\left(\frac{\dot{m}_0}{\dot{m}_a}\right) + 0.9816 \qquad \textbf{Equation 6-39.}$$

The proposed modelling equations were assessed using the conditions in which flow was introduced through the PJ nozzle only (ψ_{CAJ}=0%) and in which impingement on the duct walls was observed within the imaged region. The jet axis bias from the nozzle centreline and any other slight imperfections in the experimental geometry such as deviations from concentricity were included in the model. The location at which the model 2% concentration contour reached the "break radius", r_{break}, was defined as the "break axial distance", x_{break}. The validity of using the model to calculate impingement was then tested by plotting the predicted axial break location against the mea-

sured break location, see Figure 6-58. Perfect correlation between the model and experiments would mean all data points collapsed onto the line $y=x$, indicated with the dashed line.

Figure 6-58 indicates that there is a discrepancy between the predicted location of the break axial distance and that measured in the present experiments. The deviation from perfect correlation is possibly due to incorrect incorporation of jet bias effects into the model and errors in determining the location of the measured break point, which was a subjective process in some cases. However, the most likely explanation for the difference is the departure of the radial mean concentration profile from a Gaussian distribution near the wall. This is also suggested by the radial profiles of mean concentration shown in Figure 6-23. Hence although the far field effects of co-flow, confinement and central axial jet are well described by the proposed modelling equations, the local effects of the duct walls on the jet concentration distribution are significant, so Equation 6-24 to Equation 6-29 should only be applied to predict the mean concentration upstream of the "break point", i.e. where wall effects are not significant. This implies that impingement is non-linear and not well described by Equation 6-24 to Equation 6-29, and hence accurate predictions of impingement should instead be made by physical modelling in a small-scale model designed according to the procedure outlined in Section 6.6.4. Equation 6-39 provides an easy and effective method of determining the break radius. Importantly it also indicates that the degree of recirculation and impingement induced by the flow from a PJ nozzle in a confined environment is controlled by the mass flux ratio.

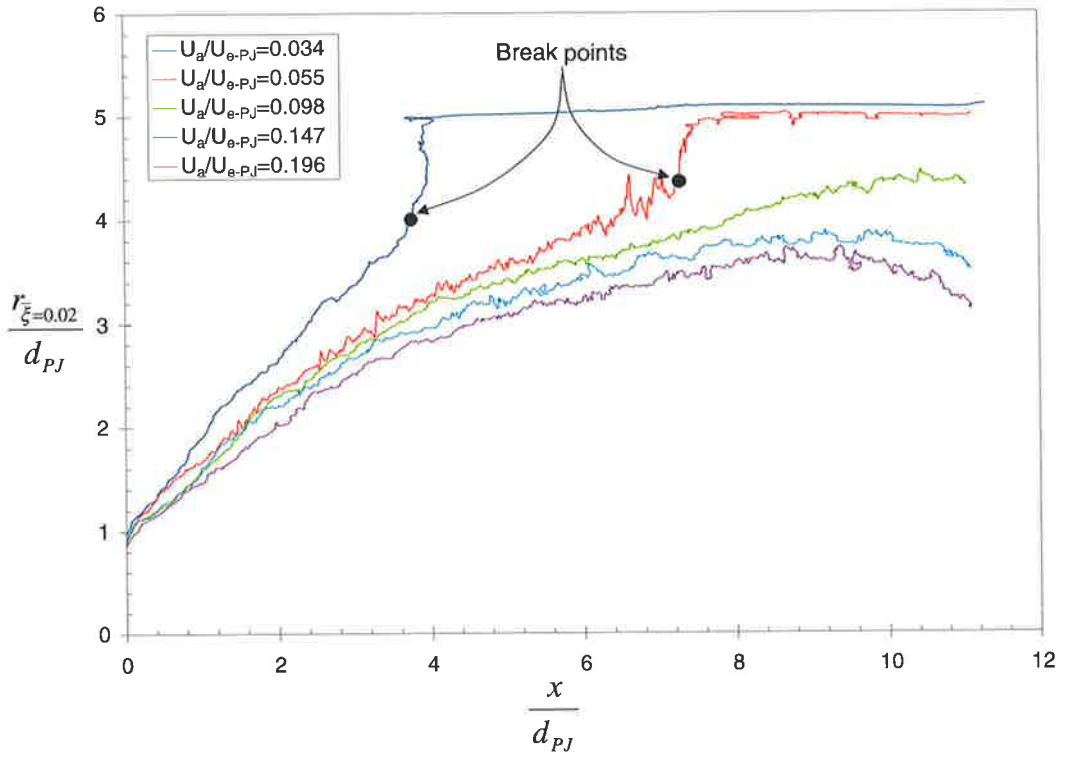

Figure 6-56. The effect of co-flow velocity ratio on the mean 2% jet concentration contour of the d_{PJ}=38mm PJ nozzle. Conditions: PJ flow only (ψ_{CAJ}=0%), Reynolds number=66,100, D_{duct}/d_{PJ}=10.3. The approximate location of the break points for the two jet conditions that touch the duct wall are also illustrated.

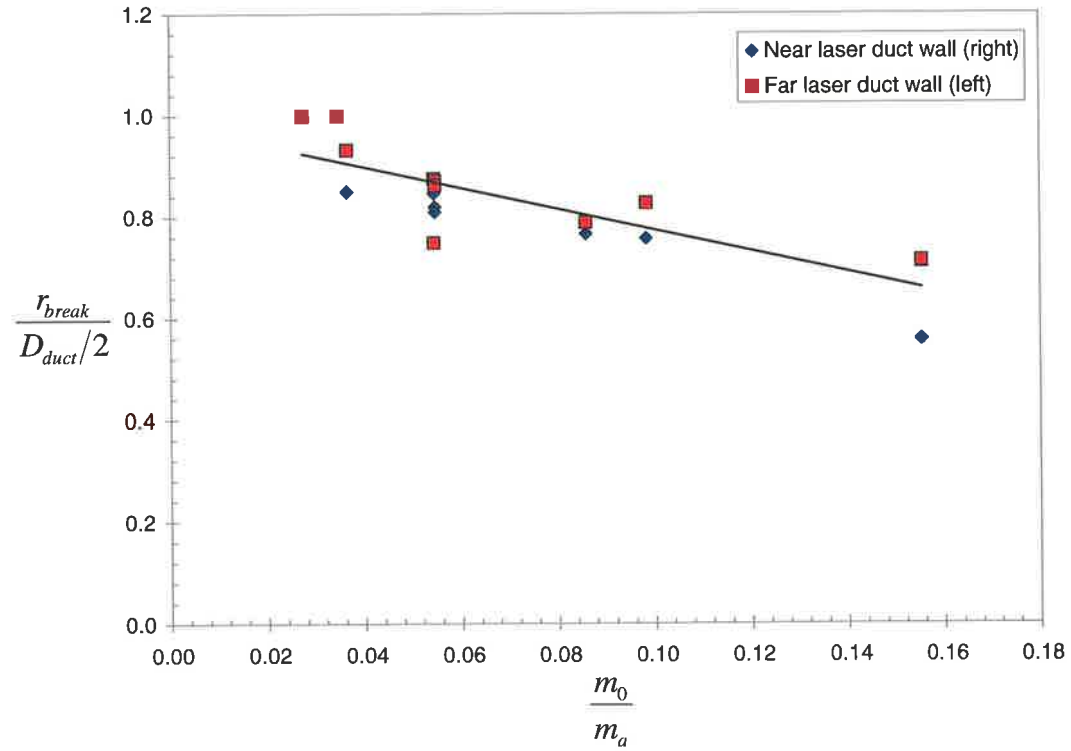

Figure 6-57. The radial location of the "break" point of the 2% jet concentration contour normalised to the duct half-width, $r_{break}/(D_{duct}/2)$ with the mass flux ratio of jet fluid to co-flowing fluid. Break points are shown for both the near laser side (right hand side of the images) and far laser side (left hand side of the images).

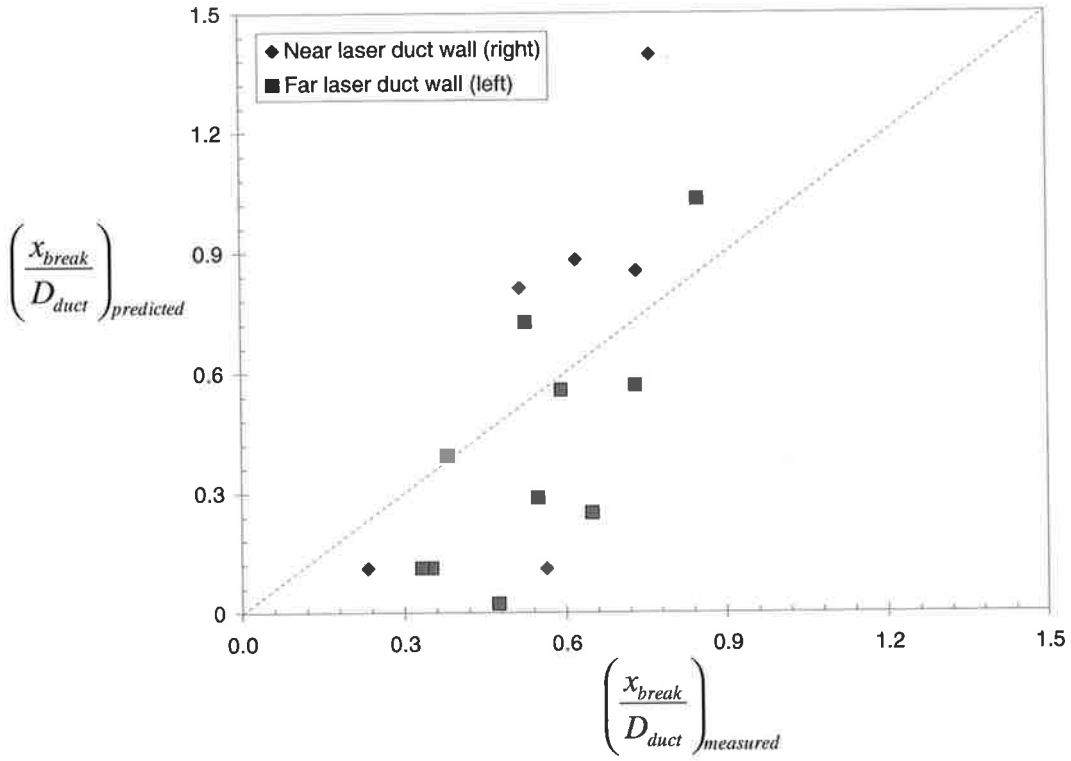

Figure 6-58. The correlation between the predicted axial location of the 2% jet concentration "break" point and the measured location of the break point from experimental data. Perfect correlation is indicated by the dashed line, $y=x$.

6.7 Comparison with Combustion Results

The main aim of the present experiments was to develop a scaling methodology for the confined combustion case of a precessing jet nozzle. Unfortunately, it is difficult to fully assess the validity of the present isothermal measurements by comparing them with the pilot-scale rotary kiln simulator measurements as the non-reacting experiments were a fundamental examination of the effects of co-flow and confinement with well defined boundary conditions which did not replicate the non-uniform co-flow conditions of the pilot-scale facility. In addition, the present experiments intentionally examined only the mixing close to the nozzle exit, while the pilot-scale combustion experiments examined the whole flame length in order to simulate the entire enclosed flame in a full scale industrial kiln. The pilot-scale simulator has limited measurement ports in the near-burner region, so the closest upstream in-flame measurement was located 0.82 kiln diameters downstream from the burner tip and the second closest port was at x/D_{duct}=1.76. The isothermal experiments were designed to investigate the effects of co-flow, confinement and central axial jet proportion and to ensure reasonable spatial resolution of each measurement volume. Hence the furthermost measurement location in the quantitative PLIF experiments is at x/D_{duct}=1.3 for the 390mm duct, which has been shown, using the proposed scaling procedure, to correspond most closely with the conditions required for an accurate, reduced scale isothermal model.

The pilot-scale combustion experiments described in Section 5.3.2 measured the in-flame species concentration of O_2, CO, CO2 and NO_x. From these measurements alone it is not possible to determine accurately the concentration of a conserved scalar, e.g. the mixture fraction of fuel Therefore, while a quantitative comparison of the isothermal mixture fraction measurements and the pilot-scale combustion data is not possible, no quantitative comparison can be made. Since the traverse performed at x/D_{duct}=0.82 is well within the main volume of the flame, see Section 5.3.2, where the in-flame temperatures are typically over 1700°C and the reaction rates are rapid, we would expect the mean concentration of CO to scale roughly with the mean fuel mixture fraction, if it is assumed that there is minimal transportation. Thus we would expect the "edge" of the flame to correspond roughly to the "edge" of the cold jet if the proposed scaling criterion is valid. For this reason the radial profiles of jet concentration measured in the isothermal quantitative PLIF experiments are compared with the radial profiles of CO from the in-flame measurements in Figure 6-59 and Figure 6-60.

One of the conditions for which CO profiles are available for comparison with isothermal results is that with all flow through the PJ nozzle (ψ_{CAJ}=0%), at x/D_{duct}=0.82. This data is presented in Figure 6-59. Figure 6-60 presents the measurements in the isothermal and pilot-scale combustion facilities for the same CAJ flow rate proportion, ψ_{CAJ}=25%, but slightly different momentum ratios, Γ_{CAJ}=0.17 for the isothermal jet and Γ_{CAJ}=0.25 for the pilot-scale flame. The CO measurements at different secondary air pre-heat temperatures and hence different co-flow velocity ratios are shown for the combustion experiments. The isothermal concentration measurements are shown at two different duct diameters and hence confinement ratios. The nozzle configuration and mass flux ratio of the isothermal experiments was constant and approximately the same as in the pilot-scale facility. Hence the co-flow velocity ratio is different for each of the duct diameters investigated. Of most interest are the CO measurements at 640°C secondary air pre-heat and the concentration measurements in the 390mm duct (D_{duct}/d_{PJ}=10.3). These conditions correspond to the same modified Thring-Newby parameter and hence satisfy the similarity conditions

described in Section 6.6.4. The isothermal measurements in the 490mm duct (D_{duct}/d_{PJ}=10.3) are also included as this condition maintains geometric similarity between the different scales.

Figure 6-60 shows there is remarkable similarity in the overall shape of the radial jet concentration and CO concentration profiles for the ψ_{CAJ}=25% PJ nozzle configuration. Both sets of curves show comparable spread and are approximately Gaussian in shape. The combustion profiles are reasonably similar at the different secondary air temperatures and also follow an approximately Gaussian distribution. Figure 6-59 shows that for the case of PJ flow only, the isothermal jet concentration profiles agree reasonable well for the different confinements. However, there appears to be a significant change in the combustion experiments due to the effect of secondary air temperature, although there is only limited data available to make this comparison. The effects of asymmetry in the co-flow velocity profile on CO measurements are also considerably more pronounced for this flow condition, although it is not clear why this should be detected at ψ_{CAJ}=0% and not also at ψ_{CAJ}=25%.

Figure 6-59 and Figure 6-60 suggest that the spreading rates of the reacting and isothermal experiments are significantly close for the model to be used as a useful predictor of impingement effects. The main difference between the reacting and non-reacting experiments appears to be a slightly increased jet spreading rate in the reacting environment compared with the isothermal experiments. The reference concentration ratio, κ, described in the scaling procedure in the previous section, was calculated to have a value of κ=0.88 for scaling of the pilot-scale combustion facility. The data, corrected for κ, in the 390mm duct is also shown in Figure 6-59 and Figure 6-60. This correction increases the jet spread in the isothermal facility slightly, but not enough to account for the observed difference with the combustion measurements. The remainder of this difference can be deduced to be attributable to the effect of density changes due to heat release with the flame, which reduces entrainment and increases the spreading of the flame, and are not included in the present form of the scaling procedure. Therefore, from the limited comparison possible of the present measurements, it appears that the isothermal experiments model the conditions in the confined, pilot-scale experiments reasonably although they appear to slightly under-estimate the spread.

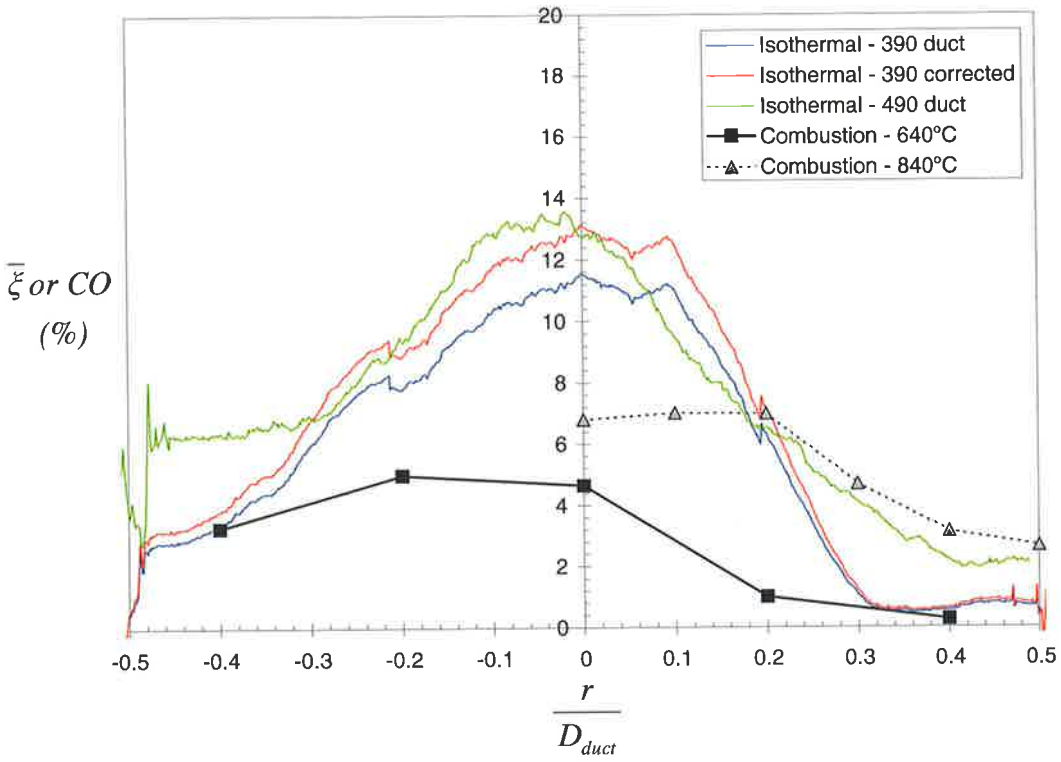

Figure 6-59. Comparison of isothermal jet concentration measurements and CO concentration in combustion experiments for PJ flow only (ψ_{CAJ}=0%). Isothermal conditions: Re_{PJ}=66,100, 390m duct: $U_d/U_{e\text{-}PJ}$=0.055 and D_{duct}/d_{PJ}=10.3, 490mm duct: $U_d/U_{e\text{-}PJ}$=0.035 and D_{duct}/d_{PJ}=12.9. Combustion conditions: 2MW fuel input, D_{duct}/d_{PJ}=13.5, 640°C pre-heat: $U_d/U_{e\text{-}PJ}$=0.050, 840°C pre-heat: $U_d/U_{e\text{-}PJ}$=0.063. The corrected isothermal concentration profile is based on a value of κ=0.88 for the reference concentration ratio, see Table 6-9.

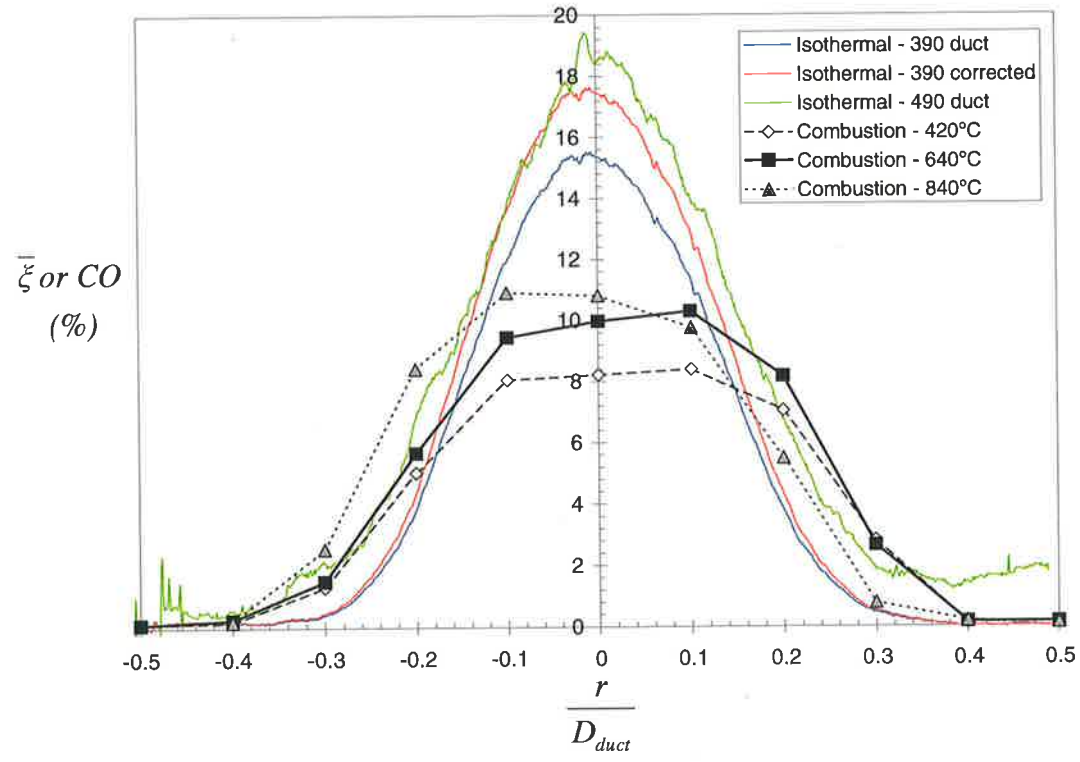

Figure 6-60. Comparison of isothermal jet concentration measurements and CO concentration in combustion experiments for the PJ nozzle with ψ_{CAJ}=25%. Isothermal duct and combustion conditions as for Figure 6-59, but incorporating CAJ proportion and with $U_d/U_{e\text{-}PJ}$=0.039 at 420°C pre-heat (for ψ_{CAJ}=0%).

6.8 Conclusions

A novel Planar Laser-Induced Fluorescence technique using a Nd:YAG laser with carboxy-dichlorofluorescein fluorescent dye has been used to investigate the effect of co-flow and confinement on the combined precessing jet and central axial jet flows. The PLIF technique has been validated by comparing the centreline and radial statistics of the concentration of dye issuing from a pipe jet with results reported in the literature for other passive scalar investigations. Analysis of the centreline concentration decay constant, K_1, and jet spreading rate, K_2, compared with previous simple jet measurements provides strong evidence that the Schmidt number is important in comparing the results of jet experiments conducted in gas or liquid phases. The difference between the validation pipe jet measurements and previous pipe jet measurements are hence attributed to Schmidt number effects and the effect of the ambient surrounding environment on entrainment. Overall, the pipe jet measurements are satisfactory compared with the previous data and therefore demonstrate the laser-dye system is appropriate for the quantitative measurement of passive scalar concentration from a jet.

The mixing from a PJ nozzle was investigated at constant nozzle conditions for a range of co-flow velocities, confinement ratios and central axial jet proportions. The respective effects are compared qualitatively using the instantaneous images and quantitatively using the inverse concentration on the jet axis, concentration half-width and intensity of jet concentration fluctuations on the jet axis. The instantaneous distribution of jet concentration from the PJ nozzle is characterised by the formation of large-scale flow structures which dominate the mixing field and have been observed previously in precessing jet flows. The quantitative measurements on the jet axis show that the PJ nozzle is characterised by a rapid decay in jet concentration within the first nozzle diameter downstream of the nozzle exit, followed by a more gradual and also approximately constant rate of decay. The PJ nozzle is also characterised by concentration fluctuations of almost the same magnitude as the mean concentration on the jet axis at a point close to the location where the decay rate changes abruptly, termed the "elbow point". Most of these results are similar to the observations of Newbold (1997). Comparison of the jet mixing statistics of the present measurements with those of Newbold (1997) suggests that differences in the nozzle inlet conditions are significant in the flow downstream from the nozzle chamber. The relative difference in mixing between the PJ flows and that of the jet through the inlet jet alone is consistent for the two experiments, although the absolute values differ significantly. Overall, the present results are consistent with those of Newbold (1997) and highlight the significantly different mixing characteristics of a PJ flow compared to that of a simple jet.

The effect of increasing the ratio of co-flow to the estimated PJ nozzle exit velocity is shown in the present investigation to result in a "stretching" of the "helical" flow structure created by the precessing motion of the jet exiting from the PJ nozzle. This acts to:

- reduce the mean concentration measured at a given point along the jet axis, but to have no effect on the rate of concentration decay in the far field;
- have only a slight effect upon the spreading rate of the jet, which is to reduce the spreading rate in the far field and move the virtual origin upstream;
- increase the peak and asymptotic value of the concentration fluctuation intensity along the jet axis, but to have no effect on the location of the peak; and to

- have minimal effect upon the distribution of concentrations along the jet axis in the far field, with a slight shift towards lower concentrations.

The effects of confinement on the scalar mixing from a PJ nozzle are demonstrated by increasing the duct diameter relative to the nozzle diameter. The effects of confinement are hence shown to:

- appear significant in instantaneous images only in the local region where the jet actually impinges on the duct wall, although the quantitative jet statistics indicate that the effect of confinement is more far reaching than this;
- have no effect upon the mean concentration along the jet axis if the axial distance is normalised by the diameter of the duct indicating that the duct diameter is the most appropriate length scale for the mean concentration;
- have no clear effect on the jet spreading rate at low co-flow velocity ratios, while at high co-flow velocity ratios the contours defining the jet spread at different confinements collapse onto a single profile;
- have no effect upon the intensity of jet concentration fluctuations along the jet axis, if the axial distance is normalised by the nozzle diameter, which is the appropriate because the main feature, the peak, is a function of the nozzle characteristics; and
- increase the range of concentrations measured along the jet axis in the far field and increase the value of the most probable jet concentration.

The proportion of jet flow through the central axial jet is shown to greatly influence the flow characteristics and so provides a wide degree of control over the mixing characteristics from a precessing jet nozzle. The qualitative observations and quantitative statistics of the effect of central axial jet proportion are shown to reflect the results of Chapter 3, in particular that at low momentum ratios, $\Gamma_{CAJ}<0.2$ (CAJ proportions $\psi_{CAJ}\leq 25\%$), the combined flow is in the precessing jet dominated regime and for $\Gamma_{CAJ}>0.23$ ($\psi_{CAJ}\geq 30\%$) the flow is in the CAJ dominated regime. Increasing ψ_{CAJ} is shown to:

- reduce the mean concentration measured at a given point on the jet axis for $0\leq \psi_{CAJ} \leq 25\%$ and increase the mean concentration for $\psi_{CAJ}\geq 30\%$,
- increase the rate of mixing on the jet axis in the far field only slightly in the PJ dominated flow regime, and more dramatically in the CAJ dominated flow regime, which is manifested as a decrease in the concentration decay constant, K_1, in direct proportion to the momentum ratio;
- reduce the mean concentration at the elbow point (the location of the change from rapid to gradual decay rate) until this feature disappears in the CAJ dominated regime and the concentration decays at a single, constant rate;
- have no clear or appreciable effect upon the asymptotic value of the intensity of jet concentration fluctuations;
- decrease the combined jet spreading rate in the far field in the PJ dominated regime with a minimum at $\psi_{CAJ}=20\%$ ($\Gamma_{CAJ}=0.12$) and cause a step change in the spreading rate in the transition to the CAJ dominated regime at $\Gamma_{CAJ}\approx 0.2\text{-}0.23$;
- decrease the magnitude of the characteristic peak in the intensity of jet concentration fluctuations for $0\leq\psi_{CAJ}\leq 25\%$ until in the CAJ dominated regime the peak is no longer present; and
- have a significant effect upon the distribution of concentration values on the jet axis in the far field, dependent on the dominant flow regime.

Hence the highest concentration at a given point on the jet axis and broadest range of jet concentration values in the far field are found to occur at ψ_{CAJ}=25%, which corresponds to a momentum ratio of Γ_{CAJ}=0.17. This configuration corresponds to a similar momentum ratio to that found to produce the highest heat release in the pilot-scale combustion experiments and the minimum inferred global strain rate in the unconfined combustion experiments.

The separate effects of co-flow, confinement and central axial jet on the mixing from a PJ nozzle have been combined to form an empirical model for the mean distribution of jet concentration from a PJ nozzle. The derived model is based on correlating the jet axis concentration decay constant, K_1, virtual origin, $x_{0,1}/D_{duct}$, spreading rate, K_2, and virtual origin, $x_{0,2}/d_{PJ}$, with non-dimensional parameters relating to the co-flow, confinement and CAJ proportion in the far field of the jet. Following the findings outlined above, the model for PJ only flow (ψ_{CAJ}=0%) is based on the following linear relations:

$$K_1 = 0.00774\left(\frac{D_{duct}}{d_{PJ}}\right) + 0.0948 \qquad \textbf{Equation 6-40.}$$

$$\frac{x_{0,1}}{D_{duct}} = -3.386\left(\frac{U_a}{U_{e-PJ}}\right) - 0.3903 \qquad \textbf{Equation 6-41.}$$

$$\frac{1}{K_2} = 0.1138\left(\frac{m_a}{m_0}\right) + 4.8311 \qquad \textbf{Equation 6-42.}$$

$$\frac{x_{0,2}}{d_{PJ}} = -0.2240\left(\frac{m_a}{m_0}\right) - 5.7547 \qquad \textbf{Equation 6-43.}$$

The effects of the central axial jet on the mixing from a PJ nozzle are assumed to be independent of the effects of co-flow and confinement in the present model. Hence K_1, $x_{0,1}/D_{duct}$, K_2, and $x_{0,2}/d_{PJ}$ are correlated with the momentum ratio Γ_{CAJ} and the dominant flow regime by the following relations:

For $0<\Gamma_{CAJ}\leq 1$

$$\frac{K_{1,\Gamma}}{K_{1,\Gamma=0}} = -0.7699\,\Gamma_{CAJ} + 1.1136 \qquad \textbf{Equation 6-44.}$$

For $0<\Gamma_{CAJ}<0.2$:

$$\frac{x_{0,1,\Gamma}}{x_{0,1,\Gamma=0}} = -4.7341\,\Gamma_{CAJ} + 1.0753$$

For $0.23<\Gamma_{CAJ}\leq 1$:

$$\frac{x_{0,1,\Gamma}}{D_{duct}} = \frac{x_{0,1,\Gamma=0}}{D_{duct}} = -0.118 \qquad \textbf{Equation 6-45.}$$

For $0<\Gamma_{CAJ}<0.2$:

$$\frac{K_{2,\Gamma}}{K_{2,\Gamma=0}} = 11.028\,\Gamma^2_{CAJ} - 1.9294\,\Gamma_{CAJ} + 0.9909$$

For $0.23<\Gamma_{CAJ}\leq 1$:

$$\frac{K_{2,\Gamma}}{K_{2,\Gamma=0}} = -0.8599\,\Gamma_{CAJ} + 1.557 \qquad \textbf{Equation 6-46.}$$

For $0<\Gamma_{CAJ}<0.2$:

$$\frac{x_{0,2,\Gamma}}{x_{0,2,\Gamma=0}} = -4.5574\,\Gamma_{CAJ} + 1.1201$$

For $0.23<\Gamma_{CAJ}\leq 1$:

$$\frac{x_{0,2,\Gamma}}{d_{PJ}} = \frac{x_{0,2,\Gamma=0}}{d_{PJ}} = -0.74 \qquad \textbf{Equation 6-47.}$$

The modelling equations that describe the effects of co-flow and confinement on the mixing from a PJ nozzle, as outlined above, have been extended to the scaling of large-scale combustion installations of the PJ nozzle. The extension of the model is based on maintaining similarity of the jet mixing characteristics in the large-scale and laboratory isothermal facilities. This is achieved by maintaining the mass flux ratio of co-flowing fluid to jet fluid and distorting the geometric ratio of duct diameter the nozzle diameter according the density correction factor of a modified Thring-Newby criterion. However, due to the change in confinement ratio, a further correction is also required to correct for the different concentration decay constants, i.e. K_1, in the large-scale and laboratory isothermal facilities. The difference in decay rate is corrected for by a concentration reference ratio, κ, based on the ratio of K_1 in the model to K_1 in the combustion facility, which are both calculated according to the expression derived from the present experimental results, Equation 6-40 (with Equation 6-44 to account for the CAJ). The concentration reference ratio effectively distorts the stoichiometry in the model from that in the actual combustion plant. Hence, based on the empirical model derived from the present experiments, the procedure to accurately model the characteristics of a PJ nozzle in an operating rotary kiln using a small-scale isothermal facility is:

1. Calculate the mass flux ratio of secondary fluid to jet fluid, m_a/m_0, in the combustion facility.
2. Calculate the density ratio of secondary air to fuel (at the inlet orifice of the PJ nozzle), ρ_a/ρ_0, in the combustion facility.
3. Calculate the confinement ratio, D_{duct}/d_{PJ}, in the combustion facility.
4. Calculate the predicted jet axis concentration decay constant in the combustion facility, $K_{1,plant}$, using Equation 6-40.
5. If a central axial jet is used, calculate the momentum ratio Γ_{CAJ} and hence the modification to $K_{1,plant}$ using Equation 6-44.
6. Calculate the confinement ratio, D_{duct}/d_{or}, in the model using the modified Thring-Newby criterion:

$$\left(\frac{D_{duct}}{d_{or}}\right)_{model} = \sqrt{\frac{\rho_a}{\rho_0}}\left(\frac{D_{duct}}{d_{or}}\right)_{plant} \qquad \textbf{Equation 6-48.}$$

7. Either specify the size and flow conditions of the PJ nozzle in the small scale model and hence calculate the duct diameter and co-flow velocity based on maintaining the mass flux ratio constant, or
8. Alternatively to (7), specify the duct diameter and co-flow velocity in the small scale model and hence calculate the size and flow conditions of the PJ nozzle to satisfy the scaling criterion.
9. Calculate the concentration decay constant in the small scale model, $K_{1,model}$, using Equation 6-40.
10. If a central axial jet is used, calculate the momentum ratio Γ_{CAJ} and hence the modification to $K_{1,model}$ using Equation 6-44.
11. Calculate the reference concentration ratio in the model, κ, using the expression:

$$\kappa = \frac{K_{1,\,model}}{K_{1,\,plant}} \qquad \textbf{Equation 6-49.}$$

12. Correct the measured concentration in the small scale model by κ and hence determine the concentration in the combustion facility.

This scaling procedure was used to calculate the geometry and flow conditions required to model the pilot-scale combustion facility used in Chapter 5 and industrial installations of the PJ nozzle. The results are consistent with the observations of the present experiments and within the range of reasonably expected values, suggesting the scaling procedure is appropriate for the modelling of precessing jet burners in large-scale rotary kilns with a small-scale isothermal experimental facility. A comparison of the mean jet concentration in the present experiments with the profiles of CO concentration measured in the pilot-scale kiln simulator test facility at the same axial location indicates remarkable qualitative agreement between the present isothermal measurements and the combustion measurements, providing more evidence for the validity of the proposed scaling procedure.

While the proposed scaling procedure provides a means to calculate the conditions of reduced scale experiments, the modelling equations have limited validity when applied to the mathematical prediction of jet impingement on the duct walls. This was demonstrated by comparing the measured location where wall effects become important from the PLIF experiments with the location calculated by the modelling equations. The radial location where wall effects on the jet become significant was found to correlate with the mass flux ratio, indicating this also controls the degree of recirculation induced by the flow from a PJ nozzle. The poor correlation between the predicted and measured locations is attributed to the radial mean concentration profile departing from the assumed Gaussian distribution close to the wall. Hence the accuracy of the modelling equations are not suitable for mathematically predicting local effects close to the duct walls and should only be applied within the region upstream of the point of impingement. This implication has no effect upon the validity of the physical modelling procedure for the precessing jet nozzle. Indeed, accurate prediction of impingement must be determined instead by physically modelling the kiln geometry and conditions in a small-scale model designed according to the procedure outlined above.

The present quantitative PLIF technique has enabled the effects of co-flow, confinement and central axial jet on the mixing from a PJ nozzle to be determined. The effect of the central axial jet has shown that, consistent with previous experiments, the momentum ratio, $\Gamma_{CAJ}=G_{CAJ}/(G_{PJ}+G_{CAJ})$, controls the mixing characteristics of the combined flows and that two broad types of flow regime exist depending on the momentum ratio and hence the proportion of flow through the CAJ. The CAJ experiments have also shown that unique mixing conditions are associated with the momentum ratio corresponding to the maximum heat release measured in the combustion experiments. The open flame experiments suggested that the maximum heat release and minimum emissions occurred for a flow configuration with a momentum ratio in the range $0.19\leq\Gamma_{CAJ}<0.36$. The confined pilot-scale combustion experiments demonstrated that the maximum heat transfer occurs for a momentum ratio in the range $0.11\leq\Gamma_{CAJ}<0.25$. The present isothermal experiments demonstrated that a flow configuration with $\Gamma_{CAJ}=0.17$ has the highest mean jet concentration and broadest range of concentration values on the jet axis in the far field of any PJ-CAJ combination investigated. This suggests that these mixing conditions are associated with the maximum heat release and minimum NO_x emissions.

Based on Equation 6-40 and Equation 6-41, it can be shown that the maximum mean concentration on the jet axis of the PJ nozzle is achieved at the momentum ratio that defines the transition of the virtual origin location, $x_{0,1}$, from being linearly proportional to Γ_{CAJ} to a constant value. This corresponds to a momentum ratio of $\Gamma_{CAJ}=0.227$. The momentum ratio defining the virtual origin transition is similar to the value determined from the flow visual-

isation experiments that defines the transition from PJ dominated flow regime to CAJ dominated flow regime, Γ_{CAJ}≈0.2-0.23. Hence for the present nozzle configuration, the mixing conditions that optimise the combustion characteristics of a combined precessing jet and central axial jet burner occur at the maximum momentum ratio that still produces a flow that can be characterised as precessing jet dominated, which is estimated to be within the range $0.17 \leq \Gamma_{CAJ} \leq 0.23$.

Chapter 7

Conclusions and Further Work

7.1 Conclusions

The flow from a novel, self-excited precessing jet flow, in combination with a simple jet flow, has been examined under reacting and non-reacting conditions to further the understanding of the physical mechanisms by which the control and optimisation of heat transfer and pollutant emissions from natural gas burners for rotary kilns can be achieved. The precessing jet-simple jet nozzle has been shown to provide continuous control of mixing characteristics such as the spread angle, decay rate and probability distribution of concentration. The wide variation in mixing conditions has been found to correspond to a wide variation in combustion characteristics such as radiation, heat transfer and pollutant emissions. The effects of co-flow and confinement on the mixing and combustion characteristics of the precessing jet flow have also been examined in detail. Hence the mixing characteristics corresponding to the maximum heat transfer and minimum emissions of gas-fired burners for rotary kiln applications have been determined, the conditions under which the precessing jet nozzle produces such mixing characteristics have been quantified and a scaling procedure to relate the results of small-scale isothermal mixing experiments using a precessing jet nozzle to operating rotary kilns has been developed. High quality quantitative measurements of the scalar concentration field from a PJ nozzle have also been obtained which can be used to validate a numerical method for simulating the flow from precessing jet, if and when developed in the future. The overall conclusions of the research program are presented in the context of these outcomes.

7.1.1 Control of Mixing and Combustion by Combined Precessing and Shaping Jet Flows

7.1.1.1 Qualitative Description of the Control of Mixing Characteristics

The control of mixing characteristics from a combined Precessing Jet (PJ) and shaping jet nozzle was investigated by conducting isothermal experiments in water. Isothermal techniques were used to allow a more detailed examination of the interaction between a shaping jet and a precessing jet than is possible in flames. A two-colour Planar Laser-Induced Fluorescence (PLIF) flow visualisation technique was used to investigate the effectiveness of different shaping jets in controlling the mixing characteristics. A quantitative PLIF technique was used to measure the concentration of jet fluid and quantify the separate effects of co-flow, confinement and a specific type of shaping jet, the Central Axial Jet (CAJ), on the mixing from a precessing jet nozzle.

The two-colour flow visualisation experiments showed clearly that the two jet flows interact strongly and merge. The initial scale of the largest turbulent motions in a combined precessing jet and axial jet flow can be controlled by altering the proportion of flow through the PJ and shaping jet. The proportion of mass flow rate through the shaping jet, relative to the total flow through both jets, has been denoted $\psi_{shaping}$. However, a semi-quantitative technique for determining the spread angle of the combined flows within the first 3 chamber diameters of the nozzle exit demonstrated clearly that the jet spread, and hence the size of the largest scale motions, is controlled by the ratio of shaping jet momentum to combined jet momentum, $\Gamma_{shaping}=G_{shaping}/(G_{PJ}+G_{shaping})$. The flow visualisation results indicate that within the range $0<\Gamma_{shaping}<0.6$, to a first order, the jet spreading rate decreases in direct proportion to this momentum ratio. For momentum ratios greater than 0.6 the jet spreading rate is approximately constant and is about the same as that of the shaping jet on its own.

As a source of high momentum, an axisymmetric simple jet is shown to require a much smaller proportion of the total flow to produce a significant change in the flow characteristics of the precessing jet compared to an annular shaping jet of typical dimensions. Therefore a simple jet is considered the most effective form of shaping jet. The flow visualisation results also show that the effectiveness of the simple shaping jet depends upon the relative locations of the simple and precessing jet exit. Hence it is demonstrated that a central axial jet located in the centre-body of the PJ nozzle with a relatively protrusion length from the centre-body of one CAJ diameter or less is the most effective means for controlling the mixing characteristics of the combined flow from a PJ nozzle.

The flow visualisation image sequences of the combined PJ and CAJ flows show that a broad spectrum of flow characteristics can be generated, from those typical of a precessing jet flow to those typical of a simple jet flow. For momentum ratios in the range $0\leq\Gamma_{CAJ}\leq0.2$ (corresponding to low ψ_{CAJ}), the combined flow field visually appears to have the same characteristics as the flow from the precessing jet on its own. Hence the flow field is described as "precessing jet dominated". For momentum ratios in the range $0.23\leq\Gamma_{CAJ}\leq1$, the flow visually appears dominated by the features of the central axial jet.

7.1.1.2 Statistical Quantification of the Control of Mixing by a Central Axial Jet

The quantitative PLIF experiments were used to determine the effect of variation in Γ_{CAJ} on the mixing of a conserved scalar by the combined flow. The results of these experiments are consistent with the results of the flow visualisation experiments. In particular, the effect of the CAJ was quantified in the far field of the jet, where the normalised radial profiles of mean concentration have become self-similar, by calculating the line of best fit between the inverse concentration and the normalised axial distance from the jet exit, expressed in general form in Equation 7-1, the line of best fit between the concentration half-width or jet spread and normalised axial distance, Equation 7-2, and the intensity of concentration fluctuations, $\xi_{rms}/\bar{\xi}$.

$$\frac{1}{\bar{\xi}} = \frac{1}{K_1}\left(x - \frac{x_{0,1}}{d}\right) \qquad \textbf{Equation 7-1.}$$

$$\frac{r_{1/2}}{d} = K_2\left(x - \frac{x_{0,2}}{d}\right) \qquad \textbf{Equation 7-2.}$$

Here x is the distance from the nozzle exit, d is a characteristic length scale, $\overline{\xi}$ is the mean concentration, $r_{1/2}$ is the radial location at which the mean concentration is half the centreline value and K_1, K_2, $x_{0,1}$ and $x_{0,2}$ are constants that depend on the mixing characteristics of the jet.

For flow only through the PJ nozzle, the instantaneous distribution of jet concentration is characterised by the formation of large-scale structures which dominate the mixing field. The mixing on the jet axis is characterised by a rapid decay in jet concentration in the first nozzle chamber diameter downstream from the nozzle exit. The rate of concentration decay then changes abruptly at a location termed the "elbow point". After the elbow point the concentration decay rate is constant and significantly lower than that upstream from the elbow point. The concentration decay constant, K_1, is approximately double the value of the decay constant of the jet from the inlet orifice with the chamber removed, indicating the concentration decay rate is halved. The spreading of the precessing jet only flow, as defined by the concentration half-width, follows a similar trend of a rapid increase in the first chamber diameter and a more gradual rate of spreading in the jet far field. Although the jet spreading rate, K_2, is only slightly greater than the value of the jet corresponding to the inlet orifice of the PJ nozzle with the chamber removed, the jet half-width contour is much larger than the simple jet flow as the location of the virtual origin is much further upstream. For precessing jet flow only, the mixing is characterised by concentration fluctuations of almost the same magnitude as the mean concentration on the jet axis close to the "elbow point". In the far field of the jet the concentration fluctuation intensity on the jet axis, $\xi_{rms\text{-}c}/\overline{\xi}_c$, asymptotes to a value of approximately 0.3, about 50% greater than the inlet jet on its own. Comparison of the jet mixing statistics of the present measurements with those of Newbold (1997) indicates that the inlet orifice conditions of the PJ nozzle are significant in affecting the mixing outside the nozzle chamber.

Consistent with the qualitative effect of the CAJ on the mixing of combined flow, the concentration decay constant, K_1, jet spreading rate, K_2 and virtual origin locations, $x_{0,1}$ and $x_{0,2}$ in the Equation 7-1 and Equation 7-2 are shown to controlled by the momentum ratio, Γ_{CAJ}, and change significantly in the PJ dominated flow regime and CAJ dominated flow regime. The quantitative PLIF experiments demonstrate that the effect of the CAJ on the mixing is approximately independent of the effects of co-flow and confinement. Hence increasing the momentum ratio and the proportion of flow through the CAJ, Ψ_{CAJ}, produces the following effects on the mixing of the combined jets:

- The concentration decay rate on the jet axis, measured downstream from the elbow point, increases in direct proportion to the momentum ratio. This translates to an increase in the concentration decay constant, K_1, with momentum ratio defined by the same relationship in both the PJ and CAJ dominated flow regimes, when normalised to the value for PJ flow only (Γ_{CAJ}=0, Ψ_{CAJ}=0%), see Equation 7-3. The maximum value of K_1 is shown to occur at the smallest proportion of CAJ flow investigated in the quantitative PLIF experiments, Γ_{CAJ}=0.01 and is a factor of 1.31 greater than that of the PJ on its own. The minimum value occurs for flow only through the CAJ, Ψ_{CAJ}=100% (Γ_{CAJ}=1) and is a factor of 0.44 times that of the PJ on its own.

For $0<\Gamma_{CAJ}\leq 1$

$$\frac{K_{1,\Gamma}}{K_{1,\Gamma=0}} = -0.7699\,\Gamma_{CAJ} + 1.1136 \qquad \textbf{Equation 7-3.}$$

- The location of the far field concentration decay virtual origin, normalised to the diameter of the confining duct, $x_{0,1}/D_{duct}$, moves upstream in direct proportion with the momentum ratio in the PJ dominated flow regime. In the CAJ dominated flow regime the virtual origin location is approximately the same as that of the central axial jet on its own. Hence, the location of the inverse concentration virtual origin, in a confined environment, relative to the value for PJ flow only (Γ_{CAJ}=0, Ψ_{CAJ}=0%) is given by:

For $0<\Gamma_{CAJ}<0.2$:
$$\frac{x_{0,1,\Gamma}}{x_{0,1,\Gamma=0}} = -4.7341\,\Gamma_{CAJ} + 1.0753$$

For $0.23<\Gamma_{CAJ}\leq 1$:
$$\frac{x_{0,1,\Gamma}}{D_{duct}} = \frac{x_{0,1,\Gamma=0}}{D_{duct}} = -0.118$$

Equation 7-4.

- The change in concentration decay rate and virtual origin location associated with an increase in the momentum ratio, Γ_{CAJ}, causes the mean concentration measured at a given point on the jet axis to increase in the PJ dominated flow regime, with the maximum value measured at Γ_{CAJ}=0.17. The maximum mean concentration on the jet axis of the PJ nozzle is shown to occur at the momentum ratio that defines the transition of the virtual origin location, $x_{0,1}$, from being linearly proportional to Γ_{CAJ} to a constant value, Γ_{CAJ}=0.227. Further increases in the momentum ratio in the CAJ dominated flow regime cause the mean concentration on the jet axis to decrease.
- The change in concentration decay rate and virtual origin location also causes the mean concentration measured at the elbow point to decrease with momentum ratio in the PJ dominated flow regime. In the CAJ dominated regime the elbow point is not observed and the concentration decays at a single, constant rate. Hence the PJ and CAJ dominated flow regimes can be distinguished by the presence of two distinct decay rates or a single decay rate respectively.
- The far field spreading rate, K_2, of the combined flow changes significantly depending on the dominant flow regime. The relationship between spreading rate and momentum ratio is approximately quadratic in the PJ dominated flow regime, with a minimum spreading rate at approximately Γ_{CAJ}=0.12. A step increase in spreading rate occurs at the transition from PJ to CAJ dominated flow regime at Γ_{CAJ}=0.2-0.23, after which the jet spreading rate decreases in proportion to the momentum ratio. Hence, the jet spreading rate, relative to the value for PJ flow only (Γ_{CAJ}=0, Ψ_{CAJ}=0%) is given by Equation 7-5. (Note that the relationship in Equation 7-5 is significantly different to that deduced from the flow visualisation experiments, principally because the quantitative PLIF experiments extended into the far field of the jet flow, while the region investigated in the flow visualisation experiments was limited to the near field of the combined flow).

For $0<\Gamma_{CAJ}<0.2$:
$$\frac{K_{2,\Gamma}}{K_{2,\Gamma=0}} = 11.028\,\Gamma^2_{CAJ} - 1.9294\,\Gamma_{CAJ} + 0.9909$$

For $0.23<\Gamma_{CAJ}\leq 1$:
$$\frac{K_{2,\Gamma}}{K_{2,\Gamma=0}} = -0.8599\,\Gamma_{CAJ} + 1.557$$

Equation 7-5.

- The location of the far field jet spreading rate virtual origin normalised to the diameter of the PJ nozzle chamber, $x_{0,2}/d_{PJ}$, moves upstream in direct proportion with the momentum ratio in the PJ dominated flow regime. In the CAJ dominated flow regime the virtual origin location is approximately the same as the central axial jet on its own. Hence, the location of the jet spread virtual origin, relative to the value for PJ flow only (Γ_{CAJ}=0, ψ_{CAJ}=0%) is given by:

For $0<\Gamma_{CAJ}<0.2$: $$\frac{x_{0,2,\Gamma}}{x_{0,2,\Gamma=0}} = -4.5574\,\Gamma_{CAJ} + 1.1201$$

For $0.23<\Gamma_{CAJ}\leq 1$: $$\frac{x_{0,2,\Gamma}}{d_{PJ}} = \frac{x_{0,2,\Gamma=0}}{d_{PJ}} = -0.74$$

Equation 7-6.

- The peak magnitude of the intensity of jet concentration fluctuations, $\xi_{rms\text{-}c}/\overline{\xi}_c$, decreases with increasing momentum ratio and ψ_{CAJ} in the PJ dominated flow regime, from a maximum value of about 0.7. In the CAJ dominated regime the peak in the concentration fluctuation intensity is not detected.
- The asymptotic value of the intensity of jet concentration fluctuations in the far field does not change significantly with central axial jet momentum ratio and remains approximately constant at $\xi_{rms\text{-}c}/\overline{\xi}_c$=0.3.
- The distribution of jet concentrations measured on the jet axis in the far field changes significantly depending on the dominant flow regime, from a maximum of $0.0375\leq \overline{\xi}_c \leq 0.4625$ for Γ_{CAJ}=0.17 to a minimum of $0.0375\leq \overline{\xi}_c \leq 0.3225$ for Γ_{CAJ}=1. The range of jet concentrations appears to increase with momentum ratio in the PJ dominated flow regime and decrease with momentum ratio in the CAJ dominated flow regime.

7.1.1.3 Control of the Combustion Characteristics

The control of combustion characteristics from a PJ nozzle by a central axial jet has been examined in small-scale unconfined flame experiments and in a 2MW pilot-scale cement kiln simulator facility. The unconfined flame experiments were intended as a relatively quick and easy method to measure the effect of central axial jet proportion, ψ_{CAJ}, and hence momentum ratio, Γ_{CAJ}, on the flame dimensions and so deduce implications regarding the expected effect on the radiant fraction, global residence time, global strain rate and thermal NO_x emissions of combined PJ and CAJ flames. Experiments in the pilot-scale cement kiln simulator were conducted to quantify the flame shapes, heat flux and NO_x emissions of the PJ nozzle with CAJ in a well controlled confined facility and compare their performance with that of a conventional burner. The issue of thermodynamic similarity between the experimental and the industrial scales was also addressed by comparing the results from the pilot-scale kiln simulator with those obtained in operating rotary kilns.

The results of the unconfined flame experiments demonstrate that the combined precessing jet and central axial jet flows allow a wide range of heat transfer and emission characteristics to be produced. Consistent with the isothermal mixing experiments, the results indicate that the momentum ratio, Γ_{CAJ}, controls the combustion characteristics of the combined precessing and central axial jets. In particular, the relationship of flame volume, length, width and intensity with momentum ratio is different for $\Gamma_{CAJ}<0.2$, the precessing jet dominated flow regime, and $\Gamma_{CAJ}>0.23$, the CAJ dominated flow regime. Photographs of the base of the entire flame demonstrated that the lift-off height and hence flame stability is not affected significantly by the change in dominant flow regime and is approximately constant for $0\leq \Gamma_{CAJ} \leq 0.57$.

In general, increasing the momentum ratio, Γ_{CAJ}, in the PJ dominated flow regime increases the spread and size of the structures within the flame, while in the CAJ dominated flow regime the spread and size of the structures decrease with increasing momentum ratio. Hence the spread and size of the flame are a maximum at a momentum ratio within the range $0.19 \leq \Gamma_{CAJ} \leq 0.36$. This trend is observed to be the case for the mean flame volume, flame length, width and signal intensity. Based on scaling relationships described in the literature, the measured variation in flame volume, length and width with momentum ratio were correlated with other properties of unconfined flames. Hence the radiant fraction and global residence time are expected to follow the same trend with momentum ratio as the flame volume and signal intensity. The emissions of thermally generated oxides of nitrogen are predicted to follow an inverse trend. Hence the radiant fraction and global residence time are expected to be a maximum at Γ_{CAJ}=0.19 and decrease with a further increase in momentum ratio. The emissions of thermally generated nitrogen oxides are predicted to follow an inverse trend such that the minimum thermal NO_x emissions occur at Γ_{CAJ}=0.19 and further increasing the momentum ratio increases the NO_x emission index.

The pilot-scale confined combustion experiments also demonstrated that varying the proportion of central axial jet fuel flow rate to total fuel flow rate provides good control of the flame characteristics. Increasing ψ_{CAJ} over the range 0-31% and hence Γ_{CAJ} from 0 to 0.32 pushes the peak heat flux further down the kiln by approximately one kiln diameter and also broadens the profile so that the peak heat flux is slightly reduced. The total heat release varies by approximately 3%, depending on ψ_{CAJ}, with the highest total heat flux appearing to be produced from flames with ψ_{CAJ}=15-25% (Γ_{CAJ}=0.11-0.25), consistent with the results of the unconfined flame experiments. The trends in the high momentum, multi-channel burners are consistent with previous predictions based on the Craya-Curtet parameter: the high momentum, low recirculation flame (Craya-Curtet parameter of 0.6, MCB-CC0.6) has poor heat transfer, low NO_x and high CO emissions and the high recirculation flame (Craya-Curtet parameter of 2.7, MCB-CC.7) has good heat transfer characteristics and good burnout. The general shape of the heat release profile of the MCB-CC2.7 flame is comparable with those of the PJ burner flames. However the shape of the heat release profile from the MCB-CC0.6 flame is significantly different, peaking some two kiln diameters further downstream. The peak heat flux from the MCB-CC2.7 flame was 7% lower than that of the PJ burner flames. Based on the measured wall surface temperatures, the heat transfer through the kiln walls shows that the PJ burner flames also typically produce 3% more total heat release than the MCB-CC2.7 flame over the first ten kiln diameters, and 8% more total heat release than the MCB-CC0.6 flame. Using the radiation measurements, the PJ burner flames produced 12% more total radiation heat release than MCB-CC2.7 flame and 20% more than the MCB-CC0.6 flame.

The raw measurements in the pilot-scale facility suggest, at first sight, that the PJ burner flames produce NO_x emissions comparable with those of the high recirculation conventional burner flame, MCB-CC2.7. When considered in isolation, this trend appears to be irreconcilable with the trends obtained in full scale operating rotary kilns, which have demonstrated a significant reduction in NO_x emissions with the installation of a PJ burner. However, a comparison of the relationship between the heat flux and NO_x emissions has demonstrated reasonable agreement to be found in the trends of the performance of the different burner systems when compared in the different facilities. A crude method of describing the relationship between heat flux and NO_x emissions is proposed by plotting total heat flux through the walls against total NO_x emissions. Extrapolation of the heat flux from the PJ burner to

equal that from the comparable typically good multi-channel burner flame, MCB-CC2.7, results in an apparent reduction in NO_x emissions of 35-50%, the same order as those measured in full-scale plant. This result demonstrates that different types of mixing within the flame can result in a different relationship between NO_x emissions and heat flux with all other parameters held constant, for both the pilot facility and the operating plant. This result also highlights the difficulties in maintaining thermal similarity between experimental facilities and operating plant. This is particularly true when comparing either different combustion systems, for example those with different mixing characteristics, or when the control of heat flux in the pilot facility is different from that in the operating plant.

7.1.2 Scaling of a Confined Precessing Jet Flow in a Co-Flow

The results of the present isothermal mixing investigations have illustrated that the flow from a PJ nozzle is complex, three-dimensional and transient in nature. This means it is not yet possible to mathematically model the scalar mixing from a confined precessing jet nozzle. Hence a scaling criterion for the PJ nozzle is required to relate small-scale model results to industrial rotary kiln applications so that the combustion characteristics can be optimised prior to installation. The most suitable pre-existing methods for scaling enclosed flames from conventional, momentum dominated burners, the Craya-Curtet and Becker parameters, assume the burner can be treated as a point source of momentum, based on the far field similarity of a simple jet. However, the results of the isothermal experiments have demonstrated that the nature of the mixing from a PJ nozzle is fundamentally different to that of a simple jet and does not depend solely on axial momentum to mix the jet and ambient fluids. Hence a different, validated scaling criterion for the PJ nozzle is necessary for the accurate prediction of combustion performance.

The proposed scaling model was developed based on dimensional arguments and an empirical correlation with measured results of the mixing of a passive scalar from a PJ nozzle.To assess independently the effects of confinement and co-flow for the development of a potential scaling model, the effects of different confining duct diameters and co-flow velocities on the mixing from a PJ nozzle operated at constant conditions were compared qualitatively using instantaneous images and quantitatively using the inverse concentration on the jet axis, concentration half-width and intensity of jet concentration fluctuations on the jet axis measured using the quantitative PLIF technique.

The effect of increasing the ratio of co-flow to the estimated PJ nozzle exit velocity is shown in the present investigation to result in a "stretching" of the "helical" flow structure created by the precessing motion of the jet exiting from the PJ nozzle. This acts to:

- reduce the mean concentration measured at a given point on the jet axis, but to have no effect on the rate of concentration decay in the far field;
- have only a slight effect upon the spreading rate of the jet, which is to reduce the spreading rate in the far field and move the virtual origin upstream;
- increase the peak and asymptotic value of the concentration fluctuation intensity along the jet axis, but to have no effect on the location of the peak; and to
- have minimal effect upon the distribution of concentrations along the jet axis in the far field, with a slight shift towards lower concentrations.

The effects of confinement on the scalar mixing from a PJ nozzle are investigated by increasing the duct diameter relative to the nozzle diameter. The effects of confinement were shown to:

- have the most significant effect on the instantaneous flow in the local region where the jet actually impinges on the duct wall, based on qualitative comparison of the PLIF images;
- have no effect upon the mean concentration along the jet axis if the axial distance is normalised by the diameter of the duct indicating that the duct diameter is the most appropriate length scale for the mean concentration;
- have no effect upon the fluctuation of jet concentration along the jet axis normalised to the mean concentration, if the axial distance is normalised by the nozzle diameter, which is appropriate because the main feature, the peak, is a function of the nozzle characteristics;
- have no clear effect on the jet spreading rate at low co-flow velocity ratios, while at high co-flow velocity ratios the contours defining the jet spread at different confinements collapse onto a single profile; and
- increase the probability distribution of concentration along the jet axis in the far field and increase the value of the most probable jet concentration.

The separate effects of co-flow, confinement and central axial jet on the mixing from a PJ nozzle have been combined to form an empirical model for the mean distribution of jet concentration from a PJ nozzle. The derived model is based on correlating the jet axis concentration decay constant, K_1, virtual origin, $x_{0,1}/D_{duct}$, spreading rate, K_2, and virtual origin, $x_{0,2}/d_{PJ}$, with non-dimensional parameters relating to the co-flow, confinement and CAJ proportion in the far field of the jet. Following the findings outlined above, the model for PJ only flow (ψ_{CAJ}=0%) is based on the following linear relations:

$$K_1 = 0.00774\left(\frac{D_{duct}}{d_{PJ}}\right) + 0.0948 \qquad \textbf{Equation 7-7.}$$

$$\frac{x_{0,1}}{D_{duct}} = -3.386\left(\frac{U_a}{U_{e-PJ}}\right) - 0.3903 \qquad \textbf{Equation 7-8.}$$

$$\frac{1}{K_2} = 0.1138\left(\frac{m_a}{m_0}\right) + 4.8311 \qquad \textbf{Equation 7-9.}$$

$$\frac{x_{0,2}}{d_{PJ}} = -0.2240\left(\frac{m_a}{m_0}\right) - 5.7547 \qquad \textbf{Equation 7-10.}$$

The modelling equations that describe the effects of co-flow and confinement on the mixing from a PJ nozzle, as outlined above, have been extended to the scaling of large-scale combustion installations of the PJ nozzle. The extension of the model is based on maintaining similarity of the jet mixing characteristics in the large-scale and laboratory isothermal facilities. This is achieved by maintaining the mass flux ratio of co-flowing fluid to jet fluid and distorting the geometric ratio of duct diameter the nozzle diameter according to the density correction factor of a modified Thring-Newby criterion. However, due to the change in confinement ratio, a further correction is also required to correct for the different concentration decay constants, i.e. K_1, in the large-scale and laboratory isothermal facilities. The difference in decay rate is corrected for by a concentration reference ratio, κ, based on the ratio of K_1 in the model to K_1 in the combustion facility, which are both calculated according to the expression derived

from the present experimental results, Equation 7-7. Equation 7-3 must also be applied to account for the effect of the central axial jet, if used. The concentration reference ratio effectively distorts the stoichiometry in the model from that in the actual combustion plant. Hence, based on the empirical model derived from the present experiments, the procedure to accurately model the characteristics of a PJ nozzle in an operating rotary kiln using a small-scale isothermal facility is:

1. Calculate the mass flux ratio of secondary fluid to jet fluid, m_a/m_0, in the combustion facility.
2. Calculate the density ratio of secondary air to fuel (at the inlet orifice of the PJ nozzle), ρ_a/ρ_0, in the combustion facility.
3. Calculate the confinement ratio, D_{duct}/d_{PJ}, in the combustion facility.
4. Calculate the predicted jet axis concentration decay constant in the combustion facility, $K_{1,plant}$, using Equation 7-7.
5. If a central axial jet is used, calculate the momentum ratio Γ_{CAJ} and hence the modification to $K_{1,plant}$ using Equation 7-3.
6. Calculate the confinement ratio, D_{duct}/d_{or}, in the model using the modified Thring-Newby criterion:

$$\left(\frac{D_{duct}}{d_{or}}\right)_{model} = \sqrt{\frac{\rho_a}{\rho_0}}\left(\frac{D_{duct}}{d_{or}}\right)_{plant} \qquad \textbf{Equation 7-11.}$$

7. Either specify the size and flow conditions of the PJ nozzle in the small scale model and hence calculate the duct diameter and co-flow velocity based on maintaining the mass flux ratio constant, or
8. Alternatively to (7), specify the duct diameter and co-flow velocity in the small scale model and hence calculate the size and flow conditions of the PJ nozzle to satisfy the scaling criterion.
9. Calculate the concentration decay constant in the small scale model, $K_{1,model}$, using Equation 7-7.
10. If a central axial jet is used, calculate the momentum ratio Γ_{CAJ} and hence the modification to $K_{1,model}$ using Equation 7-3.
11. Calculate the reference concentration ratio in the model, κ, using the expression:

$$\kappa = \frac{K_{1,\,model}}{K_{1,\,plant}} \qquad \textbf{Equation 7-12.}$$

12. Correct the measured concentration in the small scale model by κ and hence determine the concentration in the combustion facility.

This scaling procedure was used to calculate the geometry and flow conditions required to model the 2MW pilot-scale combustion facility and industrial installations of the PJ nozzle. The results are consistent with the observations of the present experiments and within the range of reasonably expected values, suggesting the scaling procedure is appropriate for the modelling of precessing jet burners in large-scale rotary kilns with a small-scale isothermal experimental facility. A comparison of the mean jet concentration in the present experiments with the profiles of CO concentration measured in the pilot-scale kiln simulator test facility at the same axial location indi-

cates remarkable agreement between the present isothermal measurements and the combustion measurements, suggesting that the spread of a flame is not very different from the spread predicted by the isothermal model.

While the proposed scaling procedure provides a means to calculate the conditions of reduced scale experiments, the modelling equations cannot be applied to the mathematical prediction of jet impingement on the duct walls. This was demonstrated by comparing the measured location where wall effects become important from the PLIF experiments with the location calculated by the modelling equations. The radial location where wall effects on the jet become significant was found to correlate with the mass flux ratio, indicating this also controls the degree of recirculation induced by the flow from a PJ nozzle. The poor correlation between the predicted and measured locations is indicative of the radial mean concentration profile departing from the ideal Gaussian distribution close to the wall. Hence the accuracy of the modelling equations are not suitable for mathematically predicting local effects close to the duct walls and should only be applied within the region upstream of the point of impingement. This implication has no effect upon the validity of the physical modelling procedure for the precessing jet nozzle. Indeed, accurate prediction of impingement must be determined instead by physically modelling the kiln geometry and conditions in a small-scale model designed according to the procedure outlined above.

7.1.3 Optimisation of the Combined PJ-CAJ Flows for Rotary Kiln Flames

The results of the isothermal and combustion experiments are consistent and demonstrate that the momentum ratio of shaping jet to the combined jet momentum, $\Gamma_{shaping}=G_{shaping}/(G_{PJ}+G_{shaping})$, controls the combined jet mixing and combustion characteristics. In particular, for the central axial shaping jet, the mixing field is characterised by two flow regimes in which the relationship between the momentum ratio, Γ_{CAJ}, and mixing and combustion properties is significantly different. The flow visualisation experiments indicated that for momentum ratios in the range $\Gamma_{CAJ}<0.2$ (corresponding to low Ψ_{CAJ}), the flow field can be characterised as precessing jet dominated, while at momentum ratios of approximately $\Gamma_{CAJ}>0.23$ the flow appears visually dominated by the features of the central axial jet.

The results of the unconfined combustion experiments suggest that the maximum global residence time and radiant fraction and minimum NO_x emissions of the combined PJ and CAJ nozzle occur at a momentum ratio in the range $0.19\leq\Gamma_{CAJ}<0.36$. The maximum ratio of flame width to length also occurs for the same conditions, implying that the strain rate at the flame tip is minimised at a flow condition within this momentum ratio. The confined, pilot-scale combustion experiments demonstrated that the total heat release was maximised at CAJ proportions of Ψ_{CAJ}=15-25%, corresponding to momentum ratios of Γ_{CAJ}=0.11-0.25. The results of the pilot-scale experiment did not allow the effect of the central axial jet on NO_x emissions to be fully quantified because of the interrelationship between the heat flux, wall temperatures and NO_x emissions. Nevertheless a relationship which accounts for the trend of increasing NO_x emissions with increasing heat flux suggests that the maximum heat flux and minimum NO_x emissions also occur at about the same momentum ratio. This finding is consistent with trends in operating plants in which increased heat flux is compensated by increased throughput to maintain similar product and wall temperatures.

The quantitative PLIF experiments showed that distinctive mixing characteristics are associated with the PJ and CAJ dominated flow regimes and the flow condition within the range of momentum ratios associated with the optimal combustion characteristics. At a momentum ratio of Γ_{CAJ}=0.17, the measured concentration on the jet axis at a given point is the highest and the range of concentrations on the jet axis was the largest of any jet from the combined flows investigated. At this condition, the profile of concentration fluctuation intensity profile does not peak close to the nozzle exit, characteristic of a CAJ dominated flow condition, but approaches the asymptotic concentration fluctuation intensity value more rapidly than any of the CAJ dominated flow conditions. This suggest that such mixing characteristics are desired from any natural gas burner for the maximum efficiency and lowest emissions in a rotary kiln.

For the precessing jet burner, the maximum mean concentration on the jet axis of the PJ nozzle is shown to occur at a momentum ratio of Γ_{CAJ}=0.227, as this defines the transition of the virtual origin location, $x_{0,1}$, from being linearly proportional to Γ_{CAJ} to a constant value. This momentum ratio is similar to the value determined from the flow visualisation experiments that defines the transition from PJ dominated flow regime to CAJ dominated flow regime, Γ_{CAJ}=0.2-0.23. Therefore the mixing conditions that produce the maximum heat transfer and minimum emissions from the combined precessing jet and central axial jet burner occur for the maximum momentum ratio within the PJ dominated flow regime, which is estimated to be within the range $0.17 \leq \Gamma_{CAJ} \leq 0.23$.

The mixing characteristics of the flow from the PJ-CAJ nozzle at a momentum ratio of Γ_{CAJ}=0.17, at the lower end of the range associated with the optimal combustion characteristics, have been measured in the quantitative PLIF experiments. The mixing statistics in the far field of the flow at this jet condition, scaled to simulate the mixing conditions in the pilot-scale experiments (total jet flow rate of 1400L/hr through a d_{PJ}=38mm chamber diameter PJ nozzle with a co-flow velocity of U_a=0.06m/s and a confining duct diameter of D_{duct}=390mm) for the maximum heat transfer and minimum NO_x emissions are hence:

- Centreline concentration decay constant normalised to the chamber diameter, K_1=0.151 (normalised to the inlet orifice diameter, K_1=7.83)
- Centreline concentration decay virtual origin relative to the PJ nozzle exit, $x_{0,1}/d_{PJ}$=-1.68 (normalised to the inlet orifice and inlet location, $x_{0,1}/d_{or}$=4.82)
- Jet spreading rate, K_2=0.128,
- Jet spreading rate virtual origin relative to the PJ nozzle exit $x_{0,2}/d_{PJ}$=-3.56 (normalised to the inlet orifice and inlet location, $x_{0,2}/d_{or}$=-4.70)
- Centreline concentration fluctuation intensity asymptote, $\xi_{rms\text{-}c}/\overline{\xi}_c$=0.279, with no peak in the near field,
- Range of concentrations on the centreline in the far field, normalised to the mean concentration, of $0.164 \leq \xi_c/\overline{\xi}_c \leq 2.048$,
- Range of concentrations on the centreline at a distance of 12 chamber diameters from the PJ nozzle exit of $0.0375 \leq \overline{\xi}_c \leq 0.4625$

The optimal conditions shown above indicate that the concentration decay rate, K_1, and jet spreading rate, K_2, are not too dissimilar from typical simple jet values. Hence, the main effect of the optimal precessing jet-central axial jet combination relative to the jet at the inlet to the nozzle chamber is to shift the location of the virtual origin loca-

tions, $x_{0,1}$ and $x_{0,2}$ and to increase the concentration fluctuations, which results in a higher mean concentration and a broader range of mixture fractions at a given axial location in the far field.

7.1.4 The Effect of Schmidt Number on Jet Mixing

A simple jet was also investigated in the isothermal quantitative PLIF experiments, principally to validate the technique by comparing the centreline and radial statistics of the concentration of dye issuing from a pipe jet with results reported in the literature for other passive scalar investigations. Separating the results of previous simple jet investigations according to the nozzle type (smooth contraction or pipe jet) and phase (liquid or gas) was shown to provide strong evidence that the Schmidt number (the ratio of the relative importance of turbulent transportation and molecular diffusion) has a significant, albeit secondary, effect on the mixing from a jet. Hence the results of the present pipe jet experiments, which indicated the jet is narrower and the concentration decay rate lower than previous pipe jet investigations, is attributed, at least in part, to the significant difference in Schmidt number when comparing mixing experiments conducted in water and in gases. The disparity between the present quantitative PLIF simple jet measurements and those of comparable investigations of pipe jets in water using a PLIF technique are attributed to real differences in the experimental arrangements, in particular to different boundary conditions of the surrounding ambient environment.

7.2 Recommendations for Further Work

7.2.1 Modelling the Confined PJ Nozzle

The present work has resulted in the development of a procedure for modelling the mixing characteristics of large-scale industrial installations of the PJ nozzle by use of reduced scale isothermal facilities. However, this study intentionally only investigated the region close to the nozzle exit in order to examine the effects of confinement, co-flow and central axial jet proportion on the mixing from a PJ nozzle at a fundamental level. Hence further experiments that examine a region corresponding to the entire flame length are required to test the validity of the proposed scaling procedure for modelling the entire flame. Experiments that investigate the entire flame length and accurately replicate the co-flow conditions would also provide the data necessary to compare the proposed scaling procedure with the in-flame and heat flux measurements from the pilot-scale rotary kiln simulator. A suitable technique for performing such an investigation is the acid-alkali flame modelling technique, as variation in the concentration reference ratio, κ, can be achieved by altering the stoichiometry of acid to alkali in the secondary fluid and jet fluid respectively. Such experiments could also investigate any correlation between the effects of heat release and the simulated flame length, as this is not incorporated into the present scaling procedure.

The equations that form the basis of the model proposed here imply that it is possible to calculate mathematically the mean concentration distribution from a PJ nozzle in a confined environment, given the flow conditions and geometry. The mathematical description of the mean concentration from a PJ nozzle could also be refined so that it can be incorporated into the heat transfer model of Jenkins and Moles (1981). The successful integration of the model equations into this heat transfer model would enable, for the first time, the mathematical prediction of heat flux profiles from a PJ nozzle in a rotary kiln installation. However, the present experimental work has shown that, in the region near the wall, the assumption of a Gaussian distribution of mean concentration is not appropriate, so the current modelling equations cannot be applied to predict concentration near the wall. Hence, if a mathematical prediction of impingement is desirable, further work or analysis of the present results is required so that the mean concentration can be accurately predicted in the region where wall effects are significant. This would enable the accurate calculation of the point of impingement and the mean concentration downstream from the location of impingement.

The present results demonstrate that the instantaneous flow from the PJ nozzle can depart significantly from the mean. This departure has been quantified by measurement of the concentration fluctuations. Hence a complete model of the mixing from the PJ-CAJ nozzle in a confined, co-flowing environment would benefit from including the fluctuating component of concentration into the present model. This is likely to have a significant effect upon heat transfer modelling and the prediction of impingement effects. Hence further work is required to correlate the concentration fluctuation intensity with co-flow, confinement and central axial jet proportion.

7.2.2 Optimising the PJ Nozzle Combustion Characteristics

The present work has shown that the optimal combustion characteristics from the PJ-CAJ nozzle are obtained with the maximum momentum ratio that generates a flow that can be characterised as precessing jet dominated, i.e. within the range $0.17 \leq \Gamma_{CAJ} \leq 0.23$. The present work has investigated the effect of Γ_{CAJ} on the concentration field from the PJ nozzle. Further work is recommended to measure the effect of Γ_{CAJ} on the velocity field from the PJ nozzle. This would provide information on strain rates and residence times within different regions of the combined flow field and hence further examine what unique mixing features are associated with a CAJ momentum ratio of $0.17 \leq \Gamma_{CAJ} \leq 0.23$. Velocity measurements in a laboratory scale flame would also be extremely valuable to correlate the mixing characteristics with the optimal combustion characteristics. Due to the transient and highly three dimensional nature of the flow from the PJ nozzle, a particle image velocimetry technique which instantaneously resolves the spatial distribution of two velocity components would be the most appropriate technique to pursue this goal. A characteristic global strain rate can also be measured using volume rendering, following Newbold *et al.* (1997), who adopted the technique of Mungal *et al.* (1991).

A basic form of swirl nozzle was included in the present quantitative PLIF research program. However, the results of this investigation, in which the swirl number was varied at constant confinement and co-flow velocity, have not been processed. It is highly desirable that these results be analysed with respect to the relevant scalar statistical information to compare the mixing characteristics with the precessing jet, and hence if similar optimal mixing characteristics to those determined for the PJ nozzle are detected in the swirling flow. These mixing characteristics should also be compared with the pilot-scale combustion results for further investigation of the correlation between mixing conditions and the optimal combustion requirements.

The present form of the CAJ momentum ratio, velocity ratio and Thring-Newby scaling are referenced to the inlet orifice of the PJ nozzle as the conditions are well defined at this point, while they are not at the exit of the nozzle. Phenomenologically, these ratios should be referenced to the exit conditions as it is physically more relevant to the interaction of with the CAJ. Velocity measurements to characterise the PJ nozzle exit conditions and derive a more appropriate form of the present momentum ratio and velocity ratio would improve the understanding and modelling of these processes greatly. (It is noted that the Ph.D. program of Mr. Chong Wong should provide such information.)

Comparison of the present experiments with the concentration measurements of Newbold (1997) has indicated the inlet conditions of the PJ nozzle may be significant on the downstream mixing. Further work is recommended to assess this effect for the optimisation of downstream mixing conditions for combustion and hence the desired inlet conditions to the PJ nozzle for the maximum heat transfer and minimum emissions.

Appendix A

Pilot-Scale In-Flame Species Concentration Measurements

A.1 Precessing Jet Only Flames (ψ_{CAJ}=0%)

A.1.1 640°C Secondary Air Pre-Heat Temperature

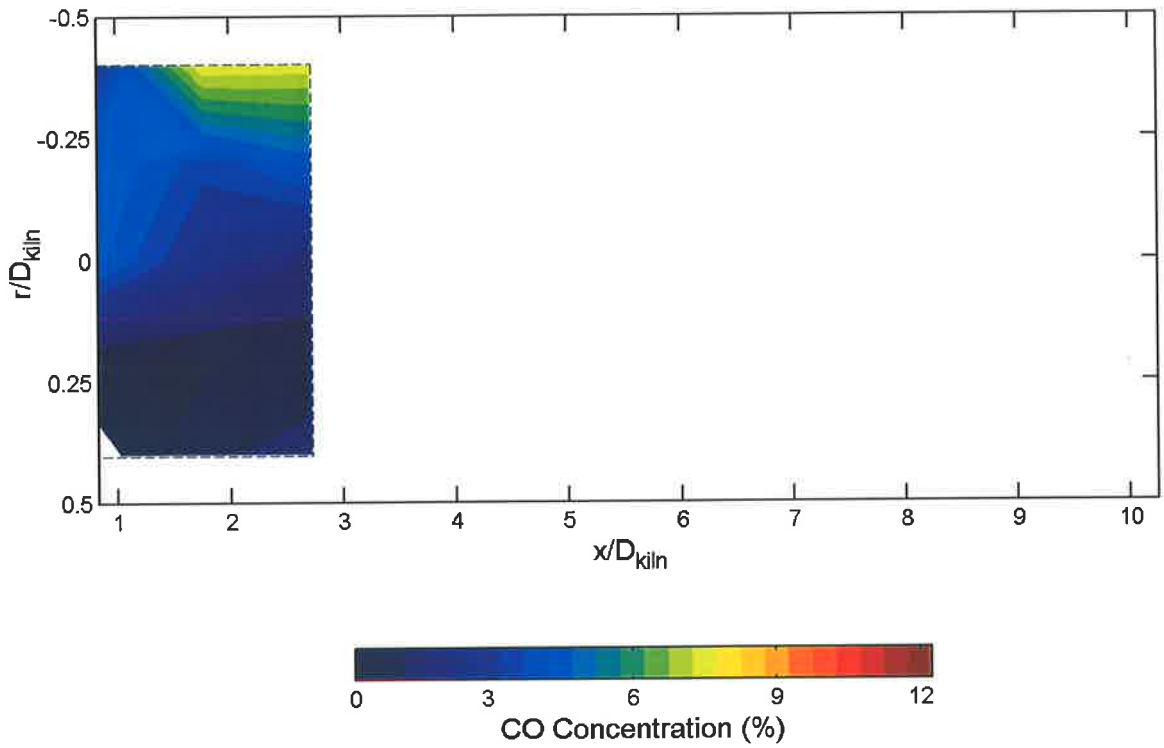

Figure A-1. Concentration contours of carbon monoxide measured in the pilot-scale kiln for the precessing jet burner with flow only through the PJ nozzle (ψ_{CAJ}=0%) at a secondary air pre-heat temperature of 640°C (PJ-ψ0-640 flame). Contours are in steps of 0.5% and the colour map is identical to that used for all the in-flame CO results. The dashed line indicates the boundary of the in-flame measurement region.

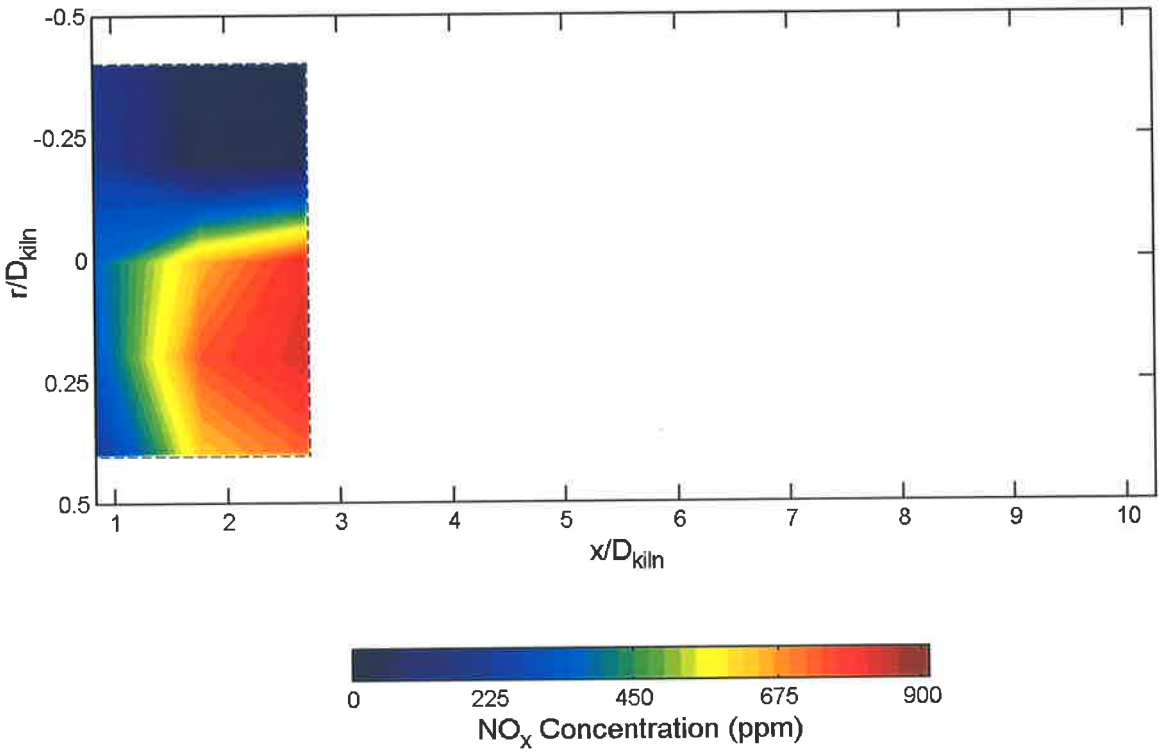

Figure A-2. Concentration contours of NO_x measured in thepilot-scale kiln for the precessing jet burner with flow only through the PJ nozzle (ψ_{CAJ}=0%) at a secondary air pre-heat temperature of 640°C (PJ-ψ0-640 flame). Contours are in steps of 25ppm and the colour map is identical to that used for all the in-flame NO_x results at 640°C pre-heat. The dashed line indicates the boundary of the in-flame measurement region.

A.1.2 840°C Secondary Air Pre-Heat Temperature

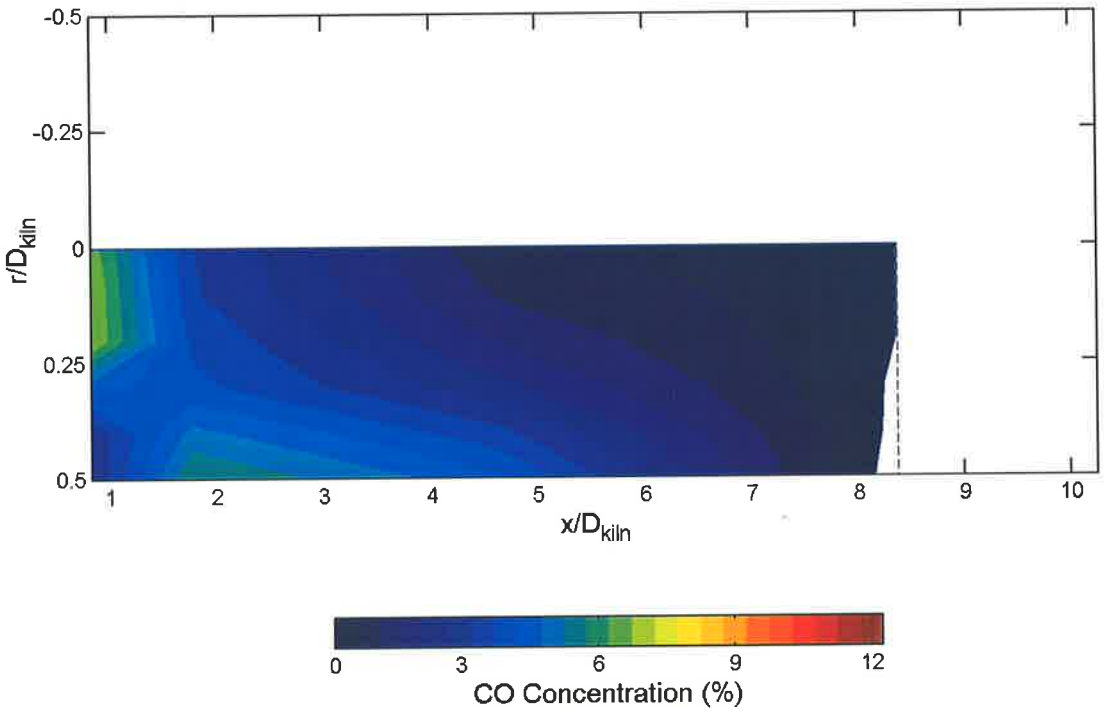

Figure A-3. Concentration contours of carbon monoxide measured in the pilot-scale kiln for the precessing jet burner with flow only through the PJ nozzle (ψ_{CAJ}=0%) at a secondary air pre-heat temperature of 840°C (PJ-ψ0-840 flame). Contours are in steps of 0.5% and the colour map is identical to that used for all the in-flame CO results. The dashed line indicates the boundary of the in-flame measurement region.

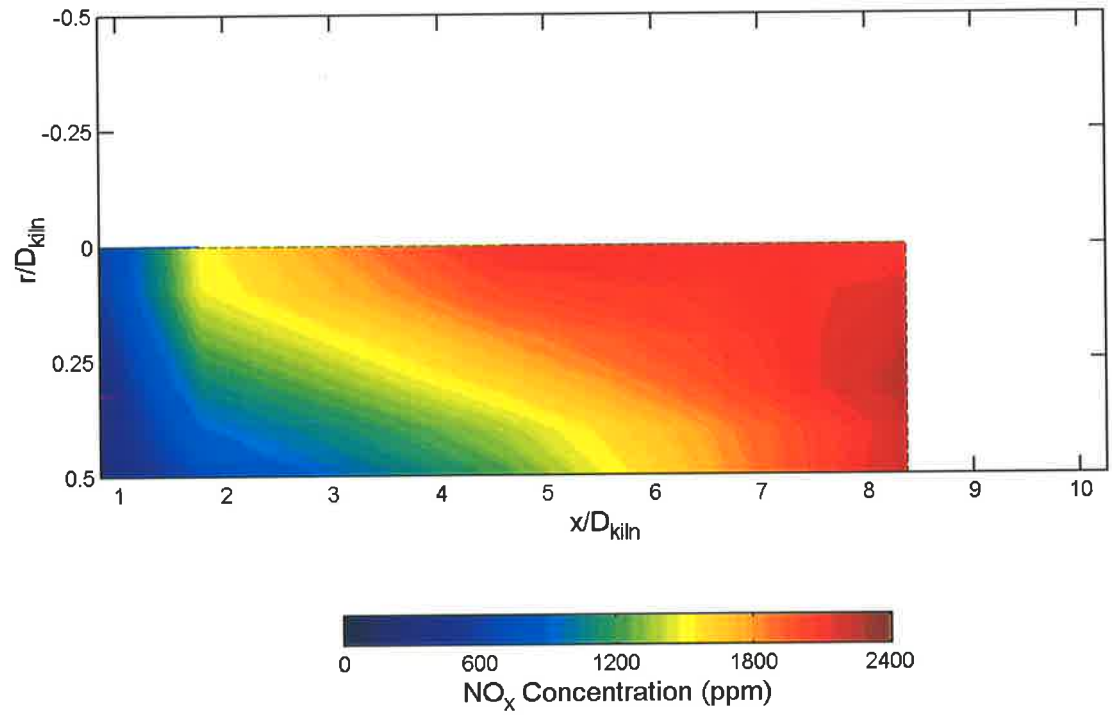

Figure A-4. Concentration contours of NO_x measured in the pilot-scale kiln for the precessing jet burner with flow only through the PJ nozzle (ψ_{CAJ}=0%) at a secondary air pre-heat temperature of 840°C (PJ-ψ0-640 flame). Contours are in steps of 25ppm, but the colour map is changed due to the higher NO_x concentrations at 840°C pre-heat. The dashed line indicates the boundary of the in-flame measurement region.

A.2 Precessing Jet with CAJ Flames (ψ_{CAJ}=25%)

A.2.1 420°C Secondary Air Pre-Heat Temperature

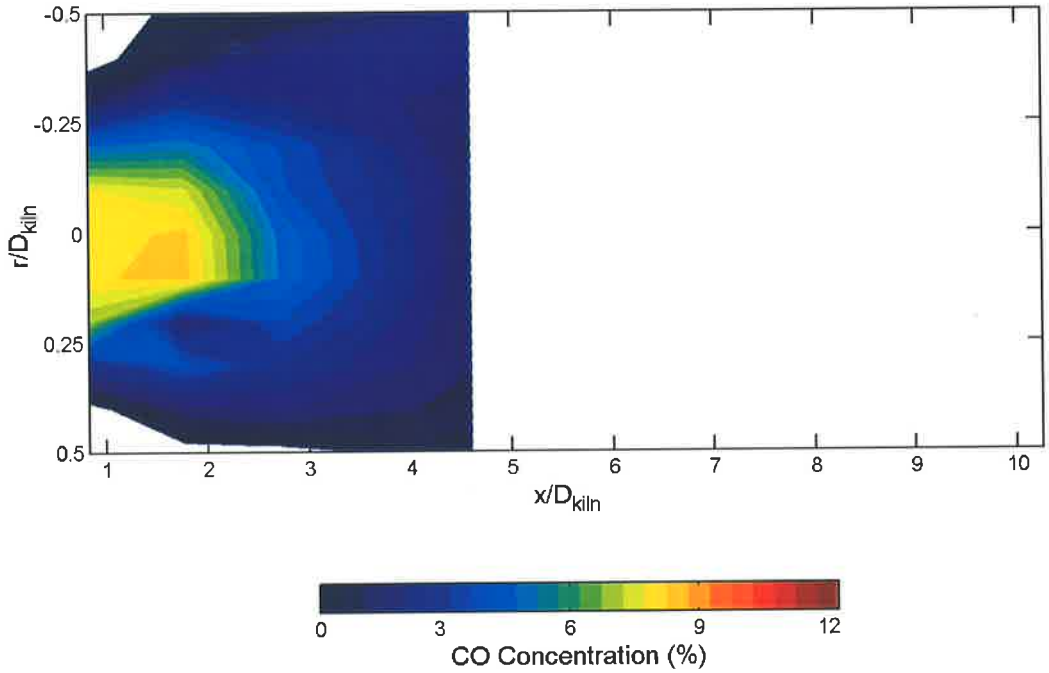

Figure A-5. Concentration contours of carbon monoxide measured in the pilot-scale kiln for the precessing jet burner with central axial jet (ψ_{CAJ}=25%, Γ_{CAJ}=0.25) at a secondary air pre-heat temperature of 420°C (PJ-ψ25-420 flame). Contours are in steps of 0.5% and the colour map is identical to that used for all the in-flame CO results. The dashed line indicates the boundary of the in-flame measurement region.

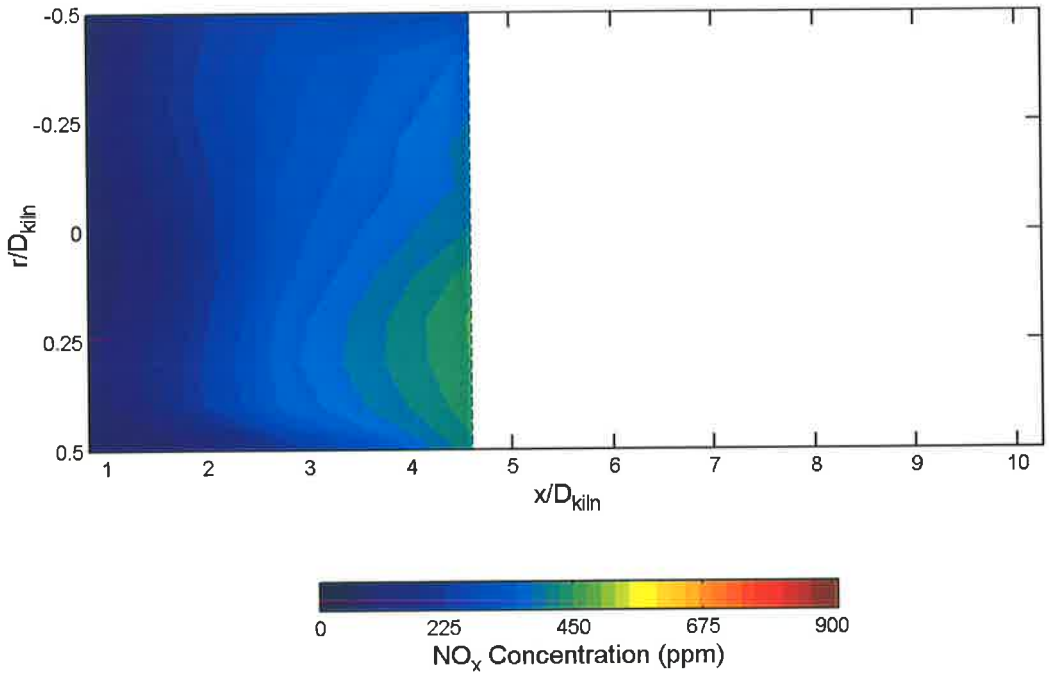

Figure A-6. Concentration contours of NO_x measured in the pilot-scale kiln for the precessing jet burner with central axial jet (ψ_{CAJ}=25%, Γ_{CAJ}=0.25) at a secondary air pre-heat temperature of 420°C (PJ-ψ25-420 flame). Contours are in steps of 25ppm and the colour map is identical to that used for all the in-flame NO_x results at 640°C pre-heat. The dashed line indicates the boundary of the in-flame measurement region.

A.2.2 840°C Secondary Air Pre-Heat Temperature

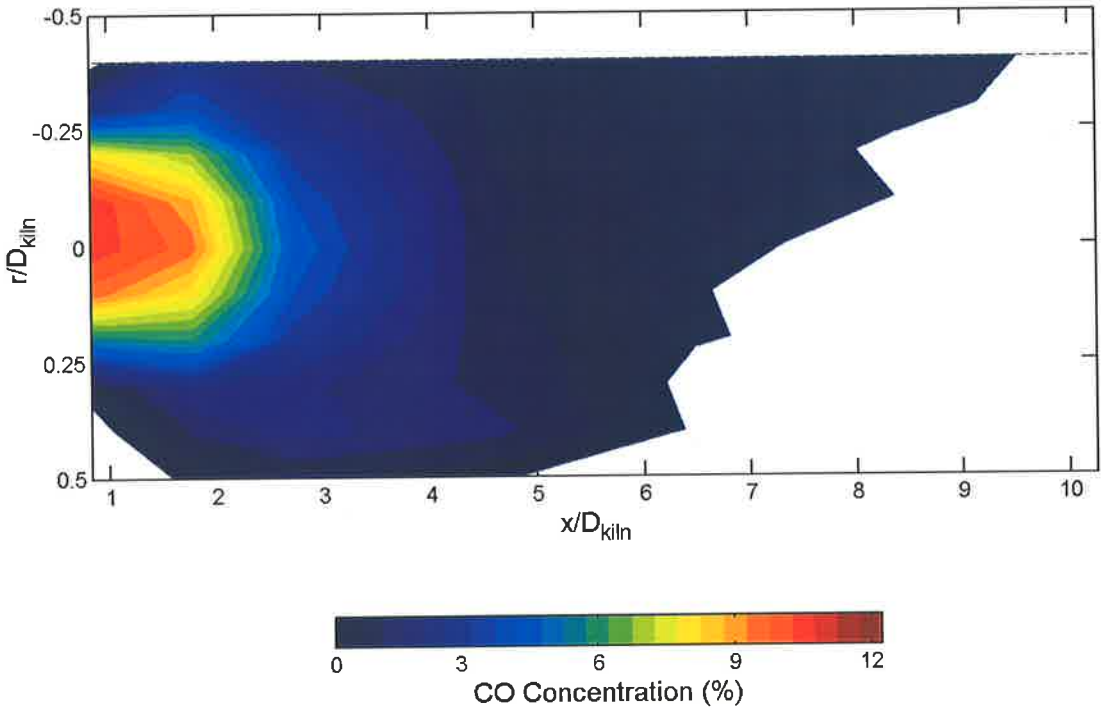

Figure A-7. Concentration contours of carbon monoxide measured in the pilot-scale kiln for the precessing jet burner with central axial jet (ψ_{CAJ}=25%, Γ_{CAJ}=0.25) at a secondary air pre-heat temperature of 840°C (PJ-ψ25-840 flame). Contours are in steps of 0.5% and the colour map is identical to that used for all the in-flame CO results. The dashed line indicates the boundary of the in-flame measurement region.

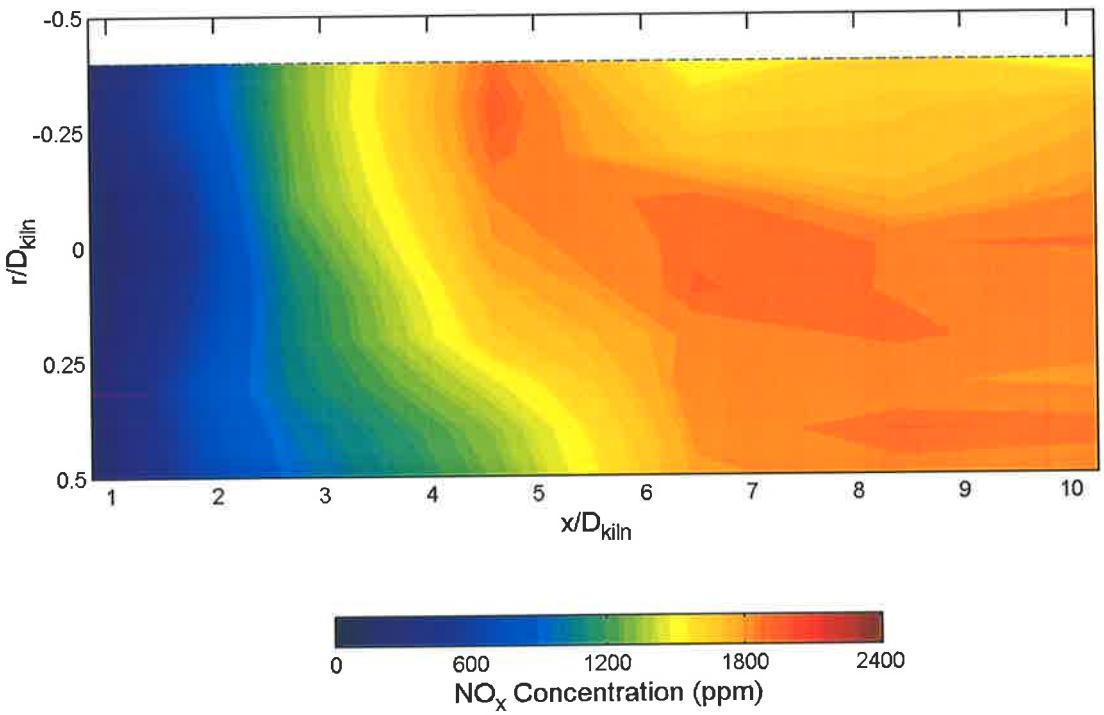

Figure A-8. Concentration contours of NO_x measured in the pilot-scale kiln for the precessing jet burner with central axial jet (ψ_{CAJ}=25%, Γ_{CAJ}=0.25) at a secondary air pre-heat temperature of 840°C (PJ-ψ25-840 flame). Contours are in steps of 25ppm, but the colour map is changed due to the higher NO_x concentrations at 840°C pre-heat. The dashed line indicates the boundary of the in-flame measurement region.

Appendix C

Additional PJ Nozzle Concentration Statistics

C.1 The Effect of Co-Flow Velocity on PJ mixing

3.1.1 Confinement of D_{duct}/d_{PJ}=7.6.

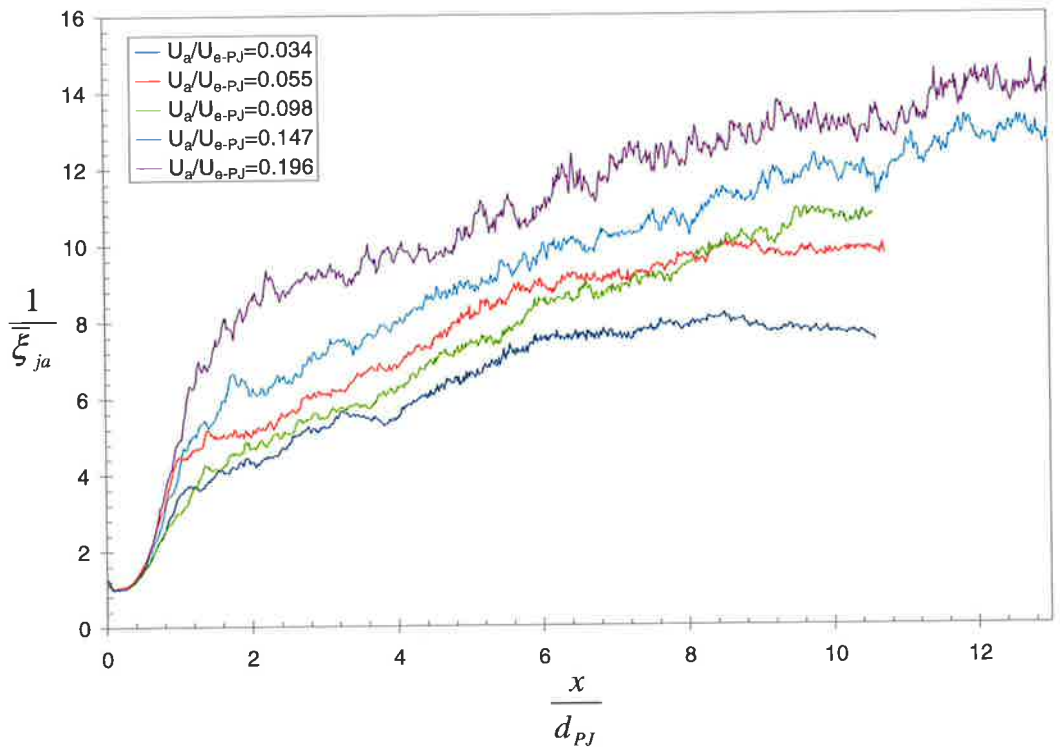

Figure C-1. The effect of co-flow velocity ratio on the inverse mean jet concentration on the jet axis, $\overline{\xi}_{ja}$, of the d_{PJ}=38mm PJ nozzle. Conditions: PJ flow only (ψ_{CAJ}=0%), Reynolds number=66,100, D_{duct}/d_{PJ}=7.6.

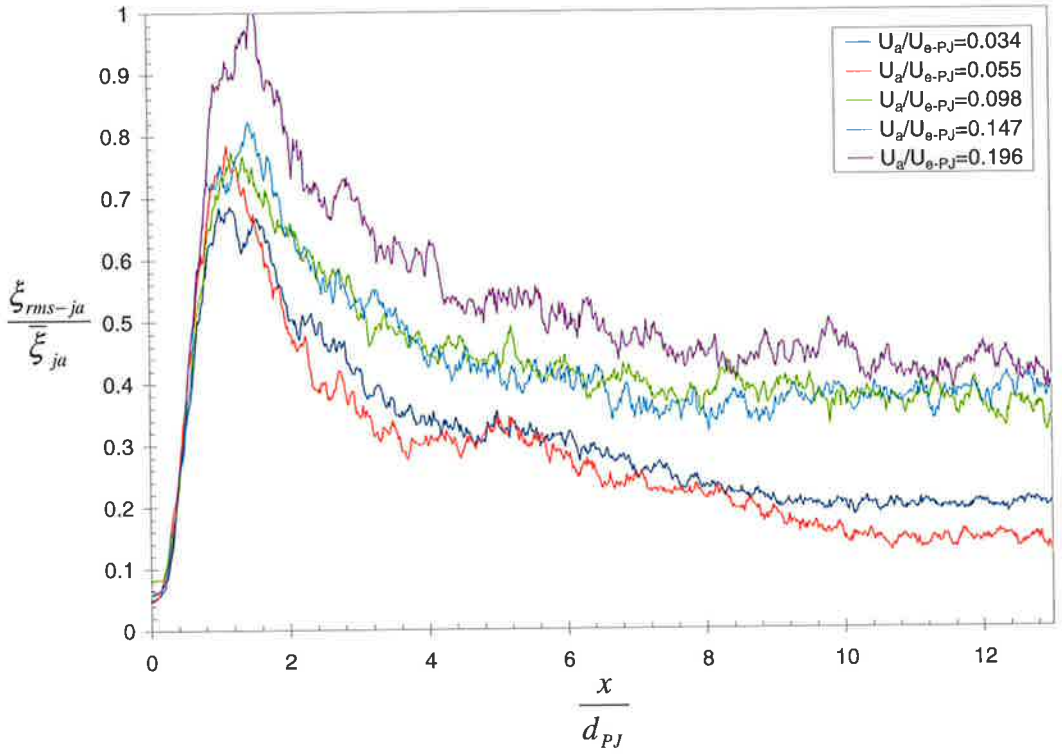

Figure C-2. The effect of co-flow velocity ratio on the concentration fluctuation intensity, $\xi_{rms\text{-}ja}/\bar{\xi}_{ja}$, on the jet axis of the d_{PJ}=38mm PJ nozzle. Conditions: PJ flow only (ψ_{CAJ}=0%), Reynolds number=66,100, D_{duct}/d_{PJ}=7.6.

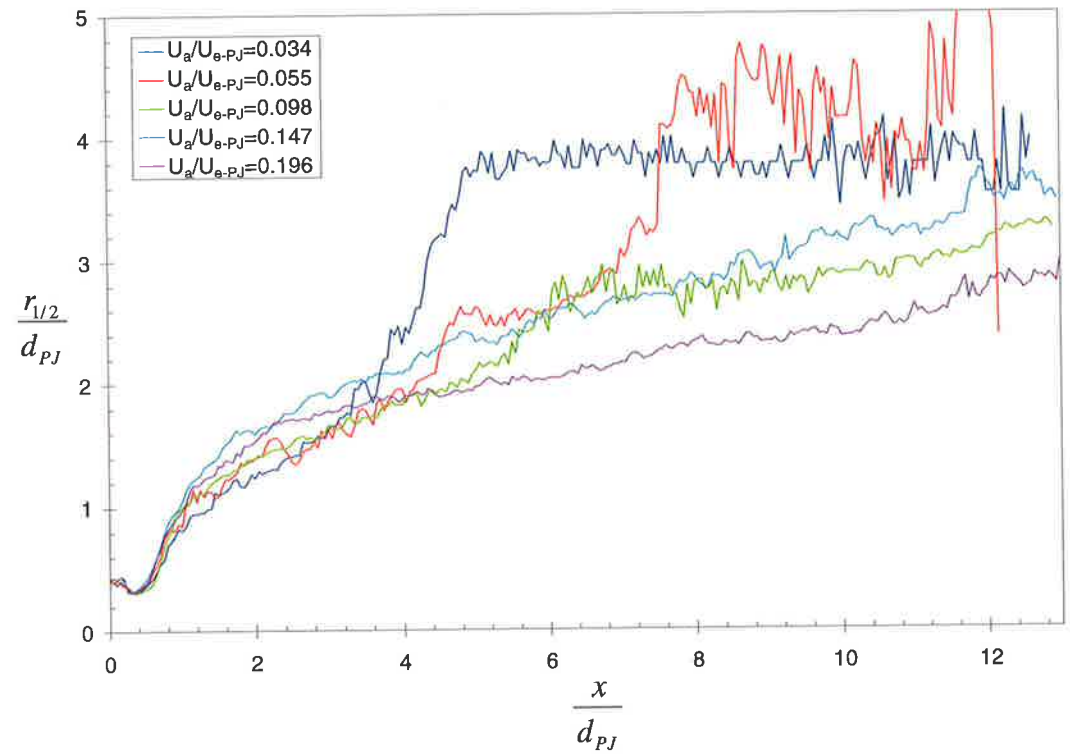

Figure C-3. The effect of co-flow velocity ratio on the concentration half-width, $r_{1/2}/d_{PJ}$, of the d_{PJ}=38mm PJ nozzle. Conditions: PJ flow only (ψ_{CAJ}=0%), Reynolds number=66,100, D_{duct}/d_{PJ}=7.6.

3.1.2 Confinement of D_{duct}/d_{PJ}=12.9.

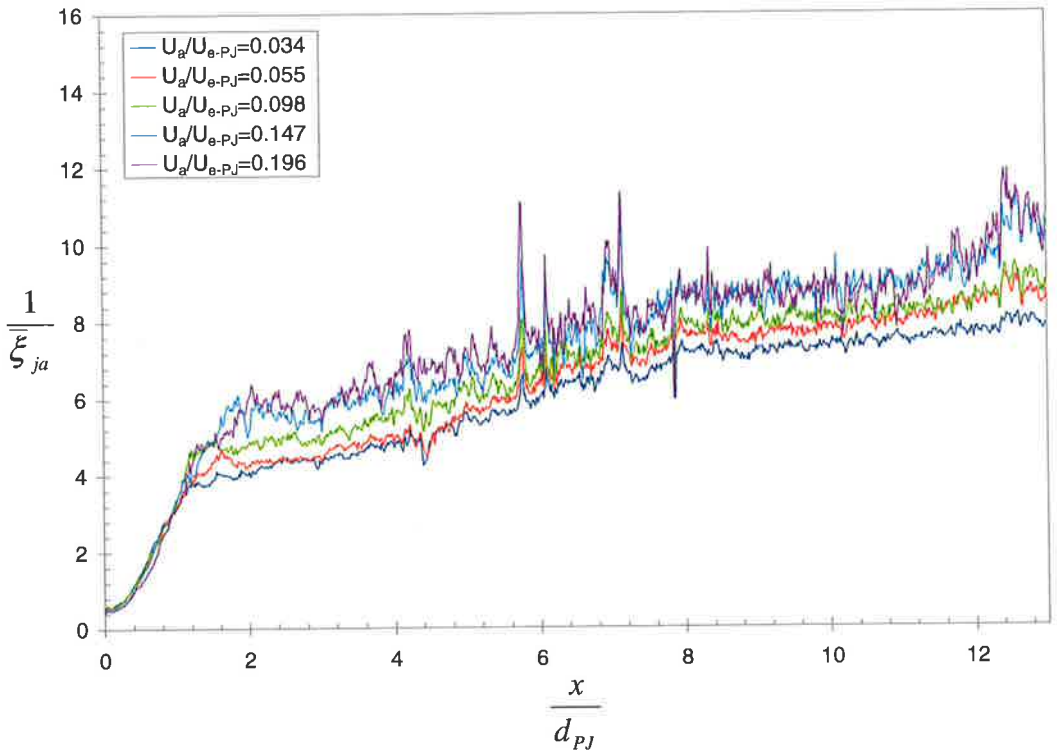

Figure C-4. The effect of co-flow velocity ratio on the inverse mean jet concentration on the jet axis, $\overline{\xi}_{ja}$, of the d_{PJ}=38mm PJ nozzle. Conditions: PJ flow only (ψ_{CAJ}=0%), Reynolds number=66,100, D_{duct}/d_{PJ}=12.9.

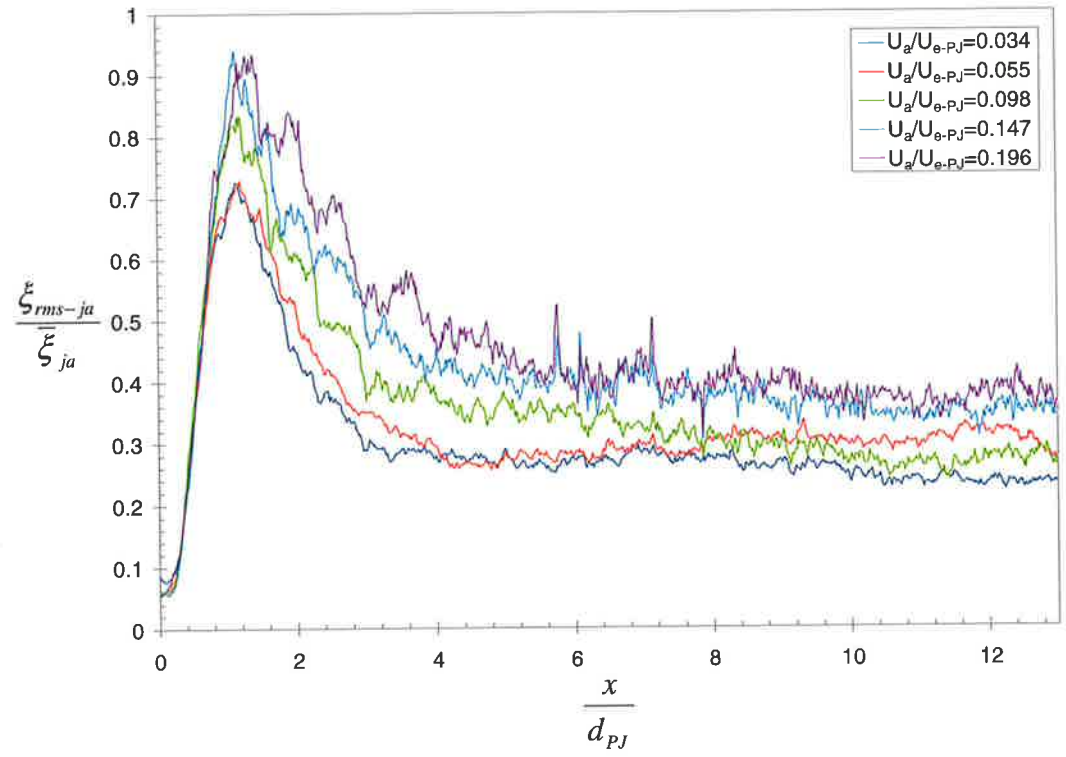

Figure C-5. The effect of co-flow velocity ratio on the concentration fluctuation intensity, $\xi_{rms\text{-}ja}/\overline{\xi}_{ja}$, on the jet axis of the 38mm PJ nozzle. Conditions: PJ flow only (ψ_{CAJ}=0%), Reynolds number=66,100, D_{duct}/d_{PJ}=12.9.

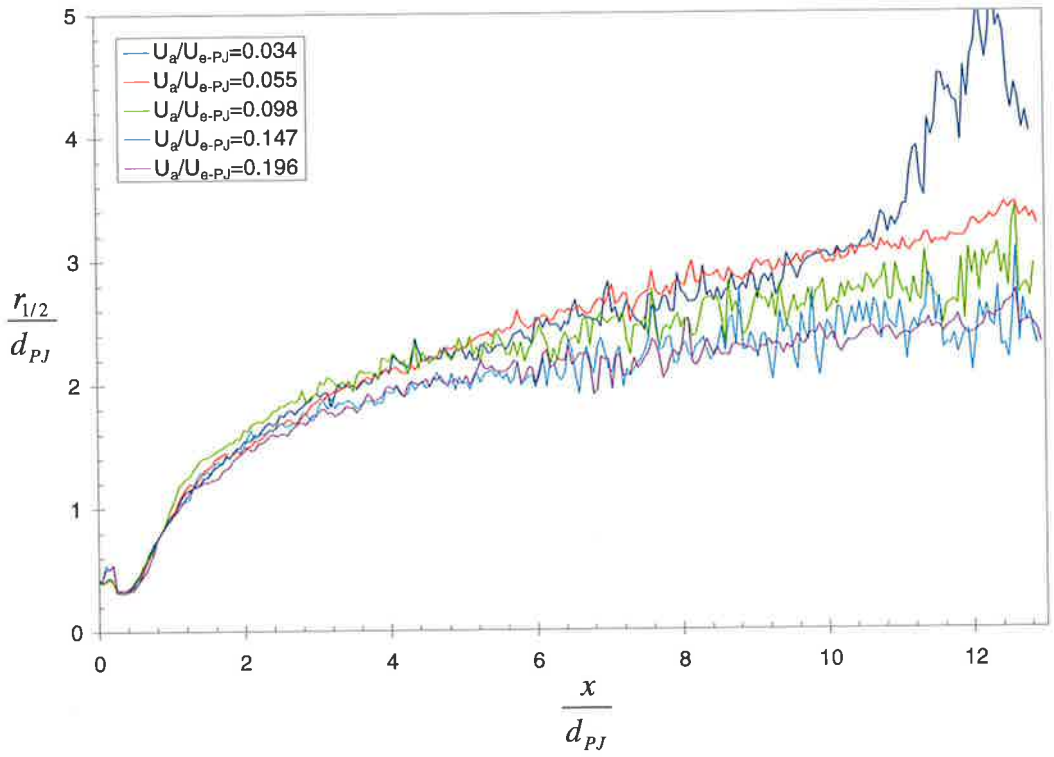

Figure C-6. The effect of co-flow velocity ratio on the concentration half-width, $r_{1/2}/d_{PJ}$, of the d_{PJ}=38mm PJ nozzle. Conditions: PJ flow only (ψ_{CAJ}=0%), Reynolds number=66,100, D_{duct}/d_{PJ}=12.9.

3.1.3 Confinement of D_{duct}/d_{PJ}=10.4.

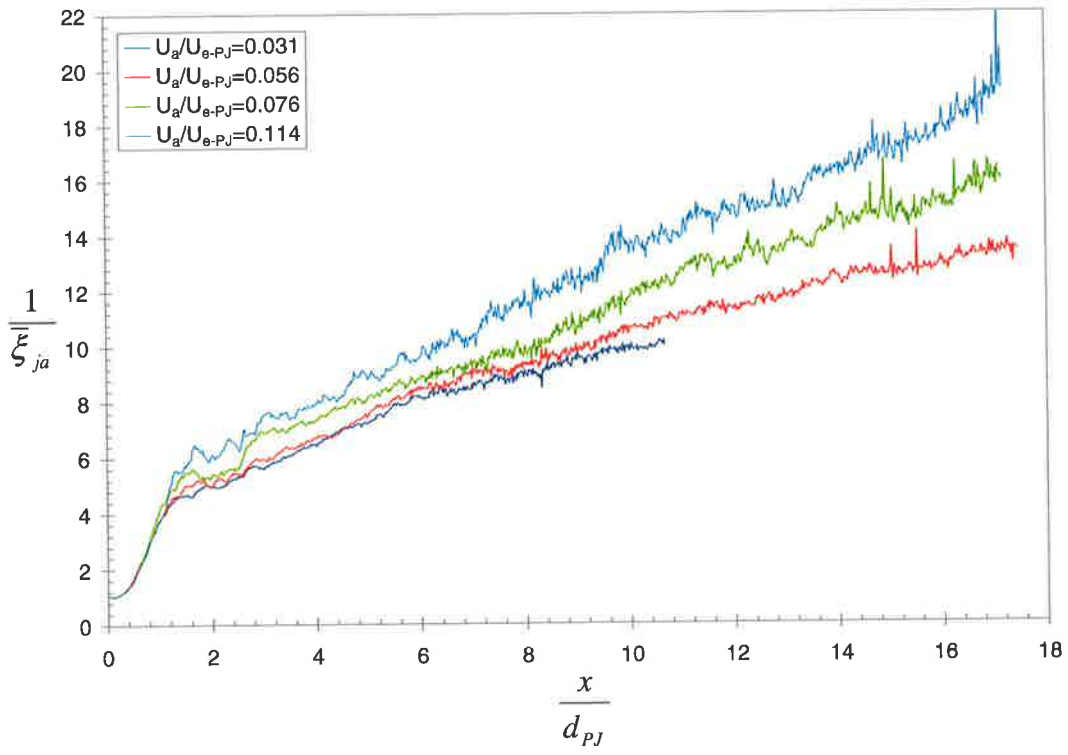

Figure C-7. The effect of co-flow velocity ratio on the inverse mean jet concentration on the jet axis, $\overline{\xi}_{ja}$, of the 28mm PJ nozzle. Conditions: PJ flow only (ψ_{CAJ}=0%), Reynolds number=62,400, D_{duct}/d_{PJ}=10.4.

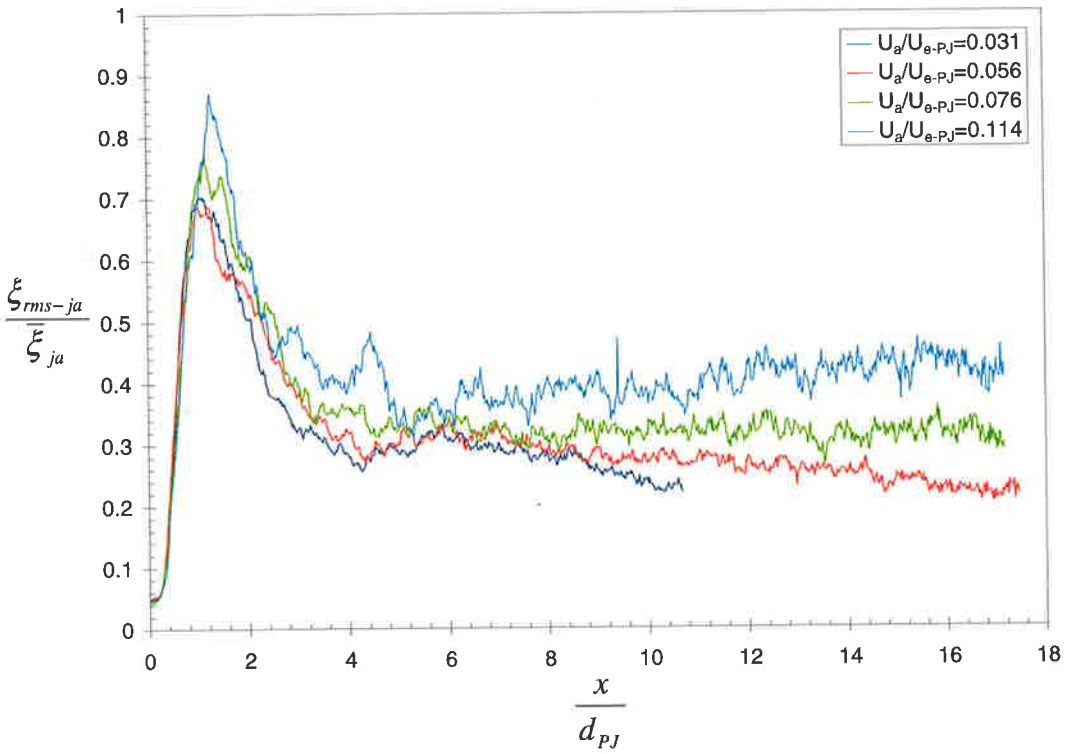

Figure C-8. The effect of co-flow velocity ratio on the concentration fluctuation intensity, $\xi_{rms\text{-}ja}/\overline{\xi}_{ja}$, on the jet axis of the 28mm PJ nozzle. Conditions: PJ flow only (ψ_{CAJ}=0%), Reynolds number=62,400, D_{duct}/d_{PJ}=10.4.

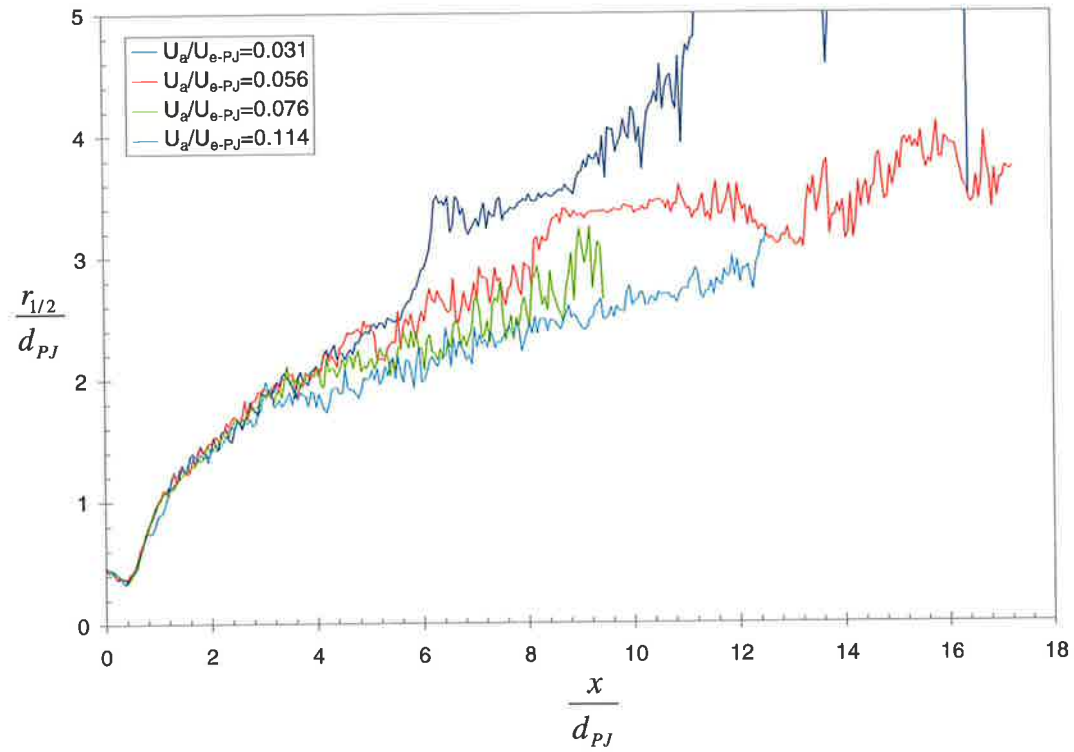

Figure C-9. The effect of co-flow velocity ratio on the concentration half-width, $r_{1/2}/d_{PJ}$, of the 28mm PJ nozzle. Conditions: PJ flow only (ψ_{CAJ}=0%), Reynolds number=62,400, D_{duct}/d_{PJ}=10.4.

3.1.4 Confinement of D_{duct}/d_{PJ}=13.9.

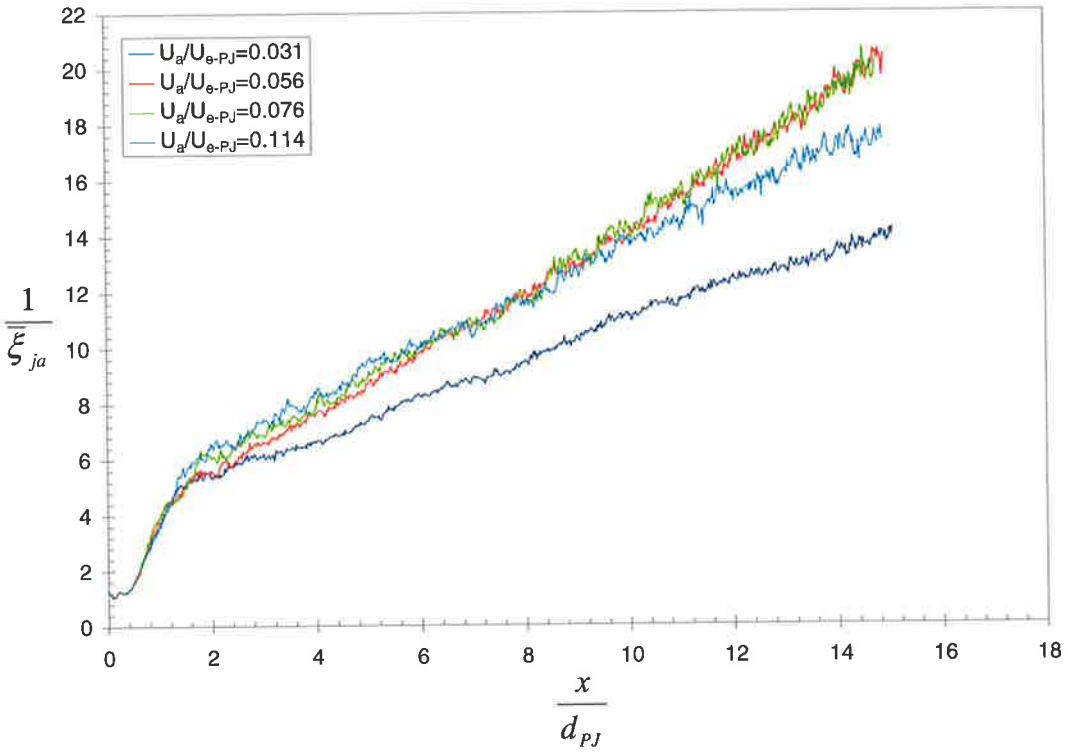

Figure C-10. The effect of co-flow velocity ratio on the inverse mean jet concentration on the jet axis, $\overline{\xi}_{ja}$, of the 28mm PJ nozzle. Conditions: PJ flow only (ψ_{CAJ}=0%), Reynolds number=62,400, D_{duct}/d_{PJ}=13.9.

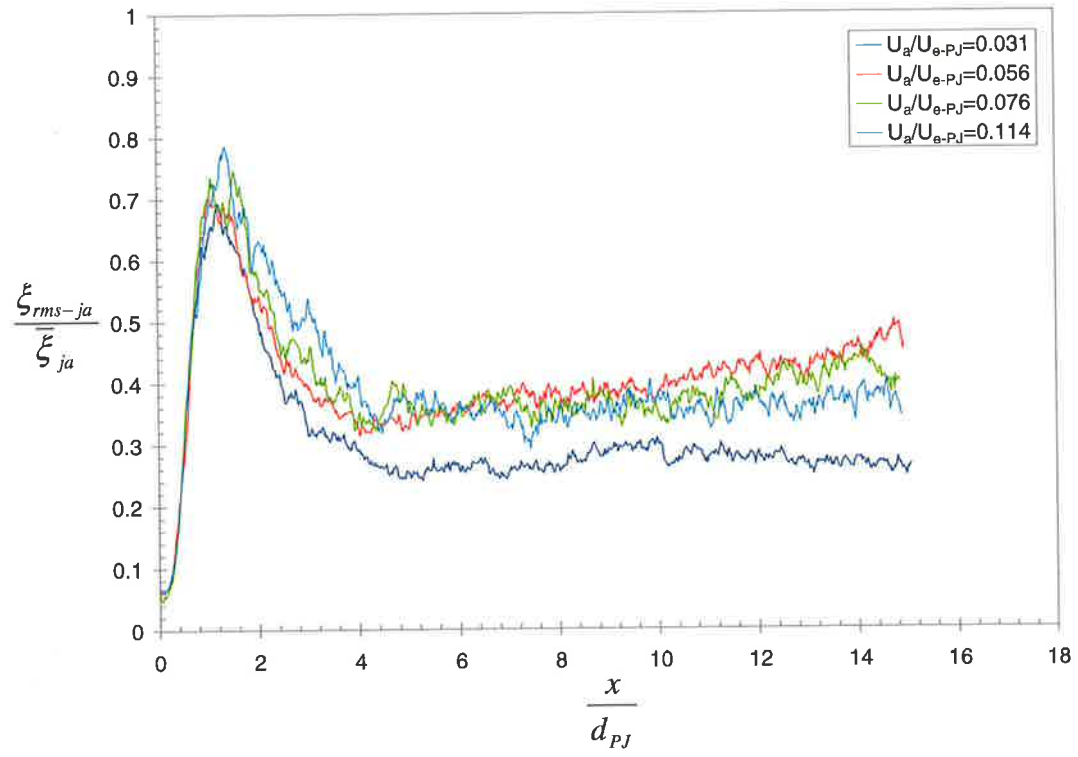

Figure C-11. The effect of co-flow velocity ratio on the concentration fluctuation intensity, $\xi_{rms\text{-}ja}/\overline{\xi}_{ja}$, on the jet axis of the 28mm PJ nozzle. Conditions: PJ flow only (ψ_{CAJ}=0%), Reynolds number=62,400, D_{duct}/d_{PJ}=13.9.

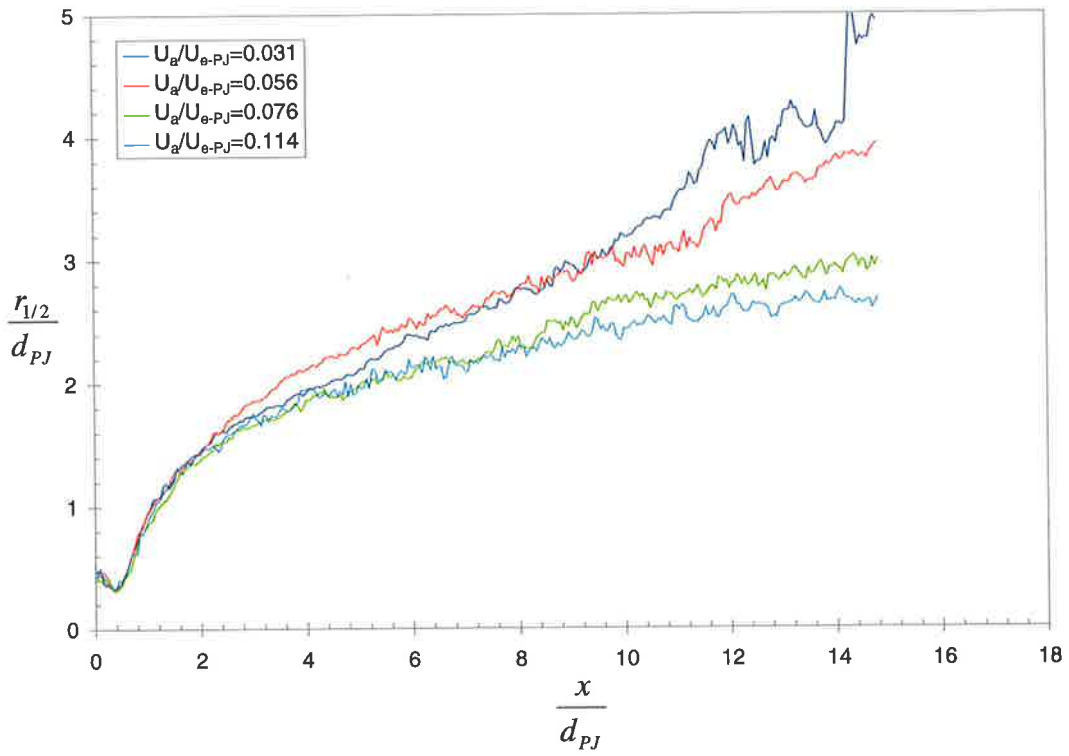

Figure C-12. The effect of co-flow velocity ratio on the concentration half-width, $r_{1/2}/d_{PJ}$, of the 28mm PJ nozzle. Conditions: PJ flow only (ψ_{CAJ}=0%), Reynolds number=62,400, D_{duct}/d_{PJ}=13.9.

C.2 The Effect of Confinement on PJ mixing

3.2.1 Co-flow Velocity Ratio of $U_a/U_{e\text{-}PJ}$=0.035

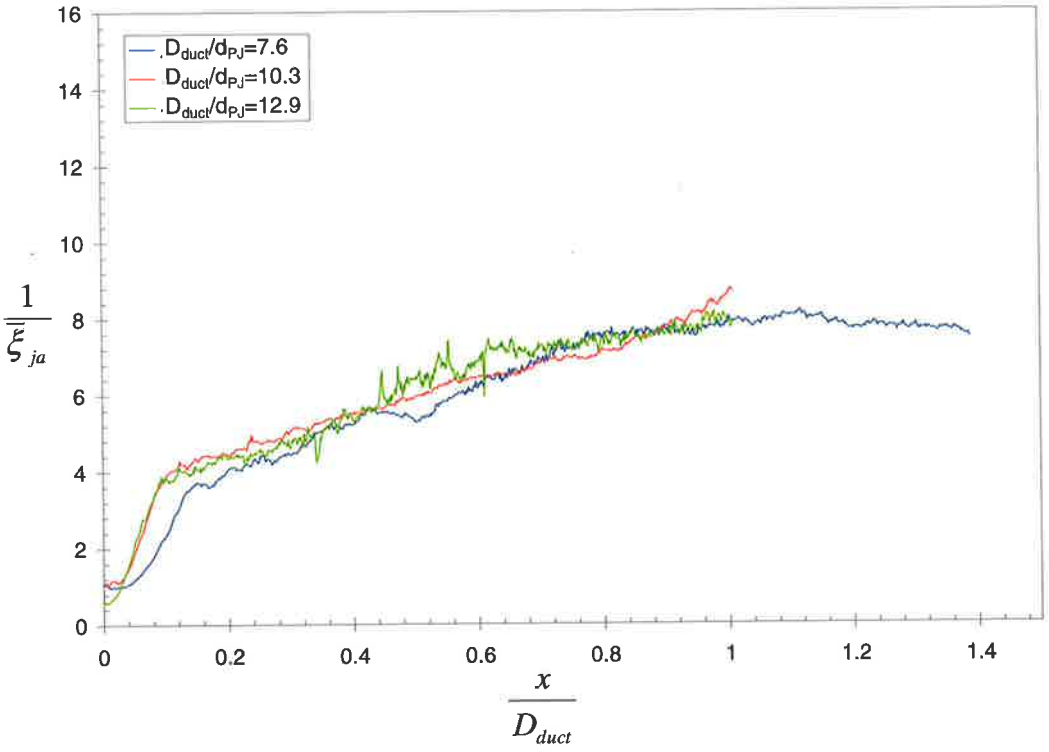

Figure C-13. The effect of confinement on the inverse mean jet concentration on the jet axis, $\overline{\xi}_{ja}$, of the d_{PJ}=38mm PJ nozzle. Conditions: PJ flow only (ψ_{CAJ}=0%), Reynolds number=66,100, $U_a/U_{e\text{-}PJ}$=0.035 (U_a=0.038m/s). Axial distance from the nozzle exit is normalised to the duct diameter, D_{duct}.

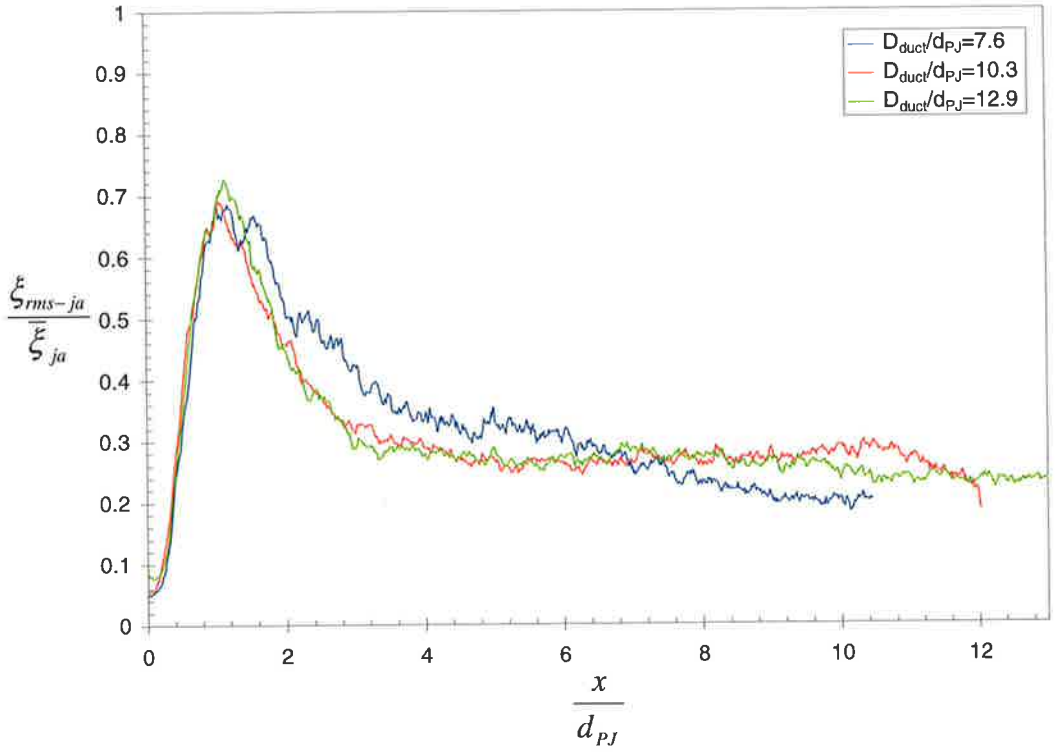

Figure C-14. The effect of confinement on the concentration fluctuation intensity on the jet axis, $\xi_{rms\text{-}ja}/\overline{\xi}_{ja}$, of the d_{PJ}=38mm PJ nozzle. Conditions: PJ flow only (ψ_{CAJ}=0%), Reynolds number=66,100, $U_a/U_{e\text{-}PJ}$=0.035 (U_a=0.038m/s). Axial distance is normalised to the PJ nozzle chamber diameter, d_{PJ}.

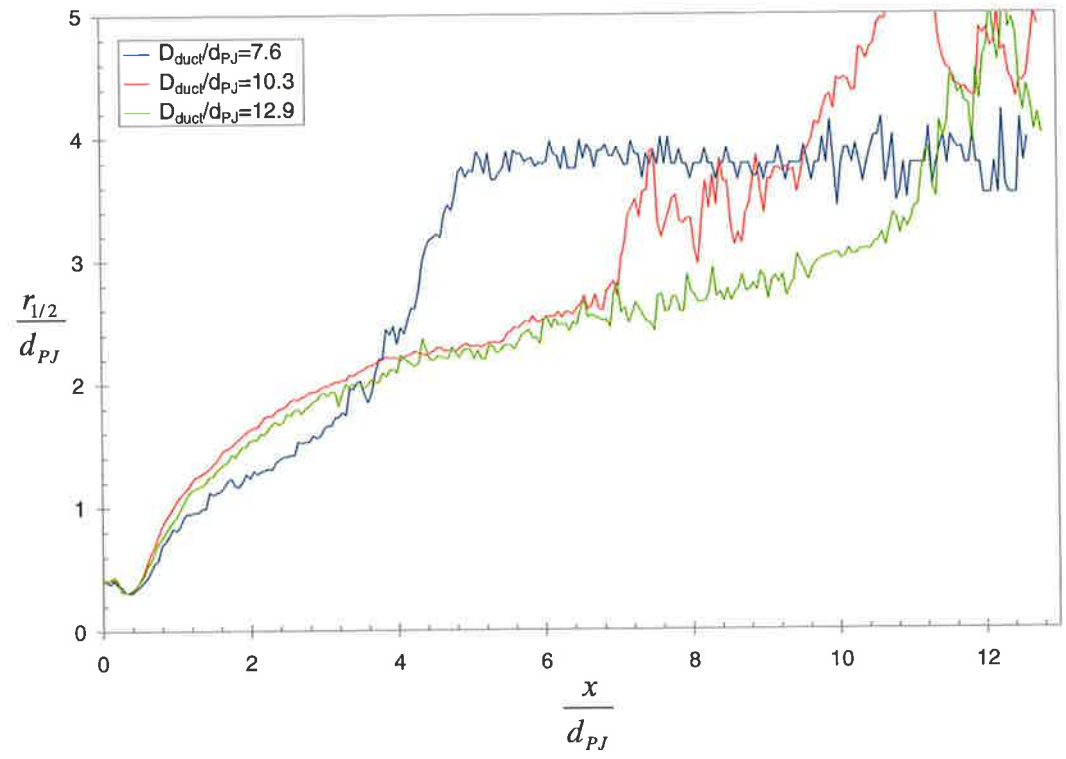

Figure C-15. The effect of confinement on the concentration half-width, $r_{1/2}/d_{PJ}$, of the d_{PJ}=38mm PJ nozzle. Conditions: PJ flow only (ψ_{CAJ}=0%), Reynolds number=66,100, $U_a/U_{e\text{-}PJ}$=0.035 (U_a=0.038m/s). Axial distance is normalised to the PJ nozzle chamber diameter, d_{PJ}.

3.2.2 Co-flow Velocity Ratio of $U_a/U_{e\text{-}PJ}$=0.098

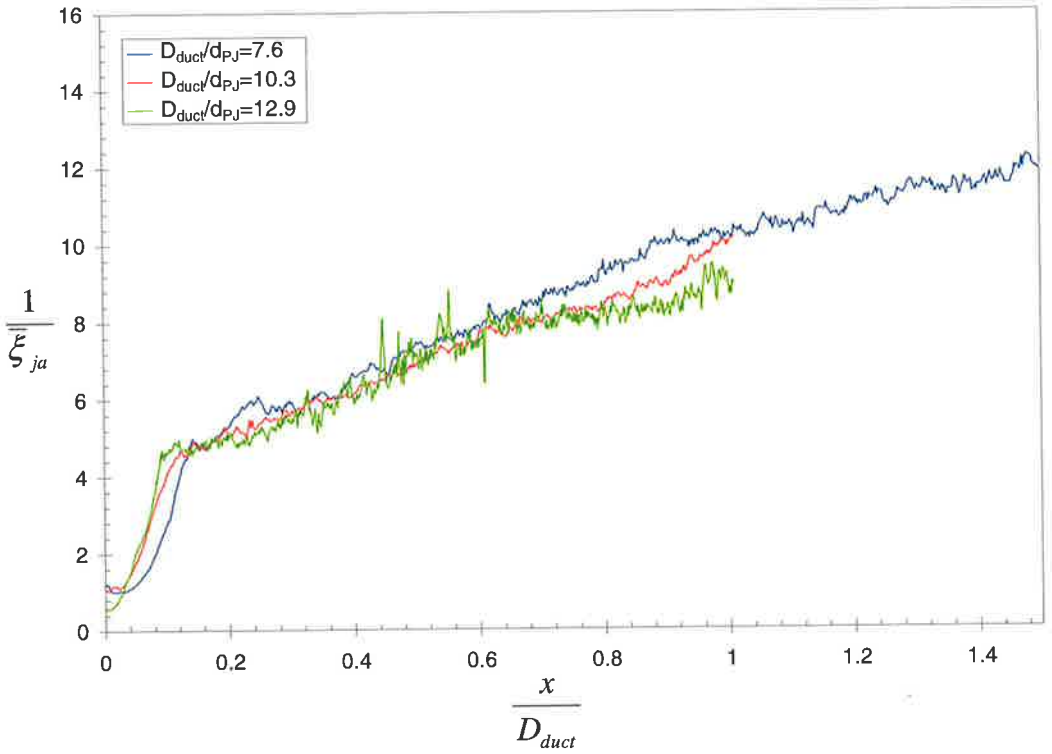

Figure C-16. The effect of confinement on the inverse mean jet concentration on the jet axis, $\bar{\xi}_{ja}$, of the d_{PJ}=38mm PJ nozzle. Conditions: PJ flow only (ψ_{CAJ}=0%), Reynolds number=66,100, $U_d/U_{e\text{-}PJ}$=0.098 (U_a=0.108m/s). Axial distance from the nozzle exit is normalised to the duct diameter, D_{duct}.

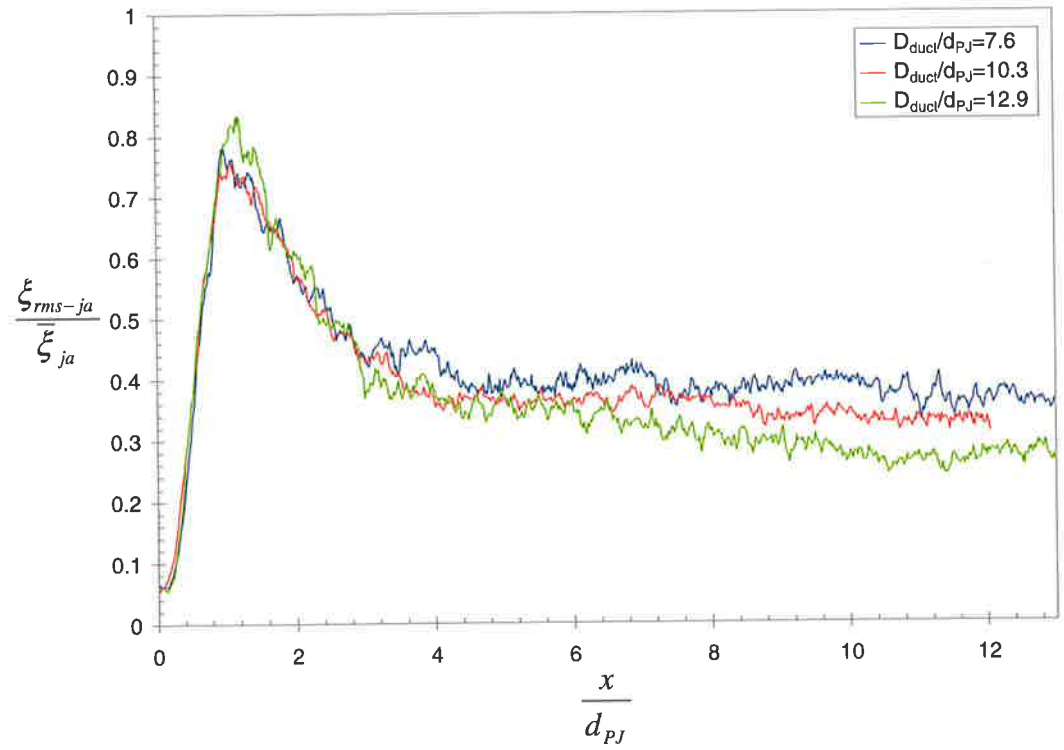

Figure C-17. The effect of confinement on the concentration fluctuation intensity on the jet axis, $\xi_{rms\text{-}ja}/\bar{\xi}_{ja}$, of the d_{PJ}=38mm PJ nozzle. Conditions: PJ flow only (ψ_{CAJ}=0%), Reynolds number=66,100, $U_d/U_{e\text{-}PJ}$=0.098 (U_a=0.108m/s). Axial distance is normalised to the PJ nozzle chamber diameter, d_{PJ}.

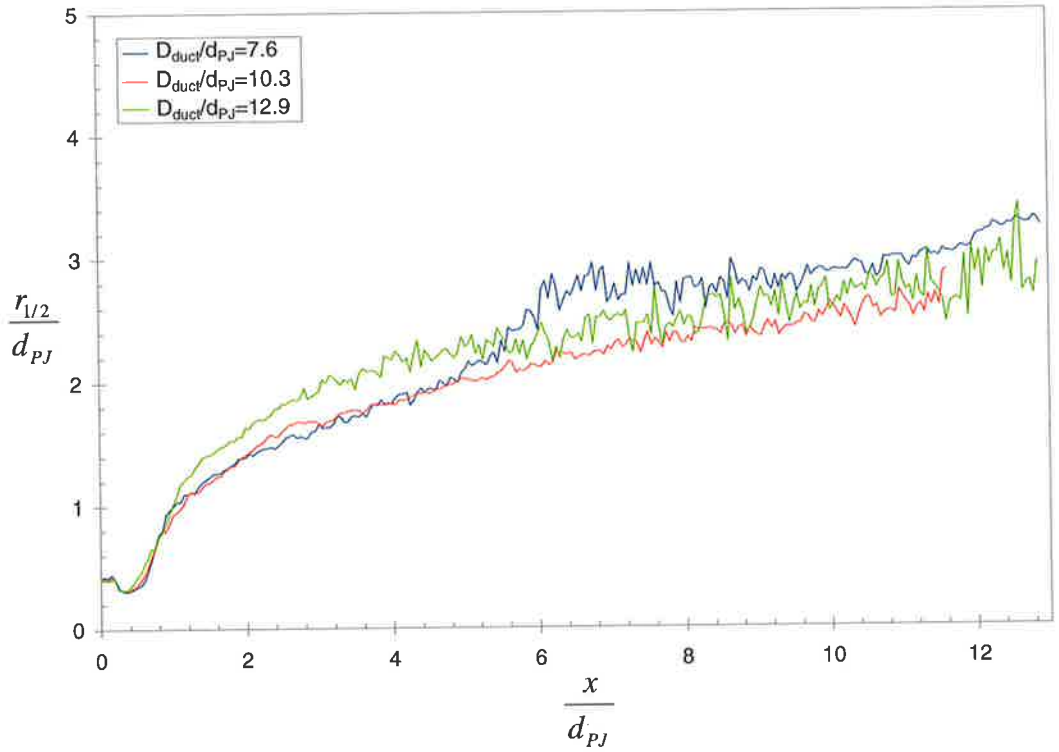

Figure C-18. The effect of confinement on the concentration half-width, $r_{1/2}/d_{PJ}$, of the d_{PJ}=38mm PJ nozzle. Conditions: PJ flow only (ψ_{CAJ}=0%), Reynolds number=66,100, $U_a/U_{e\text{-}PJ}$=0.098 (U_a=0.108m/s). Axial distance is normalised to the PJ nozzle chamber diameter, d_{PJ}.

3.2.3 Co-flow Velocity Ratio of $U_a/U_{e\text{-}PJ}$=0.147

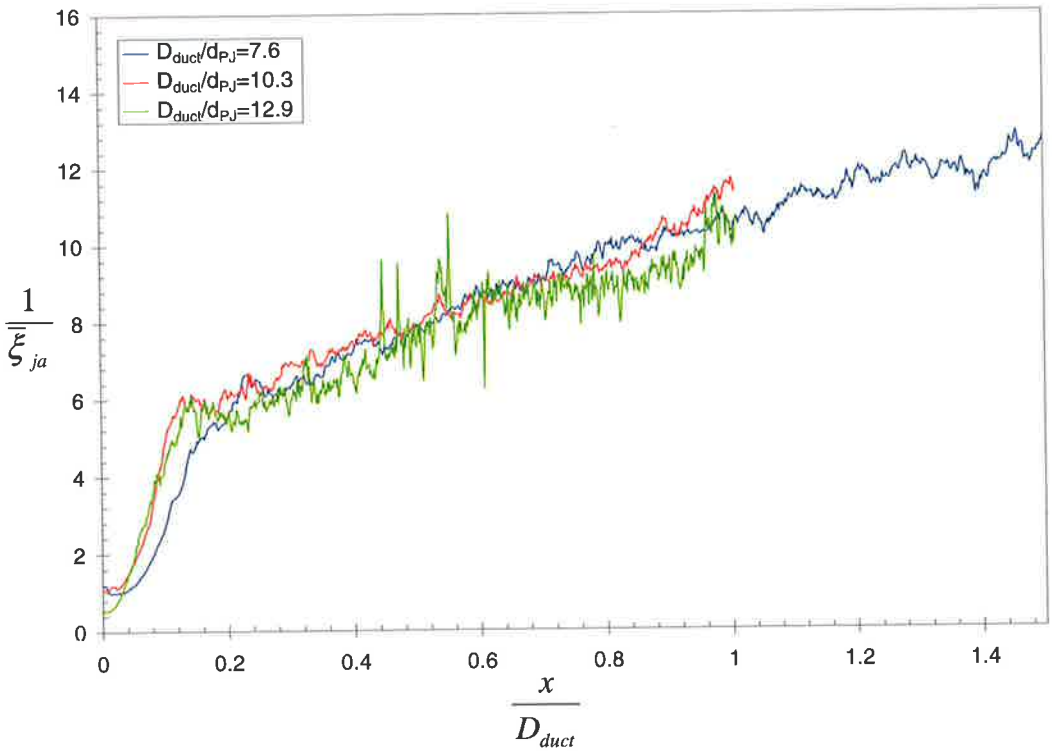

Figure C-19. The effect of confinement on the inverse mean jet concentration on the jet axis, $\bar{\xi}_{ja}$, of the d_{PJ}=38mm PJ nozzle. Conditions: PJ flow only (ψ_{CAJ}=0%), Reynolds number=66,100, $U_a/U_{e\text{-}PJ}$=0.147 (U_a=0.162m/s). Axial distance from the nozzle exit is normalised to the duct diameter, D_{duct}.

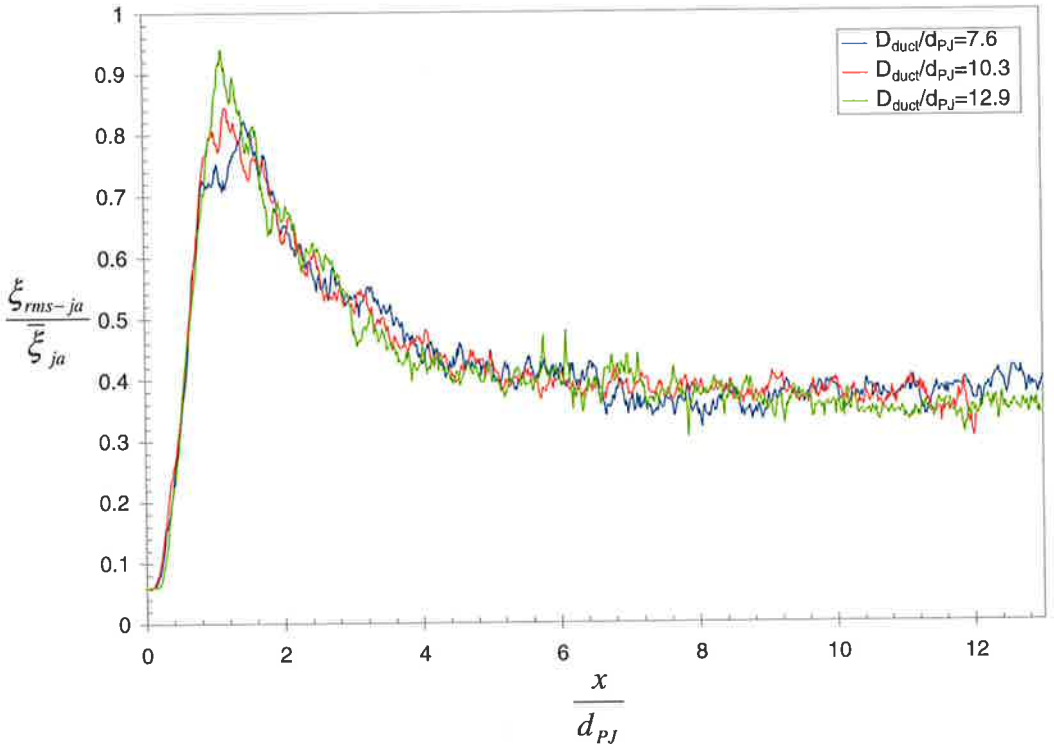

Figure C-20. The effect of confinement on the concentration fluctuation intensity on the jet axis, $\xi_{rms\text{-}ja}/\overline{\xi}_{ja}$, of the d_{PJ}=38mm PJ nozzle. Conditions: PJ flow only (ψ_{CAJ}=0%), Reynolds number=66,100, $U_a/U_{e\text{-}PJ}$=0.147 (U_a=0.162m/s). Axial distance is normalised to the PJ nozzle chamber diameter, d_{PJ}.

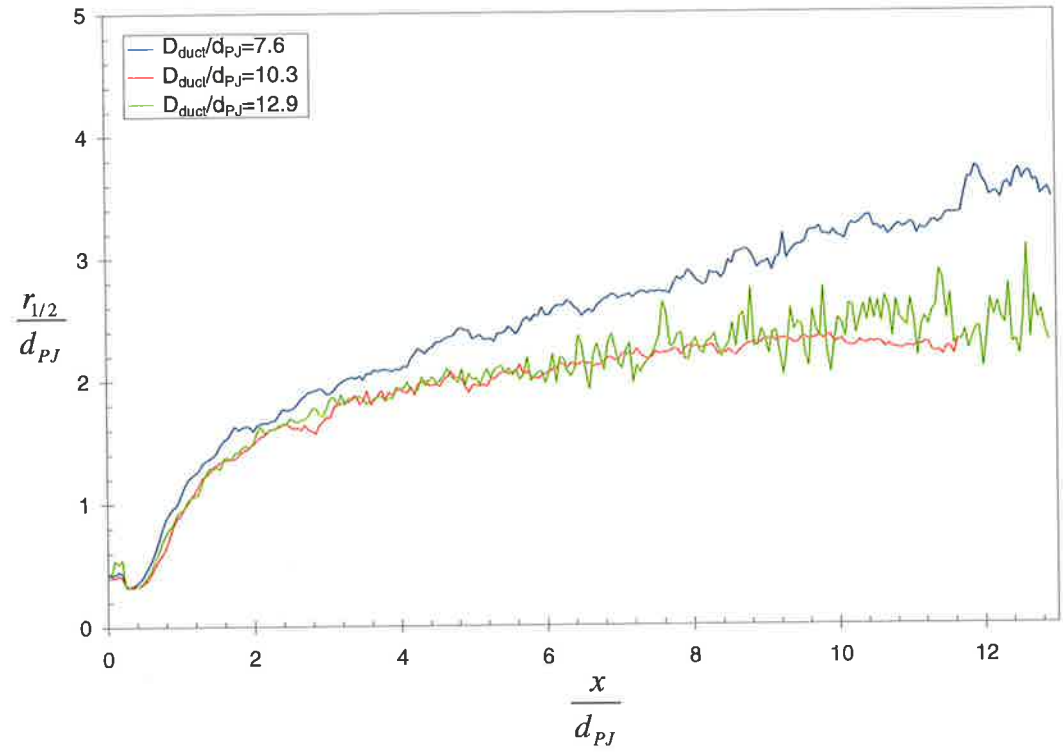

Figure C-21. The effect of confinement on the concentration half-width, $r_{1/2}/d_{PJ}$, of the d_{PJ}=38mm PJ nozzle. Conditions: PJ flow only (ψ_{CAJ}=0%), Reynolds number=66,100, $U_a/U_{e\text{-}PJ}$=0.147 (U_a=0.162m/s). Axial distance is normalised to the PJ nozzle chamber diameter, d_{PJ}.

3.2.4 Co-flow Velocity Ratio of $U_a/U_{e\text{-}PJ}$=0.196

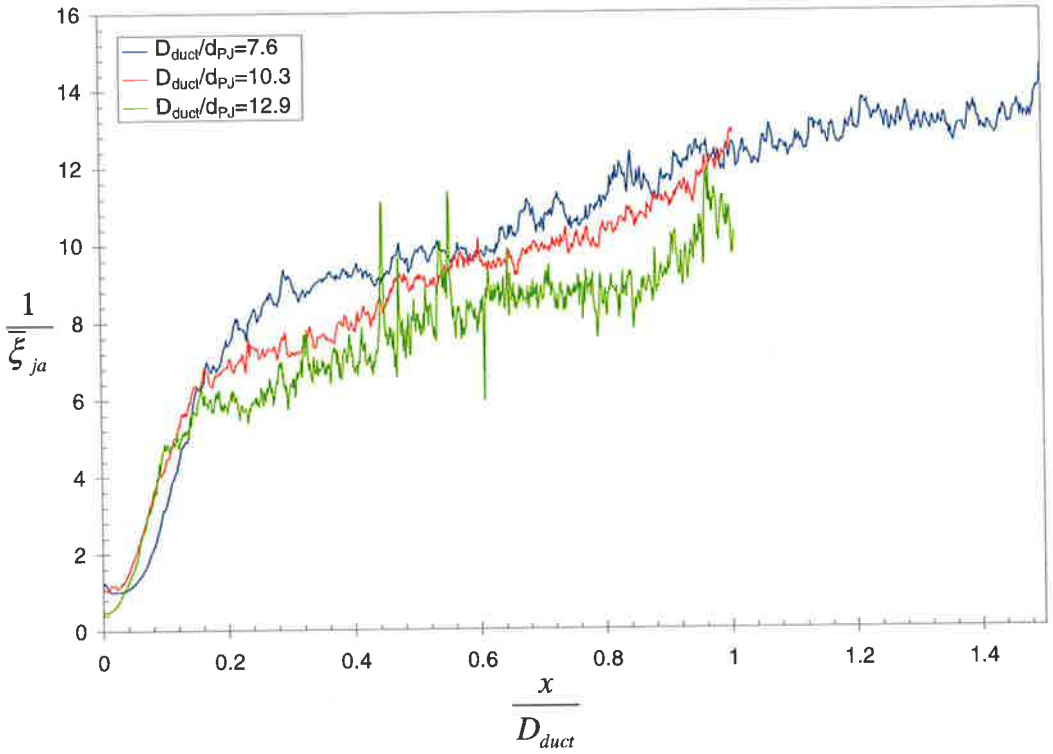

Figure C-22. The effect of confinement on the inverse mean jet concentration on the jet axis, $\overline{\xi}_{ja}$, of the d_{PJ}=38mm PJ nozzle. Conditions: PJ flow only (Ψ_{CAJ}=0%), Reynolds number=66,100, $U_a/U_{e\text{-}PJ}$=0.196 (U_a=0.216m/s). Axial distance from the nozzle exit is normalised to the duct diameter, D_{duct}.

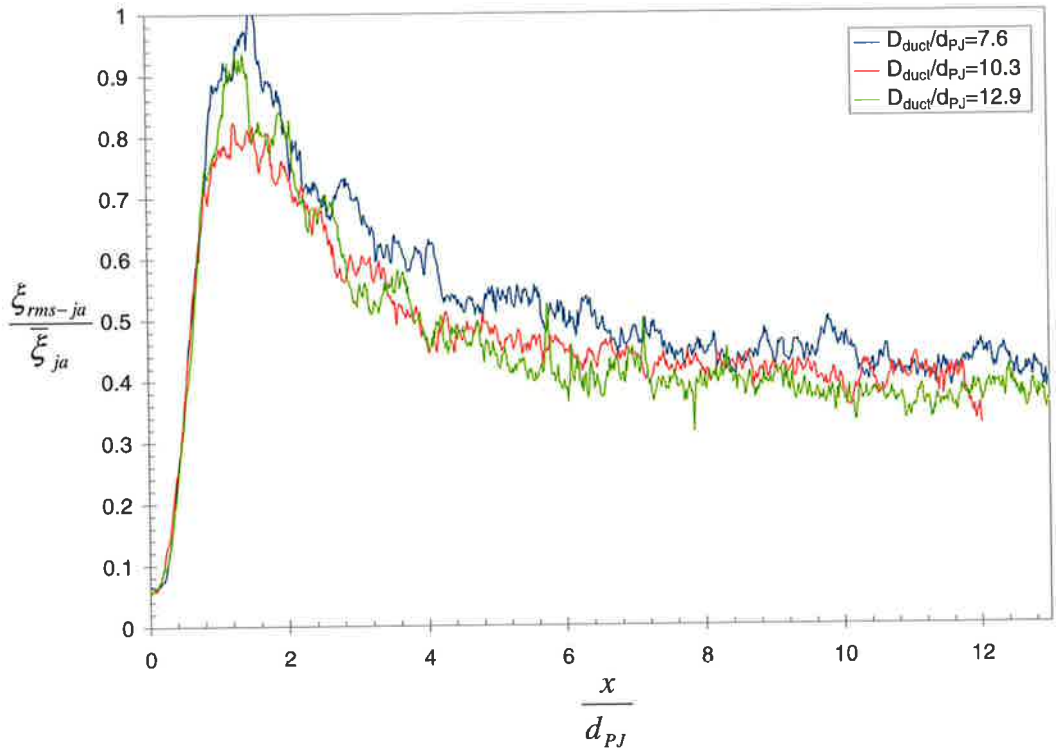

Figure C-23. The effect of confinement on the concentration fluctuation intensity on the jet axis, $\xi_{rms\text{-}ja}/\overline{\xi}_{ja}$, of the d_{PJ}=38mm PJ nozzle. Conditions: PJ flow only (Ψ_{CAJ}=0%), Reynolds number=66,100, $U_a/U_{e\text{-}PJ}$=0.196 (U_a=0.216m/s). Axial distance is normalised to the PJ nozzle chamber diameter, d_{PJ}.

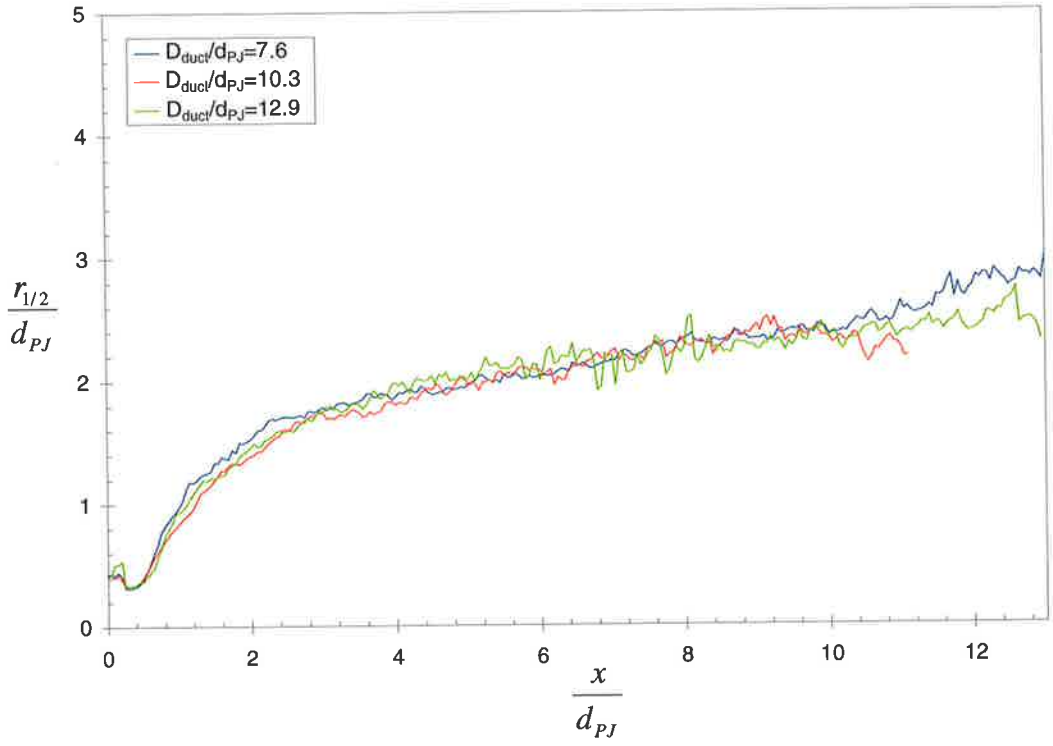

Figure C-24. The effect of confinement on the concentration half-width, $r_{1/2}/d_{PJ}$, of the d_{PJ}=38mm PJ nozzle. Conditions: PJ flow only (ψ_{CAJ}=0%), Reynolds number=66,100, $U_a/U_{e\text{-}PJ}$=0.196 (U_a=0.216m/s). Axial distance is normalised to the PJ nozzle chamber diameter, d_{PJ}.

C.3 The Effect of the Central Axial Jet on PJ mixing

3.3.1 Confinement of D_{duct}/d_{PJ}=7.6, Co-Flow Velocity of U_a=0.108m/s.

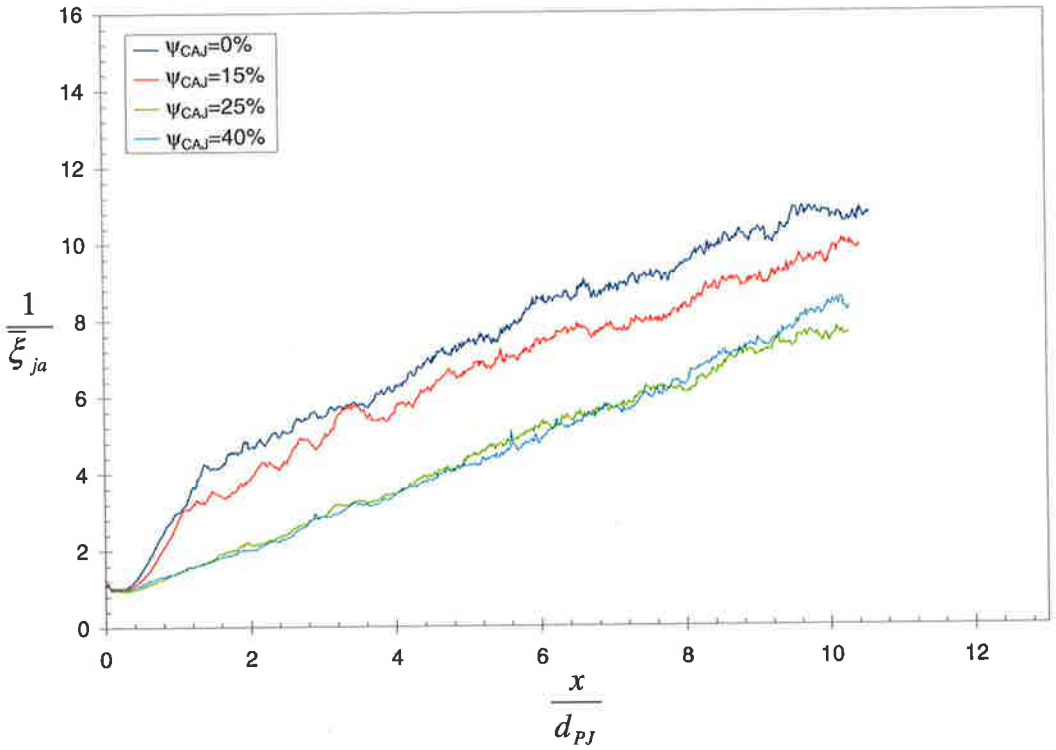

Figure C-25. The effect of CAJ proportion, ψ_{CAJ}, on the mean jet concentration on the jet axis, $\bar{\xi}_{ja}$, of the 38mm PJ nozzle. Conditions: co-flow velocity U_a=0.108m/s, confinement D_{duct}/d_{PJ}=7.6, mass flux ratio m_a/m_0=18.4.

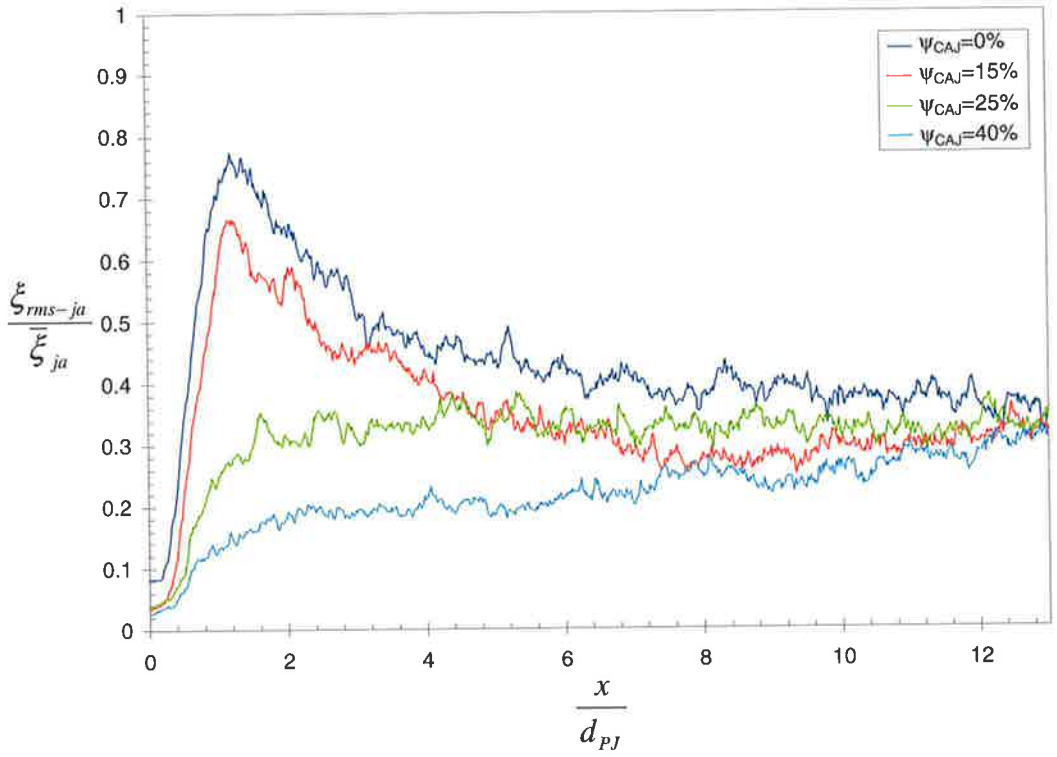

Figure C-26. The effect of CAJ proportion, ψ_{CAJ}, on the concentration fluctuation intensity, $\xi_{rms\text{-}ja}/\bar{\xi}_{ja}$, on the jet axis of the d_{PJ}=38mm PJ nozzle. Conditions: co-flow velocity U_a=0.108m/s, confinement D_{duct}/d_{PJ}=7.6, mass flux ratio m_a/m_0=18.4.

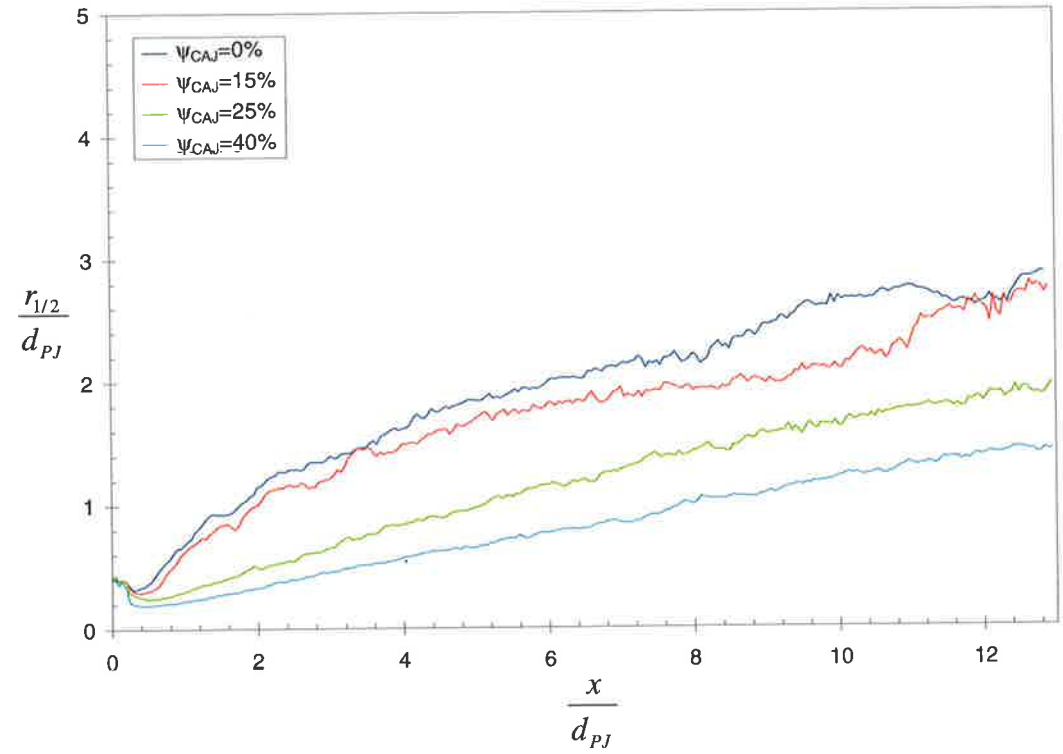

Figure C-27. The effect of CAJ proportion, ψ_{CAJ}, on the concentration half-width, $r_{1/2}/d_{PJ}$, of the d_{PJ}=38mm PJ nozzle. Conditions: co-flow velocity U_a=0.108m/s, confinement D_{duct}/d_{PJ}=7.6, mass flux ratio m_a/m_0=18.4.

3.3.2 Confinement of D_{duct}/d_{PJ}=12.9, Co-Flow Velocity of U_a=0.038m/s.

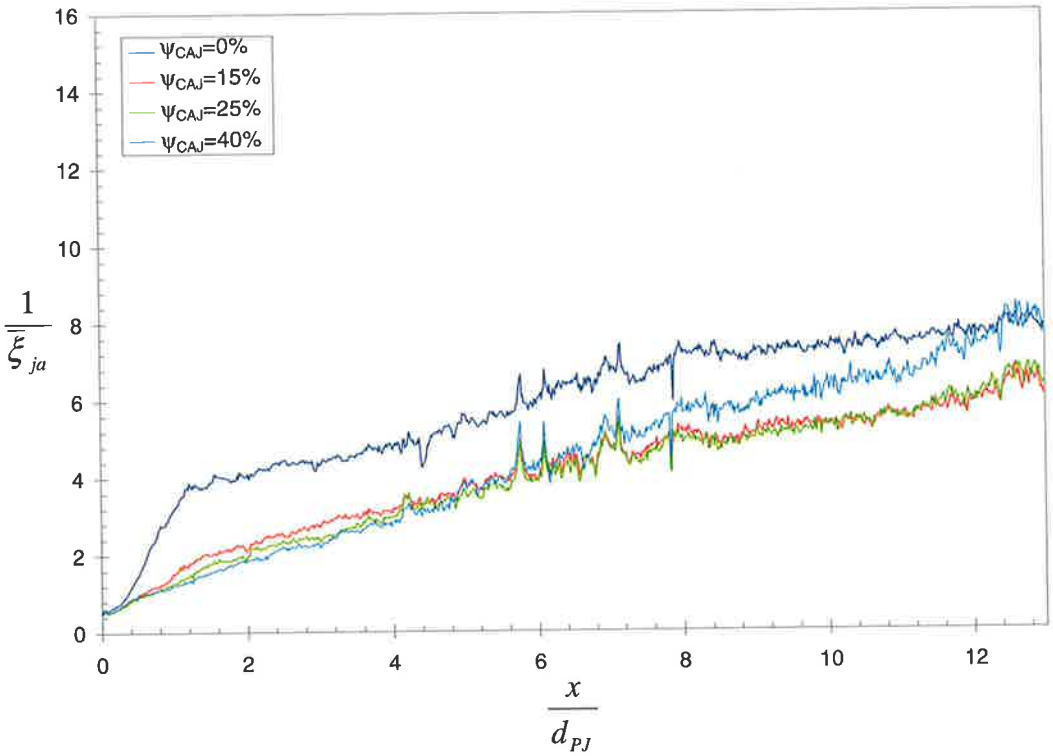

Figure C-28. The effect of CAJ proportion, ψ_{CAJ}, on the mean jet concentration on the jet axis, $\bar{\xi}_{ja}$, of the 38mm PJ nozzle. Conditions: co-flow velocity U_a=0.038m/s, confinement D_{duct}/d_{PJ}=10.9, mass flux ratio m_a/m_0=18.4.

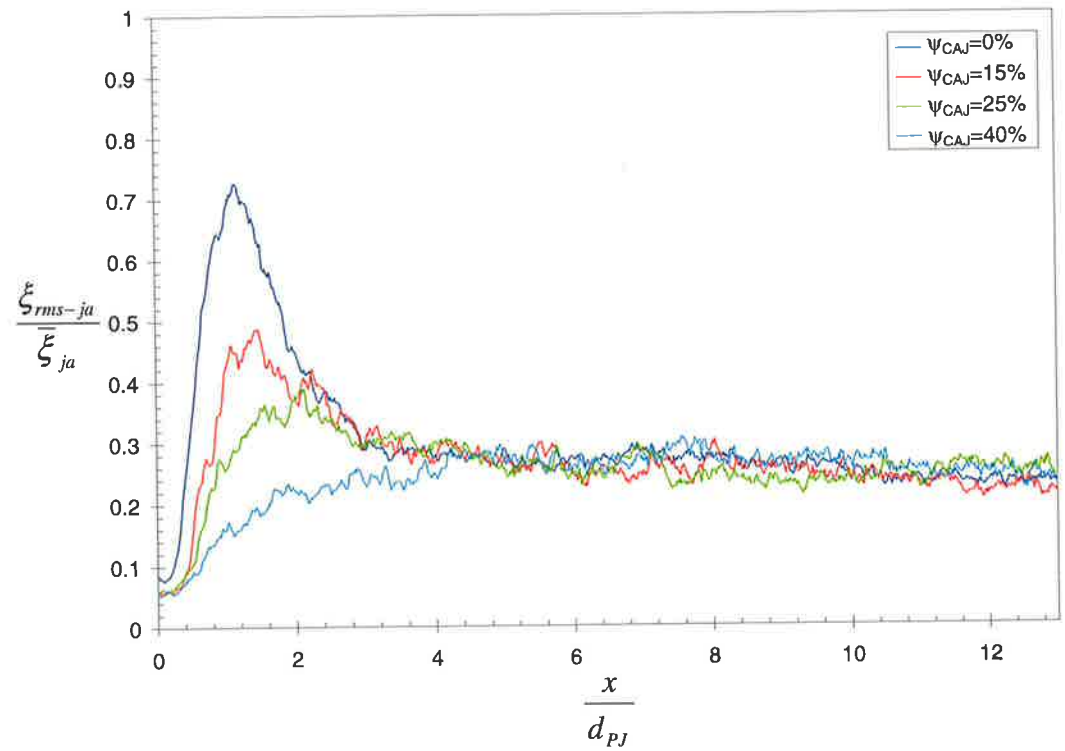

Figure C-29. The effect of CAJ proportion, ψ_{CAJ}, on the concentration fluctuation intensity, $\xi_{rms\text{-}ja}/\bar{\xi}_{ja}$, on the jet axis of the d_{PJ}=38mm PJ nozzle. Conditions: co-flow velocity U_a=0.038m/s, confinement D_{duct}/d_{PJ}=10.9, mass flux ratio m_a/m_0=18.4.

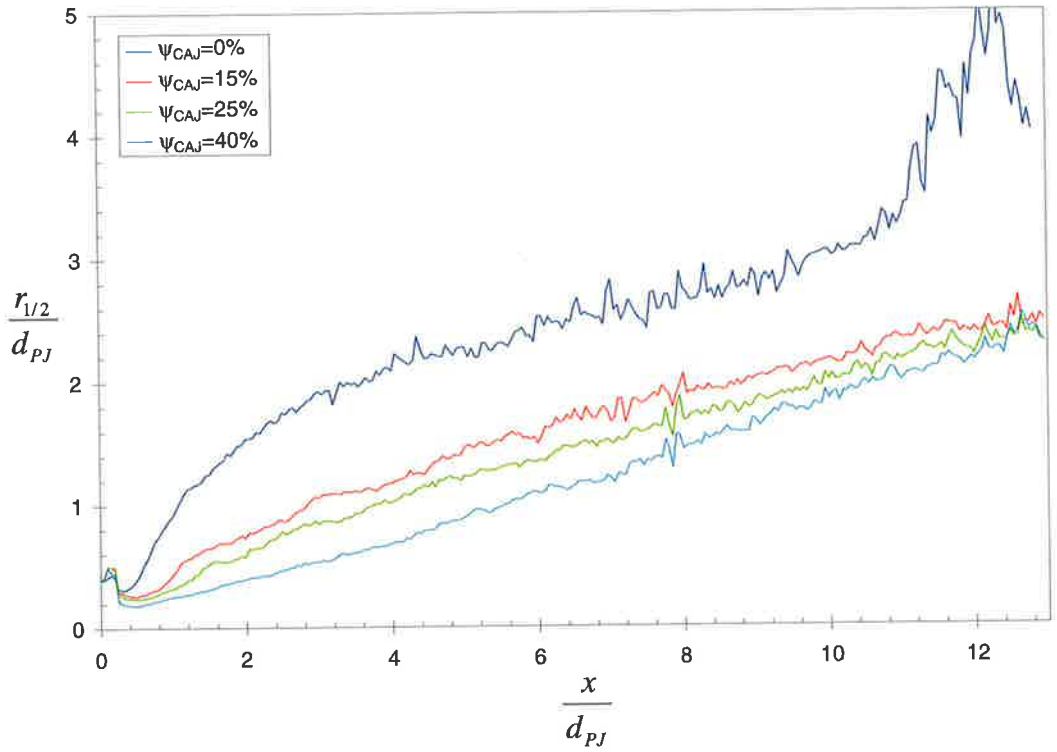

Figure C-30. The effect of CAJ proportion, ψ_{CAJ}, on the concentration half-width, $r_{1/2}/d_{PJ}$, of the d_{PJ}=38mm PJ nozzle. Conditions: co-flow velocity U_a=0.038m/s, confinement D_{duct}/d_{PJ}=10.9, mass flux ratio m_a/m_0=18.4.

Publications Arising From This Thesis

[1] Nathan, G.J., Parham, J.J., Smart, J.P. and Jenkins, B.G. (1997). The heat flux and emission characteristics of a gas-fired Gyro-Therm burner in a 2MW test facility. *Fuel and Combustion Technology*, Internal Document, Report No. RT617.

[2] Parham, J.J. (1998). Prediction and control of heat flux and NO_x emissions in gas fired rotary kilns, Upgrade Report, Dept. Mech. Eng., The University of Adelaide.

[3] Parham, J.J., Nathan, G.J. and Luxton, R.E. (1998). The interaction between an axial jet and a precessing jet, *The Album of Visualization*, **15**, The Visualization Society of Japan.

[4] Parham, J.J., Nathan, G.J., Smart, J.P., Jenkins, B.G. and Luxton, R.E. (1998). Control of heat flux profiles from rotary kiln burners by modification of mixing, *Developments in Chemical Engineering and Mineral Processing*, **7** (3-4), 333-344.

[5] Parham, J.J., Nathan, G.J. and Luxton, R.E. (1998). Control of initial growth rate of a jet by combined precessing and axial jet flows, *Thirteenth Australasian Fluid Mechanics Conference*, Monash University, Victoria, Australia, 595-598.

[6] Parham, J.J., Nathan, G.J. and Alwahabi, Z.T. (2000). The influence of a co-flow on the instantaneous structure of a confined precessing jet flow, *The Album of Visualization*, **17**, The Visualization Society of Japan.

[7] Parham, J.J., Nathan, G.J., Smart, J.P., Hill, S.J. and Jenkins B.G. (2000). The relationship between heat flux and NO_x emissions in gas-fired rotary kilns, *J. Inst. Energy*, **73** (494), 25-34.

[8] Parham, J.J., Nathan, G.J. and Mi, J. (2001). The effect of Schmidt number on scalar mixing in axisymmetric jets, *Phys. Fluids A*, submitted.

References

[1] Anderson, I. and Johnston, D. (1997). Burner development for a recuperative glass furnace, *Level IV Project Report*, Dept. Mech. Eng. University of Adelaide, Australia.

[2] Arcoumanis, C., McGuirk, J.J., and Palma, J.M.L.M. (1990). On the use of fluorescent dyes for concentration measurements in water flows, *Expt. Fluids*, **10**, 177-180.

[3] Antonia, R.A. and Bilger, R.W. (1973). An experimental investigation of an axisymmetric jet in a co-flowing air stream, *J. Fluid Mech.*, **61** (4), 805-822.

[4] Badri Naranyan, M.A. and Platzer, M.F. (1987). The mixing mechanism by organised turbulence structures in a plane jet excited by a novel method, *Proceedings of the IUTAM Symposium on Turbulence Management and Relaminarisation*, Bangalore, January 19-23.

[5] Becker, H.A., Hottel, H.C. and Williams, G.C. (1963). Mixing and flow in ducted turbulent jets, *Proc. Combust. Inst.*, **9**, 7-19.

[6] Becker, H.A., Hottel, H.C. and Williams, G.C. (1965). Concentration intermittency in jets, *Proc. Combust. Inst.*, **10**, 1253-1263

[7] Becker, H.A., Hottel, H.C., and Williams, G.C. (1967a). The nozzle-fluid concentration field of the round, turbulent, free jet, *J. Fluid Mech.*, **30** (2), 285-303.

[8] Becker, H.A., Hottel, H.C. and Williams, G.C. (1967b). Concentration fluctuations in ducted turbulent jets, *Proc. Combust. Inst.*, **10**, 791-797

[9] Beltagui, S.A., Kenbar, A.M.A. and Maccallum, N.R.L. (1993). Heat transfer and emission studies in a gas fired furnace, *First International Conference on Combustion and Emissions Control*, The Institute of Energy, London, 275-296.

[10] Bilger, R.W. and Beck, R.E. (1975). Further experiments on turbulent jet diffusion flames. *Proc. Combust. Inst.*, **15**, 541-552.

[11] Bilger, R.W. (1976). Reaction zone thickness and formation of nitric oxide in turbulent diffusion flames. *Combust. Flame*, **26** (1), 115-123.

[12] Birch, A.D., Brown, D.R., Dodson, M.G. and Thomas, J.R. (1978). The turbulent concentration field of a methane jet, *J. Fluid Mech.*, **88**, 431-449.

[13] Bowman, C.T. (1992). Control of combustion-generated nitrogen oxide emissions: technology driven by regulation, *Proc. Combust. Inst.*, **24**, 859-878.

[14] Breidenthal, R.E. (1981). Structure in turbulent mixing layers and wakes using chemical reaction, *J. Fluid Mech.*, **109** (1), 1-24.

[15] Broadwell, J.E. and Mungal, M.G. (1984). Turbulent mixing and combustion in a reacting shear layer, *AIAA Journal*, **22** (6), 797-800.

[16] Broadwell, J.E. and Mungal, M.G. (1991). Large-scale structures and molecular mixing, *Phys. Fluids A*, **3** (5), 1193-1206.

[17] Broadwell, J.E., and Lutz, A.E. (1998). A turbulent jet chemical reaction model: NO_x production in jet flames, *Combust. Flame*, **114**, 319-335.

[18] Brown, G.L. and Roshko, A. (1974). On density effects and large structure in turbulent mixing layers. *J. Fluid Mech.*, **64**, 775-816.

[19] Buriko, Y.Y. and Kuznetsov, V.R. (1978). Possible mechanism of the formation of nitrogen oxides in turbulent diffusional combustion. *Combust. Explos. Shock Waves*, **14** (3) 296-303.

[20] Chedaille, J. and Braud, Y. (1972). Measurements in flames, in: Industrial Flames, Vol.1 (ed. Beer & Thring). Edward Arnold, London.

[21] Chen, R-.H. and Driscoll, J.F. (1990). Nitric oxide levels of jet diffusion flames: effects of coaxial air and other mixing parameters, *Proc. Combust. Inst.*, **23**, 281-288.

[22] Chen, R.-H., Driscoll, J.F., Kelly, J., Namazian, M. and Schefer, R.W. (1990). A comparison of bluff-body and swirl-stabilized flames, *Combust. Sci. and Tech.*, **71**, 197-217.

[23] Chu, P.C.K., Lee, J.H. and Chu, V.H. (1999). Spreading of a turbulent round jet in coflow, *J. Hydraul.Eng.*, **125** (2), 193-204.

[24] Chua, L.P. and Antonia, R.A. (1986). The turbulent interaction region of a circular jet, *Int. Commun. Heat Mass Transfer*, **13** (5), 545-558.

[25] Claypole, T.C. and Syred, N. (1982). The stabilization of flames in swirl combustors, *J. Inst. Energy*, **55**, 14-19.

[26] Corrsin, S. and Uberoi, M.S. (1950). Further experiments on the flow and heat transfer in a heated turbulent jet, *NASA Report*, No. 998, 859-875.

[27] Crow, S.C. and Champagne, F.H. (1971). Orderly structure in jet turbulence, *J. Fluid Mech.*, **483**, 547-591.

[28] van Cruynigen, I., Lozano, A., and Hanson, R.K. (1990). Quantitative imaging of concentration by planar laser-induced fluorescence, *Expt. Fluids*, **10**, 41-49.

[29] Curtet, R. (1958). Confined jets and recirculation with cold air, *Combust. Flame*, **2**, 383-411.

[30] Dahm, W.J.A. and Dimotakis, P.E. (1987). Measurements of entrainment and mixing in turbulent jets, *AIAA Journal*, **25** (9), 1216-1223.

[31] Dahm, W.J.A. and Dimotakis, P.E. (1990). Mixing at large Schmidt number in the self-similar far field of turbulent jets, *J. Fluid Mech.*, **217**, 299-330.

[32] Dahm, W.J.A., Frieler, C.E. and Tryggason, G. (1992). Vortex structure and dynamics in the near field of a coaxial jet, *J. Fluid Mech.*, **241**, 371-402.

[33] Dimotakis, P.E., Miake-Lye, R.C. and Papantoniou, D.A. (1983). Structure and dynamics of round turbulent jets, *Phys. Fluids*, **26** (11), 3185-3192.

[34] Dimotakis, P.E. (2000). The mixing transition in turbulent flows, *J. Fluid Mech.*, **409**, 69-98.

[35] Dowling, D.R. and Dimotakis, P.E. (1990). Similarity of the concentration field of gas-phase turbulent jets, *J. Fluid Mech*, **218**, 109-141.

[36] Driscoll, J.F., Chen, R.-H. and Yoon, Y. (1992). Nitric oxide levels of turbulent jet diffusion flames: effects of residence time and Damkohler Number, *Combust. Flame*, **88**, 37-49.

[37] Dyer, T.M. (1979). Rayleigh scattering measurement of time-resolved concentration in a turbulent propane jet, *AIAA Journal*, **17** (8), 912-914.

[38] Ebrahimi, I. and Kleine, R. (1977). The nozzle fluid concentration fluctuation field in round turbulent free jets and jet diffusion flames, *Proc. Combust. Inst.*, **16**, 1711-1723.

[39] Ellis, J. (2000). An initial view on methodologies for emission baselines: cement case study, OECD Information Paper, Annex I Expert Group, Paris, http://www.oecd.org/env/cc.

[40] Garg, A. (1994). Specify better low-NO_x burners for furnaces, *Chem. Eng. Prog.*, **90** (1), 46-49.

[41] Grandmaison, E.W., Rathgeber, D.E. and Becker, H.A. (1982). Some characteristics of concentration fluctuations in free turbulent jets, *Can. J. Chem. Eng.*, **60**, 212-219.

[42] Guilbault, G. (1973). Practical Fluorescence: Theory, Methods and Techniques, Marcel Dekker Inc., New York.

[43] Gutmark, E., Parr, T.P., Parr, D.M. and Schadow, K.C. (1989). Planar imaging of vortex dynamics in flames, *J. Heat Transfer*, **111**, 148-155.

[44] Gutmark, E., Parr, T.P., Hanson-Parr, D.M. and Schadow, K.C. (1990). Coherent and random structure in reacting jets, *Expt. Fluids*, **10**, 147-156.

[45] Hawthorne, W.R., Weddell, D.S. and Hottel, H.C. (1951). Mixing and combustion in turbulent gas jets, *Proc. Combust. Inst.*, **3**, 266-288.

[46] Hill, S.J., Nathan, G.J. and Luxton, R.E. (1992). Precessing and axial flows following a sudden expansion in an axisymmetric nozzle, *Eleventh Australasian Fluid Mechanics Conference*, University of Tasmania, Hobart, Australia, 14-18 December, 1113-1116.

[47] Hill, S.J., Rapson, D.S. and Nathan, G.J. (1995). Control of flame shape and heat flux in a rotary kiln, *The Australian Symposium on Combustion*, The Combustion Institute (Australia), Gawler, South Australia, November.

[48] Hill, S.J. (2000a). Precession in flows through axisymmetric sudden expansions, *Ph.D. Thesis* (to be submitted), Dept. Mech. Eng. University of Adelaide, Australia.

[49] Hill, S.J. (2000b). *Private Communication*, 5th December.

[50] Hsieh, T.-C.A., Dahm, W.J.A. and Driscoll, J.F. (1998). Scaling laws for NO_x emission performance of burners and furnaces from 30kW to 12MW, *Combust. Flame*, **114**, 54-80.

[51] International Panel on Climate Change (IPCC) (1995). 1995 Summary for policy makers: Working group I, Madrid, November 29.

[52] Jenkins, B.G. and Moles, F.D. (1981). Modelling of heat transfer from a large enclosed flame in a rotary kiln, *Transactions of the Institute of Chemical Engineers*, **59**, 17-25.

[53] Jenkins, B.G. (1998). Modelling - it's Plastic, Mathematic, Stochastic Elastic and Fantastic, *Thermal Energy Engineering and the Environment*, McLaren Vale, South Australia, 9-10 February.

[54] van de Kamp, W.L. and Daimon, J. (1996). Further studies on the effects of burner design variables and fuel properties on the characteristics of cement kiln flames, *International Flame Research Foundation*, Report F97/y/3.

[55] van de Kamp, W.L. and Smart, J.P. (1992). The effect of burner design and operation and fuel type on the properties of the cement kiln flame, *International Flame Research Foundation,* Report F97/y/1.

[56] van de Kamp, W.L. (1996). Evaluation of cement kiln flames from coal, delayed coke, sewage sludge and plastic waste, *International Flame Research Foundation,* Report D91/y/12.

[57] Karasso, P.S. (1994). Experiments on mixing and reaction in plane and curved shear layers, *Ph.D. Thesis*, Dept. Mech. Eng., Stanford University, USA.

[58] Karasso, P.S. and Mungal, M.G. (1996). Scalar mixing and reaction in plane liquid shear layers, *J. Fluid Mech.*, **323**, 23-63.

[59] Karasso, P.S. and Mungal, M.G. (1997a). Mixing and reaction in curved liquid shear layers, *J. Fluid Mech.*, **334**, 381-409.

[60] Karasso, P.S. and Mungal, M.G. (1997b). PLIF measurements in aqueous flows using the Nd:YAG laser, *Expt. Fluids*, **23**, 382-387.

[61] Kent, J.H. and Bilger, R.W. (1977). Prediction of turbulent diffusion flame fields and nitric oxide formation. *Proc. Combust. Inst.*, **16**, 1643-1656.

[62] Khodadadi, J.M. and Vlachos N.S. (1989). Experimental and numerical study of confined coaxial turbulent jets, *AIAA Journal*, **27** (5), 532-541.

[63] Koochesfahani, M.M. and Dimotakis, P.E. (1985). Laser-induced fluorescence measurements of fluid concentration in a liquid plane shear layer, *AIAA Journal*, **23** (11), 1700-1707.

[64] Kristmanson, D. and Danckwerts, P.V. (1961). Studies in turbulent mixing - I: Dilution of a jet, *Chem. Eng. Sci.* **16**, 267-277.

[65] Law, A.W.-K. and Wang, H. (2000). Measurement of mixing processes with combined digital particle image velocimetry and planar laser induced fluorescence, *Exp. Therm. Fluid Sci.*, **22**, 213-229.

[66] Li, X. and Tankin, R.S. (1987). A study of cold and combusting flow around bluff-body combustors, *Combust. Sci. and Tech.*, **52**, 173-206.

[67] Lockwood, F.C. and Moneib, H.A. (1980). Fluctuating temperature measurements in a heated round free jet, *Combust. Sci. and Tech.*, **22**, 63-81.

[68] Lovett, J.A. and Turns, S.R. (1990). Experiments on axisymmetrically pulsed turbulent jet flames, *AIAA Journal*, **28** (1), 38-46.

[69] Lowes, T.M. and Evans, L.P. (1989). Optimisation of the design and operation of coal flames in cement kilns, *J. Inst. Energy*, **62**, 220-228.

[70] Lu, G., Yan, Y. and Ward, D.D. (2000). Advanced monitoring, characterisation and evaluation of gas fired flames in a utility boiler, *J. Inst. Energy*, **73**, 43-49.

[71] Luxton, R.E., Nathan, G.J. and Luminis Pty. Ltd. (1991). Controlling the motion of a fluid jet. *USA Letters Patent*, No. 5,060,867.

[72] Maczynski, J.F.J. (1962). A round jet in an ambient co-axial stream, *J. Fluid Mech.*, **13**, 597-608.

[73] Manias, C.G. and Nathan, G.J. (1993). The precessing jet gas burner - a low NO_x burner providing process efficiency and product quality improvements, *World Cement*, **24** (3), 4 -11.

[74] Manias, C.G. and Nathan, G.J. (1994). Low NO_x clinker production, *World Cement*, **25** (5), 54-56.

[75] Manias, C.G., Balendra, A. and Retallack, D. (1996). New combustion technology for lime production, *World Cement*, **27** (12), 34-39.

[76] Marks, L.S. (1996). Mechanical engineer's handbook (ed. Avallone, E.A. and Baumeister, T.), McGraw-Hill, New York.

[77] McManus, K.R., Vandsburger, U. and Bowman, C.T. (1990). Combustor performance enhancement through direct shear layer excitation, *Combust. Flame*, **10**, 147-156.

[78] McQueen, A.T., Bortz, S.J., Hatch, M.S. and Leonard R L. (1995). Cement kiln NO_x control, *IEEE Transactions on Industrial Applications*, **31** (1), 36-43.

[79] Mi, J., Nathan, G.J. and Luxton, R.E. (1997). Frequency spectra of turbulence in a precessing jet, *Seventh Asian Congress on Fluid Mechanics*, India, December.

[80] Mi, J., Nathan, G.J. and Nobes, D.D. (2000a). Mixing characteristics of axisymmetric free jets from a contoured nozzle, an orifice plate and a pipe, *J. Fluids Eng.* (submitted).

[81] Mi, J., Nobes, D.S. and Nathan, G.J. (2000b). Influence of jet exit conditions on the passive scalar field of an axisymmetric free jet, *J. Fluid. Mech.*, to appear.

[82] Miller, P.L. and Dimotakis, P.E. (1991). Reynolds number dependence of scalar fluctuations in a high Schmidt number turbulent jet, *Phys. Fluids A*, **3** (5), 1156-1163.

[83] Moles, F.D., Watson, D. and Lain, P.B. (1972). The aerodynamics of the rotary cement kiln, *Fourth Symposium on Flames and Industry*, Imperial College, London, 2-10.

[84] Mullinger, P.J. (1994). Cement kiln firing and clean air requirements, *World Cement*, **25** (12), 27-31.

[85] Mullinger, P.J. (1999). The relevance of predictive techniques to industrial combustion and heat transfer problems, *Developments in Chemical Engineering and Mineral Processing*, **7**, (3-4), 225-244.

[86] Mungal, M.G. and Dimotakis, P.E. (1984). Mixing and combustion with low heat release in a turbulent mixing layer, *J. Fluid. Mech.*, **148**, 349-382.

[87] Mungal, M.G., Karasso, P.S. and Lozano, A. (1991). The visible structure of turbulent jet diffusion flames: large-scale organisation and flame tip oscillation, *Combust. Sci. and Tech.*, 76, 165-185.

[88] Nakamura, I., Sakai, Y. and Miyata, M. (1982). A study on the fluctuating concentration field in a turbulent jet, *Memoirs of the Faculty of Engineering*, Nagoya University, **34** (1), 113-124.

[89] Nakamura, T., Smart, J.P. and van de Kamp, W.L. (1993). The effect of fuel air mixing on NO_x reduction and heat transfer in high temperature, gas fired, glass melting furnaces, *First International Conference on Combustion and Emissions Control*, The Institute of Energy, London, 213-229.

[90] Namazian, M., Kelly, J. and Schefer, R.W. (1992). Concentration imaging measurements in turbulent concentric-jet flows, *AIAA Journal*, **30** (2), 384-394.

[91] Nathan, G.J. (1988). The enhanced mixing burner, *Ph.D. Thesis*, Dept. Mech. Eng., The University of Adelaide, Australia.

[92] Nathan, G.J. and Luxton, R.E. (1991). The entrainment and combustion characteristics of an axis-symmetric, self-exciting, enhanced mixing nozzle, *Third ASME-JSME Thermal Engineering Joint Conference*, Reno, USA, March 17-22, **5**, 145-152.

[93] Nathan, G.J., Manias, C.G. and Luxton, R.E. (1991). Potential increases in the efficiency of a rotary kiln using an enhanced mixing burner, *I.E.Aust. International Mechanical Engineering Congress*, Sydney, Australia, July, **4**, 58-61.

[94] Nathan, G.J. and Luxton, R.E. (1992). A low NO_x gas burner with a radiant flame, *International Conference on Energy Efficiency in Process Technology*, Athens, Greece, October 19-22, 883-892, Elselvier.

[95] Nathan, G.J., Brumale, S., Proctor, D. and Luxton, R.E. (1993). NO_x reduction in flames by modification of turbulence with jet precession. *First International Conference on Combustion and Emissions Control*, The Institute of Energy, London, 145.

[96] Nathan, G.J. and Manias, C.G. (1995). The role of process and flame interaction in reducing NO_x emissions, *Second International Conference on Combustion and Emissions Control*, The Institute of Energy, London, 309-318.

[97] Nathan, G.J. and Rapson, D.S. (1995). Simultaneous optimisation of heat transfer profile and NO_x emissions in a cement kiln, *The Australian Symposium on Combustion*, The Combustion Institute (Australia), Gawler, South Australia, November.

[98] Nathan, G.J., Smart, J.P. and Jenkins, B.G. (1995). Criterion for modelling GyroTherm burners - Draft I, *Fuel and Combustion Technology*, Internal Report.

[99] Nathan, G.J., Turns, S.R. and Bandaru, R.V. (1996). The influence of jet precession on NO_x emissions and radiation from turbulent flames, *Combust. Sci. And Tech.*, **112**, 211-230.

[100] Nathan, G.J., Nobes, D.S., Mi, J., Schneider, G.M., Newbold, G.J.R., Alwahabi, Z.T., Luxton, R.E. and King, K.D. (1997). Exploring the relationship between mixing, radiation and NO_x emissions from natural gas flames, *Third International Conference on Combustion and Emissions Control*, The Institute of Energy, London, 49-69.

[101] Nathan, G.J., Hill, S.J. and Luxton, R.E. (1998). An axisymmetric 'fluidic' nozzle to generate jet precession, *J. Fluid Mech.*, **380**, 347-380.

[102] Newbold, G.J.R., Nobes, D.S., Nathan, G.J., Luxton, R.E., Alwahabi, Z.T. and King, K.D. (1996). Visualisation and mixing in the precessing jet flow, *First Australian Conference on Laser Diagnostics in Fluid Mechanics and Combustion*, The University of Sydney, Australia, December 5-6, 253.

[103] Newbold, G.J.R., Nathan, G.J. and Luxton, R.E. (1997). Large-scale dynamics of an unconfined precessing jet flame, *Combust. Sci. Tech.*, **126** (1-6), 53.

[104] Newbold, G.J.R. (1997). Mixing and combustion in precessing jet flows, *Ph.D. Thesis*, Dept. Mech. Eng., The University of Adelaide, Australia.

[105] Newbold, G.J.R. and Nathan, G.J. (1998). The influence of changes to mixing on the sooting and NO_x emission characteristics of unconfined turbulent jet diffusion flames, *Developments in Chemical Engineering and Mineral Processing*, **7** (3-4), 361-374.

[106] Newbold, G.J.R., Nathan, G.J., Nobes, D.S. and Turns, S.R. (2000). Measurement and prediction of NO_x emissions from unconfined propane flames from turbulent-jet, bluff-body, swirl and precessing jet burners, *Proc. Combust. Inst.*, **28**.

[107] Nickels, T.B. and Perry, A.E. (1996). An experimental and theoretical study of the turbulent coflowing jet, *J. Fluid Mech.*, **309**, 157-182.

[108] Nobes, D.S. (1996). The effect of a co-flow and/or combustion on a precessing jet flow field, *Upgrade Report*, Dept. Mech. Eng., University of Adelaide, Australia.

[109] Nobes, D. S., Newbold G. J. R., Nathan, G. J., Luxton, R. E., Alwahabi, Z. T., and King, K. D. (1997). The mixing field of a simple round turbulent jet and a fluidic precessing jet, *Asia-Pacific Conference on Combustion*, Osaka University, Japan, May 12-15, 334-337.

[110] Nobes, D.S. (1997). The generation of large-scale structures by jet precession, *Ph.D. Thesis*, Dept. Mech. Eng., The University of Adelaide, Australia.

[111] Nobes, D.S., Newbold, G.J.R., Hasselbrink, E.F., Su, L., Mungal, M.G. and Nathan, G.J. (2000). PIV and PLIF measurements in precessing and round jets, *Internal Report*, Dept. Mech. Eng., The University of Adelaide, Australia.

[112] Ono, Y. (1980). Microscopial estimation of burning condition and quality of clinker, *Seventh International Congress on the Chemistry of Cement*, **2**, 206-211.

[113] Papanicolaou, P.N. and List, E.J. (1987). Statistical and spectral properties of tracer concentration in round buoyant jets, *Int. J. Heat Mass Transfer*, **30** (10), 2059-2071.

[114] Papanicolaou, P.N. and List, E.J. (1988). Investigations of round vertical turbulent buoyant jets, *J. Fluid Mech.*, **195**, 341-391.

[115] Parekh, D.E., Reynolds, W.C. and Mungal, M.G. (1987). Bifurcation of round jets by dual-mode acoustic excitation, *AIAA Paper* 87-0164.

[116] Paschereit, G.O, Oster, D., Long, T.A., Fiedler, H.E. and Wygnanski, I. (1992). Flow visualisation of interactions among large coherent structures in an axisymmetric jet, *Expt. Fluids*, **12**, 189-199.

[117] Peters, N. and Donnerhack, S. (1981). Structure and similarity of nitric oxide production in turbulent diffusion flames, *Proc. Comb. Inst.*, **18**, 33-42.

[118] Pitts, W.M. and Kashiwagi, T. (1984). The application of laser-induced Rayleigh light scattering to the study of turbulent mixing, *J. Fluid Mech.*, **141**, 391-420.

[119] Pitts, W.M. (1991). Effects of global density ratio on the centerline mixing behavior of axisymmetric turbulent jets, *Expt. Fluids*, **11**, 125-134.

[120] Prasad, R.R. and Sreenivasan, K.R. (1990). Quantitative three-dimensional imaging and the structure of passive scalar fields in fully turbulent flows, *J. Fluid Mech.*, **216**, 1-34.

[121] Prather, M.J. and Logan, J.A. (1994). Combustion's impact on the global atmosphere, *Proc. Combust. Inst.*, **25**, 1513-1527.

[122] Rapson, D., Stokes, B. and Hill, S. (1995). Kiln flame shape optimisation using a Gyro-Therm gas burner, *World Cement*, **26** (7), 2-5.

[123] Rhine, J.M. and Tucker, R.J. (1991). Modelling of Gas-Fired Furnaces and Boilers, McGraw Hill.

[124] Richards, C.D. and Pitts, W.M. (1993). Global density effects on the self-preservation behaviour of turbulent free jets, *J. Fluid Mech.*, **254**, 417-435.

[125] Røkke, N.A., Hustad, J.E., Sønju, O.K. and Williams, F.A. (1992). Scaling of nitric oxide emissions from buoyancy-dominated hydrocarbon turbulent-jet diffusions flames, *Proc. Combust. Inst.*, **24**, 384-393.

[126] Røkke, N.A., Hustad, J.E., and Sønju, O.K. (1994). A study of partially premixed unconfined propane flames, *Combust. Flame*, **97**, 88-106.

[127] Sayre, A., Lallemant, N., Dugué, J. and Weber, R. (1994). Effect of radiation on nitrogen oxide emissions from nonsooty swirling flames of natural gas, *Proc. Combust. Inst.*, **25**, 235-242.

[128] Schefer, R.W, Namazian, M. and Kelly, J. (1987). Velocity measurements in a turbulent nonpremixed bluff-body stabilised flame, *Comb. Sci. Tech.*, **56**, 101-138.

[129] Schneider, G.M. (1997). Flow structures and turbulence characteristics in a precessing jet, *Ph.D. Thesis*, Dept. Mech. Eng., the University of Adelaide, Australia.

[130] Schneider, G.M., Froud, D., Syred, N., Nathan, G.J. and Luxton, R.E. (1997). Velocity measurements in a precessing jet flow using a three dimensional LDA system, *Expt. Fluids*, **23**, 89-98.

[131] Smart, J.P. and Morgan, D.J. (1994). Exploring the effects of employing different scaling criteria on swirl stabilised pulverised coal burner performance, *Comb. Sci Tech.*, **100**, 331-343.

[132] Smith (2000). The influence of the spectrum of jet turbulence on the stability, NO_x emissions and heat release profile of pulverised coal flames, *Ph.D. Thesis*, Dept. Mech. Eng., University of Adelaide, Australia.

[133] Spalding, (1962). The art of partial modelling, *Proc. Combust. Inst.*, **9**, 833.

[134] Stapountzis, H., Westerweel, J., Bessem, J.M., Westendorp, A. and Nieuwstadt, F.T.M. (1992). Measurement of product concentration of two parallel reactive jets using digital image processing, *Appl. Sci. Res.*, **49**, 245-259.

[135] Tennekes, H. and Lumley, J.L.A. (1972). A First Course in Turbulence, The MIT Press.

[136] Thring, M.W. and Newby, M.P. (1953). Combustion length of enclosed turbulent jet flames, *Proc. Combust. Inst.*, **4**, 789-796.

[137] Tomeczek, J., Goral, J. and Gradon, B. (1995). Gasdynamic abatement of NO_x emission from industrial natural gas jet diffusion flames, *Combust. Sci. And Tech.*, **105**, 55-65.

[138] Turns, S.R. and Myhr, F.H. (1991). Oxides of nitrogen emissions from turbulent jet flames: Part I - Fuel effects and flame radiation, *Combust. Flame*, **87**, 319-335.

[139] Videgar, R. (1997). Gyro-Therm technology solves burner problems, *World Cement Case Studies*, November.

[140] Viskanta, R. (1991). Enhancement of heat transfer in industrial combustion systems: problems and future challenges, *ASME/JSME Thermal Engineering Proceedings*, **5**, 161-173.

[141] Walker, D.A. (1987). A fluorescence technique for measurement of concentration in mixing liquids, *J. Phys., E, J. Scient. Instrum.*, **20**, 217-224.

[142] Weber, R. (1996). Scaling characteristics of aerodynamics, heat transfer, and pollutant emissions in industrial flames, *Proc. Combust. Inst.*, **26**, 3343-3354.

[143] Wilson, R.A.M. and Danckwerts, P.V. (1964). Studies in turbulent mixing - II: A hot-air jet, *Chem. Eng. Sci.*, **19**, 885-895.

[144] Wood, S.C. (1994). Select the right NO_x control technology, *Chem. Eng. Prog.*, **90** (1), 32-38.

[145] Yoda, M., Hesselink, L. and Mungal, M.G. (1994). Instantaneous three-dimensional concentration measurements in the self-similar region of a round high-Schmidt-number jet, *J. Fluid Mech.*, **279**, 313-350.

[146] Yoda, M. and Fiedler, H.E. (1996). The round jet in a uniform counterflow: flow visualisation and mean concentration measurements, *Expt. Fluids*, **21**, 427-436.

[147] Yule, A.J. and Damou, M. (1991). Investigations of ducted jets, *Exp. Therm. Fluid Sci.*, **4**, 469-490.